Disarming the immune system's "atomic bomb" cells p. 1067

The origins of peanut allergy p. 1072

A central psychosomatic stress pathway p. 1105

Science

$15
6 MARCH 2020
sciencemag.org

AAAS



ACTIVE MATTER

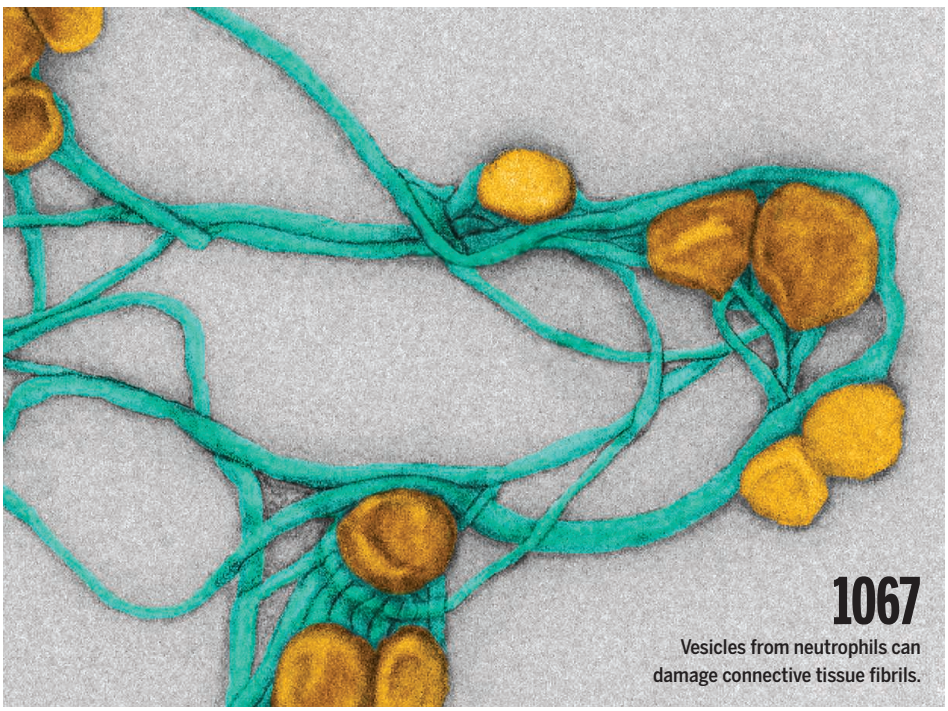
Watching liquid crystal defect dynamics pp. 1075 & 1120

CONTENTS



1070
How are health outcomes related to breastmilk?

6 MARCH 2020 • VOLUME 367 • ISSUE 6482



1067
Vesicles from neutrophils can damage connective tissue fibrils.

NEWS

IN BRIEF

1058 News at a glance

IN DEPTH

1061 Can China's COVID-19 strategy work elsewhere?
Rapid decline in case numbers is real, expert mission concludes—but it came at a high cost
By K. Kupferschmidt and J. Cohen

1062 Why weather systems are apt to stall
A new theory tries to explain enigmatic "blocks" that bring heat waves and drought
By P. Voosen

1064 Unplanned experiment could help save a key farmed fish
Random outbreak at research center points to tilapia variants that resist the deadly emerging tilapia lake virus
By E. Stokstad

1065 Pentagon's social science research faces threat
Minerva initiative falls out of favor in latest DOD review of spending priorities
By J. Mervis

1066 New telescope promises boon for Turkish science
The 4-meter Eastern Anatolia Observatory aims to become an affordable regional hub *By U. Farooq*

FEATURES

1067 The body's dangerous defenders
Neutrophils fiercely attack infections, but can also trigger disease. Researchers are trying to tame them *By M. Leslie*

INSIGHTS

PERSPECTIVES

1070 Understanding the mother-breastmilk-infant "triad"
Breastmilk research holds important opportunities to improve maternal-child health *By L. Bode* et al.

1072 Origins of peanut allergy-causing antibodies
Analysis of gut-produced antibodies raises questions about how food allergy arises
By D. R. Wesemann and C. R. Nagler
SCIENCE IMMUNOLOGY RESEARCH ARTICLE BY R. A. HOH *ET AL.* 10.1126/SCIIMMUNOL.AAY4209

1074 Coding functions of "noncoding" RNAs
Hundreds of RNA regions that encode microproteins are found to regulate cell growth *By L.-H. Wei and J. U. Guo*
REPORT p. 1140

1075 Rings rule three-dimensional active matter
Dynamical defect networks are imaged in viral-particle liquid crystals driven by biomotors *By D. Bartolo*
REPORT p. 1120

1077 Frank Press (1924–2020)
Policy adviser and National Academy of Sciences president *By M. McNutt*

POLICY FORUM

1078 Overcoming obstacles to experiments in legal practice
The biggest ethical concern is failing to seek reliable evidence to guide the legal profession
By H. Fernandez Lynch et al.

BOOKS *ET AL.*

1081 Evolution makes a splash
An underwater arms race drives a vibrant new game *By A. Chuang and O. Schwery*



1064

CREDITS (FROM TOP): N. CARY/*SCIENCE*; TOMASZ SZUL AND DEREK W. RUSSELL; WORLDFISH/FLICKR/CC BY-NC-ND

Published by AAAS

1082 The landmark case that almost never was
A law professor investigates the legal decision to regulate U.S. greenhouse gases
By M. B. Gerrard

LETTERS

1083 Protect Australia's Gondwana Rainforests
By R. M. Kooyman et al.

1083 Post-2020 goals overlook genetic diversity
By L. Laikre et al.

1084 Outreach that sticks
By L. Jardine-Wright

RESEARCH

IN BRIEF

1086 From *Science* and other journals

RESEARCH ARTICLES

1089 Germ cell development
ZGLP1 is a determinant for the oogenic fate in mice *S. I. Nagaoka* et al.
RESEARCH ARTICLE SUMMARY; FOR FULL TEXT: DX.DOI.ORG/10.1126/SCIENCE.AAW4115

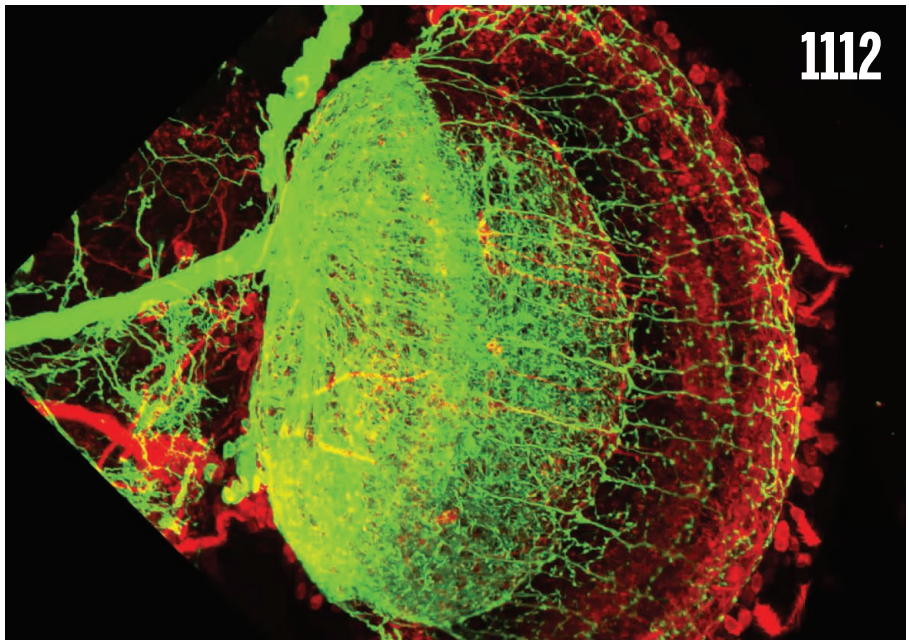
1090 Integrative omics
An atlas of the protein-coding genes in the human, pig, and mouse brain
E. Sjöstedt et al.
RESEARCH ARTICLE SUMMARY; FOR FULL TEXT: DX.DOI.ORG/10.1126/SCIENCE.AAY5947

1091 Cell surface mapping
Microenvironment mapping via Dexter energy transfer on immune cells
J. B. Geri et al.

1097 Solar cells
Triple-halide wide–band gap perovskites with suppressed phase segregation for efficient tandems *J. Xu* et al.

1105 Neuroscience
A central master driver of psychosocial stress responses in the rat
N. Kataoka et al.

1112 Neurodevelopment
A neurodevelopmental origin of behavioral individuality in the *Drosophila* visual system
G. A. Linneweber et al.



Developmental randomness drives behavioral divergence among individual *Drosophila* flies.

REPORTS

1120 Liquid crystals
Topological structure and dynamics of three-dimensional active nematics *G. Duclos et al.*
PERSPECTIVE p. 1075

1124 Electron microscopy
Single-atom vibrational spectroscopy in the scanning transmission electron microscope
F. S. Hage et al.

1128 Quantum simulation
A scalable realization of local U(1) gauge invariance in cold atomic mixtures *A. Mil* et al.

1131 Neuroscience
Replay of cortical spiking sequences during human memory retrieval *A. P. Vaz* et al.

1135 Solar cells
Efficient tandem solar cells with solution-processed perovskite on textured crystalline silicon *Y. Hou* et al.

1140 Molecular biology
Pervasive functional translation of noncanonical human open reading frames
J. Chen et al.
PERSPECTIVE p. 1074

1147 Microbiology
PE/PPE proteins mediate nutrient transport across the outer membrane of *Mycobacterium tuberculosis* *Q. Wang* et al.

1151 Transcription
Sequencing metabolically labeled transcripts in single cells reveals mRNA turnover strategies
N. Battich et al.

DEPARTMENTS

1057 Editorial
Learning to deal with dual use
By Megan J. Palmer

1162 Working Life
Learning to say 'yes, and'
By Ellen K. W. Brennan

ON THE COVER



Fluorescence microscopy image of a composite three-dimensional active nematic liquid crystal. Light-sheet microscopy reveals the structure and dynamics of disclination defects, which are fundamental features of nematic liquid crystals and other fluids with orientational order. See pages 1075 and 1120.
Image: Ray Adkins

New Products.....1157
Science Careers.....1158

SCIENCE (ISSN 0036-8075) is published weekly on Friday, except last week in December, by the American Association for the Advancement of Science, 1200 New York Avenue, NW, Washington, DC 20005. Periodicals mail postage (publication No. 484460) paid at Washington, DC, and additional mailing offices. Copyright © 2020 by the American Association for the Advancement of Science. The title SCIENCE is a registered trademark of the AAAS. Domestic individual membership, including subscription (12 months): $165 ($74 allocated to subscription). Domestic institutional subscription (51 issues): $2148; Foreign postage extra: Air assist delivery: $98. First class, airmail, student, and emeritus rates on request. Canadian rates with GST available upon request, GST #125488122. Publications Mail Agreement Number 1069624. **Printed in the U.S.A.**
Change of address: Allow 4 weeks, giving old and new addresses and 8-digit account number. **Postmaster:** Send change of address to AAAS, P.O. Box 96178, Washington, DC 20090–6178. **Single-copy sales:** $15 each plus shipping and handling available from backissues.sciencemag.org; bulk rate on request. **Authorization to reproduce** material for internal or personal use under circumstances not falling within the fair use provisions of the Copyright Act can be obtained through the Copyright Clearance Center (CCC), www.copyright.com. The identification code for *Science* is 0036-8075. *Science* is indexed in the *Reader's Guide to Periodical Literature* and in several specialized indexes.

CREDIT: LINNEWEBER *ET AL.*

Published by AAAS

EDITORIAL

Learning to deal with dual use

Biological research is profoundly valuable but can carry profound risks. The coronavirus outbreak reminds us of our vulnerability to biological threats and that research on pathogens is vital to threat mitigation. But such research can lead to catastrophic safety and security incidents. A global proliferation of tools and capabilities, driven by economic and national security interests, is also generating risks that fall outside current governance frameworks. We must learn to manage risks as quickly as we learn to manipulate life, but it remains unclear how well we are doing. One opportunity to learn is found in a new charge to the U.S. National Science Advisory Board for Biosecurity (NSABB), which reconvened in January after a 2-year hiatus, to assess the effectiveness of U.S. dual-use research oversight policies. To meet the charge and suggest improvements, the NSABB must address a neglected need for an evidence base for adaptive risk management. Building this evidence base will require revisiting success criteria, creating data infrastructures, and fostering adaptive policies and testbeds.

Clear criteria for success form the foundation of an evidence base. Criteria for policies designed to prevent rare incidents can be challenging to develop, but there are leading indicators that can validate design goals and assumptions. These can range from enhanced stakeholder participation and expressions of trust to reductions in near misses. Such criteria form the basis for sound policy design and implementation and must be regularly revisited.

The next step is to collect and analyze data to assess whether goals were met. A 2011 U.S. government–commissioned risk and benefit analysis of gain-of-function research exposed the dearth of data available to inform many risk management decisions. The NSABB and other groups have called—to no avail—for systems to collect and analyze data on incidents and near-misses as well as oversight. Failure of the U.S. government to quickly act on these recommendations means that the NSABB will again confront this data gap. Moreover, biosafety and biosecurity research, which seeks to understand and improve practices for risk management, remains chronically underfunded despite being called out as a priority in the U.S. National Biodefense Strategy. This research should be supported as an essential part of all major biological research programs so that it evolves alongside and is integrated with the latest advances.

Unfortunately, even when limited data are collected, they are often not shared lest they expose vulnerabilities or tarnish reputations. Legitimate security concerns abound, but an unknown and growing risk exposure is also dangerous. Many organizations do not fully exercise their ability to share details of their risk management process; they should do so to promote cross-organizational learning and to avoid repeating the same mistakes.

Policies designed to adapt to emerging evidence can provide standards and incentives for gathering data. Yet dual-use policies are typically narrowly scoped to prioritize limiting oversight burden over learning where concerns arise. This priority is misplaced in preparing for the future. As the scope of research broadens, our definitions of dual use will change, and we need to continue moving toward functional definitions of activities that could be hazardous that aren't reliant on quickly outdated lists. In many instances where there is uncertainty over appropriate scope, we should update policies regularly and prioritize observing activities over restricting them to gain visibility into the evolving landscape.

> **"We must learn to manage risks as quickly as we learn to manipulate life..."**

Communities of practitioners need testbeds to experiment with policy approaches and to learn from each other in real time. One example is the international Genetically Engineered Machine (iGEM) competition, where thousands of students from dozens of countries work on hundreds of projects that can often expose policy gaps. The competition has becomes a nexus to test strategies for managing dual-use technologies across many cases with yearly iteration. Such testbeds should be cultivated at many scales—from individual labs, to universities, to regional and national networks.

Biological science and technology will only become more essential to our societies, and we need strategies to learn to manage their power. Investing in an evidence base for adaptive risk management is essential to ensure that the future of the life sciences is one in which we want to live.

–Megan J. Palmer



PHOTO: ROD SEARCY/STANFORD UNIVERSITY

Megan J. Palmer is a senior research scholar at the Center for International Security and Cooperation (CISAC) at Stanford University, Stanford, CA, USA. mjpalmer@stanford.edu

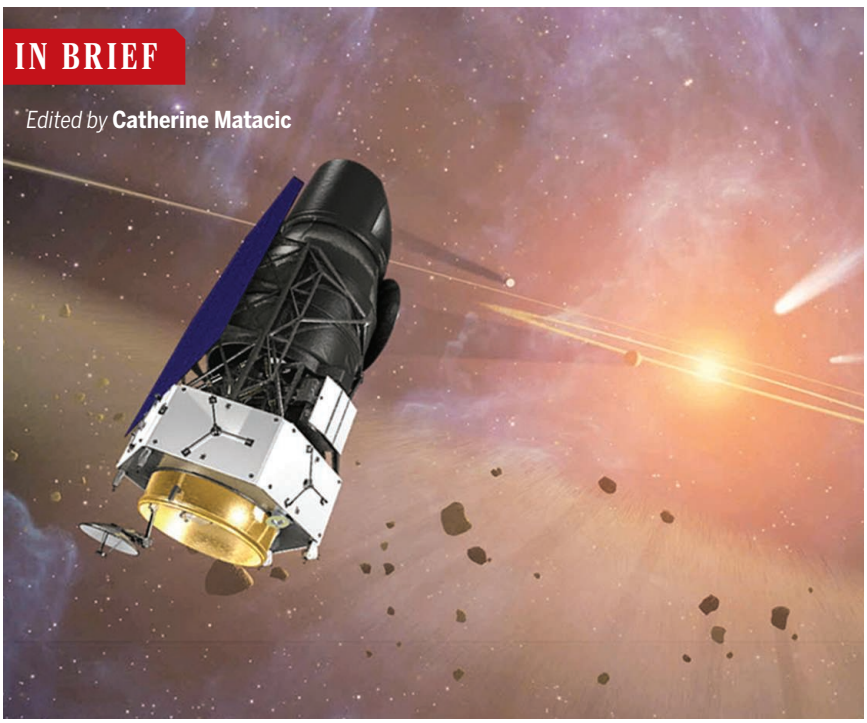
Published online 27 February 2020; 10.1126/science.abb1466

Published by AAAS

> “You don’t want to go to war with a president … but you got to [make] sure you continue to tell the truth.”
>
> **National Institute of Allergy and Infectious Diseases Director Anthony Fauci**, to *Politico* last week on the “fine balance” needed for a credible U.S. government response to the coronavirus crisis.

IN BRIEF

Edited by **Catherine Matacic**



An artist’s rendition of the Wide Field Infrared Survey Telescope.

ASTRONOMY

NASA survey scope wins approval

NASA’s Wide Field Infrared Survey Telescope (WFIRST), a big orbiting observatory planned for launch in the mid-2020s, has reached a major milestone. On 2 March, the agency said the project passed its confirmation review and could begin to build hardware. Thanks to a 2.4-meter mirror donated in 2011 by the U.S. Department of Defense’s National Reconnaissance Office, WFIRST will peer deep into the cosmos with the sensitivity of the Hubble Space Telescope, but 100 times the field of view. It will track the shapes, positions, and distances of millions of galaxies to understand how dark matter influenced their formation and how dark energy is boosting cosmic expansion. It will also carry a coronagraph, a mask to block out a star’s light so that orbiting exoplanets can be seen directly. To keep within its $3.2 billion budget, the project eased the requirements of the coronagraph and its attached spectrograph (*Science*, 27 October 2017, p. 433). Last month, the Trump administration proposed killing the project in its 2021 budget request, but astronomers hope Congress will reverse that, as it did after similar budget requests for 2019 and 2020.

Coronavirus KOs major meeting

MEETINGS | Citing the spread of the new coronavirus, the American Physical Society (APS) abruptly canceled its largest meeting of the year, just 36 hours before more than 10,000 physicists were to convene this week in Denver. APS made the decision on 29 February, hours after the U.S. Centers for Disease Control and Prevention advised against nonessential travel to South Korea and Italy, APS CEO Kate Kirby told *Science*. More than 500 people were registered from those countries. Although the cancellation inconvenienced many, Kirby says APS leaders were concerned about the health of registrants, vendors, and local residents. They had also envisioned a “nightmare scenario” in which a few infected attendees might cause thousands to be quarantined. As *Science* went to press, many major conferences were still on, including the spring meeting of the American Chemical Society and the European Congress of Clinical Microbiology and Infectious Diseases.

Earth’s fly-by-night visitor

PLANETARY SCIENCE | Some 18 months ago, Earth’s gravity roped in a car-size asteroid, making it the planet’s second detected “minimoon,” astronomers reported last week. (Another captured asteroid orbited Earth from 2006 to 2007.) Discovered by Kacper Wierzchos and Theodore Pruyne of the Catalina Sky Survey at the Mount Lemmon Observatory and provisionally dubbed 2020 CD3, the rock, of unknown composition, likely won’t stick around: CD3 has a wobbly orbit that in a few weeks will fling it from Earth and return it to its orbit around the Sun. Smaller minimoons occur frequently, scientists think, but visitors the size of CD3 may come only once a decade.

Trials must post missing data

CLINICAL TRIALS | Drug companies, device manufacturers, and universities must make public data from hundreds of clinical trials conducted in the United States from 2007–17, a federal judge ruled last week. The ruling, from the Southern District of New York, says that government agencies including the National Institutes of Health,

PHOTO: JPL/NASA

Published by AAAS



BIODIVERSITY

Glow-in-the-light amphibians

Most salamanders don't stand out: Their mottled, earth-toned skin helps them blend into the background of forests and streams around the world. But shine the right type of light on them, and they light up like glow sticks. That's the finding of a new study, which reveals for the first time that most amphibians—from salamanders to frogs—have fluorescent compounds in their skin, bones, and even urine that absorb the surrounding light and re-emit it at specific wavelengths. When researchers put 32 species of amphibians under a blue or ultraviolet light, all were biofluorescent, emitting a greenish to yellow light from their skin, they reported last week in *Scientific Reports*. This widespread occurrence suggests biofluorescence appeared early in the evolutionary history of amphibians.

An eastern tiger salamander exposed to regular light (top) and blue light (bottom).

PHOTO: JENNIFER Y. LAMB AND MATTHEW P. DAVIS

the Food and Drug Administration, and the Department of Health and Human Services for years misinterpreted a law requiring them to make clinical trial sponsors post the data to ClinicalTrials.gov. If the ruling is upheld, it will likely discourage drug companies from keeping unfavorable results from the public, and it could offer vital information for patients and doctors. Still unclear is how quickly the agencies might move to fill in the 10-year gap in compliance—and what the consequences would be for clinical trial sponsors that don't comply.

Canada steps up whale safeguards

CONSERVATION | With only about 400 North Atlantic right whales (*Eubalaena glacialis*) remaining, Canada is stepping up its efforts to keep them safe from ships and dangerous fishing gear, even as it tries to keep its lucrative snow crab and lobster fisheries thriving. New regulations announced last week expand the area in which whales will be protected by "dynamic" restrictions—which trigger only after the animals have been spotted—to the entire Gulf of St. Lawrence and the Bay of Fundy. The new restrictions should give fishers more harvesting opportunities than seasonlong shutdowns. But it also means fishing gear could already be in the water when the whales arrive. "That creates a huge risk," says Kristen Monsell, an attorney for the Center for Biological Diversity.

Wind power tops water in U.S.

ENERGY | Last year, wind energy for the first time surpassed hydropower as the top source of renewable electricity generation in the United States, according to a report out last month from the U.S. Energy Information Administration. In 2019, wind turbines produced 300 million megawatt hours (MWh), compared with 274 million MWh from dams and 146 million MWh from all other renewables. The United States is second only to China in wind energy production; that country generated more than 366 million MWh in 2018, the last year for which statistics are available. Globally, hydropower continues to be the largest source of renewable energy.

A satellite that foils space junk

SPACE SCIENCE | One satellite docked autonomously last week with another, derelict one and rescued it, a milestone for a spaceflight industry increasingly concerned with space junk. Some 36,000 kilometers above Earth, Northrop Grumman's Mission Extension Vehicle (MEV-1) latched onto Intelsat 901 (IS-901), a 19-year-old

Published by AAAS

THREE QS

When English is a barrier

English is the lingua franca of modern science. But for the millions of scientists whose mother tongue isn't English, the language can be a barrier to publishing papers, presenting at conferences, and even reviewing the scientific literature. Valeria Ramírez Castañeda, a Ph.D. student in biology at the University of California, Berkeley, who grew up in Colombia and studied science communication in Spain, decided to survey fellow researchers about publishing in a language that is not their own. Her findings were posted last month on the preprint server bioRxiv. *Science* spoke (in Spanish) to Ramírez Castañeda about the problem, and possible solutions.

Q: How did you come up with this idea?
A: When I was in university in Colombia, I was privileged to be able to read in English—most of my classmates understood little to nothing. While doing my master's, I had the choice of writing my thesis in English. I tried, but in the end, I couldn't do it. It was very frustrating. And I knew many other students felt the same.

Q: What did you find?
A: Of 49 students, 43.5% said they had papers rejected because of English. On average, they spent 10 more days preparing a manuscript in English than they did in Spanish; 33% of them didn't attend meetings where they were required to present in English. Beyond the numbers, the response has been very emotional. Colleagues have told me they thought of leaving science … and some haven't been able to graduate because they cannot pay for English courses. It's emotionally hard to realize. Everyone deserves and has the right to be a scientist.

Q: What should scientists do?
A: Right now, the responsibility falls on individuals to learn English, no matter where they were born, whether they're poor, or whether they have trouble learning another language. And that cannot happen anymore! Institutions, scientific publishers, government agencies, professors, and meeting organizers must provide solutions. Most already exist: including proofreading services in publishing fees, promoting spaces in publications for second languages, providing editing and university training to science students, and hiring [interpreters] at international meetings.

SCIENCEMAG.ORG/NEWS
Read more news from *Science* online.

communications satellite nearly out of propellant. For a cost of about $13 million annually, MEV-1 will serve as a sort of jetpack, keeping IS-901 in a geostationary orbit. After 5 years, MEV-1 will move IS-901 to a higher "graveyard" orbit, release its companion, and attach itself to a new satellite. More than 5000 satellites orbit Earth, but just 40% are still operational. Researchers have been testing different ways to collect or eliminate space junk, including nets, harpoons, and lasers.

Constant unmoved by black hole

ASTROPHYSICS | The constant of nature that sets the strength of the electromagnetic force isn't altered by the gravity of a supermassive black hole, astronomers reported last week in *Physical Review Letters*. Researchers observed five stars orbiting the black hole in the center of our galaxy, a behemoth 4 million times as massive as the Sun. In the stars' atmospheres, elements including sodium, titanium, and silicon absorb certain wavelengths of starlight, creating dark lines in the stars' spectra. The lines' spacing depends on the strength of the electromagnetic force and the fine structure constant. Researchers found no change in their spacing, putting a dent in speculative theories in which the fine structure constant could change in intense gravitational fields.

Freeman Dyson dies at 96

PHYSICS | Theoretical physicist, futurist, and writer Freeman Dyson died last week in Princeton, New Jersey, where he spent his career at the Institute for Advanced Study. Born and raised in the United Kingdom, Dyson established himself in 1949, when he proved that two competing quantum theories of electricity, magnetism, and light—one more practical and ad hoc and the other more comprehensive but unwieldy—were equivalent. But he did not share in the 1965 Nobel Prize in Physics, which honored the theory of quantum electrodynamics. In the late 1950s, Dyson joined Project Orion to design a spaceship propelled by atomic bombs, a goal abandoned after a 1963 arms control treaty banned nuclear explosions in space. In 1960, he mused that an alien civilization might surround its star with an array of energy absorbers, later known as a "Dyson sphere," detectable from afar. In his later years, he angered peers by denying and downplaying the threat of climate change.

SCIENCE POLICY

And the Vannevar goes to …

The U.S. National Science Foundation (NSF) owes a lot to Vannevar Bush, whose seminal 1945 report made the case for federal funding of academic research. So when NSF officials learned that a bronze sculpture of the former Massachusetts Institute of Technology engineering dean was tucked away in a warehouse of the Smithsonian Institution, they wanted to bring it to NSF's new headquarters in Alexandria, Virginia. But Smithsonian officials said NSF didn't have the proper environmental controls needed to house the 57-centimeter-tall statue, made for a 1944 exhibit on "50 notable men of wartime." NSF applied some of the "Yankee ingenuity" Bush had lauded in his report, *Science, The Endless Frontier*. Using 3D printing, it replicated the sculpture (right) and installed it in the office of NSF Director France Córdova. And now, it's making miniature versions. Last week, as the National Academy of Sciences hosted a 75th anniversary celebration of Bush's report, Córdova presented NAS President Marcia McNutt with the first "Vannevar," calling it the scientific equivalent of an Oscar.



PHOTO: JIM CRAWFORD AND ANNE DUVIVIE

Published by AAAS



IN DEPTH

Bruce Aylward of the World Health Organization holds up a graphic showing China's plummeting coronavirus cases at a 24 February press conference in Beijing.

PHOTO: XINHUA/XING GUANGLI/GETTY IMAGES

INFECTIOUS DISEASES

Can China's COVID-19 strategy work elsewhere?

Rapid decline in cases is real, expert mission concludes—but it came at a high cost

By **Kai Kupferschmidt** *and* **Jon Cohen**

Chinese hospitals overflowing with COVID-19 patients a few weeks ago now have empty beds. Trials of experimental drugs can't find enough eligible patients. And the number of new cases reported each day in China is dropping precipitously.

These are some of the startling observations in a report released on 28 February by a team of 12 Chinese and 13 foreign scientists who toured five cities in China to study the state of the COVID-19 epidemic and the effectiveness of the country's response. Even some on the team, organized jointly by the World Health Organization (WHO) and the Chinese government, say they were surprised. "I thought there was no way those numbers could be real," says epidemiologist Tim Eckmanns of the Robert Koch Institute in Berlin.

But the report is unequivocal. "China's bold approach to contain the rapid spread of this new respiratory pathogen has changed the course of a rapidly escalating and deadly epidemic," it says. To Bruce Aylward, a Canadian WHO epidemiologist who led the mission and briefed journalists in Beijing and Geneva last week, the effort was a huge success. "Hundreds of thousands of people in China did not get COVID-19 because of this aggressive response," he says.

Aylward and other members of the task force say the rest of the world should learn from China. But critics say the report failed to acknowledge the human rights costs of the most severe measures imposed by China's authoritarian government: massive lockdowns and electronic surveillance of millions of people. "I think there are very good reasons for countries to hesitate using these kinds of extreme measures," says Lawrence Gostin, a global health law scholar at Georgetown University. Many also worry that a resurgence of the disease will occur after the country lifts some of its strictest control measures and restarts its economy, which has taken a huge hit.

The report comes at a critical time in what many epidemiologists now consider a nascent pandemic. The number of affected countries is rising rapidly—it stood at 72 as *Science* went to press, according to WHO. Alarmingly, in many of these countries, the virus has quickly gained a foothold and started to spread in communities.

But cases have plummeted in China. On 10 February, the first day of the mission, the country reported 2478 new cases. Two weeks later, when the foreign experts packed their bags, the daily number of new cases had dropped to 409. (On 3 March it had dropped further to 129 new cases, compared with 1848 in the rest of the world.) China's epidemic appears to have peaked in late January, according to the report.

Members of the team traveled to Beijing, Shenzhen, Guangzhou, Chengdu, and the hardest hit city, Wuhan. They visited hospitals, laboratories, companies, live animal markets, train stations, and local government offices. "Everywhere you went, anyone you spoke to, there was a sense of responsibility and collective action—and there's a war footing to get things done," Aylward says.

As part of the effort, Chinese scientists have compiled a massive data set that gives the best available picture of the disease. The mission report says about 80% of infected people had mild to moderate disease, marked by fever and a dry cough; 13.8% had severe symptoms; and 6.1% had life-threatening episodes of respiratory failure, septic shock, or organ failure. The case fatality rate was highest for people over age 80 (21.9%), and people who had heart disease, diabetes, or hypertension, but 3.8% overall. Children made up a mere 2.4% of the cases, and almost none was severely ill. People with mild and moderate illness took 2 weeks on average to recover.

Published by AAAS

The report highlights how China achieved what many public health experts thought was impossible: containing the spread of a widely circulating respiratory virus. "China has rolled out perhaps the most ambitious, agile, and aggressive disease containment effort in history," the report notes. The most dramatic—and controversial—measure was the lockdown of Wuhan and nearby cities in Hubei province, putting at least 50 million people under a mandatory quarantine since 23 January. That has "effectively prevented further exportation of infected individuals to the rest of the country," the report concludes. Most of China did not face such severe measures: People were asked, but not required, to quarantine themselves if they felt ill, and neighborhood leaders monitored their movements.

Chinese authorities also built two dedicated hospitals in Wuhan in about 1 week, sent health care workers from all over China to Hubei, and launched an unprecedented effort to trace contacts of confirmed cases. In Wuhan alone, more than 1800 teams traced tens of thousands of contacts. Aggressive "social distancing" measures implemented in the entire country included canceling sporting events and shuttering theaters, schools, and businesses. Anyone who went outdoors had to wear a mask.

Two widely used mobile phone apps, AliPay and WeChat—which in recent years have replaced cash in China—have helped enforce the restrictions, because they allow the government to keep track of people's movements and even stop people with confirmed infections from traveling. "Every person has sort of a traffic light system," says mission member Gabriel Leung, dean of the Li Ka Shing Faculty of Medicine at the University of Hong Kong. Color codes on mobile phone screens—in which green, yellow, or red designate a person's health status—let guards at train stations and other checkpoints know who to let through.

"As a consequence of all of these measures, public life is very reduced," the report notes. But the measures did work. In the end, infected people rarely spread the virus to anyone except members of their own household, Leung says. Once all the people living together were exposed, the virus had nowhere else to go and chains of transmission ended. "That's how the epidemic truly came under control," Leung says.

It's debatable how much of this could be done elsewhere. "China is unique in that it has a political system that can gain public compliance with extreme measures," Gostin says. The country also has an extraordinary ability to do labor-intensive, large-scale projects quickly, says Jeremy Konyndyk, a senior policy fellow at the Center for Global Development: "No one else in the world really can do what China just did."

Nor should they, says lawyer Alexandra Phelan, a China specialist at Georgetown's Center for Global Health Science and Security. "There are plenty of things that would work to stop an outbreak that we would consider abhorrent in a just and free society," Phelan says.

The report urges China "to more clearly communicate key data and developments internationally." But it is mum on the coercive nature of China's control measures and the toll they have exacted. "The one thing that's completely glossed over is the whole human rights dimension," says Devi Sridhar, a global public health specialist at the University of Edinburgh. Instead, the report praises the "deep commitment of the Chinese people to collective action in the face of this common threat."

"To me, as somebody who has spent a lot of time in China, it comes across as incredibly naïve—and if not naïve, then willfully blind to some of the approaches being taken," Phelan says. Singapore and Hong Kong may be better examples to follow, Konyndyk says: "There has been a similar degree of rigor and discipline but applied in a much less draconian manner." Jennifer Nuzzo of the Johns Hopkins University Bloomberg School of Public Health also wonders what effects China's strategy had on, for instance, the treatment of cancer or HIV patients, whose care may have been interrupted. "I think it's important when evaluating the impact of these approaches to consider secondary, tertiary consequences," she says.

And the benefit may be short-lived. "There's no question they suppressed the outbreak," says Mike Osterholm, head of the Center for Infectious Disease Research and Policy at the University of Minnesota, Twin Cities. Reducing the peak number of cases buys a health system time to deal with later ones, public health experts say. But once the restrictions are lifted, "It'll come roaring right back," Osterholm predicts.

Aylward and the other visiting scientists on the team were well aware of the "reality of different political systems," he says, but they spoke with hundreds of people around the country and "everyone agreed with the approach." He hopes China's successes so far will encourage other countries to act quickly. "We're getting new reports daily of new outbreaks in new areas, and people have a sense of, 'Oh, we can't do anything,'" Aylward says. "Well, sorry. There are really practical things you can do to be ready to be able to respond to this, and that's where the focus will need to be." ■

ATMOSPHERIC SCIENCE

Why weather systems are apt to stall

A new theory tries to explain enigmatic "blocks" that bring heat waves and drought

By **Paul Voosen**

It was the summer of 2003 in Europe, and, for a while, it seemed as if Earth's weather system had broken down. For weeks a huge mass of air stalled over the continent, slowly subsiding and suppressing cloud formation, leaving day after day of brilliantly clear skies. The mercury rose, and a record-breaking heat wave gripped countries including France and Germany, causing 70,000 deaths. Then, as abruptly as it set in, the persistent atmospheric block eased, and high winds brought relief.

Few weather phenomena are as widely experienced—but poorly understood—as an atmospheric block. When a block arises, typically at the western edge of a continent, the jet stream splits, trapping a blob of seemingly static air thousands of kilometers across. Such blocks can last for weeks, and drive heat waves, drought, and winter cold snaps. At the same time, the persistent flows around the edges of a block can route storm after storm to the same spot. A block "has very different impacts in different seasons," says Tim Woollings, an atmospheric dynamicist at the University of Oxford. "But it's always quite extreme." Yet atmospheric scientists have long struggled to understand why blocks occur and last so long, and how they might change in a warming world.

Several new theories are offering answers. A leading idea links blocking to the behavior at high latitudes of the Coriolis force, an effect of Earth's rotation that can cause the jet stream to meander and contort. The theory, developed by Harvard University atmospheric scientist Lei Wang, is unlikely to be the full picture, but it has a sobering implication. As the world warms, the jet stream is likely to move to higher latitudes, which could lead to even more blocking events.

The new ideas about blocking emerged from debate over another potential impact of climate change. Researchers led by Jennifer

Published by AAAS



In 2018, an atmospheric block caused drought that dried out the Rhine River in Germany.

Francis, a climate scientist at the Woods Hole Research Center, have suggested a warming Arctic is leading to more severe winter storms in the midlatitudes (*Science*, 18 April 2014, p. 250). Francis has argued that the encroaching warmth is slowing the jet stream and causing it to form larger blocklike meanders, exacerbating winter weather. But other scientists are skeptical of the mechanism. The controversy has exposed just how much there is to learn about blocking, Wang says. "The lack of theory is really the root cause of a lot of confusion we now have."

Scientists did have a standard explanation for what sustains blocks. Published in 1983, the idea stems from close study of a single block in 1976 that led to drought in Europe. Once the block was established, the split jet stream seemed to shear later weather systems apart. The energy of these atmospheric eddies then fed into the slowly rotating trapped airmass, creating a feedback loop that reinforced and sustained the block. It was an elegant idea, says Stephan Pfahl, an atmospheric dynamicist at the Free University of Berlin, but "its connection to more realistic cases has always been a question mark."

Wang revisited this work. First, he simulated blocking events in a series of simple atmospheric models, hoping to detect the eddy feedback, as it's known. He was shocked—it didn't exist. Looking at the original calculations from the 1980s, Wang saw an error: They generated the feedback even when the block was missing. He then used modern weather records to examine some 100 similar blocking events over several decades. He found that eddies played a minimal role, at most, in maintaining them, as he reported this year at the annual meeting of the American Meteorological Society. All signs pointed to one conclusion, he says. "The existence of the feedback that was discovered in that paper is a false alarm."

Two years ago, Wang's former adviser, atmospheric scientist Noboru Nakamura at the University of Chicago, proposed an alternative explanation for blocks. Over the years, he had painstakingly developed an equation to track large meanders in the jet stream. Such bends can eventually break, causing the jet to split. Nakamura found that these meanders seemed to behave like cars on a highway; pile enough together on the jet, and a traffic jam—a block—arises, he argued 2 years ago in *Science*. Atmospheric scientists are still digesting Nakamura's proposal. But Wang and others suspect it may be more complicated than needed.

Wang and his co-author, Zhiming Kuang, also at Harvard, have come up with their own theory. While a student at the University of Chicago, Wang had pulled off the lunchroom shelf the dissertation of Tu-cheng Yeh, who studied in Chicago with pioneering geophysicist Carl-Gustaf Rossby in the 1940s. Yeh, who became a famed meteorologist in China, had noted that blocking events are more common and last longer when the jet stream moves to higher latitudes.

That pattern, Yeh proposed, is set by the atmosphere's inherent dispersiveness—essentially, the noise and chaos in the system. At low latitudes, the atmosphere is too noisy to sustain a long-term pattern. For example, giant undulations in airflows like the jet stream, called Rossby waves, are quickly canceled out by other waves of different amplitudes and frequencies. But at higher latitudes, where the globe gets narrower, the waves generated by the Coriolis force are squeezed into a smaller band. That squeeze makes them more likely to align, which can amplify them, forcing the jet to split and give rise to a block.

Yeh had demonstrated his idea only in a simple, 1D model. But now, Wang and Kuang have found it holds in more complex simulations. The work is still under review, with one part posted on the preprint server arXiv. "But it's potentially a breakthrough," says Jian Lu, a climate dynamicist at the Pacific Northwest National Laboratory. "Fundamentally, blocking may be a simpler phenomenon than we previously thought." In the past, simple explanations couldn't explain why long-lasting blocks are so frequent. In Wang's model, the latitude dependence does just that, says Eric DeWeaver, a program manager for climate and large-scale dynamics at the National Science Foundation. "It's very appealing as a back to basics rethink."

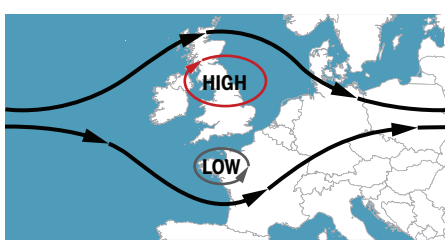
Wang's theory shares a flaw with its predecessors, however: They all treat the atmosphere as dry. Over the past 5 years, Pfahl and others have shown that moisture is crucial to sustaining blocks. Indeed, Pfahl found in case studies and models that many blocks persist only if fed air in which water vapor has condensed into clouds and rain, releasing heat that uplifted the air mass. "For me this is the really new thing," Woollings says.

The next step will be to see whether the new insights can improve forecasts of weather and climate. Current models project a small decline in the frequency of blocks as the world warms, but scientists have low confidence in that prediction, says Olivia Martius, an atmospheric dynamicist at the University of Bern. "There is no simple answer" for how to improve such predictions. But the new theories could identify thresholds—specific atmospheric conditions—at which blocks are likely to proliferate, Nakamura says. "If you can nail the threshold condition, then you can ask how climate changes that threshold."

Wang's theory suggests one answer. Warming is expected to push the polar jet stream in the Northern Hemisphere farther north. And Wang has found that shifting the stream 10° closer to the pole could bring a 10-fold increase in blocks—and the heat waves and droughts they foster. "Northern Europe would experience many more," Lu says. "Especially Russia. It's a huge impact." ■

No change in the weather

In a "dipole" atmospheric block, the jet stream splits, wrapping around slowly rotating high- and low-pressure air masses and trapping them.



CREDITS: (PHOTO) CHRISTOPHE GATEAU/DPA/ALAMY LIVE NEWS; (MAP) X. LIU/*SCIENCE*; (DATA) U.K. MET OFFICE/OPEN GOVERNMENT LICENSE V1.0

Published by AAAS



Farm-raised tilapia at a market in Egypt, where growers have had outbreaks of a damaging fish virus.

ANIMAL HEALTH

Unplanned experiment could help save a key farmed fish

Random outbreak at research center points to tilapia variants that resist the deadly emerging tilapia lake virus

By **Erik Stokstad**

About a decade ago, farm-raised tilapia in Israel began to die mysteriously. The fish had ulcerated skin and internal hemorrhages; sometimes ponds full of fish were wiped out. In 2014, researchers identified the culprit: a previously unknown virus they named tilapia lake virus. Since then, the virus has been detected on farms in Asia, Africa, and the Americas. There's no cure and no vaccine, and the virus is likely spreading, threatening one the world's most important farmed fish. "It's a major global problem," says John Benzie, a geneticist at WorldFish, an international publicly funded research center.

New findings, however, are providing hope that Nile tilapia (*Oreochromis niloticus*), the most common kind of farmed tilapia, could be bred to resist the virus. In a lucky break, in 2018 the virus struck a pond at WorldFish holding numerous tilapia produced for breeding experiments, and some of the fish proved completely resistant to the virus, Benzie and colleagues reported last month in *Aquaculture*. "It's good news for the tilapia sector," says Morten Rye, a fish geneticist at Benchmark Genetics, a company that breeds tilapia and other aquacultural species.

Tilapia is the second most popular fish in aquaculture, after carp, with farmers in more than 120 countries now harvesting about 6 million tons per year. It's especially important in developing nations, many of which rely on a productive strain first developed in the 1990s at WorldFish.

The emerging virus affects several types of farmed tilapia, and was probably causing problems for at least several years before its discovery. Although researchers know some regions have been hit hard, the overall distribution and impact of the virus are not clear. Because the World Organisation for Animal Health has not certified a diagnostic test that works in all situations, countries are only required to report major outbreaks. More than a dozen countries do voluntarily report additional data, but, "We really need descriptive and analytical epidemiological studies to help us understand the situation in the field," says Mona Dverdal Jansen, a veterinary epidemiologist at the Norwegian Veterinary Institute.

In the meantime, researchers at WorldFish are working with the University of Edinburgh's Roslin Institute to breed Nile tilapia that resist the virus. The 2018 outbreak in WorldFish's pond in Malaysia is helping them identify promising genetic variants. In all, the pond contained 1821 individually tagged tilapia belonging to 124 groups of siblings. Each group had different pairs of parents. Nearly 40% of all the fish died; that was enough to allow the researchers to pick out which groups of siblings had the highest survival rates.

Just as encouraging, the WorldFish outbreak enabled researchers to show that about 50% of the variation in survival was due to genetics. "That bodes well for future breeding to improve resistance to the virus," says co-author Ross Houston, a fish geneticist at the Roslin Institute. The researchers also found that bigger—and more valuable—fish were just as likely to resist the disease as the smaller fish. That finding suggests breeders won't have to sacrifice yield to boost resistance, which would be a problem for growers.

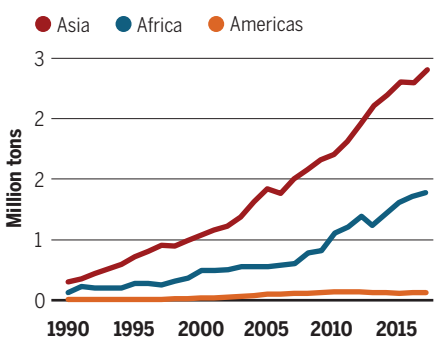
Still, getting resistant tilapia into the world's ponds could take years. Researchers need a genomic test that would allow breeders to quickly identify fish with desirable genes, and they need a reliable and realistic way to infect the fish to find out whether they really are resistant. Rye cautions that even if breeders develop a winning strain, mass-producing the fish in hatcheries and distributing them—especially in the developing world—will be a tall order. "It's not changing everything overnight," he says.

Some companies are pursuing a different approach: developing a vaccine against tilapia lake virus. But viable candidates are still far off, and even a highly effective vaccine might not be cheap enough to be economically viable, especially because tilapia is a relatively low-value fish often grown by poor farmers.

Given such issues—and the threat that the virus is continuing to spread—creating hardier tilapia breeds has become "a matter of urgency," Benzie says. "We're going hell for leather on this." ■

A threatened bounty

Production of pond-raised Nile tilapia has been booming in Asia and Africa, helping the species become the second most popular farmed finfish in the world, behind carp.



CREDITS: (PHOTO) WORLDFISH/FLICKR/CC BY-NC-ND; (GRAPHIC) D. MALAKOFF/*SCIENCE*; (DATA) FOOD AND AGRICULTURE ORGANIZATION OF THE UNITED NATIONS

Published by AAAS

U.S. RESEARCH FUNDING

Pentagon's social science research faces threat

Minerva initiative falls out of favor in latest DOD review of spending priorities

By **Jeffrey Mervis**

The U.S. Department of Defense (DOD) wants to kill a unique social science research program meant to help it understand nontraditional threats to national security, from the rapid growth of China's technological prowess to radical Islamic terrorism.

The $20 million Minerva Research Initiative is in jeopardy after Defense Secretary Mark Esper ordered a review that identified some $5 billion worth of programs deemed less essential to DOD's mission. Michael Griffin, DOD undersecretary for research and engineering, has made developing hypersonic weapons a top priority, and DOD watchers say Minerva doesn't meet Griffin's definition of what his office, which controls a $16.1 billion research budget, should fund. In its 2021 budget request, DOD proposed cuts that could lead to the program's demise, but Congress could save it.

"The current undersecretary doesn't believe that Minerva is science," says a Democratic congressional staffer. "He thinks it's soft, and his priorities are elsewhere."

The Minerva program began under former President George W. Bush. "Too many mistakes have been made over the years because our government and military did not understand—or even seek to understand—the countries or cultures we were dealing with," then–Defense Secretary Robert Gates said in an April 2008 speech announcing the program.

Gates envisioned a role for researchers in promoting "soft power—the elements of national power beyond guns and steel." He also hoped that Minerva would improve what he called the often "hostile" relationship between DOD and social scientists.

A 2019 evaluation by the U.S. National Academies of Sciences, Engineering, and Medicine found that Minerva has met both those goals over the past decade. Its 111 grants—which now average $1.5 million over 3 years—"have produced a substantial body of research in a variety of areas of importance to national security … [and have] had a positive impact on the amount of dialogue between DOD and the social science community." But the findings from Minerva projects, it added, have been slow to reach the intended audience of policymakers within the Pentagon and commanders in the field.

Although Minerva projects represent a tiny fraction of DOD's $2.6 billion investment in basic research, they have gotten outsize media attention. One example is work conducted by researchers including cultural anthropologist Scott Atran of the University of Michigan, Ann Arbor, and the University of Oxford. It probes the psychology of suicide bombers, for example, by using brain scans to track how people react to perceived threats to their deeply held values.

Economist Eli Berman of the University of California, San Diego, has worked on Minerva projects that embedded social scientists with U.S. military leaders in Afghanistan to seek ways to strengthen local institutions and combat insurgency movements. "The goal was always to be useful right away," Berman says.



Afghan security forces trained by the U.S. military inspect travelers at a checkpoint near the Pakistani border.

PHOTO: REUTERS/PARWIZ/TPX IMAGES OF THE DAY

As social scientists, Minerva grantees focus on promoting understanding and preventing conflicts, often through interdisciplinary teams. For example, one project sent anthropologists to do ethnographic studies of Indonesian communities, allowed sociologists to conduct attitudinal surveys in West Africa, and funded computer scientists to analyze online data related to social movements in several regions of the world. The result was a web-based tool, called LookingGlass, that allows authorities to track emerging threats by displaying information about these movements in real time.

That approach contrasts with the Pentagon's traditional emphasis on tapping basic research to improve its chances of winning battles. "Minerva is not going to support the science needed to develop the tools for projects that the undersecretary considers a priority, like hypersonic weapons," says Erin Fitzgerald, who directed Minerva for 5 years and is now a research administrator at the University of Maryland, College Park. "But it might help us avoid the need to deploy those weapons." As Atran puts it: "If superior machines and hardware were the way to win wars, we'd have been out of Afghanistan in 2002 and Iraq in 2003. But it's people. And we still don't understand them."

Griffin declined comment, but a DOD spokesperson says Esper's review allowed Griffin's office to "scrutinize and revector our fiscal year 2021 budget request to align more directly with the department's modernization priorities." Asked specifically about the value of Minerva, the spokesperson said, "The question was not, 'Is this a good effort?' but rather, 'Is a dollar spent on this effort more important to our military capability than spending that same dollar on" a priority area?

DOD's proposed budget would put Minerva on a path to a rapid demise. It would eliminate the $11 million contribution from the basic research office, leaving Minerva with some $4 million that Congress has recently earmarked for research on how other government are using social media to undermine U.S. institutions and sway public opinion and to examine the threat posed by China, Russia, North Korea, and Iran.

The Navy and Air Force could continue to fund projects they think are useful, although observers say they are likely to bow out once money from the basic research office disappears. (The Navy has proposed spending $3 million in FY2021; the Air Force doesn't break out Minerva but has invested roughly $2 million annually in recent years.)

Minerva backers are hoping its track record will persuade Congress to protect the program. "Our biggest concern is to make sure that the research doesn't stop," the Democratic staffer says. "We think that Minerva is so important in helping DOD achieve its mission." ■

Published by AAAS

ASTRONOMY

New telescope promises boon for Turkish science

The 4-meter Eastern Anatolia Observatory aims to become an affordable regional hub

By **Umar Farooq**

International megaprojects that cost well over $1 billion generate most of the excitement in observational astronomy today: the 39-meter Extremely Large Telescope under construction in Chile, for example, or the Thirty Meter Telescope, controversial because of its proposed location on Mauna Kea, a mountain sacred to some Native Hawaiians.

But smaller telescopes still do cutting-edge science as well. And Turkish scientists are eagerly awaiting the completion of the new Eastern Anatolia Observatory (DAG), a 4-meter optical and infrared telescope expected to come online next year. Its main structure is scheduled to be shipped to the site, a 3170-meter mountaintop in northeastern Turkey, this month; polishing and grinding of the primary mirror is nearly done.

Despite its modest $34 million price tag, DAG will be one of Asia's largest optical telescopes and Turkey's largest science project. Its developers hope DAG will make Turkey a regional astronomy hub and help nurture its astronomy community. "We are dreaming of using the instruments on DAG," says Ozgur Basturk, an exoplanet scientist at Ankara University. "With a 4-meter telescope, we can do much better and be more competitive in our field."

Turkey's largest telescope today is a 1.5-meter reflector near the city of Antalya on the Mediterranean coast. The new facility will sit well above haze and humidity and far from urban light pollution, and enjoy 288 clear nights per year on average. Its design and construction, financed by the Turkish government, has involved scientists at 40 universities in the region, along with European academic and industrial partners. "It's not a 40-meter telescope of course," says Laurent Jolissaint of the University of Applied Sciences and Arts of Western Switzerland, the project's lead optical engineer, "but we put everything into it. The optics system is the same essentially as the very newest systems." DAG will be run by the Astrophysics Research and Application Center at Atatürk University in Erzurum, a city in eastern Turkey.

Turkish scientists have little access to the world's largest telescopes. The European Southern Observatory (ESO) in Chile, for instance, prioritizes observing time for projects led by scientists from the 16 nations that have helped pay for the facility and contribute to its €162 million annual budget. "In principle anyone can apply to use these telescopes, but the competition is very high, so the research quality [of your proposals] should be high," says astronomer Sinan Alis of Istanbul University. "You have to somehow reach that level to be able to compete." In 2010, Turkish astronomers began to lobby their government to apply for ESO membership, but they gave up a few years ago, their hopes dashed by Turkey's economic crisis. (Another developing country, Brazil, dropped its membership bid last year because it could not afford €270 million in fees over the next decade.)



A new telescope, under construction on a 3170-meter mountaintop in eastern Turkey, is expected to come online next year.

PHOTO: ATATÜRK UNIVERSITY ASTROPHYSICS RESEARCH AND APPLICATION CENTER/ANADOLU IMAGES

Unable to make observations themselves, many Turkish astronomers fall back on archival data from large telescopes that have already been picked over by other astronomers, who can take years to release them. Some Turkish astronomers have struck up collaborations with teams from ESO member countries, but even then, getting travel funded is often difficult.

That's why the new telescope will be such a boon, Basturk says—for instance, for his exoplanet research. DAG will allow him to use one of the standard strategies for hunting exoplanets: monitoring stars for a wobbling motion that results from the gravitational tug of an orbiting planet. But like other premier telescopes, DAG will also have a coronagraph, an instrument that masks bright stars to remove their glare so that dim planets orbiting them can be imaged directly. New technology will enable the coronagraph to block multiple stars at the same time, needed to hunt for exoplanets in star systems that, unlike our own, have two stars or more.

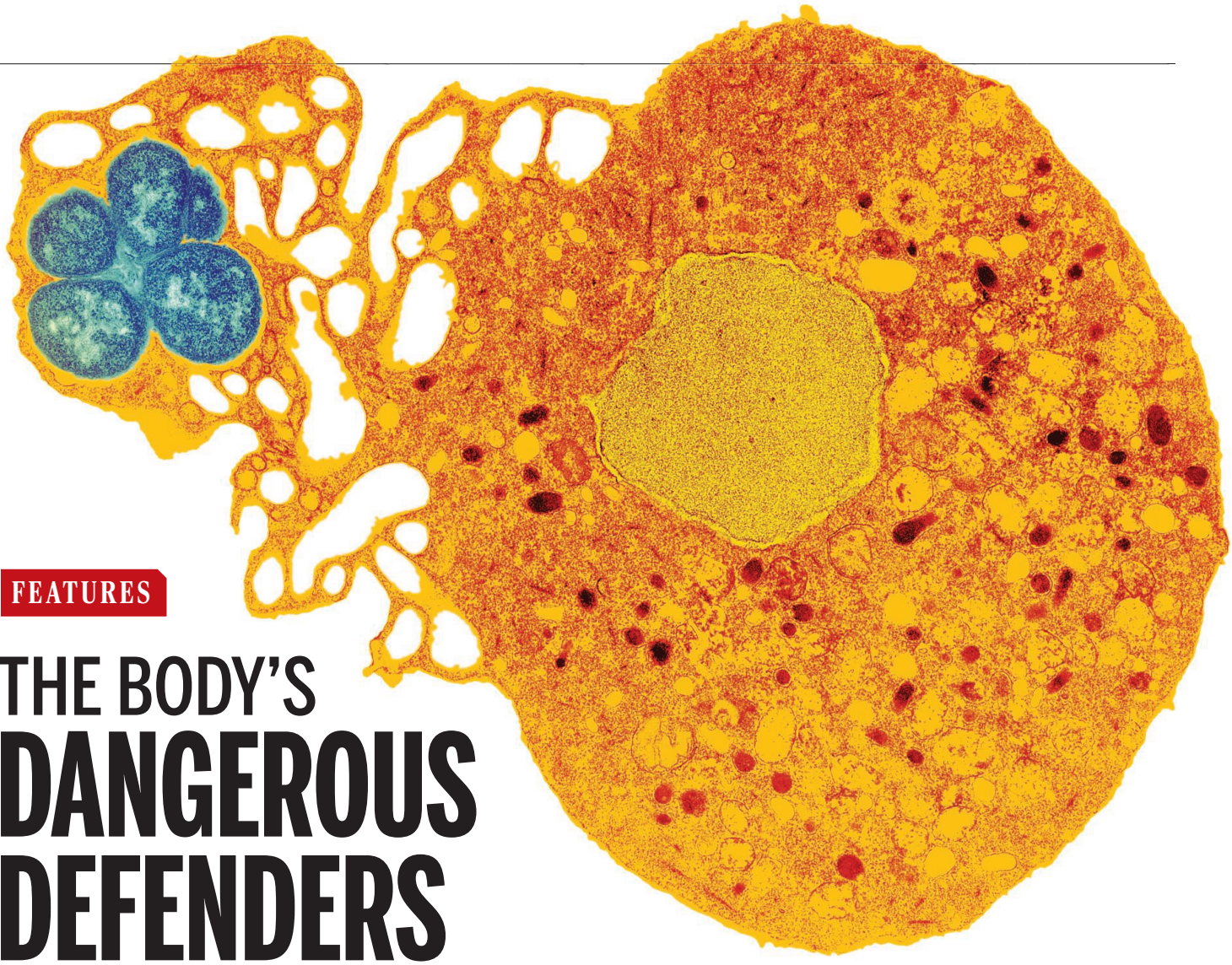
DAG's large aperture will enable it to capture light from distant, faint objects like high redshift galaxies, allowing astronomers to probe far back into the universe's history. That's important for Alis, who hopes to use DAG to follow up on data from the Spektr-RG space observatory, a Russian-German satellite launched last year to map the x-ray sky (*Science*, 14 June 2019, p. 1020). Many objects can produce x-rays, from black holes at the centers of galaxies to smaller black holes or neutron stars consuming mass from a companion star. "We need to follow up with optical and infrared to see what they actually are," Alis said.

In an ironic twist, DAG officials say astronomers from several European countries have shown interest in Turkey's new observatory, despite their access to ESO's mega-telescopes, drawn by the location—there are few others in the Northern Hemisphere at that longitude—and affordable observation time. "We envision DAG as an international observatory," says the project's director, Cahit Yeşilyaprak of Atatürk University. "We do not have a preference about the origin of the proposals, as long as the best science cases are proposed and conducted."

But the biggest impact will be in Turkey itself. Designing the telescope has already pushed science in other fields. For instance, dozens of optical, mechanical, and computer engineers helped design the telescope's adaptive optics system, which will sharpen its images, and its derotator, a device that keeps the telescope trained on the same spot as the Earth rotates. "These are big deals for a developing country," Yeşilyaprak says. And the telescope itself will invigorate Turkish astronomy, Alis says. "Once we have the telescope, the expertise will pop up." ■

Umar Farooq is a journalist based in Istanbul.

Published by AAAS



FEATURES

THE BODY'S DANGEROUS DEFENDERS

Neutrophils fiercely attack infections, but can also trigger disease. Researchers are trying to tame them

By **Mitch Leslie**

Seeking a new treatment for people who have dangerous blockages in their coronary arteries, doctors in London are trying to disarm the body's own defenders. The 90 patients in the study receive the usual treatments for heart disease, such as small tubes called stents to prop open their narrowed arteries. But half of the patients in the phase II trial, conducted by clinical pharmacologist Albert Ferro of King's College London and colleagues, also pop pills targeting a class of immune cells called neutrophils. Researchers think that by invading the fatty obstructions, or plaques, in clogged arteries, neutrophils make them even more dangerous. The drug is designed to steer the cells away.

Interfering with neutrophils is an audacious idea. Neutrophils make up some 70% of the white cells in blood, with billions spawned every day by stem cells nestled in the bone marrow. The cells patrol the bloodstream and wage war on pathogens, and their defensive role is so vital that people who lose their neutrophils in the course of cancer treatment can die from infections.

But their scorched-earth tactics are tough on the body. "They are the classic double-edged sword," says immunologist Michael Fessler of the U.S. National Institute of Environmental Health Sciences. For example, the enzyme neutrophil elastase, which neutrophils release to kill invading bacteria, also erodes the extracellular matrix, the mesh of proteins and sugars that cradles cells and provides structural support for tissue.

A neutrophil (orange) traps bacteria by extruding a net of DNA—a protective response that can backfire.

Neutrophils can also malfunction. In some conditions, such as chronic obstructive pulmonary disease (COPD), they seem to lose their sense of direction: Instead of homing in on bacteria, they wander. Researchers suspect these vagrant neutrophils release neutrophil elastase and other molecules at the wrong spots, including the lungs, causing the tissue damage seen in COPD. And as people age, neutrophils become less effective at combating infections and more harmful to the body.

"We are now beginning to understand that neutrophils are linked to many diseases that blight our population," says pulmonologist Elizabeth Sapey of the University of

PHOTO: SPL/SCIENCE SOURCE

Published by AAAS

Birmingham in the United Kingdom. With that realization has come optimism that these cells aren't off-limits for medical interventions. Researchers have been cautious about targeting neutrophils, fearing that doing so would leave patients at the mercy of pathogens. "The age-old idea was that you couldn't touch neutrophils," Sapey says. But a series of clinical trials has offered reassurance that it can be safe to restrain the cells.

Although some of those trials yielded mediocre results, researchers have pressed on—and their persistence may be paying off. Two clinical trials with neutrophil-focused drug candidates reported encouraging findings last year; one could lead to the approval of the first medication targeting these immune cells, in a rare autoimmune condition. The trial Ferro and his colleagues are conducting, the first to attempt to stem cardiovascular disease by interfering with neutrophils, is expected to have results by 2021 or 2022. And a burst of new findings about the cells' diversity and behavior is likely to inspire new ways to manipulate them. "There is real hope in this field," Sapey says.

NEUTROPHILS FLOCK to the site of an injury or infection, wherever it occurs. The cells navigate to trouble spots with the help of receptors on their surface, such as one known as CXCR2, which detects a trail of alarm molecules released by damaged tissue. If the cells happen upon microbes, they launch a multipronged attack, gobbling the pathogens, spilling corrosive chemicals, and sometimes launching webs of DNA, known as neutrophil extracellular traps (NETs), that snag and kill the invaders. Hematopoietic stem cell transplants given to some cancer patients to replace their bone marrow underscore the importance of these defenses. "If the graft doesn't take, you will have no neutrophils, and that is not survivable," says immunologist Klaus Ley of the La Jolla Institute for Immunology.

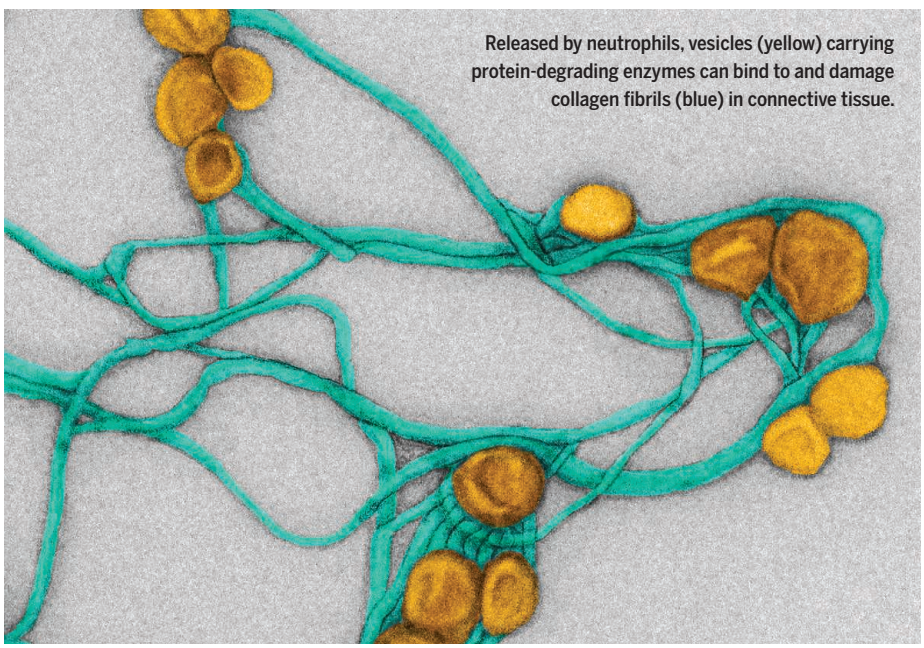
Yet studies over the past 2 decades have darkened their image. The cells in effect "drop atomic bombs" in the body, says immunologist Paul Kubes of the University of Calgary. Neutrophil elastase and other chemicals they discharge may drive inflammation and damage to the airways in cystic fibrosis and intractable cases of asthma. NETs, for their part, can provoke the immune system to attack a patient's own cells in the autoimmune disease lupus, and they spur formation of blood clots in the potentially lethal condition deep-vein thrombosis. NETs can also worsen arterial plaques by promoting inflammation, cell biologist Venizelos Papayannopoulos of the Francis Crick Institute in London and colleagues found in 2015. Neutrophils can even abet cancer, spurring growth of new blood vessels that feed tumors and helping the abnormal cells spread to other parts of the body.

More than 10 years ago, such disease links prompted some companies to begin to develop compounds that inhibit neutrophil elastase. Others tried to restore neutrophils' navigational abilities, which are faulty in COPD and other conditions, by blocking the protein PI3K, an enzyme involved in controlling cell movement.

More than a dozen clinical trials scrutinized these potential drugs in many conditions. The good news is that the compounds didn't cripple defenses against infections. But most of the trials found minimal benefits. As a result, several big pharmaceutical companies have given up. In 2019, GlaxoSmithKline jettisoned danirixin and nemiralisib, the two neutrophil-targeting drug candidates it had been developing for lung diseases. Merck and AstraZeneca have also recently abandoned once-promising compounds.

But researchers say there's still hope, arguing they haven't yet pinned down what doses to use, how best to deliver potential drugs, and which aspects of neutrophil biology to target. In trials for COPD and other lung disorders, Sapey notes, patients inhaled the compounds. But because most neutrophils ply the bloodstream, inhaled drugs may not reach faulty cells, she says. Nervous about side effects, investigators may also have kept doses too low.

Hematologist and oncologist Steven Pavletic of the U.S. National Cancer Institute and his colleagues think they can do better. In a phase I safety trial, Pavletic and his team have started to give larger amounts



Released by neutrophils, vesicles (yellow) carrying protein-degrading enzymes can bind to and damage collagen fibrils (blue) in connective tissue.

PHOTO: TOMASZ SZUL AND DEREK W. RUSSELL

Blunting the attack

Ongoing clinical trials aim to treat a range of diseases by targeting proteins that abet tissue damage by neutrophils. Earlier tests had reassured researchers that the strategy would not leave patients defenseless against infections.

CONDITION	TARGET	DRUG	STATUS	DRUG MANUFACTURER
ANCA vasculitis	C5a (molecule that helps switch on neutrophils)	Avacopan	Phase III completed	ChemoCentryx
Chronic obstructive pulmonary disease	CXCR2 (receptor that helps guide neutrophils to damaged tissue)	Danirixin	Phase II completed	GlaxoSmithKline
Cardiovascular disease	CXCR2	AZD5069	Phase II underway	AstraZeneca
Asthma	PI3K (protein that helps control neutrophil migration)	Nemiralisib	Phase II completed	GlaxoSmithKline
Cystic fibrosis	Neutrophil elastase (tissue-damaging enzyme)	POL6014	Phase I/II underway	Santhera Pharmaceuticals
Pulmonary arterial hypertension	Neutrophil elastase	Elafin	Phase I underway	Proteo Biotech

Published by AAAS

of the neutrophil elastase inhibitor alvelestat to patients with the lung condition bronchiolitis obliterans. The ailment strikes a significant percentage of people who receive hematopoietic stem cell transplants during cancer treatment, developing when immune cells from the transplant attack the recipient's own tissue. Neutrophils swarm into the lungs and may encourage scar tissue to build up in the bronchioles, the lungs' smallest airways, which can cause them to clog. For transplant recipients, bronchiolitis obliterans is like having an unstoppable asthma attack, Pavletic says.

He adds that alvelestat probably won't reverse bronchiolitis obliterans, but by blocking neutrophil elastase, it could stop the disease from getting worse. "Even a marginal improvement could lead to a major improvement in lung function."

Researchers are further along in evaluating a way to target neutrophils to treat a rare autoimmune disease in which the immune system produces antibodies against its own neutrophils—a condition known as antineutrophil cytoplasmic autoantibody (ANCA) vasculitis. The antibodies glom onto the cells, which then get stuck in small blood vessels and release their chemical load, leading to inflammation that can cause kidney damage and other problems. In the first year after diagnosis, patients with the disease are nine times more likely to die than people in the general population, and current treatments, which include steroids and immune-suppressing drugs, are one reason for this high mortality, notes nephrologist David Jayne of the University of Cambridge.

In a recent trial involving 331 ANCA vasculitis patients, Jayne and colleagues tested the experimental drug avacopan, which stymies C5a, a protein in the blood that helps spur neutrophils to release their inflammation-promoting contents. The results of the phase III trial, announced late last year, revealed that the drug was about 20% more likely to produce remissions after 1 year than steroids were. It improved patients' kidney function and was also less harmful than steroids. Jayne predicts avacopan will be approved by the U.S. Food and Drug Administration and "will be a complete replacement for steroids" in treatment of ANCA vasculitis.

Although many efforts to target neutrophils aim to inhibit them, Sapey and her colleagues believe rejuvenating neutrophils could help boost immune function in older people. An existing drug, the cholesterol-lowering medication simvastatin, may do the job, they found. Simvastatin had caught their attention because some evidence suggested people taking it for high cholesterol are less vulnerable to infections. When the team members exposed neutrophils to simvastatin in the lab, they found it boosts the cells' migration accuracy and improves their performance in other ways. And in a phase II trial of the drug in 62 older people with bacterial pneumonia and sepsis, Sapey and her colleagues determined that adding simvastatin to the normal treatment regimen reduced the severity of infections and allowed the patients to spend more time out of the hospital over the next year.

"That was highly unexpected and very exciting," says Sapey, whose team reported the findings last year in the *American Journal of Respiratory and Critical Care Medicine*. They are now planning a larger study of the drug, and she says it might also work against other common bacterial problems in the elderly, such as urinary tract and skin infections.

"Neutrophils are linked to many diseases that blight our population."
Elizabeth Sapey, University of Birmingham

THE THERAPEUTIC possibilities are likely to broaden as researchers learn more about the biology of neutrophils. The cells have traditionally been seen as the immune system's cannon fodder—simple, expendable killers. But neutrophils, it turns out, aren't so simple after all. "They are not merely the cells that clear microbes from infected sites," Papayannopoulos says.

"The most exciting thing is that the cells are much more heterogeneous than we thought," says immunologist Leo Koenderman of University Medical Center Utrecht in the Netherlands. With techniques such as single-cell RNA sequencing, researchers have discovered that neutrophils come in multiple varieties. And their properties can vary by time of day. In humans, the cells are much more aggressive toward pathogens at night than during daylight hours, and they crank up different genes depending on the hour.

This diversity enables the cells to specialize and take on more tasks than researchers expected. Some neutrophils have moved up the chain of command and help control the activity of other immune cells. For example, they can either spur T cells to attack pathogens or rein them in. The cells can also take on alternative roles when they enter damaged tissue. If they encounter microbes, they become fighters. But if an injury is not infected, they become healers. Chemicals they release can stimulate new blood vessels to form and spark the production of replacement cells.

Intravital microscopy, which reveals the movements of cells within the body, suggests the lives of these immune cells are eventful. Researchers long assumed that once neutrophils left the bloodstream and moved into infected or injured tissues, they would eventually self-destruct, allowing the inflammation at the site to clear. But several microscopy studies have revealed more complex migrations. In a 2011 study, for example, Anna Huttenlocher of the University of Wisconsin, Madison, and colleagues tracked neutrophils in zebrafish that had wounds on their fins. The scientists found that individual neutrophils moved into and out of a wound several times before eventually departing for good.

Now, Ferro and his colleagues are trying to interrupt one leg of the neutrophils' journey. In patients with heart disease, the cells worm into the fatty plaques lining the coronary arteries. There, they release chemicals, including neutrophil elastase, that may make these plaques more likely to fracture and spawn blood clots, which can trigger heart attacks.

The drug candidate that Ferro and colleagues are testing in people with serious plaques, AZD5069, blocks CXCR2, the receptor that helps neutrophils navigate to infected and inflamed locations. In animal tests, the compound deters neutrophils from entering sites of inflammation.

Death rates from cardiovascular diseases have been dropping for decades in many countries thanks to lifestyle changes, such as a decline in smoking, as well as drugs that lower cholesterol and combat blood clotting. But heart disease still kills more than 600,000 people in the United States every year. "There's clearly a big gap that remains in therapy for these patients," Ferro says. Within a couple of years, he hopes to know whether deflecting neutrophils can help.

Some researchers remain skeptical that the current crop of experimental neutrophil-targeting drugs will work outside certain rare diseases. The cells have multiple redundant pathways that control their activity, Koenderman notes. A neutrophil "is extremely robust," he says. The idea that a single drug could correct its misbehavior "is pretty naïve," he says.

However, researchers are already developing new approaches, including DNA-destroying enzymes that might slice up NETs and prevent blood clots. And as scientists dig deeper into the cells' biology, they may find new ways to keep these immune soldiers in check, Fessler says. "There is hope that with increasing understanding of neutrophils, we will have more sophisticated approaches down the line." ■

Published by AAAS



PHYSIOLOGY

Understanding the mother-breastmilk-infant "triad"

Breastmilk research holds important opportunities to improve maternal-child health

By **Lars Bode[1], Arjun S. Raman[2], Simon H. Murch[3], Nigel C. Rollins[4], Jeffrey I. Gordon[2]**

Breastfeeding and breastmilk exert remarkable influence on infant survival and health (*1*, *2*), including reduced risk from infections and promoting various aspects of postnatal development. The many maternal benefits include protection from breast and ovarian cancer and cardiometabolic disorders. Although the mechanisms underlying some of these benefits have been elucidated, the origins of others that have been reported, such as influence on adult IQ and later protection against obesity and diabetes, remain more obscure. Hence, timely investments in research designed to clarify the operations and biological effects of the mother-breastmilk-infant "triad," and their translation into public health, are needed.

Breastmilk does not stand alone; maternal physiology, breastmilk composition, and infant physiology are parts of a coadapting system, with variations in each influencing the trajectory of infant development and maternal health. In addition to macronutrients and micronutrients essential for child survival, breastmilk contains other myriad bioactive components, including cells and microbes (*3*, *4*). Breastmilk can be considered a "live tissue" whose composition varies between women and changes over the course of lactation. Structurally diverse human milk oligosaccharides (HMOs) represent the third most abundant nonaqueous component of breastmilk (after lactose and lipids). One

[1]Department of Pediatrics and Larsson-Rosenquist Foundation, Mother-Milk-Infant Center of Research Excellence, University of California, San Diego, La Jolla, CA, USA. [2]The Edison Family Center for Genome Sciences and Systems Biology, and the Center for Gut Microbiome and Nutrition Research, Washington University School of Medicine, St. Louis, MO, USA. [3]Warwick Medical School, University of Warwick, Coventry, UK. [4]Departments of Maternal, Newborn, Child, and Adolescent Health and Ageing, World Health Organization, Geneva, Switzerland. Email: lbode@ucsd.edu, jgordon@wustl.edu

PHOTO: FRED DUFOUR/AFP VIA GETTY IMAGES

Published by AAAS

A Rohingya Muslim refugee holds her malnourished child in Bangladesh. Better understanding of breastmilk could improve therapeutic foods to treat undernutrition.

prominent example illustrating how maternal genotype affects breastmilk composition is a single-nucleotide polymorphism that introduces a premature stop codon in the fucosyltransferase-2 (*FUT2*) gene. This mutation abolishes the ability to synthesize α(1-2)-fucosylated HMOs. The presence or absence of these HMOs creates specific maternal "lactotypes," known as secretors and nonsecretors, respectively, with the breastmilk of secretors conveying reduced risk of common forms of infectious diarrhea (*5*).

Comprehensive characterization of the components of each axis of the triad through longitudinal and cross-sectional studies of maternal-infant cohorts has expanded markedly. Increasingly, high-throughput analytical methods have been used to characterize more than 150 different HMO structures, and intra- and interpersonal variations in their representation within and across different populations (*6*). Other components of breastmilk, including compounds associated with the membrane that surrounds milk fat globules, microRNAs, and bacterial constituents, as well as antibodies and immune cells, are being actively cataloged and characterized. In addition to quantifying the products of metabolism in infants and their mothers by mass spectrometry, platforms are now available for simultaneously measuring the concentration of thousands of proteins circulating in blood that are biomarkers and regulators of numerous physiologic, metabolic, and immune processes, as well as other facets of growth and homeostasis (*7*). Furthermore, recent studies have highlighted how, with the use of culture-independent methods, features of gut microbial community development in infants and young children can be used as a readout for their nutritional status (*8*, *9*).

Although datasets pertaining to each axis are available, considerably more work is needed to quantitatively relate how environmental influences affect the triad and in turn, how variations in each of its axes influence the other (see the figure). For example, it will be interesting to discover what other maternal genetic factors affect biosynthesis of HMOs and other milk constituents. The mechanisms that link maternal nutritional status and other aspects of their physiology to breastmilk features and infant growth phenotypes are also an important issue. Additionally, which signaling pathways allow infant health status to regulate maternal biology, including breastmilk composition, should be investigated. How varied sociocultural, behavioral, and environmental factors shape and perturb the development of the triad is important to understand so that a "normal" range can be defined. Two disorders, childhood malnutrition and necrotizing enterocolitis (NEC), illustrate how a deeper understanding of the mother-breastmilk-infant triad could improve child health with potential lifelong benefits, and how some of the analytic challenges might be surmounted.

Childhood malnutrition contributes to 45% of deaths worldwide in those under the age of five; it manifests early in life and involves disruption of multiple biological systems fundamental to healthy growth, including host pathways influenced by the developing gut microbiota, which are key consumers of breastmilk constituents (*8*, *9*). One approach for obtaining new insights about disease pathogenesis is to conduct longitudinal studies of healthy and malnourished children living in areas where disease burden is high, and to comprehensively characterize the plasma proteomes, metabolomes, and developing microbial communities of malnourished infants and their healthy counterparts, their mothers' breastmilk composition, and the products of microbial HMO utilization.

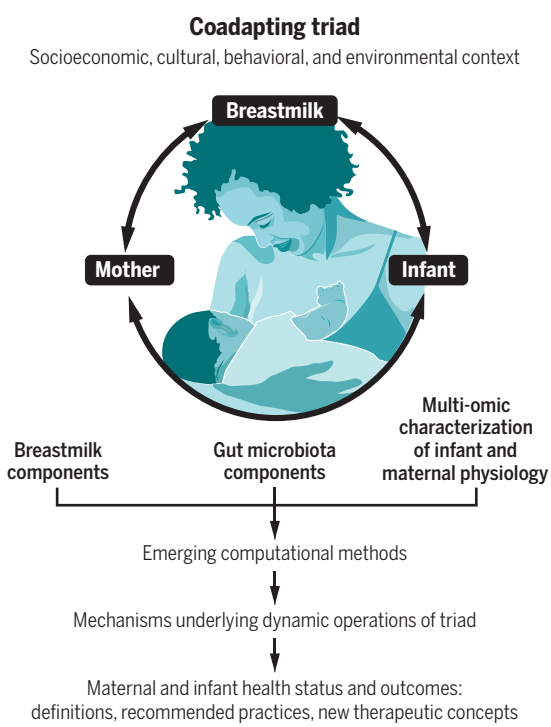
A strategy for defining functionally important interactions between triad components is to borrow from studies conducted in disparate fields where statistical covariation is used for "feature reduction." Components that covary with each other are deemed important for defining the behaviors or functions of dynamic complex systems. Applying this approach to the developing gut microbiota of healthy members of a Bangladeshi birth cohort sampled monthly from 1 to 60 months of age disclosed a network composed of 15 covarying bacterial taxa (*9*). The abundances of these taxa describe normal gut microbial community assembly in healthy members of birth cohorts residing in diverse geographic locales and are useful for quantifying the degree of impaired microbial community development in children with moderate and severe acute malnutrition.

From the limited evidence available, microbiota immaturity associated with these conditions is not repaired with standard therapeutic foods. Affordable, culturally acceptable complementary foods have been identified that in combination repair the gut microbiota of Bangladeshi children with moderate acute malnutrition toward a state resembling that of age-matched, healthy growing children. This is accompanied by increases in numerous blood plasma protein biomarkers and mediators of growth, bone formation, neurodevelopment, metabolism, and immune function (*8*, *9*).

These findings support the idea that healthy growth is linked in part to healthy development of the gut microbiota. They also raise the question of what factors shape microbial community development during the period of exclusive breastmilk feeding, and as children transition to complementary foods during the weaning period. Members of the bacterial genus *Bifidobacterium*, notably *B. longum* subsp. *infantis*, have suites of genes involved in the import and metabolism of HMOs. It is important that efforts be directed to defining the representation of *B. infantis* and other HMO-consuming bacteria in healthy versus malnourished in-

How does breastmilk affect maternal and infant health?

Mechanistic insights hold the promise of providing more informative definitions of health status, better predictions of health outcomes, improved recommendations for preventing disease, and new therapeutic targets.



GRAPHIC: N. CARY/*SCIENCE*

Published by AAAS

fants and their mothers. This information, together with characterizing the representation of genes involved in HMO acquisition and degradation in different bacterial strains cultured from these children, would allow an assessment of (i) whether and how the presence of these different organisms and their genome features correlate with maternal breastmilk composition and (ii) the degree to which products of breastmilk metabolism correlate with host features. The answers, from analyses of human biospecimens as well as animal models colonized with consortia of human gut microbes representing different stages of community assembly (*10*, *11*), could have important therapeutic implications. These include the development of new probiotic, HMO-based prebiotic and/or synbiotic (prebiotic combined with probiotic) therapies (*12*).

NEC provides a different type of opportunity to characterize the mother-breastmilk-infant triad. One of the most common and fatal gastrointestinal disorders in preterm infants, NEC develops within the first few weeks of delivery. It is characterized by destruction of the integrity of the intestinal wall, invasion of luminal bacteria, marked inflammation, and sepsis. Maternal and infant physiology are immature after preterm delivery in terms of producing and digesting breastmilk. Moreover, the use of antibiotics and other medications and interventions, when both mother and infant face serious and often life-threatening crises, further disrupts the mother-breastmilk-infant triad, including initial colonization of the infant intestine. Although breastmilk composition is not fully adapted to the physiological needs of the premature infant, breastmilk feeding, compared to enteral feeding with specialized breastmilk substitutes, reduces NEC incidence by 6- to 10-fold (*13*). The mechanisms underlying these protective effects remain largely uncharacterized.

HMOs significantly improve survival and reduce pathology in a neonatal rat model of NEC, leading to the identification of the HMO, disialyllacto-*N*-tetraose (DSLNT), as a protective factor (*14*), likely through its direct interactions with gut epithelial and immune cells. A multicenter study of mothers and their very-low-birthweight infants found that infants who developed NEC received breastmilk containing less DSLNT than infants who did not develop NEC (*15*). Proof of a causal relationship requires a randomized controlled clinical trial, which raises several challenges, including the availability of DSLNT and ethical considerations if control groups of high-risk infants were to be treated with formula alone. More generally, NEC illustrates the need to comprehensively define states of "triad immaturity." This would entail longitudinal studies of the set of features that define breastmilk given to prematurely born neonates who do and do not develop this devastating disease. It would also require a simultaneous effort to obtain comprehensive definitions of the biological characteristics of chronologically age-matched preterm infants with and without NEC, as well as of their mothers.

Mothers face a "balancing-act" between various socioeconomic, cultural, and even marketing pressures to maintain or forego breastfeeding and their motivation to provide their infants with what is best for their health and development. This balancing act is perpetuated in part by confusion surrounding the respective attributes of breastmilk versus breastmilk substitutes, with consumer understanding being heavily influenced by commercial interests. Aspirational goals include new parameters for defining health status and deeper understanding of how health outcomes are related to breastfeeding and breastmilk components. Within a risk-stratified continuum of care, knowledge of the latter has potential therapeutic implications and opportunities, personalized to the circumstances of an individual mother and her infant (*1*). Such efforts will not only provide new appreciation of the remarkable properties of nature's first food, but also serve to further develop analytic approaches that yield insights into the dynamic systems that direct infant development. ■

REFERENCES AND NOTES

1. C. G. Victora *et al.*, *Lancet* **387**, 475 (2016).
2. N. C. Rollins *et al.*, *Lancet* **387**, 491 (2016).
3. M. Witkowska-Zimny, E. Kaminska-El-Hassan, *Cell. Mol. Biol. Lett.* **22**, 11 (2017).
4. A. Boix-Amorós, M. C. Collado, A. Mira, *Front. Microbiol.* **7**, 492 (2016).
5. L. Mottram, G. Wiklund, G. Larson, F. Qadri, A.-M. Svennerholm, *Sci. Rep.* **7**, 10649 (2017).
6. L. Bode, *Glycobiology* **22**, 1147 (2012).
7. B. Lollo, F. Steele, L. Gold, *Proteomics* **14**, 638 (2014).
8. J. L. Gehrig *et al.*, *Science* **365**, eaau4732 (2019).
9. A. S. Raman *et al.*, *Science* **365**, eaau4735 (2019).
10. C. A. Cowardin *et al.*, *Proc. Natl. Acad. Sci. U.S.A.* **116**, 11988 (2019).
11. L. Feng *et al.*, *Proc. Natl. Acad. Sci. U.S.A.* **117**, 2622 (2020).
12. B. M. Henrick *et al.*, *Pediatr. Res.* **86**, 749 (2019).
13. J. Meinzen-Derr *et al.*, *J. Perinatol.* **29**, 57 (2009).
14. E. Jantscher-Krenn *et al.*, *Gut* **61**, 1417 (2012).
15. C. A. Autran *et al.*, *Gut* **67**, 1064 (2018).

ACKNOWLEDGMENTS

We thank M. Barratt and S. Moukarzel for helpful input during writing. L.B. and A.S.R. contributed equally to this work. L.B. is a coinventor on patent applications related to the use of HMOs in preventing NEC and other inflammatory diseases. J.I.G. is a cofounder of Matatu, Inc., which characterizes the role of diet-by-microbiota interactions in animal health.

10.1126/science.aaw6147

IMMUNOLOGY

Origins of peanut allergy-causing antibodies

Analysis of gut-produced antibodies raises questions about how food allergy arises

By **Duane R. Wesemann**[1] *and* **Cathryn R. Nagler**[2,3]

Some people produce immunoglobulin E (IgE) antibodies to proteins in common foods. As a result, these foods can trigger severe allergic inflammation (anaphylaxis). There are several structurally and functionally distinct antibody isotypes (IgM, IgD, IgG, IgA, and IgE), and which isotype binds to a target molecule (antigen) influences what happens next. For example, IgG that binds peanut proteins is harmless, but IgE bound to the same proteins can induce anaphylaxis and death. Therefore, how, where, and why allergen-reactive IgE is made are decades-old questions. Hoh *et al.* (*1*) found that gut tissue is a likely place for IgE development in peanut-allergic individuals. In addition, despite vast sequence possibilities, they found that many individuals share similar peanut-reactive IgE DNA sequences. This suggests that IgE antibodies in different individuals recognize peanut proteins in a similar manner, which could inform strategies for pharmacological interventions.

Antibodies are produced by cells of the B lymphocyte lineage and consist of four Ig polypeptide chains—two identical heavy (H) chains and two identical light (L) chains—and each chain has a variable (V) region and a constant (C) region. The V region forms the surface that physically binds to antigens such as peanut proteins. The C region of IgH (CH) dictates antibody

[1]Department of Medicine, Division of Allergy and Clinical Immunology, Brigham and Women's Hospital and Harvard Medical School, Boston, MA, USA. [2]Department of Pathology, Biological Sciences Division, The University of Chicago, Chicago, IL, USA. [3]Pritzker School of Molecular Engineering, The University of Chicago, Chicago, IL, USA. Email: dwesemann@bwh.harvard.edu; cnagler@bsd.uchicago.edu

Published by AAAS

function largely by triggering processes that lead to neutralization, elimination, or induction of inflammation. Assembly of multiple *IGH* gene segments through the process of V(D)J recombination results in enormous sequence diversity, particularly in the exon encoding the V region, which comprises much of the antigen binding surface. Next to the V exon are a variety of C-region exons arranged in tandem (e.g., Cμ, Cγ, Cϵ, and Cα), which define the different antibody isotypes (*2*).

Newly assembled Ig is produced as IgM. However, during an immune response, the same V region of IgH (VH) can be expressed in the context of another C-region isotype through a process called class switch recombination (CSR). This positions an alternative CH region next to the VH exon by permanent excision of the intervening DNA and associated CH-encoding exons. The position of CH exons relative to each other thus determines which IgH isotypes are available for secondary switch events. For example, an IgM-expressing B cell can switch to IgG1, and then that same IgG1$^+$ B cell can switch to IgE because Cϵ is 3′ (downstream) to Cγ1 in the *IGH* locus. However, IgE-expressing B cells cannot switch to IgG1 (or any other isotype whose CH is positioned 5′ to Cϵ). Somatic hypermutation (SHM) further diversifies V regions by introducing mutations that can enhance affinity to antigen (*3*).

The V(D)J recombination–, CSR-, and SHM-mediated processing of *IGH* enable phylogenetic mapping of how B-lineage cells and the antibodies they produce are related to one another. To gain insights into the origins of IgE production and the relationships between antibody-producing cells, Hoh *et al.* sequenced the *IGH* genes from B-lineage plasma cells in upper digestive tract tissues of 19 peanut-allergic individuals and compared them with those of nonallergic controls. They found more IgE-expressing cells in gut tissue in food-allergic individuals, confirming previous findings (*4*). Multiple clonally related VH-encoding sequences in IgE antibodies were also shared with other IgH isotypes. These findings suggest that B cells undergo CSR to IgE in the gut tissue as opposed to undergoing CSR to IgE elsewhere before migrating to the gut. This is different to the case of bone marrow, which is a major destination for antibody-producing cells after CSR elsewhere. This raises an important question: What features of the gut environment favor CSR to IgE? Moreover, because the bone marrow is a major location of antibody production, including IgE in allergic disease (*5*), the degree to which gut-derived versus bone marrow–derived IgE affects clinical disease, prognosis, and treatment approaches remains to be determined (see the figure).

Hoh *et al.* identified antibody sequences that are reactive to the peanut protein Ara h 2 (*Arachis hypogaea* allergen 2) and found groups of similar sequences among multiple individuals. Similar sequences were also found in analyses of IgE$^+$ B cells from peripheral blood in individuals with peanut allergy (*6*), further validating the concept of convergent IgE development to peanut proteins. Nonallergic individuals also had Ara h 2–reactive sequences, but only in non-IgE isotypes such as IgM, IgG, and IgA.

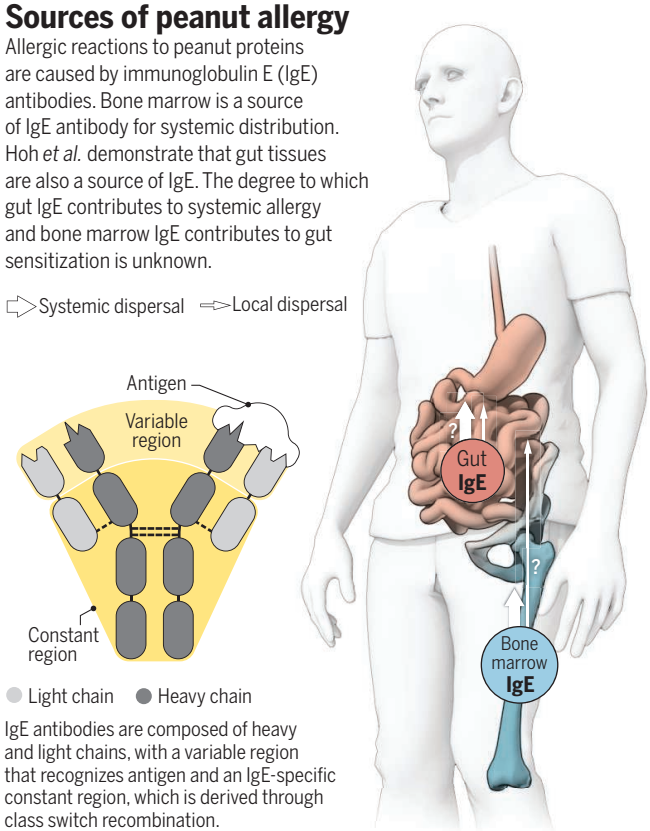
These findings highlight how antibodies that induce a food-allergic response are generated. The production of antibodies that bind peanut proteins does not seem to be the problem per se; instead, the switching of that antibody to the IgE isotype appears to be key. This is consistent with observations that humans make IgG to a variety of dietary proteins without correlation to food allergy (*7*). In addition, it is possible that IgG to food antigens may be protective from food allergy by either blocking IgE binding or otherwise interfering with IgE function (*8*, *9*). Perhaps an intervention that discourages gut IgE CSR could prevent food allergy.

The convergence of IgE sequences in multiple peanut-allergic individuals suggests that immune recognition may occur through antibody binding to a few finite regions on key proteins. In this regard, drugs that block IgE binding to these regions holds promise as a therapy in allergic disease. There is proof of principle: Two therapeutic monoclonal IgG antibodies against a cat allergen inhibited IgE binding, and treatment with the combination of these two antibodies alone was sufficient to reduce allergic symptoms in 34 cat-allergic individuals in a clinical trial (*10*). Blocking IgE to peanut antigens may be similarly efficacious.

Although seemingly innocuous, food allergens may influence the gut environment to generate conditions that induce CSR to IgE. In this regard, allergenic foods may have properties that induce allergic inflammation, as has been proposed (*11*, *12*). Understanding the influences of the gut microbiota, age of exposure, and environment on the regulation of allergic responses to food (*13*, *14*) promises to provide clues to elucidating how IgE CSR is regulated. ■

Sources of peanut allergy

Allergic reactions to peanut proteins are caused by immunoglobulin E (IgE) antibodies. Bone marrow is a source of IgE antibody for systemic distribution. Hoh *et al.* demonstrate that gut tissues are also a source of IgE. The degree to which gut IgE contributes to systemic allergy and bone marrow IgE contributes to gut sensitization is unknown.



IgE antibodies are composed of heavy and light chains, with a variable region that recognizes antigen and an IgE-specific constant region, which is derived through class switch recombination.

GRAPHIC: V. ALTOUNIAN/*SCIENCE*

REFERENCES AND NOTES

1. R. A. Hoh *et al.*, *Sci. Immunol.* **5**, eaay4209 (2020).
2. P. Tong, D. R. Wesemann, *Curr. Top. Microbiol. Immunol.* **388**, 21 (2015).
3. L. Mesin, J. Ersching, G. D. Victora, *Immunity* **45**, 471 (2016).
4. C. Caffarelli, E. Romanini, P. Caruana, M. E. Street, G. De' Angelis, *Pediatr. Res.* **44**, 485 (1998).
5. S. Asrat *et al.*, *Sci. Immunol.* **5**, eaav8402 (2020).
6. D. Croote, S. Darmanis, K. C. Nadeau, S. R. Quake, *Science* **362**, 1306 (2018).
7. J. Gocki, Z. Bartuzi, *Postepy Dermatol. Alergol.* **33**, 253 (2016).
8. O. T. Burton *et al.*, *J. Allergy Clin. Immunol.* **134**, 1310 (2014).
9. O. T. Burton, J. M. Tamayo, A. J. Stranks, K. J. Koleoglou, H. C. Oettgen, *J. Allergy Clin. Immunol.* **141**, 189 (2018).
10. J. M. Orengo *et al.*, *Nat. Commun.* **9**, 1421 (2018).
11. M. Profet, *Q. Rev. Biol.* **66**, 23 (1991).
12. N. W. Palm, R. K. Rosenstein, R. Medzhitov, *Nature* **484**, 465 (2012).
13. O. I. Iweala, C. R. Nagler, *Annu. Rev. Immunol.* **37**, 377 (2019).
14. D. R. Wesemann, C. R. Nagler, *Immunity* **44**, 728 (2016).

ACKNOWLEDGMENTS

D.R.W. is supported by the NIH (AI121394, AI139538, and AI137940), the Burroughs Wellcome Fund, and an anonymous donor. C.R.N. is supported by the NIH (AI106302, AI134923, and AI146099) and the Sunshine Charitable Foundation. C.R.N. is president and co-founder of ClostraBio, Inc.

10.1126/science.aba8974

Published by AAAS

MOLECULAR BIOLOGY

Coding functions of "noncoding" RNAs

Hundreds of RNA regions that encode microproteins are found to regulate cell growth

By **Lian-Huan Wei** and **Junjie U. Guo**

High-throughput RNA sequencing studies have revealed pervasive transcription of the human genome, which generates a variety of long noncoding RNAs (lncRNAs) that have no apparent protein-coding functions (*1*). Subsequent studies that globally monitor translation have similarly identified numerous translation events outside of canonical protein-coding sequences (*2*–*4*), suggesting pervasive translation of the transcriptome. However, only a few examples of functional peptides encoded by RNA regions previously thought to be noncoding have been reported to regulate distinct biological processes (*5*–*9*). On page 1140 of this issue, Chen *et al.* (*10*) provide evidence for an expanded repertoire of functional peptides encoded by lncRNAs and other "untranslated" RNA regions.

Sequencing of ribosome-protected messenger RNA (mRNA) fragments (RPFs) allows researchers to globally identify RNA regions that are translated (open reading frames, or ORFs). In addition to the canonical open reading frames (main ORFs) of mRNAs, RPFs have also been found in the untranslated regions (UTRs) of mRNAs and in many lncRNAs (*2*–*4*). Although some RPFs may not represent bona fide translation (*11*), the question remains whether translation of lncRNAs and UTRs is functional or represents an inconsequential amount of translation that occurs on all cytosolic 5′-capped RNAs (see the figure).

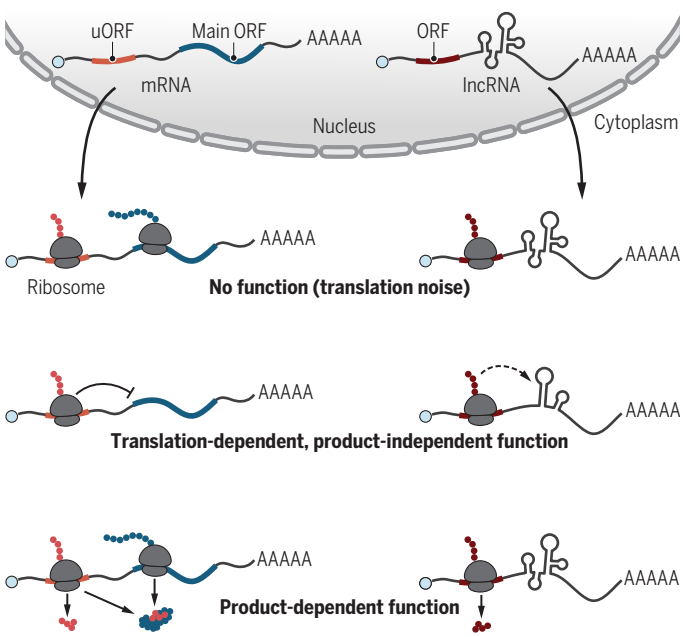
Chen *et al.* used genome-wide loss-of-function screens to systematically assess the functionality of noncanonical ORFs in cell growth. They first filtered RPFs obtained from several human cell types and identified more than 5000 previously unannotated ORFs that showed robust evidence of active translation. These newly identified ORFs include variants of canonical ORFs (e.g., canonical ORFs with an alternative initiation position), upstream ORFs (uORFs) within 5′UTRs, and ORFs within transcripts that are annotated as lncRNAs. Consistent with previous studies, these ORFs are shorter (fewer than 100 amino acids; hence, they are also called microproteins) and less conserved than canonical ORFs. They often use near-cognate translation start codons such as CUG, whereas canonical ORFs are predominantly initiated at AUG start codons. More than 200 newly identified microproteins were validated by orthogonal proteomic and peptidomic analyses in multiple human cell lines, suggesting that at least some microproteins accumulate in cells to detectable concentrations.

Using CRISPR-Cas9, Chen *et al.* disrupted each of 2353 selected unannotated ORFs and identified more than 400 ORFs that promoted cell growth in both human K562 leukemia cells and induced pluripotent stem cells. In addition to changes in cell growth, the disruption of many unannotated ORFs also caused specific changes in gene expression. Consistent with translation being essential, the authors found that start codons were critical for the functions of a few ORF-containing lncRNAs. However, among all the lncRNAs that affected cell growth when they were transcriptionally silenced by CRISPR interference, only a small subset showed consistent phenotypes when their embedded ORFs were disrupted, suggesting noncoding functions of the remaining lncRNA loci.

Peptides encoded by lncRNAs and uORFs within 5′UTRs showed specific subcellular localization and protein interactions. Notably, some uORF-encoded peptides formed complexes with the proteins encoded by the corresponding main ORFs. The functional importance of such interactions remains to be tested, as well as the generality of eukaryotic mRNAs encoding multiple subunits of a protein complex. Also unresolved is the extent to which the growth phenotypes of some uORFs may be partly due to their regulation of main ORF translation and independent of the uORF-translated peptides (i.e., translation-dependent, product-independent), which is a well-established function of uORFs (*12*). Future studies on the genetic interactions between uORFs and main ORFs within the same mRNAs should provide an answer. Analogous to the translation regulation function of uORFs, translation may also regulate the function and stability of some bona fide lncRNAs by remodeling RNA structures and/or ribonucleoprotein composition, a possibility that remains largely unexplored.

Possible functions of noncoding RNA translation

Aside from the main open reading frames (ORFs) of messenger RNAs (mRNAs), translation also occurs in upstream ORFs (uORFs) within 5′ untranslated regions (UTRs) as well as ORFs within cytosolic long noncoding RNAs (lncRNAs). These translation events may either have no function, regulate main ORF translation, regulate noncoding functions of lncRNAs, produce functional peptides that interact with main ORF-encoded proteins, or function independently.



GRAPHIC: KELLIE HOLOSKI/*SCIENCE*

Department of Neuroscience, Yale University School of Medicine, New Haven, CT 06520, USA.
Email: junjie.guo@yale.edu

Published by AAAS

The study of Chen *et al.* demonstrates the challenge of identifying microproteins by evolutionary conservation. Many short ORFs that encode conserved peptides, including some lncRNA ORFs identified by Chen *et al.*, have indeed been annotated as such in some databases. However, most microproteins found to be important for cell growth do not show strong evolutionary conservation of their amino acid sequences, as canonical proteins typically do. Perhaps not all the ORFs that regulate cell growth in vitro would have similar impact on organismal fitness (*13*). Nevertheless, extrapolating from this study, many more interesting peptides encoded by noncanonical ORFs must exist and regulate far more biological processes than currently known. Their frequent usage of non-AUG start codons may allow for translational control that is distinct from canonical ORFs.

Noncanonical translation has been linked to a variety of neurological diseases caused by the expansion of short tandem repeats in the genome (*14*). For example, expanded GGC repeats within the 5′UTR of human fragile X mental retardation 1 (*FMR1*) mRNA is translated into polyglycine by a uORF-like mechanism (*15*). It is unclear whether most repeat-associated non-AUG translation occurs this way. However, the pervasive translation of cytosolic RNAs and the widespread usage of alternative initiation codons in producing physiologically functional peptides provide a parsimonious explanation for the pathological translation events in noncoding regions. ■

REFERENCES AND NOTES

1. I. Ulitsky, D. P. Bartel, *Cell* **154**, 26 (2013).
2. A. A. Bazzini *et al.*, *EMBO J.* **33**, 981 (2014).
3. N. T. Ingolia *et al.*, *Cell Rep.* **8**, 1365 (2014).
4. Z. Ji, R. Song, A. Regev, K. Struhl, *eLife* **4**, e08890 (2015).
5. D. M. Anderson *et al.*, *Cell* **160**, 595 (2015).
6. T. Kondo *et al.*, *Nat. Cell Biol.* **9**, 660 (2007).
7. A. Pauli *et al.*, *Science* **343**, 1248636 (2014).
8. E. G. Magny *et al.*, *Science* **341**, 1116 (2013).
9. S. R. Starck *et al.*, *Science* **351**, aad3867 (2016).
10. J. Chen *et al.*, *Science* **367**, 1140 (2020).
11. M. Guttman, P. Russell, N. T. Ingolia, J. S. Weissman, E. S. Lander, *Cell* **154**, 240 (2013).
12. T. G. Johnstone, A. A. Bazzini, A. J. Giraldez, *EMBO J.* **35**, 706 (2016).
13. W. F. Doolittle, T. D. Brunet, S. Linquist, T. R. Gregory, *Genome Biol. Evol.* **6**, 1234 (2014).
14. F. B. Gao, J. D. Richter, D. W. Cleveland, *Cell* **171**, 994 (2017).
15. M. G. Kearse *et al.*, *Mol. Cell* **62**, 314 (2016).

ACKNOWLEDGMENTS

We thank A. Giraldez, I. Ulitsky, N. DeRuiter, and other members of the Guo lab for comments. J.U.G. is a NARSAD Young Investigator and a Klingenstein-Simons Fellow in Neuroscience. Our work is supported by the Yale Scholar in Neuroscience Fund, the Ludwig Family Foundation, an NIH New Innovator Award (DP2 GM132930), and the Muscular Dystrophy Association (MDA602934).

10.1126/science.aba6117

PHOTO: RAY ADKINSSS

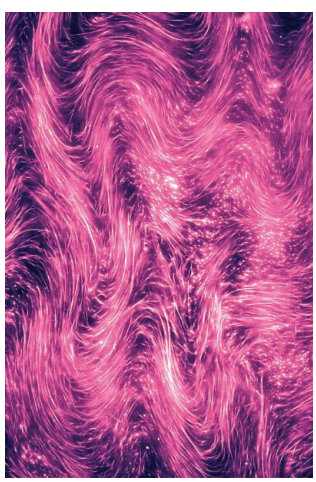
LIQUID CRYSTALS

Rings rule three-dimensional active matter

Dynamical defect networks are imaged in viral-particle liquid crystals driven by biomotors

By **Denis Bartolo**

We are active matter, in that we move and deform on our own without resorting to external forces. During the past 10 years, fluids and soft solids have been turned into active matter animated by spontaneous flows and deformations, usually by seeding a fluid with self-propelled units that convert chemical or electric energy into directed motion. Animated by spontaneous flows and deformations driven from within, active fluids are usually powered by dispersing active particles that self-assemble into coherent dynamical structures. Active materials—including polymer gels, liquid emulsions, or colloidal suspensions with mesmerizing emergent dynamics (*1*–*3*)—have been mostly limited to two-dimensional (2D) materials. However, thin films are unlikely to host more than a small fraction of the full complexity of active matter. On page 1120 of this issue, Duclos *et al.* (*4*) report the synthesis and the observation of 3D active liquid crystals (see the image) and elucidate the elementary excitations responsible for their complex inner dynamics.



The active 3D nematic was imaged with wide-field fluorescent microscopy.

Nematic liquid crystals are formed of elongated molecules or colloidal particles that fluctuate in their orientation, but on average, all locally point along the same direction, described as the director. In ordinary passive nematics, shear deformations are unhindered as in normal fluids, but bending deformations are suppressed by elastic stresses in favor of homogeneously aligned states (see the figure, top). In stark contrast, when a nematic includes active components that power internal stresses that distort the fluid, the smallest bending deformations can be exponentially amplified (see the figure, top). This generic instability yields unsteady bulk flows casually termed "active turbulence" (*5*). Unlike turbulence in normal fluids, the chaotic flows of active nematics are devoid of self-similar structures (ones that repeat identically at all scales). The flows originate from the formation and disappearance of vortices that have a well-defined size set by the competition between active and elastic stresses.

The spatial structure of 2D chaotic vortices is easily inferred from a static picture of the nematic director that defines its local orientation. In 2D active nematic films, each vortex is centered on pointwise singularities of the director sketched in the figure, top. Nematic defects are a signal of a finite local winding of the director field and interact at a distance, much like electric charges. Topological charge being a conserved quantity, no net charge can develop in a defect-free nematic, and in two dimensions, no smooth deformation can morph a +½ into a −½ charge. This topological constraint implies that active stresses can only nucleate pairs of oppositely charged defects in response to bending instabilities, and in two dimensions (see the figure, top).

The mapping of the unsteady and heterogeneous flows of active nematics on the motion of interacting charged particles was the key to understanding 2D active turbulence. However, in 3D liquid crystals, the nature of the fundamental excitations is drastically different (*6*). The director field in 3D nematics can host spatially extended topological excitations in the form of disclination lines and loops. Although these singularities were vastly explored in passive systems, they remained out of reach of active matter until the study of Duclos *et al.*, who assembled liquid crystals from micrometer-long filamentous bacteriophage viruses instead of

Laboratoire de Physique, Ecole Normale Supérieure de Lyon, Université de Lyon, France. Email: denis.bartolo@ens-lyon.fr

Published by AAAS

the more typical small molecules that from nematic phases.

These slender biological colloids provide a prototypical nematic phase at room temperature (*7*). The authors built on earlier works from Dogic and co-workers and dispersed a small fraction of cross-linked microtubules and molecular motors extracted from eukaryotic cells into this liquid crystal to create an active material (*8*). When fueled with adenosine triphosphate, the molecular motors elongated the microtubule bundles, which in turn generated active stresses that drove bending instabilities and bulk flows throughout the entire sample.

The authors then solved the second formidable challenge of observing the inner chaotic structure of this chimera of nematic molecules and motors. Elucidating the spatiotemporal structure of a 3D active nematic must overcome two conflicting constraints. One is imaging the nematic orientation from micrometer to millimeter scales, which is a time-consuming task, and the other is computing the spatial-orientation maps with high temporal resolution. The optical transparency of the active material made it possible to resolve this technical conflict by taking advantage of multiview light-sheet microscopy (*9*). This high-speed, high-resolution evolution of selective-plane illumination microscopy provided the quantitative measurements of the local director field over the entire volume of a 3D active material. The potential of this state-of-the-art experiment can be immediately grasped from the authors' supplementary movies, which also illustrate the much faster flows in active nematics.

As the molecular motors drove activity, a living network of disclinations emerged and constantly rewired its connectivity (see the figure, bottom left, which reveals the regions of space where the active-nematic director is singular or discontinuous). These living networks of singularities do not reflect built-in heterogeneities of the nematic structure. Duclos *et al.* instead found that the fundamental excitations of 3D active nematics are disclination loops that can nucleate, shrink, open, and merge to form spatially extended structures out of smooth and homogeneous regions of space (see the figure, bottom right). A careful analysis of the nematic orientation around the singular loops revealed that two ring-shape excitations chiefly rule the emergent distortions in the liquid crystal.

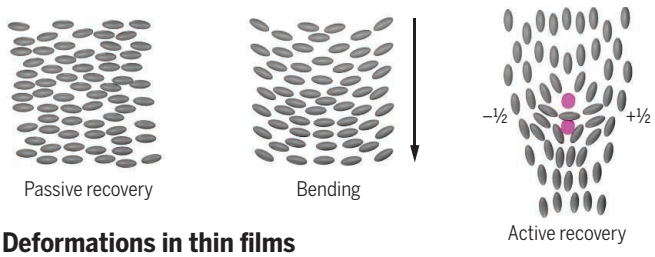
Both families of disclination loops are topologically neutral but are at the core of geometrically distinct textures. Wedge-twist loops connect sections of spaces hosting the familiar +½ and −½ defects found in 2D nematics (see the figure, bottom right). This continuous connection is made possible by a smooth 3D rotation of the nematic units along the loop. At mid-distance between the two planar wedges, the variations of the director around the centerline of the disclination line forms the equivalent of a Möbius strip, a one-sided shape that can be visualized by taping together the ends of a paper band after applying a half-turn twist (*10*).

The second and most abundant ring-shape singularities are pure-twist loops along which Möbius conformations encircle the entire defect line. Comparisons with numerical resolutions further confirmed these observations and established that the two elementary ring singularities originate from activity-induced flows, so that active hydrodynamic theories delivered compelling accuracy. However, 3D active turbulence cannot be reduced to interacting-particle models. Quantitative connections between defect topology, loop geometry, and flows are only emerging and remain to be elucidated.

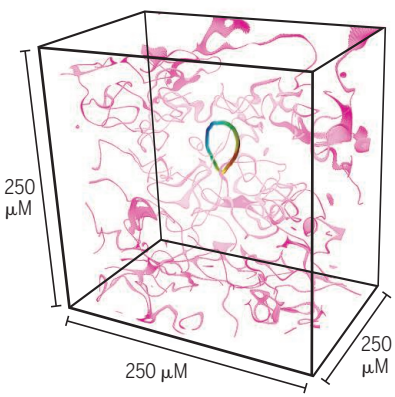
In a field dominated by numerical simulations and theory, Duclos *et al.* offer a formidable experimental platform with which to gain a deep insight in active matter. One can envision the synthesis of active smectics (that have a layered structure) or chiral nematics that have no 2D counterpart. Another appealing prospect would be manipulation of disclination networks around solid inclusions. Particle-laden liquid crystals are not bound to hosting only neutral topological excitations. For example, isolated point charges exist in three dimensions, such as hedgehogs, in which the director orientations resemble hedgehog spikes. Activity could be put to work to dynamically twist, braid, and knot disclination lines or to couple them to point defects not yet observed in the experiments of Duclos *et al.* (*6*, *11*). The number of opportunities delivered by the combination of a versatile active material and a state-of-the art observation tool seems virtually unlimited. Last, the production of actual volumes of synthetic active nematics is a major milestone on the route toward practical application of smart active materials. ■

Topological defects in active liquid crystals

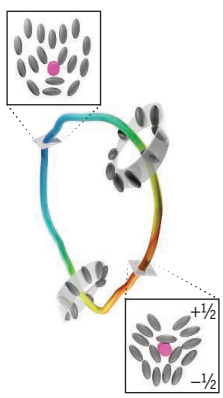
In active matter, internal molecular motors can drive fluid or particle motion and amplify responses to external stimuli such as bending forces. Most examples have been thin films, but Duclos *et al.* now report three-dimensional (3D) active matter, a viral particle liquid crystal (LC) driven by embedded microtubule networks.



Deformations in thin films
Bending a nematic LC (middle) distorts the molecular alignment. In a passive nematic (left), the orientation along the director simply relaxes back. In an active LC (right), distortions are exponentially amplified and create pairs of +½ and −½ topological defects.



Deformations in 3D LCs
Duclos *et al.* used high-resolution microscopy to image the director field. They located the extended defects (the linear structures) formed by internally driven bending instabilties.



Defect connections
The wedge-twist loop connects +½ and −½ defects like a Möbius strip. This smooth evolution can only occur in 3D materials and not in thin films.

REFERENCES AND NOTES

1. M. C. Marchetti *et al.*, *Rev. Mod. Phys.* **85**, 1143 (2013).
2. J. Zhang, E. Luijten, B. A. Grzybowski, S. Granick, *Chem. Soc. Rev.* **46**, 5551 (2017).
3. A. Doostmohammadi, J. Ignés-Mullol, J. M. Yeomans, F. Sagués, *Nat. Commun.* **9**, 3246 (2018).
4. G. Duclos *et al.*, *Science* **367**, 1120 (2020).
5. L. Giomi, *Phys. Rev. X* **5**, 031003 (2015).
6. G. P. Alexander, B. Gin-ge Chen, E. A. Matsumoto, R. D. Kamien, *Rev. Mod. Phys.* **84**, 499 (2012).
7. Z. Dogic, S. Fraden, *Curr. Opin. Colloid Interface Sci.* **11**, 47 (2006).
8. T. Sanchez, D. T. N. Chen, S. J. DeCamp, M. Heymann, Z. Dogic, *Nature* **491**, 431 (2012).
9. U. Krzic, S. Gunther, T. E. Saunders, S. J. Streichan, L. Hufnagel, *Nat. Methods* **9**, 730 (2012).
10. Y. Bouligand, *J. Phys. (Paris)* **35**, 215 (1974).
11. U. Tkalec, M. Ravnik, S. Čopar, S. Žumer, I. Muševič, *Science* **333**, 62 (2011).

10.1126/science.aba5319

GRAPHIC: A. KITTERMAN/*SCIENCE*

Published by AAAS

RETROSPECTIVE

Frank Press (1924–2020)

Policy adviser and National Academy of Sciences president

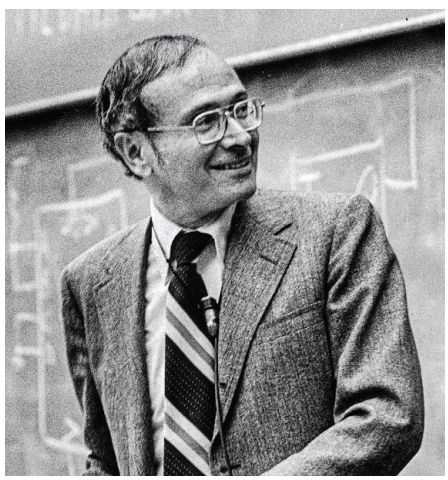
By **Marcia McNutt**

Frank Press, geophysicist and two-term president of the National Academy of Sciences (NAS), died on 29 January. He was 95. This soft-spoken son of Jewish immigrants advised four U.S. presidents, built institutions to prominence, and provided the scientific guarantee for the nuclear test ban treaty. No scientist had more impact on the American science-policy interface in the late 20th century.

Born in Brooklyn, New York, Press earned his bachelor's degree in physics from City College of New York before completing a Ph.D. in geophysics at Columbia University with the famed geophysicist and oceanographer Maurice "Doc" Ewing in 1949. Press was appointed to the faculty of Columbia, where he developed the Press-Ewing seismometer and cofounded the Lamont Geological Observatory (now the Lamont-Doherty Earth Observatory). In 1955, he was recruited to the Seismological Laboratory at the California Institute of Technology (Caltech), where just 2 years later he succeeded its founder, Beno Gutenberg, to become the director, leapfrogging more senior seismologists. As a member of the international "Conference of Experts" in Geneva in 1958, Press convinced world leaders that a worldwide seismic network could be designed to monitor compliance with a nuclear test ban treaty. This assurance that such a treaty could be verified was instrumental to its ultimate success. At Caltech, Press championed the use of computers to digitize the increasing volume of seismic data. Along with colleagues, he used this processing power to make the first observational detection of the excitation of Earth's normal modes from the 1960 Chilean earthquake.

In 1965, the Massachusetts Institute of Technology (MIT) recruited Press to head the Department of Geology and Geophysics. Press transformed the classical department into a modern-day Department of Earth and Planetary Sciences (now known as the Department of Earth, Atmospheric, and Planetary Sciences), addressing the cutting-edge issues of the day. For Neil Armstrong's first walk on the Moon, Press designed a seismic experiment to passively detect moonquakes and asteroid impacts. The experiment returned the first information on the internal structure of the Moon and proved this concept for probing planetary interiors. The Joint Program between MIT and the Woods Hole Oceanographic Institution that educates graduate students in ocean sciences and engineering is one of Press's more successful innovations during his MIT years.

President Jimmy Carter appointed Press as his science adviser and director of the Office of Science and Technology Policy in 1977. By that time, Press was no stranger to Washington, D.C., policy circles. He had already served 3 years on the President's Science Advisory Committee under John Kennedy and Lyndon Johnson and 6 years on the National Science Board under Richard Nixon. While in the White House, he championed federal investment in research and international cooperation. He created the first opportunities for Chinese students to study at U.S. universities, a cohort that grew to 100,000 young scholars in just 5 years.



In 1981, Press was elected president of the NAS. Despite what the research community viewed as the Reagan administration's assaults on science budgets, science-based policy, and the environment, Press managed to avoid politicizing the NAS and deftly piloted its advisory mission to new prominence by supplying unassailable advice based on science. For example, the Supreme Court ruled in the late 1980s that requiring creationism to be taught in public schools along with evolution was unconstitutional under the First Amendment, influenced by a NAS publication (*Science and Creationism*, 1984) that pointed out that creationism is not supported by scientific evidence. In an environmental win, a report on acid rain (*Acid Deposition: Atmospheric Processes in Eastern North America*, 1983) led the Reagan administration to cap the emissions of nitrogen dioxide. A year later, Congress amended the Clean Air Act to address sulfur dioxide emissions. Press was also a defender of the social sciences, stating that their research is evidence based and that they belong in the NAS.

Two high-profile consensus reports changed the course of the nation during Press's NAS tenure. *Confronting AIDS* (1986) spurred a reluctant administration to action to prevent HIV infections from becoming a nationwide public health epidemic. Within a few years, several African nations that did not act saw life expectancy fall. In 1988, *Mapping and Sequencing the Human Genome* launched a project that spawned multibillion-dollar industries and has contributed immeasurably to human health. In 2000, recognizing that Press had positioned the NAS as the most trusted adviser in science for policy, the NAS honored him as its first-ever "president emeritus."

After his retirement from NAS in 1993, Press founded the Washington Advisory Group (WAG). WAG worked with, among others, the King Abdullah University of Science and Technology. Press and colleagues helped Saudi Arabia develop a first-class research university.

When Frank Press talked, people listened. I was one of those people. I was the final hire into "the department that Frank built" at MIT before he left to head the NAS. Later, he helped recruit me to lead the Monterey Bay Aquarium Research Institute for an idyllic dozen years, where he served on the board. His office was my first stop for advice after being asked to lead the U.S. Geological Survey in 2009. I was wavering on accepting the Washington, D.C., position because it would require a long separation from my family in California. When Press learned that I would also be science adviser to the secretary of the interior, he was adamant that I accept. Press saw an important opportunity to ensure that science would have a direct route into Cabinet-level decisions. He made me realize that choices were no longer about me but rather what was best for the nation.

I also followed Press's advice to benefit from the fresh perspectives of new colleagues and a new mission by changing positions frequently. I could not be more fortunate to have had such an amazing mentor choose me. His passing is a loss not just for the nation but for the many he inspired. ■

President of the National Academy of Sciences, Washington, DC, and chair of the National Research Council of the National Academies of Sciences, Engineering, and Medicine, Washington, DC. Email: mmcnutt@nas.edu

PHOTO: COURTESY MIT MUSEUM

10.1126/science.abb2626

Published by AAAS

POLICY FORUM

RESEARCH ETHICS AND LAW

Overcoming obstacles to experiments in legal practice

The biggest ethical concern is failing to seek reliable evidence to guide the legal profession

By **H. Fernandez Lynch,[1] D. J. Greiner,[2] I. G. Cohen[3]**

The importance of evidence-based policy rooted in experimental methods is increasingly recognized, from the Oregon Medicaid experiment to the efforts to address global poverty that were awarded a 2019 Nobel Prize. Over the past several decades, there have been attempts to extend this scientific approach to legal systems and practice. Yet, despite progress in empirical legal studies and experimental social policy research, judges, lawyers, and legal services providers often fail to subject their own practices to empirical study or to be guided by empirical data, with a particular aversion to randomized controlled trials (RCTs) (*1*). This is troubling, as many questions fundamental to legal practice and those it affects, such as allocation of attorney services, bail decisions, and use of mandatory mediation, could and should be informed by a rigorous evidentiary foundation. Although there are practical obstacles to undertaking legal practice RCTs, they have also been stymied by cultural barriers within the legal profession. Whereas medical practitioners are expected to subject their practices to randomized study and rely on the data produced, the default in legal practice is to rely on experience, common wisdom, and professional judgment, often in settings in which clients face constraints on their freedom. To address ethical concerns stemming from this cultural difference, we draw on lessons from biomedical and policy research, as well as experiences of the Access to Justice Lab (A2JL), a leading institution promoting the use of RCTs to inform legal practice.

RCTs in law face funding challenges, a dearth of lawyers trained in experimental methods, and blanket roll-out of new laws and legal interventions across entire populations in a manner that often precludes randomization. But the most fundamental challenges are ethical. When field RCTs of legal practice interventions have been proposed, practitioners have sometimes raised concerns about violating both perceived professional obligations and the individual rights of research subjects. Institutional review boards (IRBs), responsible for assessing the permissibility of research, also sometimes exhibit difficulty applying familiar research ethics concepts to nonmedical settings, a phenomenon exhibited toward social science research more broadly. Ethical objections have posed real barriers to A2JL's work (see the table), which have occasionally been resolved through education and negotiation, but have more often led to abandonment of important, ethical studies.

There have been growing calls to systematize and expand efforts to subject legislative and regulatory interventions to randomized experimentation (*2*), as well as increasing attention to the ethics of policy experiments more broadly (*3*–*6*). We build on this work, but because our goal is to highlight objections rooted in concerns over randomization in lieu of the individual judgments of legal professionals, the principles of biomedical research ethics are the best starting point for potential solutions. The medical profession has been able to manage many ethical concerns raised by RCTs and to create an evidence-based culture, a portent of what the legal profession could achieve. The ethics of clinical research have also developed in a way that addresses the traditional fiduciary obligations of physicians, whereas perspectives regarding the obligations of legal practitioners seem to be generating erroneous resistance to legal practice RCTs.

Although there are differences between medical and legal settings, including the role of democratic authority, protected legal rights, and the unavoidably coercive nature of the criminal justice system, many ethical challenges facing field RCTs of legal practice interventions, including those related to randomization and consent, are familiar in biomedical research. Therefore, we seek to apply lessons from that context to law—and to identify novel ethical considerations where further attention is warranted. Research ethics regulations will not always apply to legal practice RCTs, depending on institutions and funding. Nonetheless, public trust, researcher obligations, and pragmatic considerations all demand that ethical principles be both clarified and upheld.



PHOTO: ICEDMOCHA/SHUTTERSTOCK

EVIDENCE-BASED LEGAL PRACTICE

The core idea of evidence-based medicine is that because few medical interventions are so obviously safe and effective that they can be adopted without testing, patient care should be guided by scientific evidence. Although observational studies and historical controls can be superior to anecdote, randomization and contemporaneous controls help minimize confounders and support causal conclusions. As a result, RCTs are rightly regarded by the medical profession as essential to quality care, albeit with their own methodological constraints.

These same concepts apply to legal practice but have not been widely endorsed by the legal profession, even when stakes are high, with implications for freedom (e.g., incarceration), safety (e.g., protection from domestic violence), and access to resources essential to fundamental human needs (e.g., legal assistance in securing government benefits). Although legal practitioners may rely on certain guidelines when available, these

[1]Department of Medical Ethics and Health Policy, Perelman School of Medicine; Leonard Davis Institute of Health Economics, University of Pennsylvania, Philadelphia, PA, USA. [2]Access to Justice Lab, Harvard Law School, Cambridge, MA, USA. [3]Petrie-Flom Center for Health Law Policy, Biotechnology, and Bioethics, Harvard Law School, Cambridge, MA, USA. Email: lynchhf@pennmedicine.upenn.edu

Published by AAAS

Examples of legal practice research questions, RCT designs, objections, and replies

QUESTION	STUDY DESIGN	OBJECTIONS	RESPONSE
Does availability of risk assessment scores improve judicial bail decisions?	Randomize arrestees as to whether bail judge receives their risk assessment score	Too much at stake (freedom v. incarceration)	High stakes demand empirical study
			Equipoise as to utility of risk assessment scores
		Voluntary consent from arrestees not practicable	Either practice (scores or no scores) is permissible without consent outside research; no entitlement to either policy
Can legal professionals effectively allocate scarce resources for greatest benefit?	Randomize criminal defendants to have public defender decide whether to assign a social worker or allocate services by some other process	Unfair to defendants who would have been assigned a social worker but for the study	Scarcity of social workers
			Equipoise as to quality of attorney allocation decisions
			Either practice (public defender triage or other approach) permissible outside research; no entitlement to either a particular triage process or social work assistance
Does a combative litigation style produce superior client results compared to a facilitative, deal-making style?	Randomize whether legal aid attorneys in summary eviction cases litigate aggressively (e.g., demand jury trials, file motions, make ambitious settlement demands) or nonaggressively	Contrary to responsibility of attorneys to use their best professional judgment about ideal strategy for each individual case	Equipoise as to ideal litigation strategy
			Either practice permissible outside research; both strategies within the "standard of care"

are also often not evidence-based, being instead informed by politics or the subjective collective wisdom of professional authorities. Even when evidence is available from one of the few dozen legal practice RCTs conducted in the United States to date, and even when that evidence fails to support the use of interventions that are costlier than their alternatives, it has not been used to change practice (*1*). When aspects of legal practice are rooted in philosophical and normative claims about rights and interests, empirical study may have little to add. But when interventions aim to achieve certain instrumental outcomes, as is often the case, evidence is critical (*1*, *2*).

RANDOMIZATION

One commonly articulated objection to legal practice RCTs is that it is unethical to randomize legal interventions in a way that temporarily precludes individualized professional judgment. For example, in objecting to a proposed A2JL study in which tenants facing eviction litigation would be randomized to participate in a mandatory pretrial settlement conference or proceed without one, local legal services providers argued on the basis of their anecdotal experience that settlement conferences assist in keeping low-income tenants in their homes, despite reason to question that assumption. Similarly, organizations running charitable bail funds have refused to discuss RCTs, even when they lack sufficient resources to assist all eligible arrestees, arguing that because they "already know" the difference it makes to have bail posted, it is wrong to randomize "lifesaving" legal "treatments."

These examples are indicative, in part, of the legal profession's lagging understanding of foundational principles of research design and ethics. Similar objections have long been considered resolved in the realm of clinical research, where one might also be concerned that randomized participants could be harmed by the denial of some perceived benefit in a way that violates the physician's professional obligation to provide individualized care (*7*). However, an RCT can be ethical—and perhaps ethically mandatory—when there is sufficient professional uncertainty, or "equipoise," regarding the safety or efficacy of the experimental intervention compared to the standard of care. In these cases, randomization violates no professional obligation because it will not result in practitioners knowingly exposing participants to harm.

In addition to the culture shift needed in law to adopt this view, it is also essential to challenge faulty moral intuitions exhibited in the legal profession and elsewhere that it is permissible to roll out an untested intervention across an entire population, but not to randomize population groups to rigorously examine the intervention's effect (*8*). Moreover, because resolving extant uncertainty is essential to the professional's fiduciary obligation to provide the best care or services, it would be logically incoherent to refuse to subject unproven approaches to study unless or until evidence is produced to challenge their effectiveness.

Even when there is relative certainty as to which intervention to prefer in ideal circumstances, practical constraints may render that intervention neither attainable nor sustainable for some or all of the relevant population (*5*, *9*). In such cases, researchers should work to resolve "policy equipoise" (*5*), developing evidence needed to inform open questions, such as how to optimally allocate the intervention and whether a less resource-intensive approach might suffice. Doing this work through RCTs is methodologically ideal and in many cases ethically permissible. However, one further consideration particularly relevant to legal practice interventions is that the ethical permissibility of an RCT that fails to provide all subjects with the preferred intervention depends on the absence of legal or ethical entitlement to that intervention. Although patients may have ethical entitlements, they have few legal entitlements to medical services, at least in the United States. Those affected by legal practice interventions may have stronger claims.

Consider an offer of representation by a lawyer. This is a federal constitutional entitlement in the United States only for serious criminal charges and a few other narrow matters; in these contexts, it would be legally impermissible to withhold the offer from some individuals, even for research purposes. However, there are other circumstances in which an individual may be expected to benefit from an offer of legal representation without being legally entitled to it. In the face of scarcity, a legal clinic could reasonably randomize similarly situated individuals to receive either an offer of traditional representation, an offer of self-help resources only, or no offer at all to research how to maximize benefits across the population. Individuals randomized without entitlement have either not been harmed, because they might not have received the benefit outside the RCT, or have not been unreasonably harmed, because even if they would have received the benefit, they lack a greater claim to it than others facing similar need.

VOLUNTARY CONSENT

Other objections to legal practice RCTs are based on concerns that RCTs may be inherently coercive. Perceived or actual coerciveness might stem from the involvement of

Published by AAAS

lawyers, who like physicians are often in a position of power compared with prospective subjects; the provision of desired legal services only to study participants (or select participants); or the constraints on freedom present in criminal settings.

Concerns about professional power dynamics can be addressed in part by emphasizing, where true, that participation in research is voluntary and refusal will involve "no penalty or loss of benefits to which the subject is otherwise entitled" (*10*). Nonetheless, potential subjects may feel pressured when research is the only way to access a desired intervention, a concern that has been a persistent point of confusion in research ethics. This pressure is not coercive absent entitlement to the desired intervention (*11*), and it is not unduly influential if the risks of participation are reasonable and not so great as to outweigh the benefits of the desired intervention (*12*). In fact, where research risks are reasonable and there is the prospect of direct benefit to subjects, one might worry less about constraints on voluntary consent because research participation will be objectively reasonable.

This is important because one distinctive feature of legal practice RCTs is the inherent involuntariness of some aspects of the legal system, particularly in the context of criminal justice. Unlike medicine, where there is an expectation of informed consent to justify interventions on a patient's body, individuals who have been arrested, are facing prosecution, or have been convicted have little control over what happens to them. At least partly in recognition of these circumstances, U.S. research regulations demand special protections for individuals involuntarily confined or detained in penal institutions (*10*), which can also guide research in other legal settings.

To the extent voluntariness concerns persist, further analysis is warranted to evaluate whether securing traditional research consent is a reasonable expectation for all legal practice research interventions. Current norms permit consent waiver only for minimal risk research that would be impractical to conduct if consent were required (*10*). This would likely cover RCTs assessing mandatory mediation or online dispute resolution, for example, but "minimal risk" is challenging to define and the subject of intense debate in research ethics, especially when evaluating practices that may be part of the existing standard of care, despite remaining unproven (*13*). And at least some legal practice interventions will pose greater than minimal risk, such as a heightened possibility of incarceration (e.g., for arrest, bail, and sentencing interventions) or inability to access government benefits (e.g., for comparisons of self-help models versus assistance of counsel). The response to concerns about voluntary consent must not be to inhibit legal practice RCTs, however, because without them, potentially harmful legal interventions may be adopted and potentially beneficial interventions may be dismissed without either evidence or consent (*8*).

Similar questions arise in circumstances in which it may be infeasible to secure individual consent, a challenge faced across medical, policy, and legal practice intervention research. For example, it may not be possible to study an intervention without mandatory application to some group, such as use of a sentencing algorithm to substitute for judicial discretion. Similarly, use of randomized cluster design can sometimes preclude individual consent, such as when different legal services clinics are each randomized to offer only a single approach, removing choice from each clinic's clients unless they seek services elsewhere. It is important to recognize that these interventions could be implemented without consent outside a research context (and sometimes already have been), which may render the inability to secure research consent less ethically concerning (*2*, *8*). Nevertheless, alternative protections may be appropriate. For example, the data collection required for research purposes should not unduly infringe participants' autonomy and privacy rights (*6*), and research should avoid disproportionately testing interventions designed to justify reducing resources allocated to vulnerable populations (*14*).

BYSTANDERS

A final concern that may arise for legal practice RCTs, as well as other types of studies, centers on their potential impact on both incidental bystanders and intended third-party beneficiaries, an understudied area in research ethics generally (*15*). For example, research interventions regarding bail decisions might be intended to achieve public safety goals, to advance the interests of arrestees, or both. Where third parties are affected by research but not directly intervened upon, there are further questions of consent. They may not be individually identifiable in advance (e.g., the future victim of an arrestee released on bail due to a study intervention), making their consent impossible. Even if bystanders are identifiable, however, it is unclear that they should be given the authority to withhold consent and preclude research that offers the prospect of direct benefit to research subjects and future individuals like them (e.g., arrestees that may benefit from a bail decision). Yet, to the extent bystanders face research risks, those risks seem worthy of consideration when assessing a study's ethical permissibility. Conversely, although we traditionally consider risks to research subjects, where research interventions are intended to produce social rather than individual benefit, and the intervention does not entail any breach of a subject's rights or entitlements, it is not clear that subjects should be allowed to withhold their consent. Although IRBs are directed to consider benefits that extend beyond study participants when assessing a study's risk-benefit profile, they have not typically considered risks to bystanders. This area deserves further attention in both law and medicine.

CONCLUSION

Although objections to legal practice RCTs often have been framed in ethical terms related to randomization and consent, the biggest ethical challenge lies in failing to seek reliable answers to guide the legal profession. The profession—and IRBs—should embrace RCTs, while being thoughtful about their methodological limits and devoting further attention to unresolved issues, including which legal interventions should be viewed as entitlements; when research consent should be required; how to address bystander interests; which RCTs should be prioritized; when it may be appropriate to proceed with a promising intervention in the absence of confirmatory evidence; and how to best engage with communities that would be affected by this research. ■

REFERENCES AND NOTES

1. D. J. Greiner, A. Matthews, *Annu. Rev. Law Soc. Sci.* **12**, 295 (2016).
2. M. Abramowicz, I. Ayres, Y. Listokin, *U. Penn. Law Rev.* **159**, 929 (2011).
3. A. S. Venkataramani, K. Underhill, K. G. Volpp, *JAMA* **323**, 21 (2020).
4. World Health Organization, Ethical considerations for health policy and systems research (2019); www.who.int/alliance-hpsr/resources/publications/ethical-considerations-hpsr/en/.
5. D. MacKay, *Bioethics* **32**, 59 (2018).
6. D. MacKay, A. Chakrabarti, *Public Health Ethics* **12**, 188 (2019).
7. S. Joffe, F. G. Miller, *Nat. Rev. Clin. Oncol.* **9**, 230 (2012).
8. M. N. Meyer *et al.*, *Proc. Natl. Acad. Sci. U.S.A.* **116**, 10723 (2019).
9. R. A. Crouch, J. D. Arras, *Hastings Cent. Rep.* **28**, 26 (1998).
10. 45 C.F.R. 46.116 (2018).
11. A. Wertheimer, *Coercion* (Princeton Univ. Press, 2016).
12. E. J. Emanuel, *Am. J. Bioeth.* **5**, 9, discussion W8-11, W17 (2005).
13. S. Joffe, A. Wertheimer, *Ethics Hum. Res.* **36**, 16 (2014).
14. J. Blustein, *J. Policy Anal. Manage.* **24**, 824 (2005).
15. S. K. Shah *et al.*, *Science* **360**, 158 (2018).

ACKNOWLEDGMENTS

Some of Access to Justice Lab's work is supported by Arnold Ventures, The Chan Zuckerberg Initiative, The Charles Koch Foundation, The NOMIS Foundation, and The Robert Wood Johnson Foundation. Support for elements of this article was provided in part by The Pew Charitable Trusts. The opinions, findings, and conclusions or recommendations expressed here do not necessarily reflect the views of any of the entities listed. H.F.L. is funded by the Greenwall Foundation as a Faculty Scholar.

10.1126/science.aay3005

Published by AAAS



Increasingly powerful beasts emerge from *Oceans*' deeper waters.

EVOLUTIONARY BIOLOGY

Evolution makes a splash

An underwater arms race drives a vibrant new game

By **Angela Chuang**[1] *and* **Orlando Schwery**[2]

North Star Games' new board game *Oceans* simulates marine evolution, modeling the fierce struggle for existence among competing species in an "eat or be eaten" environment. It does this by enabling players to create species whose feeding strategies are dictated by one of 12 trait cards. "Filter feeders," for example, forage exclusively from the fish tokens in the game's reef zone. "Apex predators," on the other hand, must successfully attack other players' species. Players can react with defensive behaviors, such as "inking" and "schooling," which, in turn, create pressure on other players to produce predators with ever-stronger attacks, in a coevolutionary arms race. The food tokens a player earns from feeding attempts are added to the individual board of each species and are eventually converted into the final points that determine victory at the game's conclusion.

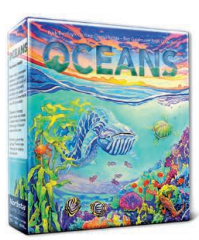
Oceans is the latest addition to the highly praised North Star Games *Evolution* series (*1*–*3*). Veterans of the earlier games in that series will recognize Catherine Hamilton's mesmerizing illustrations on the box and on the game's main ("surface") deck of cards. Her vibrant watercolors simultaneously capture the elegance of real species' forms while leaving room for players' imaginations to complete the canvas of their new creations. The "deep" deck, however, which comprises 89 unique abilities, includes designs from other talented artists, lending to their distinctive feel.

The game preserves one of the key elements of its predecessors, illustrating trade-offs associated with certain feeding strategies. Food tokens are limited, and either players must keep the reef well stocked, or species that feed from the reef must eventually adapt to life in deeper habitats. But *Oceans* really ups the ante when it comes to species and player interactions.

The game cleverly incorporates a host of traits that create symbiotic relationships between and among players' species. For instance, "parasitic" creatures leech food tokens from adjacent species, whereas "shark cleaners" gain tokens when a large attack has been made. A single feeding event can trigger a cascade of effects among a species's symbionts, highlighting the interconnectedness of life in such ecosystems and illustrating the vital role of keystone species. Abrupt changes to these species send reverberations across the community and spell extinction for those that cannot evolve fast enough. Players are also discouraged from allowing their species to indulge in unbridled feeding frenzies: Those that gain too many fish tokens overpopulate, and their numbers collapse by half.

Every game of *Oceans* features an event known as the Cambrian Explosion, named for the period in Earth's history characterized by rapid speciation rates and a burst of morphological innovation. Here, players use double the amount of trait cards per turn, thus hastening the evolutionary turnover of traits. This second half of the game also requires species to consume more food per round to survive, intensifying the game's tempo.

While it is possible to play the game using only the 12 surface trait cards, the game gets really weird (in a good way) if players choose to add in the cards from the deep deck after the Cambrian Explosion. This deck features powerful and mysterious cards that lean into science fiction and embrace the unknown lurking in our thalassic depths, as deep-sea krakens, leviathans, and behemoths rear their heads. It also features a range of real, magnificent, and game-changing traits found in the deep sea, such as intelligence, bioluminescence, and coprophagia (yes, the game goes there). It is worth noting that gentle giants can also evolve with great success, lest it seem as though the game is biased toward aggressive strategies at this phase.



Oceans
Nick Bentley, Dominic Crapuchettes, Ben Goldman, and Brian O'Neill
North Star Games, 2020.

Oceans invites players to marvel at the rich diversity of ocean life, from the vivacious reef to the mysterious ocean depths. Building on the prior successes of the series, it packages all this into a fast-paced and dynamic strategy game with high replay value. ■

REFERENCES AND NOTES

1. S. West, *Nature* **528**, 192 (2015).
2. A. Chuang, *Science* **355**, 587 (2017).
3. M. R. Muell *et al.*, *Evolution* 10.1111/evo.13924 (2020).

10.1126/science.aba9172

[1]Department of Psychology and Department of Ecology and Evolutionary Biology, University of Tennessee, Knoxville, TN 37996, USA. [2]New Mexico Consortium, Los Alamos, NM 87544, USA. Email: angelachuang@utk.edu

CREDITS (TOP TO BOTTOM): GUILLAUME DUCOS; CATHERINE HAMILTON

Published by AAAS

ENVIRONMENTAL POLICY

The landmark case that almost never was

A law professor investigates the legal decision to regulate U.S. greenhouse gases

By **Michael B. Gerrard**

The U.S. Supreme Court's 2007 decision in *Massachusetts* v. *Environmental Protection Agency* is widely seen as the most important U.S. environmental ruling of all time. But the suit, which led to a ruling that the Clean Air Act of 1970 empowered the U.S. Environmental Protection Agency (EPA) to regulate greenhouse gases, was almost never brought. Richard J. Lazarus's wonderful new book, *The Rule of Five*, is the inside story of how this case came to be, how its lawyers struggled and fought over theories and roles, and how the late Justice John Paul Stevens patched together the five votes needed to secure a majority.

Lazarus is ideally suited to tell this story. A law professor at Harvard, he has represented the government and environmental groups in 40 Supreme Court cases and presented oral argument in 14. He also roomed with John Roberts during law school, and they later taught a course on the history of the Supreme Court together. For this project, he interviewed almost everyone involved in the case, including several of the judges and justices and (with their permission) their law clerks, and had access to internal memos and drafts of opinions.

The case in question was the brainchild of Joe Mendelson, a lawyer working for a little-known environmental group in Washington, D.C., called the International Center for Technology Assessment. In 1998, he drafted a 35-page petition to the EPA, arguing that it was the agency's responsibility to regulate carbon dioxide and other greenhouse gases as pollutants, and put it in a drawer, awaiting the right time to file. A year later he decided that the time had come, but leaders of other environmental organizations pleaded and then pressured him not to file, thinking it would be better to wait for the expected ascension of a climate champion, Vice President Al Gore, to the presidency in January 2001. Mendelson filed anyway.

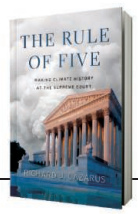
The EPA sat on the petition until after the November 2000 election. When George W. Bush took office, the agency's newly instated political appointees fumbled the response in a way that made it easier to challenge in court. In 2013, 30 parties filed suits in the U.S. Court of Appeals for the District of Columbia, but the court dismissed them in a 2-to-1 split.



The *Massachusetts* v. *EPA* decision empowered the EPA to regulate domestic greenhouse gases.

There are always long odds when one seeks to persuade the Supreme Court to take a case, but they are even longer when a side has legions of squabbling lawyers with different legal theories and just one chance to file a brief. But Lisa Heinzerling, a professor at Georgetown Law School, wrote what all agreed was a brilliant brief on behalf of the petitioners, and—to everyone's shock—the Supreme Court took the case. Then began the fight over who would get to argue it.

The Rule of Five: Making Climate History at the Supreme Court
Richard J. Lazarus
Harvard University Press, 2020. 368 pp.



This honor ultimately fell to James Milkey, a lawyer in the Massachusetts Attorney General's Office who had never argued before the Supreme Court. As they had done with Mendelson, many other lawyers working on the case tried to get Milkey to step aside, claiming that he was not up to the task. But Milkey persisted, and—with the help of additional brilliant briefs led by Heinzerling—on argument day, he shone. In the months that followed, Justice Stevens found ways to persuade his colleague Anthony Kennedy to give him the crucial fifth vote needed to prevail.

Lazarus walks readers through all of the procedural steps and legal theories that surrounded this case, using lucid prose that is easy for nonlawyers to follow. The book is a master class in how the Supreme Court works and, more broadly, how major cases navigate through the legal system.

The *Massachusetts* v. *EPA* decision was the basis for almost all of the Obama administration's actions on climate change, which included stricter regulations of emissions from motor vehicles and power plants. These actions, in turn, gave President Obama the legitimacy to press fellow world leaders to reach a landmark agreement on climate change in Paris in December 2015. However, in February 2016, the Supreme Court put Obama's Clean Power Plan on hold, and President Trump has pressed to repeal it, to weaken the motor vehicle rule, and to pull the United States out of the Paris Agreement. As Lazarus rightly concludes, the most important legal decisions are made not in the courtroom, but at the ballot box. ■

The reviewer is at the Sabin Center for Climate Change Law, Columbia Law School, New York, NY 10027, USA, and is the co-editor of *Legal Pathways to Deep Decarbonization in the United States* (Environmental Law Institute, 2019). Email: mgerra@law.columbia.edu

10.1126/science.aba8125

PHOTO: FENG CHENG/SHUTTERSTOCK.COM

Published by AAAS



LETTERS

Wildfires burned parts of Australia's ancient rainforests, including the lowland rainforest in Terania Creek, Nightcap National Park.

PHOTO: ROBERT M. KOOYMAN

Edited by **Jennifer Sills**

Protect Australia's Gondwana Rainforests

Recent fires in the Gondwana Rainforests of eastern Australia, a UN Educational, Scientific and Cultural Organization (UNESCO) World Heritage site (*1*), exposed the country's inability to protect these unique forests. Rich in diversity and global fossil heritage, the Gondwana Rainforests harbor the highest concentrations of threatened species in subtropical southeast Queensland and northern New South Wales, and they protect more than 40 million years of globally significant rainforest evolutionary history (*2*–*9*). Australia must take steps to ensure that these forests will not be lost in future natural disasters.

Australia began to break from Gondwana (Antarctica) around 40 million years ago (*3*), carrying its remnant of Austral paleorainforest and deep time evolutionary history. On its journey north, the Australian continent escaped the ravages of Antarctic freezing, only to heat up and dry out much later as it approached the tropics (*4*, *5*). The Paleo-Antarctic rainforest lineages (PARLs) retreated to the few remaining, geographically restricted and still shrinking wet places (*2*, *4*). PARLs are living plant taxa with fossil records in the mid-high latitude paleorainforests of the Cretaceous and Paleogene Southern Hemisphere (*2*, *3*), and their existence in Australia's living World Heritage Gondwana Rainforests preserves a vestige of the mostly vanished, late-Gondwana rainforest ecosystems that once covered much of the southern half of the planet (*4*, *6*–*9*). The greatest concentration of threatened rainforest plant species in Australia, many of them PARLs, now resides in the Nightcap Range in northern New South Wales (*10*). Efforts to protect this incredible concentration of diversity have proven inadequate (*11*).

Although the fires are now under control, more than 50% of the Gondwana Rainforests were affected by them (*11*). Australia must learn from this experience. Before the next threat arrives, Australian state governments should identify natural assets that are at risk and put policies in place to improve fire planning, streamline fire responses, and protect these forests. Legislation should prioritize areas of high conservation value, implement strategic fire planning to protect the forests, and avoid implementing broad-area industrial-scale controlled burns. Meanwhile, scientists must work to generate baseline scientific data for these areas immediately, which can be used to assess the damage from the recent fires and better predict fire behavior in the future. If policy-makers fail to heed the lessons of the recent fires, the world could lose Australia's ancient Gondwana Rainforests.

Robert M. Kooyman[1]*, James Watson[2], Peter Wilf[3]
[1]Department of Biological Sciences, Macquarie University, Sydney, NSW 2019, Australia. [2]Centre for Biodiversity and Conservation Science, School of Earth and Environmental Sciences, University of Queensland, Brisbane 4072, Australia. [3]Department of Geosciences, Pennsylvania State University, University Park, PA 16802, USA.
*Corresponding author.
Email: robert.kooyman@mq.edu.au

REFERENCES AND NOTES

1. UNESCO, World Heritage List, Gondwana Rainforests of Australia (https://whc.unesco.org/en/list/368/).
2. R. M. Kooyman *et al.*, *Am. J. Bot.* **101**, 2121 (2014).
3. L. A. Lawver, L. M. Gahagan, I. W. D. Dalziel, in *Tectonic, Climatic, and Cryospheric Evolution of the Antarctic Peninsula*, J. B. Anderson, J. S. Wellner, Eds. (American Geophysical Union, Washington, DC, 2011), pp. 5–33.
4. R. S. Hill, Ed., *History of the Australian Vegetation: Cretaceous to Recent* (Cambridge Univ. Press, Cambridge, UK, 1994).
5. R. Hall, *Geol. Soc. London Spec. Publ.* **355**, 75 (2011).
6. P. Wilf, N. R. Cúneo, I. H. Escapa, D. Pol, M. O. Woodburne, *Annu. Rev. Earth Planet. Sci.* **41**, 561 (2013).
7. L. Merkhofer *et al.*, *Am. J. Bot.* **102**, 1160 (2015).
8. M. A. Gandolfo, E. J. Hermsen, *Ann. Bot.* **119**, 507 (2017).
9. R. S. Hill, T. J. Brodribb, *Aust. J. Bot.* **47**, 639 (1999).
10. NSW Government, Office of Environment and Heritage, Threatened species, South Eastern Queensland (www.environment.nsw.gov.au/threatenedspeciesapp/AreaHabitatSearch.aspx?cmaname=South+Eastern+Queensland).
11. NSW Government, Understanding the impact of the 2019-20 fires (2020); www.environment.nsw.gov.au/topics/parks-reserves-and-protected-areas/fire/park-recovery-and-rehabilitation/recovering-from-2019-20-fires/understanding-the-impact-of-the-2019-20-fires.

10.1126/science.abb2046

Post-2020 goals overlook genetic diversity

In January, the secretariat of the Convention on Biological Diversity (CBD) released the first draft of a post-2020 global biodiversity framework with goals and targets for biodiversity (*1*, *2*). We are deeply concerned that the goal suggested for genetic diversity—the basic element for evolutionary processes and all biological diversity—is weak. Abundant scientific evidence recognizes the crucial role of intraspecific genetic diversity in ecosystem resilience, species survival, and adaptation, especially under increased threats of climate change, habitat loss, and diseases (*3*). The new goals should correct omissions in the previous strategy document.

The previous biodiversity strategy, CBD 2011–2020, includes Aichi Target 13 on

Published by AAAS



A Royal Society Summer Science Exhibition attendee learns about the helium atom microscope.

OUTSIDE THE TOWER

Outreach that sticks

I stood in our booth at the Royal Society's 215th Summer Science Exhibition, eagerly awaiting a chance to share with the attendees the hands-on activities describing the physics of our cutting-edge research—the result of a collaboration between two groups half a world apart. A group of three teenagers hesitantly approached the exhibit, nervous as to whether to engage. "Would you like to try our challenge?" I asked. "Match the pictures of the object to the image from our microscope." Immediately, their apprehension vanished, and they set about the task.

I watched as they matched macroscopic images of a honeybee and a spider to a close-up of the hairs on the bee's eye and the fang in the spider's tiny mouth. When the students finished analyzing the images, I explained that the close-up photographs were created using a novel helium atom microscope, which shows extraordinary details at micrometer scale without damaging the sample. By then, they had overcome their preconceptions about the difficulty of physics, and their questions flowed: "How were these images made?" "Why is this microscope different?" "What can it be used for?" Their natural scientific curiosity and confidence had been revitalized.

Call for submissions
Outside the Tower is an occasional feature highlighting scientists' advocacy experiences. Submit your advocacy story at http://cts.sciencemag.org.

Our exhibit accomplished our mission for the day—to engage an audience ranging from young children to distinguished Fellows of the Society. However, it was only the first step to lifelong learning in science, technology, engineering, and mathematics (STEM). Although one-off interventions can inspire, the lack of participation in STEM will not be solved just by increasing interest (*1*).

To boost the long-term effects of our outreach efforts, we sent students and teachers on their way with curriculum-linked resources provided through an online program (*2*). With hints, videos, and teacher support available online, they could solve problems related to the exhibition and make connections between science lessons in school and a career in research. We hope that our model of inspiration followed by long-term engagement will allow students to experience the euphoria of success and the resilience needed to become the researchers of the future.

Lisa Jardine-Wright
Isaac Physics, University of Cambridge, Cambridge, CB3 0HE, UK. Email: ljw21@cam.ac.uk

REFERENCES AND NOTES

1. King's College London, "ASPIRES: Young people's science and career aspirations, age 10–14" (2013); www.kcl.ac.uk/ecs/research/aspires/aspires-final-report-december-2013.pdf.
2. Isaac Physics (https://isaacphysics.org/).

COMPETING INTERESTS

L.J.-W. is employed by the University of Cambridge as the Director of the Isaac Physics project, which is funded by grants from the Department for Education England and The Ogden Trust.

10.1126/science.aaz9726

genetic diversity, which focuses on "cultivated plants and farmed and domesticated animals" and their wild relatives. Indicators associated with Target 13 follow trends, number, and threat status of domestic animal breeds and crops (*4*). Although the post-2020 CBD draft includes a much-needed goal to maintain genetic diversity, it does not explicitly state that genetic diversity maintenance is crucial for all species, not just a few. Because no indicators to follow trends of genetic diversity of wild animals and plants are suggested in the draft, genetic diversity could continue to be considered only for domestic organisms, as it was under Target 13.

The newly proposed framework should incorporate several revisions before it is finalized. The post-2020 framework should explicitly commit to maintaining genetic diversity within all species and to implementing strategies to halt genetic erosion and preserve adaptive potential of populations of both wild and domesticated species. The framework should also define indicators of progress toward this goal (*5*). Such indicators could include collecting data on the number of species, populations, or metapopulations that are large enough to maintain genetic diversity as well as those that are not. A widely used measure in this context is the "genetically effective population size," which quantifies the rate at which a population loses genetic variation. When the effective size is measured as 500 "ideal individuals," the population is considered "genetically safe" (*6*, *7*). We therefore suggest monitoring the number of populations above and below the genetically effective size of 500. The effective size is assessed from genetic or demographic data and is usually much lower—by about an order of magnitude (*8*)—than the total number of mature individuals. Another indicator could be the number of species or populations in which genetic diversity is being monitored by national agencies or universities using DNA-markers. A third indicator could be measuring rates of loss of distinct populations within species.

It is encouraging that the CBD post-2020 draft includes genetic diversity in one of the five main goals. However, including explicit protection for genetic diversity in wild as well as domestic species, and strategies to measure the effectiveness of efforts toward that goal, will ensure that signatories prioritize this important aspect of biodiversity conservation.

Linda Laikre[1,2]*, Sean Hoban[3,2], Michael W. Bruford[4,2], Gernot Segelbacher[5,2], Fred W. Allendorf[6,2], Gonzalo Gajardo[7], Antonio González Rodríguez[8,2], Philip W. Hedrick[9], Myriam Heuertz[10,11], Paul A. Hohenlohe[12], Rodolfo Jaffé[13,14,2], Kerstin Johannesson[15], Libby

PHOTO: SHEENA MARTIN

Published by AAAS

Liggins[16], Anna J. MacDonald[17,2], Pablo Orozco-terWengel[4,2], Thorsten B. H. Reusch[18], Hernando Rodríguez-Correa[19], Isa-Rita M. Russo[4,2], Nils Ryman[1], Cristiano Vernesi[20,2,21]
[1]Department of Zoology, Stockholm University, SE 10691 Stockholm. [2]Conservation Genetics Specialist Group, International Union for Conservation of Nature (IUCN), 1196 Gland, Switzerland. [3]Center for Tree Science, The Morton Arboretum, Lisle, IL 60532, USA. [4]School of Biosciences, Cardiff University, Cardiff, UK. [5]Wildlife Ecology and Management, University Freiburg, Freiburg, Germany. [6]Division of Biological Sciences, University of Montana, Missoula, MT 59812, USA. [7]Universidad de Los Lagos, Lab Genetics, Aquaculture & Biodiversity, Osorno, Chile. [8]Instituto de Investigaciones en Ecosistemas y Sustentabilidad, Universidad Nacional Autónoma de México, Morelia, Michoacán, Mexico. [9]School of Life Sciences, Arizona State University, Tempe, AZ 85287, USA. [10]Biodiversity, Genes, & Communities (BIOGECO), Joint Research Unit (UMR) of French National Institute for Agriculture, Food, and Environment (INRAE) and University of Bordeaux, FR-33610 Cestas, France. [11]Faculté des Sciences, Évolution Biologique et Écologie, Université Libre de Bruxelles, BE-1050 Brussels, Belgium. [12]Department of Biological Sciences, Institute for Bioinformatics and Evolutionary Studies, University of Idaho, Moscow, ID 83844–3051, USA. [13]Instituto Tecnológico Vale, 66055–090 Belém PA, Brazil. [14]Department of Ecology, University of São Paulo, 05508–090 São Paulo SP, Brazil. [15]Department of Marine Sciences, University of Gothenburg, Tjärnö, Sweden. [16]School of Natural and Computational Sciences, Massey University, Auckland, New Zealand. [17]The John Curtin School of Medical Research/ Research School of Biology, The Australian National University, Acton, ACT 2601, Australia. [18]GEOMAR Helmholtz Centre for Ocean Research Kiel, Kiel, Germany. [19]Escuela Nacional de Estudios Superiores Unidad Morelia, Universidad Nacional Autónoma de México, Morelia, Michoacán, México. [20]Department of Sustainable Agroecosystems and Bioresources, Research and Innovation Centre–Fondazione Edmund Mach, San Michele All'Adige, TN, Italy. [21]Genomic Biodiversity Knowledge for Resilient Ecosystems (G-BiKE) Action network of the European Cooperation in Science & Technology (COST CA18134) c/o Department of Sustainable Agroecosystems and Bioresources, Research and Innovation Centre–Fondazione Edmund Mach, San Michele All'Adige, TN, Italy.
*Corresponding author.
Email: linda.laikre@popgen.su.se

REFERENCES AND NOTES

1. CBD, "Zero draft of the post-2020 global biodiversity framework" (2020); www.cbd.int/doc/c/efb0/1f84/a892b98d2982a829962b6371/wg2020-02-03-en.pdf.
2. CBD, "Zero draft of the post-2020 global biodiversity framework, Appendix 1 (2020); https://www.cbd.int/doc/c/2c69/df5a/01ee87752c3612d3ba7ec341/wg2020-02-03-add1-en.pdf
3. The European Cooperation in Science & Technology (COST) Action Genomic Biodiversity Knowledge for Resilient Ecosystems (G-BiKE), "Genetic variation—key to adapting to environmental change" (2019); https://sites.google.com/fmach.it/g-bike-genetics-eu/reports-publications?authuser=0.
4. D. P. Tittensor *et al.*, *Science* **346**, 241 (2014).
5. M. E. Hunter, S. M. Hoban, M. W. Bruford, G. Segelbacher, L. Bernatchez, *Evol. Appl.* **11**, 1029 (2018).
6. F. W. Allendorf, N. Ryman, in *Population Viability Analyses*, S. R. Beissinger, D. R. McCullough (Eds.) (University of Chicago Press, Chicago, 2002).
7. I. G. Jamieson, F. W. Allendorf, *Trends Ecol. Evol.* **27**, 578 (2012).
8. R. Frankham, *Genet. Res.* **66**, 95 (1995).

COMPETING INTERESTS

M.H. receives funding from an "Investissement d'Avenir" grant managed by Agence Nationale de la Recherche [Centre d'étude de la biodiversité amazonienne (CEBA), ref. ANR-10-LABX-25-01].

10.1126/science.abb2748

Where Science Gets Social.

AAAS.ORG/ COMMUNITY

AAAS' Member Community is a one-stop destination for scientists and STEM enthusiasts alike. It's "Where Science Gets Social": a community where facts matter, ideas are big and there's always a reason to come hang out, share, discuss and explore.

Member COMMUNITY AAAS

AAAS Travels

Members and friends of AAAS are invited to join AAAS Travels on fascinating trips to all 7 continents!

Discover Greenland!
September 11-21, 2020



On board M/V Hondius, a superb new ice class vessel, explore Scoresbysund in East Greenland by zodiac, ship, and on shore excursions. Sail from Northern Iceland to Greenland, and then discover this immense fjord system during the time of fall color. Watch the Aurora Borealis dance across the night sky!

From $4,500 quad + air
to $6,950 twin window + air.

Discover Egypt
November 18 - December 1, 2020



Optional Red Sea Extension to December 5

Discover the amazing antiquities and colossal monuments of Egypt. Visit the fabulous new Alexandria Library and National Museum, and the ultimate monuments of the Old Kingdom, the Great Pyramids and Sphinx! Explore the Valley of the Kings, cruise on the Nile, and delight in the exquisite Nubia and Luxor Museums! Optional Extension to Abu Simbel.

$ 4,995 pp twin share + air

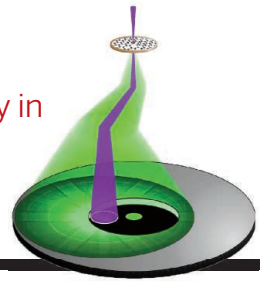
For a detailed brochure, please call (800) 252-4910
All prices are per person twin share + air

Betchart Expeditions Inc.
17050 Montebello Rd
Cupertino, California 95014
Email: AAASInfo@betchartexpeditions.com
www.betchartexpeditions.com

RESEARCH

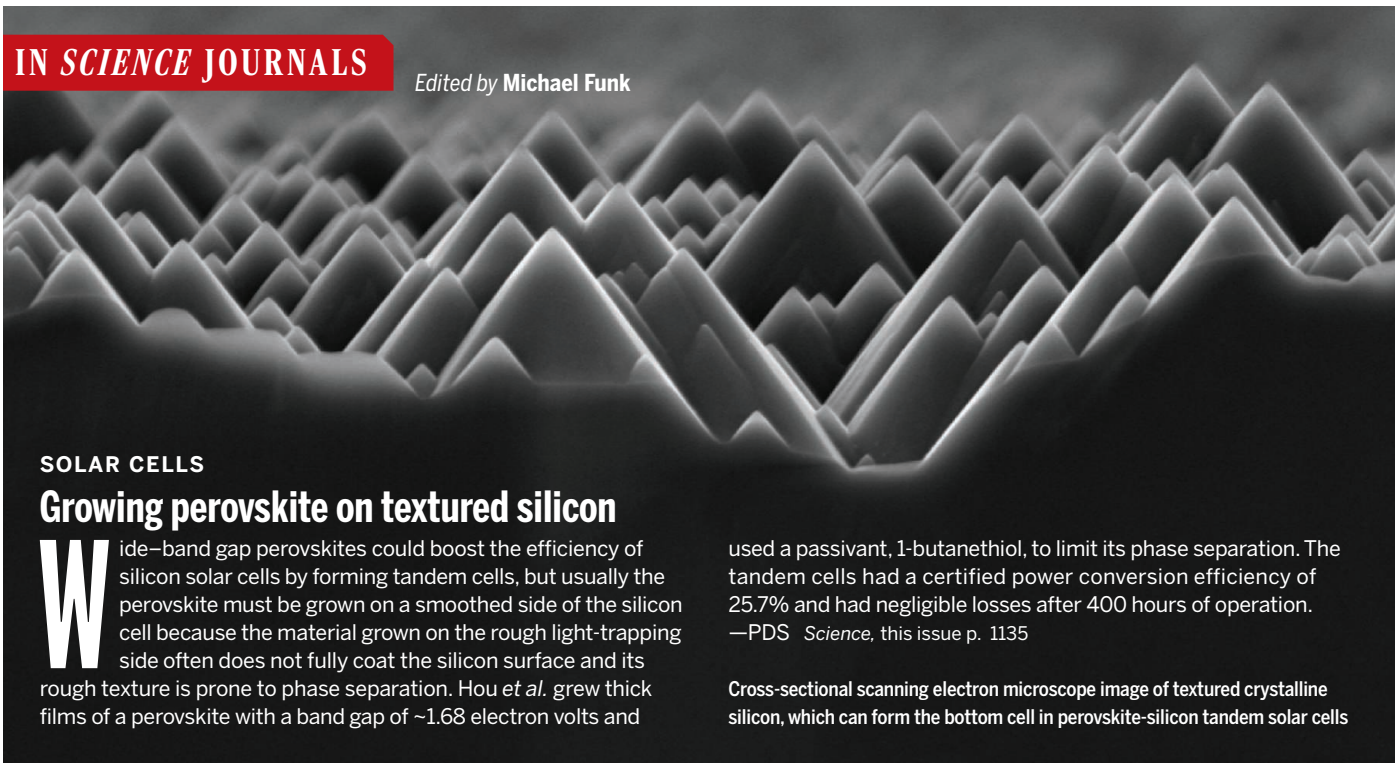
Vibrational spectroscopy in an electron microscope

Hage et al., *p. 1124*



IN *SCIENCE* JOURNALS

Edited by **Michael Funk**



SOLAR CELLS

Growing perovskite on textured silicon

Wide–band gap perovskites could boost the efficiency of silicon solar cells by forming tandem cells, but usually the perovskite must be grown on a smoothed side of the silicon cell because the material grown on the rough light-trapping side often does not fully coat the silicon surface and its rough texture is prone to phase separation. Hou *et al.* grew thick films of a perovskite with a band gap of ~1.68 electron volts and used a passivant, 1-butanethiol, to limit its phase separation. The tandem cells had a certified power conversion efficiency of 25.7% and had negligible losses after 400 hours of operation. —PDS *Science,* this issue p. 1135

Cross-sectional scanning electron microscope image of textured crystalline silicon, which can form the bottom cell in perovskite-silicon tandem solar cells

QUANTUM SIMULATION

Gauge invariance with cold atoms

There is considerable interest in developing quantum computational technologies that can simulate a series of physical phenomena inaccessible by classical computers. Mil *et al*. propose a modular scheme for quantum simulation of a U(1) lattice gauge theory based on heteronuclear spin-changing collisions in a mixture of two bosonic quantum gases isolated in single wells of a one-dimensional optical lattice. They engineered the elementary building block for a single well and demonstrate its reliable operation that preserves the gauge invariance. The potential for scalability of the proposed scheme opens up opportunities to address challenges in quantum simulating the continuum limit of the gauge theories. —YS

Science, this issue p. 1128

HIV

Clearing a path for an HIV cure

Curing HIV is more feasible if we better understand the formation of the latent viral reservoir. Leyre *et al*. studied longitudinal blood and tissue samples obtained from individuals during acute HIV infection. The large pool of infected cells present at the early stages of infection did not survive antiretroviral treatment. Infected cells at later stages were more prevalent in lymphoid tissues than in blood. These results show that most infected targets are cleared with early treatment, but HIV-positive cells that remain after a certain stage are more likely to persist. These persistent cells are the ones that will need to be eradicated for a cure to be achieved. —LP

Sci. Transl. Med. **12**, eaav3491 (2020).

MOLECULAR BIOLOGY

Expanding the human proteome

Using mass spectrometry, ribosome profiling, and several CRISPR-based screens, Chen *et al*. identified hundreds of previously uncharacterized functional micropeptides in the human genome (see the Perspective by Wei and Guo). Protein translation outside of annotated open reading frames (ORFs) in messenger RNAs and within ORFs in long noncoding RNAs is pervasive. A functional screen using CRISPR-Cas9 with single-cell transcriptomics suggested critical roles for hundreds of micropeptides. Micropeptides encoded by multiple short, upstream ORFs form stable protein complexes with the downstream canonical proteins encoded on the same messenger RNAs. —SYM

Science, this issue p. 1140; see also p. 1074

TRANSCRIPTION

RNA life span at single-cell resolution

RNA transcripts are an easily accessed representation of gene expression, but we lack a comprehensive view of the life span of RNA within the single cell. Battich *et al*. developed a method to sequence messenger RNA labeled with

CREDITS (FROM TOP) HAGE *ET AL.*; HOU *ET AL.*

Published by AAAS

5-ethynyl-uridine (EU) in single cells (scEU-seq), which allows estimation of RNA transcription and degradation rates. When examining intestinal organoid cells, scEU-seq data can be used to discern between transcription and degradation during development, indicating that this method can be applied to better understand the relationship between gene expression and RNA degradation during development. —LMZ

Science, this issue p. 1151

CELL SURFACE MAPPING

Pinpointing proteins

To develop drugs that target a specific cell surface protein, it's helpful to know which other proteins reside in its vicinity. Geri *et al*. report a light-triggered labeling technique that improves the spatial resolution for this type of mapping. Specifically, they rely on a photocatalyst with a very short energy-transfer range to activate a carbene-based label that can only diffuse a short distance in water before reacting. They showcase the technique by mapping the environment of the programmed-death ligand 1 (PD-L1) protein on B cell surfaces, a system of considerable interest in cancer immunotherapy. —JSY

Science, this issue p. 1091

NEURODEVELOPMENT

Diversity from development

When given a line to follow, some fruit flies do so carefully and others weave. Linneweber *et al*. now show that these behaviors are stable for an individual but diverse in an isogenic population. Key to generating individual diversity in the population is the inherent chaos of normal development. A set of neurons in the visual system is wired up in a variable manner, resulting in brain circuit asymmetry unique to each fly that guides its line-walking behavior. With more asymmetry in its brain circuit, a fly is better able to orient to the line. —PJH

Science, this issue p. 1112

NEUROSCIENCE

Human brain activity during memory

Animal studies suggest that sequence replay of neuronal activity may underlie memory retrieval and consolidation. However, there is no direct evidence that the replay of spiking activity sequences is important for these processes in the human brain. Vaz *et al*. simultaneously recorded single-unit spikes, local field potential, and intracranial electroencephalography signals in the brain while participants performed a memory task. Sharp wave ripple oscillations in the temporal lobe cortex reflected bursts of neural spiking, and these bursts of spikes organized into sequences during memory formation. These sequences were replayed during successful memory retrieval. The extent of sequence replay during correct recall was related to the extent to which cortical spiking activity was coupled with ripples in the medial temporal lobe. —PRS

Science, this issue p. 1131

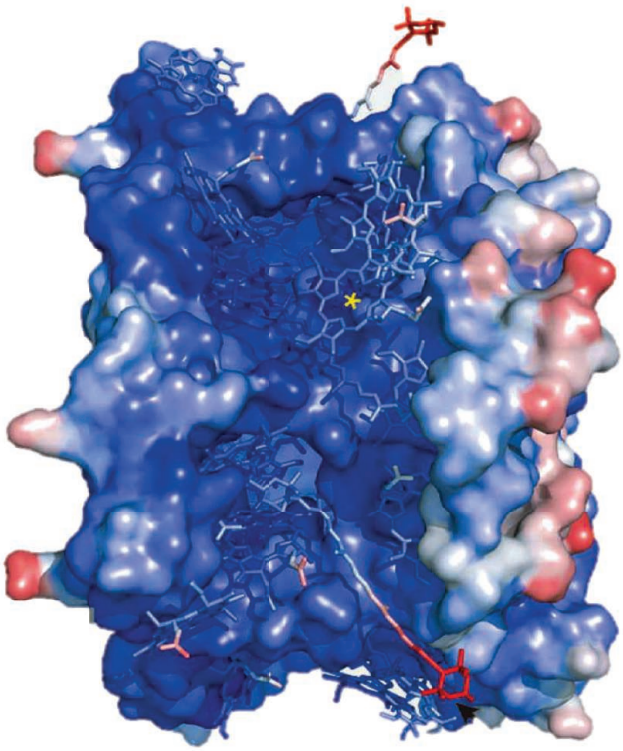


PHOTO: NG IMAGES/ALAMY STOCK PHOTO

Behavioral patterns in fruit flies, *Drosophila melanogaster*, vary by individual.

IN OTHER JOURNALS

Edited by **Caroline Ash** *and* **Jesse Smith**



Model of the light-harvesting complex II trimer structure for membranes containing only bilayer-forming lipids

PHOTOSYNTHESIS

Bulky lipids for light-harvesting control

Lipid membranes are extraordinarily complex, with many different acyl chains, head groups, and proteins contributing to their shape, curvature, and fluidity. In membranes with specialized functions, such as the thylakoid membranes within chloroplasts, these properties can influence the function of the embedded membrane proteins. Tietz *et al*. measured changes in the behavior of proteoliposome-reconstituted light-harvesting complex II, a protein that normally gathers light for photosystem II, in the presence or absence of the non–bilayer-forming lipid monogalactosyldiacylglycerol. In this assay, the lipid stimulated energy quenching, which would divert light energy into heat and be photoprotective in high-intensity light. The authors suggest that changes in lateral membrane pressure caused by the bulky lipids may influence pigment conformations within the protein and thus alter the amount of light energy moving through the system. —MAF

J. Biol. Chem. **295**, 1857 (2020).

ORGANIC CHEMISTRY

Sulfurous glue for heterocycles

Palladium catalysts can stitch together a wide variety of carbon-based aromatic rings, but they often get hung up if both rings contain nitrogen. Qin *et al*. report that a sulfur reagent can help fill this gap. Specifically, they show that isopropyl sulfinyl chloride can react successively with two Grignard-activated heterocycles, such as pyridine rings, and then couple them together by elimination. The reaction was compatible with a wide variety of five- and

Published by AAAS



Dogs have an amazing sense of smell, which can be put to use in the early detection of tree diseases.

PLANT DISEASE

Sniffing out disease

Dogs have extraordinary noses and can detect odors at sensitivities well beyond human technologies. Gottwald *et al*. tested the talents of dogs for sniffing out the pandemic and economically severe bacterial disease of citrus trees called huanglongbing. The dogs were first trained by positive reinforcement on potted citrus plants. Gradually, the tests were scaled up to grids of 10 trees by 10 trees and finally to orchard conditions. The dogs detected 30-day-old infections compared with genetic testing that only started to identify infections 3 months after insect-vectored transmission. If two dogs were used, detection accuracies of 100% were achieved, not only in commercial orchards but also among a range of plants in residential areas known to be foci of infection. By modeling the data, the authors estimated that dogs could save up to 92% of the trees in an orchard by early detection followed by removal of individual infected trees. —CA

Proc. Natl. Acad. Sci. U.S.A. **117**, 3492 (2020).

six-membered rings, including thiazoles and azaindoles. —JSY

Angew. Chem. Int. Ed. 10.1002/anie.201915425 (2020).

PHYSIOLOGY

Humans on a chip

Organ chips are devices in which epithelial and/or stromal cells are grown in a chamber filled with medium connected by a porous matrix-like membrane to another chamber lined with endothelial cells and containing a blood substitute. Depending on the cell types used and the contents of the blood substitute and medium, these chips can model organ-specific environments. Novak *et al*. devised an automated system to connect up to 10 different organ chips with a common blood substitute to model physiological systems. In a series of reports, they show that this system could be used to predict drug dynamics and drug toxicity. These devices have numerous potential applications, including modeling complex environments and disease development. —GKA

Nat. Biomed. Eng. 10.1038/s41551-019-0497-x, s41551-019-0498-9, s41551-019-0495-z (2020).

SCIENTIFIC WORKFORCE

It takes a village

STEM Ph.D. students often select a lab based on the reputation of the principle investigator (PI), who mentors students as they develop research skills. Feldon *et al*. sought to empirically determine how PI mentorship affects students' skill development in a long-term study involving 336 Ph.D. students in the biological sciences. Specifically, skills including establishing testable hypotheses, experimental design, and data analysis were measured using writing samples and additional qualitative data that were collected. Results showed that the mentoring activities of PIs do not significantly predict students' skill development trajectories. In fact, Ph.D. students were more than four times as likely to have positive skill development when engaging with postdocs, supporting the idea that "cascading mentorship" is an effective and critical element of Ph.D. training. —MMc

Proc. Natl. Acad. Sci. U.S.A. **116**, 20910 (2019).

MICROBIAL GENOMICS

Closing the loop on sequencing

Sequencing of microorganisms in the context of metagenomes, such as human microbiomes, can be difficult. It is not only the diversity of species but also the occurrence of repeated sequences, such as transposable elements, that are challenging. Furthermore, long-read sequencing often requires large amounts of DNA, which can be difficult to obtain from a microbiome. To assemble full bacterial genomes for analysis of the role of repeats in bacterial genomes, Moss *et al*. used nanopore sequencing, assembly, and error correction to extract closed bacterial genomes from microbiomes. From this, they were able to resolve difficult-to-assemble bacterial genomes. —LMZ

Nat. Biotechnol. 10.1038/s41587-020-0422-6 (2020).

IMMUNOLOGY

Wisdom of the crowd

Quorum sensing is used by bacteria to sense local cell density in order to regulate and coordinate a wide array of functions, including biofilm formation. Muldoon *et al*. report that a somewhat analogous process may play a role in macrophage responses. Macrophages exposed to bacterial lipopolysaccharide—a potent immune stimulant—showed a bimodal activation profile that could be tuned by adjusting cell density before stimulation. The authors then used dynamical modeling and single-cell tracking to propose a mechanism they termed quorum licensing. In bacterial quorum sensing, all players are uniformly activated. By contrast, quorum licensing entails the transformation of "digital" single-cell decisions into "analog" population-wide outputs. This phenomenon may help macrophages limit inflammatory responses to local sites of injury and infection. —STS

Nat. Commun. **11**, 878 (2020).

PHOTO: MARYBETH OKERSON/ALAMY STOCK PHOTO

Published by AAAS

ALSO IN *SCIENCE* JOURNALS

Edited by **Michael Funk**

DEVELOPMENT

Paths to understanding breastmilk

Breastfeeding is important for infant and maternal health. Some of the mechanisms that account for the benefits of breastmilk include improved nutritional and immune status, but much is still unknown about how breastmilk confers health benefits. In a Perspective, Bode *et al*. discuss paths to understanding the mother-breastmilk-infant triad. They focus on how improved knowledge of the triad could inform research on two key issues for infant health: childhood undernutrition and necrotizing enterocolitis, a fatal gastrointestinal disorder that affects preterm infants. —GKA

Science, this issue p. 1070

GERM CELL DEVELOPMENT

Commencing oogenesis

In mice, embryonic stem cells and induced pluripotent stem cells have been shown to differentiate into primordial germ cell–like cells that can give rise to functional oocytes. In this system, Nagaoka *et al*. identified the gene *Zglp1* as a necessary and sufficient factor for conferring the oogenic fate to sexually undetermined germ cells. As a downstream effector of bone morphogenetic protein signaling, conserved transcriptional regulator ZGLP1 activates the oogenic program repressed by Polycomb activities, whereas retinoic acid signaling assists the maturation of such activation and also the repression of the primordial germ cell program. This study thus refines our understanding of mammalian oogenic fate determination. —BAP

Science, this issue p. 1089

INTEGRATIVE OMICS

Mapping the mammalian brain

The diverse physiology of the brain is reflected in its complex organization at regional, cellular, and subcellular levels. Sjöstedt *et al*. combined data—both newly acquired and from other large-scale brain mapping projects—from transcriptomics, single-cell genomics, in situ hybridization, and antibody-based protein profiling to map the molecular profiles in human, pig, and mouse brain. The analysis is consistent with a conserved basic brain architecture during mammalian evolution, but it does show differences in regional gene expression profiles. —VV

Science, this issue p. 1090

NEUROSCIENCE

A major psychosocial stress circuit

Psychological stress induces various physiological responses by activating the sympathetic nervous system. The brain circuits involved in these functions are still not completely understood. In a rat model, Kataoka *et al*. combined anatomical tracing, immediate early gene expression analysis, pharmacology, optogenetics, electrophysiology, and genetic cell ablation to provide evidence for the prominent role of a ventral part of the medial prefrontal cortex in sympathetic responses to social defeat stress. This brain region sends excitatory projections to the dorsomedial hypothalamus as a central coordinator of the psychosocial stress responses. This pathway is crucial for understanding how psychosocial stress influences a variety of body functions. —PRS

Science, this issue p. 1105

LIQUID CRYSTALS

Watching defects flow and grow

Orientational topological defects in liquid crystals, known as disclinations, have been visualized in polymeric materials or through mesoscale simulations of the local orientation of the molecules. Duclos *et al*. report the experimental visualization of the structure and dynamics of disclination loops in active, three-dimensional nematics using light-sheet microscopy to watch the motion of nematic molecules driven by the motion of microtubule bundles (see the Perspective by Bartolo). This setup makes it possible to directly watch the nucleation, deformation, recombination, and collapse of spatially extended topological defects in three dimensions. —MSL

Science, this issue p. 1120; see also p. 1075

MICROBIOLOGY

Porin' through the wax

Mycobacterium tuberculosis has a distinctive physiology that allows it to persist in the human body, including a wax-like cell coat that is largely impermeable and can resist attack by host immune response effectors. Wang *et al*. identified a simple molecule that effectively crosses this cell coat and kills *M. tuberculosis* cells. Whole-genome sequencing of mutants resistant to this molecule, 3,3-*bis*-di(methylsulfonyl)propionamide, showed scattered mutations in a protein called PPE51, and these mutants resulted in a spectrum of nutrient-related growth defects. Experiments suggest that PE/PPE family proteins are small molecule–selective channels analogous to outer membrane porins, which allow *M. tuberculosis* to take up nutrients while maintaining an otherwise impermeable barrier. —CA

Science, this issue p. 1147

CANCER

Palmitoylation makes the switch for EGFR

Aberrant epidermal growth factor receptor (EGFR) signaling through two important pathways, RAS–mitogen-activated protein kinase (RAS-MAPK) and phosphatidylinositol 3-kinase (PI3K), promotes tumor growth. EGFR inhibitors are rarely effective in tumors with mutations in the protein KRAS, which stimulate the MAPK pathway independently of EGFR activity. Kharbanda *et al*. found that EGFR palmitoylated on the intracellular tail interacted preferentially with a PI3K subunit rather than a MAPK adaptor protein. Blocking palmitoylation reduced PI3K signaling activity and sensitized cells to PI3K inhibitors. These results explain why EGFR inhibitors are effective only in cancer cells in which EGFR is palmitoylated. —LKF

Sci. Signal. **13**, eaax2364 (2020).

THYMUS

PAX1 in the thymus

Severe combined immunodeficiency encompasses a wide spectrum of genetic disorders. Yamazaki *et al*. studied immune deficits in six patients with otofaciocervical syndrome type 2, a genetic abnormality attributed to biallelic mutations in the transcription factor PAX1. In addition to immunodeficiency, the disease is also characterized by facial dysmorphism, hearing loss, and skeletal abnormalities. The patients were subjected to hematopoietic stem cell transplantation to rectify their immunodeficiency. Despite successful engraftment in three of the patients, all three failed to develop T cells. By generating patient-derived induced pluripotent stem cells and differentiating them ex vivo into thymic epithelial progenitor (TEP) cells, the authors found that PAX1 plays an important

Published by AAAS

role in regulating the development of TEP cells. —AB

Sci. Immunol. **5**, eaax1036 (2020).

SOLAR CELLS

Tuning band gaps with three halides

Tandem solar cells can boost solar cell efficiency by using two active layers to absorb the solar spectrum more completely, provided that the two cells are current-matched. Inorganic-organic perovskites tuned to the appropriate wide band gap (~1.7 electron volts) as top cells that contained iodine and bromine or bromine and chlorine have short carrier diffusion lengths and undergo photo-induced phase segregation. Xu *et al*. now report a method for incorporating chloride that allows for fabrication of stable triple-halide perovskites with a band gap of 1.67 electron volts. Two-terminal tandem silicon solar cells made with this material had a power conversion efficiency of 27%. —PDS

Science, this issue p. 1097

ELECTRON MICROSCOPY

Seeing single silicon atom vibrations

Vibrational spectroscopy can achieve high energy resolution, but spatial resolution of unperturbed vibrations is more difficult to realize. Hage *et al*. show that a single-atom impurity in a solid (a silicon atom in graphene) can give rise to distinctive localized vibrational signatures. They used high-resolution electron energy-loss spectroscopy in a scanning transmission electron microscope to detect this signal. An experimental geometry was chosen that reduced the relative elastic scattering contribution, and repeated scanning near the silicon impurity enhanced the signal. The experimental vibration frequencies are in agreement with ab initio calculations. —PDS

Science, this issue p. 1124

Published by AAAS

RESEARCH ARTICLE SUMMARY

GERM CELL DEVELOPMENT

ZGLP1 is a determinant for the oogenic fate in mice

So I. Nagaoka, Fumio Nakaki, Hidetaka Miyauchi, Yoshiaki Nosaka, Hiroshi Ohta, Yukihiro Yabuta, Kazuki Kurimoto, Katsuhiko Hayashi, Tomonori Nakamura, Takuya Yamamoto, Mitinori Saitou*

INTRODUCTION: Mammals generate sexually dimorphic germ cells, oocytes and spermatozoa, which form the basis for sexual reproduction. Studies in mice have shown that in embryonic ovaries, retinoic acid (RA) and its downstream effector, STRA8, induce sexually uncommitted germ cells into the oogenic fate, whereas in embryonic testes, RA is degraded by Sertoli cells and other mechanisms elicit the spermatogenic pathway. Conversely, our recent study has shown that RA and STRA8 are not sufficient to induce in vitro mouse primordial germ cell–like cells (mPGCLCs) into the oogenic fate. Instead, bone morphogenetic protein (BMP), which is expressed in granulosa cells, and RA synergistically confer the oogenic pathway on mPGCLCs. This finding creates an experimental framework for a systematic understanding of the mechanism of oogenic fate determination.

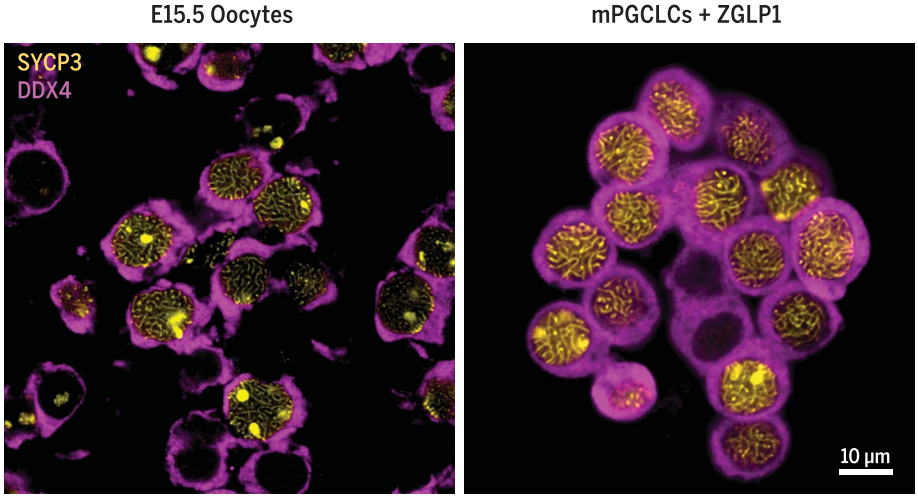
RATIONALE: Using mouse embryonic stem cells (mESCs) as a starting material, our in vitro system reconstitutes PGC specification, epigenetic reprogramming, and oogenic fate determination under a defined condition. We reasoned that this system should serve as a powerful platform with which to analyze the mechanism of germ cell development, including that for oogenic fate determination. Here, we set out to identify a transcriptional regulator that functions downstream of BMP signaling for oogenic fate determination by screening with RNA sequencing and to explore the regulation and function of a key candidate using both the in vivo model and the in vitro system through loss- or gain-of-function experiments. We reasoned that these experiments should clarify the distinctive functions of the BMP and RA pathways in oogenic fate determination.

RESULTS: We identified *Zglp1*, which encodes an evolutionary conserved transcriptional regulator with GATA-like zinc fingers, as a gene that showed specific up-regulation in mPGCLCs in response to BMP, but not to RA. In females, ZGLP1 showed specific and transient expression in embryonic germ cells during oogenic fate determination [from embryonic day (E) 12.0 to E15.5], whereas in males, it was not detected in embryonic germ cells undergoing spermatogenic fate determination but was expressed in postnatal undifferentiated or differentiating spermatogonia. In females, *Zglp1* was essential for the oogenic fate determination, with no germ cells differentiating into oocytes in the meiotic prophase in *Zglp1*-knockout mice, whereas in males, it was dispensable for germ cell sex determination but was required in the spermatogonia for an efficient completion of meiotic prophase. ZGLP1 overexpression replaced the functions of the BMP signaling and induced mPGCLCs into the oogenic fate and meiotic prophase with up-regulation of *Stra8* in the absence of RA. We found that the key role of RA signaling was to contribute to maturation of the overall oogenic program and to repression of the PGC program. Consistently, *Zglp1* showed a broad regulatory coverage of the transcriptome for the oogenic program, which included the program for RNA processing, transcription and chromatin modification, retrotransposon regulation, meiosis, and oocyte development, whereas *Stra8*, which functioned in part downstream of *Zglp1*, mainly regulated the meiotic program. Chromatin immunoprecipitation sequence analysis suggested that ZGLP1 preferentially activates key genes repressed by Polycomb activities in sexually uncommitted germ cells.

ON OUR WEBSITE

Read the full article at http://dx.doi.org/10.1126/science.aaw4115

CONCLUSION: Our results demonstrate that BMP signaling and ZGLP1 play a central role in establishing the key programs for the oogenic fate, with RA signaling assisting in the maturation of these programs, including repression of the early PGC program. These findings provide an integrated paradigm for mammalian oogenic fate determination. The distinct function of ZGLP1 between females and males represents a sexual dichotomy of the mechanism for the onset and progression of the oogenic and spermatogenic processes, including meiosis. A better understanding of the mechanism of sex determination in germ cells should serve as a key, not just for further promoting in vitro gametogenesis (IVG) studies, including human IVG, but also for delineating the etiology of critical diseases such as infertility and genetic and epigenetic disorders of offspring. Furthermore, an in vitro system that induces meiotic recombination in a physiologically relevant context propels future studies to understand the mechanisms for generating genetic diversity. ■



ZGLP1 induces the oogenic fate in mice. Images show immunofluorescence staining of SYCP3 (yellow) and DDX4 (magenta) expression in E15.5 oocytes (left) and mPGCLCs in vitro overexpressing ZGLP1 (right). ZGLP1 alone, which acts downstream of the BMP signaling, is sufficient to induce mPGCLCs into oocyte-like cells in the meiotic prophase with SYCP3-positive synaptonemal complexes. Scale bar, 10 μm.

The list of author affiliations is available in the full article online.
***Corresponding author. Email: saitou@anat2.med.kyoto-u.ac.jp**
Cite this article as S. I. Nagaoka *et al.*, *Science* 367, eaaw4115 (2020). DOI: 10.1126/science.aaw4115.

RESEARCH ARTICLE

GERM CELL DEVELOPMENT

ZGLP1 is a determinant for the oogenic fate in mice

So I. Nagaoka[1,2], Fumio Nakaki[2]*, Hidetaka Miyauchi[2]†, Yoshiaki Nosaka[1,2], Hiroshi Ohta[1,2], Yukihiro Yabuta[1,2], Kazuki Kurimoto[2]‡, Katsuhiko Hayashi[2]§, Tomonori Nakamura[1,2], Takuya Yamamoto[1,3,4,5], Mitinori Saitou[1,2,3]‖

Sex determination of germ cells is vital to creating the sexual dichotomy of germ cell development, thereby ensuring sexual reproduction. However, the underlying mechanisms remain unclear. Here, we show that ZGLP1, a conserved transcriptional regulator with GATA-like zinc fingers, determines the oogenic fate in mice. ZGLP1 acts downstream of bone morphogenetic protein, but not retinoic acid (RA), and is essential for the oogenic program and meiotic entry. ZGLP1 overexpression induces differentiation of in vitro primordial germ cell–like cells (PGCLCs) into fetal oocytes by activating the oogenic programs repressed by Polycomb activities, whereas RA signaling contributes to oogenic program maturation and PGC program repression. Our findings elucidate the mechanism for mammalian oogenic fate determination, providing a foundation for promoting in vitro gametogenesis and reproductive medicine.

In mammals, the chromosomes specify the sex of somatic cells, which in turn activates the oogenic or spermatogenic program in developing germ cells. This manifests at around embryonic day (E) 12.5 in mouse germ cells that are colonized in embryonic ovaries or testes (*1*). A prevalent hypothesis posits that in females, retinoic acid (RA) induces the expression of STRA8, which acts as a key regulator for germ cells (oogonia) to adopt the oogenic fate and enter into the meiotic prophase, whereas in males, RA is degraded by CYP26B1 in embryonic Sertoli cells, and germ cells (prospermatogonia) ensheathed by such cells enter the spermatogenic pathway (*2*–*4*). However, in a recent in vitro analysis, we showed that RA and the expression of STRA8 are not sufficient to induce the oogenic fate in mouse primordial germ cell–like cells (mPGCLCs) derived from mouse embryonic stem cells (mESCs). Instead, bone morphogenetic proteins (BMPs), which are expressed strongly in embryonic granulosa cells (*5*, *6*), and RA synergistically confer the oogenic pathway and meiotic program on mPGCLCs (*7*). This finding not only defines a signaling principle that drives the oogenic pathway, but also creates an experimental framework for its systematic analysis. Here, we identify a key transcription factor (TF) downstream of BMP and establish an integrated paradigm for oogenic fate determination.

[1]Institute for the Advanced Study of Human Biology (ASHBi), Kyoto University, Yoshida-Konoe-cho, Sakyo-ku, Kyoto 606-8501, Japan. [2]Department of Anatomy and Cell Biology, Graduate School of Medicine, Kyoto University, Yoshida-Konoe-cho, Sakyo-ku, Kyoto 606-8501, Japan. [3]Center for iPS Cell Research and Application (CiRA), Kyoto University, 53 Kawahara-cho, Shogoin, Sakyo-ku, Kyoto 606-8507, Japan. [4]AMED-CREST, AMED, 1-7-1 Otemachi, Chiyoda-ku, Tokyo, 100-0004, Japan. [5]Medical-risk Avoidance based on iPS Cells Team, RIKEN Center for Advanced Intelligence Project (AIP), Kyoto, 606-8507, Japan.
*Present address: Multicellular Systems Biology Group, European Molecular Biology Laboratory (EMBL) Barcelona, 08003 Barcelona, Spain. †Present address: Department of Surgery, Division of Hepato-Biliary-Pancreatic Surgery and Transplantation, Graduate School of Medicine, Kyoto University, Kyoto 606-8507, Japan. ‡Present address: Department of Embryology, Nara Medical University, Nara 634-8521, Japan. §Present address: Department of Developmental Stem Cell Biology, Faculty of Medical Sciences, Kyushu University, Fukuoka 812-8582, Japan.
‖Corresponding author. Email: saitou@anat2.med.kyoto-u.ac.jp

A system for identifying key TFs for the oogenic fate

In the in vitro system, mPGCLCs isolated by fluorescence-activated cell sorting (FACS) for the expression of Prdm1-mVenus [also known as Blimp1-mVenus (BV)] and Dppa3-ECFP [also known as Stella-ECFP (SC)] transgenes are cultured in the presence of forskolin and rolipram, which elevate intracellular cAMP levels and enhance PGC(LC) expansion (*8*), and these cells are provided with BMP and RA from culture day 3 (c3) onward (Fig. 1A) (*7*). Under these conditions, mPGCLCs differentiate into fetal oocyte–like cells that are positive for SYCP3, a key synaptonemal complex component, and proceed into meiotic prophase, reaching the pachytene stage at c9 (Fig. 1, A and B) (*7*). BMP alone can also induce mPGCLCs into fetal oocyte–like cells, albeit with low efficiency (Fig. 1, A and B) (*7*). Using RNA-sequencing (RNA-seq) technology (*9*), we screened genes encoding TFs preferentially up-regulated in response to BMP (fig. S1A and tables S1 and S2). Considering genes known to function in meiotic initiation (*10*, *11*), we selected eight genes, *Dazl*, *Gata2*, *Id1*, *Id3*, *Msx1*, *Msx2*, *Stra8*, and *Zglp1*, for further analyses (fig. S1, A and B).

We established a system to overexpress the candidates in mPGCLCs in a doxycycline (Dox)-dependent fashion (Fig. 1A) (*12*, *13*). Immunofluorescence (IF) analyses revealed that the provision of Dox and RA to the eight-gene transfectants from c3 onward leads to the induction of SYCP3$^+$ fetal oocyte–like cells in most BV$^+$ and SC$^+$ cells at c9 (Fig. 1, A and B), suggesting that one or more of the eight factors acts as a BMP effector and, together with RA, induces the oogenic fate. The provision of Dox alone also induced the SYCP3$^+$ cells (Fig. 1, A and B). We therefore performed eight sets of experiments by providing Dox and RA to the seven-gene transfectants produced by withdrawing each of the eight genes in turn, which revealed that each of the seven-gene combinations, except that lacking *Zglp1*, resulted in the induction of SYCP3$^+$ cells (Fig. 1, A and B). Accordingly, *Zglp1* overexpression, but not overexpression of the other genes, including *Gata2*, *Id1*, and *Msx1*, and the provision of RA resulted in a robust induction of SYCP3$^+$ cells (Fig. 1, A and B, and fig. S1, C and D). *Zglp1* overexpression without RA also generated SYCP3$^+$ cells as a substantial fraction of BV$^+$ and SC$^+$ cells (Fig. 1, A and B) (see below). We therefore explored the function of *Zglp1* in oogenic fate determination.

ZGLP1 is essential for the oogenic fate

Zglp1 encodes a transcriptional regulator bearing a GATA-like zinc finger conserved across the metazoan phyla (fig. S2) (*14*, *15*). It has been reported that *Zglp1* is expressed in gonadal somatic cells, but not in germ cells, and is essential both for oogenesis and spermatogenesis (*14*, *15*). However, our RNA-seq and IF analyses revealed that during the embryonic period, *Zglp1*/ZGLP1 exhibits specific and transient expression in DDX4$^+$ germ cells in females, but not in somatic cells or males, beginning at E12.0 and waning after E14.5, a key period for the sex determination of germ cells (Fig. 2, A and B, and fig. S1B). ZGLP1 preceded STRA8 in expression by a period of >1 day (Fig. 2, A and B). Postnatally, *Zglp1* showed specific expression in *Zbtb16*$^+$-undifferentiated and *Kit*$^+$-differentiating spermatogonia (fig. S3, A to C) (*16*).

We analyzed *Zglp1* homozygous knockout (*Zglp1*$^{-/-}$) mice (fig. S4A) (*14*, *15*). Compared with wild-type ovaries, *Zglp1*$^{-/-}$ ovaries at postnatal day (P) 8 and at 6 weeks were highly atrophic with no ovarian follicles. Ovaries as early as E17.5 contained a drastically reduced number of DDX4$^+$ cells (Fig. 2, C and D, and fig. S4B). At E15.5, although a substantial number of DDX4$^+$ cells remained in *Zglp1*$^{-/-}$ ovaries, a majority of them (≳90%) were negative for SYCP3 even though they expressed STRA8 (Fig. 2, D to F, and fig. S4, C to E; see below for the level of *Stra8*/STRA8 in *Zglp1*$^{-/-}$ cells). The less prevalent SYCP3$^+$ cells did not display features suggestive of meiotic entry, such as telomere clustering (*17*) or the expression of DMC1 (*18*, *19*) or γH2AX (*20*) (Fig. 2, E and F, and fig. S4, F and G). Note that the *Zglp1*$^{-/-}$ female germ cells bore more severe phenotypes than the *Stra8*$^{-/-}$ cells, some of which survived to form mature ovarian follicles despite their failure in meiosis (*21*).

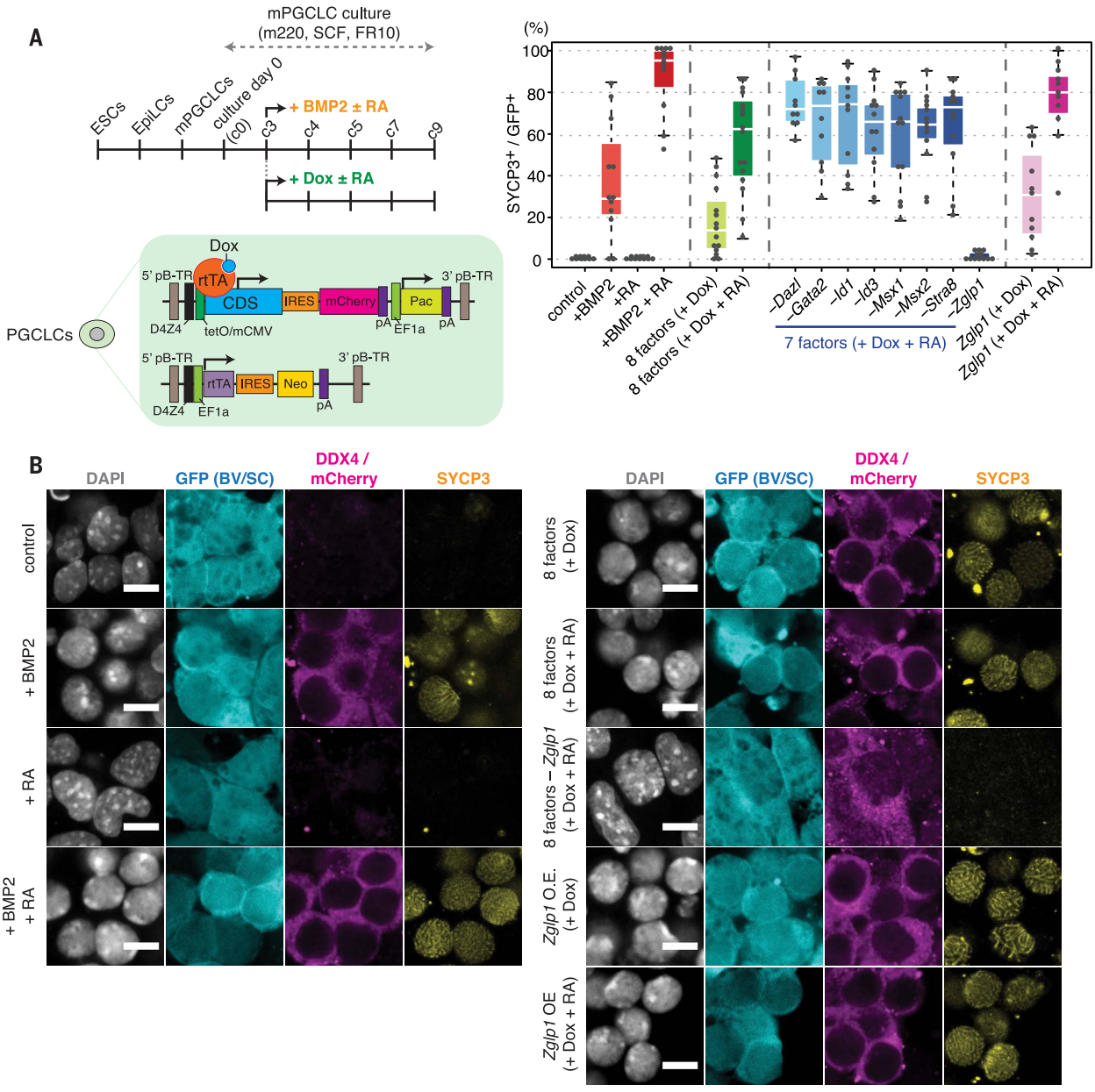


Fig. 1. Identification of a TF inducing the oogenic fate. (**A**) Left: Top, Scheme for the oogenic fate induction by BMP2- or Dox-induced TF overexpression with or without RA in mPGCLCs. m220, m220 feeder cells; SCF, stem cell factor; FR10, forskolin and rolipram (10 μM each). Bottom: Vectors for the Dox-inducible system. D4Z4, an insulator; EF1a, elongation factor 1α promoter; CDS, a coding DNA sequence from a candidate gene; IRES, internal ribosome entry site; Neo, neomycin-resistance gene; Pac, puromycin-resistance gene; pB-TR, *piggyBac* terminal repeat; rtTA, reverse tetracycline transactivator; tetO/mCMV, tetracycline operator fused to the minimal cytomegalovirus promoter. Right: Percentages of SYCP3$^+$ cell induction among GFP$^+$ (BV$^+$ and SC$^+$) mPGCLC-derived cells at c9 under the conditions indicated. For each condition, mPGCLC-derived cells were imaged so that a minimum of 20 BV$^+$ and SC$^+$ cells were included per image and at least 10 such images were acquired from two to four biological replicates. (**B**) Representative images for the expressions of GFP (BV and SC) (cyan), DDX4/mCherry (magenta), and SYCP3 (yellow) in mPGCLC-derived cells at c9 under the conditions indicated. Cells were counterstained with DAPI (gray). Scale bars, 10 μm.

The *Zglp1*$^{-/-}$ male germ cells developed normally until at least P7 (fig. S5, A and B). Subsequently, they exhibited severe impairment in the first wave of spermatogenesis: unlike in females, they entered into meiotic prophase but mostly failed to progress beyond the zygotene stage, resulting in a large fraction of abnormal pachytene cells both at P15 and P20 (fig. S5, A to F). The *Zglp1*$^{-/-}$ adults exhibited severe defects in spermatogenesis and were infertile (fig. S5, G and H) (*14*, *15*). Nonetheless, upon aging, a small fraction of the *Zglp1*$^{-/-}$ cells generated round or elongated spermatids, which, with intracytoplasmic sperm injection, contributed to apparently healthy offspring (fig. S5, I to O). Thus, in females, *Zglp1* is essential for activating the oogenic program, including meiotic prophase, whereas in males, it is dispensable for germ cell sex determination but is required in the spermatogonia for an efficient completion of meiotic prophase.

ZGLP1 is sufficient to create the foundation of the oogenic fate

Next, we explored the regulation and function of *Zglp1*. We examined the expression of *Zglp1* and other relevant genes by mPGCLC-derived

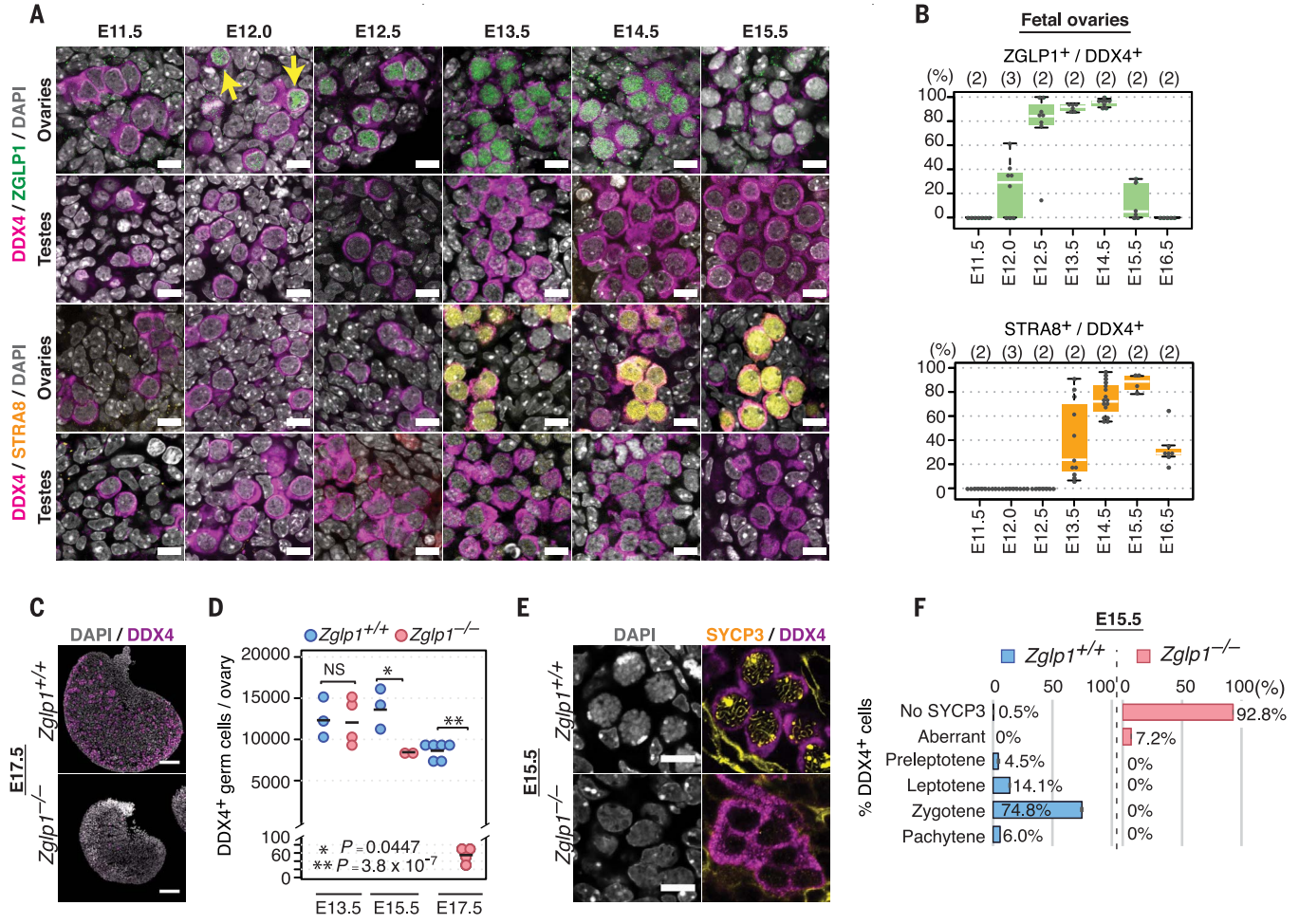


Fig. 2. Expression and requirement of ZGLP1 in oogenic fate determination. (**A**) Expression of ZGLP1 (green) and STRA8 (yellow) in DDX4$^+$ (magenta) germ cells in fetal ovaries and testes from E11.5 to E15.5. Cells were counterstained with DAPI (gray). Yellow arrows indicate ZGLP1$^+$ cells in E12.0 fetal ovaries. Scale bars, 10 μm. (**B**) Percentages of ZGLP1$^+$ or STRA8$^+$ cells among DDX4$^+$ cells per ovarian section (see the materials and methods). The numbers in parentheses represent the number of embryos analyzed. (**C**) Ovarian sections of *Zglp1*$^{+/+}$ and *Zglp1*$^{-/-}$ mice at E17.5 immunostained for DDX4 (magenta). Scale bars, 100 μm. (**D**) Numbers of DDX4$^+$ cells per ovary from *Zglp1*$^{+/+}$ and *Zglp1*$^{-/-}$ mice at E13.5, E15.5, and E17.5 (see the materials and methods). Two to three embryos were analyzed for each genotype at each time point. Black bars represent mean values. NS, not significant. (**E**) Expression of SYCP3 (yellow) in DDX4$^+$ (magenta) cells in ovaries of *Zglp1*$^{+/+}$ and *Zglp1*$^{-/-}$ mice at E15.5. Scale bars, 10 μm. (**F**) Percentages of DDX4$^+$ cells in ovaries of *Zglp1*$^{+/+}$ and *Zglp1*$^{-/-}$ mice at E15.5 showing distinct SYCP3 staining as categorized in fig. S4C. Two embryos for each genotype and at least 250 DDX4$^+$ cells were analyzed per embryo. Error bars indicate SD.

cells under four conditions: control culture or a culture with BMP2, RA, or both BMP2 and RA. *Zglp1* was undetectable in the control, whereas it was up-regulated as early as 24 hours after BMP2 stimulation and elevated further thereafter (fig. S6A). The manner of up-regulation of *Zglp1* in response to BMP2 was similar to that of *Id1*, a well-known BMP target (*22*) (fig. S6A). There was no up-regulation of *Zglp1* in response to RA (fig. S6A). Combined with the data showing that *Zglp1* up-regulation by BMP2 is impaired by LDN193189, a selective inhibitor of ALK2/3 receptors (fig. S6B), these findings confirm that *Zglp1* is a downstream target of BMP signaling. Although *Stra8* was up-regulated as early as 24 hours after RA stimulation and elevated further thereafter, it was also up-regulated, albeit at lower levels, in the control at late stages such as c7 and c9 (fig. S6C). Such up-regulation could be an effect of genome-wide DNA demethylation, including the demethylation of the *Stra8* promoter, during the mPGCLC culture (*8*, *23*) (fig. S6D). Note that BMP2 enhanced *Stra8* and *Rec8* expression at late stages such as c7 and c9 (fig. S6C), and these enhancements could have occurred, at least in part, through the action of ZGLP1 (see below). By contrast, RA-responsive genes (*24*) with no apparent roles in the oogenic pathway (*Cyp26a1*, *Rarb*, and *Hoxa1*) were undetectable in the control culture or the culture with BMP2 (fig. S6C), indicating that there is little, if any, RA activity in the culture.

We cloned mESC lines expressing high (A2), middle (C2), and low (H2) levels of *Zglp1*, respectively, upon Dox administration (fig. S7, A and B). ZGLP1 overexpression alone in mPGCLCs up-regulated key genes for the oogenic fate and meiotic entry (*Ddx4*, *Dazl*, *Stra8*, *Rec8*, *Sycp3*, *Spo11*, and *Dmc1*) and induced SYCP3$^+$ cells in a dose-dependent manner: notably, the A2 clone with the highest *Zglp1* expression activated oogenic and meiotic genes robustly and induced as much as ~90% of mPGCLCs into SYCP3$^+$ cells (fig. S7, C to E). RA enhanced such activations, particularly in the H2 and C2 clones with low and middle ZGLP1-overexpression levels, respectively (fig. S7, C and E). These findings suggest that ZGLP1 is sufficient to induce the oogenic fate, whereas RA augments the ZGLP1-activated oogenic program. We validated that although LDN193186 impaired the BMP-dependent up-regulation of oogenic and meiotic genes, it had no impact on that by ZGLP1 (fig. S7F), corroborating that ZGLP1 is a key BMP effector for the oogenic fate.

We examined the consequences of ZGLP1 overexpression in a culture lacking fetal bovine serum and including WIN18,446, an inhibitor of aldehyde dehydrogenases and thereby of RA biosynthesis from retinol (*25*), a condition under which the presence of RA can be negated more formally. Even under this condition, ZGLP1 attained a robust induction of the SYCP3$^+$ cells (fig. S8, A to C). We explored the effect of BMS493, an inverse agonist of RA receptors (RARs) that enhances the interaction of RARs with their corepressors (*26*). BMS493 therefore stabilizes a repressive chromatin state near RAR-bound genes, compromising their activation irrespective of the presence of RA (*26*). BMS493 inhibited the induction of SYCP3$^+$ cells by ZGLP1 to a substantial extent; however, even in the presence of 1 or 10 μM BMS493, which fully prevents the activity of 100 nM RA (fig. S8D), ZGLP1 induced ~20% of BV$^+$ and SC$^+$ cells into SYCP3$^+$ cells and up-regulated the relevant genes (fig. S8, E to G). Collectively, these findings indicate that ZGLP1 is sufficient to create the foundation of the oogenic fate in the absence of RA, that this function involves the activation of oogenic and meiotic genes both through RAR-dependent (BMS-sensitive) and RAR-independent (BMS-insensitive) mechanisms, and that RA enhances this pathway through RAR-mediated transcriptional regulation.

ZGLP1 reconstitutes key transcriptome programs for the oogenic fate

To examine the extent to which ZGLP1 overexpression recapitulates the oogenic program, we determined the transcriptome dynamics associated with ZGLP1 overexpression in mPGCLCs (the A2 clone) under the various conditions examined thus far (tables S1 and S3). Principal component analysis (PCA) revealed that mPGCLCs with ZGLP1 alone, as well as those under a serum-free condition with WIN18,446, progressed along the oogenic pathway, gaining, at c9, properties similar to those of E14.5 and E15.5 fetal oocytes (Fig. 3A and fig. S9A). A spread analysis revealed that up to 3% of mPGCLCs with ZGLP1 alone proceed to the pachytene stage by c9 (Fig. 3, B and C). mPGCLCs with ZGLP1 and BMS493 also adopted the oogenic program, gaining, at c9, more advanced properties than E13.5 fetal oocytes (fig. S9B). The addition of RA facilitated the ZGLP1-activated oogenic program, with mPGCLCs with ZGLP1 and RA attaining a transcriptome similar to that of E14.5 and E15.5 fetal oocytes at c7 (Fig. 3A) and up to 14% of them proceeding to the pachytene stage by c9 (Fig. 3C).

We defined the early PGC (315 genes: *Nanog*, *Sox2*, *Prdm1*, *Prdm14*, *Tfap2c*, etc.), late germ cell (250 genes: *Dazl*, *Ddx4*, *Piwil2*, *Mael*, *Mov10l1*, etc.), and fetal oocyte (468 genes: *Stra8*, *Rec8*, *Sycp3*, *Dmc1*, *Sycp1*, etc.) genes that characterize the transition of transcription profiles for the oogenic program (*7*). mPGCLCs with ZGLP1 (without RA, serum-free with WIN18,446) activated late germ cell and fetal oocyte genes to an extent comparable to fetal oocytes in vivo (fig. S9C), and mPGCLCs with ZGLP1 and BMS493 also activated such genes, with up-regulation of genes including *Stra8* and *Rec8* as early as 24 hours after Dox administration (fig. S9D). Conversely, mPGCLCs with ZGLP1 repressed early PGC genes moderately, and mPGCLCs with ZGLP1 and BMS493 failed, to a greater extent, to repress them (fig. S9C). By contrast, mPGCLCs with ZGLP1 and RA activated late germ cell and fetal oocyte genes and repressed the early PGC genes in a manner parallel to female germ cells in vivo (fig. S9C), highlighting the role of RA signaling in augmenting the activation of the oogenic program and repressing the early PGC program.

Compared with the control, mPGCLCs with ZGLP1 up-regulated 489 genes, which were enriched in gene ontology (GO) terms key to the oogenic fate, such as "oogenesis," "meiotic cell cycle," and "piRNA metabolic process" (Fig. 3D). mPGCLCs with BMP2, with ZGLP1 (serum-free with WIN18,446), and with ZGLP1 and BMS493 up-regulated a similar number of genes (457, 505, and 413 genes, respectively) with key GO enrichment (Fig. 3E), and the ZGLP1-overexpressing cells showed no up-regulation of typical BMP downstream genes, including *Id1/3* and *Msx1* (fig. S9, E and F). mPGCLCs with ZGLP1 and RA up-regulated a larger number of genes (1178), which encompassed nearly all of the genes up-regulated in mPGCLCs with ZGLP1 (Fig. 3D). Nonetheless, the genes specifically up-regulated above the threshold [$\log_2$(fold change) > 2] by ZGLP1 and RA (713 genes, with enrichment for "cilium assembly," "protein ubiquitination/phosphorylation," and "gametogenesis") were up-regulated, albeit to a lesser extent, by ZGLP1 alone (fig. S9G).

mPGCLCs with ZGLP1 down-regulated 294 genes, which were enriched in GO terms such as "regulation of transcription" and "glycolytic process" (Fig. 3F). Consistently, mPGCLCs with BMP2, with ZGLP1 (serum-free with WIN18,446), and with ZGLP1 and BMS493 down-regulated a similar number of genes (107, 187, and 185 genes, respectively) (Fig. 3G). mPGCLCs with ZGLP1 and RA down-regulated 1063 genes, which encompassed nearly all of the genes down-regulated in mPGCLCs with ZGLP1 (Fig. 3F). The genes specifically down-regulated above the threshold [$\log_2$(fold change) > 2] by ZGLP1 and RA (795 genes, with enrichment for "metabolic process," "stem cell maintenance," and "G1/S transition of mitotic cell cycle") were down-regulated only to a small extent by ZGLP1 alone (fig. S9H). Collectively, these findings demonstrate that the BMP signaling and ZGLP1 play a central role in establishing the key programs for the oogenic fate, with RA signaling assisting its maturation, including the repression of the early PGC program.

STRA8 activates meiotic genes in a ZGLP1-dependent context

To compare the role of *Zglp1* with that of *Stra8*, we generated *Zglp1* and *Stra8* homozygous knockout (*Zglp1*$^{-/-}$ and *Stra8*$^{-/-}$, respectively) mESCs (fig. S10, A to D). At least two *Zglp1*$^{-/-}$ and two *Stra8*$^{-/-}$ independent clones gave essentially identical phenotypes (see below), and we present representative data hereafter. The *Zglp1*$^{-/-}$ mESCs differentiated into apparently normal mPGCLCs, which propagated in culture in the presence of forskolin and rolipram; however, upon stimulation with BMP and RA, the *Zglp1*$^{-/-}$ mPGCLCs were retarded in down-regulating BV and SC expression, failed to establish premeiotic DNA replication, and failed to differentiate into SYCP3$^+$ fetal oocyte–like cells (fig. S10, E to H).

The transcriptome analyses revealed that in response to BMP2, *Zglp1*$^{-/-}$ mPGCLCs failed to up-regulate most of the genes that were up-regulated in wild-type mPGCLCs except genes such as *Id1* and *Id2* (Fig. 4, A and B). Accordingly, *Zglp1*$^{-/-}$ mPGCLCs with BMP and RA progressed very poorly along the female pathway, only gaining properties similar to those of ~E12.5 germ cells even at c9 (Fig. 4C). *Stra8*$^{-/-}$ mPGCLCs with BMP and RA also failed to establish premeiotic DNA replication and to fully differentiate into fetal oocyte–like cells (fig. S10, I and J) (*7*), yet they progressed further than *Zglp1*$^{-/-}$ mPGCLCs, acquiring the properties of germ cells between E13.5 and E14.5 to E15.5 (fig. S11A) (*7*). Although *Zglp1* expression was unaffected in *Stra8*$^{-/-}$ cells, *Stra8*/STRA8 was reduced to less than half in *Zglp1*$^{-/-}$ cells (Fig. 4, D and E). Furthermore, although the addition of RA at higher concentrations (1 and 10 μM) reinforced *Stra8* up-regulation in *Zglp1*$^{-/-}$ cells, it had no impact on the up-regulation of other oogenic or meiotic genes in these cells (Fig. 4F). To explore whether *Zglp1* overexpression overcomes the defects in *Stra8*$^{-/-}$ cells, we disrupted *Stra8* in the A2 clone (fig. S11, B and C). The mPGCLCs from the *Stra8*$^{-/-}$ A2 clone with Dox and RA exhibited phenotypes similar to those of the *Stra8*$^{-/-}$ mPGCLCs with BMP2 and RA (fig. S11, D and E). Thus, although *Zglp1* is essential for launching the overall oogenic program, *Stra8* is an indispensable downstream effector of *Zglp1* for the meiotic program.

The number of genes that failed to be up-regulated in *Zglp1*$^{-/-}$ mPGCLC-derived cells with BMP and RA (530 genes) was much greater than that in *Stra8*$^{-/-}$ cells (224 genes) (Fig. 4G). Although such genes in *Stra8*$^{-/-}$ cells, a majority of which (199/224 genes, ~89%) also failed to

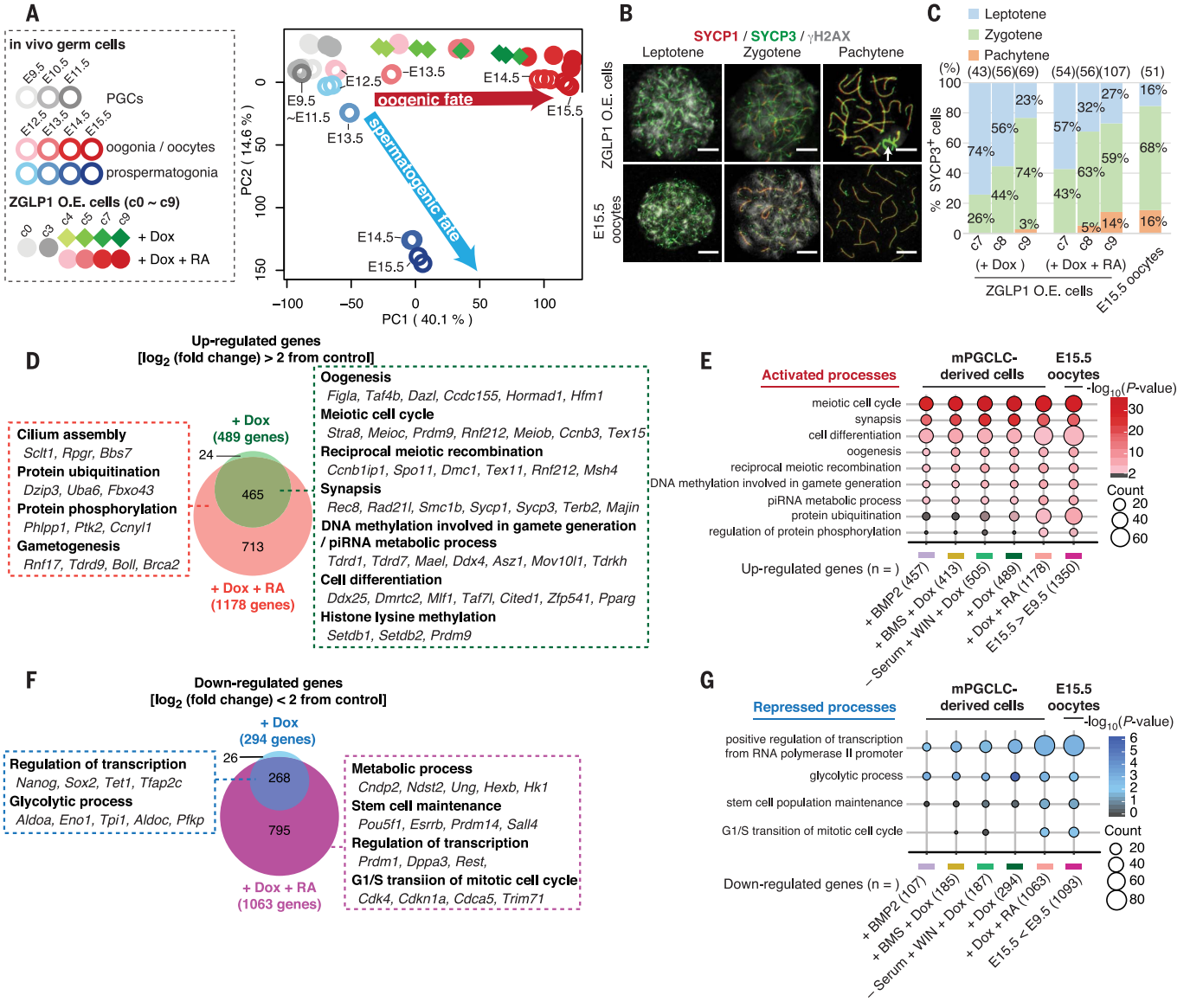


Fig. 3. Induction of the oogenic program by ZGLP1 and its augmentation by RA. (**A**) PCA of the transcriptomes of germ cells in vivo (E9.5 to E11.5 PGCs, E12.5 to E15.5 female or male germ cells) and mPGCLCs from *Zglp1*-overexpressing (O.E.) clones cultured with Dox or with Dox and RA. Each plot represents one transcriptome. Transcriptomes from two replicates (for E9.5 PGCs and E14.5 to E15.5 oocytes, three replicates) are plotted. The color code is as indicated. (**B**) Representative images showing the substages of meiotic prophase I in ZGLP1 O.E. mPGCLC-derived cells and E15.5 oocytes. Germ cells were spread and immunostained for SYCP1 (red), SYCP3 (green), and γH2AX (gray). Arrow indicates an unsynapsed X chromosome (this clone is XO) (fig. S7B). Scale bars: 5 μm for ZGLP1 O.E. cells, 10 μm for oocytes. (**C**) Meiotic progression of SYCP3^{+} mPGCLC-derived cells (at c7, c8, and c9) and E15.5 oocytes (see the materials and methods). The numbers of SYCP3^{+} cells analyzed are shown in parentheses above each bar. (**D** and **F**) Overlap of up-regulated or down-regulated genes between mPGCLCs overexpressing ZGLP1 without or with RA. The numbers of the genes up-regulated or down-regulated [$\log_2$(RPM + 1) > 4, $\log_2$(fold change) > 2 from the control, either at c4, c5, c7, or c9] are shown. Key GO enrichments are shown. (**E** and **G**) GO enrichment among genes up-regulated or down-regulated in mPGCLC-derived cells and in E15.5 oocytes. For mPGCLC-derived cells, the numbers of the genes up-regulated or down-regulated [$\log_2$(RPM + 1) > 4, $\log_2$(fold change) > 2, at c4, c5, c7, or c9] from the control culture (clone H18 for BMP2-treated and the *Zglp1* O.E. clone A2 for other treatments) are shown. For E15.5 oocytes, the numbers of genes up-regulated or down-regulated from E9.5 PGCs are shown.

be up-regulated in *Zglp1*$^{-/-}$ cells, were mainly associated with the processes for the meiotic prophase such as "synapsis" and "meiotic cell cycle," the genes that failed to be up-regulated exclusively in *Zglp1*$^{-/-}$ cells included those with wider implications for fetal oocyte development, such as "oogenesis," "RNA secondary structure unwinding," and "transcription and chromatin modification," in addition to those associated with the meiotic prophase (Fig. 4G). Similarly, the number of genes that failed to be down-regulated in *Zglp1*$^{-/-}$ cells with BMP and RA (281 genes) was greater than that in *Stra8*$^{-/-}$ cells (152 genes) (Fig. 4H). We conclude that *Zglp1* broadly regulates the oogenic program, whereas *Stra8*, which functions at least in part downstream of *Zglp1*, mainly regulates the meiotic program.

A mechanistic basis of ZGLP1 function

We used chromatin immunoprecipitation sequencing (ChIP-seq) to determine the genome-wide binding profiles of ZGLP1 in c7 or c8 mPGCLC-derived cells overexpressing V5-tagged

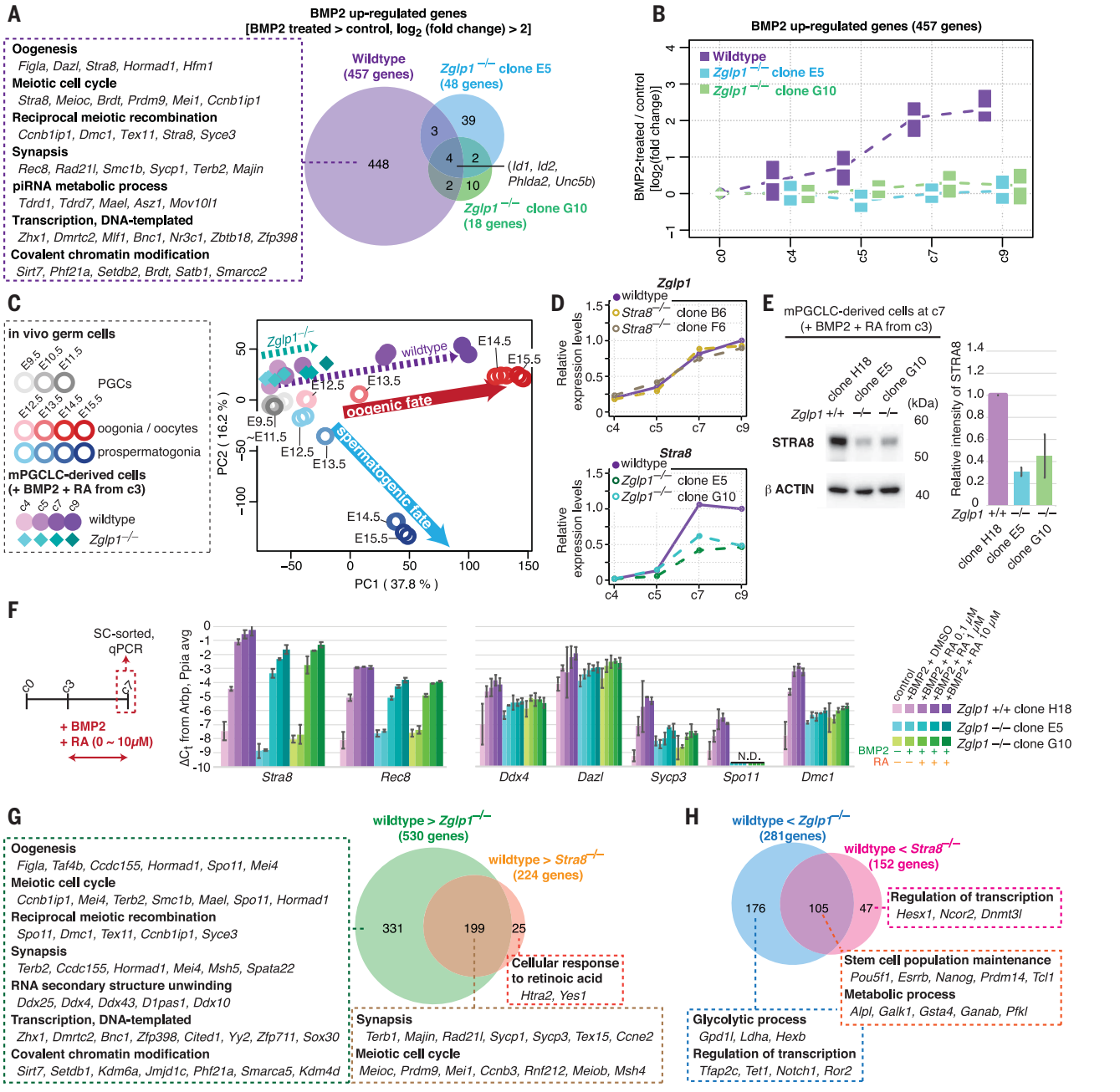


Fig. 4. Regulatory coverages of ZGLP1 and STRA8 for the oogenic program. (**A**) Overlap of genes up-regulated by BMP2 between the wild-type and *Zglp1*$^{-/-}$ mPGCLC-derived cells. The numbers of the genes up-regulated [$\log_2$(RPM + 1) > 4, $\log_2$(fold change) > 2 from the control at c4, c5, c7, or c9] in the respective clones are shown. Key GO enrichments are shown. (**B**) Expression kinetics of the 457 up-regulated genes (A) in the wild-type and *Zglp1*$^{-/-}$ mPGCLC-derived cells at c4, c5, c7, and c9. Fold changes from the control culture are shown for the respective clones. Box plots represent values for the 25th, 50th, and 75th percentiles. (**C**) PCA of the transcriptomes of germ cells in vivo (E9.5 to E11.5 PGCs and E12.5 to E15.5 female or male germ cells) and wild-type and *Zglp1*$^{-/-}$ mPGCLC-derived cells (G10) cultured with BMP2 and RA from c3. Each plot represents one transcriptome. Transcriptomes from two replicates (for E9.5 PGCs and E14.5 to E15.5 oocytes, three replicates) are plotted. The color code is as indicated. (**D**) Expression dynamics of *Zglp1* and *Stra8* in the wild-type, *Zglp1*$^{-/-}$, and *Stra8*$^{-/-}$ mPGCLC-derived cells cultured with BMP2 and RA from c3 onward (relative to the wild-type mPGCLC-derived cells at c9). (**E**) Left: Western blot analysis of the STRA8 expression at c7 in the wild-type and *Zglp1*$^{-/-}$ mPGCLC-derived cells cultured with BMP2 and RA from c3 onward. Right: STRA8 levels (normalized by β-ACTIN) from two biological replicates. The mean value for the wild-type mPGCLC-derived cells is set as 1.0. Error bars indicate SDs. (**F**) Expression of key oogenic and meiotic genes at c7 in the wild-type and *Zglp1*$^{-/-}$ mPGCLC-derived cells in the cultures as indicated. The expression in SC^{+} cells sorted by FACS was analyzed by quantitative polymerase chain reaction. The ΔC_t from the average C_t values of two housekeeping genes, *Arbp* and *Ppia*, is shown for each gene. The mean values from two independent experiments, each with two technical replicates, are shown. Error bars indicate SDs. N.D., not detected. The color code is as indicated. (**G** and **H**) Overlap of differentially expressed genes (DEGs) [$\log_2$(RPM + 1) > 4, $\log_2$(fold change) > 2 at c4, c5, c7, or c9] between the wild-type and *Zglp1*$^{-/-}$ PGCLC-derived cells (common DEGs in clone E5 and G10; 530 up-regulated and 281 down-regulated) and DEGs between the wild-type and *Stra8*$^{-/-}$ mPGCLC-derived cells (common DEGs in clone B6 and F6; 224 up-regulated and 152 down-regulated). Key GO enrichments are shown.

ZGLP1 from c3 onward without or with RA (fig. S12, A to C, and tables S4 and S5), and analyzed them with reference to the chromatin modification states of cultured mPGCLCs at c7 (*8*, *27*) (Fig. S12, D to F, and table S6). Under the condition without or with RA, we defined 16,576 and 14,662 ZGLP1-binding peaks in common in c7 and c8 cells, respectively, and assigned 16,290 and 14,409 peaks to the transcription start sites (TSSs), respectively (fig. S12G). Under both conditions, the majority of the peaks (>90%) were located within 15 kb of the TSSs, and approximately half of them were associated with promoters, binding to a majority of the promoters or genes expressed in c7 or c8 cells [~74% and ~70% of genes expressed at $\log_2(\text{RPM} + 1) > 4$, respectively] (fig. S12, G to I, and table S5). Accordingly, under the two conditions, a majority (≥79%) of the ZGLP1-bound genes overlapped (fig. S12J and table S5), suggesting that ZGLP1 functions at gene proximities independently from RA.

To identify ZGLP1–DNA interactions critical to the oogenic fate, we analyzed ZGLP1 binding to genes that were up-regulated in response to ZGLP1 overexpression. Upon ZGLP1 overexpression at c3 without RA, 41, 181, 671, and 829 genes were up-regulated from c3 at c4, c5, c7, and c9, respectively (Fig. 5, A and B, and fig. S12I). ZGLP1 bound to ~51% (21/41), ~54% (98/181), ~64% (426/671), and ~63% (520/829) of the c4, c5, c7, and c9 genes, respectively (Fig. 5, A and B, fig. S12I, and table S5). Notably, a dominant fraction of the c4 genes bound by ZGLP1 originally bore a repressive state; ~52% (11/21) and ~14% (3/21) showed bivalent modifications and H3K27me3 enrichment, respectively, and only ~29% (6/21) exhibited H3K4me3 enrichment (Fig. 5, A and B, and table S6). This trend was also the case for the c5 genes bound by ZGLP1, with ~37% (36/98) and ~18% (18/98) being bivalent and H3K27me3 enriched, respectively (Fig. 5, A and B, and table S6). By contrast, similar to the overall ZGLP1-binding profile in c7 and c8 cells, most (>67%) of the c7 and c9 genes bound by ZGLP1 were active genes with H3K4me3 enrichment (Fig. 5, A and B, and table S6). Similarly, a dominant fraction of the c4 and c5 genes up-regulated by ZGLP1 and RA and bound by ZGLP1 originally bore a repressive state (fig. S12, K and L, and table S6).

The H3K27me3-enriched genes bound by ZGLP1 exhibited higher up-regulation at c4

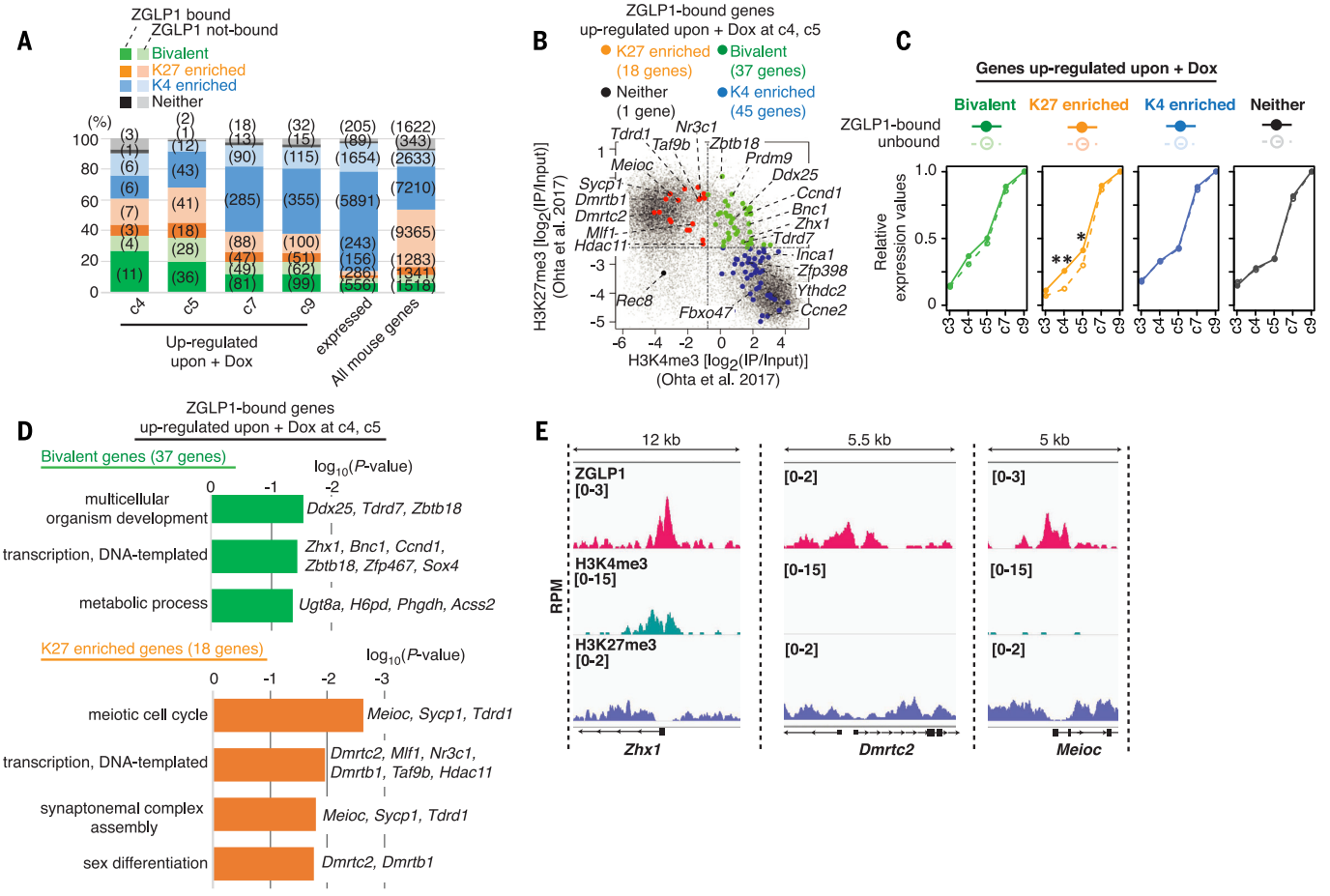


Fig. 5. Activation of Polycomb-repressed genes by ZGLP1. (**A**) Percentages of up-regulated genes [$\log_2$(fold change) > 2 from c3, at c4, c5, c7, and c9] in mPGCLC-derived cells cultured with Dox from c3 onward classified on the basis of ZGLP1 binding and the enrichment of two histone modifications (H3K4me3 and H3K27me3) (see table S6). The numbers of genes for each category are shown in parentheses. The color coding is as indicated. (**B**) Scatter plot showing the immunoprecipitation (IP) levels for H3K4me3 and H3K27me3 around the TSSs. The dotted lines represent the threshold IP levels for each histone modification (see the materials and methods). Genes bound by ZGLP1 and up-regulated from c3 to c4 or from c3 to c5 by Dox treatment (101 genes in total) are colored as indicated. Representative ZGLP1 up-regulated genes are annotated. (**C**) Expression dynamics of ZGLP1-bound and ZGLP1-unbound genes. The expression levels [$\log_2$(RPM + 1)] for each gene are normalized by its peak expression levels between c3 and c9, and then the median values are plotted. *$P < 0.05$. **$P < 0.005$. (**D**) GO term enrichment among bivalent and H3K27me3-enriched genes bound by ZGLP1 and up-regulated from c3 to c4 or from c3 to c5. (**E**) ChIP-seq tracks for ZGLP1, H3K4me3, and H3K27me3 around *Zhx1*, *Dmrtc2*, and *Meioc*. The ChIP-seq data for the two histone modifications are from sexually uncommitted mPGCLCs during culture (*8*).

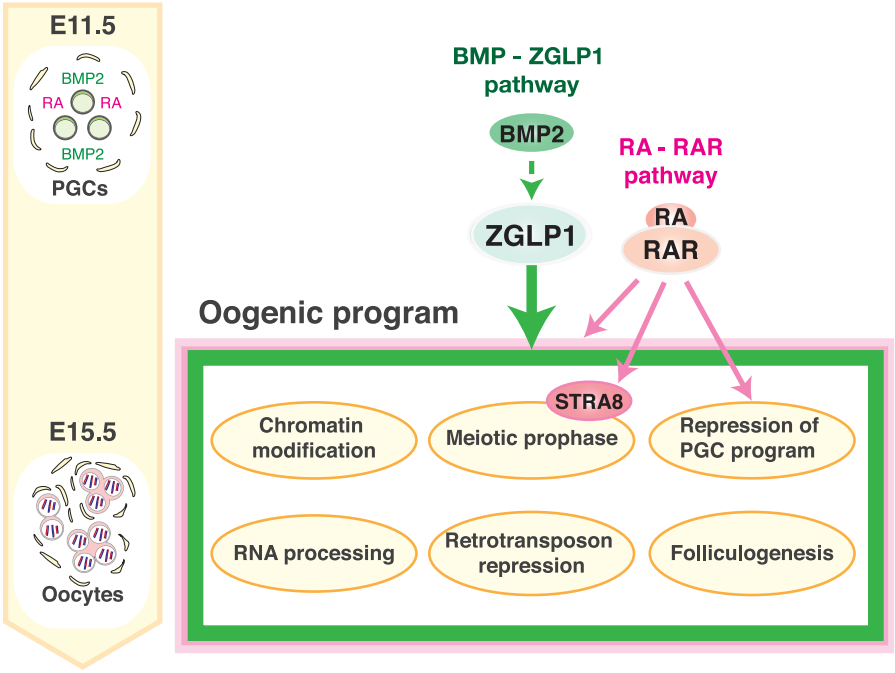


Fig. 6. Model for oogenic fate determination in mice. BMP2, most likely secreted from embryonic granulosa cells (*5*, *6*), up-regulates ZGLP1 in PGCs, which activates key oogenic programs, including those for "chromatin modification," "RNA processing," "retrotransposon repression," "folliculogenesis," and "meiotic cell cycle," whereas RA signaling contributes to the overall maturation of the oogenic program as well as to "repression of the PGC program." STRA8 mainly regulates the meiotic program in a ZGLP1-dependent context.

and at c5 than those not bound by ZGLP1, whereas the H3K4me3-enriched genes were up-regulated similarly irrespective of the ZGLP1 binding (Fig. 5C). The bivalent and H3K27me3-enriched genes bound by ZGLP1 and up-regulated by c5 were enriched with those for "multicellular organism development," "transcription," "meiotic cell cycle," and "sex differentiation," and included *Ddx25*, *Zbtb18*, *Zhx1*, *Meioc*, *Sycp1*, *Tdrd1*, *Dmrtc2*, *Dmrtb1*, *Taf9b*, and *Hdac11* (Fig. 5, D and E). The trend for the preferential up-regulation of the repressed genes bound by ZGLP1 at c4 and c5 was also observed and even appeared to be augmented in mPGCLCs with ZGLP1 and RA (fig. S12, M and N), with bivalent genes also showing higher up-regulation at c4. Collectively, these findings support the idea that ZGLP1 activates key genes for the oogenic program, including meiotic prophase, which are in poised and/or repressed states with bivalent or H3K27me3 modifications in sexually uncommitted germ cells.

Discussion

On the basis of both in vivo and in vitro studies in mice, we have demonstrated that BMP signaling and its downstream effector, ZGLP1, specify the oogenic program through the regulation of genes involved in "RNA processing," "transcription and chromatin modification," "retrotransposon regulation," "meiotic cell cycle," and "oocyte development," whereas RA signaling contributes to the overall maturation of the oogenic program as well as to the repression of the PGC program (Figs. 3 and 6 and fig. S9). The finding that RA plays a role in repression of the PGC program, which involves a network of TFs for pluripotency, is consistent with a well-known function of RA in stem cell differentiation (*28*). Thus, our findings provide an integrated paradigm for the signaling pathway and transcriptional mechanism for the oogenic program in mice (Fig. 6). Transcriptome analysis of human fetal germ cells and gonadal somatic cells revealed the potential involvement of the BMP–ZGLP1 pathway in human oogenic fate determination (*29*), suggesting that the BMP–ZGLP1 pathway may play a conserved function in oogenic fate determination in a wide range of species. Clarification of the biochemical mechanism of action of ZGLP1 will be a critical future challenge.

We have shown that *Zglp1* plays a critical function in allowing the spermatogonia, not to enter, but to efficiently accomplish the meiotic prophase, and only a small fraction of the *Zglp1*$^{-/-}$ cells generate round or elongated spermatids (*14*, *15*) (fig. S5). The distinct phenotypes between females and males represent a sexual dichotomy of the mechanism for the onset and progression of the oogenic and spermatogenic processes, including meiosis, which also warrants further investigation. Notably, the *Stra8*$^{-/-}$ male germ cells show more severe phenotypes: depending on the genetic background, they either fail to enter the meiotic prophase itself or fail to complete the meiotic prophase, with no formation of secondary spermatocytes or round or elongated spermatids (*30*, *31*). Thus, *Stra8* exhibits indispensable functions in ensuring the meiotic prophase both in females and males. A further understanding of the mechanism for the sex determination of germ cells will serve as a key not only for clarifying the etiology of relevant disease states, including infertility, but also for promoting in vitro gametogenesis in diverse mammalian species.

REFERENCES AND NOTES

1. C. Spiller, P. Koopman, J. Bowles, Sex determination in the mammalian germline. *Annu. Rev. Genet.* **51**, 265–285 (2017). doi: 10.1146/annurev-genet-120215-035449; pmid: 28853925
2. J. Bowles *et al.*, Retinoid signaling determines germ cell fate in mice. *Science* **312**, 596–600 (2006). doi: 10.1126/science.1125691; pmid: 16574820
3. A. E. Baltus *et al.*, In germ cells of mouse embryonic ovaries, the decision to enter meiosis precedes premeiotic DNA replication. *Nat. Genet.* **38**, 1430–1434 (2006). doi: 10.1038/ng1919; pmid: 17115059
4. J. Koubova *et al.*, Retinoic acid regulates sex-specific timing of meiotic initiation in mice. *Proc. Natl. Acad. Sci. U.S.A.* **103**, 2474–2479 (2006). doi: 10.1073/pnas.0510813103; pmid: 16461896
5. H. H. Yao *et al.*, Follistatin operates downstream of Wnt4 in mammalian ovary organogenesis. *Dev. Dyn.* **230**, 210–215 (2004). doi: 10.1002/dvdy.20042; pmid: 15162500
6. S. A. Jameson *et al.*, Temporal transcriptional profiling of somatic and germ cells reveals biased lineage priming of sexual fate in the fetal mouse gonad. *PLOS Genet.* **8**, e1002575 (2012). doi: 10.1371/journal.pgen.1002575; pmid: 22438826
7. H. Miyauchi *et al.*, Bone morphogenetic protein and retinoic acid synergistically specify female germ-cell fate in mice. *EMBO J.* **36**, 3100–3119 (2017). doi: 10.15252/embj.201796875; pmid: 28928204
8. H. Ohta *et al.*, *In vitro* expansion of mouse primordial germ cell-like cells recapitulates an epigenetic blank slate. *EMBO J.* **36**, 1888–1907 (2017). doi: 10.15252/embj.201695862; pmid: 28559416
9. T. Nakamura *et al.*, SC3-seq: A method for highly parallel and quantitative measurement of single-cell gene expression. *Nucleic Acids Res.* **43**, e60 (2015). doi: 10.1093/nar/gkv134; pmid: 25722368
10. Y. Lin, M. E. Gill, J. Koubova, D. C. Page, Germ cell-intrinsic and -extrinsic factors govern meiotic initiation in mouse embryos. *Science* **322**, 1685–1687 (2008). doi: 10.1126/science.1166340; pmid: 19074348
11. R. Le Bouffant *et al.*, Msx1 and Msx2 promote meiosis initiation. *Development* **138**, 5393–5402 (2011). doi: 10.1242/dev.068452; pmid: 22071108
12. F. Nakaki *et al.*, Induction of mouse germ-cell fate by transcription factors in vitro. *Nature* **501**, 222–226 (2013). doi: 10.1038/nature12417; pmid: 23913270
13. Y. Kojima *et al.*, Evolutionarily distinctive transcriptional and signaling programs drive human germ cell lineage specification from pluripotent stem cells. *Cell Stem Cell* **21**, 517–532.e5 (2017). doi: 10.1016/j.stem.2017.09.005
14. S. Li, M. M. Lu, D. Zhou, S. R. Hammes, E. E. Morrisey, GLP-1: A novel zinc finger protein required in somatic cells of the gonad for germ cell development. *Dev. Biol.* **301**, 106–116 (2007). doi: 10.1016/j.ydbio.2006.07.048; pmid: 16982049
15. T. J. Strauss, D. H. Castrillon, S. R. Hammes, GATA-like protein-1 (GLP-1) is required for normal germ cell development during embryonic oogenesis. *Reproduction* **141**, 173–181 (2011). doi: 10.1530/REP-10-0376; pmid: 21123517
16. B. P. Hermann *et al.*, The mammalian spermatogenesis single-cell transcriptome, from spermatogonial stem cells to spermatids. *Cell Rep.* **25**, 1650–1667.e8 (2018). doi: 10.1016/j.celrep.2018.10.026
17. Y. Chikashige *et al.*, Telomere-led premeiotic chromosome movement in fission yeast. *Science* **264**, 270–273 (1994). doi: 10.1126/science.8146661; pmid: 8146661

18. D. L. Pittman *et al*., Meiotic prophase arrest with failure of chromosome synapsis in mice deficient for Dmc1, a germline-specific RecA homolog. *Mol. Cell* **1**, 697–705 (1998). doi: 10.1016/S1097-2765(00)80069-6; pmid: 9660953
19. K. Yoshida *et al*., The mouse RecA-like gene Dmc1 is required for homologous chromosome synapsis during meiosis. *Mol. Cell* **1**, 707–718 (1998). doi: 10.1016/S1097-2765(00)80070-2; pmid: 9660954
20. S. K. Mahadevaiah *et al*., Recombinational DNA double-strand breaks in mice precede synapsis. *Nat. Genet.* **27**, 271–276 (2001). doi: 10.1038/85830; pmid: 11242108
21. G. A. Dokshin, A. E. Baltus, J. J. Eppig, D. C. Page, Oocyte differentiation is genetically dissociable from meiosis in mice. *Nat. Genet.* **45**, 877–883 (2013). doi: 10.1038/ng.2672; pmid: 23770609
22. T. López-Rovira, E. Chalaux, J. Massagué, J. L. Rosa, F. Ventura, Direct binding of Smad1 and Smad4 to two distinct motifs mediates bone morphogenetic protein-specific transcriptional activation of Id1 gene. *J. Biol. Chem.* **277**, 3176–3185 (2002). doi: 10.1074/jbc.M106826200; pmid: 11700304
23. K. Shirane *et al*., Global landscape and regulatory principles of DNA methylation reprogramming for germ cell specification by mouse pluripotent stem cells. *Dev. Cell* **39**, 87–103 (2016). doi: 10.1016/j.devcel.2016.08.008; pmid: 27642137
24. J. E. Balmer, R. Blomhoff, Gene expression regulation by retinoic acid. *J. Lipid Res.* **43**, 1773–1808 (2002). doi: 10.1194/jlr.R100015-JLR200; pmid: 12401878
25. J. K. Amory *et al*., Suppression of spermatogenesis by bisdichloroacetyldiamines is mediated by inhibition of testicular retinoic acid biosynthesis. *J. Androl.* **32**, 111–119 (2011). doi: 10.2164/jandrol.110.010751; pmid: 20705791
26. A. le Maire *et al*., A unique secondary-structure switch controls constitutive gene repression by retinoic acid receptor. *Nat. Struct. Mol. Biol.* **17**, 801–807 (2010). doi: 10.1038/nsmb.1855; pmid: 20543827
27. K. Kurimoto *et al*., Quantitative dynamics of chromatin remodeling during germ cell specification from mouse embryonic stem cells. *Cell Stem Cell* **16**, 517–532 (2015). doi: 10.1016/j.stem.2015.03.002; pmid: 25800778
28. D. R. Soprano, B. W. Teets, K. J. Soprano, Role of retinoic acid in the differentiation of embryonal carcinoma and embryonic stem cells. *Vitam. Horm.* **75**, 69–95 (2007). doi: 10.1016/S0083-6729(06)75003-8; pmid: 17368312
29. L. Li *et al*., Single-cell RNA-Seq analysis maps development of human germline cells and gonadal niche interactions. *Cell Stem Cell* **20**, 858–873.e4 (2017). doi: 10.1016/j.stem.2017.03.007
30. E. L. Anderson *et al*., Stra8 and its inducer, retinoic acid, regulate meiotic initiation in both spermatogenesis and oogenesis in mice. *Proc. Natl. Acad. Sci. U.S.A.* **105**, 14976–14980 (2008). doi: 10.1073/pnas.0807297105; pmid: 18799751
31. M. Mark *et al*., STRA8-deficient spermatocytes initiate, but fail to complete, meiosis and undergo premature chromosome condensation. *J. Cell Sci.* **121**, 3233–3242 (2008). doi: 10.1242/jcs.035071; pmid: 18799790

ACKNOWLEDGMENTS

We thank the members of our laboratory for their helpful input on this study and Y. Nagai, Y. Sakaguchi, N. Konishi, and M. Kawasaki of the Saitou Laboratory and T. Sato and M. Kabata of the Yamamoto Laboratory for technical assistance.

Author contributions: S.I.N. performed all the experiments and analyzed the data. F.N., H.M., Y.N., H.O., and K.H. assisted in the induction, expansion, and female differentiation by cytokines and transgene overexpression of PGCLCs. K.K. contributed to the ChIP-seq. T.N. and T.Y. contributed to the RNA-seq. Y.Y. contributed to the analyses of RNA-seq and ChIP-seq data. S.I.N. and M.S. designed the experiments and wrote the manuscript. **Funding:** This work was supported by a Japan Society for the Promotion of Science (JSPS) Research Fellowship for Young Scientists to S.I.N. and a Grant-in-Aid for Specially Promoted Research from JSPS (17H06098), a JST-ERATO grant (JPMJER1104), a grant from HFSP (RGP0057/2018), and grants from the Pythias Fund and the Open Philanthropy Project to M.S. **Competing interests:** The authors declare no competing interests. **Data and materials availability:** All data are available in the manuscript or the supplementary material. The accession number for the RNA-seq and ChIP-seq data generated in this study is GSE124262. All cell lines are available upon request through a material transfer agreement with Kyoto University.

SUPPLEMENTARY MATERIALS

science.sciencemag.org/content/367/6482/eaaw4115/suppl/DC1
Materials and Methods
Figs. S1 to S12
Tables S1 to S8
References (*32*–*63*)

18 December 2018; resubmitted 17 October 2019
Accepted 31 January 2020
Published online 13 February 2020
10.1126/science.aaw4115

RESEARCH ARTICLE SUMMARY

INTEGRATIVE OMICS

An atlas of the protein-coding genes in the human, pig, and mouse brain

Evelina Sjöstedt, Wen Zhong, Linn Fagerberg, Max Karlsson, Nicholas Mitsios, Csaba Adori, Per Oksvold, Fredrik Edfors, Agnieszka Limiszewska, Feria Hikmet, Jinrong Huang, Yutao Du, Lin Lin, Zhanying Dong, Ling Yang, Xin Liu, Hui Jiang, Xun Xu, Jian Wang, Huanming Yang, Lars Bolund, Adil Mardinoglu, Cheng Zhang, Kalle von Feilitzen, Cecilia Lindskog, Fredrik Pontén, Yonglun Luo, Tomas Hökfelt, Mathias Uhlén*†, Jan Mulder*†

INTRODUCTION: The brain is the most complex organ of the mammalian body, boasting a diverse physiology combined with intricate cellular organization. In an effort to expand our basic understanding of the neurobiology of the brain and its diseases, we performed a comprehensive molecular dissection of the main regions of the human, pig, and mouse brain using transcriptomics and antibody-based mapping. With this approach, we have identified regional expression profiles and observed similarities and differences in expression levels between these three mammalian species.

RATIONALE: There is a need for a comprehensive overview of genes expressed in the mammalian brain categorized by organ, brain region, and species specificity. To address this need, a brain-centered knowledge resource of RNA and protein expression in the brain of three mammalian species has been created and used for cell topological analysis, systems modeling, and data integration. The regional expression of all protein-coding genes is reported, and this classification is integrated with results from the analysis of tissues and organs of the whole human body. All generated data, including high-resolution images and metadata, have been made publicly available in an open-access Human Protein Atlas (HPA) Brain Atlas.

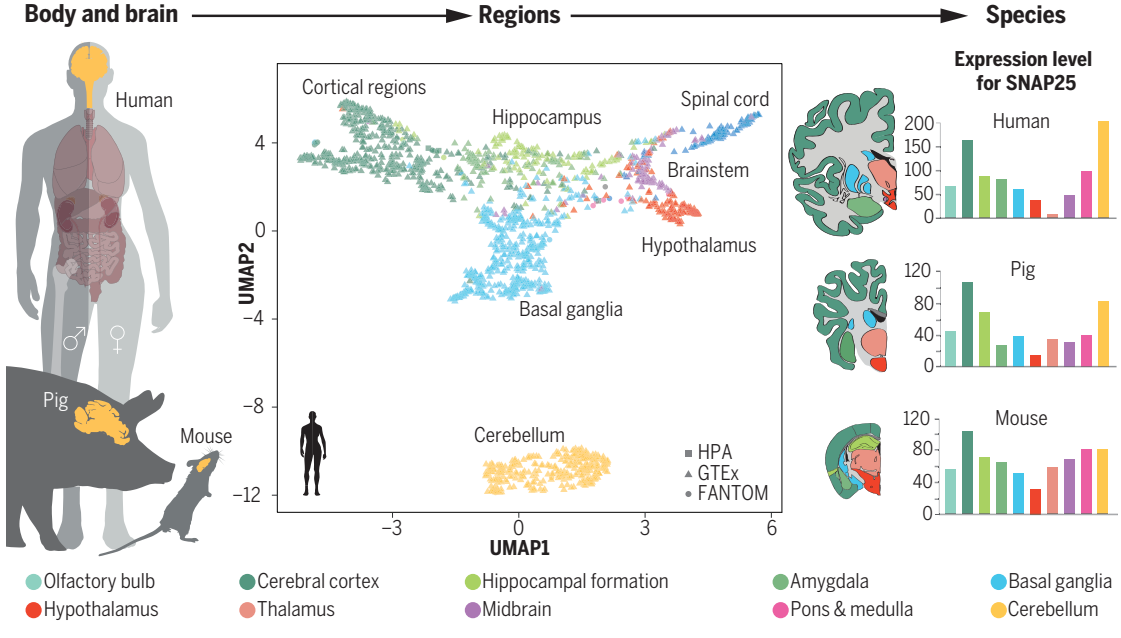
RESULTS: The global analysis suggests similar regional organization and expression patterns in the three mammalian species, consistent with the view that basic brain architecture is preserved during mammalian evolution. However, there is considerable variability between species for many neurotransmitter receptors, in particular between human and mouse. This calls for caution when using the mouse as a model system for the human brain, for example, in attempts to develop therapeutic strategies. For some of the brain regions, such as the cerebellum and hypothalamus, the human global expression profile is closer to that of the pig than it is to that of the mouse, suggesting that the pig might be considered a preferred animal model to study many brain processes. We show that many "signature genes" identified previously for specific brain cell types (such as astrocytes, microglia, oligodendrocytes, and neurons) are expressed at even higher levels in peripheral organs. In fact, our results support a view of shared functions between many genes in microglia and immune cells, and a large number of genes previously identified as signature genes for astrocytes are shown to be shared with liver or skeletal muscle. The cerebellum stands out as having a distinct molecular signature with many regionally enriched genes. Several genes suggested to be involved in neuropsychiatric diseases are selectively expressed in the cerebellum.

ON OUR WEBSITE

Read the full article at http://dx.doi.org/10.1126/science.aay5947

CONCLUSION: The integration of data from several sources has allowed us to combine data from transcriptomics, single-cell genomics, in situ hybridization, and antibody-based protein profiling. This integrative approach for mapping the molecular profiles in the human, pig, and mouse brain has generated a detailed multilevel genome-wide view on the protein-coding genes of the mammalian brain, where we compared tissue specificity across the whole body, as classified in the HPA (www.proteinatlas.org). The open-access HPA Brain Atlas resource offers the opportunity to explore individual genes and classes of genes and their expression profiles in the various parts of the mammalian brain. ■

The list of author affiliations is available in the full article online.
*These authors contributed equally to this work.
†Corresponding author. Email: mathias.uhlen@scilifelab.se (M.U.); jan.mulder@ki.se (J.M.)
Cite this article as E. Sjöstedt *et al.*, *Science* **367**, eaay5947 (2020). DOI: 10.1126/science.aay5947



Genome-wide transcriptomics analysis of anatomically dissected regions in mammalian brains uncovers regional and species-specific expression. Multiple regions of the human, pig, and mouse brain were dissected and analyzed. A uniform manifold approximation and projection (UMAP) analysis (middle) shows the global expression patterns of 1710 samples in the human brain, with the cerebellum as the outlier. The HPA Brain Atlas (right) shows the expression of individual genes, for example, synaptosomal-associated protein 25 (*SNAP25*), in the different brain regions in the three mammalian species.

RESEARCH ARTICLE

INTEGRATIVE OMICS

An atlas of the protein-coding genes in the human, pig, and mouse brain

Evelina Sjöstedt[1,2], Wen Zhong[2], Linn Fagerberg[2], Max Karlsson[2], Nicholas Mitsios[1], Csaba Adori[1], Per Oksvold[2], Fredrik Edfors[2], Agnieszka Limiszewska[1], Feria Hikmet[3], Jinrong Huang[4,5,6,7], Yutao Du[5,8], Lin Lin[4,6], Zhanying Dong[4,5,6], Ling Yang[4,5,6], Xin Liu[5,8], Hui Jiang[9], Xun Xu[5,8], Jian Wang[5,8], Huanming Yang[5,8], Lars Bolund[4,5,6], Adil Mardinoglu[2], Cheng Zhang[2], Kalle von Feilitzen[2], Cecilia Lindskog[3], Fredrik Pontén[3], Yonglun Luo[4,5,6], Tomas Hökfelt[1], Mathias Uhlén[1,2]*†, Jan Mulder[1]*†

The brain, with its diverse physiology and intricate cellular organization, is the most complex organ of the mammalian body. To expand our basic understanding of the neurobiology of the brain and its diseases, we performed a comprehensive molecular dissection of 10 major brain regions and multiple subregions using a variety of transcriptomics methods and antibody-based mapping. This analysis was carried out in the human, pig, and mouse brain to allow the identification of regional expression profiles, as well as to study similarities and differences in expression levels between the three species. The resulting data have been made available in an open-access Brain Atlas resource, part of the Human Protein Atlas, to allow exploration and comparison of the expression of individual protein-coding genes in various parts of the mammalian brain.

The brain is an extraordinarily complex organ owing to its diverse physiology, complex cellular organization, and abundance of expressed genes. Identifying the molecular organization of the brain at regional, cellular, and subcellular levels will advance our understanding of its function under normal and diseased conditions. The Human Protein Atlas (HPA) program aims to combine antibody-based profiling with genome-wide transcriptomics analysis to explore the spatial expression levels of transcripts and proteins across cells, tissues, and organs (*1*). The Tissue Atlas (*1*, *2*)—a subsection of the HPA—includes only a limited number of human brain regions (the cerebral cortex, hippocampus, caudate nucleus, and cerebellum). Here, we describe genome-wide expression profiles for the protein-coding genes in 10 major well-defined mammalian brain regions to capture the complexity of the cellular organization. To identify differences and similarities of the brain in different phylogenetic orders, the expression profiles have been analyzed in three species: primates (human), Cetartiodactyla (pig), and Rodentia (mouse).

The effort described here is complementary to several brain mapping projects focused on basic organization and regional or cellular gene expression of the mammalian brain. The Allen Institute for Brain Science (https://alleninstitute.org) hosts several knowledge resources, including an in situ hybridization atlas of the adult (*3*) and developing (*4*) mouse brain; and a microarray-based atlas of the adult human brain (*5*) has been complemented with a map of the human brain during development (*6*). More recently, brain atlas strategies have been launched on the basis of different approaches: fluorescence-activated cell sorting in mouse (*7*), antibody-based cell sorting in human (*8*), single-cell gene expression in mouse (*9*) and human (*10*, *11*), and covariation analysis of transcriptomics expression (*12*). These efforts have been further complemented with several large-scale mapping programs, including the National Institutes of Health (NIH) BRAIN Initiative Cell Census Network (*13*), the European Human Brain Project (*14*), the NIH Human BioMolecular Atlas Program (*15*), and the Human Cell Atlas project (*16*).

Here, we present the HPA Brain Atlas (*17*), where the data collected have been used for cell topological analysis, systems modeling, and data integration, with the aim to create a knowledge resource of messenger RNA and protein expression in the mammalian brain. We complement the transcriptomics with antibody-based protein profiles of selected proteins in multiple regions of the mouse brain. In this open-access resource, transcriptomics data from three external sources—the Genotype-Tissue Expression (GTEx) portal (*18*), the Functional Annotation of Mammalian Genomes 5 (FANTOM5) project (*19*), and the Allen Mouse Brain Atlas (*3*)—are presented together with RNA profiles and protein stainings generated "in-house." The classification of all protein-coding genes with regard to brain regional specificity is reported, and this is integrated with the tissue and organ specificity across the human body.

Transcriptomics analysis of the human brain

Transcriptomics analysis was performed on anatomically dissected human, pig, and mouse brain regions (Fig. 1A and figs. S1 to S3). For the human brain, we integrated publicly available RNA sequencing (RNA-seq) data generated by the GTEx consortium (*18*) and cap analysis of gene expression (CAGE) data from the FANTOM consortium (*19*), with data from the HPA (*1*), for a total of 1710 samples from selected human brain regions (table S1). The combined dataset contains 23 human brain regions, including white matter (corpus callosum) and spinal cord, as outlined in Fig. 1B. Several issues complicate the combining of datasets. First, samples may not be homogeneous, especially for regions with a high level of cellular heterogeneity, such as the hypothalamus, midbrain, pons, and medulla oblongata. Furthermore, both HPA and GTEx data are based on RNA-seq protocols using polyadenylate [poly(A)] tail enrichment, whereas CAGE data are based on the selection and sequencing of the 5′ cap. As a result, genes lacking the poly(A) tail, such as canonical histone mRNA, are only detected by CAGE. Despite these complications, the large number of included samples and our gene classification approach enable us to generate a comprehensive overview of biologically relevant gene expression and regional and species variation.

We used normalization strategies to avoid batch effects caused by sampling, technology platforms, and differences in transcriptome size between different types of tissues and also to allow both within-sample and between-sample comparisons (*20*, *21*). The within-sample normalization was based on protein-coding transcripts per million (pTPM), while the between-sample normalization was based on trimmed means of M values (TMM) (*22*), Pareto scaling per gene (*23*), and *limma* (*24*), resulting in normalized expression (NX) values calculated for all genes across all tissue types, as outlined in Fig. 1C and described in detail in the supplementary information (figs. S4 to S6).

The uniform manifold approximation and projection (UMAP) (fig. S7) of all 1710 human brain samples shows the expected global expression patterns after normalization. Developmentally related anatomical regions cluster together, with the cerebellum being an outlier

[1]Department of Neuroscience, Karolinska Institutet, 171 77 Stockholm, Sweden. [2]Department of Protein Science, Science for Life Laboratory, KTH-Royal Institute of Technology, 17121 Stockholm, Sweden. [3]Department of Immunology, Genetics and Pathology, Uppsala University, 751 85 Uppsala, Sweden. [4]Lars Bolund Institute of Regenerative Medicine, BGI-Qingdao, Qingdao 266555, China. [5]BGI-Shenzhen, Shenzhen 518083, China. [6]Department of Biomedicine, Aarhus University, 80000 Aarhus, Denmark. [7]Department of Biology, University of Copenhagen, 2100 Copenhagen, Denmark. [8]China National GeneBank, BGI-Shenzhen, Shenzhen 518083, China. [9]MGI, BGI-Shenzhen, Shenzhen 518083, China.
*These authors contributed equally to this work.
†Corresponding author. Email: mathias.uhlen@scilifelab.se (M.U.); jan.mulder@ki.se (J.M.)

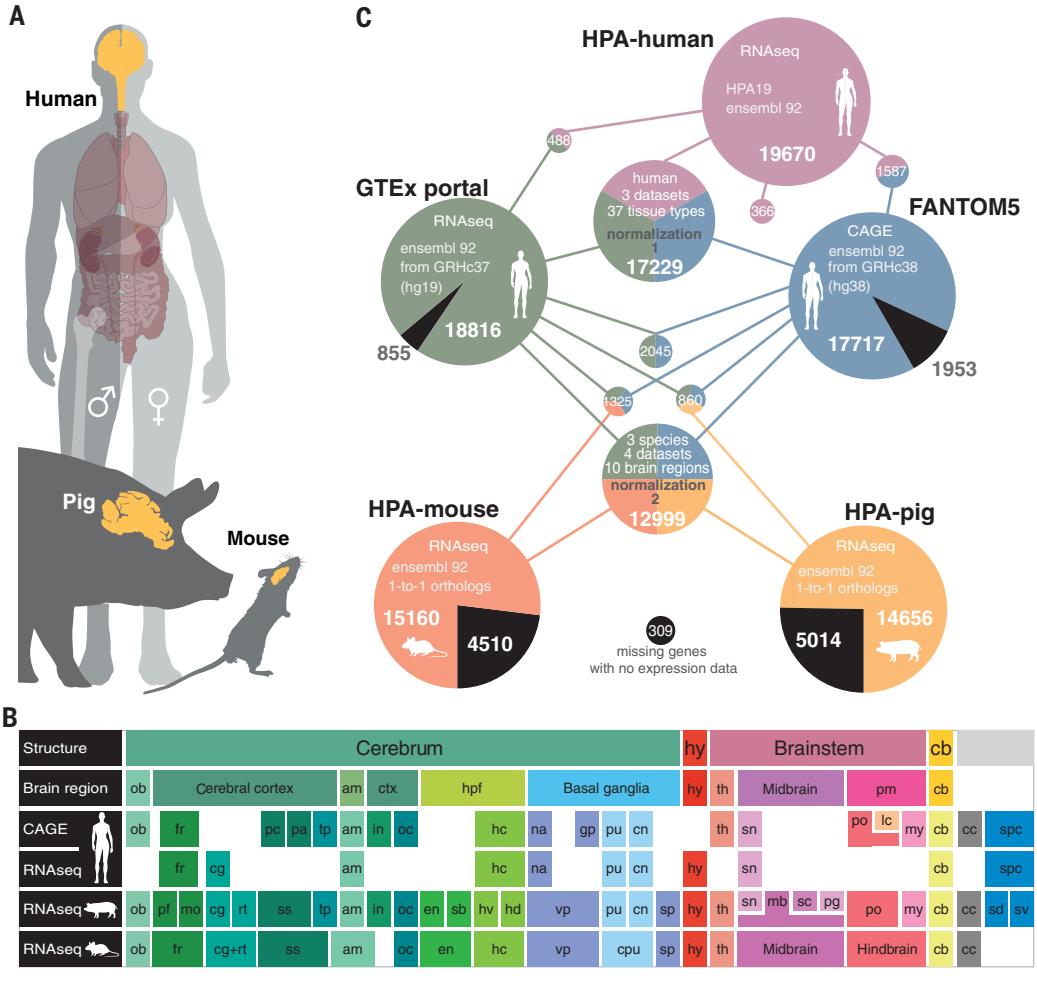


Fig. 1. Genome-wide transcriptomics analysis of anatomically dissected regions in mammalian brains. (**A**) Multiple regions of the human, pig, and mouse brain were dissected and analyzed using transcriptomics methods. (**B**) A summary of the included brain subregions, with 23 human, 30 pig, and 17 mouse samples, in 10 main brain regions (for an anatomical overview, see figs. S1 to S3). The subregions are as follows: olfactory bulb, ob; prefrontal cortex, pf; frontal lobe, fr; motor cortex, mo; cingulate cortex, cg; retrosplenial cortex, rt; somatosensory cortex, ss; paracentral gyrus, pa; postcentral gyrus, pc; temporal lobe, tp; insula cortex, in; occipital lobe, oc; entorhinal cortex, en; subiculum, sb; amygdala, am; hippocampus, hc (ventral, hv, and dorsal, hd); nucleus accumbens, na; ventral pallidum, vp; globus pallidus, gp; putamen, pu; caudate nucleus, cn; caudate putamen, cpu; septum, sp; hypothalamus, hy; thalamus, th; substantia nigra, sn; midbrain, mb; superior colliculus, sc; periaqueductal gray, pg; pons, po; locus coeruleus, lc; medulla oblongata, my; cerebellum, cb; corpus callosum, cc; spinal cord, spc (dorsal, sd, and ventral, sv). (**C**) Overview of the data normalization approach, combining five separate datasets. Total gene numbers for respective datasets are shown, as well as genes overlapping and nonoverlapping between datasets (see fig. S5 for extended version).

compared with other brain regions. No bias between the different platforms for transcriptomics analysis (HPA, GTEx, and FANTOM) was observed. The expression data for all analyzed human brain regions covering 19,670 human protein-coding genes are presented in a gene-specific manner in the HPA Brain Atlas (see below). The regional expression data in the human brain include 15,157 protein-coding genes detected in at least one region of the brain, ranging from 13,068 to 14,332 expressed genes per brain region (fig. S8).

Transcriptomics analysis of the pig brain

Brain transcriptome analysis of two male and two female adult pigs (Bama minipig, aged 1 year) was performed for anatomically dissected brain regions covering the whole brain, as outlined in table S2. The pig brain was divided into 30 anatomically defined brain regions (Fig. 1B). A normalization protocol using TMM and Pareto scaling was used, as outlined in fig. S4. A UMAP analysis of the transcript expression profiles of all samples (fig. S9) indicates the overall similarity between subregions and illustrates the expression variation between the cerebrum regions and regions of the brainstem. On the basis of the pig gene build Ensembl 92 and a detection cutoff at NX = 1, a total of 18,686 genes were detected in the pig brain, with 15,601 to 17,394 genes detected in individual brain regions (fig. S10). Expression data for 14,656 protein-coding genes with a one-to-one pig ortholog can be found in the gene-specific pages of the HPA Brain Atlas (*17*).

Transcriptomics analysis of the mouse brain

A genome-wide transcriptomics analysis was performed on multiple regions of two male and two female adult mice (C57bl/6n, aged 2 months). The mouse brain was divided into 17 anatomically defined brain regions (table S3). A normalization protocol using TMM and Pareto scaling was used, as outlined in fig. S4. The UMAP plot of the global expression patterns shows the expected pattern with developmentally related anatomical regions clustering together (fig. S11). On the basis of a cutoff for detection at NX = 1, a total of 15,823 brain-expressed mouse genes were detected, with 12,977 to 14,402 genes per brain region (fig. S12). Data for 15,160 protein-coding genes with a mouse one-to-one ortholog are presented in the gene-specific pages of the HPA Brain Atlas (*17*).

Genome-wide classification of all protein-coding genes based on regional brain expression

Expression data for the various brain regions of the three species were summarized into 10 main regions (Fig. 2, A to C). On the basis of the maximum expression in any of the analyzed subregions, a consensus result of the 10 regions for three species was generated. These regions are the olfactory bulb, all cerebral cortex regions, subfields of the hippocampus, the amygdala, regions of the basal ganglia, the hypothalamus, the thalamus, subfields of the midbrain, the pons and medulla oblongata, and the cerebellum (Fig. 1B). A hierarchical clustering of the 10 main regions was performed using the global expression profiles

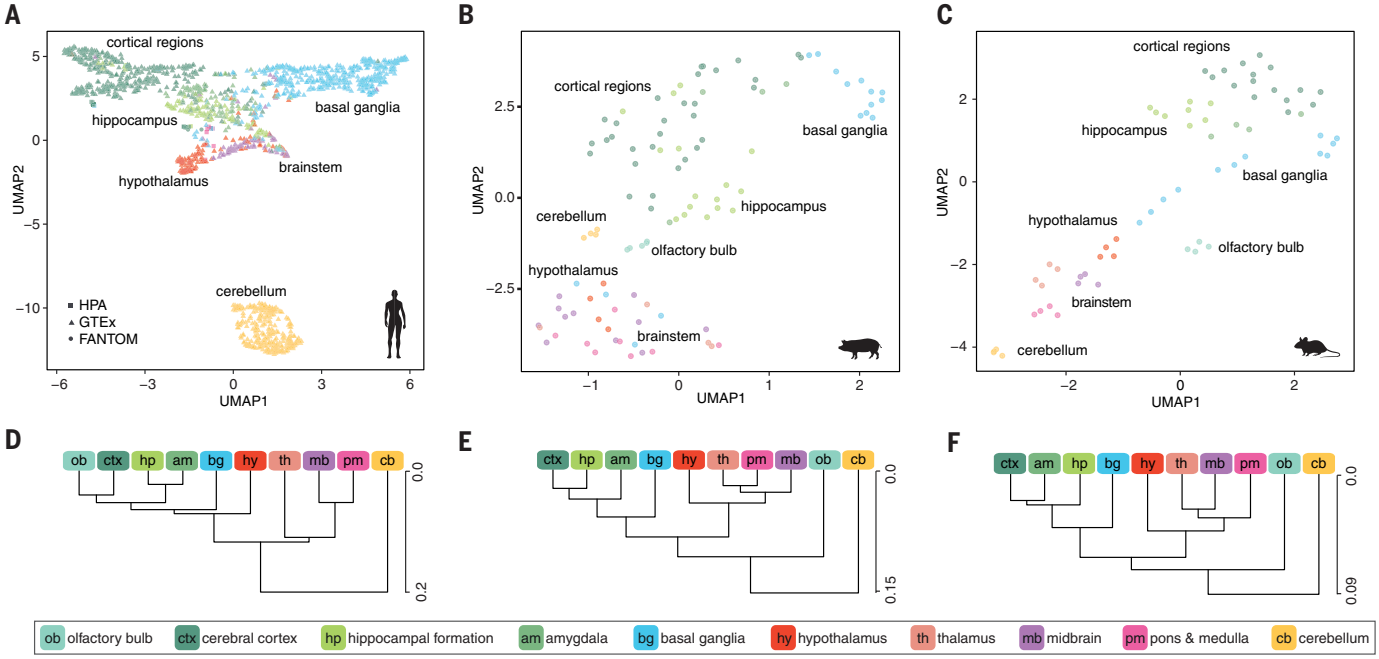


Fig. 2. Regional comparison based on global expression in three mammalian species. (**A**) Uniform manifold approximation and projection (UMAP) analysis showing the global expression patterns of all samples in 10 human brain regions (1616 total) from HPA, GTEx, and FANTOM. (**B**) UMAP plot of pig brain samples in 10 regions (107) used for mapping regional transcript expression in the pig brain. (**C**) UMAP plot of mouse brain samples in 10 regions (64) analyzed in this study from the mouse brain. (**D**) Hierarchical clustering based on pair-wise Spearman correlation of the transcript expression levels in 10 main brain regions is shown. (**E** and **F**) Same as (D), but for pig and mouse brain regions, respectively.

of all the protein-coding genes. The results for each of the three mammalian brains are shown in Fig. 2, D to F, with details in fig. S13. The hierarchical trees show a similar structure, with the cerebellum as an outlier in all three species and with the three cerebrum regions (cerebral cortex, hippocampus, and amygdala) close together, next to the basal ganglia. Similarly, the three brainstem regions (midbrain, thalamus, and pons and medulla) cluster together in all three species, next to the hypothalamus. The analysis confirms that the global expression patterns in the different regions of the three mammalian brains are preserved during mammalian evolution.

To identify regionally specific molecular features, regionally elevated genes were classified according to their expression across the 10 main brain regions. Elevated genes were further stratified into regionally enriched (fourfold higher expression compared with any other brain region), group enriched (several brain regions with fourfold higher values than all other regions), and regionally enhanced (fourfold higher expression than the average expression of the 10 regions). Genes not elevated in a single region or group of brain regions are classified as genes with low regional specificity (the classification is described in detail in table S4). This classification was performed across all protein-coding genes on the basis of NX values. The numbers of regionally enriched, group enriched, and regionally enhanced genes are shown in fig. S14 and in the HPA Brain Atlas resource (see below). Heatmaps show the distribution of regionally enriched, group-enriched, and regionally enhanced genes in the 10 regions of the human (fig. S15), pig (fig. S16), and mouse (fig. S17) brain. In all three species, the cerebellum contains the largest number of regionally enriched genes, while most group enriched genes are shared among the regions of the cerebrum and brainstem, respectively (fig. S18).

Comparative analysis of transcriptomics, in situ RNA hybridization, and immunofluorescence protein staining

A comprehensive and extensively used mouse brain gene expression atlas has been generated by the Allen Institute using probe-based in situ transcriptomics (*3*). In the HPA Brain Atlas, we have integrated expression profiles from the Allen Brain Atlas for all mouse genes (with a human one-to-one ortholog) with the HPA-generated RNA-seq and antibody-based protein distribution data. The two transcriptomics sets are highly complementary, because RNA-seq expression data provide sensitive quantitative transcript information, although these data have the disadvantage that mixtures of cell types are analyzed. The in situ hybridization data provide spatial expression data on a single-cell level, but this probe-based method is less quantitative than the count-based RNA-seq method. In addition, for selected proteins, an immunofluorescence protein distribution map was generated, allowing visualization of protein distribution on a cellular level, including neuronal processes, with high spatial resolution. An advantage of this protein staining is that anatomically stacked images can be generated, and this has allowed us to annotate more than 120 regions and subfields of the brain. Together, the three complementary datasets provide genome-wide regional profiles of the protein-coding genes and their expression in the different regions of the brain.

The results are displayed in the HPA Brain Atlas, and this resource allows for comparisons of the HPA data (RNA-seq), the probe-based in situ hybridization (ISH), and the antibody-based protein immunofluorescence (IF) staining for all 10 regions of the mouse brain, as exemplified for five genes in Fig. 3A. Insulin-like growth factor binding protein 5 (IGFBP5) is shown to be expressed in all analyzed regions of the mouse brain according to all datasets. However, both the mRNA location (ISH) and immunoreactivity (IF) reveal a distinct expression pattern in the mouse olfactory bulb with expression in mitral cells, localized both in soma and proximal dendrites. For NECAB1, an N-terminal EF-hand calcium binding protein with unknown function, brain-wide expression is also observed. The ISH and

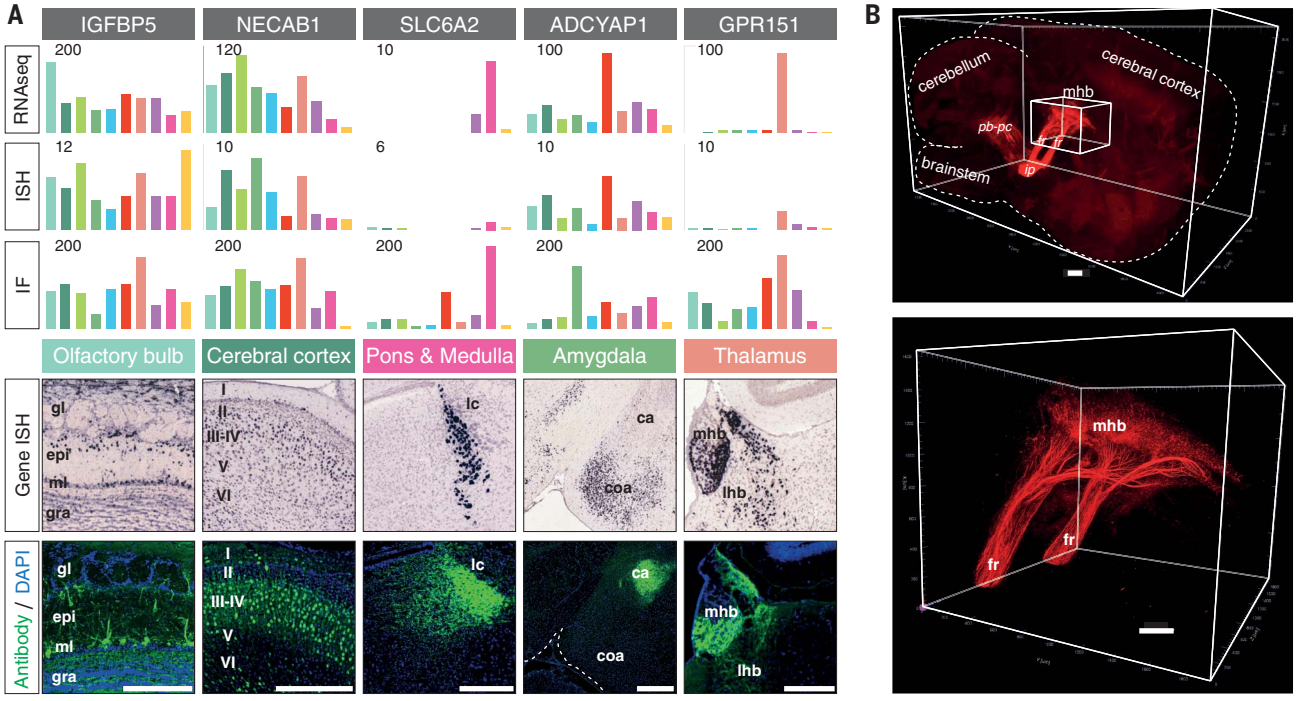


Fig. 3. Comparison of mouse regional data from transcriptomics, in situ hybridization, and immunofluorescence. (**A**) Examples of expression profiles from the HPA Brain Atlas, with mouse expression shown as data from RNA-seq (this study), in situ hybridization (ISH) data from the Allen Brain Atlas, and regional staining intensity based on antibody-based immunofluorescence (IF) profiling (this study). The color codes are the same as in Fig. 2. Below are examples of ISH and IF staining for each gene, from left to right: insulin-like growth factor binding protein 5 (IGFBP5); N-terminal EF-hand calcium binding protein 1 (NECAB1); norepinephrine transporter, also called solute carrier family 6 member 2 (NET1 or SLC6A2); adenylate cyclase–activating polypeptide 1 (ADCYAP1); and G protein–coupled receptor 151 (GPR151). Glomerular layer, gl; external plexiform layer, epi; mitral cell layer, ml; granule cell layer, gra; locus coeruleus, lc; central amygdala, ca; cortical amygdala, coa; lateral habenula, lhb. (**B**) iDISCO+ volume immunostaining of a whole mouse brain for GPR151 receptor. The medial habenula (mhb), fasciculus retroflexus (fr), interpeduncular nucleus (ip), and parabrachial-pericoerulear region (pb-pc) are strongly stained. The boxed region in the top image is enlarged in the bottom image. Scale bars, 250 μm.

the IF data indicate a distinct neuronal expression of NECAB1 in subsets of neurons in various regions of the thalamus and forebrain, including pyramidal neurons in the cerebral cortex. The (nor)epinephrine uptake transporter (SLC6A2), also called NET1, is an example of an apparent partial discrepancy between the RNA and the protein location: The RNA transcript is detected in cell bodies of the locus coeruleus in the pons with an expression pattern resembling that of the well-characterized (nor)epinephrinergic neurons. However, this transporter protein cannot be detected in the cell bodies with IF. This is because NET1 is rapidly transported into the extensive axonal network. Adenylate cyclase–activating polypeptide 1 (ADCYAP1) is known to stimulate the generation of cyclic adenosine monophosphate (cAMP), and all three datasets show widespread expression across the brain regions, with the highest levels in the hypothalamus and amygdala. In the latter region, ISH shows that this gene is expressed by cells located in the cortical amygdaloid nucleus, whereas protein labeling is found in nerve terminals in the central amygdaloid nucleus, which is known to receive an input from the cortical amygdala. The results suggest that this protein is primarily presynaptic and support a role in cAMP-mediated synaptic plasticity. Expression of the orphan G protein–coupled receptor 151 (GPR151) can be visualized both with ISH and IF in neuronal cell bodies in the habenular nucleus of the mouse thalamus. However, the protein staining also shows the projection from the thalamus to the interpeduncular nucleus in the midbrain. This orphan receptor is thus visualized in the neuronal soma, in axons running in the fasciculus retroflexus, and in the presynaptic terminals. This expression pattern can also be shown using three-dimensional imaging of solvent-cleared brain (iDISCO) encompassing a whole mouse hemisphere (Fig. 3B). In addition, this analysis revealed that a portion of the axons pass the interpeduncular nucleus and innervate the parabrachial-pericoerulear region. Movie S1 shows the three-dimensional location of this orphan receptor. Together, these examples illustrate how combining three different approaches for spatial transcriptomics and proteomics results in insights offering detailed information on cellular expression and protein location.

Species comparisons of regional brain expression

To compare the expression profiles in the three mammalian brains, all genes with one-to-one orthologs in human, mouse, and pig were identified, and a total of 12,999 protein-coding genes were analyzed (fig. S19A). Additional genes can be included in the analysis in the future, as additional one-to-one gene orthologs are identified. A combined hierarchical tree including all regions of the three species based on all regionally elevated genes across the 10 main regions is shown in Fig. 4A. The results again support a preserved brain architecture, where the hypothalamus and cerebellum of all three species cluster in proximity to each other. Similarly, the brainstem regions and the cerebrum regions cluster together. Neighboring regions from one species cluster together, but clustering is less tight for corresponding regions from different species. The olfactory bulbs from pig and mouse are clustered tightly together, and the outlier is the olfactory bulb from humans, which shows similarities with the cerebrum regions of humans. This might be due to sampling error, as discussed above, but could also reflect the

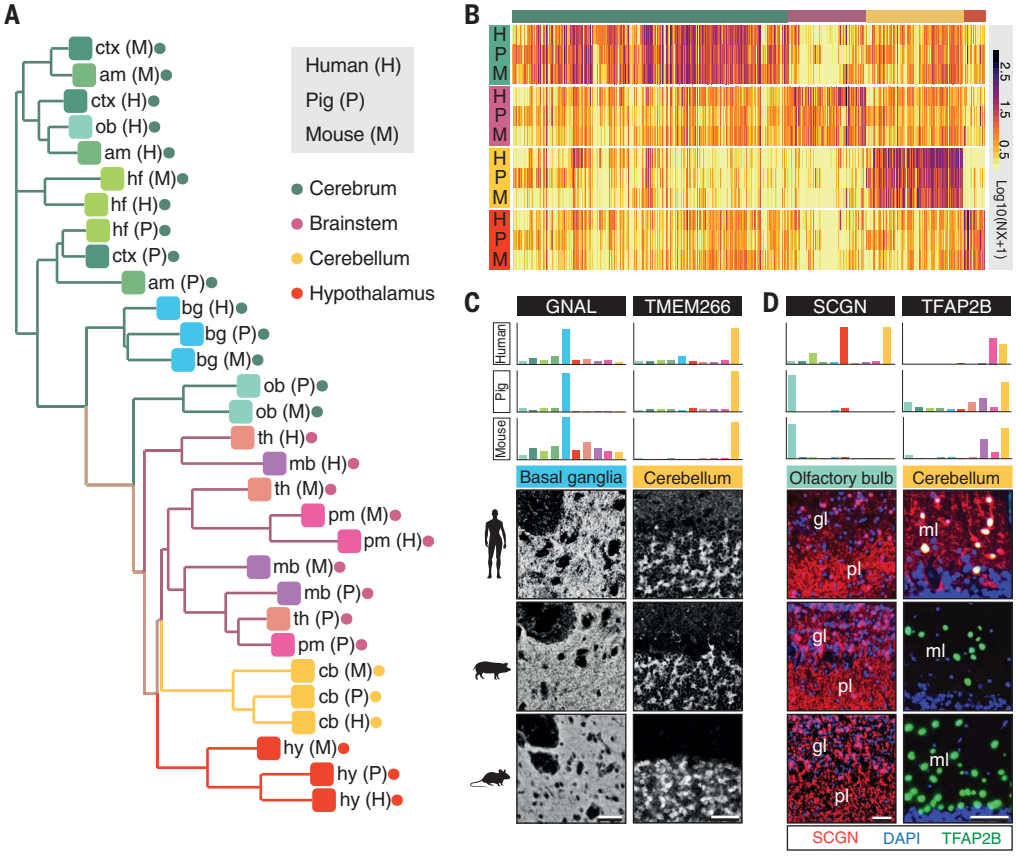


Fig. 4. Species comparison of regional expression in the mammalian brain. (**A**) The expression levels of 1422 genes classified as regionally elevated in either human, pig, or mouse were used for hierarchical clustering analysis, showing the relationship of the 10 main brain regions from the three species. (**B**) A heatmap showing the expression levels in the different brain structures in human (H), pig (P), and mouse (M) brain of enriched genes shared by the three species, based on brain structure comparison shown in Venn diagrams (fig. S19B). The same expression data, but visualized with the 10 regions of the brain, are shown in fig. S20. (**C**) Examples of regionally enriched genes in the mammalian brain and the protein location shown using immunofluorescence. GNAL is enriched in basal ganglia of human and pig brain, and this protein shows highest expression in basal ganglia (neuropil) in all three species. TMEM266 is cerebellum-enriched in all three species and located in synaptic glomeruli of the granular layer. (**D**) SCGN is expressed in the olfactory bulb in all three species with a higher expression in granule cells (gl) in the mouse and pig. In cerebellum, SCGN is only expressed in the molecular layer (ml) of the human and is not detected in pig or mouse cerebellum. In contrast, the transcription factor TFAP2B, coexpressed with SCGN in human, is expressed in the molecular layer of the cerebellum in all three species. External plexiform layer, pl. Scale bars, 50 μm.

more extended pig and rodent olfactory systems, which have olfactory bulbs that are larger than the more rudimentary human olfactory bulbs.

To analyze the differences in elevated genes in the three species, the regions were organized into four main brain structures (cerebrum, brainstem, cerebellum, and hypothalamus) (Fig. 4A), and the molecular features of each brain structure shared by all three species were identified. Genes with the highest expression in the same brain structure in all three species with enriched expression in at least one species were identified, and a list of 537 genes was obtained (fig. S19B). Heatmaps of the expression levels of these 537 brain structure–enriched genes are displayed in Fig. 4B and fig. S20, demonstrating the similarity of expression pattern for these genes across the regions of the brain in the three species. Many known genes are found among these 537 genes with brain structure–enriched expression, including the neuropeptides galanin, oxytocin, and vasopressin (hypothalamus); transcription factors such as T-box brain protein 1 (TBR1), special AT-rich sequence-binding protein 2 (SATB2), and neurogenic differentiation factor 6 (NEUROD6) (cerebrum); and hox genes (brainstem), but less well characterized genes are also found (table S5). The former include the G protein subunit alpha L (GNAL), which is highly expressed in the basal ganglia and known to couple to adenosine A2A and dopamine type 1 receptors (Fig. 4C) (*25*). The protein staining suggests synaptic location in the caudate nucleus or caudate putamen of all three species. Similarly, cerebellum-enriched transmembrane protein 266 (TMEM266, also known as HVRP1) is selectively detected in the synaptic glomeruli in the granular layer in all three species (Fig. 4C). This detection is in line with the reported role of this postsynaptic protein in the communication between mossy fibers and granule cells (*26*).

The normalized data also allowed us to identify genes with differential brain expression across the three species. Volcano plots show the overall fold difference in gene expression based on the 10 regions (figs. S21 to S23 and table S6), and these data were combined in scatterplots (figs. S24 to S26) showing species-specific molecular features (one versus two species). Many proteins show similar expression in the three species, as exemplified in Fig. 4D for transcription factor AP-2-beta (TFAP2B) expressed by γ-aminobutyric acid–releasing (GABAergic) interneurons (*27*), including stellate cells, in all three species. However, many differentially expressed genes associated to specific brain functions could also be identified, such as the low expression of the astrocytic genes glial fibrillary acidic protein (GFAP) and clusterin (CLU) in mouse compared with human and pig. For each of the 10 brain regions, a triangle plot indicates the relative expression of each gene in the three species (fig. S27). As an example, secretagogin (SCGN) is an EF-hand calcium binding protein expressed in the olfactory bulb (*28*) that is also seen in the stellate cells in the molecular layer of the human cerebellum. This contrasts with pig and mouse, where this protein cannot be detected in the cerebellum (Fig. 4D).

The neurochemical architecture of the mammalian brain

Brain functions are driven by complex circuits composed of different types of neurons with chemical phenotypes adapted to receive and generate signals. To identify species similarities and variations that characterize these types of neurons and their neurotransmitter systems, as well as other classes of cells, we analyzed the distribution of cell identity genes in all three mammalian species. These include (i) transcription factors (n = 1053 genes), which

are essential for differentiation and maintenance of cell identities in the postmitotic brain (*29*); (ii) cell identity genes, including neuropeptides, proteins, and enzymes responsible for the production, transport, and clearance of neurotransmitters (n = 63); and (iii) all known neurotransmitter and neuropeptide receptors and receptor subunits (n = 118). Comparing the correlation values between species for these protein classes reveals a higher correlation for transcription factors (P < 0.001), cell identity genes (P < 0.001), and receptors (P < 0.01) relative to the gene expression of all other 11,765 genes with their one-to-one ortholog (Fig. 5A).

We found that expression of some transcription factors is highly conserved across the three species, while other transcription factors have a less-maintained expression profile, thus affecting the overall correlation (fig. S28). Examples of some of the transcription factors with conserved distribution across the brain regions are illustrated in Fig. 5B. Homeobox protein 1 (EMX1), known to be expressed by most of the neurons in the cerebral cortex and hippocampus (*30*), has a similar expression pattern and expression levels in all three species. Class E basic helix-loop-helix protein 22 (BHLHE22, or Bhlhb5), which regulates postmitotic differentiation of cortical neurons (*31*), has a highly similar expression pattern in the cerebrum regions. In contrast, expression of the transcription factor SIX6 is restricted to the hypothalamus of all three species, which is in line with earlier reports (*32*). Pituitary homeobox 3 (PITX3) is mainly expressed in the midbrain in all three species, with the highest expression in the substantia nigra in pig, also supporting earlier observations that PITX3 plays a role in the development of dopaminergic neurons of the substantia nigra in mice (*33*). Homeobox protein Hox-B5 (HOXB5) is specifically expressed in the pons–medulla oblongata region, supporting the observation that Hox genes are expressed in the hindbrain and known to be important for the segmental patterning of this part of the brain. Neurogenic differentiation factor 1 (NEUROD1) is essential for the development of the cerebellum in rats (*34*). We find that this transcription factor is restricted to the cerebellum in all three species

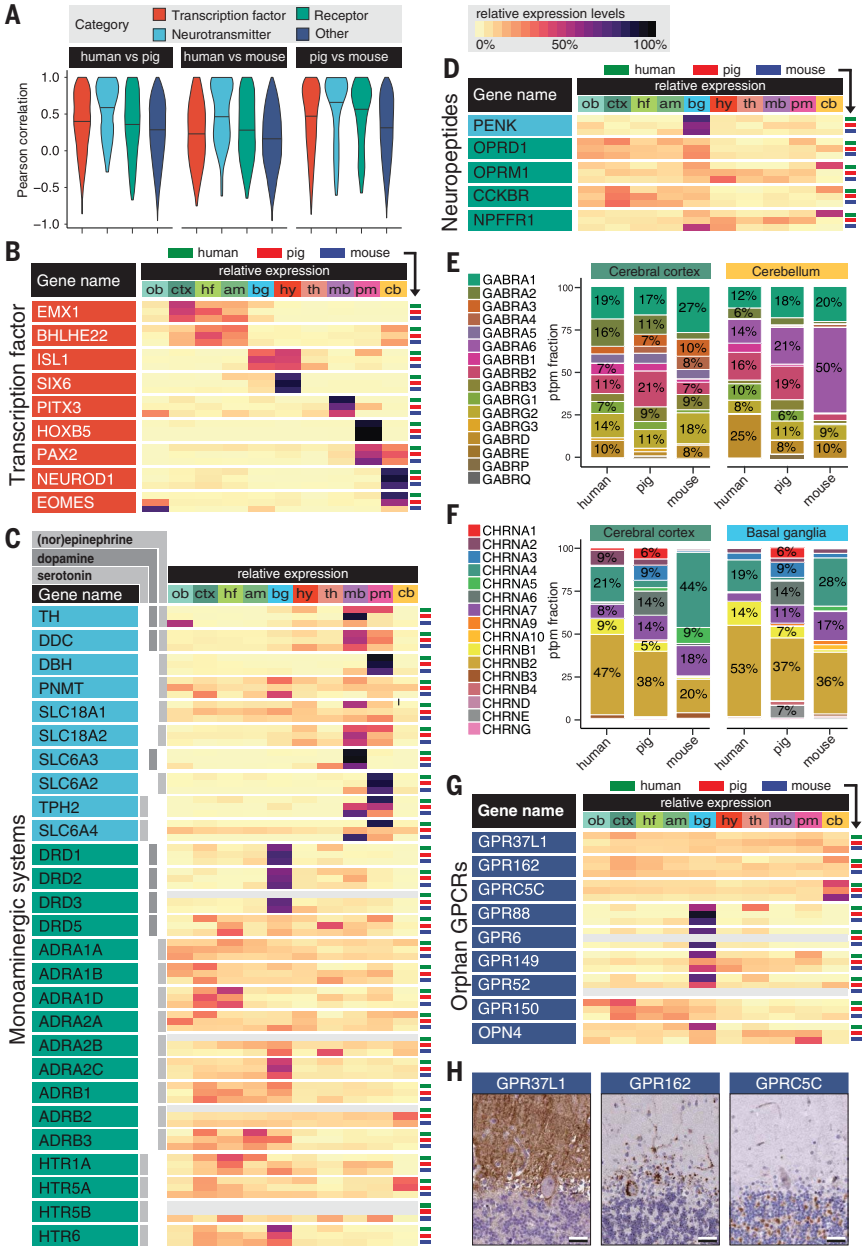


Fig. 5. Expression profiles of cell identity genes in the mammalian brain. (**A**) Overall Pearson correlation between species for transcription factors (red), genes involved in the production and processing of neurotransmitters and neuropeptides (blue), and metabotropic and ionotropic neurotransmitter and neuropeptide receptors (green) in contrast to all other genes (dark blue). (**B**) Examples showing the relative expression in the 10 regions of human, pig, and mouse brains display elevated expression in developmental and anatomical defined regions of the brain. (**C**) Comparing the relative distribution of the monoaminergic systems and (**D**) selected neuropeptide genes reveals a conserved pattern of expression, especially of the enzymes responsible for the production of dopamine (TH, DDC), noradrenaline (+DBH), adrenaline (+PNMT), and serotonin (TPH2) as well as the opioid peptide proenkephalin (PENK). Although many neurotransmitter receptors show a similar distribution profile [DDRs, ADRs, HTR1A, and 5-hydroxytryptamine receptor 6 (HTR6)], several exceptions with clear on/off differences between species could be observed, especially in the cerebellum (HTR5A, OPRM1, OPRD1, CCKBR, and NPFFR1). (**E**) Relative expression of all $GABA_A$ receptor subunits in the cerebral cortex and cerebellum and (**F**) nicotinic receptor subunits in all three species suggests alternative nicotinic subunit composition in different species, especially the pig. (**G**) Four brain-elevated orphan GPCRs (GPR6, GPR52, GPR88, and GPR149) are elevated in the caudate and putamen, whereas GPR150 is group-enriched in the forebrain regions. The nonvisual photoreceptor melanopsin (OPN4) is only expressed in the human basal ganglia. Missing values (gray bars) are due to missing one-to-one orthologs or genes not included in all used datasets. (**H**) The relative distribution of brain-elevated GPCRs with unknown function reveals widespread expression of the orphan GPR37L1 and GPR162, including the cerebellum, whereas GPRC5C expression is elevated in cerebellum. Scale bars, 40 um. Full overviews with NX for all transcription factors, neurotransmitters, and GPCRs are available in figs. S28 to S30.

(Fig. 5B). Notably, NEUROD1 is also expressed in retina of mouse and pig but not human (see gene-specific page of HPA Brain Atlas). An example of a transcription factor with a differential regional expression pattern is eomesodermin (EOMES, or TBR2), which has a high expression level in the human cerebellum but is expressed mainly in the olfactory bulb in the mouse brain. In pig, however, this transcription factor is expressed at equal levels in the cerebellum and olfactory bulb. Overall, these results show an evolutionarily preserved distribution and regulatory role of some of the transcription factors, which likely provide a foundation for basic brain architecture during evolution. However, these data also reveal substantial species variation in the distribution of transcription factors, including many uncharacterized transcription factors not yet linked to a cell type.

The neurotransmitters

The expression patterns of the proteins involved in brain signaling were analyzed in the various regions of the human, pig, and mouse brain, revealing a strong correlation between all species for genes essential for the production and transport of neurotransmitters and peptides (Fig. 5A). This confirms the known similarities between species with regard to the distribution of cell types and functions in the brain. In Fig. 5C, the relative distribution of molecular components of the neuromodulatory monoaminergic systems is shown, consisting of the (nor)adrenergic, dopaminergic, and serotonergic systems. In general, the enzymes responsible for the production of these neurotransmitters are distributed similarly in the three species, indicating a conserved organization in the mammalian brain, although there are some exceptions that might have neuropharmacological implications. For example, lysergic acid diethylamide (LSD) has a high affinity for several serotonin [5-hydroxytryptamine (5-HT)] receptors (*35*). Rodents have genes coding for serotonin receptors 5A and 5B (HTR5A and HTR5B) (*36*), whereas humans and pigs lost the gene for HTR5B during evolution. In mouse, HTR5A and HTR5B are expressed throughout the brain, with lowest expression in the cerebellum. Human and pig show a similar distribution to each other, with the highest expression of HTR5A in the cerebellum (Fig. 5C).

Another example of species differences is tyrosine hydroxylase (TH), the rate-limiting enzyme in the synthesis of the catecholamines dopamine, noradrenaline, and adrenaline. TH is expressed in the mouse olfactory bulb in a substantial number of mainly periglomerular, often GABAergic neurons, but this transcript is under the detection cutoff in human and pig. The human olfactory bulb does contain TH-positive neurons (*37*) and, as mentioned previously, the human results on the bulb may be compromised by dissection problems. Notably, the transcription factor PITX3 (Fig. 5B), known to bind with high affinity to the TH promotor (*38*), shows a similar species variation. The results also show a surprisingly strong and wide distribution of phenylethanolamine *N*-methyltransferase (PNMT) (Fig. 5C), the enzyme converting noradrenaline to adrenaline. As expected, PNMT is present in the pons and medulla oblongata of all three species (*39*, *40*), but unexpectedly high expression is found in mouse and human basal ganglia, in mouse cortex, and in pig olfactory bulb. A transient and wide expression of PNMT transcript and protein has been observed in the rat brain, but only during the first postnatal month (*39*). A pronounced species difference is also seen for the expression of the sodium-dependent serotonin transporter (SLC6A4) expressed in the brain regions containing serotonergic neurons in mouse and human, while the pig has more widespread expression (Fig. 5C). It has earlier been reported (*41*) that the expression of this transporter in the human and mouse developing brain is widespread before its expression is restricted to serotonergic neurons in the adult brain. Thus, our data suggest that SLC6A4 retains its developmental distribution in adult pigs.

The analysis of the genes coding for neuropeptide systems also revealed similarities and differences in expression between the species; for example, in the opioid system there is a highly conserved expression of the ligand proenkephalin (PENK) combined with a dissimilar regional expression of the delta (OPRD1) and mu (OPRM1) opioid receptors, both G protein–coupled receptors (GPCRs) (Fig. 5D). Our data support earlier observations that OPRM1 is expressed in the human cerebellum (*42*) but not in the mouse cerebellum (*43*), and here we show that this receptor cannot be detected in the cerebellum of pig. Instead, the expression profiles show the presence of OPRD1 in the pig cerebellum. The neuropeptide receptor NPFFR1 is here shown to be predominantly expressed in the human cerebellum, although this receptor binds the opioid-modulating peptide NPFF expressed in the cerebellum of all three species. Similarly, the gastrin/cholecystokinin type B receptor (CCKBR) is expressed in the human cerebellum, whereas the transcripts for the ligands (cholecystokinin and/or gastrin) could not be detected in this part of the brain. The ligands may have an extracerebellar origin.

We subsequently analyzed the genes coding for the γ-aminobutyric acid type A ($GABA_A$) and nicotinic receptor subunits (nACHRs) (Fig. 5, E and F). Both receptor types can form ligand-gated ion channels with different physiological properties by variations in the subunit compositions. Many of the studies related to these receptors have been performed in mice and rats, and it is therefore also relevant to compare the expression of the various $GABA_A$ and nACHRs in humans and pigs. Variation in subunit composition between brain regions has been reported (*44*), and it is known that the α6 (GABRA6) subunit, which has the highest potency for GABA, is only expressed in the cerebellum, unlike receptors containing the α1 and α2 subunits, which are more widespread throughout the brain. Carriers of a variant allele of the *GABRA6* gene have an increased risk for suicide (*45*), suggesting that the cerebellum might be implicated in mental disorders.

Comparing the expression of the GABA receptors in the three species suggests a conserved subunit composition, as exemplified by the subunit distribution pattern in cerebral cortex and cerebellum (Fig. 5E). In contrast, comparing the relative and absolute expression of nACHR subunits reveals a high degree of phylogenetic differences between mouse, human, and pig (Fig. 5F). For example, pigs express low levels of neuronal acetylcholine receptor subunit α4 (CHRNA4) but higher levels of subunits α1 (CHRNA1), α3 (CHRNA3), and α6 (CHRNA6) in the cerebral cortex and basal ganglia compared with mouse and human. Furthermore, both human and pig express higher levels of the β1 subunit (CHRNB1) compared with mice, and pigs express the ε subunit (CHRNE) in the basal ganglia only. The β1, α1, and ε subunits are all considered to be exclusive mammalian muscular nicotinic receptor subunits. The results presented here therefore suggest alternative nicotinic receptor composition in different mammalian species and the possibility of "muscular" nicotinic receptor subunits involved in the formation of functional nicotinic receptors in the central nervous system (CNS). These examples confirm the shared basic architecture of the mammalian brain with regard to cell types, neurotransmitter systems, and physiological functions. However, we identified examples of clear species variation in the expression levels and distribution of receptors that suggest an important role for receptors in brain evolution and adaptation. This reinforces the need for caution when comparing the function of, for examples, serotonergic, opioid, and cholinergic receptors on the basis of animal experiments using rodents without considering the expression pattern of the ortholog receptor in humans. This is particularly important in the context of drug development, given that at least 30% of today's prescribed drugs act via GPCRs (*46*).

GPCRs with unknown functions

We next analyzed the expression profiles of all GPCRs to explore differences and similarities in expression pattern across the brain regions in the three mammalian species (fig. S30).

These GPCRs include many olfactory receptors with highest mRNA levels in the olfactory bulb, possibly located in the axons of the olfactory receptor cells. In addition to the GPCRs associated with olfaction and neurotransmission, we identified several human orphan GPCRs with brain-elevated expression (n = 30 genes). These include the GPR37L1 and GPR162 expressed in many brain regions (Fig. 5G), such as the cerebellum (Fig. 5H), but also several brain-elevated orphan GPCRs with regionally elevated expression, including GPRC5C, mainly expressed in the cerebellum in all three species. We confirm the exclusive expression of GPR88 in the basal ganglia (*47*) of human, pig, and mouse, but we were also able to identify four brain orphan GPCRs with elevated expression in the basal ganglia (Fig. 5G). The nonvisual photoreceptor melanopsin (OPN4) shows high expression in the human basal ganglia but very low expression in the brains of pig and mouse. OPN4 is expressed by ganglion cells in the retina and plays a role in the regulation of circadian rhythms (*48*), although the function of this photoreceptor deep in the "dark" core of the brain is unclear. It was recently reported that melanopsin also acts as a thermoreceptor mediating heat-activated expression of clock genes (*49*). Our data, based on the expression pattern found here, suggest a possible temperature-sensing role of OPN4 in the human basal ganglia that is not shared with mice or pigs.

Whole-body versus brain regional tissue specificity classification

The data presented here have made it possible to compare the brain enrichment of all genes with the whole-body tissue specificity using the Tissue Atlas resource (*1*). The NX data across all samples were used to classify all protein-coding genes according to organ and tissue expression, where the brain was classified as a single organ, and 36 additional organs and tissues were scored across the human body. These tissue types include, for example, liver, pancreas, intestine, lung, reproductive organs, and lymphoid tissues, as well as a group of cell types summarized as "blood," including 18 single blood cell types and peripheral blood mononuclear cells (*50*). For the brain, the maximum NX value for a given gene in one of the brain regions was used as the brain expression value. We previously reported 1113 genes with elevated expression in the brain on the basis of the comparison of the cerebral cortex with 26 peripheral tissue types (*1*, *51*). Here, we analyzed many more brain regions as well as spinal cord and corpus callosum, and we identified many more genes (n = 2587) with elevated expression in at least one region of the brain compared with peripheral tissues (fig. S31). In addition, 5298 genes were found to be expressed in the brain but had elevated expression levels in a peripheral organ. A total of 8342 genes showed low tissue specificity across all 37 tissues and organs (fig. S31 and table S7). Only 33 genes could be specifically defined as enriched in the brain and not detected in any of the peripheral tissues. Many of these "specific" genes were transcription factors, such as neurogenic differentiaton factors 2 and 6 (NEUROD2 and NEUROD6), BarH-like 1 homeobox protein (BARHL1), and GPCRs such as GPR101 and GPR26.

We analyzed the expression levels of the 2587 human genes classified as brain-elevated across all analyzed human peripheral tissues (fig. S32A). The analysis demonstrates two major clusters: the first with relatively restricted expression across the peripheral tissues, and the second containing genes with a more tissue-wide expression. An analysis of the first cluster shows smaller and more specific expression clusters, such as a subcluster of genes with expression in testis and fallopian tube, in addition to the brain. Most of these genes encode proteins specifically expressed in ciliated cells, including ependymal cells lining the ventricular wall in the brain (fig. S32B). Other notable subclusters harbor genes with elevated expression in the brain but also high expression in peripheral tissues, such as cardiac and skeletal muscles (fig. S32C) and liver (fig. S32D). The large cluster of genes with elevated expression in the brain, but with a more general tissue-wide expression pattern, includes a small cluster of genes encoding immune tissue–associated proteins (fig. S32, E and F).

The relationship between the whole-body specificity and the regional brain specificity was then analyzed for all protein-coding genes. In Fig. 6, all genes detected in any of the human tissues and organs are included with a gene-to-gene comparison to the regional brain specificity. Only 520 genes that are classified as brain-elevated have regional brain specificity expression, while a large fraction of the brain-elevated genes (n = 1776) have low regional specificity within the brain. The latter include (i) several well-known astrocyte markers, including GFAP and aquaporin 4 (AQP4); (ii) oligodendrocyte genes involved in myelination, including myelin basic protein (MBP) and proteolipid protein 1 (PLP1); and (iii) pan-neuronal genes expressed by most neurons, for example, sodium/potassium-transporting adenosine triphosphatase subunit alpha-3 (ATP1A3). The 520 genes classified as both regionally and brain-elevated include genes known to be expressed by different neuronal populations and genes involved in inter- and intracellular signaling cascades, such as (i) receptors, e.g., adenosine receptor 2A (ADORA2A) enriched in the basal ganglia; (ii) ion channels, e.g., calcium voltage-gated channel auxiliary subunit gamma 3 (CALCNG3) elevated in regions of the cerebrum; and (iii) components of intracellular signaling pathways, such as GTPases, e.g., Rho guanine nucleotide exchange factor 33 (ARHGEF33) enriched in the cerebellum.

Many of the genes that have regional brain specificity expression are not brain-elevated from a whole-body perspective but instead have elevated expression in one or a group of peripheral tissue types. For example, ankyrin-1 (ANK1), with expression enriched in skeletal muscle and tongue, is selectively expressed in the cerebellum and, on the protein level, associated with the membrane of Purkinje cells (Fig. 6). However, most of the genes classified as elevated in tissue types other than brain are classified as having low regional specificity within the brain, such as a number of proteins detected in astrocytes or oligodendrocytes. These proteins include crystallin alpha B (CRYAB) and aldehyde dehydrogenase 6 family member A1 (ALDH6A1), as well as many of the microglia proteins, such as the well-characterized allograft inflammatory factor 1 (AIF1) and the neuropil-associated protein regulatory factor X2 (RFX2) elevated in testis. The group of genes (n = 8027) classified as both low tissue specific and low regional specific in the brain include many housekeeping proteins but also proteins with a more selective location to certain cell types, such as Acyl–coenzyme A (CoA) synthetase long chain family member 4 (ACSL4) mainly detected in neuronal cell bodies, and A-kinase anchoring protein 17A (AKAP17A) detected in the nucleus of glial cells and neurons in the cerebellar granular layer (Fig. 6).

Global and regional expression landscape of cortical cell type signature genes

A large number of differentially expressed genes have previously been identified using various approaches, including single-cell genomics and coexpression analysis. Here, we have analyzed the whole-body expression pattern of a consensus set of signature genes for cortical neurons, astrocytes, oligodendrocytes, and microglia using an immunopanning approach (*8*) and a coexpression analysis of publicly available expression data (*12*). From these two datasets, 420 genes were identified as putative human cerebral cortex cell type signature genes (listed in table S9), with 196 neuron-specific, 180 astrocyte-specific, 65 oligodendrocyte-specific, and 51 microglia-specific genes. Analyzing the expression variance of these cell type signature genes across the different regions of the brain showed multiple outliers differentially expressed in different parts of the brain for both neuronal and astrocyte genes (Fig. 7A). Oligodendrocytes and microglia signature genes are less variable across the different brain regions. A large fraction of neuronal and oligodendrocyte genes are classified as brain-enriched (Fig. 7B, table S10,

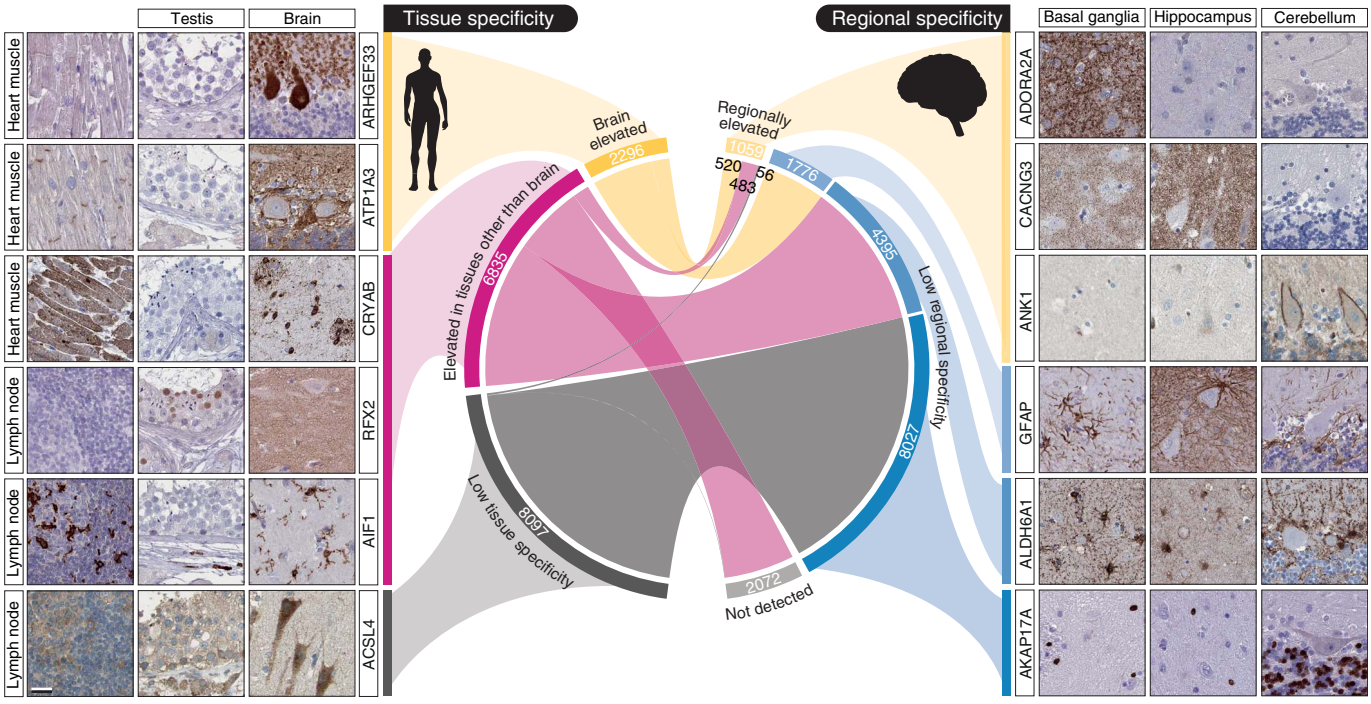


Fig. 6. The regional expression in brain compared with whole-body expression. Gene classification based on tissue specificity using transcript expression data in 37 different tissue types enables separation of genes into brain-elevated, elevated in tissues other than brain, and low tissue specificity. This is compared to the classification based on regional expression in the brain. Of 1059 genes, 520 with regionally elevated expression were also classified as brain-elevated. Genes classified as elevated in tissues other than the brain are often detected in brain but expressed with low regional specificity. Rho guanine nucleotide exchange factor 33 (ARHGEF33) is brain-enriched, including cerebellum-enriched, and here detected in Purkinje cells (HPA041051). ATPase Na^+/K^+ transporting subunit alpha 3 (ATP1A3) is group-enriched in brain and heart muscle and detected in all brain regions with low regional specificity. Immunohistochemistry using HPA056446 displayed the intercalated discs in heart muscle and had a synaptic location in brain. Crystallin alpha B (CRYAB) is tissue-enhanced in striated muscle, found in all brain regions with low tissue specificity, and detected in oligodendrocytes (HPA057100). Regulatory factor X2 (RFX2) is elevated in testis and detected in all brain regions with low regional specificity, and with a nuclear localization in testis and neuropil in brain (HPA048969). AIF1 is enhanced in blood and lymphoid tissues, while also detected in microglia in all brain regions with low regional specificity (HPA049234). ACSL4 is classified as low specificity both in tissues as well as brain regions (HPA005552). ADORA2A is group-enriched in lymphoid tissues and brain, including basal ganglia–enriched (HPA075997). Calcium voltage-gated channel auxiliary subunit gamma 3 (CACNG3) is brain-enriched and group-enriched in cerebrum regions but was not detected in cerebellum, also verified at the protein level (HPA077238). ANK1 is group-enriched in skeletal muscle and tongue as well as cerebellum-enhanced in brain, where the protein is selectively associated with the Purkinje cell membrane (HPA004842). GFAP is brain-enriched and detected in all brain regions with low regional specificity (HPA056030). ALDH6A1 is group-enriched in kidney and liver, detected in all brain regions with low regional specificity, and, as GFAP, localized to astrocytes (HPA029074). AKAP17A is expressed in all tissue types with low tissue specificity as well as low regional specificity in the brain; the protein is detected in subsets of cell nuclei and in brain in glial cells as well as granular cells in cerebellum (HPA043247). Scale bar, 25 μm.

and fig. S35), while many astrocyte and microglia genes are classified as elevated in other tissues. In fact, several astrocyte signature genes are highly expressed in liver and/or muscle tissue, whereas many microglia signature genes are enriched in lymphoid tissue, bone marrow, and/or blood. In summary, the global analysis reveals that most of the putative astrocyte and microglia signature genes are highly expressed in selective peripheral tissues, often exceeding the expression levels in the brain.

We superimposed the putative cell type signature genes on the global tissue expression landscape using the data from this study (Fig. 7C). Expression of only 180 of the human cerebral cortex cell type signature genes (43%) was classified as brain-elevated with regard to expression, and 158 genes (38%) were classified as elevated in expression in nonbrain tissues and the expression of the remaining genes (n = 82) classified as low tissue specific. To further explore this lack of "brain specificity" of many of the putative brain signature genes, we analyzed some of these genes further, as shown in Fig. 7D. The microglia signature genes arachidonate 5-lipoxygenase (ALOX5) and integrin subunit beta 2 (ITGB2) both showed elevated expression in blood (lymphoid tissues), while other microglia signature genes showed elevated expression in specific blood cells. For example, the gene for PYD and CARD domain containing protein (PYCARD) is expressed by granulocytes, monocytes, and dendritic cells. These results confirm the notion of shared origin and functions between microglia and immune cells. In contrast, several astrocyte signature genes are classified as genes with elevated expression in liver or muscle tissue. Out of the 19 genes with liver-elevated expression, six are transport-related genes, including solute carrier family 13 member 5 (SLC13A5), detected in the membrane of hepatocytes and end feet of astrocytes in brain, and nine genes code for metabolic enzymes such as aldehyde dehydrogenase 1 family member L1 (ALDH1L1), detected in cytoplasm of hepatocytes and astrocytes. Genes classified as having muscle-elevated expression include several proteins with structural function, such as syntrophin alpha 1 (SNTA1), detected both in astrocytes and skeletal muscle. All three are thus classified as showing elevated expression in tissues other than brain on the tissue level. These results highlight the shared function of astrocytes

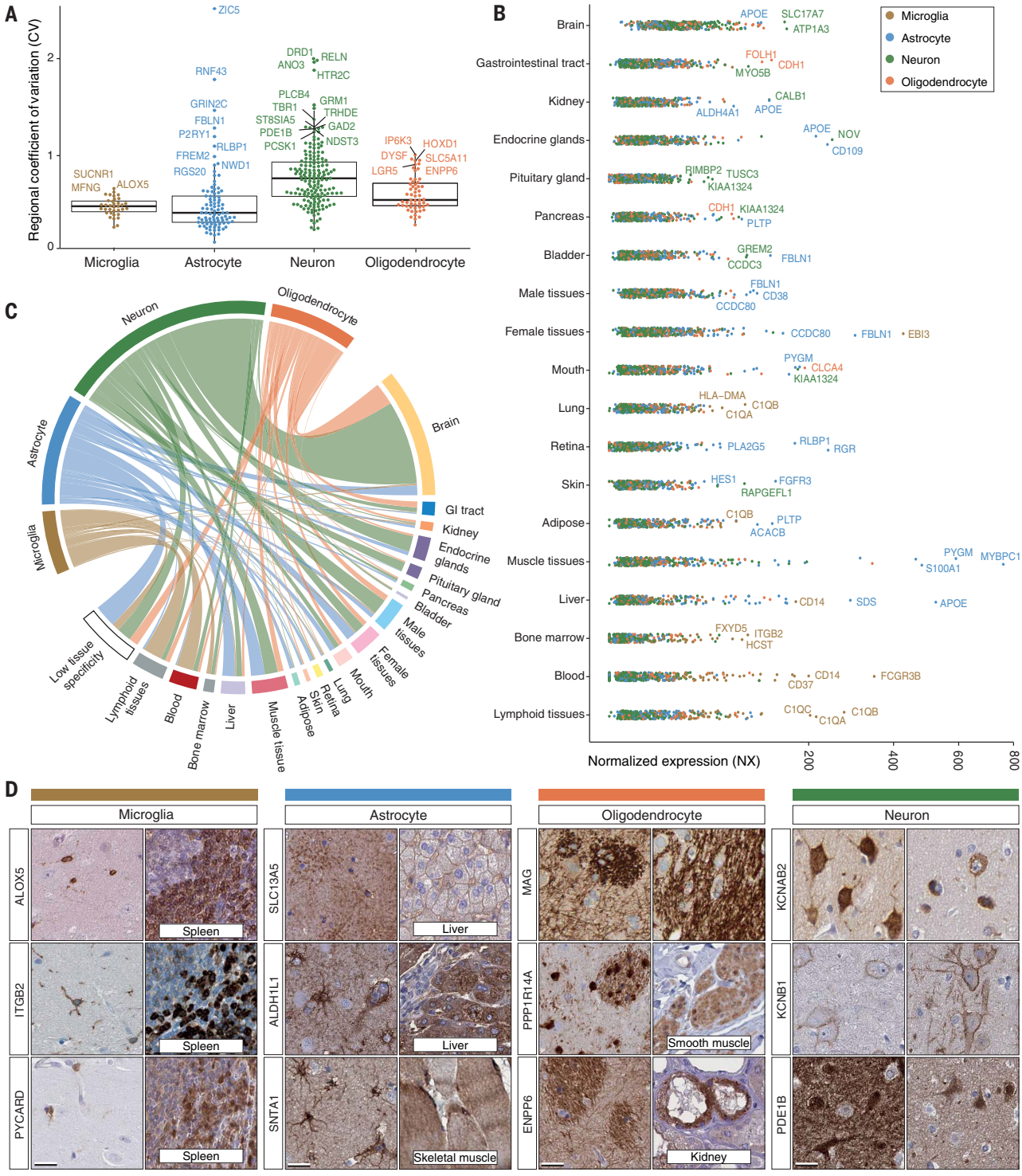


Fig. 7. The gene expression landscape of 420 putative brain cell type signature genes in cerebral cortex. (**A**) The expression variation for the 420 signature genes in the different brain regions was analyzed on the basis of the coefficient of variation (CV) of NX values across the 10 regions (see figs. S33 and S34 for expression heatmap and scatterplot across the 10 regions). (**B**) The expression levels for the individual signature genes in the different tissue types. The most abundant genes are indicated by gene names (see fig. S32 for expression heatmap of the signature genes across all tissues). (**C**) Chord diagram shows the tissue specificity of brain cell type signature genes. Each link represents the number of cell type signature genes that are elevated at a tissue level in the analyzed organ and tissue types. (**D**) Examples of signature genes and their protein localization in the different cell types. Microglia signature genes (ALOX5, ITGB2, and PYCARD) are highly expressed in spleen. Several astrocyte signature genes, including SLC13A5 and ALDH1L1, have elevated expression in liver, whereas SNTA1 is highly expressed in skeletal muscle. Neuronal examples (KCNAB2, KCNB1, and PDE1B) are located in neuronal cell bodies in the brain, while oligodendrocyte proteins, including MAG, are detected in white matter of the brain as well as in smooth muscle (PPP1R14A) and renal tubule of kidney (ENPP6). More detailed expression profiles for all cell signature genes are shown in figs. S33 to S35. Scale bars, 25 μm.

and hepatocytes in the metabolism of secreted substrates.

We subsequently analyzed the signature genes for oligodendrocytes. Expression of some putative oligodendrocyte signature genes is here classified to have low tissue specificity, such as protein phosphatase 1 regulatory inhibitor subunit 14A (PPP1R14A). Others are classified as having elevated expression in peripheral tissues, such as ectonucleotide pyrophosphatase 6 (ENPP6), which is elevated in kidney. The expression of putative neuronal signature genes is here mainly classified as brain-elevated, such as potassium voltage-gated channel subfamily A regulatory beta subunit 2 (KCNAB2), potassium voltage-gated channel subfamily B member 1 (KCNB1), and phosphodiesterase 1B (PDE1B), all detected on the protein level, using antibody-based localization, in a subset of neurons and with different subcellular locations (Fig. 7D). However, several neuronal signature genes also showed elevated expression in endocrine tissues, the pituitary gland, or male tissues. The analysis shows that caution should be taken regarding genes identified as signature genes, because the identification of these is context-dependent, and many of the genes previously identified as signature genes for specific cell types in the brain are in fact also highly expressed in peripheral tissues.

The HPA Brain Atlas

As part of this work, a brain atlas database has been launched to present and integrate all the data reported here, and this is an extension of the HPA portal, with a brain-centric summary page for each gene with expression data in human, pig, and mouse brain regions. The resource is presented (*17*) with an expression summary for all protein-coding genes. For selected genes, the distribution of the corresponding protein is visualized by antibody-based protein detection. Gene expression in the CNS is visually summarized on the basis of the 10 brain regions as well as spinal cord, corpus callosum, retina, and pituitary gland, with underlying data for many more subregions (21 subregions in human, 27 in pig, and 16 in mouse). Each of the 10 regions can also be reviewed in individual pages, which provide a classification overview, interactive lists, and figures, as well as highlighted examples of regionally specialized cells and proteins. A selection of 815 proteins is shown at the protein level in human tissues, and 271 genes include a complete mouse brain profile through a high-resolution virtual microscope. These 271 genes were analyzed with immunofluorescence-based imaging and include protein expression levels for 120 subregions of the brain.

Outlook

The expression profiles for the protein-coding genes in all major brain regions have been determined to capture the complexity of the cellular organization of the brain and to enable comparison between species. The integration of data from several sources has allowed us to combine data from transcriptomics, single-cell genomics, in situ hybridization, and antibody-based protein profiling. The rapid technological improvements in the field of spatial transcriptomics and single-cell genomics will in the future allow for an even higher degree of molecular granularity. The analysis presented here, relying on anatomical dissection of the different regions of the brain, allowed us to classify all of the individual protein-coding genes on a genome-wide level, where each gene is scored for its regional distribution. The resource provides detailed molecular transcriptomics maps of the mouse, pig, and human brains, and these maps are combined with immunofluorescence-based imaging of single cells using antibodies toward proteins identified as being of neurological and neuropsychiatric interest. In this manner, genes could be identified that are shown to be differentially expressed between organs and within the brain. By including more brain regions, the number of transcripts detected in the human brain has increased compared with previous studies. The number of regionally elevated genes in all three species is relatively small, with ~1000 genes identified in each species with an elevated expression (regional enriched, group enriched, or regional enhanced) across the 10 brain regions.

Analysis of the regionally elevated genes in the three species presented here supports the concept of a similar basic molecular brain architecture during mammalian evolution. The genes involved in production, vesicular transport, uptake, and degradation of the main neurotransmitter systems show overall high similarity among the three species, although notable differences have been identified. Thus, for example, some of the catecholamine-synthesizing enzymes show distinct species differences with regard to localization and expression levels, and several metabotropic and ionotropic receptors also exhibit species differences. Many neurotransmitter receptors, in particular the nicotinic and opioid receptors, show high variability in the different species, in particular between human and mouse. These types of gene differences between species highlight the fact that mouse models may not provide data that can be used to understand and treat human mental disorders. For some of the brain regions, such as cerebellum and hypothalamus, the global expression profile of pig is closer to that of human, suggesting that pig might be an attractive animal model to study many neurological and mental processes.

Many "signature genes" identified previously for specific brain cell types (such as astrocytes, microglia, oligodendrocytes, and neurons) are expressed at higher levels in peripheral organs, demonstrating that caution should be taken when using such genes as markers of specific brain cell types. In fact, our results support a view of shared functions between microglia and immune cells, with many genes elevated in both types of cells. Similarly, many genes previously identified as signature genes for astrocytes have a functional role in transport, and the elevated expression of these genes in astrocytes is often shared with liver or skeletal muscle. Cerebellum stands out with regard to the number of regional enriched genes and genes differentially expressed between species. This is also the brain region with the most distinct pattern of active cis regulatory elements compared with cortical and subcortical structures, and the cerebellum also has the highest degree of alteration within predicted enhancers among primates (*52*). Several genes suggested to be involved in neuropsychiatric diseases are found to be selectively expressed in the human cerebellum, which might be surprising for a brain region traditionally linked to fine-tuning motor behaviors. However, these data support the emerging notion that this part of the brain is associated with many neurological and psychiatric conditions.

We describe an integrative approach for mapping the molecular profiles in human, pig, and mouse brain that generates a detailed multilevel view on the protein-coding genes of the mammalian brain. We also compare the regional differences of the human brain with a genome-wide, whole-body tissue-specificity classification. An open-access Human Brain Atlas knowledge-based resource is presented as part of the HPA to allow the exploration of individual genes and classes of genes and their expression profiles in the various parts of the mammalian brain as well as all other major parts of the human body.

Material and methods

Animal procedures

The animal experiments conformed to the European Communities Council Directive (86/609/EEC), and all efforts were made to minimize the suffering and the number of animals used. Mouse brain tissue samples used for transcriptomic and proteomic analyses were collected and handled in accordance with Swedish laws and regulations, and all experiments were approved by the local ethical committee (Stockholms Norra Djurförsöksetiska Nämd N183/14). The experimental minipigs (Chinese Bama Minipig) were provided by the Peral Lab Animal Sci & Tech Co., Ltd (Permit number SYXK2017-0123). Brain tissue samples used for analysis were collected and handled in accordance with national guidance for large experimental animals and under permission of the local ethical committee (ethical permission numbers 44410500000078 and BGI-IRB18135)

and experiments were conducted in line with European directives and regulations.

Wild-type male (n = 2) and female (n = 2) C57BL/6J mice (2 months old) were obtained from Charles River Laboratories and maintained under standard conditions on a 12-hour day/night cycle, with water and food ad libitum. Mice were deeply anesthetized and transcardially perfused with 0.9% saline solution. Brains were quickly removed from the skull and dissected on a glass plate on ice. The entire brain was carefully dissected into 16 subregions, and corpus callosum, pituitary gland, and retina were also collected. A complete list of samples and subregions is provided in table S3. Tissue samples were collected into tubes, snap frozen in dry ice, and stored at −80°C until further processing.

For immunofluorescence and iDISCO analysis, mice were anesthetized and transcardially perfused using balanced Tyrode's solution followed by fixation with modified Zamboni fixative (4% paraformaldehyde, 0.2% picric acid in 0.1 M phosphate buffer). For cryosectioning, brains were post-fixed for 90 min and transferred to PBS containing 30% sucrose and 0.1% sodium azide. After cryopreservation, brains were snap frozen using CO_2 and 16-μm-thick coronal sections were cut on a cryostat (Leica, CM1950) and thaw-mounted on SuperFrost Plus glass slides (VWR). For iDISCO experiments, samples were placed in PBS containing 0.1% sodium azide until further processing.

Male (n = 2) and female (n = 2) Chinese Bama minipigs (1 year old), were obtained from the Pearl Lab Animal Sci & Tech Co., Ltd. All animals were housed in a specific pathogen-free stable facility under standard conditions. Pigs were deeply anesthetized and slaughtered by terminal bleeding. The entire pig brain was quickly removed from the scull and submerged into ice-cold PBS buffer for 2 min to remove excess blood and stiffen the tissue. The brain was cut in coronal slabs at the level of (i) frontal lobe/olfactory tract, (ii) optic chiasm, and (iii) between hypothalamus and cerebral peduncle. Slaps were divided in two hemispheres, exposing all main brain structures. Sample blocks of one hemisphere were immersion-fixed in phosphate-buffered saline containing 4% paraformaldehyde for 1 week followed by storage in phosphate-buffered saline containing 0.1% sodium azide at 4°C. For mRNA analysis, pieces of cerebral cortex and cerebellum were collected on the basis of a sampling strategy collecting a representative sample containing all cell layers. All other regions were dissected and collected in their entirety, subregional samples are listed in table S2. Two samples (somatosensory cortex and periaqueductal gray) are missing from female 1, as these two regions could not be identified with 100% certainty and thus were excluded. Duplicate samples were taken from olfactory bulb from female 2, resulting in 119 brain samples and an additional 8 samples (retina and pituitary gland), for a total of 127 samples. All samples were stored at −80°C until RNA extraction took place, within one month.

For immunofluorescence analysis, samples were immersed in 70% ethanol before dehydration in absolute alcohol and xylene before paraffin embedding. Sections were cut (4 μm by Microm HM 355S, Thermo Fisher Scientific) and placed on SuperFrost Plus glass slides (VWR), baked, and then used for staining or stored in −20°C until stained.

RNA sequencing of pig and mouse brain samples

For mouse brain RNA extraction, the tissue was homogenized mechanically using a TissueLyser LT (Qiagen) and total RNA was prepared using the RNeasy Mini isolation kit (Qiagen) for each of the 19 samples. This generated high-quality RNA, with 84% of the samples having RNA integrity values >8.0, with only one sample removed owing to very low RIN value (<6.0). RNA integrity (RIN) was assessed using Agilent RNA 6000 Nano Kit (Agilent Technologies). In total, 75 samples were subsequently used for library construction with Illumina TruSeq Stranded mRNA reagents. The Illumina HiSeq2500 platform was used for sequencing at ~20 million reads depth. Detailed information about the samples and sequencing quality control is listed in table S11. The output analysis was performed using Kallisto v.0.43.1 and mapped to the mouse Ensembl v92 with 22,333 protein-coding genes, for the initial analysis. Human and mouse orthologs were defined as a one-to-one translation, resulting in a total of 15,160 genes.

For pig brain RNA extraction, the tissue was homogenized mechanically using a Dounce tissue grinder in liquid nitrogen. Total RNA was then extracted with a standardized protocol based on TRIzol reagent (Invitrogen). First, total mRNA and noncoding RNAs were enriched by removing ribosomal RNA (rRNA) using a MGIEasy rRNA depletion kit (MGI Tech, China). Enriched RNAs were then mixed with RNA fragmentation buffer resulting in short fragments (180 to 300 base pairs). Third, complementary DNA (cDNA) was synthesized from the fragmentated RNAs using N6 random primers, followed by end repair and ligation to BGISEQ sequencer compatible adapters. The quality and quantity of the cDNA libraries were assessed using Agilent 2100 BioAnalyzer (Agilent Technologies). Finally, the libraries were sequenced on the BGISEQ-500 with 100 paired-end read (PE100). A few randomly selected libraries were also resequenced and co-validated with MGI2000 sequencer. An average of 200 million reads were generated for each library. Sequencing reads that contained adapters and/or had low quality, aligned to rRNA were filtered before following bioinformatic analysis. An overview of the total reads, Q30 clean reads, and mapping ratio to the pig genome (Sscrofa11.1) is provided in table S12. More than 94% of the samples have <10% rRNA of total reads, indicating a highly efficient rRNA removal and RNA quality. One sample (pituitary gland from female 2) was excluded from final data analyzed because of high rRNA inclusion (table S12). The output analysis was performed using Kallisto v.0.43.1 and mapped to the pig Ensembl build 92 with 22,342 protein-coding genes, for the initial analysis. Human and pig orthologs were defined as a one-to-one translation, resulting in a total of 14,656 genes.

Human sequencing datasets

The Functional Annotation of Mammalian Genomes 5 (FANTOM5) project (*19*) provides transcriptomic profiles and functional annotation of mammalian cell types using cap analysis of gene expression (CAGE) (*53*), a method developed at RIKEN that is based on several full-length cDNA technologies. Expression data files with CAGE peaks and ontology for 77 samples (representing 30 different tissue types) were obtained from the version 4 FANTOM5 repository (https://fantom.gsc.riken.jp/5/datafiles/reprocessed/), which we mapped to Ensembl for calculation of the normalized tags per million for each gene. The Genotype-Tissue Expression (GTEx) (*18*) is an extensive project that has collected and analyzed thousands of human postmortem tissue samples. RNA-seq data from 26 tissue types (including more than 8000 patient samples) were mapped using RSEMv1.2.22 (v7,GTEx_Analysis_2016-01-15_v7_RSEMv1.2.22_transcript.tpm.txt.gz) and generated transcript per million (TPM) values that are included in the Human Protein Atlas. The in-house RNA-seq analysis on human tissue types includes 172 tissue samples covering 33 of the 37 tissue types representing the whole human body. The detailed protocol used for RNA-sequencing in the HPA has been described previously (*1*, *51*).

Normalization of human data

To enable expression classification and mapping of all human protein-coding genes across all tissue types and samples, TPM expression values were obtained by mapping processed human reads to the human reference genome GRCh37/hg19 based on Ensembl build 92 (*54*) gene models using Kallisto (v.0.43.1) (*55*). Next, the gene expression levels were calculated by summing up the TPM values of all alternatively spliced protein coding transcripts for the corresponding gene for a total of 19,670 protein-coding genes. The average TPM value of all individual samples for each tissue, brain region, or cell type was used to estimate the gene expression level. Data analysis and visualization were performed using R (version

3.5.1 Feather Spray) (*56*). To allow the three datasets (HPA, GTEx, and FANTOM) to be combined (*1*, *18*, *19*), a pipeline was set up to normalize the data for all samples (fig. S4). In brief, we first scaled all TPM values per sample so that the sum was one million, to compensate for the noncoding transcripts that had been previously removed and to obtain pTPM values per sample. Next, all TPM values were TMM normalized (*22*) between all the samples in each data source (HPA tissues, HPA blood cells, GTEx, and FANTOM5, respectively), then each gene was Pareto scaled (*23*) within each data source. Tissue data from multiple sources were integrated using batch correction implemented as removeBatchEffect in the R package *limma* (*24*) using the data source as a batch parameter. The resulting transcript expression values, here called normalized expression (NX), are calculated for each gene in every sample. In the Human Protein Atlas, the NX value for every gene in every sample is calculated and visualized on the gene summary page together with the pTPM value. The expression classification across the 37 tissue types included four tissues with combined data: brain, intestine, lymphoid tissues, and blood cells, all represented by the maximum NX value within each group. In general, tissues, cells, or regions including multiple data sources or multiple subtissues were all represented by a consensus NX value, calculated for each gene as the maximum NX value in the subtissues/regions or cell types.

Normalization of pig and mouse data

All TPM values of pig and mouse datasets were TMM normalized (*22*) between all samples, respectively, and then each gene was Pareto scaled (*23*) within each species (fig. S4). NX for each gene was calculated in every sample as described for human, including calculation of pTPM values. In the HPA, the pTPM value for every gene in every sample is visualized on the gene summary page and the more detailed tissue pages. For regions containing multiple subregions, a consensus NX value was calculated for each gene as the maximum NX value of the subregions (Fig. 1B).

Comparisons of three species

Protein-coding genes with one-to-one orthologs in human, mouse, and pig were identified to compare the expression profiles in the three mammalian brains, and altogether 12,999 genes were analyzed (fig. S19A). All NX values of the 12,999 genes were then TMM normalized (*22*) between 10 brain regions in three species (figs. S4 to S6).

Classification based on RNA expression

All protein-coding genes were classified according to a new strategy based on categorization on both tissue specificity (expression abundance between tissues, table S4) and tissue distribution (detection level above cutoff NX =1, table S8). Tissue specificity highlights genes with elevated expression in one or a group of tissue types compared with the rest, with the three elevated categories being "enriched" (fourfold higher expression in one tissue compared with the second highest), "group enriched" (fourfold higher expression in a group of tissues compared with other tissues), and "enhanced" (fourfold higher expression in one or several tissues compared with the mean of all tissues) (table S4). These classification rules were applied to the expression profiles of the 37 tissue types representing the whole human body as well as the different brain regions in human, pig, and mouse (Fig. 2). The tissue distribution defines the number of tissues with expression levels above cutoff (NX = 1) (table S8). The combination of tissue specificity and distribution from a brain perspective (genes detected in brain distributed into the different categories) is shown in table S7. Tissue-based classification, highlighting the brain-elevated genes compared with peripheral tissues, is available for all human protein-coding genes, while the regional classification in human brain is limited by the availability of external expression data (GTEx and FANTOM) (Fig. 1C and fig. S5 for more details about the gene coverage and combinations of the datasets). A second step of normalization was introduced to enable comparison of the expression levels across species. All human protein-coding genes with one-to-one orthologs in both mouse and pig (12,999 genes) were adjusted by TMM normalization, as illustrated in the schematic overview of the normalization pipeline, fig. S4.

Hierarchical clustering and UMAP analysis

Clustering in heatmaps and dendrograms based on Spearman correlation were created by first calculating a correlation matrix of Spearman's ρ (*57*) between all brain regions. The correlation was converted to a distance metric (1 – ρ) and was clustered using unsupervised top-down hierarchical clustering, where, at each stage, the distances between clusters are recomputed by the Lance-Williams dissimilarity update formula according to average linkage. Dendrograms showing gene expression in heatmaps have been clustered using the Ward2 algorithm (*58*), an implementation of Ward's minimum variance method (*59*) implemented as "Ward.D2" in the hclust function in the R package stats, where clusters are chosen at each stage such that the increase in cluster variance is minimized after merging. The hierarchical clustering of brain regions in three species was conducted by using the neighbor-joining approach in the ape package (*60*) in R, based on pairwise Pearson correlational distances between samples. The reliability of branches was assessed using 100 bootstrap replicates. The phylogenetic tree was drawn using the plot.phylo function in ape. Uniform Manifold Approximation and Projection (UMAP) has been performed on NX values of brain samples by using the R packages UMAP (*61*) with default parameters.

Differential expression analysis of three species

Differential expression analysis was conducted by using normalized NX values of 10 regions of three species. The R package *limma*, which includes lmFit, eBayes, and topTable functions, was used for pairwise comparison of DEGs. False discovery rate (FDR) was calculated by using p.adjust() function in R, using the Benjamini-Hochberg method. Genes with FDRs less than 0.01 and absolute fold change larger than 2 were considered as differentially expressed genes.

Defining cell type signature genes

Human cerebral cortex signature genes for neurons, astrocytes, oligodendrocytes, and microglia were determined on the basis of the agreement between two independent (data source and approach) datasets. RNA-seq results of cells selected using immunopanning (*8*) were obtained from www.brainrnaseq.org, and results based on coexpression analysis (*12*) were obtained from http://oldhamlab.ctec.ucsf.edu/. By varying the inclusion criteria for RNA-seq data (fold-enrichment >2 to >5) and coexpression analysis (p-value 0.95 to 1) the optimal settings creating the maximum overlap between these datasets for each cell type were determined (Table 1). Human cerebral cortex cell type signature genes were defined as genes associated with the same cell type based on both datasets with an FPKM value of >1 in only one cell type based on RNA-seq. The list of 420 genes, here defined as cell type signature genes, are listed in table S9.

Antibody-based profiling of protein distribution

Protein profiling in human brain tissues was performed within the Human Protein Atlas pipeline, following previously published protocols (*1*). Formalin fixed paraffin embedded (FFPE) tissue samples were used for tissue microarray (TMA) construction, where 144 separate 1-mm cores were placed in a recipient paraffin block (*62*) representing 44 different tissue types. Sections were cut (4 μm by Microm HM 355S, Thermo Fisher Scientific) and placed on SuperFrost Plus glass slides (VWR). The sections were dewaxed, H_2O_2-incubated, and antigen retrieved by heat-induced epitope retrieval (HIER) in pH6 citric acid solution before commencing the staining procedure. The Leica Biosystems CV5030 immunostainer was used for pretreatment as well as in later steps of counterstaining and coverslipping. Staining protocols were standardized and executed in a

Table 1. Criteria used for best overlap in two independent datasets, defining the cell type signature genes. Percentages in parentheses represent maximal overlap between two datasets used for selection of inclusion criteria.

Cell type	RNA-seq enrichment (fold)	Coexpression analysis (*P* value)	Number of genes (two datasets)	Number of signature genes
Neurons	>2	>0.98	679 (30.0%)	196
Astrocytes	>3	>0.98	324 (40.2%)	180
Oligodendrocytes	>2	1	212 (32.3%)	65
Microglia	>5	>0.95	135 (19.4%)	51

LabVision Autostainer 480 using LabVision reagents and protocols with primary antibody incubation 30 min in room temperature and HRP-polymer secondary antibody and DAB (3,3-diaminobenzidine) chromogenic visualization. All slides were counterstained in HTXplus (Histolab) before coverslipping, and image digitalization was performed in Scanscope AT2 (Aperio Vista) using a 20× objective.

Protein profiling in mouse brain tissues was performed as described previously (*63*). Complete brain profiles were represented by 20 to 25 sections having a 400-μm interval, covering all major regions of the mouse brain. Briefly, sections were incubated with primary antibody (16 to 72 hours at 4°C), blocked in TNB buffer (0.1 M Tris-HCl, pH 7.5; 0.15 M NaCl; 0.5% blocking reagent) followed by HRP-conjugated secondary antibody (Dako), and immunoreactivity was visualized using the tyramide signal amplification system (TSA-Plus; NEN Life Science Products, Inc.). Fluorescent images were obtained using a "VSlide" slide scanning microscope (MetaSystems) equipped with a CoolCube 2 camera (12-bit grayscale), a 10× objective and filter sets for 4′,6-diamidino-2-phenylindole (DAPI) (EX350/50–EM470/40), Fluorescein isothiocyanate (FITC) (EX493/16–EM527/30), Cyanine (Cy) 3 (EX546/10–EM580/30), Cy3.5 (EX581/10–EM617/40), and Cy5 (EX630/20–647/long pass). Finally, the individual images were stitched together (VSlide) to generate a large image of the entire section, while the images (vsi-files) were additionally extracted to high quality .jpeg files for further analysis using the software Metaviewer (Metasystems). All images were manually evaluated and scored, always including verification by a second observer.

The human brain antibody-based chromogen stainings are all available on the Human Protein Atlas portal (www.proteinatlas.org). Antibody IDs and antibody dilutions are listed in table S13. More details about antibody validation and antigen design for respective antibodies are found on the respective antibody information page in the portal. Fluorescent mouse brain staining shown in Fig. 3 are examples from full mouse protein profiles available online, performed according to the protocol described above (list of antibodies in table S13). The examples shown for species comparison in human, pig, and mouse are all performed on FFPE tissue sections (4 μm), placed on SuperFrost Plus glass slides (VWR), baked before dewaxing and antigen retrieved according to standard procedure for FFPE sections as described previously, including H_2O_2-incubated and HIER in pH 6 citric acid solution. The sections were then incubated overnight at 4°C with primary antibody (list of antibodies and dilution in table S13), followed by blocking and secondary HRP-conjugated secondary antibody. The staining protocol followed was according to the mouse profiling standard using TSA amplification.

iDISCO+ volume immunostaining

iDISCO+ volume immunostaining and clearing process were performed as earlier described by Renier and colleagues (*64*). Briefly, whole mouse brains (one hemisphere was laterally slightly trimmed) were washed in 0.01 M PBS three times in 5-ml Eppendorf tubes and then dehydrated in a series of methanol/water solutions for 1 hour each. The samples were then bleached with 5% hydrogen peroxide in 100% methanol overnight at +4°C. Then, they were rehydrated, incubated in permeabilization solution for 2 days, and followed by blocking solution for an additional 2 days, both at 37°C (0.2% Triton-X100/20% DMSO/0.3 M glycine in 0.01 M PBS + 0.02% sodium azide, 0.2% Triton-X100/10% DMSO/6% normal donkey serum in 0.01 M PBS + 0.02% sodium azide, respectively). The samples were then incubated with a rabbit polyclonal primary antibody raised against human GPR151 (HPA065728, 1:150) solution for 7 days at 37°C (antibody diluent: 0.2% Tween-20/10 μg/ml heparin/5% DMSO/3% normal donkey serum in 0.01 M PBS + 0.02% sodium azide). After extensive washing, the blocks were incubated in secondary antibody (1:150; goat anti-rabbit, conjugated with Alexa Fluor 647; Molecular Probes, Oregon, USA) solution (0.2% Tween-20/10 μg/ml heparin/3% normal donkey serum in 0.01 M PBS + 0.02% sodium azide). The blocks were dehydrated in methanol/water series, incubated in 66% dichloromethane/33% methanol for 3 hours and in 100% dichloromethane for 2 × 15 min. Finally, the blocks were moved to tubes and stored in 100% dibenzyl ether for the long term.

A light sheet microscope (Ultramicroscope II, Lavision Biotec, Bielefeld, Germany) and the Imspector software were used for image acquisition of the whole mouse brains. The microscope was equipped with an sCMOS camera (Andor Neo) and a 2×/0.5 objective lens (MVPLAPO 23), with a 6.5-mm working distance spherical aberration corrected dipping cap.

The trimmed full mouse brain (cut at lateral ca −2.5 mm) was fixed on the sample holder with the surface of the trimmed hemisphere side down and acquired in sagittal position from ca. lateral −2.00 until the top of the other side cortex (ca 6.5 mm altogether). To obtain the required X/Y/Z resolution, homogeneous illumination within the entire focal plane and minimal photobleaching, the following microscope parameters were applied: 2× objective, 1.6× zoom body, and additional magnification of the dipping cap lens (altogether 3.6× effective magnification), 70% laser power (OBIS 647 laser), bilateral illumination (blend merging algorithm), 100-ms exposure time, max sheet numerical aperture (0.149), dynamic horizontal focus process with 13 steps (blend merging algorithm after precalibration process), 70% sheet width, 2-μm Z-step thickness, mosaic acquisition mode (six tiles with 15% overlap). Stitching was achieved by the Terastitcher-Imspector python script (LaVision Biotec, 2017), where the serials of 16-bit uncompressed stitched tiff images (ca. 3500 z-levels, ca 100 GB) were then converted to IMS file, and the 3D vision of acquisitions was reconstructed in the Imaris 9.1.2 (Bitplane, UK) software for inspection and quality control.

REFERENCES AND NOTES

1. M. Uhlén *et al*., Tissue-based map of the human proteome. *Science* **347**, 1260419 (2015). doi: 10.1126/science.1260419; pmid: 25613900
2. The HPA Tissue Atlas; www.proteinatlas.org/tissue.
3. E. S. Lein *et al*., Genome-wide atlas of gene expression in the adult mouse brain. *Nature* **445**, 168–176 (2007). doi: 10.1038/nature05453; pmid: 17151600
4. C. L. Thompson *et al*., A high-resolution spatiotemporal atlas of gene expression of the developing mouse brain. *Neuron* **83**,

309–323 (2014). doi: 10.1016/j.neuron.2014.05.033; pmid: 24952961
5. M. J. Hawrylycz *et al*., An anatomically comprehensive atlas of the adult human brain transcriptome. *Nature* **489**, 391–399 (2012). doi: 10.1038/nature11405; pmid: 22996553
6. J. A. Miller *et al*., Transcriptional landscape of the prenatal human brain. *Nature* **508**, 199–206 (2014). doi: 10.1038/nature13185; pmid: 24695229
7. Y. Zhang *et al*., An RNA-sequencing transcriptome and splicing database of glia, neurons, and vascular cells of the cerebral cortex. *J. Neurosci.* **34**, 11929–11947 (2014). doi: 10.1523/JNEUROSCI.1860-14.2014; pmid: 25186741
8. Y. Zhang *et al*., Purification and characterization of progenitor and mature human astrocytes reveals transcriptional and functional differences with mouse. *Neuron* **89**, 37–53 (2016). doi: 10.1016/j.neuron.2015.11.013; pmid: 26687838
9. A. Zeisel *et al*., Molecular architecture of the mouse nervous system. *Cell* **174**, 999–1014.e22 (2018). doi: 10.1016/j.cell.2018.06.021; pmid: 30096314
10. B. B. Lake *et al*., Integrative single-cell analysis of transcriptional and epigenetic states in the human adult brain. *Nat. Biotechnol.* **36**, 70–80 (2018). doi: 10.1038/nbt.4038; pmid: 29227469
11. R. D. Hodge *et al*., Conserved cell types with divergent features in human versus mouse cortex. *Nature* **573**, 61–68 (2019). doi: 10.1038/s41586-019-1506-7; pmid: 31435019
12. K. W. Kelley, H. Nakao-Inoue, A. V. Molofsky, M. C. Oldham, Variation among intact tissue samples reveals the core transcriptional features of human CNS cell classes. *Nat. Neurosci.* **21**, 1171–1184 (2018). doi: 10.1038/s41593-018-0216-z; pmid: 30154505
13. J. R. Ecker *et al*., The BRAIN Initiative Cell Census Consortium: Lessons learned toward generating a comprehensive brain cell atlas. *Neuron* **96**, 542–557 (2017). doi: 10.1016/j.neuron.2017.10.007; pmid: 29096072
14. H. Markram, The human brain project. *Sci. Am.* **306**, 50–55 (2012). doi: 10.1038/scientificamerican0612-50; pmid: 22649994
15. HuBMAP Consortium, The human body at cellular resolution: The NIH Human Biomolecular Atlas Program. *Nature* **574**, 187–192 (2019). doi: 10.1038/s41586-019-1629-x; pmid: 31597973
16. A. Regev *et al*., The Human Cell Atlas. *eLife* **6**, e27041 (2017). doi: 10.7554/eLife.27041; pmid: 29206104
17. The HPA Brain Atlas; www.proteinatlas.org/brain.
18. GTEx Consortium, Genetic effects on gene expression across human tissues. *Nature* **550**, 204–213 (2017). doi: 10.1038/nature24277; pmid: 29022597
19. S. Noguchi *et al*., FANTOM5 CAGE profiles of human and mouse samples. *Sci. Data* **4**, 170112 (2017). doi: 10.1038/sdata.2017.112; pmid: 28850106
20. J. E. Coate, J. J. Doyle, Variation in transcriptome size: Are we getting the message? *Chromosoma* **124**, 27–43 (2015). doi: 10.1007/s00412-014-0496-3; pmid: 25421950
21. J. Lovén *et al*., Revisiting global gene expression analysis. *Cell* **151**, 476–482 (2012). doi: 10.1016/j.cell.2012.10.012; pmid: 23101621
22. M. D. Robinson, A. Oshlack, A scaling normalization method for differential expression analysis of RNA-seq data. *Genome Biol.* **11**, R25 (2010). doi: 10.1186/gb-2010-11-3-r25; pmid: 20196867
23. R. A. van den Berg, H. C. Hoefsloot, J. A. Westerhuis, A. K. Smilde, M. J. van der Werf, Centering, scaling, and transformations: Improving the biological information content of metabolomics data. *BMC Genomics* **7**, 142 (2006). doi: 10.1186/1471-2164-7-142; pmid: 16762068
24. M. E. Ritchie *et al*., *limma* powers differential expression analyses for RNA-sequencing and microarray studies. *Nucleic Acids Res.* **43**, e47 (2015). doi: 10.1093/nar/gkv007; pmid: 25605792
25. J. C. Corvol, J. M. Studler, J. S. Schonn, J. A. Girault, D. Hervé, $G\alpha_{olf}$ is necessary for coupling D1 and A2a receptors to adenylyl cyclase in the striatum. *J. Neurochem.* **76**, 1585–1588 (2001). doi: 10.1046/j.1471-4159.2001.00201.x; pmid: 11238742
26. I. H. Kim *et al*., Evidence for functional diversity between the voltage-gated proton channel Hv1 and its closest related protein HVRP1. *PLOS ONE* **9**, e105926 (2014). doi: 10.1371/journal.pone.0105926; pmid: 25165868
27. N. Zainolabidin, S. P. Kamath, A. R. Thanawalla, A. I. Chen, Distinct activities of Tfap2A and Tfap2B in the specification of GABAergic interneurons in the developing cerebellum. *Front. Mol. Neurosci.* **10**, 281 (2017). doi: 10.3389/fnmol.2017.00281; pmid: 28912684
28. J. Mulder *et al*., Secretagogin is a Ca^{2+}-binding protein specifying subpopulations of telencephalic neurons. *Proc. Natl. Acad. Sci. U.S.A.* **106**, 22492–22497 (2009). doi: 10.1073/pnas.0912484106; pmid: 20018755
29. E. S. Deneris, O. Hobert, Maintenance of postmitotic neuronal cell identity. *Nat. Neurosci.* **17**, 899–907 (2014). doi: 10.1038/nn.3731; pmid: 24929660
30. H. Guo *et al*., Specificity and efficiency of Cre-mediated recombination in Emx1-Cre knock-in mice. *Biochem. Biophys. Res. Commun.* **273**, 661–665 (2000). doi: 10.1006/bbrc.2000.2870; pmid: 10873661
31. P. S. Joshi *et al*., Bhlhb5 regulates the postmitotic acquisition of area identities in layers II-V of the developing neocortex. *Neuron* **60**, 258–272 (2008). doi: 10.1016/j.neuron.2008.08.006; pmid: 18957218
32. D. Jean, G. Bernier, P. Gruss, *Six6* (*Optx2*) is a novel murine *Six3*-related homeobox gene that demarcates the presumptive pituitary/hypothalamic axis and the ventral optic stalk. *Mech. Dev.* **84**, 31–40 (1999). doi: 10.1016/S0925-4773(99)00068-4; pmid: 10473118
33. I. Nunes, L. T. Tovmasian, R. M. Silva, R. E. Burke, S. P. Goff, Pitx3 is required for development of substantia nigra dopaminergic neurons. *Proc. Natl. Acad. Sci. U.S.A.* **100**, 4245–4250 (2003). doi: 10.1073/pnas.0230529100; pmid: 12655058
34. F. Chantoux, J. Francon, Thyroid hormone regulates the expression of NeuroD/BHF1 during the development of rat cerebellum. *Mol. Cell. Endocrinol.* **194**, 157–163 (2002). doi: 10.1016/S0303-7207(02)00133-8; pmid: 12242038
35. R. Grailhe *et al*., Increased exploratory activity and altered response to LSD in mice lacking the 5-HT(5A) receptor. *Neuron* **22**, 581–591 (1999). doi: 10.1016/S0896-6273(00)80712-6; pmid: 10197537
36. R. Grailhe, G. W. Grabtree, R. Hen, Human 5-HT(5) receptors: The 5-HT(5A) receptor is functional but the 5-HT(5B) receptor was lost during mammalian evolution. *Eur. J. Pharmacol.* **418**, 157–167 (2001). doi: 10.1016/S0014-2999(01)00933-5; pmid: 11343685
37. R. L. Smith, H. Baker, K. Kolstad, D. D. Spencer, C. A. Greer, Localization of tyrosine hydroxylase and olfactory marker protein immunoreactivities in the human and macaque olfactory bulb. *Brain Res.* **548**, 140–148 (1991). doi: 10.1016/0006-8993(91)91115-H; pmid: 1678294
38. M. Lebel, Y. Gauthier, A. Moreau, J. Drouin, Pitx3 activates mouse tyrosine hydroxylase promoter via a high-affinity binding site. *J. Neurochem.* **77**, 558–567 (2001). doi: 10.1046/j.1471-4159.2001.00257.x; pmid: 11299318
39. E. Mezey, Phenylethanolamine N-methyltransferase-containing neurons in the limbic system of the young rat. *Proc. Natl. Acad. Sci. U.S.A.* **86**, 347–351 (1989). doi: 10.1073/pnas.86.1.347; pmid: 2563164
40. N. Puskás, R. S. Papp, K. Gallatz, M. Palkovits, Interactions between orexin-immunoreactive fibers and adrenaline or noradrenaline-expressing neurons of the lower brainstem in rats and mice. *Peptides* **31**, 1589–1597 (2010). doi: 10.1016/j.peptides.2010.04.020; pmid: 20434498
41. L. C. Daws, G. G. Gould, Ontogeny and regulation of the serotonin transporter: Providing insights into human disorders. *Pharmacol. Ther.* **131**, 61–79 (2011). doi: 10.1016/j.pharmthera.2011.03.013; pmid: 21447358
42. J. Peng, S. Sarkar, S. L. Chang, Opioid receptor expression in human brain and peripheral tissues using absolute quantitative real-time RT-PCR. *Drug Alcohol Depend.* **124**, 223–228 (2012). doi: 10.1016/j.drugalcdep.2012.01.013; pmid: 22356890
43. D. L. Kaufman *et al*., Characterization of the murine μ opioid receptor gene. *J. Biol. Chem.* **270**, 15877–15883 (1995). doi: 10.1074/jbc.270.26.15877; pmid: 7797593
44. M. Mortensen, B. Patel, T. G. Smart, GABA potency at GABA(A) receptors found in synaptic and extrasynaptic zones. *Front. Cell. Neurosci.* **6**, 1 (2012). pmid: 22319471
45. X. Gonda *et al*., A new stress sensor and risk factor for suicide: The T allele of the functional genetic variant in the GABRA6 gene. *Sci. Rep.* **7**, 12887 (2017). doi: 10.1038/s41598-017-12776-8; pmid: 29018204
46. A. S. Hauser, M. M. Attwood, M. Rask-Andersen, H. B. Schiöth, D. E. Gloriam, Trends in GPCR drug discovery: New agents, targets and indications. *Nat. Rev. Drug Discov.* **16**, 829–842 (2017). doi: 10.1038/nrd.2017.178; pmid: 29075003
47. K. Mizushima *et al*., A novel G-protein-coupled receptor gene expressed in striatum. *Genomics* **69**, 314–321 (2000). doi: 10.1006/geno.2000.6340; pmid: 11056049
48. D. M. Berson, F. A. Dunn, M. Takao, Phototransduction by retinal ganglion cells that set the circadian clock. *Science* **295**, 1070–1073 (2002). doi: 10.1126/science.1067262; pmid: 11834835
49. M. N. Moraes *et al*., Melanopsin, a canonical light receptor, mediates thermal activation of clock genes. *Sci. Rep.* **7**, 13977 (2017). doi: 10.1038/s41598-017-13939-3; pmid: 29070825
50. M. Uhlen *et al*., A genome-wide transcriptomic analysis of protein-coding genes in human blood cells. *Science* **366**, eaax9198 (2019). doi: 10.1126/science.aax9198; pmid: 31857451
51. E. Sjöstedt *et al*., Defining the human brain proteome using transcriptomics and antibody-based profiling with a focus on the cerebral cortex. *PLOS ONE* **10**, e0130028 (2015). doi: 10.1371/journal.pone.0130028; pmid: 26076492
52. M. W. Vermunt *et al*., Epigenomic annotation of gene regulatory alterations during evolution of the primate brain. *Nat. Neurosci.* **19**, 494–503 (2016). doi: 10.1038/nn.4229; pmid: 26807951
53. H. Takahashi, S. Kato, M. Murata, P. Carninci, CAGE (cap analysis of gene expression): A protocol for the detection of promoter and transcriptional networks. *Methods Mol. Biol.* **786**, 181–200 (2012). doi: 10.1007/978-1-61779-292-2_11; pmid: 21938627
54. D. R. Zerbino *et al*., Ensembl 2018. *Nucleic Acids Res.* **46**, D754–D761 (2018). doi: 10.1093/nar/gkx1098; pmid: 29155950
55. N. L. Bray, H. Pimentel, P. Melsted, L. Pachter, Near-optimal probabilistic RNA-seq quantification. *Nat. Biotechnol.* **34**, 525–527 (2016). doi: 10.1038/nbt.3519; pmid: 27043002
56. R Core Team, R: A language and environment for statistical computing (R Foundation for Statistical Computing, 2018); www.R-project.org.
57. C. Spearman, The proof and measurement of association between two things. By C. Spearman, 1904. *Am. J. Psychol.* **100**, 441–471 (1987). doi: 10.2307/1422689; pmid: 3322052
58. L. Kaufman, P. J. Rousseeuw, *Finding Groups in Data: An Introduction to Cluster analysis* (Wiley Series in Probability and Statistics, Wiley, 1990).
59. F. Murtagh, P. Legendre, Ward's hierarchical agglomerative clustering method: Which algorithms implement Ward's criterion? *J. Classif.* **31**, 274–295 (2014). doi: 10.1007/s00357-014-9161-z
60. S. Bhattacharya *et al*., ImmPort, toward repurposing of open access immunological assay data for translational and clinical research. *Sci. Data* **5**, 180015 (2018). doi: 10.1038/sdata.2018.15; pmid: 29485622
61. L. McInnes, J. Healy, J. Melville, UMAP: Uniform Manifold Approximation and Projection for Dimension Reduction. arXiv:1802.03426 [stat.ML] (9 February 2018).
62. C. Kampf, I. Olsson, U. Ryberg, E. Sjöstedt, F. Pontén, Production of tissue microarrays, immunohistochemistry staining and digitalization within the Human Protein Atlas. *J. Vis. Exp.* 10.3791/3620 (2012). doi: 10.3791/3620; pmid: 22688270
63. J. Mulder *et al*., Tissue profiling of the mammalian central nervous system using human antibody-based proteomics. *Mol. Cell. Proteomics* **8**, 1612–1622 (2009). doi: 10.1074/mcp.M800539-MCP200; pmid: 19351664
64. N. Renier *et al*., Mapping of brain activity by automated volume analysis of immediate early genes. *Cell* **165**, 1789–1802 (2016). doi: 10.1016/j.cell.2016.05.007; pmid: 27238021

ACKNOWLEDGMENTS

We thank W. Gu from the School of Biotechnology, Southern Medical University, Guangzhou, for providing the pigs. We acknowledge the entire staff of the Human Protein Atlas program and the Science for Life Laboratory for their valuable contributions. Support from the National Genomics Infrastructure in Stockholm is acknowledged, with funding from Science for Life Laboratory, the Knut and Alice Wallenberg Foundation, the Swedish Research Council, and SNIC/Uppsala Multidisciplinary Center for Advanced Computational Science for assistance with massively parallel sequencing and access to the UPPMAX computational infrastructure. **Funding:** Main funding was provided by the Knut and Alice Wallenberg Foundation (WCPR) and the Erling Persson Foundation (KCAP). The pig atlas part is supported by Sanming Project of Medicine in Shenzhen (SZSM201612074). L.L. is supported by the Lundbeck Foundation (R219–2016-1375) and the DFF Sapere Aude Starting grant (8048-00072A). **Author contributions:** M.U. and J.M. conceived of and designed the study. J.H., Y.D., L.L., Z.D., X.L., H.J., and Y.L. performed pig brain experiments (sample processing, RNA extraction, quality control, NGS library constructions, sequencing, and pilot data analysis). W.Z., L.F., M.K., A.M., and C.Z. performed the bioinformatics analysis. K.v.F. and P.O. provided the infrastructure for the data. E.S., M.U., W.Z., T.H., and J.M. drafted the manuscript. All authors discussed the results and contributed to the final manuscript. **Competing interests:** T.H. has shares in Lundbeck and Bioarctic. No other authors declare any competing interests. **Data and materials availability:** Materials are available upon request from J.M. All classification information, data, and gene

information are available, open access, and downloadable from the Human Protein Atlas database. The external data from GTEx, FANTOM5, and the Allen Brain Atlas are available at their respective sources. The transcript expression values at the brain regional level for human, pig, and mouse, as well as the remapped TPM and pTPM tables for the external data, are available from the HPA download section (www.proteinatlas.org/about/download), in addition to the human data for all tissue and blood cell types. The original data for the pig brain transcriptome has been deposited to the public data depository CNGB Nucleotide Sequence Archive (CNSA; https://db.cngb.org/cnsa/) of the China National GeneBank DataBase (CNGBdb) with accession number CNP0000483.

SUPPLEMENTARY MATERIALS

science.sciencemag.org/content/367/6482/eaay5947/suppl/DC1

Figs. S1 to S35
Tables S1 to S13
Movie S1

View/request a protocol for this paper from *Bio-protocol*.

8 July 2019; accepted 6 February 2020
10.1126/science.aay5947

RESEARCH ARTICLE

CELL SURFACE MAPPING

Microenvironment mapping via Dexter energy transfer on immune cells

Jacob B. Geri[1]*, James V. Oakley[1]*, Tamara Reyes-Robles[2]*, Tao Wang[1]*, Stefan J. McCarver[1], Cory H. White[2], Frances P. Rodriguez-Rivera[3], Dann L. Parker Jr.[3], Erik C. Hett[2], Olugbeminiyi O. Fadeyi[2]†, Rob C. Oslund[2]†, David W. C. MacMillan[1]†

Many disease pathologies can be understood through the elucidation of localized biomolecular networks, or microenvironments. To this end, enzymatic proximity labeling platforms are broadly applied for mapping the wider spatial relationships in subcellular architectures. However, technologies that can map microenvironments with higher precision have long been sought. Here, we describe a microenvironment-mapping platform that exploits photocatalytic carbene generation to selectively identify protein-protein interactions on cell membranes, an approach we term MicroMap (μMap). By using a photocatalyst-antibody conjugate to spatially localize carbene generation, we demonstrate selective labeling of antibody binding targets and their microenvironment protein neighbors. This technique identified the constituent proteins of the programmed-death ligand 1 (PD-L1) microenvironment in live lymphocytes and selectively labeled within an immunosynaptic junction.

Spatial relationships between biomolecules underpin the fundamental processes of life. In the context of cell surfaces, it has long been established that proteins are localized into defined assemblies, termed microenvironments (*1*). These substructures play a critical role in intercellular communication (*2*). As such, the capacity to precisely map these cellular landscapes should provide crucial insights into fundamental biology that will have wide-reaching implications for human health and the development of therapeutic strategies (*3*). In more specific terms, improved methods for microenvironment mapping are likely to enable discoveries in areas as wide ranging as proteomics (antibody target identification and discovering protein-protein interactions) (*4*), genomics (profiling biomolecules near genetic loci) (*5*), and neuroscience (elucidating synapse dynamics) (*6*).

In recent years, several platforms have emerged that enable the specific labeling of proteins by using the concept of spatial proximity (*7*–*9*). These technologies (APEX, SPPLAT, EMARS, and BioID) (*10*, *11*) use tethered enzymes that catalytically generate reactive open-shell or electrophilic species that target specific amino acid residues in neighboring systems. Because these intermediates have extended half-lives (0.1 ms to 60 s), they undergo diffusion at rates comparable with that of labeling (Fig. 1) (*12*). These elegant strategies have primarily been applied to the proteomic profiling and imaging of larger protein architectures such as mitochondria, lipid droplets, and nuclear pores (*13*–*15*) as well as regions such as synaptic clefts (*16*), lipid rafts (*9*), nuclear lamina (*17*, *18*), and protein clusters (*19*, *20*).

Given the intrinsic value of understanding biological systems at the microenvironment level, there remains a demand for cellular mapping technologies that operate at short range and with high precision. With this in mind, we identified a series of requirements for a suitable micromapping technology that might be used across a range of cellular constructs: (i) a catalytic manifold tolerant of aqueous conditions and biomolecules; (ii) a catalyst that can be conjugated to a range of targeting modalities—antibodies, small-molecule ligands, macromolecules, DNA, and sugars (*21*); (iii) a catalysis mechanism that can selectively activate chemical probes at a diffusion-limited rate; (iv) a readily accessible labeling probe that is only activated within 1 nm of the catalyst radius; (v) a labeling probe that is sufficiently reactive not to undergo long-range diffusion after activation; and (vi) a biomolecule-labeling mechanism that is both diffusion-limited and residue agnostic. The successful realization of these goals could, therefore, be applied within spatially restricted environments that have to date proven challenging to profile with high precision, such as the immunosynapse.

Design plan

It has long been established that carbenes readily cross-link with C–H bonds found in all biomolecules [rate constant (k) = 3.1×10^9 s^{-1}] and cannot diffuse farther than 4 nm owing to fast quenching by water [$k = 3.1 \times 10^8$ s^{-1}, half-life ($T_{1/2}$) < 2 ns] (*22*, *23*). This reactivity profile renders carbenes ideal reactive intermediates for high-precision microenvironment mapping. Although diazirine-based probes have been widely applied in small-molecule target identification (*24*), the general requirement for direct excitation with ultraviolet (UV) light precludes the possibility of a target-localized activation of free diazirine substrates by using short-wavelength light. By contrast, it is well known that diazirines exhibit little to no direct absorption of blue light (410 to 490 nm) (*25*). We recently questioned whether visible light–powered iridium catalysts could sensitize diazirines by means of a Dexter energy transfer mechanism. This would allow blue light-emitting diodes (LEDs) to indirectly activate diazirines, localizing the generation of carbenes to within 0.1 nm of the photocatalyst. If that is possible, we further recognized the opportunity to apply this localized excitation to a high-precision platform for microenvironment mapping. More specifically, we envisioned a photocatalytic proximity labeling technology for carbene generation in which a spatially targeted iridium complex acts as an antenna (Fig. 1, top), absorbing the photonic energy of visible light and transferring it to a diazirine probe (Fig. 2A). Among numerous applications, we hypothesized that this approach to MicroMapping (μMap) would offer sufficient spatiotemporal resolution to profile nanoscale protein assemblies on the surface of cells.

The proposed mechanism of the transformation is outlined in Fig. 2A. First, a ground-state iridium-based photocatalyst would be excited to its S_1 state through absorption of blue (450 nm) light. Quantitative intersystem crossing to the long-lived triplet excited state (T_1) ($T_{1/2}$ = 0.2 to 3 μs) is then followed by short-range Dexter energy transfer, in which the catalyst is returned to its ground S_0 state, and diazirine is promoted to its T_1 state (*26*). The triplet diazirine undergoes elimination of N_2 to release a triplet carbene, which undergoes picosecond–time scale spin equilibration (*27*) to its reactive singlet state ($T_{1/2}$ < 1 ns) and then either cross-links with a nearby protein or is quenched by the aqueous environment. We identified four key catalyst design elements required for successful photocatalytic proximity labeling: (i) a triplet energy in excess of 60 kcal/mol, facilitating energy transfer to the diazirine substrate; (ii) a visible-light extinction coefficient (ε_{420}) greater than 1000 M^{-1} cm^{-1}, to enable the use of light sources that do not promote background diazirine photolysis; (iii) hydrophilicity for biocompatible conditions; and (iv) a suitable reactive handle for bioconjugation.

Methodology development

We first tested the feasibility of visible light–sensitized N_2 elimination from diazirines by screening a variety of photocatalysts with increasing triplet energies (Fig. 2B). Although catalysts with triplet energies below 60 kcal/mol

[1]Merck Center for Catalysis, Princeton University, Princeton, NJ 08544, USA. [2]Merck Exploratory Science Center, Merck & Co., Inc., Cambridge, MA 02141, USA. [3]Discovery Chemistry, Merck & Co., Inc., Kenilworth, NJ 07033, USA.
*These authors contributed equally to this work.
†Corresponding author. Email: olugbeminiyi.fadeyi@merck.com (O.O.F); rob.oslund@merck.com (R.C.O.); dmacmill@princeton.edu (D.W.C.M.)

did not sensitize model diazirine **1**, a catalyst with a triplet energy (E_T) exceeding this threshold {Ir[dF(CF_3)ppy]$_2$(dtbbpy)}PF_6 (**2**) (E_T = 60.1 kcal/mol) (*28*) promoted consumption of **1** under mild conditions (15 min, 25°C, 100 μM H_2O/dimethyl sulfoxide, 450 nm irradiation) in >97% yield. No reaction was observed with diazirine **1** in the absence of photocatalyst or light. We then redesigned this catalyst for biomolecular applications by increasing its water solubility through the addition of polyethylene glycol, carboxylic acid, and alkyne functional groups (**3**) (Fig. 2B). These modifications did not negatively affect its ability to sensitize N_2 elimination from **1** (supplementary materials). Diazirine sensitization could be extended to a variety of *p*- and *m*-substituted aryltrifluoromethyl diazirines bearing valuable payloads for microscopy and proteomics applications, including free carboxylic acid, phenol, amine, alkyne, carbohydrate, and biotin groups (fig. S1). The extinction coefficient of the photocatalyst (**2**) is five orders of magnitude larger than that of the diazirine (**1**) at the wavelength emitted by the blue LEDs used for sensitization (450 nm), explaining the absence of a noncatalyzed background reaction (fig. S2). Last, we assigned a short-range (Dexter) energy transfer mechanism rather than a longer-range Förster energy transfer mechanism on the basis of a lack of overlap between the absorption band of diazirine **1** and the emission band of iridium catalyst **2** even at high concentrations of **1** (0.1 M) (fig. S3). Energy transfer was highly efficient, with a rate constant of 7.9(5) × 10^7 $M^{-1}s^{-1}$ (measured through Stern-Volmer analysis; number in parentheses indicates standard deviation in trailing digit) (table S1 and figs. S4 and S5).

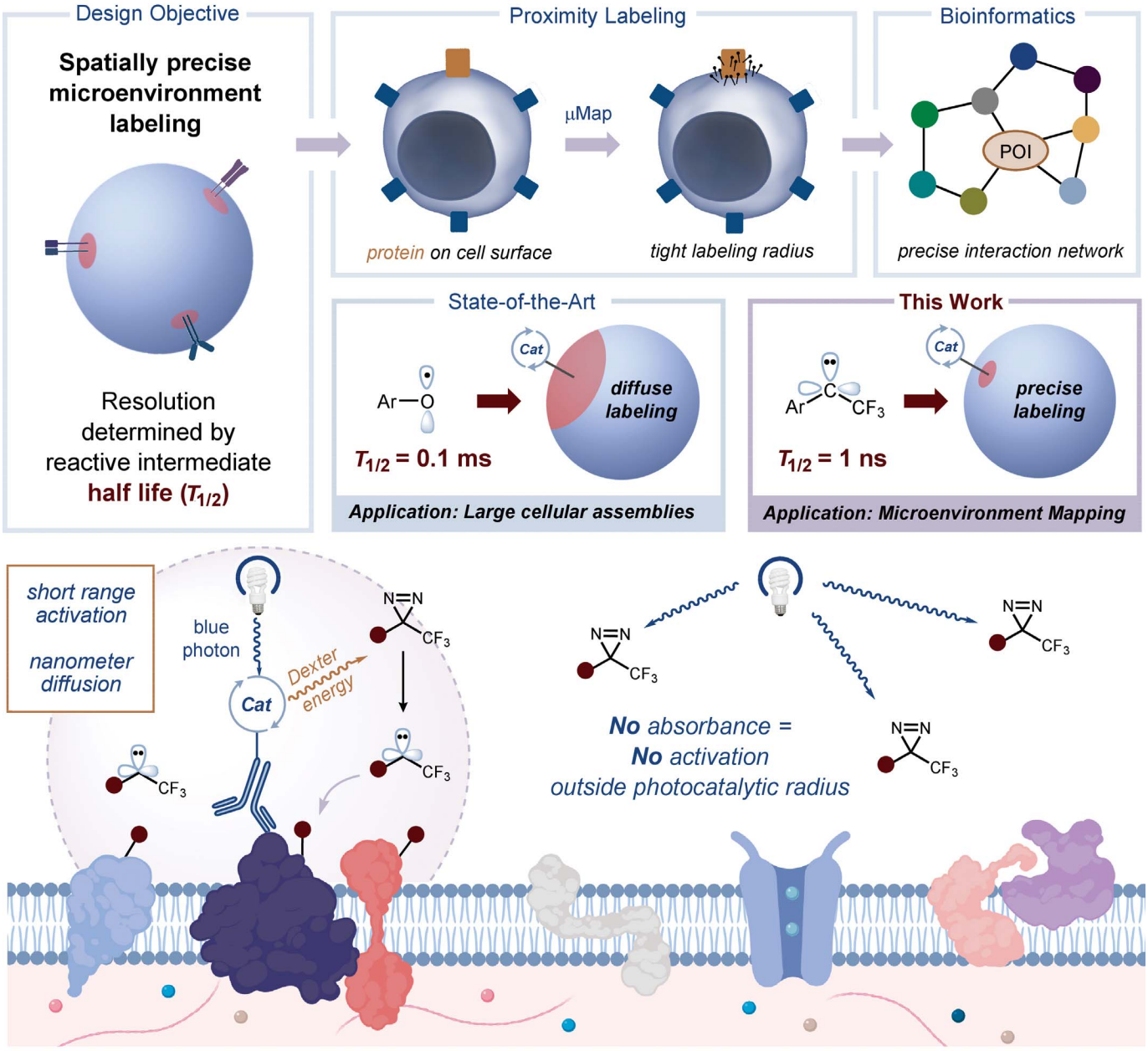


Fig. 1. High-resolution proximity-based labeling by using carbene intermediates. Spatially precise labeling enables the construction of information-rich interaction networks. (Top) The resolution of proximity-based labeling is fundamentally limited by the long solution half-life ($T_{1/2}$) of the reactive intermediates, such as phenoxyl radicals, used to label protein constituents of cell-membrane microenvironments. POI, Protein of interest. (Bottom) Using shorter-lived carbenes as reactive intermediates bypasses this limitation, enabling new applications in chemical biology.

We sought to demonstrate that carbenes generated through photocatalytic diazirine sensitization could label proteins (Fig. 2C). When a solution of bovine serum albumin (BSA) (10 μM) and a biotinylated diazirine probe **4** (100 μM) were irradiated with 375-nm light, biotinylation of BSA was detected through Western blot. When irradiated with lower-energy visible light at 450 nm, the degree of biotinylation was <0.5%

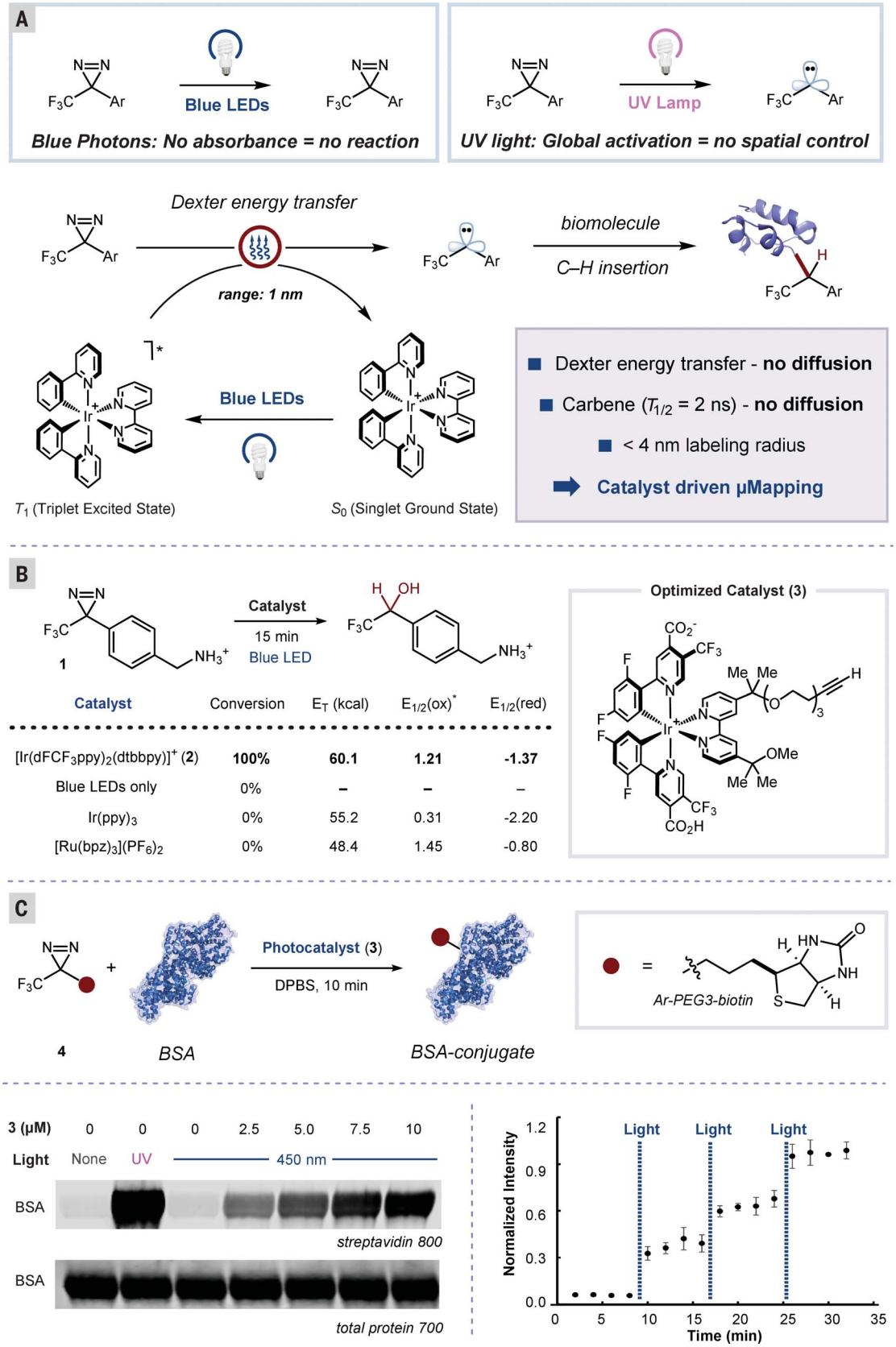


Fig. 2. Reaction design and catalyst development. (**A**) Blue light does not directly activate diazirines, whereas UV light does. In this work, we used a photocatalyst excited by using visible light for photocatalytic, energy transfer–mediated diazirine activation. (**B**) Catalyst development. Screening catalysts with a range of triplet energies demonstrated that catalytic sensitization of diazirines was possible. Catalytic activity requires a triplet energy (E_T) in excess of 60 kcal/mol, and catalysts with low triplet energies but high excited-state reduction or oxidation potentials were ineffective, suggesting an energy-transfer mechanism. Conversion was measured by means of ^{19}F–nuclear magnetic resonance spectroscopy. $E_{1/2}$, half-wave potential. (**C**) (Left) Western blot analysis of photocatalytic biotinylation of bovine serum albumin (BSA) by using a diazirine biotin conjugate (SDS–polyacrylamide gel electrophoresis, streptavidin blotting). Using light as a reagent enables fine temporal control over labeling of BSA. (Right) Short-duration illumination with light can be used to control the extent of labeling of BSA over time [streptavidin blot normalized against total protein stain; error bars are standard deviations calculated from three independent replicates (n = 3)].

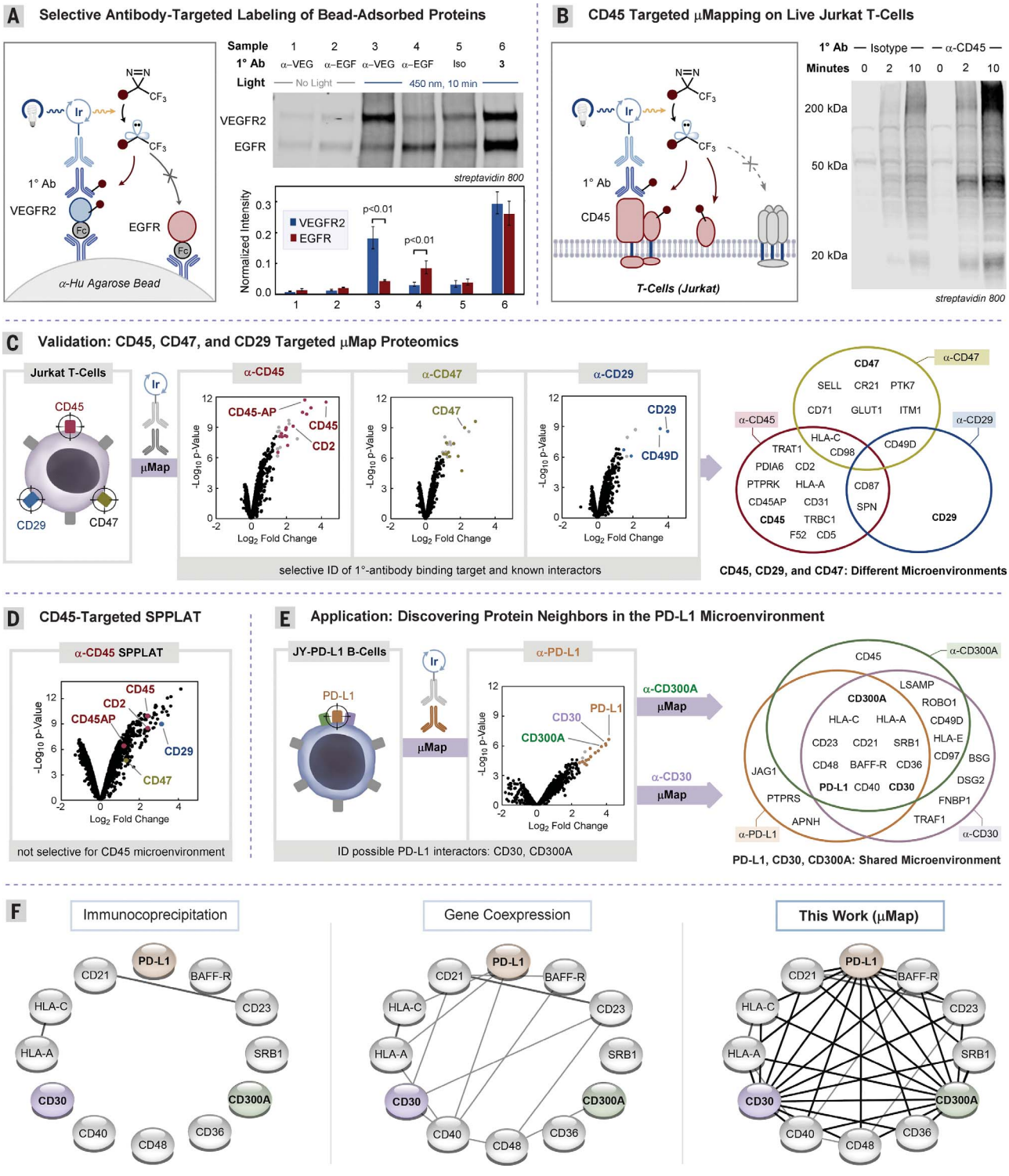


Fig. 3. μMapping on live cells. (**A**) Western blot analysis of antibody-targeted μMapping of VEGFR2-Fc or EGFR-Fc on agarose beads shows spatially selective protein labeling of VEGFR2-Fc or EGFR-Fc. Error bars in barplot are the standard deviation calculated from three independent replicates (n = 3). (**B**) Western blot analysis of antibody-targeted μMapping of CD45 on Jurkat T cells. (**C**) Selective proximity labeling of the CD45, CD47, and CD29 microenvironments using μMap. Significantly [false discovery rate (FDR)–corrected $P < 0.05$] enriched membrane proteins in volcano plots are highlighted in red (CD45), gold (CD47), or blue (CD29), and nonmembrane proteins are in gray. Venn diagram analysis of highly enriched membrane proteins shows minimal overlap. (**D**) CD45 proximity labeling on Jurkat cells by using peroxidase does not resolve CD45 and known interactors (red dots) from other proteins, including CD29 and CD47. (**E**) μMapping the PD-L1 microenvironment on JY PD-L1 B cells to reveal putative interactors. Significantly (FDR-corrected $P < 0.05$) enriched membrane proteins are highlighted in orange, and nonmembrane proteins are in gray. Labels show PD-L1 (orange), CD300A (green), and CD30 (purple) proteins. Venn diagram analysis of enriched membrane proteins shows overlap of PD-L1, CD300A, CD30, and nine other proteins. All volcano plots show averaged log2 ratios (targeted protein versus isotype) on the x axis (n = 3 replicates) and negative log10 transformed P values on the y axis. (**F**) String analysis of convergently enriched proteins.

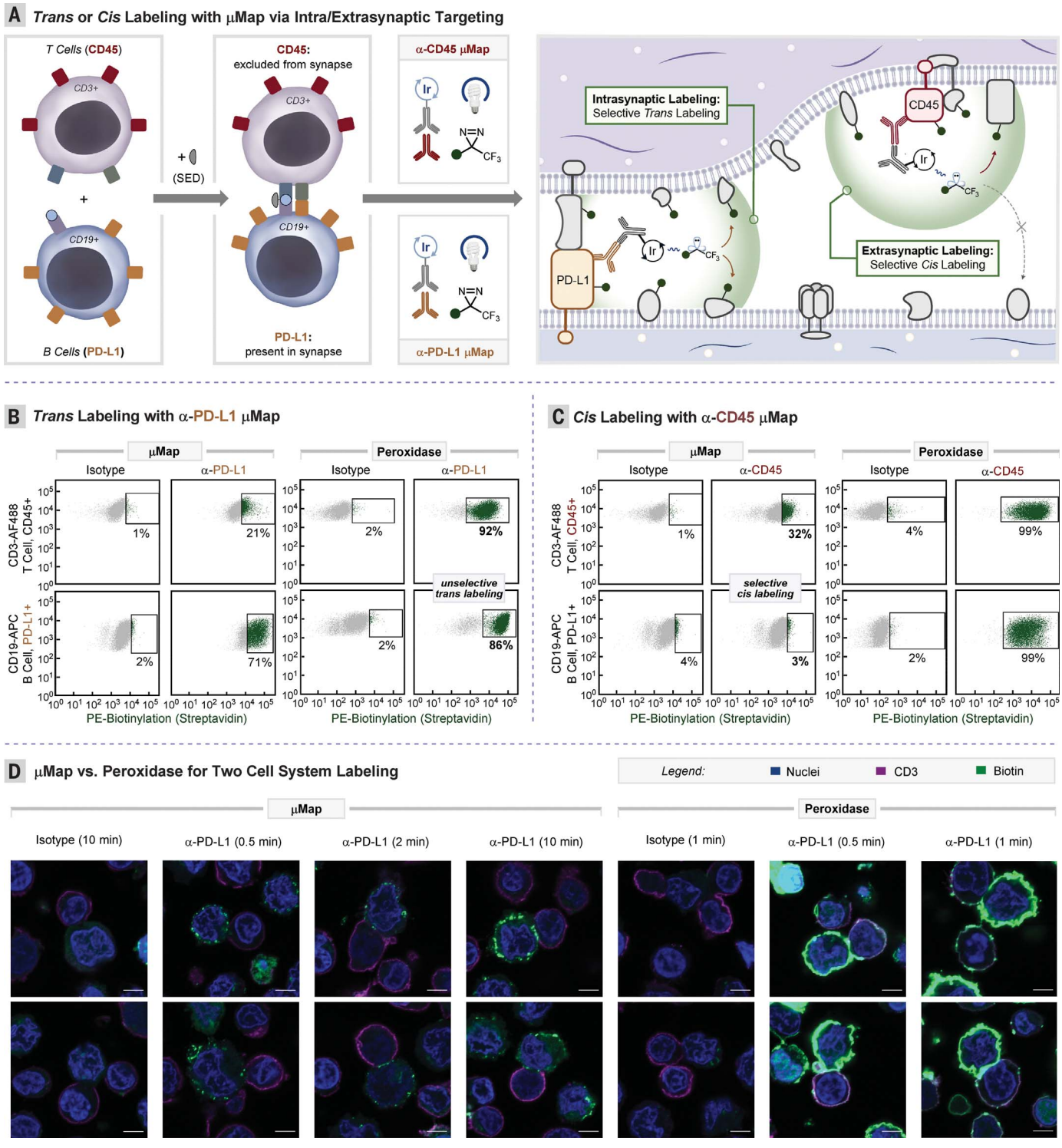


Fig. 4. Intra- and extrasynaptic μmapping within a two-cell system. (**A**) Schematic depicting Jurkat (CD45RO$^+$/PD-1$^+$/CD3$^+$) and JY (PD-L1$^+$/CD19$^+$) two-cell system enhanced by the presence of staphylococcal enterotoxin D (SED) for antibody targeting of intrasynaptic PD-L1 (expressed on JY cells) and extrasynaptic CD45RO (distinctly expressed on Jurkat cells) for selective trans or cis labeling. (**B**) Flow cytometry analysis of antibody targeting of PD-L1 on JY PD-L1 B cells with μMap by using 10-min light irradiation (left) shows both cis- and trans-cellular labeling. Peroxidase-based targeted labeling for 0.5 min (right) results in nearly complete cis- and trans-cellular labeling. (**C**) Flow cytometry analysis of antibody targeting of CD45RO on Jurkat T cells with μMap by using 10-min light irradiation (left) shows only cis-cellular labeling. Peroxidase-based targeted labeling for 0.5 min (right) results in nearly complete cis- and trans-cellular labeling. (**D**) Two-cell system confocal microscopy images of isotype-targeted (10-min light irradiation) or PD-L1–targeted (0.5-, 2-, or 10-min light irradiation) by using μMap (left) or isotype-targeted (1 min) or PD-L1–targeted (0.5 or 1 min) by using peroxidase-based labeling (right). Cells were imaged for biotinylation (green), CD3 surface expression (magenta), and nuclei (blue). Scale bar, 5 μm. Duplicate images are shown below each condition.

of the level observed through UV irradiation, establishing that the diazirine presents minimal background signal at this wavelength. However, in the presence of water-soluble iridium catalyst ***3*** (1 μM), catalyst-dependent biotinylation of BSA was observed. Photocatalytic labeling of BSA was further confirmed through intact protein mass spectrometry (fig. S6). Unlike other enzyme-based labeling methodologies, this approach requires continuous delivery of visible light to sustain diazirine sensitization for protein labeling. Accordingly, we exploited this feature to demonstrate how turning the light source on or off affords fine temporal control over the labeling process (Fig. 2C, right).

With an efficient photocatalytic system for carbene-based protein labeling in hand, we prepared a secondary antibody-photocatalyst conjugate as a general entry point for spatially targeted photocatalytic proximity labeling on cell surfaces. A goat anti-mouse (Gt/α-Ms) antibody was first decorated with azide groups through reaction with azidobutyric acid *N*-hydroxysuccinimide ester and then conjugated to alkyne-bearing iridium catalyst ***3*** by means of click chemistry, resulting in an antibody-photocatalyst ratio of 1:6. Next, to address protein-targeted labeling on a surface, we prepared a model system containing human Fc-tagged vascular endothelial growth factor receptor 2 (VEGFR2) and epidermal growth factor receptor (EGFR) proteins attached to α-human immunoglobulin G (IgG) agarose beads (Fig. 3A). These beads were sequentially incubated with a Ms/α-VEGFR2 antibody and Ir-Gt/α-Ms to position the iridium catalyst close to the VEGFR2 proteins on the bead surface. Irradiation of these beads with 450-nm light in the presence of a diazirine-biotin probe afforded selective labeling of VEGFR2 over EGFR. When Ms/α-EGFR was used as the primary antibody, the selectivity of labeling was reversed. An analogous experiment, using peroxidase-based labeling, was incapable of differentiating between EGFR or VEGFR2 (fig. S7).

Microenvironment mapping on cell membranes

We next applied antibody-targeted photocatalytic diazirine activation (μMap) to the surface of live cells. For these experiments, addition of the antibody to the cell surface was maintained at 4°C to limit antibody-mediated protein cross-linking (fig. S8) (*29*, *30*). We selected CD45, a highly abundant tyrosine phosphatase on T cell surfaces involved in antigen receptor signaling (*31*), as an initial target. Western blot analysis of CD45-targeted μMap on Jurkat cells showed light- and time-dependent protein biotinylation compared with the isotype-targeting control (Fig. 3B). Next, we used tandem mass tag (TMT)–based quantitative proteomic analysis of streptavidin-enriched proteins to identify CD45 and two known associators (CD45AP and CD2) through STRING analysis as part of a wider subset of enriched cell membrane proteins (Fig. 3C) (*32*).

With proof of concept for cell surface labeling in hand, we next questioned whether μMap could differentiate between spatially separated microenvironments on the same cell membrane. To this end, we selected CD29 and CD47 as ideal targets with, to the best of our knowledge, no known co–spatial association on the cell surface. μMapping of CD45, CD29, or CD47 on Jurkat cells resulted in the enrichment of distinct sets of proteins, which included both known (CD29:CD49D, CD45:CD45AP:CD2) and previously unknown interactors (Fig. 3C). Crucially, although several proteins were shared between pairs of targeted proteins, none were shared across all three, validating the ability of μMap to discriminate between unrelated microenvironments. By contrast, when using state-of-the-art peroxidase-based proximity labeling methods (*10*, *33*), cell surface CD45 and associated proteins were not selectively resolved from CD29 or CD47 (Fig. 3D and fig. S9).

Next, we harnessed the resolution and selectivity of μMap to investigate the proximal protein interactome of programmed-death ligand 1 (PD-L1) in B cells. As has been well established, PD-L1 plays an important role in cancer cells as an immune checkpoint ligand that can accelerate tumor progression through suppression of T cell activity (*34*). In the event, PD-L1–targeted μMap revealed CD30, a member of the tumor necrosis factor receptor family (*35*), and CD300A, an immune inhibitory receptor (Fig. 3E) (*36*), as potentially new interactors based on significant enrichment. These results highlight the potential of μMapping to provide new insights with respect to the microenvironments of checkpoint proteins.

To further validate the enriched subset of proteins identified with PD-L1 μMapping, we performed targeted labeling of these two highly enriched proteins. Targeted μMapping of these proteins within the PD-L1 microenvironment should, therefore, afford similar enrichment lists, verifying their spatial association. We found that α-CD30–, α-CD300A–, and α-PD-L1–directed μMapping identified the same set of 12 surface receptors (Fig. 3F).

It is well recognized that the development of new therapeutic oncology strategies will require an understanding of the underlying mechanisms of intercellular communication, particularly within the context of T cell activation and differentiation. Furthermore, given that localization of PD-L1 is found within the T cell/antigen-presenting cell (APC) immunosynapse (at the interface between two immunointeractive cells), we hypothesized that PD-L1–directed μMapping should lead not only to biotinylation of a PD-L1–expressing APC surface (cis-labeling) but also to the biotinylation of the adjacent synaptic T cell (trans-labeling) (Fig. 4A). As a control experiment, we further posited that when targeting a protein excluded from the synapse, such as CD45RO (*37*, *38*), the diffusion-minimized radius of μMap would preclude biotinylation of the distant trans-cell membrane.

We evaluated PD-L1– and CD45-targeted μMapping in a two-cell system composed of PD-L1–expressing JY B-lymphocytes as the APC and Jurkat T-lymphocytes distinctly expressing PD-1 and the CD45RO isoform (fig. S10). Using staphylococcal enterotoxin D (SED) to facilitate T cell receptor (TCR)–major histocompatibility complex (MHC) engagement and promote B cell/T cell immune synapse formation and signaling, we assessed the ability of μMap to selectively label within intercellular synapses (Fig. 4A and fig. S11) (*39*–*41*). Flow cytometry analysis was then used to monitor the extent of cis- and trans-cellular labeling. As anticipated, PD-L1–targeted μMap resulted in both cis- and trans-cellular labeling, whereas CD45RO-targeted μMap led to selective cis-labeling on the CD45RO-expressing Jurkat cells (Fig. 4, B and C, and fig. S12), without any labeling of the adjacent B cell. In stark contrast to μMap, peroxidase-based proximity labeling of PD-L1 or CD45RO within this two-cell system led to complete labeling of both cell types within 30 s, clearly visualized through flow cytometry and confocal microscopy (Fig. 4, B, C, and D; and fig. S12). In comparison, PD-L1–targeted μMap showed high selectivity for trans-labeling solely at the cis- and trans-cellular contact regions (Fig. 4D and fig. S12). Applying the μMap technology on PD-1 in the Jurkat-JY coculture system resulted in the reciprocal trend of cis- and trans-cellular labeling (fig. S13). Collectively, these findings clearly demonstrate that the capacity of μMap to elucidate protein-protein interactions can be directly translated toward the highly selective labeling of dynamic interfaces within complex multicellular systems.

We expect that this technology will find immediate use in antibody target identification, exploration of signal transduction pathways, profiling cell-cell junctions, and other disease-relevant microenvironments.

REFERENCES AND NOTES

1. E. Lundberg, G. H. H. Borner, *Nat. Rev. Mol. Cell Biol.* **20**, 285–302 (2019).
2. N. C. Bauer, P. W. Doetsch, A. H. Corbett, *Traffic* **16**, 1039–1061 (2015).
3. B. Z. Stanton, E. J. Chory, G. R. Crabtree, *Science* **359**, eaao5902 (2018).
4. R. R. Minter, A. M. Sandercock, S. J. Rust, *Drug Discov. Today. Technol.* **23**, 83–90 (2017).
5. D. S. Johnson, A. Mortazavi, R. M. Myers, B. Wold, *Science* **316**, 1497–1502 (2007).
6. M. Hanoun, M. Maryanovich, A. Arnal-Estapé, P. S. Frenette, *Neuron* **86**, 360–373 (2015).
7. S. S. Lam *et al.*, *Nat. Methods* **12**, 51–54 (2015).
8. J. S. Rees, X.-W. Li, S. Perrett, K. S. Lilley, A. P. Jackson, *Mol. Cell. Proteomics* **14**, 2848–2856 (2015).
9. N. Hashimoto *et al.*, *Proteomics* **12**, 3154–3163 (2012).
10. J. S. Rees, X.-W. Li, S. Perrett, K. S. Lilley, A. P. Jackson, *Curr. Protoc. Protein Sci.* **80**, 19.27.11–19.27, 18 (2015).
11. E. Choi-Rhee, H. Schulman, J. E. Cronan, *Protein Sci.* **13**, 3043–3050 (2004).
12. L. K. Folkes, M. Trujillo, S. Bartesaghi, R. Radi, P. Wardman, *Arch. Biochem. Biophys.* **506**, 242–249 (2011).
13. H.-W. Rhee *et al.*, *Science* **339**, 1328–1331 (2013).

14. D. I. Kim *et al*., *Proc. Natl. Acad. Sci. U.S.A.* **111**, E2453–E2461 (2014).
15. K. Bersuker *et al*., *Dev. Cell* **44**, 97–112.e7 (2018).
16. K. H. Loh *et al*., *Cell* **166**, 1295–1307.e21 (2016).
17. D. Z. Bar *et al*., *Nat. Methods* **15**, 127–133 (2018).
18. D. Z. Bar *et al*., *Nat. Methods* **15**, 749 (2018).
19. X.-W. Li *et al*., *J. Biol. Chem.* **289**, 14434–14447 (2014).
20. N. Kotani *et al*., *Proc. Natl. Acad. Sci. U.S.A.* **105**, 7405–7409 (2008).
21. T. Hayashi, Y. Yasueda, T. Tamura, Y. Takaoka, I. Hamachi, *J. Am. Chem. Soc.* **137**, 5372–5380 (2015).
22. A. Admasu *et al*., *J. Chem. Soc., Perkin Trans. 2* (5): 1093–1100 (1998).
23. H. C. Berg, *Random Walks in Biology* (Princeton Univ. Press, 1993).
24. S.-S. Ge *et al*., *RSC Adv.* **8**, 29428 (2018).
25. J. Brunner, H. Senn, F. M. Richards, *J. Biol. Chem.* **255**, 3313–3318 (1980).
26. D. M. Arias-Rotondo, J. K. McCusker, *Chem. Soc. Rev.* **45**, 5803–5820 (2016).
27. J. Wang, J. Kubicki, H. Peng, M. S. Platz, *J. Am. Chem. Soc.* **130**, 6604–6609 (2008).
28. A. Singh *et al*., *J. Organomet. Chem.* **776**, 51–59 (2015).
29. L. Y. Bourguignon, S. J. Singer, *Proc. Natl. Acad. Sci. U.S.A.* **74**, 5031–5035 (1977).
30. L. Y. Bourguignon, *J. Cell Biol.* **83**, 649–656 (1979).
31. M. L. Hermiston, Z. Xu, A. Weiss, *Annu. Rev. Immunol.* **21**, 107–137 (2003).
32. D. Szklarczyk *et al*., *Nucleic Acids Res.* **47** (D1), D607–D613 (2019).
33. V. Hung *et al*., *Nat. Protoc.* **11**, 456–475 (2016).
34. H. O. Alsaab *et al*., *Front. Pharmacol.* **8**, 561 (2017).
35. C. A. van der Weyden, S. A. Pileri, A. L. Feldman, J. Whisstock, H. M. Prince, *Blood Cancer J.* **7**, e603 (2017).
36. O. Zenarruzabeitia, J. Vitallé, C. Eguizabal, V. R. Simhadri, F. Borrego, *J. Immunol.* **194**, 5053–5060 (2015).
37. J. R. James, R. D. Vale, *Nature* **487**, 64–69 (2012).
38. C. B. Carbone *et al*., *Proc. Natl. Acad. Sci. U.S.A.* **114**, E9338–E9345 (2017).
39. M. L. Dustin, *Cancer Immunol. Res.* **2**, 1023–1033 (2014).
40. I. V. Pinchuk, E. J. Beswick, V. E. Reyes, *Toxins (Basel)* **2**, 2177–2197 (2010).
41. M. C. Montoya *et al*., *Nat. Immunol.* **3**, 159–168 (2002).
42. C. White, R. Oslund, O. Fadeyi, T. Reyes Robles, Flow cytometry data files for article: Microenvironment mapping via Dexter energy transfer on immune cells. Harvard Dataverse (2020).
43. C. White, Merck/Photoproximity_Labeling: Photoproximity_Labeling_v1.0. Zenodo (2020).

ACKNOWLEDGMENTS

We thank A. D. Trowbridge and C. P. Seath for their assistance with the preparation of this manuscript and D. Hazuda for insightful comments and suggestions. We also thank Efficiency Aggregators for development of the biophotoreactor used in this work.
Funding: Research reported in this publication was supported by the NIH National Institute of General Medical Sciences (R01-GM103558-03) and gifts from Merck & Co., Inc., Kenilworth, New Jersey, USA. J.B.G. acknowledges the NIH for a postdoctoral fellowship (F32-GM133133-01). J.V.O. acknowledges the NSF for a predoctoral fellowship (DGE-1656466). **Author contributions:** D.W.C.M., R.C.O., O.O.F., and S.J.M. conceived of the work. J.B.G., J.V.O., T.W., R.C.O., O.O.F., T.R.-R., and C.H.W. designed and executed experiments. D.L.P., F.P.R.-R., and E.C.H. provided insight and direction for experimental design. **Competing interests:** J.B.G., J.V.O., T.W., R.C.O., O.O.F., and D.W.C.M. have filed a provisional U.S. patent application on this work. **Data and materials availability:** Raw flow cytometry data are available through the Harvard Dataverse (*42*). Code for replicating proteomic data analysis, generation of volcano plots, and raw peptide level abundance data for each of the experiments are available in a GitHub repository (*43*). All other data are available in the main text or the supplementary materials.

SUPPLEMENTARY MATERIALS

science.sciencemag.org/content/367/6482/1091/suppl/DC1
Materials and Methods
Figs. S1 to S51
Table S1
References (*44*–*58*)
Data File S1

View/request a protocol for this paper from *Bio-protocol*.

16 June 2019; resubmitted 13 November 2019
Accepted 6 February 2020
10.1126/science.aay4106

SOLAR CELLS

Triple-halide wide–band gap perovskites with suppressed phase segregation for efficient tandems

Jixian Xu[1,2,3]*†, Caleb C. Boyd[2,4]†, Zhengshan J. Yu[5], Axel F. Palmstrom[2], Daniel J. Witter[1,2], Bryon W. Larson[2], Ryan M. France[2], Jérémie Werner[1,2], Steven P. Harvey[2], Eli J. Wolf[2,4], William Weigand[5], Salman Manzoor[5], Maikel F. A. M. van Hest[2], Joseph J. Berry[2], Joseph M. Luther[2], Zachary C. Holman[5], Michael D. McGehee[1,2,6]*

Wide–band gap metal halide perovskites are promising semiconductors to pair with silicon in tandem solar cells to pursue the goal of achieving power conversion efficiency (PCE) greater than 30% at low cost. However, wide–band gap perovskite solar cells have been fundamentally limited by photoinduced phase segregation and low open-circuit voltage. We report efficient 1.67–electron volt wide–band gap perovskite top cells using triple-halide alloys (chlorine, bromine, iodine) to tailor the band gap and stabilize the semiconductor under illumination. We show a factor of 2 increase in photocarrier lifetime and charge-carrier mobility that resulted from enhancing the solubility of chlorine by replacing some of the iodine with bromine to shrink the lattice parameter. We observed a suppression of light-induced phase segregation in films even at 100-sun illumination intensity and less than 4% degradation in semitransparent top cells after 1000 hours of maximum power point (MPP) operation at 60°C. By integrating these top cells with silicon bottom cells, we achieved a PCE of 27% in two-terminal monolithic tandems with an area of 1 square centimeter.

Compositional tuning can yield optoelectronic properties of state-of-the-art ABX_3 metal halide perovskites that are desirable for use in highly efficient solar cells, light-emitting diodes (LEDs), and detectors. Such tuning has been achieved through mixing of cations such as methylammonium (MA), formamidinium (FA), cesium (Cs), dimethylammonium (DMA), and methylenediammonium (MDA) at the A site (*1*–*6*); lead (Pb) and tin (Sn) at the B site (*7*, *8*); and iodine (I) and bromine (Br) at the X site (*9*, *10*). Wide–band gap alloys (>1.65 eV) in particular are of considerable interest for both LEDs and multijunction solar cells (*11*–*13*). The latter can overcome the Shockley-Queisser limit of single-junction cells by stacking complementary wide–band gap and narrow–band gap absorbers to reduce thermalization losses (*11*, *14*). As market-dominant silicon solar cells approach their theoretical limit of 29.1% with a lab record of 26.7% (*15*, *16*), the development of multijunction solar cells or tandem solar cells could help to further increase the power conversion efficiency (PCE) and reduce the levelized cost of photovoltaic (PV) electricity (*17*, *18*).

[1]Chemical and Biological Engineering, University of Colorado, Boulder, CO 80309, USA. [2]National Renewable Energy Laboratory, Golden, CO 80401, USA. [3]CAS Key Laboratory of Materials for Energy Conversion, Department of Materials Science and Engineering, University of Science and Technology of China, Hefei 230026, China. [4]Materials Science and Engineering, Stanford University, Stanford, CA 94305, USA. [5]School of Electrical, Computer, and Energy Engineering, Arizona State University, Tempe, AZ 85281, USA. [6]Materials Science and Engineering, University of Colorado, Boulder, CO 80309, USA.
*Corresponding author. Email: michael.mcgehee@colorado.edu (M.D.M.); jixianxu@ustc.edu.cn (J.X.)
†These authors contributed equally to this work.

Although a range of band gaps from 1.6 to 3.06 eV can be achieved through I/Br and Br/Cl alloying (*9*, *10*, *19*–*21*), wide–band gap alloys in the optimum range for use in tandem solar cells suffer from short diffusion lengths and photoinduced phase segregation, which lead to poor optoelectronic qualities and substantial open-circuit voltage (V_{oc}) deficits relative to their theoretical limit (*12*, *22*, *23*). Studies of this unexpectedly large V_{oc} deficit revealed photoinduced trap formation by halide segregation, especially when the Br fraction on the X-site was >20% (*12*, *22*, *23*). The alloyed I/Br phases segregated upon illumination and photocarriers were funneled into the low–band gap I-rich domains, which acted as traps that red-shift the photoluminescence and reduce the V_{oc} (*23*). Reduced photoinduced phase segregation and improved material quality of wide–band gap perovskites through cation substitution of Cs or DMA achieve wide band gaps while limiting the Br fraction (*2*, *24*, *25*). Additive engineering can reduce defect densities (*26*–*30*). Surface engineering techniques such as the formation of 2D/3D heterostructures have also been used for improving device V_{oc} (*31*). However, wide–band gap solar cells still are in need of both a reduced V_{oc} deficit and improved photostability (*13*).

Inspired by recent advances in achieving improved material quality with triple- or quadruple-cation perovskites (*1*, *6*) and reports suggesting that Cl as an additive may reduce defect density (*32*–*35*), we explored the triple-halide (I, Br, Cl) compositional space. Generally, previous studies have reported the use of Cl as an additive or precursor to affect morphology and surface passivation but with little or no incorporation into the bulk material. The Cl also had little impact on the band gap, independent of the Cl ratio included in the precursor (*33*–*40*). The lack of incorporation into the bulk lattice with little change in the band gap occurs because Cl typically volatilizes as MACl or FACl during annealing of the perovskite film and only acts to control film crystallization, as it resides at grain boundaries or on perovskite film surfaces in the final material.

We report that Cs and Br act as a bridge to a new phase space in wide–band gap perovskites of triple-halide alloys containing I, Br, and Cl at molar amounts >15%. We directly incorporated Cl into the lattice at much larger amounts than previously reported, observing a uniform halide distribution throughout the material with a reduction in lattice parameter and an increase in band gap corresponding to increasing amounts of Cl in the lattice. By extending the double-halide to triple-halide alloy, we observed a distinct enhancement in optoelectronic characteristics, such as factor of 2 increases in photocarrier lifetime and mobility and the suppression of light-induced phase segregation at intensities up to 100 suns. These material advances reduced the V_{oc} deficit of 1.67-eV wide–band gap solar cells by 100 mV and boosted PCE from ~18% to 20.3% (Table 1 and table S1). We demonstrated large-area (1 cm^2), wide–band gap semitransparent top cells for Si tandems with a high certified performance of 16.83% that resulted from a substantially improved V_{oc} relative to prior reports (Table 1 and table S2). The triple-halide material was also operationally stable in solar cells that maintained >96% of their initial efficiency after 1000 hours of maximum power tracking under white light illumination at 60°C, and >97% of their initial efficiency after 500 hours at 85°C. By integrating triple-halide semitransparent top cells with Si bottom cells with PCE of ~21% (*41*), we boosted their PCE by 30%, to 27% in 1-cm^2 two-terminal monolithic tandems (Table 1 and table S3).

Alloying chlorine into the perovskite lattice

We started with a targeted perovskite band gap of ~1.67 eV, which is in the range of ideal top-cell band gaps for a perovskite/Si tandem, taking into account imperfect absorption near the band edge (*42*, *43*). $FA_{0.75}Cs_{0.25}Pb(I_{0.8}Br_{0.2})_3$ has a band gap of 1.67 eV and was recently demonstrated to enable 25% PCE in two-terminal perovskite/Si tandems (*25*). We denote this perovskite family as CsFA perovskite, and denote this composition as Cs25Br20 in accordance with the percentage of Cs at the A site and the percentage of Br at the X site. Cs25Br20 outperformed its 1.67-eV counterpart Cs17Br25 in light stability and V_{oc} deficit, attributed to the reduced Br fraction and increased Cs fraction. To further improve the photostability, we reduced the Br fraction to 15% and found that Cs25Br15 has a band gap

of ~1.63 eV. To recover the optimal 1.67-eV band gap, we attempted to increase the Cs fraction but obtained lower PV performance (*25*), consistent with recent reports that a high Cs fraction might lead to halide inhomogeneity and phase segregation (*4*, *44*).

We sought to raise the band gap by alloying $MAPbCl_3$ perovskite into the lattice of CsFA perovskites. We chose $MAPbCl_3$ perovskite because it has a wide band gap (2.88 eV) and higher stability than its Br and I counterparts (*45*, *46*). When we mixed Cs25Br15 with 2 to 5 mol % $MAPbCl_3$ (referred to hereafter as Cs25Br15+Cl2 and Cs25Br15+Cl5) in solution, the band gap of the resulting films could be continuously raised from 1.63 to >1.67 eV (Fig. 1A and fig. S1). The sharp onset of the external quantum efficiency (EQE) indicated that a photoactive triple-halide perovskite phase had formed.

We used x-ray diffraction (XRD) to verify the triple-halide phase and determine the lattice constant. As indicated by the shift of the diffraction peaks (figs. S2 and S3), the perovskite single phase was retained and the lattice constant continually decreased with increasing $MAPbCl_3$ fraction. Specifically, Cs25Br15+Cl5 has a lattice constant of ~6.24 Å (Fig. 1F), which is similar to that of Cs25Br20 and evidently less than that of the host perovskite Cs25Br15, 6.27 Å.

Incorporating Cl into perovskite precursor solutions has been widely reported to increase the size of apparent grain domains in solid films, because the formation and outgassing of MACl modify the nucleation and crystal growth dynamics (*47*–*51*). Prior reports showed that the band gap remained substantially unchanged and that the Cl concentrations in the solid films were below the detection limit of energy-dispersive x-ray spectrometry (EDX) and x-ray photoelectron spectroscopy (XPS), even though a large portion of Cl was present in the precursors (*33*, *34*, *36*). In contrast, we did not observe enlargement of grain domains when more Cl was incorporated into the triple-halide films, as shown by scanning electron microscope (SEM) images (Fig. 1B and fig. S4).

In addition, we could readily detect Cl using XPS. The Cl-to-Pb ratio of films also increased when a higher fraction of Cl was included in the precursors (fig. S5). The Cl in the triple-halide films was uniformly distributed throughout the entire film thickness, similar to I and Br, as shown by time-of-flight secondary ion mass spectrometry (TOF-SIMS) depth profiling (Fig. 1C). To mitigate measurement artifacts (*52*), we recorded secondary ion clusters or molecular ion signals of Cs_2Cl^+, $Cs_4I_3^+$, and Cs_2Br^+ to track the depth profile of halides. The relative scaling of SIMS profiles between halides did not represent their stoichiometric ratio (*53*).

Taken together, the EQE, XRD, SEM, XPS, and SIMS observations show that Cl was incorporated into the perovskite lattice and increased its band gap, rather than being sacrificed as a volatile phase. Because the lattice constant of the host perovskites was reduced by the Cs and Br, Cl was closer to the ideal size for the X-site in the lattice. This explanation is consistent with the formation of MAPbBr/Cl perovskites being more thermodynamically preferred than MAPbI/Cl double-halide alloys (*19*–*21*).

Because perovskites with even wider band gaps are needed for all-perovskite tandems and possibly other applications, we identified the phase boundary of the triple-halide alloying strategy and obtained additional mechanistic insights into the perovskite phase space. When we further increased the molar ratio of Cl/(I+Br+Cl) to above 10% in Cs25Br15, we observed an inflection point in the band gap evolution curve (Fig. 1D, red line). That is, the band gap of the films began to decrease with increased Cl content, as shown in the EQE spectra (fig. S1). This increasing and then decreasing of the band gap with triple-halide alloying is anomalous and distinctly different from the monotonic growth trend reported in I/Br double-halide alloys (*9*, *10*, *23*).

Structural evolution observed with XRD (Fig. 1, E and F, and fig. S2) revealed that the band gap decrease at high Cl content was caused by phase segregation into two perovskite phases. At the phase boundary, the diffraction peaks of a segregated phase (very likely $MAPbCl_xBr_{3-x}$) emerged (fig. S2, A and D). The lattice of the host perovskite then expanded (diffraction peaks shifted to lower angles) with the growth of the segregated perovskite phase (Fig. 1F, red line, and fig. S2D), consistent with the observed band gap decrease and suggesting the segregation of a high-Br/Cl phase, which left behind an I-rich, lower–band gap host perovskite (Fig. 1D and fig. S1).

To further validate the generality of the triple-halide alloy, we also used Cs25Br30 and Cs25Br40 as the host perovskites to investigate the evolution of band gap (see EQE data in figs. S6 and S7) and lattice constant (see XRD data in figs. S8 and S9) when increasing the triple-halide alloy ratio. The trends in the band gap (Fig. 1D) and lattice constant (Fig. 1F) were consistent, further substantiating this mechanism of triple-halide alloying. In all cases, the band gap–raising rate was ~0.0078 eV, with each percent of Cl alloyed to form the single phase. The inflection point of band gap evolution (or the phase boundary between the single-phase triple-halide alloy and phase segregation) consistently increased with increased Br content, as in Cs25Br15, Cs25Br30, and Cs25Br40, indicating a wider single-phase range and greater tolerance to phase segregation in the perovskite with higher Br content. This finding verified that Br reduced the alloy barrier between I and Cl phases for triple-halide alloys. The addition of $PbCl_2$ in Cs25Br15 also increased the band gap in a manner similar to the effect of adding $MAPbCl_3$ (fig. S10), thereby reconfirming that Cl incorporation is the determinant to the band gap raising in triple-halide alloys. Adding MACl alone did not raise the band gap (fig. S10A), in agreement with previous reports that MACl volatilizes during film annealing (*47*–*51*).

Improved optoelectronic properties of triple-halide perovskites

Recent studies showcase the improvements in optoelectronic properties that result from incorporating even small amounts of Cl (<1%) (*32*–*34*, *47*, *50*). For example, small Cl ions might reduce the halogen vacancy defect density and improve the stability of perovskites in ambient air (*32*). Given that in our triple-halide perovskites, Cl-based reagents are well incorporated into the lattice, we used time-resolved microwave conductivity (TRMC) to study their electronic properties and charge-carrier dynamics (*54*). Despite no increase in apparent grain size in the triple-halide perovskites (Fig. 1B), an enhancement in both the charge-carrier

Table 1. PV parameters of solar cells using 1.67-eV triple-halide wide–band gap perovskites. Area is defined by optical aperture placed in front of devices.

Cell configuration	Area (cm^2)	V_{oc} (V)	J_{sc} (mA cm^{-2})	FF (%)	PCE (%)	Stabilized PCE (%)
Opaque single-junction	0.06	1.217	20.18	83.16	20.42	20.32
Top-illumination semitransparent	0.34	1.214	19.13	80.21	18.59	18.53
Top-illumination semitransparent	1	1.202	18.99	74.07	16.90	16.83* (certified)
Two-terminal tandem on Si	1	1.886	19.12	75.3	27.13	27.04

*11-point stabilized power output (SPO) measurement.

mobility and lifetime by nearly a factor of 2, equivalent to a doubled carrier diffusion length, was seen in comparison to our best 1.67-eV controls. Specifically, when the absorbed photon flux was ~1 × 10^{10} cm^{-2} (near 1-sun intensity), the lifetime increased from 420 to 846 ns (Fig. 2A) and the charge-carrier mobility improved from 29 to 53 cm^2 V^{-1} s^{-1} (Fig. 2B).

To disentangle the effect of Cl incorporation on the bulk and surface, we applied a passivating layer on top of the perovskite to reduce surface recombination. We chose LiF because it is insulating and suppresses nonradiative surface recombination in perovskites, thereby increasing the carrier effective lifetime (*55*). In TRMC measurements, LiF-capped perovskite samples exhibited the same mobility and lifetime as bare perovskite samples (Fig. 2), which confirmed that the enhancement in photocarrier transport in triple-halide perovskites is dominated by the bulk properties rather than surfaces. Given that there was no increase of grain size, we assert that the harmful defect density for carriers is greatly reduced by Cl incorporation in triple-halide films. Dark microwave conductivity measurements showed a factor of 2 reduction (from 7.8 × 10^{15} cm^{-3} to 2.9 × 10^{15} cm^{-3}) in dark carrier density (fig. S11), confirming the reduced defect density in triple-halide perovskites over the control. Taking into account both the potential contribution of defects to photoinstability (*26*–*30*) and the reduced Br ratio in triple-halide perovskites, we expected that the photoinduced phase segregation would also be reduced.

To compare the susceptibility of triple-halide films and our best Cs25Br20 controls to light-induced phase segregation, we carried out time- and intensity-dependent photoluminescence (PL) measurements under 488-nm continuous-wave laser illumination in a N_2 environment. A red shift or a lower-energy peak forming in the PL spectrum indicates the formation of light-induced low–band gap I-rich trap states, as seen in previous reports (*23*, *25*, *28*, *30*, *56*). Here, to avoid noise and error in peak position, we used the spectral centroid to quantitatively indicate the evolution of the population spanning the entire PL spectral range. During the course of 20 min at 10-sun–equivalent illumination, Cs25Br20 controls exhibited low-energy PL peaks and increasing peak width (Fig. 3A). In contrast, 1.67-eV triple-halide films showed no low-energy peak formation and retained their PL spectral profile, highlighting their superior photostability (Fig. 3D). At an ultrahigh injection level of 100 suns, the red shift and broadening of the PL peak became more apparent in Cs25Br20 controls (Fig. 3B), consistent with previous reports. Surprisingly, we

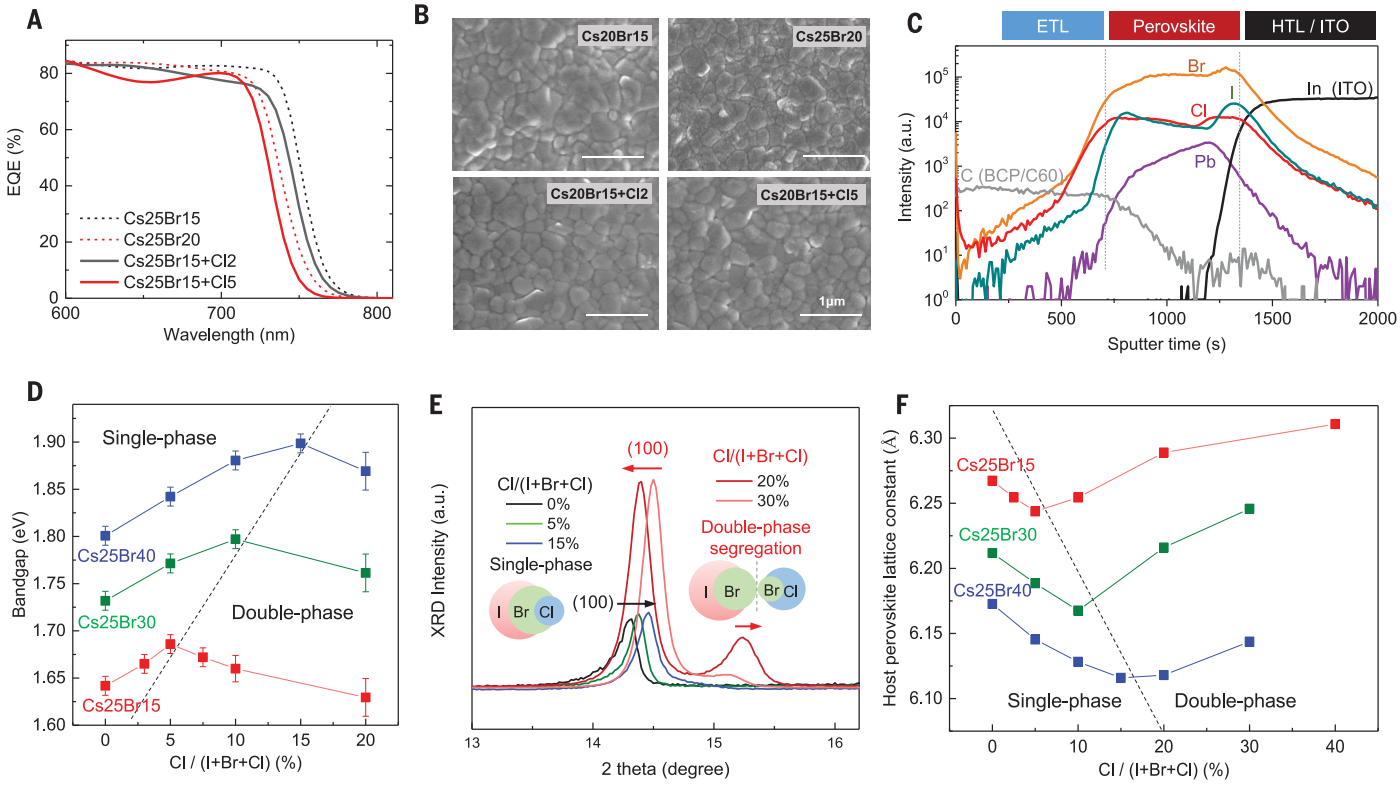


Fig. 1. Characteristics of triple-halide perovskite alloys. (**A**) EQE measurements show the band gap raising via the formation of triple-halide perovskites with 2 to 5 mol % Cl relative to host perovskites. Cs25Br15 and Cs25Br20 denote the double-halide perovskites $Cs_{0.25}FA_{0.75}Pb(I_{0.85}Br_{0.15})_3$ and $Cs_{0.25}FA_{0.75}Pb(I_{0.8}Br_{0.2})_3$, respectively. Cs25Br15+Cl2 and Cs25Br15+Cl5 denote the triple-halide perovskites with an additional 2 or 5 mol % $MAPbCl_3$ included in the Cs25Br15, respectively. (**B**) Top-view SEM images show no evident difference of apparent grain size between triple-halide perovskites and double-halide control films. (**C**) TOF-SIMS depth profiles show the uniform distribution of halides throughout the entire film thickness of the triple-halide perovskite (Cs25Br15+Cl5). Here, the Cs trace is not included because a Cs ion beam was used for sputtering to increase halide signal intensities, which makes the Cs profile through the device stack difficult to interpret. The secondary ion clusters or molecular ion signals of Cs_2Cl^+, $Cs_4I_3^+$, and Cs_2Br^+ were recorded to track the depth profile of halides. The relative scaling of SIMS profiles between halides does not represent their stoichiometric ratio. ETL (electron transport layer) is a stack of C_{60}/BCP layers. (**D**) Evolution curves of band gap for triple-halide films with increased ratio of Cl/(I+Br+Cl), based on Cs25Br15 (red), Cs25Br30 (green), and Cs25Br40 (blue), respectively. The dashed line delineates the single-phase and double-phase zones corresponding to band gap raising and band gap reducing, respectively. Error bars denote SD. (**E**) Shifting and splitting of XRD (100) peaks shows the transition from single-phase triple-halide alloy to double-phase segregation with increased Cl content. Here, the host perovskite is Cs25Br40. The intensity of XRD peaks is rescaled for ease of peak position comparison. (**F**) Evolution curves of host perovskite lattice constant with increasing ratios of Cl/(I+Br+Cl). The dashed line delineates the single-phase and double-phase zones corresponding to band gap raising and band gap reducing, respectively.

observed a PL blue shift, rather than a red shift, in triple-halide films caused by the emission growth at the PL high-energy shoulder (Fig. 3E). This opposite trend was also observed in the traces of the spectral centroid over time (Fig. 3, C and F).

This PL blue shift of wide–band gap perovskites at a high injection level is unusual and strongly suggests that incorporation of Cl into the lattice had an impact on the optoelectronic properties and halide phase-segregation pathways. Our TRMC and PL data suggested a combination of mechanisms: (i) the Moss-Burstein effect in the phase-stabilized semiconductors, which originates from the lifting of the quasi-Fermi level when the conduction band edge is fully populated at a high injection level (*57*, *58*), and (ii) a decrease in defect concentration.

Efficient and stable triple-halide perovskite/silicon tandems

To evaluate the effect of doubled charge-carrier diffusion length and better photostability in triple-halide films, we fabricated 1.67-eV single-junction solar cells with opaque metal contacts. We used a p-i-n structure (Fig. 4A): glass / indium tin oxide (ITO) / poly(4-butylphenyl-diphenyl-amine) (poly-TPD) / poly(9,9-bis(3′-(*N*,*N*-dimethyl)-*N*-ethylammonium-propyl-2,7-fluorene)-alt-2,7-(9,9-dioctylfluorene)) dibromide (PFN-Br) / perovskite / LiF / C_{60} / bathocuproine (BCP) / Ag. The statistical comparison of devices (fig. S12) showed that triple-halide devices performed better than our best Cs25Br20 controls for all PV metrics. The best-performing triple-halide device with composition Cs22Br15+Cl3 (Fig. 4B) exhibited a PCE of 20.42% and V_{oc} of 1.217 V [J_{sc} = 20.18 mA cm^{-2}, fill factor (FF) = 83.16%, active area = 0.06 cm^2], whereas the best-performing control showed a PCE of 18.16% and V_{oc} of 1.114 V. Both the control and triple-halide devices exhibited no hysteresis in *J-V* sweeps. By integrating the EQE spectrum, weighted by the AM1.5G solar spectrum (Fig. 4G), we calculated a current density of 20.6 mA cm^{-2}, in good agreement with the J_{sc} obtained in the *J-V* test. The stabilized efficiency was 20.32% after continuous operation at MPP for 5000 s (Fig. 4C). Table S1 summarizes reported p-i-n wide–band gap cells for tandems (*2*, *24*, *47*, *54*, *59*, *60*). The triple-halide devices considerably improved the V_{oc} deficit, which was reduced from >0.5 V to ~0.45 V, as well as the PCE, which increased to >20%.

To construct tandems on top of Si cells, we developed top-illuminated semitransparent devices that maximized both the near-infrared transparency and PV performance. The device structure is illustrated in Fig. 4D. The metal top contact (Ag or Au) in opaque cells was replaced with an 8-nm-thick SnO_2 / Zn:SnO_2 (ZTO) buffer layer (*2*, *41*, *54*, *61*, *62*) coated by atomic-layer deposition (ALD) and an ITO window layer to allow light through. Parasitic absorption and reflection loss created by layers in the top electrode were minimized (fig. S13) by using a polydimethylsiloxane (PDMS) scattering layer to limit reflection (*61*) and by reducing the thickness of the C_{60} and ITO layers to 10 and 60 nm, respectively (fig. S14).

To reduce the resistance of large-area devices, we evaporated a metal grid on top of the ITO window layer. Note that in top-illuminated devices, J_{sc} is typically lower than the EQE integrated current density because of the shading losses created by the metal grid. To minimize this loss, we used a metal shadow mask with a graded opening to reduce the shadow effect that occurs when metals are evaporated through high–aspect ratio holes in a mask (fig. S15). The graded-opening mask enabled us to construct ~25-μm-wide metal gridlines with a height of ~3 μm using thermal evaporation (fig. S16), which reduced the shading loss to below 0.8% without compromising FF.

With these improvements, our 1.67-eV top-illuminated semitransparent cells simultaneously achieved ~80% near-infrared transmittance (Fig. 4G) and PCEs of 18.59% (Fig. 4E). The corresponding stabilized PCE was 18.52% in the MPP tracking test (Fig. 4E, inset). The V_{oc} of 1.214 V and FF of 80.2% in 0.34-cm^2 semitransparent devices were near those achieved in the best 0.06-cm^2 opaque devices with a metallic electrode (Fig. 4B and Table 1), highlighting the quality and stability of triple-halide perovskites during ALD buffer layer deposition at 85°C and subsequent ITO sputter deposition. The active-area J_{sc} determined from the EQE spectrum (Fig. 4G) was ~19.5 mA cm^{-2}, which agrees well with the aperture-area J_{sc} of 19.13 mA cm^{-2} from *J-V* tests. The loss of J_{sc} in semitransparent top cells relative to opaque devices primarily resided in the long-wavelength region around the band edge and arose from the lack of reflection from the metal contact.

We also fabricated large-area (1 cm^2) semitransparent top cells. One such device was measured by an accredited PV laboratory (National Renewable Energy Laboratory PV Device Performance) and certified at a stabilized PCE of 16.83 ± 0.34% in an 11-point SPO (stabilized power output) test. This value appears to be the highest certified PCE reported for a 1-cm^2 semitransparent perovskite cell for tandems (table S2 and figs. S17 and S18). The performance metrics of the *J-V* curve were V_{oc} = 1.202 V, J_{SC} = 18.99 mA cm^{-2}, FF = 74.07%, and PCE = 16.90% (Fig. 4F and Table 1). The nearly identical PCEs measured in a *J-V* test and SPO test further verified the negligible hysteresis and stability of our triple-halide perovskite devices. The primary PCE loss in the large-area (1 cm^2) devices relative to small-area (0.34 cm^2) devices resided in FF, which is attributed to the limited sheet resistance (15 ohms per square) of ITO substrates used in this study; this limitation does not apply to two-terminal tandems that transport current vertically through the recombination layer between the top and bottom cells. Our semitransparent top cells exhibited both the highest PCE and highest V_{oc} of reported semitransparent top cells for tandems on Si, CIGS (copper indium gallium diselenide), or narrow–band gap perovskites (table S2) (*24*, *41*, *54*, *60*, *63*–*72*).

We examined the long-term operational stability of triple-halide devices under the combined stresses of heating and illumination (~0.77-sun sulfur plasma lamp, chamber temperature *T* = 60°C; see supplementary materials for details). An unencapsulated opaque device with metal contacts tested in ambient

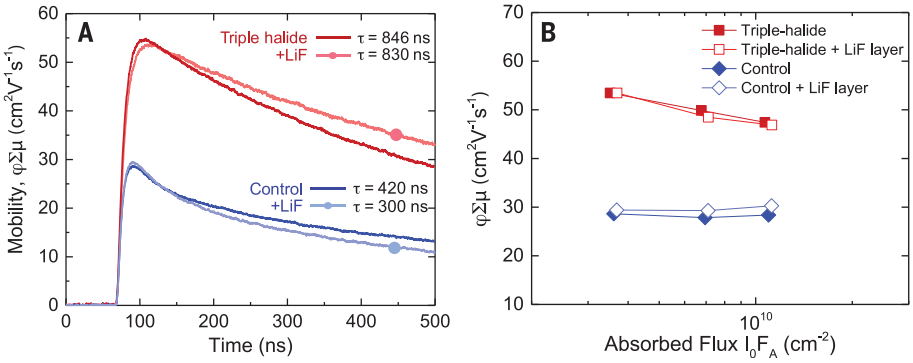


Fig. 2. Enhanced charge-carrier mobility and lifetime in triple-halide perovskite films. (**A**) Photoconductivity transient (indicative of the lifetime) measured by time-resolved microwave conductivity (TRMC), indicating doubled charge-carrier lifetime (τ) in the 1.67-eV triple-halide film (Cs22Br15+Cl3, red line) compared with the control film (Cs25Br20, blue line). (**B**) Photoconductivity under different excitation intensity. $\varphi\sum\mu$ denotes the yield-mobility product. The carrier-generation yield φ is near unity for perovskite films and therefore $\varphi\sum\mu$ is a measure of mobility. Triple-halide films exhibit nearly doubled mobility relative to control double-halide films. Perovskite/LiF bilayer samples exhibit mobilities and lifetimes similar to their corresponding bare perovskite samples.

air (relative humidity = 25 to 30%) retained 90% of its initial PCE after 250 hours of continuous operation at MPP (Fig. 4H). The thermal stability of the triple-halide material was also tested by keeping opaque devices with gold contacts at 85°C for 500 hours in nitrogen; the unencapsulated triple-halide devices and double-halide devices both retained >97% of their initial efficiency (fig. S19). Semitransparent top cells tested in N_2 exhibited negligible degradation (<4%) after 1000 hours of continuous operation at MPP near 60°C (Fig. 4H). This result confirmed the importance of encapsulation (N_2 in this case) and the role of barrier layers [an ALD buffer layer and a transparent conductive oxide (TCO) layer in this case] to suppress the reactions between metal contacts and halides, as revealed in previous reports (*73*–*75*).

We integrated our triple-halide perovskite in 1-cm^2 two-terminal monolithic tandems on silicon cells (see photos in fig. S20). Here, the ITO/glass substrate of the semitransparent device (Fig. 4D) was replaced by a front-side polished silicon heterojunction bottom cell capped with a 20-nm-thick ITO recombination layer, which allowed for solution processing of the perovskite layer rather than vapor deposition that would be required to deposit the perovskite on a pyramidally textured silicon surface (*65*, *76*). With the aid of proper light management, tandems on planar front-side wafers have been shown to deliver J_{sc} values competitive with those on fully textured wafers (*77*). Additionally, front-side planar substrates are industrially relevant, because PERC (passivated emitter and rear cell) silicon cells, which constitute ~70% of the silicon PV market, have a planar "shiny-etched" rear surface that was recently shown to allow for solution processing of the perovskite solar cell (*78*).

The full tandem structure is illustrated in Fig. 5A. Figure 5B shows a cross-sectional SEM image of the perovskite top cell on Si. Here, we developed a NiO_x / poly-TPD bilayer hole transport layer (HTL) for use in the tandems. Relative to HTLs that used only spin-cast poly-TPD, introducing a 20-nm-thick sputtered NiO_x layer between the ITO-HTL interface reduced shunting and increased the yield of 1-cm^2 tandems. In a *J-V* sweep, the best-performing tandem reached a PCE of 27.13% (V_{oc} = 1.886 V, J_{sc} = 19.12 mA cm^{-2}, and FF = 75.3%). The corresponding stabilized PCE at MPP is 27.04% (Fig. 5C and Table 1), exceeding the current record efficiency (26.7%) for Si single cells and approaching the world record value of 28% achieved by Oxford PV (*15*, *16*). The V_{oc} of >1.88 V is one of the highest reported in perovskite/Si tandems with PCE of >25% (*59*, *61*, *65*, *76*, *77*) (see summary of ≥1 cm^2–area tandems in table S3), providing further evidence of the low V_{oc} deficit achieved in the triple-halide semitransparent top cells (table S2). The EQE spectrum of the perovskite top cell matches well with those measured in top-illumination semitransparent devices (Fig. 5D). The active-area J_{sc} values calculated from the EQE spectra were 19.3 mA cm^{-2} and 19.9 mA cm^{-2} for the perovskite top cell and Si bottom cell, respectively (Fig. 5D). These calculated values indicate that the J_{sc} of our two-terminal tandem was slightly limited by the perovskite top cell.

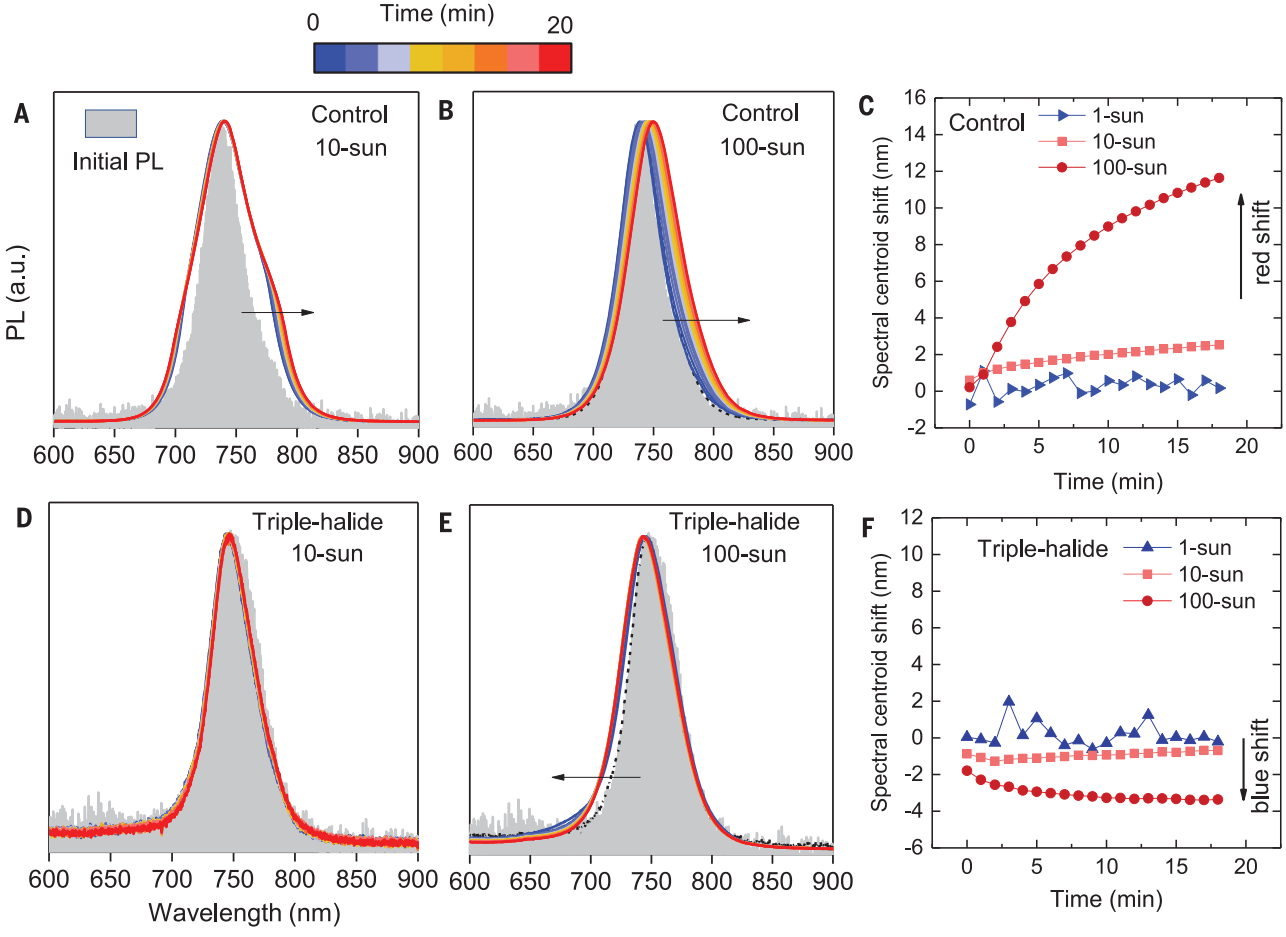


Fig. 3. Suppression of photoinduced phase segregation in triple-halide perovskites. (**A** and **B**) PL spectra of 1.67-eV control perovskite films (Cs25Br20) under 10-sun and 100-sun illumination for 20 min, respectively. Arrows indicate the direction of the PL shift over time. (**C**) The shift of the spectral centroids of control films over time. The red shift becomes more obvious under higher injection. (**D** and **E**) PL spectra of 1.67-eV triple-halide perovskites (Cs22Br15+Cl3) under 10-sun and 100-sun illumination for 20 min, respectively. (**F**) The shift of the spectral centroids of triple-halide perovskites over time. The blue shift becomes more obvious under higher injection level.

We also analyzed each subcell in our two-terminal tandems by measuring electroluminescence (EL) (Fig. 5E). After increasing the injection current density from 1 mA cm^{-2} to 100 mA cm^{-2}, the EL peak from the perovskite retained its shape and location, verifying the phase stability of triple-halide perovskites (Fig. 5F). The subcell's V_{oc} was estimated from EL quantum efficiency based on the reciprocity principle (Fig. 5G) (*79*). At an injection level of 17 to 20 mA cm^{-2} (near J_{sc} and J_{mpp}), the respective V_{oc} values of the perovskite and Si subcells were estimated to be 1.2 V and 0.7 V, aligning well with the tandem V_{oc} of ~1.9 V from *J-V* measurements.

A two-terminal tandem device was certified after being tested in air and stored in N_2 for 1 month (figs. S21 and S22). The certified efficiency (25.8%) is highly consistent with that measured in our lab (26%) (fig. S21A), verifying our rigorous protocol of in-house tandem measurement. From the comparison of EQE spectra (fig. S21B), the J_{sc} loss relative to our champion tandem (Fig. 5D) is likely caused by the absorption from a thicker C_{60} top layer, as discussed above (figs. S13 and S14). Even with this J_{sc} loss, it exhibited a V_{oc} value

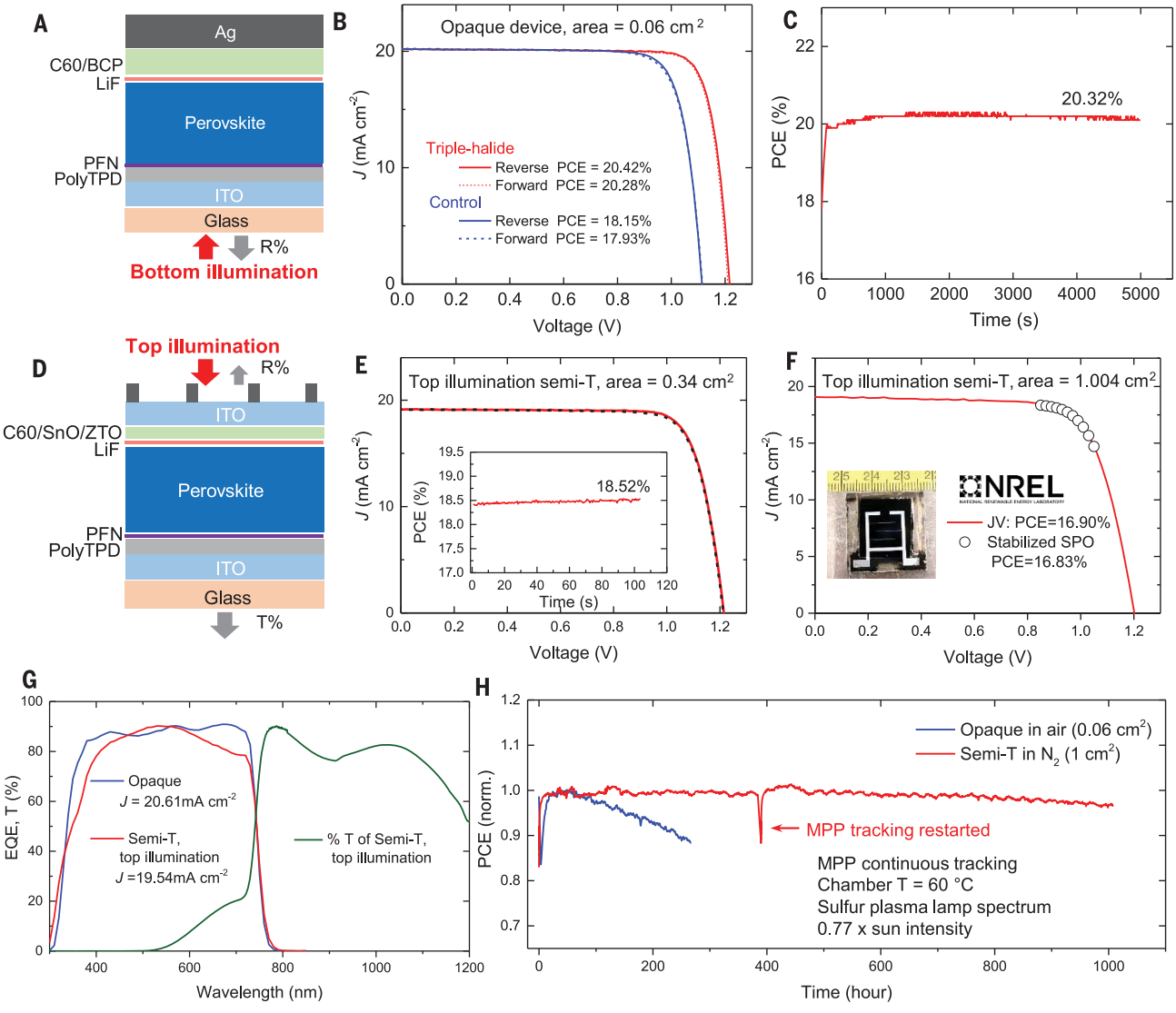


Fig. 4. PV characteristics of single-junction opaque devices and semitransparent top cells. (**A**) Schematic of the opaque device with reflective metal contact (not to scale). (**B**) *J-V* curves of the champion 1.67-eV triple-halide opaque device (red) and best control device (blue). The aperture area is 0.06 cm^2. Solid lines indicate the reverse scan (from open circuit to short circuit); dashed lines indicate the forward scan (from short circuit to open circuit). (**C**) Continuous maximum-power-point (MPP) operation of the champion triple-halide wide–band gap device for 5000 s, exhibiting stabilized PCE of 20.32%. (**D**) Schematic of the top-illuminated semitransparent device (not to scale). Light enters the cell through the top metal grid and TCO layer. (**E**) *J-V* curves of the champion semitransparent device illuminated from the top metal grid and TCO layer side. The aperture area is 0.34 cm^2. The inset shows continuous MPP operation for 100 s, exhibiting stabilized PCE of 18.52%. (**F**) A 1-cm^2 top-illuminated semitransparent device certified by NREL. The circles are the 11-point SPO (stabilized power output) measurements, showing stabilized PCE of 16.83%. The *J-V* curve shows the instantaneous PCE of 16.9%; the inset is a photo of the device. (**G**) EQE spectra of an opaque device (blue) and a top-illuminated semitransparent device (red). The green curve is the optical transmission of the top-illuminated semitransparent device, including the metal grid shading losses. (**H**) Long-term continuous MPP tracking under accelerated conditions (0.77-sun illumination and 60°C) of 1-cm^2 semitransparent (red, tested in N_2, averaged from two devices in the same batch) and opaque devices (blue, tested in air with relative humidity of ~30%).

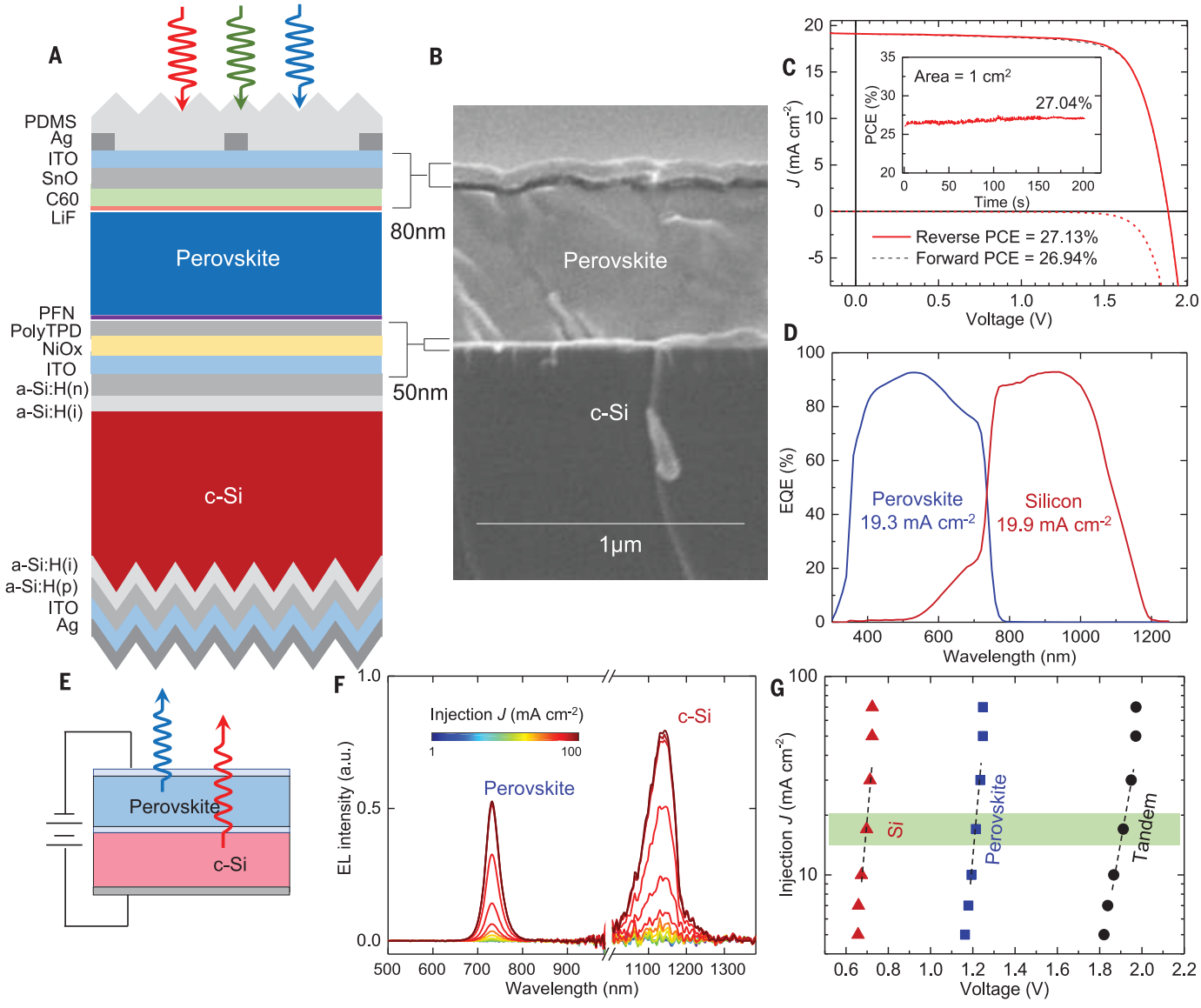


Fig. 5. PV characteristics of 1-cm² two-terminal perovskite/Si tandems. (**A**) Schematic of the two-terminal monolithic tandem structure (not to scale). a-Si:H denotes hydrogenated amorphous silicon. (**B**) Cross-sectional SEM image of a two-terminal tandem. (**C**) Light and dark *J*-*V* curves and MPP tracking (inset) of the champion tandem. (**D**) EQE spectra of the perovskite top cell (blue) and silicon bottom cell (red) of the champion tandem. (**E**) Schematic diagram of electroluminescence (EL) measurement of a two-terminal tandem. (**F**) EL spectra of the tandem under different injection levels. The triple-halide perovskite exhibits a stable EL peak up to injection levels of 100 mA cm^{-2}. (**G**) The V_{oc} contribution of each subcell estimated from EL quantum efficiency. The injection region of 17 to 20 mA cm^{-2} (near J_{sc} and J_{mpp} under 1-sun illumination) is highlighted in green.

(1.88 V) that is much improved over the best prior reports (<1.8 V) (table S3). Finally, the statistical data of tandems (fig. S23) indicates that our method was reproducible.

Outlook

We have demonstrated a low-cost tandem technology to increase the power output of a ~21% silicon solar cell by ~30%, which has major implications given that silicon currently accounts for >90% of the global PV market, which mainly consists of 19 to 21% single-junction silicon solar modules. Furthermore, triple-halide wide–band gap perovskites offer a promising path to >30% tandems because of their reduced V_{oc} deficit and record performance in wide–band gap semitransparent top cells. Although we have used a planar tandem architecture as a model in this study, the 1.67-eV, triple-halide perovskite composition also has an ideal band gap for textured perovskite/silicon tandems (*80*), with potential for a J_{sc} value of ~20 mA cm^{-2}. Both $CsPbBr_xCl_{3-x}$ perovskites and $Cs_mFA_nMA_{1-m-n}PbI_xBr_{3-x}$ perovskites with tunable band gaps have been demonstrated by co-evaporation or two-step interdiffusion methods (*65*, *76*, *81*), so there is no fundamental barrier to realizing triple-halide perovskites using vapor deposition methods required for fully textured surfaces. A perovskite/Si tandem with a J_{sc} of ~20 mA cm^{-2} and the V_{oc} and FF of triple-halide semitransparent cells presented here could have >30% PCE.

The ability to further tune the band gap to higher energies shows promise for other multijunction architectures as well, such as perovskite/perovskite and perovskite/CIGS tandems. Beyond tandems, the demonstrated suppressed photoinduced phase segregation

and improved optoelectronic properties result in stable electroluminescence at high injection current densities and stabilized perovskite PL at 100-sun–equivalent illumination, highlighting opportunities for the use of this material in LED or concentrated PV applications. More broadly, the exploration of triple-halide perovskites has identified a promising new region of perovskite single-phase stability and paves the way for another dimension of compositional engineering for perovskites.

REFERENCES AND NOTES

1. M. Saliba *et al*., *Energy Environ. Sci.* **9**, 1989–1997 (2016).
2. A. F. Palmstrom *et al*., *Joule* **3**, 2193–2204 (2019).
3. G. E. Eperon *et al*., *Energy Environ. Sci.* **7**, 982–988 (2014).
4. Z. Li *et al*., *Chem. Mater.* **28**, 284–292 (2016).
5. H. Min *et al*., *Science* **366**, 749–753 (2019).
6. M. Saliba *et al*., *Science* **354**, 206–209 (2016).
7. F. Hao, C. C. Stoumpos, R. P. H. Chang, M. G. Kanatzidis, *J. Am. Chem. Soc.* **136**, 8094–8099 (2014).
8. Y. Ogomi *et al*., *J. Phys. Chem. Lett.* **5**, 1004–1011 (2014).
9. J. H. Noh, S. H. Im, J. H. Heo, T. N. Mandal, S. I. Seok, *Nano Lett.* **13**, 1764–1769 (2013).
10. C. M. Sutter-Fella *et al*., *Nano Lett.* **16**, 800–806 (2016).
11. Z. Yu, M. Leilaeioun, Z. Holman, *Nat. Energy* **1**, 16137 (2016).
12. M. Anaya, G. Lozano, M. E. Calvo, H. Míguez, *Joule* **1**, 769–793 (2017).
13. T. Leijtens, K. A. Bush, R. Prasanna, M. D. McGehee, *Nat. Energy* **3**, 828–838 (2018).
14. W. Shockley, H. J. Queisser, *J. Appl. Phys.* **32**, 510–519 (1961).
15. M. A. Green *et al*., *Prog. Photovolt. Res. Appl.* **27**, 565–575 (2019).
16. K. Yoshikawa *et al*., *Nat. Energy* **2**, 17032 (2017).
17. Z. J. Yu, J. V. Carpenter III, Z. C. Holman, *Nat. Energy* **3**, 747–753 (2018).
18. Z. Li *et al*., *Joule* **2**, 1559–1572 (2018).
19. N. Pellet, J. Teuscher, J. Maier, M. Grätzel, *Chem. Mater.* **27**, 2181–2188 (2015).
20. C. Li *et al*., *ACS Appl. Mater. Interfaces* **8**, 11526–11531 (2016).
21. D. M. Jang *et al*., *Nano Lett.* **15**, 5191–5199 (2015).
22. E. L. Unger *et al*., *J. Mater. Chem. A* **5**, 11401–11409 (2017).
23. E. T. Hoke *et al*., *Chem. Sci.* **6**, 613–617 (2015).
24. D. P. McMeekin *et al*., *Science* **351**, 151–155 (2016).
25. K. A. Bush *et al*., *ACS Energy Lett.* **3**, 428–435 (2018).
26. M. Abdi-Jalebi *et al*., *Nature* **555**, 497–501 (2018).
27. A. J. Barker *et al*., *ACS Energy Lett.* **2**, 1416–1424 (2017).
28. R. A. Belisle *et al*., *ACS Energy Lett.* **3**, 2694–2700 (2018).
29. S. J. Yoon, M. Kuno, P. V. Kamat, *ACS Energy Lett.* **2**, 1507–1514 (2017).
30. W. Rehman *et al*., *Energy Environ. Sci.* **10**, 361–369 (2017).
31. S. Gharibzadeh *et al*., *Adv. Energy Mater.* **9**, 1803699 (2019).
32. M. I. Saidaminov *et al*., *Nat. Energy* **3**, 648–654 (2018).
33. V. L. Pool, A. Gold-Parker, M. D. McGehee, M. F. Toney, *Chem. Mater.* **27**, 7240–7243 (2015).
34. S. Colella *et al*., *Chem. Mater.* **25**, 4613–4618 (2013).
35. P.-W. Liang *et al*., *Adv. Energy Mater.* **5**, 1400960 (2015).
36. L. Cojocaru *et al*., *Chem. Lett.* **44**, 1089–1091 (2015).
37. S. Dastidar *et al*., *Nano Lett.* **16**, 3563–3570 (2016).
38. N. Ueoka *et al*., *AIP Conf. Proc.* **1929**, 020026 (2018).
39. T. Oku, Y. Ohishi, H. Tanaka, *AIP Conf. Proc.* **1929**, 020010 (2018).
40. J. Jeong *et al*., *ACS Energy Lett.* **1**, 712–718 (2016).
41. K. A. Bush *et al*., *Nat. Energy* **2**, 17009 (2017).
42. M. T. Hörantner, H. J. Snaith, *Energy Environ. Sci.* **10**, 1983–1993 (2017).
43. D. A. Jacobs *et al*., *J. Phys. Chem. Lett.* **10**, 3159–3170 (2019).
44. J.-P. Correa-Baena *et al*., *Science* **363**, 627–631 (2019).
45. R. Comin *et al*., *J. Mater. Chem. C* **3**, 8839–8843 (2015).
46. G. Maculan *et al*., *J. Phys. Chem. Lett.* **6**, 3781–3786 (2015).
47. B. Chen *et al*., *Joule* **3**, 177–190 (2018).
48. Y. Zhao, K. Zhu, *J. Phys. Chem. C* **118**, 9412–9418 (2014).
49. Q. Dong *et al*., *Energy Environ. Sci.* **8**, 2464–2470 (2015).
50. F. Xie *et al*., *Energy Environ. Sci.* **10**, 1942–1949 (2017).
51. T. Leijtens *et al*., *Sustain. Energy Fuels* **2**, 2450–2459 (2018).
52. S. P. Harvey *et al*., *ACS Appl. Mater. Interfaces* **11**, 30911–30918 (2019).
53. S. P. Harvey *et al*., *ACS Appl. Mater. Interfaces* **10**, 28541–28552 (2018).
54. D. H. Kim *et al*., *Joule* **3**, 1734–1745 (2019).
55. M. Stolterfoht *et al*., *Nat. Energy* **3**, 847–854 (2018).
56. R. E. Beal *et al*., *J. Phys. Chem. Lett.* **7**, 746–751 (2016).
57. E. Burstein, *Phys. Rev.* **93**, 632–633 (1954).
58. J. Fu *et al*., *Nat. Commun.* **8**, 1300 (2017).
59. L. Mazzarella *et al*., *Adv. Energy Mater.* **9**, 1803241 (2019).
60. T. Duong *et al*., *Adv. Energy Mater.* **7**, 1700228 (2017).
61. K. A. Bush *et al*., *ACS Energy Lett.* **3**, 2173–2180 (2018).
62. A. F. Palmstrom *et al*., *Adv. Energy Mater.* **8**, 1800591 (2018).
63. J. Tong *et al*., *Science* **364**, 475–479 (2019).
64. J. Werner *et al*., in *2017 IEEE 44th Photovoltaic Specialist Conference (PVSC)* (2017), pp. 3256–3259.
65. F. Sahli *et al*., *Nat. Mater.* **17**, 820–826 (2018).
66. C. O. Ramírez Quiroz *et al*., *J. Mater. Chem. A* **6**, 3583–3592 (2018).
67. J. Werner *et al*., *ACS Energy Lett.* **1**, 474–480 (2016).
68. Q. Han *et al*., *Science* **361**, 904–908 (2018).
69. B. Chen *et al*., *Adv. Energy Mater.* **6**, 1601128 (2016).
70. F. Fu *et al*., *Nat. Energy* **2**, 16190 (2017).
71. J. Peng *et al*., *Adv. Energy Mater.* **7**, 1601768 (2017).
72. H. Shen *et al*., *Energy Environ. Sci.* **11**, 394–406 (2018).
73. C. C. Boyd, R. Cheacharoen, T. Leijtens, M. D. McGehee, *Chem. Rev.* **119**, 3418–3451 (2019).
74. C. C. Boyd *et al*., *ACS Energy Lett.* **3**, 1772–1778 (2018).
75. J. A. Raiford *et al*., *Adv. Energy Mater.* **9**, 1902353 (2019).
76. G. Nogay *et al*., *ACS Energy Lett.* **4**, 844–845 (2019).
77. E. Köhnen *et al*., *Sustain. Energy Fuels* **3**, 1995–2005 (2019).
78. Y. Wu *et al*., in *Proceedings of the Asia-Pacific Solar Research Conference*, http://apvi.org.au/solar-research-conference/wp-content/uploads/2019/12/43_Wu-Yiliang_PV_2019.pdf (2019).
79. U. Rau, *Phys. Rev. B* **76**, 085303 (2007).
80. S. Manzoor *et al*., *Opt. Express* **26**, 27441–27460 (2018).
81. P. Du *et al*., *ACS Appl. Mater. Interfaces* **11**, 47083–47090 (2019).

ACKNOWLEDGMENTS

We thank G. Teeter for XPS measurements and A. Hazarika for supporting XRD measurements. **Funding:** This material is based on work supported by the U.S. Department of Energy's Office of Energy Efficiency and Renewable Energy (EERE) under Solar Energy Technologies Office (SETO) agreement number DE-EE0008167. Also supported by the NSF Graduate Research Fellowship under grant DGE-1656518 (C.C.B.); the Office of Naval Research under award number N00014-17-1-2525 (E.J.W.); and the De-risking Halide Perovskite Solar Cells program of the National Center for Photovoltaics, funded by the U.S. Department of Energy, Office of Energy Efficiency and Renewable Energy, Solar Energy Technology Office. Work at the National Renewable Energy Laboratory is supported by the U.S. Department of Energy under contract number DE-AC36-08GO23808. **Author contributions:** M.D.M., Z.C.H., Z.J.Y., J.M.L., and J.J.B. supervised the research; J.X. formed the idea and developed the materials and top cells; J.X. and C.C.B. fabricated and characterized the perovskites and devices; Z.J.Y. and W.W. fabricated the Si bottom cells; A.F.P. developed and deposited ALD buffer layers; S.M. fabricated the PDMS film; D.J.W. and M.F.A.M.v.H. contributed to the development and deposition of TCO layers for tandems; B.W.L. conducted the TRMC measurement; J.W. supported the material and device characterizations; R.M.F. supported the tandem characterizations; S.P.H. conducted the SIMS measurement; E.J.W. supported the stability test; M.D.M., J.X., and C.C.B. wrote the manuscript; and all authors discussed the results and revised the manuscript. **Competing interests:** A.F.P. and M.D.M. are inventors on patent application PCT/US2017/051753 submitted by Stanford University that covers the atomic layer deposition of contacts used in this work. **Data and materials availability:** All data needed to evaluate the conclusions in the paper are present in the paper or the supplementary materials. All the data are available from the corresponding authors upon reasonable request.

SUPPLEMENTARY MATERIALS

science.sciencemag.org/content/367/6482/1097/suppl/DC1
Materials and Methods
Figs. S1 to S23
Tables S1 to S3
References (*82*, *83*)

15 September 2019; resubmitted 5 December 2019
Accepted 29 January 2020
10.1126/science.aaz5074

NEUROSCIENCE

A central master driver of psychosocial stress responses in the rat

Naoya Kataoka, Yuta Shima, Keisuke Nakajima, Kazuhiro Nakamura*

The mechanism by which psychological stress elicits various physiological responses is unknown. We discovered a central master neural pathway in rats that drives autonomic and behavioral stress responses by connecting the corticolimbic stress circuits to the hypothalamus. Psychosocial stress signals from emotion-related forebrain regions activated a VGLUT1-positive glutamatergic pathway from the dorsal peduncular cortex and dorsal tenia tecta (DP/DTT), an unexplored prefrontal cortical area, to the dorsomedial hypothalamus (DMH), a hypothalamic autonomic center. Genetic ablation and optogenetics revealed that the DP/DTT→DMH pathway drives thermogenic, hyperthermic, and cardiovascular sympathetic responses to psychosocial stress without contributing to basal homeostasis. This pathway also mediates avoidance behavior from psychosocial stressors. Given the variety of stress responses driven by the DP/DTT→DMH pathway, the DP/DTT can be a potential target for treating psychosomatic disorders.

Psychological stressors induce various physiological responses by stimulating sympathetic, neuroendocrine, and behavioral mechanisms. Stress-induced sympathetic stimulation of thermogenic and cardiovascular functions is common in mammals and is recognized as a stress-coping response to boost physical performance in fight-or-flight situations. However, excessive stress may cause aberrant sympathetic symptoms such as psychogenic fever, a hyperthermia caused by intense psychological stressors (*1*). Sympathetic thermogenesis in brown adipose tissue (BAT) contributes to stress-induced hyperthermia in rats and humans (*2*, *3*). Resistance of psychogenic fever to antipyretics indicates an etiology different from that of infection-induced fever (*1*). Patients with posttraumatic stress disorder exhibit augmented cardiovascular responses to stress, which increase the risk of developing hypertension and cardiovascular diseases (*4*). Vigorous psychogenic cardiovascular responses are also observed in panic disorder, a severe anxiety disorder (*5*). However, the central circuit mechanisms by which psychological stress activates the sympathetic nervous system are not well understood.

The dorsomedial hypothalamus (DMH) is an important brain site for sympathetic stress responses (*6*, *7*). A hypothalamo-medullary pathway from the DMH to sympathetic premotor neurons in the rostral medullary raphe region (rMR) mediates BAT thermogenic and cardiovascular responses to psychological stress (*2*, *8*). However, the mechanism by which the corticolimbic circuits that process stress and emotion activate the sympathoexcitatory DMH neurons remains unknown. We sought to identify the forebrain neural pathways that transmit stress signals to the DMH by using functional neuroanatomy and in vivo physiological experiments combining genetic lesion and optogenetic manipulations of a pathway of interest. We also employed social defeat stress (SDS), an animal model of psychosocial stress caused by interindividual relationships that mimics human social stress (*9*).

Department of Integrative Physiology, Nagoya University Graduate School of Medicine, Nagoya 466-8550, Japan.
*Corresponding author. Email: kazu@med.nagoya-u.ac.jp or nkazuhir@gmail.com

SDS activates DMH-projecting neurons in the mPFC

To label neurons that project to the DMH, we injected cholera toxin b subunit (CTb), a retrograde neural tracer, into the rat DMH and consequently found many CTb-labeled neurons in the medial prefrontal cortex (mPFC) (Fig. 1, A to C). Subsequent exposure to SDS significantly increased expression of Fos, a marker for neuronal activation, in CTb-labeled neurons in specific mPFC subregions: the prelimbic cortex (PrL), infralimbic cortex (IL), and dorsal peduncular cortex (DP) and the dorsal tenia tecta (DTT) immediately rostral to the callosal commissure (Fig. 1, D to F). These double-labeled cells were mostly distributed in layers V and VI and showed the typical morphology of glutamatergic pyramidal neurons (Fig. 1E). We did not find other forebrain regions containing a substantial double-labeled population after SDS.

The DP/DTT mediates thermogenic and cardiovascular sympathetic responses to stress

The PrL and IL, which constitute the main body of the mPFC (*10*), exert inhibitory effects on stress responses (*11*, *12*). Correspondingly, optogenetic stimulation of the IL→amygdala or PrL→bed nucleus pathway reduces freezing behavior in response to stress (*13*, *14*). No literature is available on the function of the DP and DTT (hereafter, the DP/DTT). Therefore, we determined the roles of the stress-activated mPFC subregions in driving sympathetic stress responses.

SDS induced immediate increases in interscapular BAT temperature (T_{BAT}) and body core (abdominal) temperature (T_{core}) (Fig. 2), representing psychosocial stress–induced BAT thermogenesis and hyperthermia, respectively (*8*). These responses were abolished by inactivation of DP/DTT neurons with bilateral nanoinjections of muscimol: Responses were nearly suppressed by injections of 200 nl per site (T_{BAT}: 80% inhibition, T_{core}: 88% inhibition; Fig. 2, A to F) and were moderately inhibited by injections of 100 nl per site (T_{BAT}: 63% inhibition, T_{core}: 54% inhibition; fig. S1). In contrast, muscimol injections of 200 nl per site into the IL resulted in significantly reduced inhibition of the responses (T_{BAT}: 33% inhibition, T_{core}: 26% inhibition; Fig. 2, G to L) compared with injections into the DP/DTT (unpaired *t* tests comparing inhibition percentage; T_{BAT}: $t_8 = 3.16$, $P < 0.05$; T_{core}: $t_8 = 2.82$, $P < 0.05$). SDS also induced increases in heart rate (HR) and mean arterial pressure (MAP), which were diminished by injections of muscimol (100 nl per site) into the DP/DTT (HR: 53% inhibition, MAP: 77% inhibition; Fig. 2, M to Q).

DP/DTT neurons drive sympathetic responses through activation of the DMH→rMR pathway

To test whether DP/DTT neurons transmit stress signals to the DMH to drive sympathetic responses, we performed in vivo electrophysiological experiments in anesthetized rats. Stimulation of DP/DTT neurons with nanoinjection of bicuculline robustly increased BAT sympathetic nerve activity (SNA), T_{BAT}, HR, and MAP (fig. S2, A to E) (*15*). All of these responses were reversed by subsequent inactivation of DMH neurons with muscimol injections (fig. S2, A to E).

We next investigated whether the stimulation of DP/DTT neurons activated the DMH→rMR pathway. CTb injection into the rMR (fig. S2F) retrogradely labeled many neurons that bilaterally clustered in the dorsal part of the DMH (fig. S2, H and I); these include sympathoexcitatory glutamatergic neurons driving cold-defensive, febrile, and stress responses through their innervation of sympathetic premotor neurons in the rMR (*8*, *16*–*18*). Subsequent stimulation of DP/DTT neurons with a unilateral bicuculline injection under free-moving conditions increased Fos expression in the CTb-labeled population in the DMH, mainly ipsilaterally to the site of bicuculline injection (fig. S2, G to J).

Glutamatergic innervation of DMH neurons by DP/DTT neurons

Next, we determined the neurotransmitter that mediates the DP/DTT→DMH transmission. Transduction of DP/DTT neurons with palGFP, a membrane-targeted form of green fluorescent

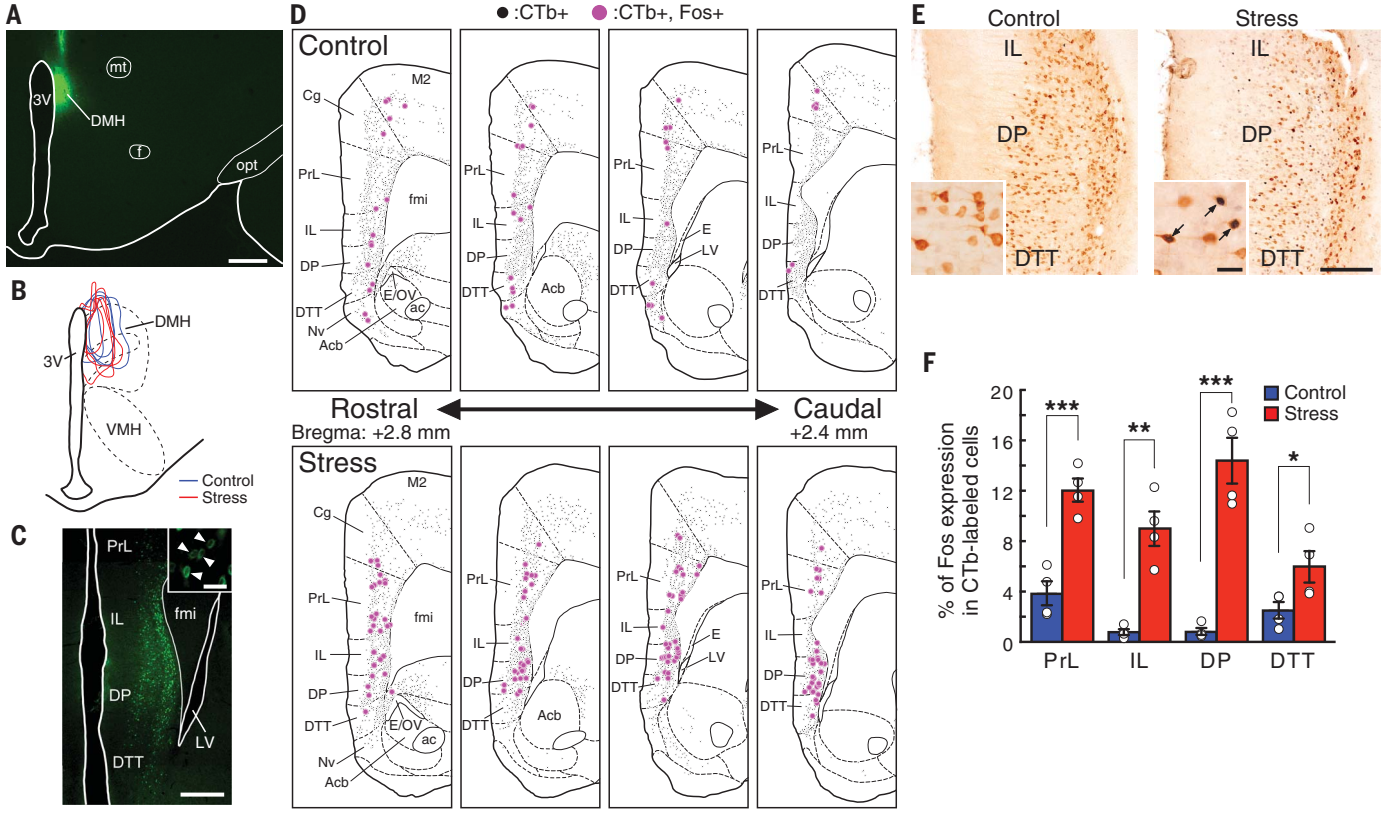


Fig. 1. SDS activates DMH-projecting neurons in the mPFC. (**A**) CTb injection into the DMH. 3V, third ventricle; f, fornix; mt, mammillothalamic tract; opt, optic tract. Scale bar, 500 μm. (**B**) CTb injection sites in the rats for which data are plotted in (F). VMH, ventromedial hypothalamic nucleus. (**C**) CTb-labeled neurons (arrowheads) in the mPFC. fmi, forceps minor of the corpus callosum; LV, lateral ventricle. Scale bars, 500 μm (main panel); 30 μm (inset). (**D**) Distribution of CTb-labeled cells with or without Fos immunoreactivity in the mPFC after sham handling (Control) or SDS (Stress). ac, anterior commissure; Acb, nucleus accumbens; Cg, cingulate cortex; E, ependymal and subependymal layer; M2, secondary motor cortex; Nv, navicular nucleus; OV, olfactory ventricle. (**E**) Stress-induced Fos expression (blue-black) in CTb-labeled (brown) cells in the DP (arrows). Note the typical pyramidal neuron morphology. Scale bars, 200 μm (main panel); 30 μm (inset). (**F**) Percentages of Fos-immunoreactive cells in CTb-labeled populations in mPFC subregions (n = 4 rats per group). *P < 0.05; **P < 0.01; ***P < 0.001 (unpaired t test; PrL, t_6 = 6.16; IL, t_6 = 5.93; DP, t_6 = 7.41; DTT, t_6 = 2.47). Error bars indicate SEM.

protein (GFP) (*19*), using adeno-associated virus (AAV) (Fig. 3A) allowed us to visualize their numerous axons projecting to the DMH. We found close association of these axons with DMH neurons retrogradely labeled with CTb from the rMR (Fig. 3, B and C, and fig. S3A), indicating putative synapses formed by DP/DTT-derived axons on DMH→rMR projection neurons. Confocal imaging revealed that the swellings of DP/DTT-derived axons apposed to rMR-projecting DMH neurons contained VGLUT1 (vesicular glutamate transporter 1), a marker for cortical glutamatergic neurons, but not VGLUT2, a subcortical glutamatergic neuron marker, or VGAT (vesicular GABA transporter), a GABAergic neuron marker (Fig. 3, D to F, and fig. S3B).

Consistent with the view that glutamatergic inputs to the DMH mediate stress responses, blockade of glutamatergic synapses in the DMH with nanoinjections of a mixture of 2-amino-5-phosphonovaleric acid and cyanquixaline (AP5/CNQX) inhibited SDS-induced sympathetic responses for the first 20 min of stress exposure (T_{BAT}: 88% inhibition, T_{core}: 80% inhibition, HR: 56% inhibition, MAP: 41% inhibition; fig. S3, C to F), after which the antagonistic effects of the drugs waned. The difference in the inhibitory effects of AP5/CNQX on the thermal and cardiovascular responses may be because the distribution of cardiovascular neurons in the DMH is broader than that of thermoregulatory neurons (*20*).

In vivo optogenetic stimulation of DP/DTT→DMH glutamatergic transmission elicits sympathetic responses

To directly examine the sympathoexcitatory role of the DP/DTT→DMH pathway, we selectively stimulated DP/DTT→DMH monosynaptic transmission by using an in vivo optogenetic technique (Fig. 3G). ChIEF, a channelrhodopsin variant (*21*), was used to induce membrane depolarization and action potentials in neurons with exposure to light. AAV transduction of DP/DTT neurons with ChIEF-tdTomato or palGFP resulted in the localization of the expressed proteins in their cell bodies in the DP/DTT and nerve endings densely distributed in the DMH (Fig. 3, H and I, and fig. S4, A and B). Illumination of ChIEF-tdTomato–containing nerve endings, but not palGFP-containing nerves, in the DMH with pulsed blue laser light for 30 s consistently increased BAT SNA, T_{BAT}, HR, and MAP in anesthetized rats (Fig. 3, J and K, and fig. S4C). Longer illumination (180 s) elicited larger increases, and the photostimulated BAT thermogenesis was as intense as that induced by SDS (fig. S4, D and E, and table S1). Photostimulation of DP/DTT→DMH transmission activated the DMH→rMR pathway (fig. S4, G to I). Consistent with the view that DP/DTT→DMH transmission driving the responses is glutamatergic, antagonizing glutamate receptors in the DMH eliminated all sympathetic responses elicited by photostimulation of DP/DTT→DMH transmission (Fig. 3, L to O, and fig. S4F).

DP/DTT-derived nerves with ChIEF-tdTomato were also distributed in the lateral hypothalamic area (LH) (Fig. 3I), which contains orexin neurons proposed to participate in

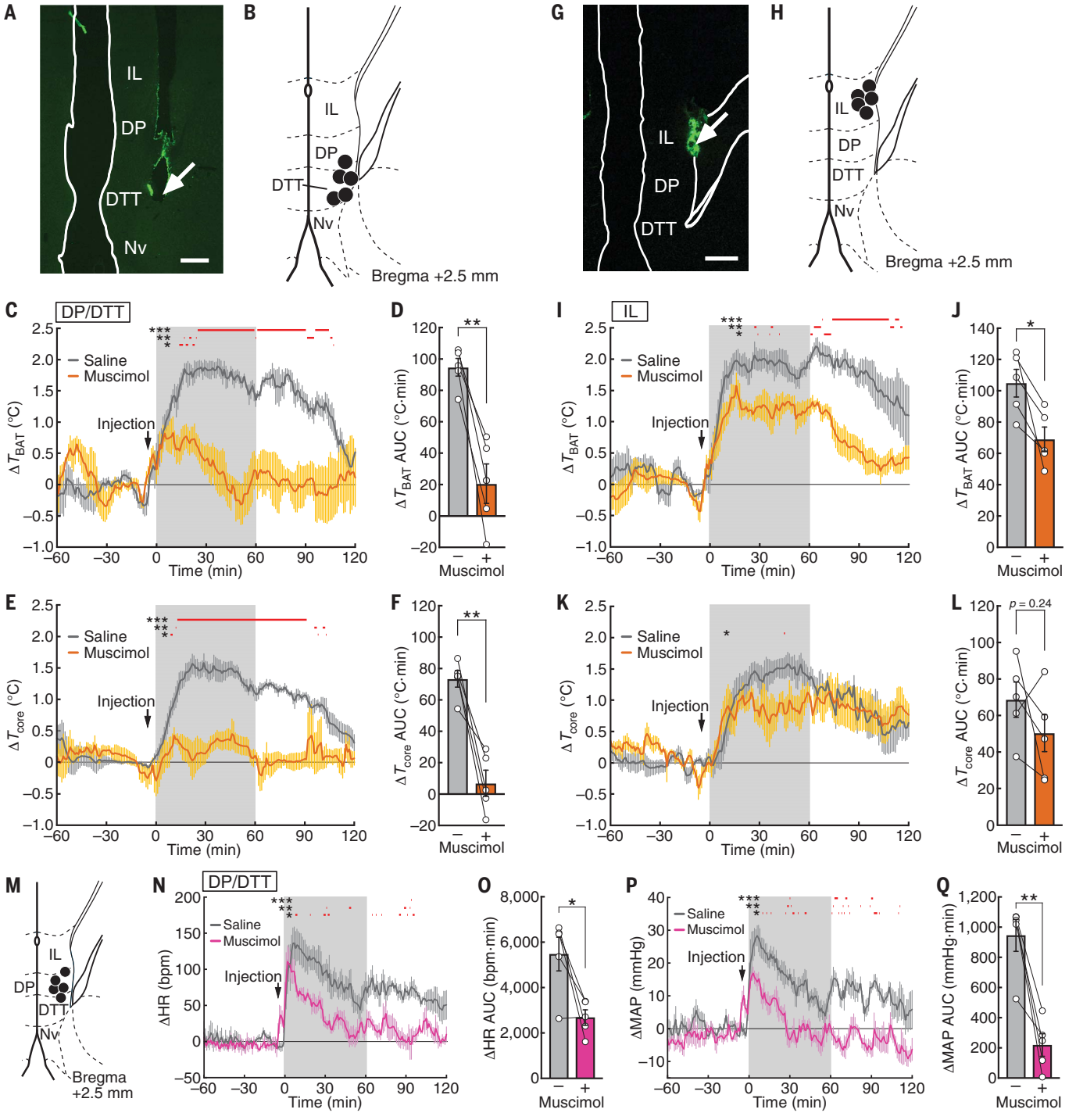


Fig. 2. Neurons in the DP/DTT, rather than the IL, mediate sympathetic stress responses. (**A** to **Q**) Effects of bilateral muscimol nanoinjections into the DP/DTT [(A) to (F) and (M) to (Q)] or the IL [(G) to (L)] on SDS-evoked BAT thermogenesis and hyperthermia [(A) to (L)] or cardiovascular responses [(M) to (Q)]. After saline or muscimol injections [1 mM; (A) to (L): 200 nl per site, (M) to (Q): 100 nl per site; marked by green microspheres in (A) and (G); scale bars, 500 μm] into the DP/DTT [(A), (B), and (M)] or the IL [(G) and (H)] (the right side of the symmetric bilateral injections is shown), animals were exposed to SDS [gray zones in (C), (E), (I), (K), (N), and (P)]. All rats (n = 5 per group) underwent two stress trials, >1 week apart, with saline (first trial) and muscimol (second trial) injections at the same sites. Time-course changes in T_{BAT}, T_{core}, HR, and MAP were analyzed by repeated measures two-way analysis of variance (ANOVA) [(C): injectant: $F_{1,4}$ = 19.85, P = 0.011, time: $F_{180,720}$ = 8.976, P < 0.001, interaction: $F_{180,720}$ = 8.68, P < 0.001; (E): injectant: $F_{1,4}$ = 36.89, P = 0.004, time: $F_{180,720}$ = 10.93, P < 0.001, interaction: $F_{180,720}$ = 10.38, P < 0.001; (I): injectant: $F_{1,4}$ = 22.5, P = 0.009, time: $F_{180,720}$ = 25.47, P < 0.001, interaction: $F_{180,720}$ = 4.63, P < 0.001; (K): injectant: $F_{1,4}$ = 0.35, P = 0.585, time: $F_{180,720}$ = 12.64, P < 0.001, interaction: $F_{180,720}$ = 2.07, P < 0.001; (N): injectant: $F_{1,4}$ = 27.99, P = 0.006, time: $F_{180,720}$ = 15.54, P < 0.001, interaction: $F_{180,720}$ = 2.48, P < 0.001; (P): injectant: $F_{1,4}$ = 55.59, P = 0.002, time: $F_{180,720}$ = 11.16, P < 0.001, interaction: $F_{180,720}$ = 2.47, P < 0.001] followed by Bonferroni's post hoc test (red bars with asterisks indicate time points with significant differences). Area under the curve (AUC) during the stress period was analyzed by paired t test [(D): t_4 = 7.57; (F): t_4 = 5.93; (J): t_4 = 3.46; (L): t_4 = 1.39; (O): t_4 = 4.39; (Q): t_4 = 6.92]. *P < 0.05; **P < 0.01; ***P < 0.001. Error bars indicate SEM. bpm, beats per minute.

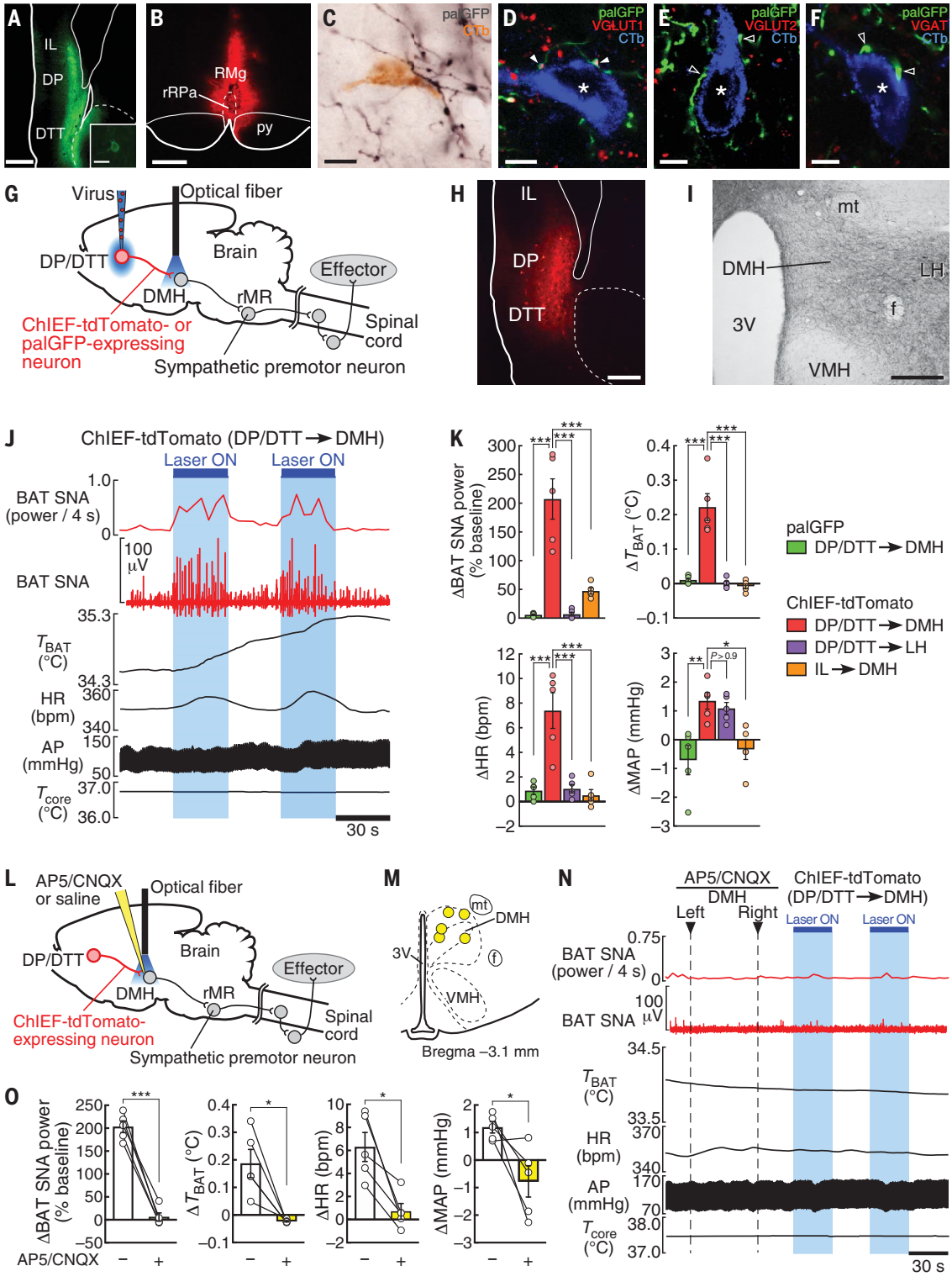


Fig. 3. Optogenetic stimulation of DP/DTT→DMH glutamatergic transmission elicits sympathetic responses. (**A** and **B**) Injections of AAV-CMV-palGFP into the DP/DTT (A) and CTb into the rMR (B). The inset in (A) shows a palGFP-expressing neuron. py, pyramidal tract; RMg, raphe magnus nucleus; rRPa, rostral raphe pallidus nucleus. Scale bars, 500 μm (main panels); 20 μm (inset). (**C**) palGFP-labeled axons closely associated with a DMH neuron retrogradely labeled with CTb. Scale bar, 10 μm. (**D** to **F**) Pseudocolored confocal images showing palGFP-labeled axon swellings (arrowheads) apposed to CTb-labeled cell bodies (asterisks) in the DMH. VGLUT1 (D) (filled arrowheads), but not VGLUT2 (E) or VGAT (F) (hollow arrowheads), was detected in these axon swellings. See also fig. S3. Scale bars, 5 μm. (**G**) In vivo optogenetic stimulation of DP/DTT→DMH nerve endings. (**H** and **I**) DP/DTT neurons transduced with ChIEF-tdTomato (H) and their axons containing ChIEF-tdTomato in the DMH [(I); immunoperoxidase staining]. Scale bars, 500 μm. (**J**) Representative example of BAT thermogenic and cardiovascular responses elicited by bilateral laser illumination of DP/DTT→DMH nerve endings with ChIEF-tdTomato. AP, arterial pressure. (**K**) Changes in physiological variables induced by illumination of selective pathways (one-way ANOVA followed by Bonferroni's post hoc test, n = 5 per group; ΔBAT SNA: $F_{3,16}$ = 28.74, P < 0.001; ΔT_{BAT}: $F_{3,16}$ = 30.46, P < 0.001; ΔHR: $F_{3,16}$ = 17.27, P < 0.001; ΔMAP: $F_{3,16}$ = 8.29, P = 0.002). *P < 0.05; **P < 0.01; ***P < 0.001. See also fig. S4. (**L**) Experiment to test the effects of blockade of glutamatergic synapses in the DMH on physiological responses to photostimulation of DP/DTT→DMH transmission. (**M**) Each circle indicates a site of saline and AP5/CNQX injections made at the same location in the DMH of each rat (saline was always injected first). The right side of symmetric bilateral injections is shown. (**N**) AP5/CNQX injections into the DMH eliminated sympathetic responses elicited by photostimulation of DP/DTT→DMH nerve endings (compare with fig. S4F, which shows a result for the saline control). (**O**) Changes in physiological variables elicited by photostimulation of the DP/DTT→DMH pathway after saline or AP5/CNQX injections into the DMH (n = 5 per group). *P < 0.05; ***P < 0.001 (paired t test; ΔBAT SNA: t_4 = 13.99; ΔT_{BAT}: t_4 = 3.98; ΔHR: t_4 = 4.07; ΔMAP: t_4 = 2.86). Error bars indicate SEM.

sympathetic stress responses (*22*). However, photostimulation of DP/DTT→LH transmission elicited no or subtle changes in the physiological variables (Fig. 3K and fig. S4J). Additionally, no response was elicited by photostimulation of IL→DMH axonal projections with ChIEF-tdTomato (Fig. 3K and fig. S4, K to M).

DP/DTT→DMH transmission is essential for sympathetic responses to psychosocial stress

We next employed genetic approaches to determine the importance of the DP/DTT→DMH

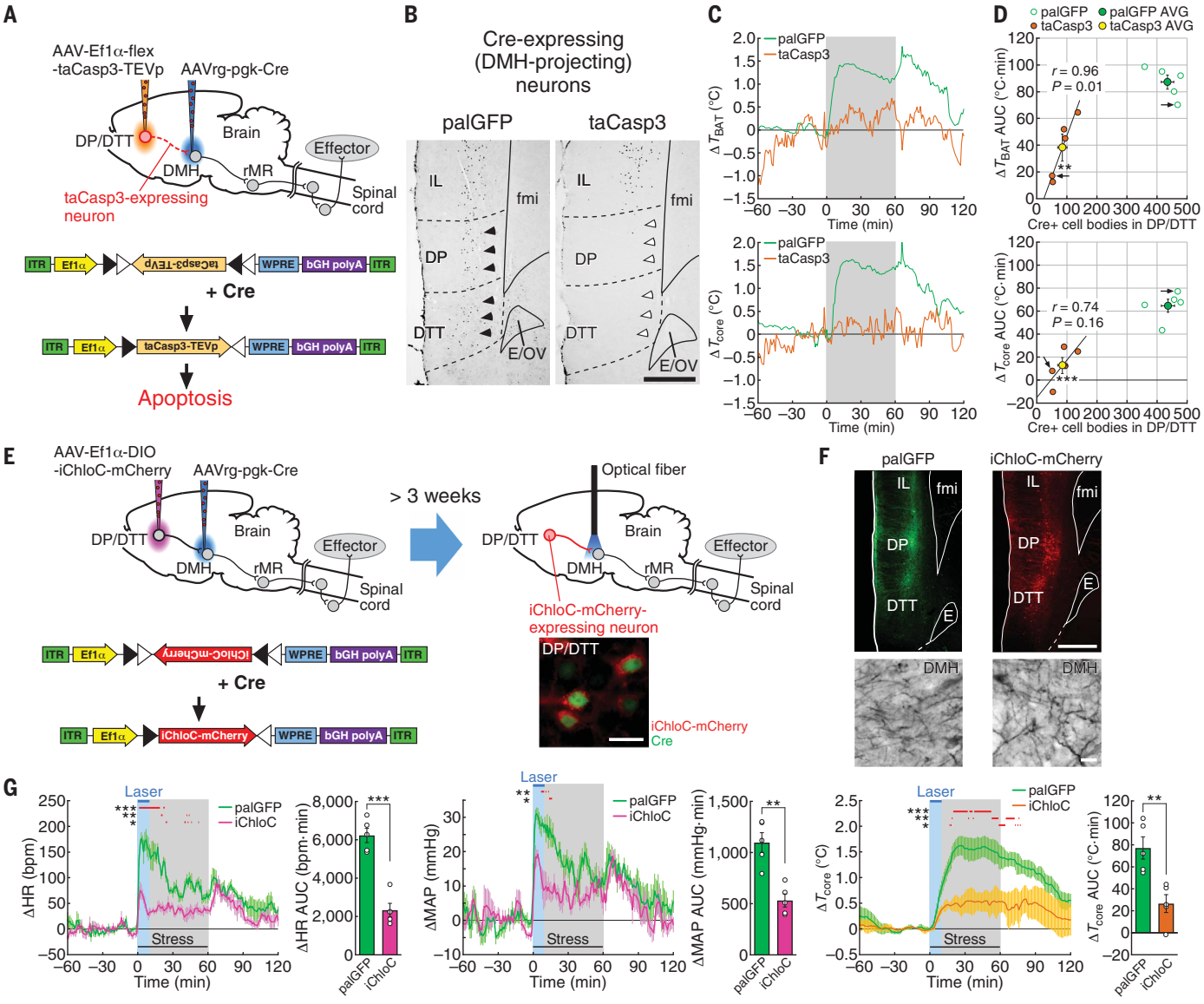


Fig. 4. Selective lesion or inhibition of the DP/DTT→DMH pathway abolishes sympathetic stress responses. (**A**) Scheme for genetic lesions of DP/DTT→DMH neurons. ITR, inverted terminal repeat; WPRE, woodchuck hepatitis virus posttranscriptional regulatory element; bGH polyA, bovine growth hormone polyadenylation signal. (**B** and **C**) Representative examples of palGFP or taCasp3 transduction of DP/DTT→DMH neurons from a single rat. (B) Cre-immunopositive (DMH-projecting) neurons were eliminated exclusively in the DP/DTT after taCasp3 transduction. Arrowheads indicate deep layers of the DP/DTT. Scale bar, 500 μm. (C) This lesioned rat failed to exhibit thermal responses to SDS (gray zone). (**D**) Relationship between the number of Cre-positive neurons remaining in the DP/DTT and stress responses (AUC of ΔT_{BAT} and ΔT_{core} during stress; see also time-course data in fig. S5A). Data from taCasp3 rats were subjected to linear regression analysis (Pearson's correlation test). The averages (AVG) of AUC were compared for the palGFP and taCasp3 groups (unpaired *t* test; $n = 5$ per group; ΔT_{BAT}: $t_8 = 4.30$; ΔT_{core}: $t_8 = 5.81$). $^{**}P < 0.01$; $^{***}P < 0.001$. Arrows indicate the cases plotted in (C). (**E**) In vivo optogenetic inhibition of DP/DTT→DMH neurons. Many Cre-immunopositive (DMH-projecting) DP/DTT neurons expressed iChloC-mCherry. Scale bar, 20 μm. (**F**) DP/DTT neurons were transduced with palGFP or iChloC-mCherry (top), and their axons with the proteins were densely distributed in the DMH (bottom; immunoperoxidase staining). Scale bars, 500 μm (top); 20 μm (bottom). (**G**) Illumination of DP/DTT→DMH nerve endings with iChloC-mCherry for the first 10 min (blue zone) of SDS inhibited cardiovascular and hyperthermic stress responses. Increases in HR and MAP after SDS were caused by stress from returning to the home cage. Time-course changes in the variables were analyzed by repeated measures two-way ANOVA ($n = 5$ per group; ΔHR: group: $F_{1,8} = 23.7$, $P = 0.001$, time: $F_{180,1440} = 23.55$, $P < 0.001$, interaction: $F_{180,1440} = 5.68$, $P < 0.001$; ΔMAP: group: $F_{1,8} = 5.98$, $P = 0.040$, time: $F_{180,1440} = 11.82$, $P < 0.001$, interaction: $F_{180,1440} = 2.24$, $P < 0.001$; ΔT_{core}: group: $F_{1,8} = 9.69$, $P = 0.014$, time: $F_{180,1440} = 31.83$, $P < 0.001$, interaction: $F_{180,1440} = 7.69$, $P < 0.001$) followed by Bonferroni's post hoc test (red bars with asterisks indicate time points with significant differences). The difference in AUC during the stress period was analyzed by unpaired *t* test (ΔHR: $t_8 = 8.21$; ΔMAP: $t_8 = 4.91$; ΔT_{core}: $t_8 = 3.91$). $^{*}P < 0.05$; $^{**}P < 0.01$; $^{***}P < 0.001$. Error bars indicate SEM.

monosynaptic pathway for driving sympathetic stress responses. First, DP/DTT→DMH projection neurons were selectively lesioned. An AAV for Cre recombinase–dependent expression of taCasp3, which induces cell-autonomous apoptosis (*23*), and a retrograde AAV (AAVrg) for Cre expression were bilaterally injected into the DP/DTT and DMH, respectively, to selectively lesion double-infected neurons (i.e., DP/DTT→DMH projection neurons) (Fig. 4A). Figure 4B shows an example of lesions of DP/DTT→DMH neurons: taCasp3 expression eliminated 88% of Cre-expressing (i.e., DMH-projecting) DP/DTT neurons in one representative rat as compared with palGFP-transduced control rats. This lesioned rat failed to exhibit BAT thermogenic and hyperthermic responses to SDS (Fig. 4C). Group data (Fig. 4D and fig. S5A) showed that stress-induced BAT thermogenesis was inhibited in proportion to the extent of lesions of DP/DTT→DMH neurons, and the stress response was totally eliminated when all the neurons were lesioned. However, the lesions of DP/DTT→DMH neurons did not affect diurnal control of T_{BAT} or T_{core} (fig. S5B).

To exclude the possible influence of long-term alterations in the circuits after neuronal lesions, we optogenetically suppressed DP/DTT→DMH transmission in free-moving rats. The Cre-dependent expression system with anterograde and retrograde AAVs was used to selectively transduce DP/DTT→DMH projection neurons with iChloC, a chloride-conducting channelrhodopsin shown to photoinhibit neuronal activity (*24*) (Fig. 4E). Expressed iChloC-mCherry proteins (or palGFP for control) were bilaterally detected in cell bodies in the DP/DTT and their nerve endings in the DMH (Fig. 4F). In vivo bilateral illumination of iChloC-mCherry–containing nerve endings in the DMH with pulsed blue light exerted potent, long-lasting inhibition on SDS-induced increases

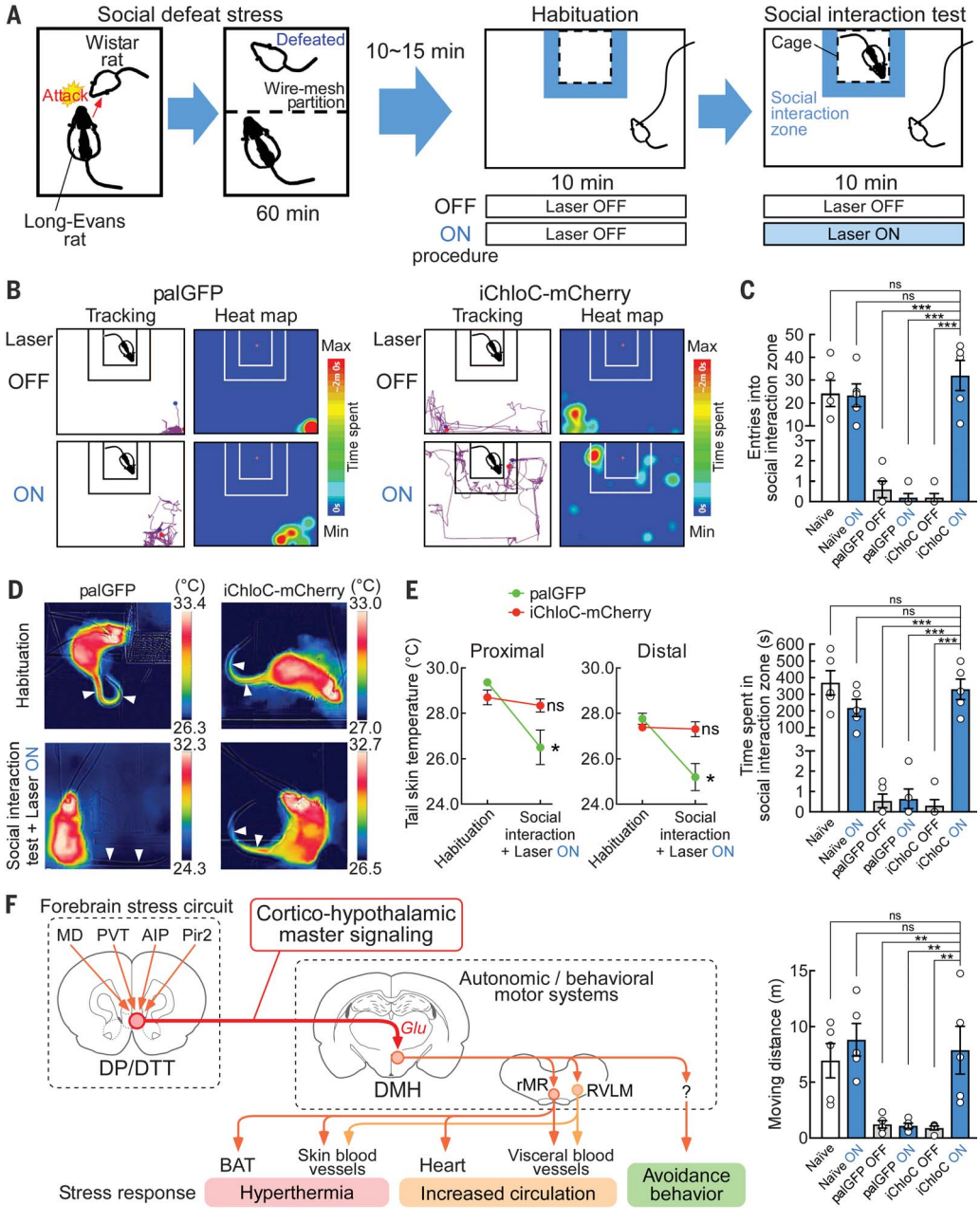


Fig. 5. Photoinhibition of the DP/DTT→DMH pathway abolishes stress-induced avoidance behavior and skin vasoconstriction. (**A**) Wistar rats in which DP/DTT→DMH neurons were transduced with iChloC-mCherry or palGFP (Fig. 4E) underwent a social interaction test after SDS. (**B**) Representative examples of behavior tracking of palGFP- and iChloC-mCherry–transduced rats during the social interaction test. (**C**) Behaviors during the social interaction test (n = 5 per group). Naïve rats did not undergo SDS before habituation and social interaction test. Data were analyzed by one-way ANOVA (Entries: $F_{5,24}$ = 12.87, P < 0.001; Time spent: $F_{5,24}$ = 15.49, P < 0.001; Moving distance: $F_{5,24}$ = 9.15, P < 0.001) followed by Bonferroni's post hoc test. ns, not significant; **P < 0.01; ***P < 0.001. Error bars indicate SEM. (**D** and **E**) Thermographic measurements at proximal and distal parts [arrowheads in (D)] on the tail skin (n = 5 per group) were analyzed by repeated measures two-way ANOVA (Proximal: treatment: $F_{1,4}$ = 17.44, P = 0.014; group: $F_{1,4}$ = 2.11, P = 0.220; interaction: $F_{1,4}$ = 9.01, P = 0.040; Distal: treatment: $F_{1,4}$ = 12.13, P = 0.025; group: $F_{1,4}$ = 10.74, P = 0.031; interaction: $F_{1,4}$ = 11.36, P = 0.028) followed by Bonferroni's post hoc test. ns, not significant; *P < 0.05 (versus habituation). Error bars indicate SEM. (**F**) Model of the central psychosomatic pathways that drive stress responses. The DP/DTT integrates signals from multiple forebrain regions processing stress and emotion and then provides a glutamatergic (Glu) master signal to the DMH to excite neuronal groups controlling different effectors. The excited DMH neurons drive sympathetic outflows to BAT, the heart, and cutaneous and visceral blood vessels through the rMR and partly through the rostral ventrolateral medulla (RVLM). Another subset of DMH neurons drives avoidance behavior through as-yet-unknown circuit mechanisms. AIP, posterior part of the agranular insular cortex; Pir2, layer II of the piriform cortex.

in HR, MAP, and T_{core} (HR: 63% inhibition, MAP: 52% inhibition, T_{core}: 66% inhibition; Fig. 4G) as compared with illumination of palGFP-expressing nerves. Commensurate with these inhibitions, iChloC-mCherry was expressed in 70 ± 2% of Cre-expressing (DMH-projecting) DP/DTT neurons (counted in three rats in which Cre immunostaining was successful; Fig. 4E). Photoinhibition of DP/DTT→DMH transmission did not reduce HR, MAP, or T_{core} below baseline levels, which indicates that this pathway is not involved in basal maintenance of these parameters.

Photoinhibition of DP/DTT→DMH transmission also suppressed BAT thermogenesis evoked by cage-exchange stress, an anticipatory anxiety model, in males and females (fig. S6), indicating that DP/DTT→DMH transmission mediates sympathetic responses to broader types of psychological stressors in both sexes. In contrast, photoinhibition of IL→DMH transmission did not impede SDS-induced stress responses (fig. S7).

The DP/DTT→DMH pathway mediates stress behaviors and skin vasoconstriction

Because the DP/DTT→DMH pathway is essential for driving the repertoire of sympathetic stress responses, we sought to examine its involvement in stress behavior. We thus investigated the effect of optogenetic inhibition of DP/DTT→DMH transmission on avoidance behavior from psychosocial stressors (*25*). A male Wistar rat in which DP/DTT→DMH neurons were selectively transduced with iChloC-mCherry or palGFP (Fig. 4E) was subjected to SDS and moved to an open field for habituation (Fig. 5A). Subsequently, the dominant male Long-Evans rat used in the SDS episode was caged and placed in the open field (Fig. 5A). All of the stressed Wistar rats that did not undergo illumination exhibited avoidance behavior by staying away from the social interaction zone surrounding the cage of the Long-Evans rat (Fig. 5, B and C). By contrast, naïve Wistar rats, which had not experienced SDS, exhibited active social interactions (Fig. 5C). The stress-induced avoidance behavior was suppressed by photoinhibition of DP/DTT→DMH transmission in iChloC-mCherry rats, and their social interactions were restored to the level exhibited by naïve rats, whereas illumination in palGFP rats had no effect (Fig. 5, B and C). Illumination administered when iChloC-mCherry rats were lying down in a relaxed state in the open field without the presence of a Long-Evans rat did not elicit locomotion (trials in four rats, five illumination episodes per rat). Therefore, it is unlikely that the behavioral effect of photoinhibition resulted from stimulation of any motivation or vigilance circuit system. In addition, photoinhibition did not alter social interactions exhibited by naïve rats (naïve ON; Fig. 5C).

Thermography revealed reduction of tail skin temperature in palGFP rats during the social interaction test (with illumination) compared with temperature during habituation (Fig. 5, D and E). This outcome represents stress-induced cutaneous vasoconstriction, a sympathetic response that contributes to stress-induced hyperthermia by reducing heat loss (*26*). Tail skin vasoconstriction was absent in iChloC-mCherry rats with photoinhibition of DP/DTT→DMH transmission (Fig. 5, D and E).

The DP/DTT receives stress-driven inputs from thalamic and cortical regions

To explore the forebrain regions that provide stress inputs to the DP/DTT, we combined retrograde tracing from the DP/DTT with detection of stress-induced Fos expression. Rats that received a CTb injection into the DP/DTT (fig. S8, A and B) underwent SDS or sham handling. Substantial numbers of neurons were labeled with CTb in several regions of the thalamus, insular and piriform cortices, and amygdala. SDS significantly increased Fos expression in CTb-labeled neurons in the mediodorsal (MD) and paraventricular (PVT) thalamic nuclei, the posterior part of the agranular insular cortex, and layer II of the piriform cortex (fig. S8, C to F). This observation suggests that the DP/DTT receives and integrates stress-driven inputs from these thalamic and cortical regions and provides the integrated signals to the DMH to drive sympathetic and behavioral stress responses (Fig. 5F).

Discussion

By using the rodent model of psychosocial stress, we discovered a prefrontal cortex–hypothalamus excitatory pathway that drives sympathetic and behavioral stress responses, in which the DP/DTT was crucial for stress signaling to the DMH. Our anatomical, physiological, and optogenetic experiments revealed that VGLUT1-positive pyramidal neurons in the DP/DTT transmit psychological stress–driven glutamatergic signals to the DMH to elicit a variety of stress responses. Most notably, selective ablation or inhibition of the DP/DTT→DMH monosynaptic pathway abolished BAT thermogenic, skin vasoconstrictor, cardiovascular, and behavioral responses to SDS without affecting basal thermoregulatory or cardiovascular homeostasis. Our present findings demonstrate that the DP/DTT→DMH excitatory transmission of psychological stress signals is a master driver of the wide range of sympathetic and behavioral stress responses (Fig. 5F).

The DP/DTT is an unexplored brain area located at the ventral limit of the mPFC. In contrast, the PrL and IL have been a central focus of stress research and have been shown to provide signals to inhibit stress responses. In this study, we discovered a group of neurons that drive stress responses in the DP/DTT. Photostimulation of DP/DTT→DMH transmission, but not that of IL→DMH, elicited sympathetic responses that mimic stress responses. Photoinhibition of DP/DTT→DMH transmission, but not that of IL→DMH, suppressed sympathetic stress responses. Also, inactivation of DP/DTT neurons suppressed stress responses, in contrast to subtle effects of inactivation of IL neurons. Thus, we propose that there are two functional units in the mPFC: the ventral (DP/DTT) unit that drives stress responses and the dorsal (PrL/IL) unit that inhibits these responses. The inhibitory unit may constitute the negative feedback mechanism in which the stress hormones, glucocorticoids, act in the PrL and IL to mitigate or terminate stress responses (*11*). This feedback inhibition might involve stress-activated PrL/IL→DMH neurons (Fig. 1) and/or local inhibition of DP/DTT neurons from the PrL/IL.

DP/DTT→DMH stress signaling activates DMH→rMR sympathoexcitatory neurons to drive stress responses (Fig. 5F). The DMH→rMR pathway also serves as the trunk pathway that controls body temperature and develops inflammatory fever, whose activity level is continuously controlled by descending inputs from the thermoregulatory center, the preoptic area (*27*). Because the DP/DTT→DMH pathway does not contribute to basal thermoregulation or cardiovascular control, the stress-driven ad hoc inputs from the DP/DTT are likely integrated in the DMH with the homeostatic tonic inputs from the preoptic area by impinging on the DMH→rMR efferent neurons. In addition, stress-induced visceral and cutaneous vasoconstriction may also be mediated in part by DMH neurons innervating the rostral ventrolateral medulla (*28*, *29*) (Fig. 5F).

The DP/DTT→DMH pathway appears to constitute a key psychosomatic connection through which stress and emotions affect the autonomic and behavioral motor systems. Although the corticolimbic circuits that process stress and emotions are undetermined, the PVT and MD thalamic nuclei, which provide stress inputs to the DP/DTT, constitute a fear stress circuit involving the amygdala (*30*, *31*). Thus, the stress and emotion signals processed by forebrain circuits are likely integrated at the DP/DTT and then transmitted to the DMH. In panic disorder, glutamatergic inputs to the DMH to develop the panic-prone state (*32*) may be provided from the DP/DTT. The DP/DTT→DMH pathway is a potential target for treating psychosomatic disorders that involve aberrant physiological responses, particularly because this pathway does not contribute to basal autonomic homeostasis.

REFERENCES AND NOTES

1. T. Oka, *Temperature* **2**, 368–378 (2015).
2. B. Lkhagvasuren, Y. Nakamura, T. Oka, N. Sudo, K. Nakamura, *Eur. J. Neurosci.* **34**, 1442–1452 (2011).

3. L. J. Robinson, J. M. Law, M. E. Symonds, H. Budge, *Exp. Physiol.* **101**, 549–557 (2016).
4. J. Park *et al.*, *J. Physiol.* **595**, 4893–4908 (2017).
5. P. L. Johnson, W. A. Truitt, S. D. Fitz, C. A. Lowry, A. Shekhar, *Neuropsychopharmacology* **33**, 2093–2107 (2008).
6. J. A. DiMicco, S. Sarkar, M. V. Zaretskaia, D. V. Zaretsky, *Auton. Neurosci.* **126-127**, 106–119 (2006).
7. R. A. L. Dampney, J. Horiuchi, L. M. McDowall, *Auton. Neurosci.* **142**, 3–10 (2008).
8. N. Kataoka, H. Hioki, T. Kaneko, K. Nakamura, *Cell Metab.* **20**, 346–358 (2014).
9. K. Björkqvist, *Physiol. Behav.* **73**, 435–442 (2001).
10. M. Laubach, L. M. Amarante, K. Swanson, S. R. White, *eNeuro* **5**, ENEURO.0315-18.2018 (2018).
11. D. Diorio, V. Viau, M. J. Meaney, *J. Neurosci.* **13**, 3839–3847 (1993).
12. R. F. Tavares, F. M. A. Corrêa, *Neuroscience* **143**, 231–240 (2006).
13. A. Adhikari *et al.*, *Nature* **527**, 179–185 (2015).
14. S. B. Johnson *et al.*, *J. Neurosci.* **39**, 1405–1419 (2019).
15. S. F. Hassan, J. L. Cornish, A. K. Goodchild, *J. Physiol.* **591**, 6069–6088 (2013).
16. Y. Nakamura *et al.*, *Eur. J. Neurosci.* **22**, 3137–3146 (2005).
17. S. Sarkar, M. V. Zaretskaia, D. V. Zaretsky, M. Moreno, J. A. DiMicco, *Eur. J. Neurosci.* **26**, 2228–2238 (2007).
18. R. A. Piñol *et al.*, *Nat. Neurosci.* **21**, 1530–1540 (2018).
19. K. Moriyoshi, L. J. Richards, C. Akazawa, D. D. M. O'Leary, S. Nakanishi, *Neuron* **16**, 255–260 (1996).
20. M. Tanaka, R. M. McAllen, *Am. J. Physiol. Regul. Integr. Comp. Physiol.* **294**, R477–R486 (2008).
21. J. Y. Lin, M. Z. Lin, P. Steinbach, R. Y. Tsien, *Biophys. J.* **96**, 1803–1814 (2009).
22. W. Zhang *et al.*, *J. Physiol.* **588**, 4117–4129 (2010).
23. C. F. Yang *et al.*, *Cell* **153**, 896–909 (2013).
24. J. Wietek *et al.*, *Sci. Rep.* **5**, 14807 (2015).
25. I. Toth, I. D. Neumann, *Cell Tissue Res.* **354**, 107–118 (2013).
26. Y. Ootsuka, W. W. Blessing, E. Nalivaiko, *Stress* **11**, 125–133 (2008).
27. K. Nakamura, *Am. J. Physiol. Regul. Integr. Comp. Physiol.* **301**, R1207–R1228 (2011).
28. J. Horiuchi *et al.*, *Am. J. Physiol. Regul. Integr. Comp. Physiol.* **287**, R824–R832 (2004).
29. Y. Ootsuka, R. M. McAllen, *Am. J. Physiol. Regul. Integr. Comp. Physiol.* **289**, R1107–R1115 (2005).
30. X. B. Li, T. Inoue, S. Nakagawa, T. Koyama, *Brain Res.* **1008**, 261–272 (2004).
31. M. A. Penzo *et al.*, *Nature* **519**, 455–459 (2015).
32. P. L. Johnson, A. Shekhar, *J. Neurosci.* **26**, 7093–7104 (2006).

ACKNOWLEDGMENTS

We thank P. Aebischer, P. Hegemann, A. Y. Karpova, R. McQuiston, D. V. Schaffer, N. Shah, J. Wells, and J. Wietek for sharing their plasmids and H. Hioki for providing anti-VGLUTs antibodies.
Funding: This study was supported by the JSPS NEXT program (LS070 to Ka.N.); MEXT KAKENHI (16H05128, 15H05932, 26118508, 26713009, and 22689007 to Ka.N.; 19K06954 and 16K19006 to N.K.); JST PRESTO (JPMJPR13M9 to Ka.N.); AMED (JP19gm5010002 to Ka.N.); and grants from the Takeda Science Foundation, Nakajima Foundation, Uehara Memorial Foundation, Ono Medical Research Foundation, Brain Science Foundation, Kowa Life Science Foundation (to Ka.N.), and Kato Memorial Bioscience Foundation (to N.K.). **Author contributions:** Ka.N. conceived the project. N.K. and Ka.N. designed experiments. All authors performed experiments and analyzed data. N.K. and Ka.N. discussed data and wrote the manuscript. Ka.N. supervised the entire project. All authors approved the manuscript.
Competing interests: The authors declare no competing interests.
Data and materials availability: All data are available in the main text or the supplementary materials. Plasmids and AAVs with Addgene numbers given in the materials and methods were obtained under material transfer agreements with Addgene.

SUPPLEMENTARY MATERIALS

science.sciencemag.org/content/367/6482/1105/suppl/DC1
Materials and Methods
Figs. S1 to S8
Table S1
References (*33*–*38*)

View/request a protocol for this paper from *Bio-protocol*.

12 September 2019; accepted 4 February 2020
10.1126/science.aaz4639

NEURODEVELOPMENT

A neurodevelopmental origin of behavioral individuality in the *Drosophila* visual system

Gerit Arne Linneweber[1,2,3], Maheva Andriatsilavo[1,2,3], Suchetana Bias Dutta[1,2,3], Mercedes Bengochea[1], Liz Hellbruegge[2,3], Guangda Liu[4,5], Radoslaw K. Ejsmont[1]*, Andrew D. Straw[6], Mathias Wernet[2], Peter Robin Hiesinger[2,3], Bassem A. Hassan[1,2,3]†

The genome versus experience dichotomy has dominated understanding of behavioral individuality. By contrast, the role of nonheritable noise during brain development in behavioral variation is understudied. Using *Drosophila melanogaster*, we demonstrate a link between stochastic variation in brain wiring and behavioral individuality. A visual system circuit called the dorsal cluster neurons (DCN) shows nonheritable, interindividual variation in right/left wiring asymmetry and controls object orientation in freely walking flies. We show that DCN wiring asymmetry instructs an individual's object responses: The greater the asymmetry, the better the individual orients toward a visual object. Silencing DCNs abolishes correlations between anatomy and behavior, whereas inducing DCN asymmetry suffices to improve object responses.

Individual variability in morphology is abundant, including among human identical twins and species that reproduce by parthenogenesis (*1*, *2*). In this regard, the brain is no exception. Examples of individual brain variation include differences of size, weight (*3*), and neuroanatomical parcellations of human brains (*4*, *5*). In invertebrates, where individual neurons can be identified across animals, single neurons show variability in morphology, wiring (*6*), synaptic connectivity, and molecular composition across individuals (*7*–*9*).

Similarly, innate behaviors, such as selective attention to stimuli, show individual variation even among genetically identical individuals (*10*–*13*). The stability of individual differences over time defines behavioral idiosyncrasies as animal individuality (*14*). It has been proposed that variability in innate behavior is due to neuromodulation of anatomically hardwired circuits (*15*–*17*). By contrast, there is evidence for developmental plasticity resulting in a range of possible circuit diagrams among individuals (*18*, *19*), but whether nonheritable individual anatomical differences in brain wiring can predict distinct behavioral outcomes is unexplored (*20*–*23*).

To test whether stochastic wiring of neural circuits affects behavioral variation, we used *Drosophila* contralateral visual interneurons called the dorsal cluster neurons (DCNs) (*24*) (also known as LC14) (*25*). DCNs exhibit up to 30% wiring variability of their axonal projections between individuals and between the left and right hemispheres of the same brain (*26*). DCN axons innervate two alternative target areas in the fly visual system called the medulla (M-DCNs) and the lobula (L-DCNs) (*24*). The decision whether any given DCN becomes a M-DCN or L-DCN is determined by an intrinsically stochastic lateral inhibition mechanism mediated by the Notch signaling pathway (*18*). To test the link between wiring variation and behavioral variation, we used a visual behavioral assay called Buridan's paradigm (*27*). In this assay, a fly is placed between two identical high-contrast stripes at 180° from each other in a uniformly illuminated arena (*28*). The stripes are unreachable, inducing the fly to walk back and forth between them during the assay.

Here we report that flies show behavioral individuality that is nonheritable and is not reduced through inbreeding. We find that the degree in left-right DCN wiring asymmetry in the medulla is a predictor of behavioral performance of individual flies. The more asymmetric the DCN medulla innervation is, the narrower the path a fly walks between the two stripes. DCN activity is necessary for this correlation, and reengineering DCN asymmetry suffices to change an individual's behavior.

Results

While analyzing object orientation responses in wild-type *Canton S* (*CS*) flies (Fig. 1A and movies S1 to S3), we noted sex-independent interindividual variability in their trajectories (Fig. 1, B and C). We focused on a parameter called absolute stripe deviation (henceforth aSD), measuring the deviation from the narrowest possible path between the stripes. Although males tend to walk narrower paths, the degree of interindividual variation in aSD is the same between males and females (Fig. 1D). We therefore continued our studies with combined populations (Fig. 1E).

Object orientation variability is independent of genetic diversity

To test whether behavioral variability correlates with genetic diversity, we screened a subset (N = 10) of the *Drosophila* genomic reference panel (DGRP) (*29*) for genetically homogeneous strains with extreme object orientation responses. This identified two strains with opposing behavioral phenotypes: *DGRP-639* showed low aSD (Fig. 1, F and G), whereas *DGRP-859* showed high aSD (Fig. 1, H and I). Similar behavioral differences were found in seven other representative behavioral parameters (fig. S1). However, despite the extreme reduction of genetic diversity, the degree of individual variation in aSD was not reduced (Fig. 1, G and I). On the contrary, *DGRP-639* showed increased behavioral variability (Fig. 1G and fig. S1), hinting at the nonheritability of this variability.

Individual object orientation responses are nonheritable

If the genotype of an individual determines its behavior, repeated breeding of parental animals with a specific behavioral trait should select for a specific behavior, creating a behaviorally homogeneous population. We mated three pairs with the lowest and highest aSD scores, respectively (Fig. 2, A and B), and object orientation responses were measured in their offspring (Fig. 2, C and D). We found no differences between the two sets of offspring in aSD scores as well as six other parameters tested (fig. S2A). The same was true for the offspring of a single pair with low and high aSD (fig. S2, B and C). We repeated the same breeding schemes with the near-isogenic *DGRP-639* and *DGRP-859* for seven generations. We found that for most parameters, a breeding pair reproduces the full range of variability in the population at every generation (figs. S3 and S4).

Individual object orientation responses are stable over time

An individual's idiosyncratic behavioral profile may not be heritable either because it is driven by internal-state modulations, or because it is driven by nonheritable developmental mechanisms. To distinguish these possibilities, we first tested the same individual *CS* flies once every other day for 3 days and found that an individual's behavior was virtually identical over the three trials (Fig. 3, A and B). Statistical analysis of aSD showed that the individual responses of *CS* flies on different days were correlated (r = 0.74 to 0.77, Fig. 3E). The same was true for

[1]Institut du Cerveau et de la Moelle Epinière (ICM)–Sorbonne Université, Inserm, CNRS, Hôpital Pitié-Salpêtrière, Paris, France. [2]Division of Neurobiology of the Institute for Biology, Free University, Berlin, Germany. [3]Einstein-BIH, Charité Universitätsmedizin, Berlin, Germany. [4]VIB Center for the Biology of Disease, VIB, 3000 Leuven, Belgium. [5]Center for Human Genetics, University of Leuven School of Medicine, 3000 Leuven, Belgium. [6]Institute of Biology I and Bernstein Center Freiburg, Faculty of Biology, Albert-Ludwigs-University Freiburg, Freiburg, Germany.
*Present address: Centre de Recherches Interdisciplinaires (CRI), 10 rue Charles V, 75004 Paris, France.
†Corresponding author. Email: bassem.hassan@icm-institute.org

path details like left- or right shifted angles (Fig. 3A and fig. S5C), distance, full walks, meander, absolute horizon deviation, absolute angle deviation, angle deviation, and center deviation. We extended this analysis over a 4-week period. We found that the object responses of individuals were stable over this extended period (Fig. 3, C and D, and fig. S6, A and B). This stability argued against state modulations and in favor of individual properties. Indeed, starvation followed by refeeding over a period of 3 days failed to reduce stability of individual performances despite obvious changes in mean population behavior (fig. S7). Finally, we asked whether

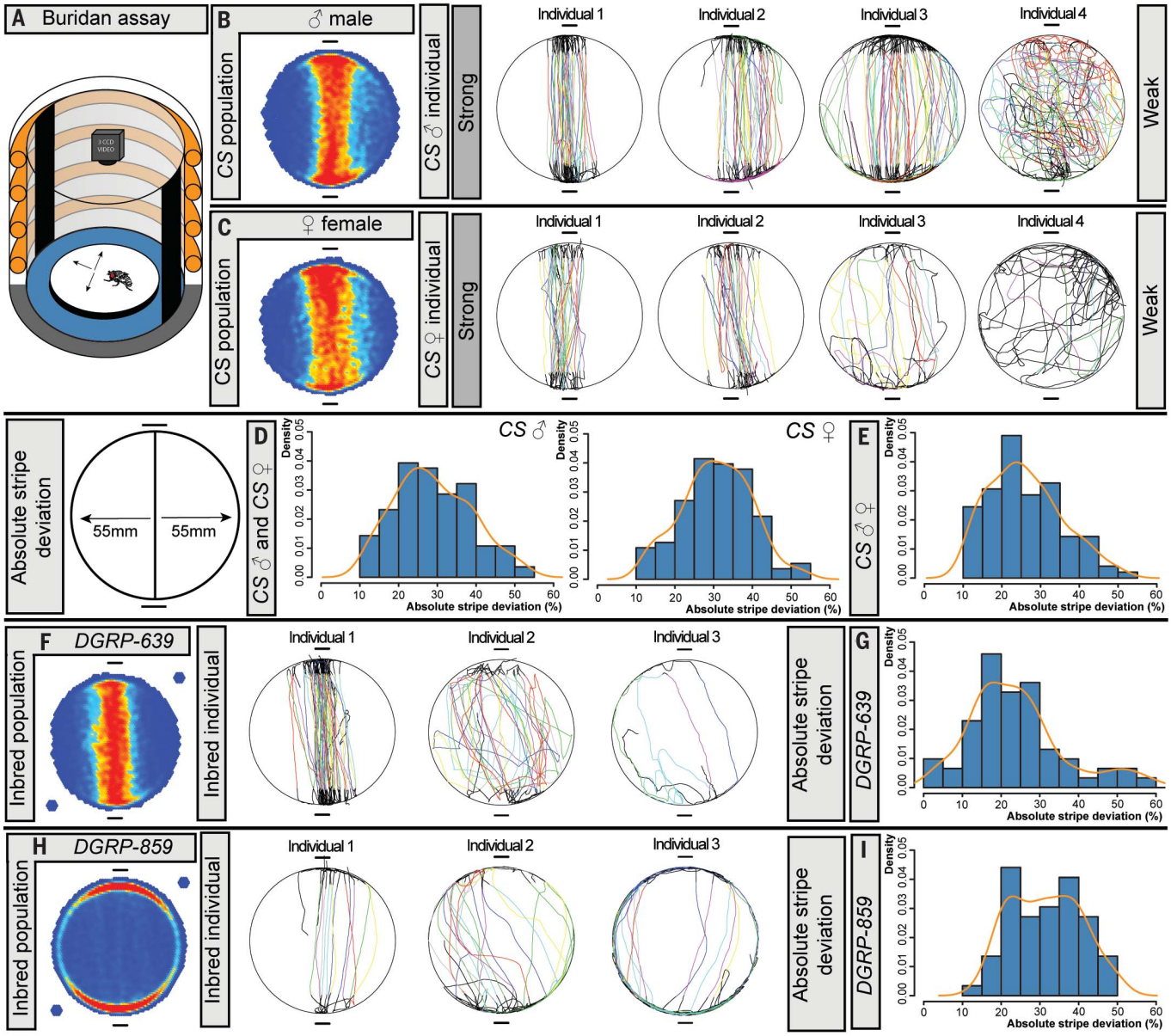


Fig. 1. Individual variation of *Drosophila* stripe responses is independent of gender or genetic diversity. (**A**) *Drosophila* object orientation responses are measured in a Buridan's paradigm arena. (**B**) Male *CS* wildtype flies (N = 50) showed on the population level (shown in a heatmap) an object orientation response toward the stripes that are located at the top and bottom. The categorization of individual responses into strong and weak object orientation responses shows the entire repertoire of responses (shown as individual fly tracks). (**C**) Female *CS* wild-type flies (N = 48) showed the same object orientation responses as their male counterparts. (**D**) The histograms for aSD show that *CS* male (N = 50) and female (N = 48) flies displayed the same range of individual responses. The histogram shows in bins of 5 % of the radius the distribution of aSD for each population. The distributions for males and females are statistically identical (Tukey test, p = 0.1). (**E**) The histogram shows the cumulative aSD for *CS* male and female flies (N = 98). (**F**) *DGRP-639* flies (N = 61) showed on the population level an object orientation response toward the stripes that exceeds even the response of *CS* (Tukey test, p = 0.01). Three examples of individual responses show the individual differences. (**G**) The histogram for aSD shows that *DGRP-639* flies (N = 61) exceed the variability of *CS* flies (F-test, $p < 0.001$). The distribution is shifted toward lower aSDs. (**H**) *DGRP-859* flies (N = 59) showed on the population level (heatmap) a weak object orientation response toward the stripes. The main population response is edge behavior. Two examples of individual responses show prevalent individual differences that include also individuals with strong object orientation responses. (**I**) The histograms for aSD indicate that *DGRP-859* flies (N = 59) show variability comparable to that of CS flies. The distribution is shifted toward higher aSDs.

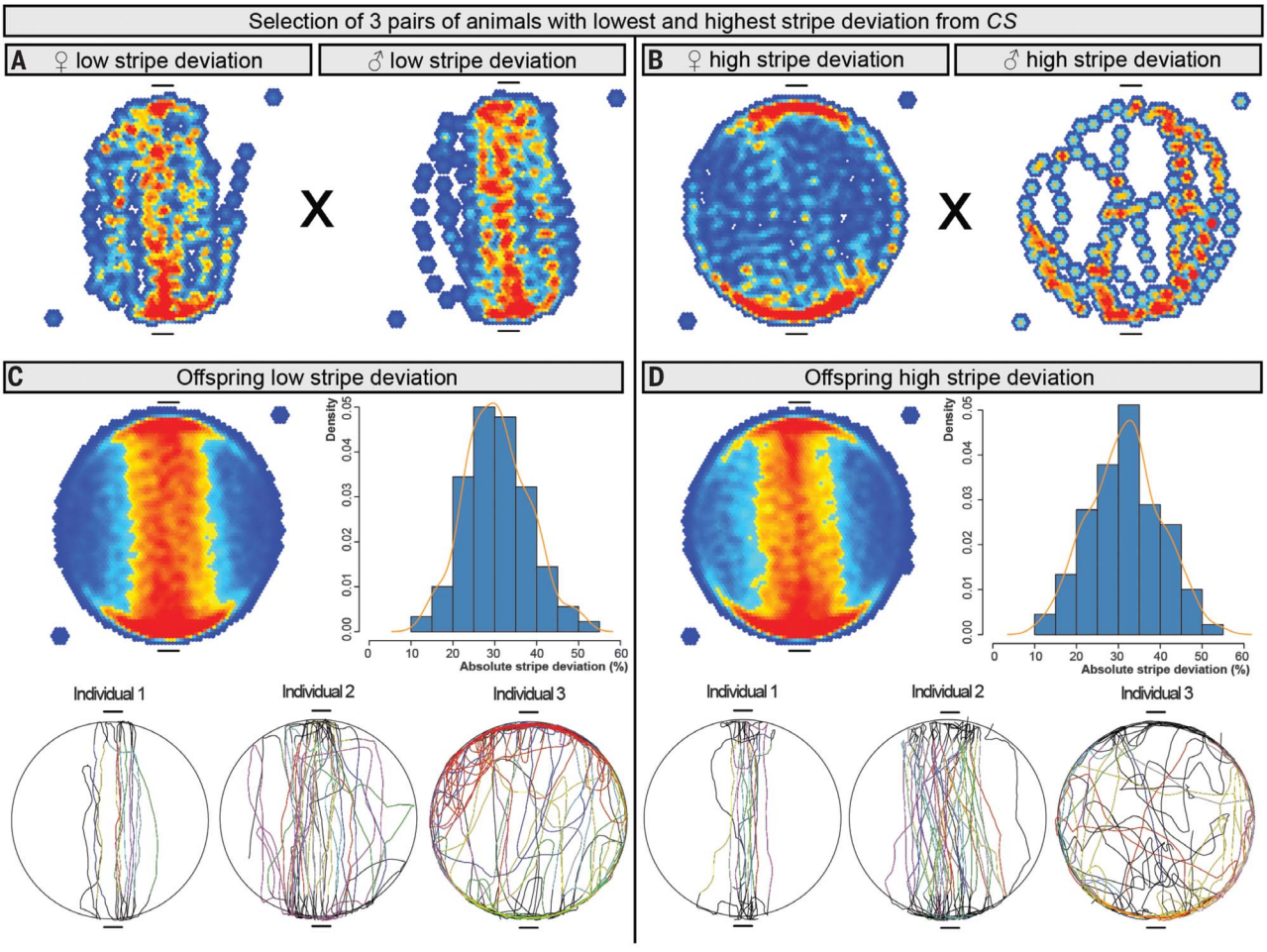


Fig. 2. Individual variation is independent of genetic selection. (**A** and **B**) The three lowest- (A) and highest-scoring couples (B) for aSD were chosen from a population of 47 *CS* males and 37 virgin *CS* females. The heatmaps in the top row show, from left to right: (i) the three virgin females and (ii) males with the lowest aSD, (iii) the three virgin females, and (iv) males with the highest aSD. (**C** and **D**) The offspring of these two populations are shown in the middle row separated by a black stripe. The behavioral heatmaps and variability histograms of the two populations of offspring are statistically indistinguishable (N = 180 for both; two-way analysis of variance (ANOVA) and Tukey HSD as post hoc test; p = 0.22). The bottom row shows examples of individuals representing the range of variability in both populations.

reduced genetic diversity affects behavioral stability. We performed repeated testing of *DGRP-639* and *DGRP-859* individual flies and found that both inbred strains showed temporally stable individual responses (Fig. 3, F and G, and fig. S5, A to C).

Together, the data show that individual variability in object orientation is a nonheritable, temporally stable trait that is independent of sex, genetic background, and genetic diversity. Where in the brain might such individuality in visual behavior originate?

A variable set of commissural visual interneurons

In 1982 Bülthoff (*30*) suggested, based on work by Zimmermann (*31*) and Götz (*32*), that object position processing in *Drosophila* (*33*) requires qualitative asymmetry of the visual percept of an object. However, direct evidence for this notion is lacking, especially that the sizes of the left and right eyes of the same fly are highly correlated (*34*). In 1986, while analyzing object responses in motion-blind flies, Heisenberg and colleagues suggested that binocular interactions, through higher-order commissural visual interneurons, are required for object orientation (*35*). Putting the two predictions together we hypothesized that variation in object orientation responses is regulated by the variation in the asymmetry of a higher-order contralateral visual circuit innervating the frontal visual field. The DCNs match this predicted circuit (Fig. 4A).

To obtain a comprehensive description of DCN wiring, we extended the previous analyses of DCNs that were based on 16 female flies (*18*), to 103 males and females. We found that the number of DCNs varied from 22 to 68 cells, with a range of 11 to 55 L-DCNs and 6 to 23 M-DCNs (Fig. 4B and fig. S8, A and B). In addition, we observed a distribution of variation in medulla-targeting asymmetry by M-DCNs (Fig. 4C, histogram distributions; fig. S8B). The distribution of all DCN asymmetries showed a peak of low asymmetries, although extreme asymmetries were present but rare. Finally, three-dimensional reconstruction showed that M-DCN axons terminate in the posterior medulla (movies S4 to S6), where visual columns from the frontal visual field are located, and the DCN wiring pattern in the medulla does not change in the adult (fig. S9 and movies S7 and S8).

Individual wiring variability drives behavioral individuality

DCNs represent an ideal candidate for an intrinsically asymmetric population of contralateral higher-order interneurons to mediate object responses (*35*). To test this hypothesis,

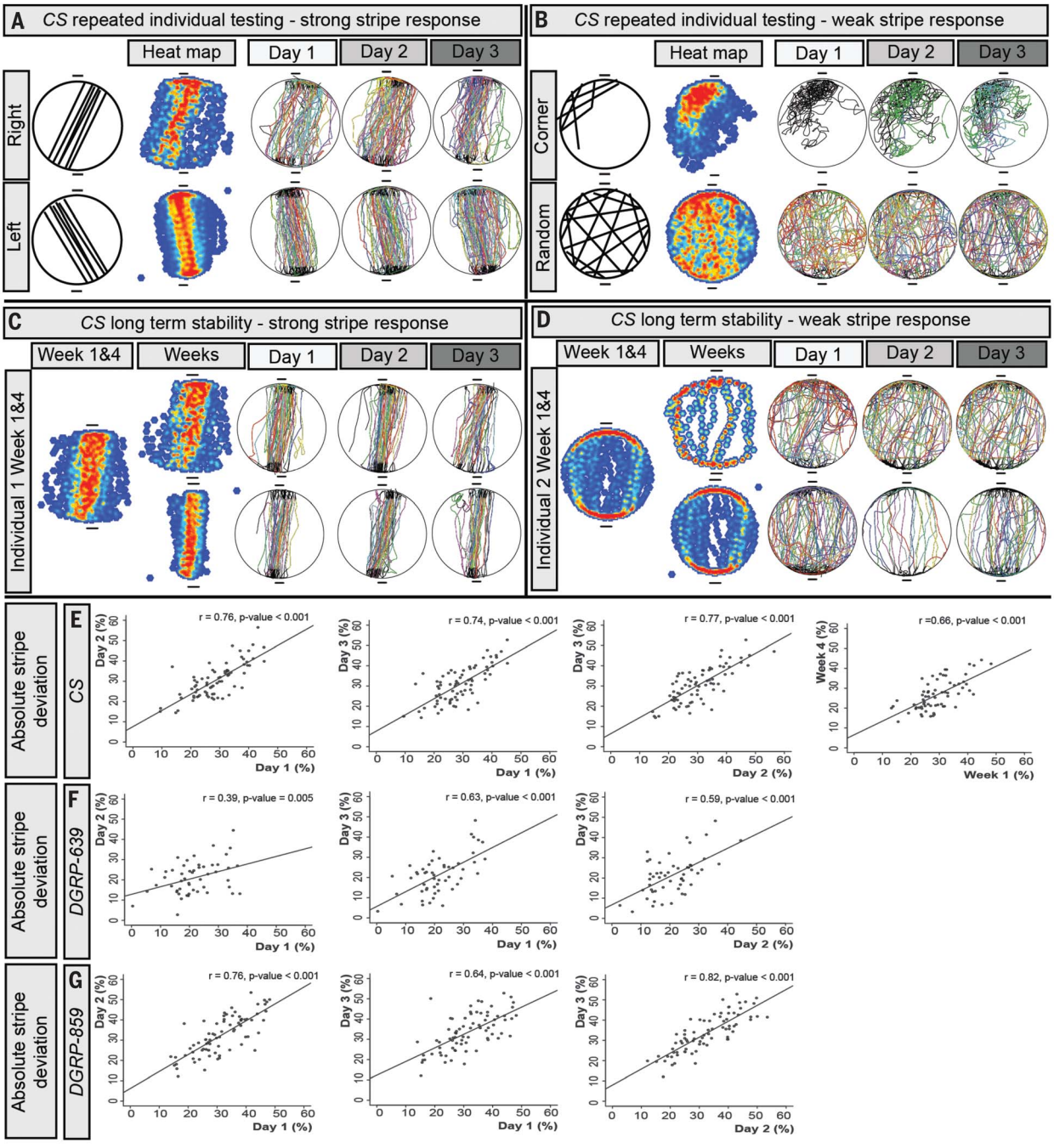


Fig. 3. Individual variation of *Drosophila* object orientation responses is stable over time. Adult *CS* flies (N = 74) were repeatedly tested over the duration of 3 days and several weeks. The flies showed marked stability in their responses irrespective of whether they responded strongly or weakly to the visual cue, or even showed no response toward the visual cue at all. (**A**) Two different examples of *CS* flies with low aSD. The heatmap and the individual tracks for the 3 days show persistent behavior. Even the angle toward the stripes is conserved throughout the 3 days. The upper row is right shifted, and the bottom row is left shifted. (**B**) Two different examples of *CS* flies with high aSD. The positional preferences are conserved between the different days. The upper row shows an animal with local preferences and the lower one performs a random walk. (**C** and **D**) Two different examples of *CS* flies with strong (individual 1) and high aSD (individual 2) that show persisting behavior throughout three consecutive days and several weeks. (**E**) Statistical analysis for aSD shows that the *CS* responses of the different days and weeks are correlated. The Pearson correlation coefficient for day 1 versus day 2 is 0.76 with $p < 0.001$. For day 1 versus day 3, the correlation coefficient is 0.76 with $p < 0.001$. For day 2 versus day 3, the correlation coefficient is 0.76 with $p < 0.001$. For week 1 versus week 4, the correlation coefficient is 0.66 with $p < 0.001$. (**F**) Similar to the *CS* data, the responses for *DGRP-639* were moderately to strongly correlated (N = 52, animals with low path length were removed; see fig. S3A for examples). The Pearson correlation coefficient for day 1 versus day 2 is 0.39 with $p = 0.0047$. For day 1 versus day 3, the correlation coefficient is 0.63 with $p < 0.001$. For day 2 versus day 3, the correlation coefficient is 0.59 with $p < 0.001$. (**G**) The correlation between days for *DGRP-859* (N = 76) even exceeds the data for *CS*. The Pearson correlation coefficient for day 1 versus day 2 is 0.76 with $p < 0.001$. For day 1 versus day 3, the correlation coefficient is 0.64 with $p < 0.001$. For day 2 versus day 3, the correlation coefficient is 0.82 with $p < 0.001$.

we first asked whether the DCNs were required for object orientation. Inactivating either all DCNs or only M-DCNs resulted in a strong increase in aSD (Fig. 4, D and E, and fig. S8, C and D). Next, we queried the relationship between individual variability in object orientation behavior and individual variability in DCN wiring (N = 103) (fig. S10). Unbiased correlation analysis between 36 behavioral parameters and 37 prominent DCN anatomical features (Fig. 5A and fig. S11, A to C) showed that left-right asymmetry in M-DCN innervation correlated with an individual's aSD (Fig. 5C, r = −0.67) and other interdependent parameters (fig. S11A). Individuals with high

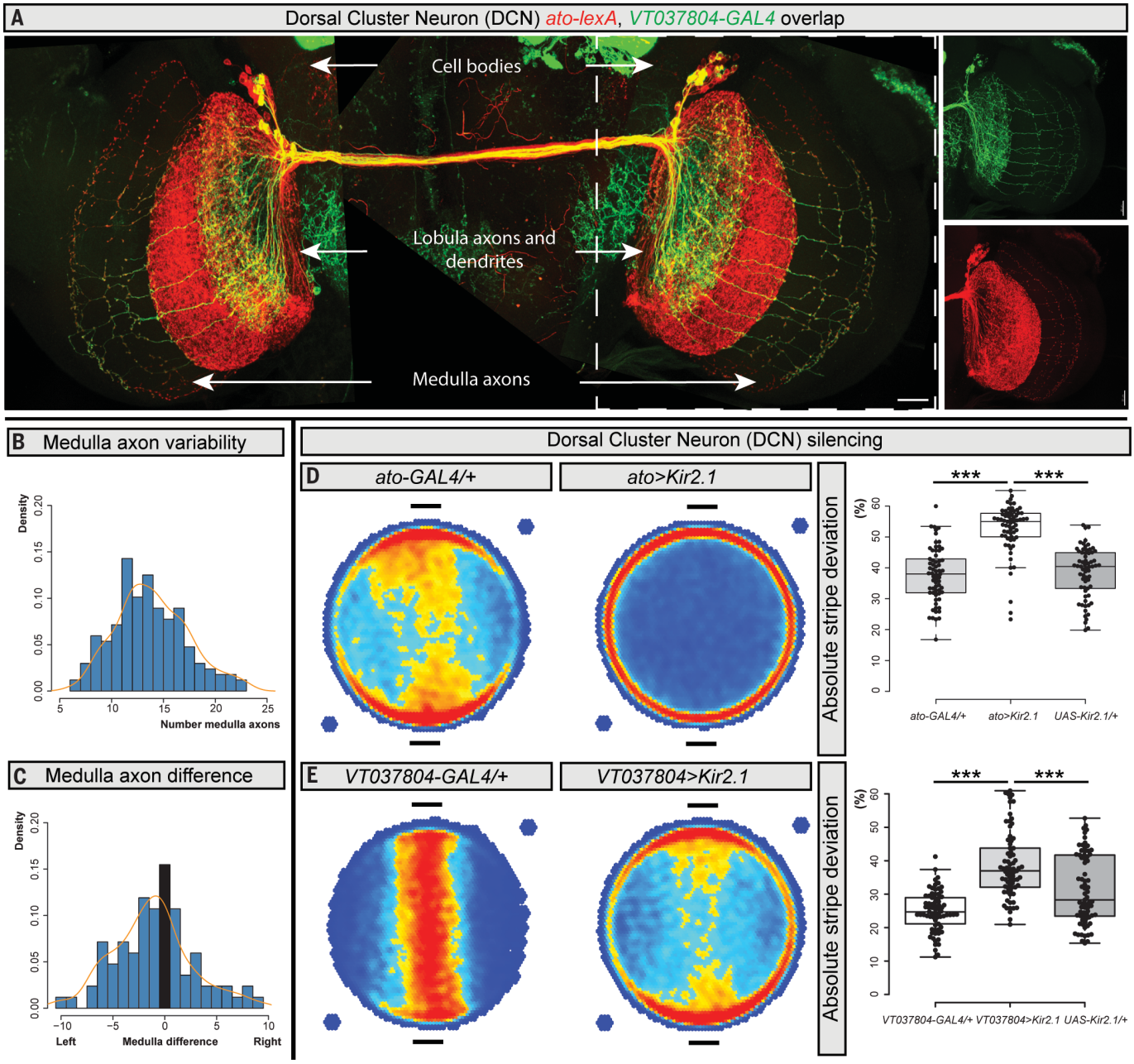


Fig. 4. Normal stripe responses require DCN function. (**A**) The DCNs are commissural neurons in the visual system of the fly. The DCNs have dorsally located cell bodies that send out an ipsilateral dendrite and a contralateral axon. This axon innervates either the visual neuropil lobula or medulla. Two independent driver lines are shown for the DCN neurons: *ato-lexA* (red, *lexAOP-myr-tdTomato*) marks all DCNs whereas *VT037804-GAL4* (green, *UAS-myr-GFP*) marks only the M-DCN neurons that innervate the medulla. (**B** and **C**) The DCNs display high variability in their axonal branching pattern, as shown for three individual brains. Statistical analysis shows that the number of medulla axon branches ranges from 6 to 23 axons with a mean of 13.99 (B). The medulla asymmetry ranges from 0 to 10 axons with a mean of 2.98 (C). (**D**) DCN neuron silencing leads to an increase in aSD. The heatmap of the control population of *ato-GAL4/+* flies shows a normal response in the two-stripe arena. This is lost upon silencing of DCN neurons in *ato>Kir2.1* animals. Statistical analysis (N = 57 to 63) of aSD shows that *ato>Kir2.1* animals show higher aSD than the controls (two-way ANOVA and Tukey HSD as post hoc test, $p < 0.001$). Higher aSD means that the animals fixate the stripes less. (**E**) Similar results are obtained by M-DCN neuron silencing with *VT037804-GAL4*. The heatmap of the control population of *VT037804-GAL4/+* flies shows normal object orientation in the two-stripe arena. This is lost upon silencing of DCN neurons in *VT037804>Kir2.1* animals. Statistical analysis (N = 72) of aSD shows that *VT037804>Kir2.1* animals show higher aSD than the controls ($p < 0.001$). Scale bars, 20 μm.

M-DCN asymmetry have a low aSD, whereas individuals with symmetric M-DCN have a high aSD (Fig. 5, B and C). To test if DCN wiring asymmetry is a functional driver of individual object orientation behavior, we silenced DCNs and repeated the analyses. This abolished the correlation between M-DCN asymmetry and aSD, but not stripe detection per se (Fig. 5, D and E, r = −0.002 and figs. S12 and S13).

DCN asymmetry determines object orientation in individuals

Our data show that nonheritable developmental variation in DCN wiring asymmetry is necessary for creating variability in object

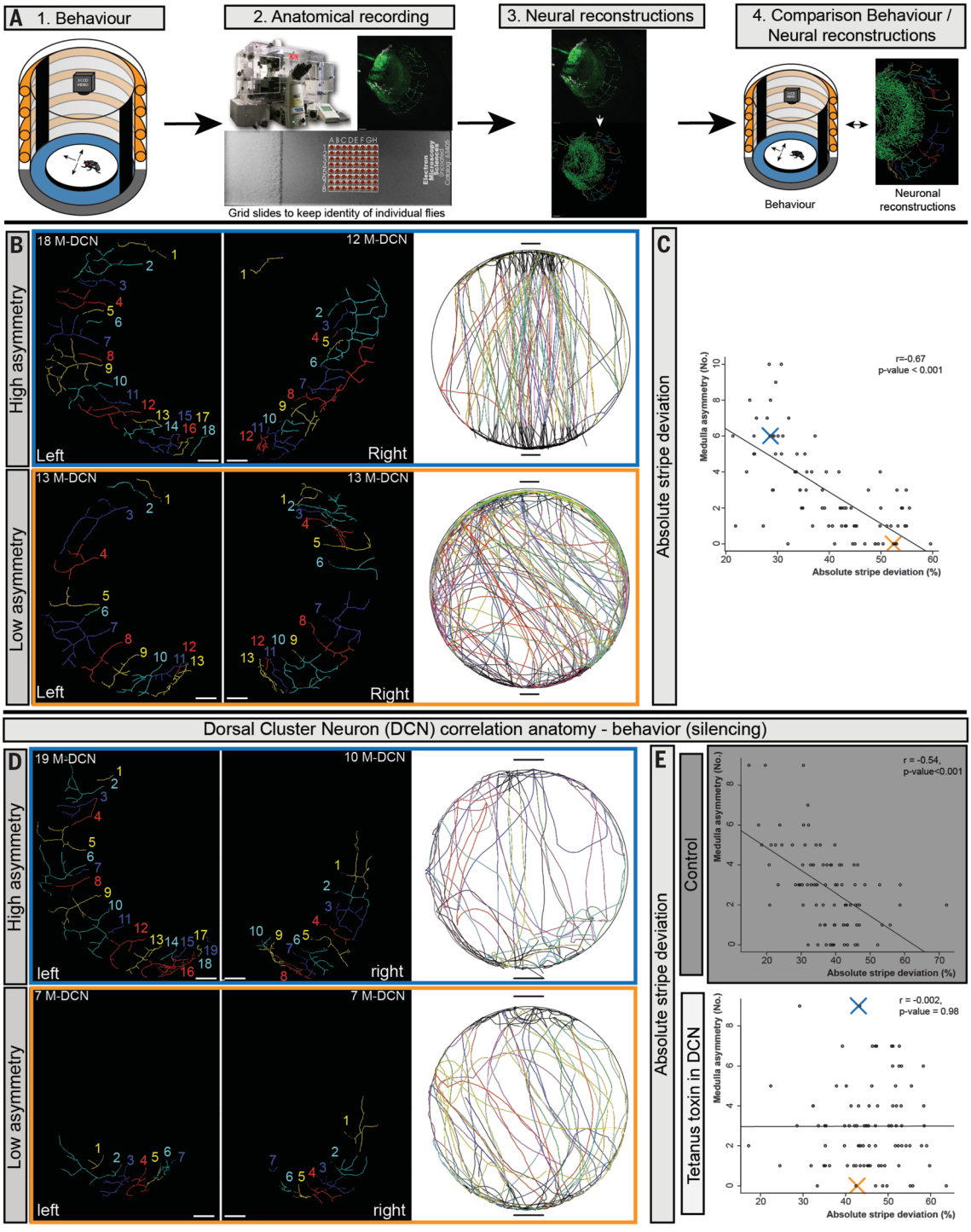


Fig. 5. Individual variation of anatomical brain asymmetry regulates behavioral variation. (**A**) To correlate behavioral variation with brain anatomical variation, flies were tested behaviorally in the Buridan arena, their brains dissected and stained, and DCN anatomy imaged, keeping individual information intact. After computational analysis of fly tracks and automated neuronal reconstruction of the brain anatomy, a cross-correlational analysis of both data sets was performed. (**B**) Animals with high left-right asymmetry of DCN axonal projections showed better performance than animals with lower asymmetry. The colored numbers show the reconstructed medulla axons in each brain hemisphere. (**C**) Statistical analysis (N = 103) shows that the medulla asymmetry correlates (r = 0.67, p < 0.001) with aSD. The blue and orange crosses mark the position of the blue and orange individuals shown in (B). (**D**) DCN silencing with tetanus toxin results in the loss of a correlation between medulla right-left asymmetry and aSD. High-asymmetry and low-asymmetry animals show approximately the same behavioral performance. (**E**) Statistical analysis shows that DCN silencing with tetanus toxin (TNT, N = 92) results in the loss of anatomy behavior correlations (r = −0.002, p = 0.98; control: N = 89, r = −0.54, p < 0.001, shaded dark gray). The examples of (D) are marked with a blue and orange cross in the correlation plot. Scale bars, 20 μm.

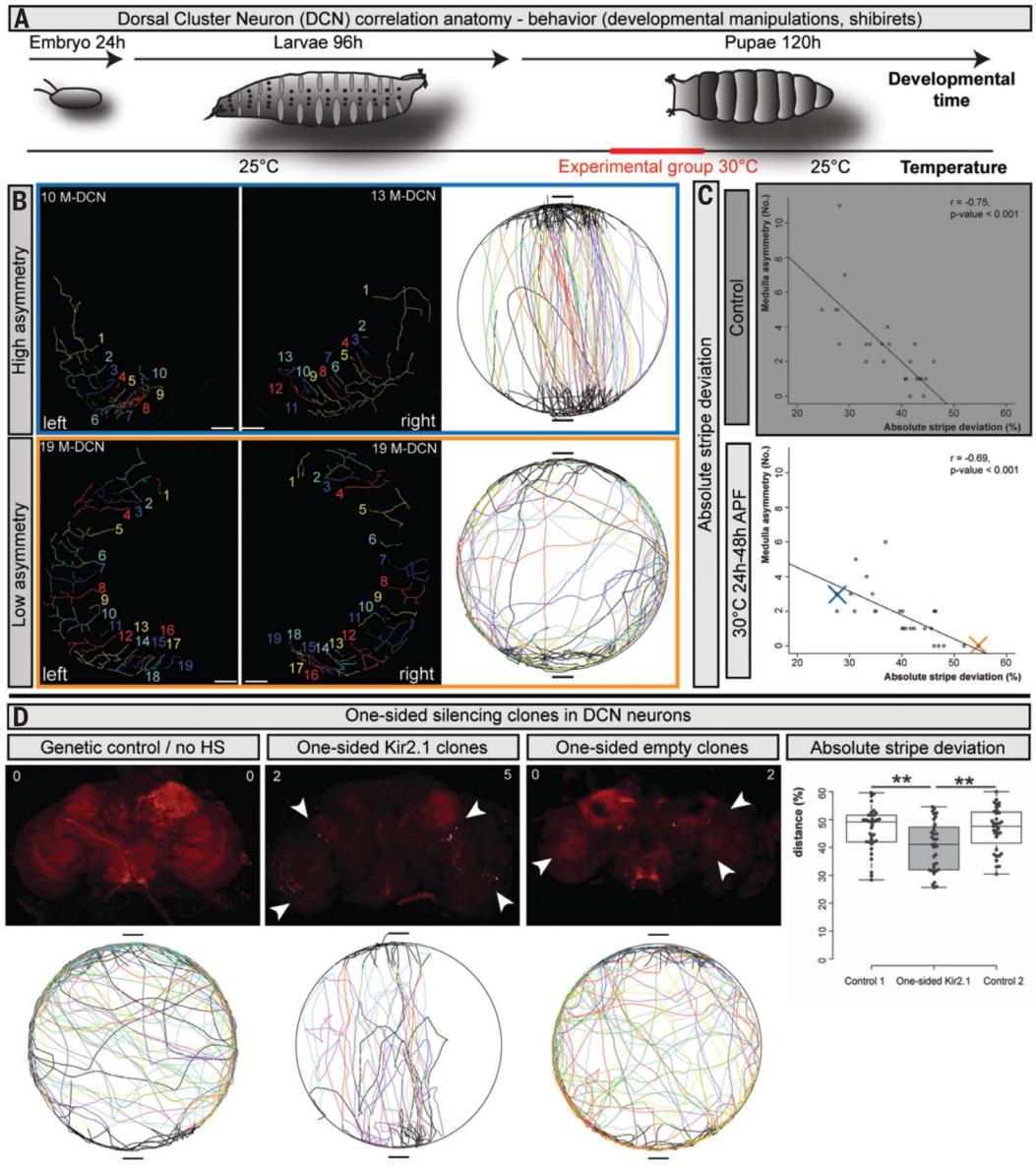


Fig. 6. Individual variation of anatomical brain asymmetry suffices for behavioral variation. (**A**) Schematic for the developmental inhibition of endocytosis using *UAS-shibire^{ts}* during the critical period (24 to 48 hours after puparium formation). The manipulation to change asymmetry is performed at the time of the choice between M-DCN or L-DCN (*18*). (**B**) Blocking endocytosis during DCN development increased the proportion of individuals with symmetric wiring and correspondingly aSD, with no effect on the correlation between anatomy and behavior in single flies. (**C**) Correlation curve of the *UAS-shibire^{ts}* individuals described in (B) (N = 27, r = −0.69, p < 0.001; control: N = 25, r = −0.75, p < 0.001, shaded dark gray). (**D**) Directed induction of one-sided clones in M-DCNs expressing Kir2.1 results in stronger object orientation responses than in the genetic control [same genotype, no heat shock (HS) clonal induction, p = 0.007] and in the HS control (identical genotype but lacking *UAS-Kir.2.1*, p = 0.006). Data were analyzed by two-way ANOVA and Tukey test. Scale bars, 20 μm.

orientation behavior across individuals. We therefore wondered if the changed object orientation responses in the DGRP strains reflect DCN asymmetry alterations. We found that the low aSD strain *DGRP-639* displayed more DCN wiring asymmetry, and the high aSD strain *DGRP-859* less DCN wiring asymmetry (fig. S14), consistent with our hypothesis. Next, we developmentally rewired the DCNs either by blocking endocytosis to inhibit developmental signaling among DCNs or by activating the Notch pathway, both in a DCN-specific fashion. This resulted in reduced DCN wiring asymmetry and a correspondingly higher aSD, while preserving the correlation between wiring and behavior (Fig. 6, A to C, and figs. S15 and S16). Finally, we genetically engineered flies to generate one-sided DCN clones expressing the neuronal silencer Kir2.1. Animals with asymmetrically silenced clones showed lower aSD scores than controls with unsilenced clones or no clones at all (Fig. 6D and fig. S17). Together, these data causally link DCN wiring asymmetry to object orientation responses.

Finally, to test our hypothesis further, we asked if generating any asymmetry in visual processing is sufficient to override high stripe deviation. Among 79 *CS* flies tested, we selected the 20 with the highest aSD indices (>40), performed monocular deprivation, and tested them again. This resulted in a reduction of aSD in these flies, as well as in the entire population (fig. S18).

Discussion

The origins of behavioral individuality are a central question in neuroscience, psychology, and evolution. The discovery of stable individual traits in nonhuman vertebrates (*16*) and invertebrates facilitated research on behavioral variation (*10*, *14*) and offered both genetic (*11*, *12*, *36*) and neuromodulatory (*11*, *15*, *36*) explanations for behavioral idiosyncrasies. Here we establish a link between variability in the development of the brain and the emergence of individuality of animal behavior. Our work shows that intrinsically stochastic mechanisms of brain wiring give rise to intraindividual variation of left-right asymmetry in the innervation of the fly visual areas, which explains the individuality of behavioral differences in object responses. The amenability of the relatively complex *Drosophila* brain to multiscale analysis, from the molecular to the behavioral, at single-animal resolution makes it a model for understanding the emergence of individuality at each of these scales. We speculate that

similar mechanisms and consequences will hold true in other species, including humans.

Previous work in *Drosophila* visual behavioral neuroscience led to the proposal that asymmetry in visual information processing influences object responses. Where such functional asymmetry lay and how it might arise has, until now, remained unclear. Independently, the study of object responses in motion-blind mutants led Heisenberg and colleagues to propose a hypothetical contralateral circuit dedicated to object responses in the frontal visual field (*28*, *30*–*32*, *35*). Our discovery that DCN asymmetry drives object orientation responses in individuals is an elegant solution combining both predictions: a contralateral asymmetric visual circuit that regulates object orientation in the frontal visual field. Future work will reveal the exact physiological consequences of morphological asymmetry, such as whether wiring asymmetry induces timing differences as in auditory navigation (*37*) or whether the absolute differences are simply summed up.

Our work provides evidence for the generation of multiple brain and behavior phenotypes from the same genotype via developmental stochasticity and noise. This can serve as a robustness factor for both the individual and the population by increasing the chances of survival of any given genome in case of strong selection pressure (*22*).

REFERENCES AND NOTES

1. P. M. Visscher, *Nat. Genet.* **40**, 489–490 (2008).
2. G. Vogt *et al.*, *J. Exp. Biol.* **211**, 510–523 (2008).
3. H. Pakkenberg, J. Voigt, *Acta Anat. (Basel)* **56**, 297–307 (1964).
4. J. S. Allen, H. Damasio, T. J. Grabowski, *Am. J. Phys. Anthropol.* **118**, 341–358 (2002).
5. A. Mohr, M. Weisbrod, P. Schellinger, M. Knauth, *Brain Res. Cogn. Brain Res.* **20**, 106–110 (2004).
6. Y. H. Chou *et al.*, *Nat. Neurosci.* **13**, 439–449 (2010).
7. V. Budnik, Y. Zhong, C. F. Wu, *J. Neurosci.* **10**, 3754–3768 (1990).
8. E. R. Graf, R. W. Daniels, R. W. Burgess, T. L. Schwarz, A. DiAntonio, *Neuron* **64**, 663–677 (2009).
9. C. S. Goodman, *J. Comp. Neurol.* **182**, 681–705 (1978).
10. W. Schuett *et al.*, *Dev. Psychobiol.* **53**, 631–640 (2011).
11. J. S. Kain, C. Stokes, B. L. de Bivort, *Proc. Natl. Acad. Sci. U.S.A.* **109**, 19834–19839 (2012).
12. J. F. Ayroles *et al.*, *Proc. Natl. Acad. Sci. U.S.A.* **112**, 6706–6711 (2015).
13. A. Renart, C. K. Machens, *Curr. Opin. Neurobiol.* **25**, 211–220 (2014).
14. S. D. Gosling, *Soc. Personal. Psychol. Compass* **2**, 985–1001 (2008).
15. S. Stern, C. Kirst, C. I. Bargmann, *Cell* **171**, 1649–1662.e10 (2017).
16. C. Pantoja *et al.*, *Neuron* **91**, 587–601 (2016).
17. E. Marder, *Neuron* **76**, 1–11 (2012).
18. M. Langen *et al.*, *eLife* **2**, e00337 (2013).
19. M. Zschätzsch *et al.*, *eLife* **3**, e01699 (2014).
20. P. R. Hiesinger, B. A. Hassan, *Trends Neurosci.* **41**, 577–586 (2018).
21. K. Honegger, B. de Bivort, *Curr. Biol.* **28**, R8–R12 (2018).
22. D. N. Fisher, M. Brachmann, J. B. Burant, *Anim. Behav.* **138**, e1–e6 (2018).
23. T. J. H. White, *J. Am. Acad. Child Adolesc. Psychiatry* **58**, 1042–1050 (2019).
24. B. A. Hassan *et al.*, *Neuron* **25**, 549–561 (2000).
25. H. Otsuna, K. Ito, *J. Comp. Neurol.* **497**, 928–958 (2006).
26. X. Zheng *et al.*, *EMBO J.* **25**, 615–627 (2006).
27. J. Colomb, L. Reiter, J. Blaszkiewicz, J. Wessnitzer, B. Brembs, *PLOS ONE* **7**, e42247 (2012).
28. H. Bülthoff, K. G. Götz, M. Herre, *J. Comp. Physiol.* **148**, 471–481 (1982).
29. T. F. Mackay *et al.*, *Nature* **482**, 173–178 (2012).
30. H. Bülthoff, *Biol. Cybern.* **45**, 71–77 (1982).
31. G. Zimmermann, thesis, Eberhard-Karls-Universitaet Tübingen, Tübingen, Germany (1975).
32. K. G. Götz, *Naturwissenschaften* **62**, 468–475 (1975).
33. W. Reichardt, *Naturwissenschaften* **60**, 122–138 (1973).
34. J. Vollmer *et al.*, *Development* **143**, 1482–1490 (2016).
35. B. Bausenwein, R. Wolf, M. Heisenberg, *J. Neurogenet.* **3**, 87–109 (1986).
36. S. M. Buchanan, J. S. Kain, B. L. de Bivort, *Proc. Natl. Acad. Sci. U.S.A.* **112**, 6700–6705 (2015).
37. T. P. Franken, M. T. Roberts, L. Wei, N. L. Golding, P. X. Joris, *Nat. Neurosci.* **18**, 444–452 (2015).

ACKNOWLEDGMENTS

We thank the Bloomington stock center (NIH P40OD018537) and Gilad Barnea for providing flies used in this study. We thank L. Fenk for insightful discussions during the initiation phase of the project and B. van Swinderen and all members of the Hassan, Hiesinger, and Wernet lab for support and valuable comments. We also thank the VIB Bio Imaging Core. **Funding:** This work was supported by the ICM Big Brain Theory Program, the program "Investissements d'avenir" (ANR-10-IAIHU-06), an ANR grant (ANR-19-CE16-0009-01), The Einstein-BIH program, the Paul G. Allen Frontiers Group, VIB, the WiBrain Interuniversity Attraction Pole network (Belspo), the FLiACT Marie-Curie Initial Training Network (FP7/2007-2013) (to B.A.H.), NIH (RO1EY018884) and the German Research Foundation (DFG: SFB 958, SFB186) (to P.R.H.), FU Berlin (to P.R.H. and M.W.), as well as EMBO Long Term Postdoctoral Fellowships (to G.A.L. and R.K.E.), VIB Omics postdoctoral fellowship (to R.K.E.), and the Marie Skłodowska Curie Actions postdoctoral fellowship in FP7 and Horizon 2020. Further support for G.A.L. was provided by FU Berlin (to P.R.H.). B.A.H. is an Allen Distinguished Investigator and a BIH-Einstein Visiting Fellow. **Author contributions:** G.A.L. and B.A.H. conceived the study, designed the experiments, and wrote the manuscript. G.A.L. conducted all behavioral experiments, immunohistochemistry, and all data analysis. M.A., S.B.D., and L.H. helped with the neuronal reconstructions. M.B. helped with control behavioral experiments. G.L. and R.K.E. provided technical expertise, G.L. helped with building the Buridan arena, and R.K.E. wrote the Python analysis software. A.D.S. shared unpublished data and reagents and provided technical expertise for behavioral experiments. M.W. and P.R.H. provided expertise and equipment and helped write the manuscript. **Competing interests:** The authors declare no competing interests. **Data and materials availability:** All data are available in the manuscript or the supplementary materials.

SUPPLEMENTARY MATERIALS

science.sciencemag.org/content/367/6482/1112/suppl/DC1
Materials and Methods
Figs. S1 to S18
Movies S1 to S8
References (*38*–*54*)

View/request a protocol for this paper from *Bio-protocol*.

18 January 2019; resubmitted 26 September 2019
Accepted 27 January 2020
10.1126/science.aaw7182

REPORT

LIQUID CRYSTALS

Topological structure and dynamics of three-dimensional active nematics

Guillaume Duclos[1]*, Raymond Adkins[2]*, Debarghya Banerjee[3,4], Matthew S. E. Peterson[1], Minu Varghese[1], Itamar Kolvin[2], Arvind Baskaran[1], Robert A. Pelcovits[5], Thomas R. Powers[6,5], Aparna Baskaran[1], Federico Toschi[7,8], Michael F. Hagan[1], Sebastian J. Streichan[2], Vincenzo Vitelli[9], Daniel A. Beller[10]†, Zvonimir Dogic[1,2]†

Topological structures are effective descriptors of the nonequilibrium dynamics of diverse many-body systems. For example, motile, point-like topological defects capture the salient features of two-dimensional active liquid crystals composed of energy-consuming anisotropic units. We dispersed force-generating microtubule bundles in a passive colloidal liquid crystal to form a three-dimensional active nematic. Light-sheet microscopy revealed the temporal evolution of the millimeter-scale structure of these active nematics with single-bundle resolution. The primary topological excitations are extended, charge-neutral disclination loops that undergo complex dynamics and recombination events. Our work suggests a framework for analyzing the nonequilibrium dynamics of bulk anisotropic systems as diverse as driven complex fluids, active metamaterials, biological tissues, and collections of robots or organisms.

The sinuous change in the orientation of birds flocking is a common but startling sight. Even if one can track the orientation of each bird, making sense of such large datasets is difficult. Similar challenges arise in disparate contexts from magnetohydrodynamics (*1*) to turbulent cultures of elongated cells (*2*), where oriented fields coupled to velocity undergo complex dynamics. To make progress with such extensive three-dimensional (3D) data, it is useful to identify effective degrees of freedom that allow a coarse-grained description of the collective nonequilibrium phenomena. Promising candidates are singular field configurations locally protected by topological rules (*3*–*9*). Examples of such singularities in 2D are the topological defects that appear at the north and south poles when covering the Earth's surface with parallel lines of longitude or latitude. These point defects are characterized by the winding number of the corresponding orientation field.

The quintessential systems with orientational order are nematic liquid crystals, which are fluids composed of anisotropic molecules. In equilibrium, nematics tend to minimize energy by uniformly aligning their anisotropic constituents, which annihilates topological defects. By contrast, in active nematic materials, which are internally driven away from equilibrium, the continual injection of energy destabilizes defect-free alignment (*10*, *11*). The resulting chaotic dynamics are effectively represented in 2D by point-like topological defects that behave as self-propelled particles (*12*–*16*). The defect-driven dynamics of 2D active nematics have been observed in many systems ranging from millimeter-sized shaken granular rods and micrometer-sized motile biological cells to nanoscale motor-driven biological filaments (*17*–*23*). Several obstacles have hindered generalizing topological dynamics of active nematics to 3D. The higher dimensionality expands the space of possible defect configurations. Discriminating between different defect types requires measurement of the spatiotemporal evolution of the director field on macroscopic scales using materials that can be rendered active away from surfaces.

The 3D active nematics that we assembled are based on microtubules and kinesin molecular motors. In the presence of a depleting agent, these components assemble into isotropic active fluids that exhibit persistent spontaneous flows (*17*). Replacing a broadly acting depletant with a specific microtubule cross-linker, PRC1-NS, enabled assembly of a composite mixture of low-density extensile microtubule bundles (~0.1% volume fraction) and a passive colloidal nematic based on filamentous viruses (Fig. 1A), a strategy that is similar to work on the living liquid crystal (*21*). Adenosine 5′-triphosphate (ATP)–fueled stepping of kinesin motors generates microtubule bundle extension and active stresses that drive the chaotic dynamics of the entire system (movie S1). Birefringence of the composite material indicates local nematic order (Fig. 1B), in contrast to active fluids lacking the passive liquid crystal component.

Elucidating the spatial structure of a 3D active nematic requires measurement of the nematic director field on scales from micrometers to millimeters. Furthermore, uncovering its dynamics requires acquisition of the director field with high temporal resolution. To overcome these constraints, we used a multiview light sheet microscope (Fig. 1C) (*24*). The spatiotemporal evolution of the nematic director field $\mathbf{n}(x,y,z,t)$ was extracted from a stack of fluorescent images using the structure tensor method. Spatial gradients of the director field identified regions with large elastic distortions (Fig. 1D and movie S2). Three-dimensional reconstruction of such maps revealed that large elastic distortions mainly formed curvilinear structures, which could either be isolated loops or belong to a complex network of system-spanning lines (Fig. 1E and movie S3). These curvilinear distortions are topological disclination lines characteristic of 3D nematics. Similar structures were observed in numerical simulations of 3D active nematic dynamics using either a hybrid lattice Boltzmann method or a finite difference Stokes solver numerical approach (Fig. 1F) (*25*, *26*).

Reducing the ATP concentration slowed down the chaotic flows, which revealed the temporal dynamics of the nematic director field. In turn, this identified the basic events governing the dynamics of disclination lines (movie S4). We focused on characterizing the closed loop disclinations because they are the objects seen to arise or annihilate in the bulk. Isolated loops nucleated and grew from undistorted, uniformly aligned regions (Fig. 2A, figs. S1 and S2, and movie S5). Likewise, loops also contracted and self-annihilated, leaving behind a uniform region (Fig. 2B, figs. S1 and S2, and movie S6). Furthermore, expanding loops frequently encountered and subsequently merged with the system-spanning network of distortion lines, whereas the distortion lines in the network self-intersected and reconnected to emit a new isolated loop (Fig. 2, C and D; figs. S1 and S2; and movies S7 and S8).

Topological constraints require that topological defects can only be created in sets that are, collectively, topologically neutral. Point-like defects in 2D active nematics thus always nucleate as pairs of opposite winding number (*13*). In 3D active nematics, an isolated disclination loop as a whole has two topological possibilities: It can either carry a

[1]Department of Physics, Brandeis University, Waltham, MA 02453, USA. [2]Department of Physics, University of California, Santa Barbara, CA 93111, USA. [3]Max Planck Institute for Dynamics and Self-Organization, 37077 Göttingen, Germany. [4]Instituut-Lorentz, Universiteit Leiden, 2300 RA Leiden, Netherlands. [5]Department of Physics, Brown University, Providence, RI 02912, USA. [6]School of Engineering, Brown University, Providence, RI 02912, USA. [7]Department of Applied Physics, Eindhoven University of Technology, 5600 MB Eindhoven, Netherlands. [8]Instituto per le Applicazioni del Calcolo CNR, 00185 Rome, Italy. [9]James Frank Institute and Department of Physics, The University of Chicago, Chicago, IL 60637, USA. [10]Department of Physics, University of California, Merced, CA 95343, USA.
*These authors contributed equally to this work.
†Corresponding author. Email: dbeller@ucmerced.edu (D.A.B.); zdogic@ucsb.edu (Z.D.)

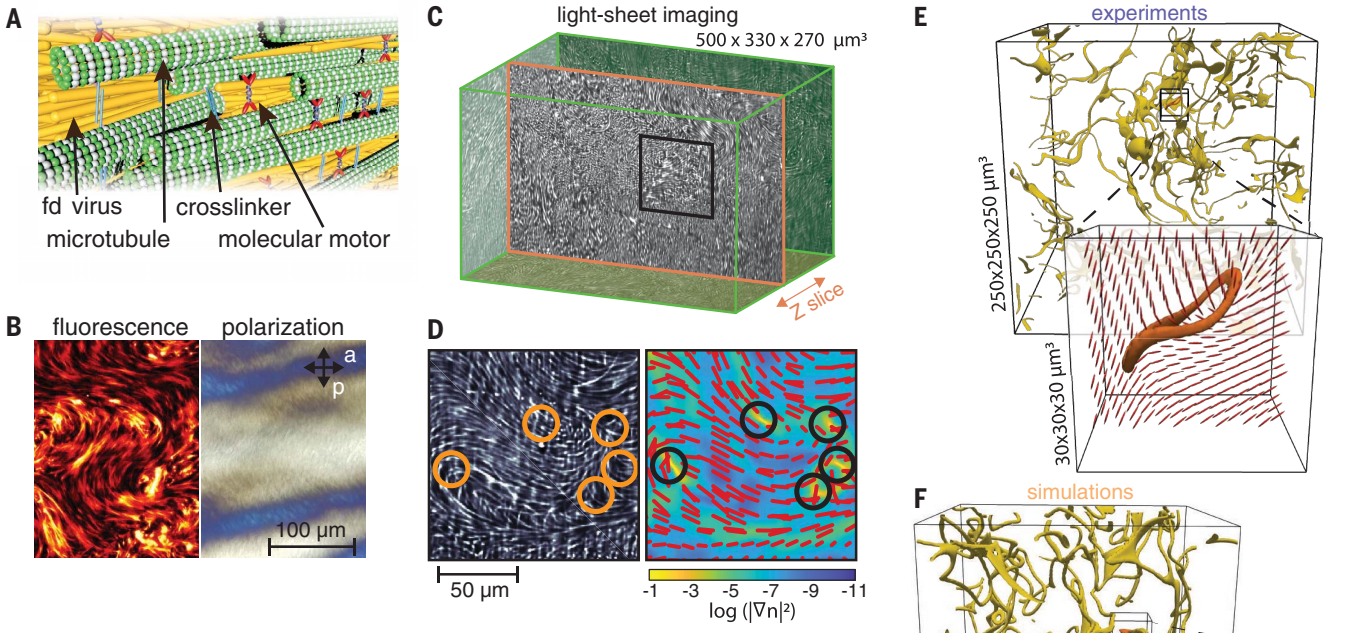


Fig. 1. Assembling 3D active nematics and imaging their director field. (**A**) Schematic of the 3D active nematic system: active stress–generating extensile microtubule bundles are dispersed in a passive colloidal liquid crystal. (**B**) Active 3D nematic imaged with widefield fluorescent microscopy (left) and polarized microscopy (right). Birefringence indicates local nematic order. (**C**) Multiview light sheet microscopy allows for 3D imaging of millimeter-sized samples with single-bundle resolution. (**D**) Left: A 2D slice of fluorescent microtubule bundles with highlighted elastic distortions. Right: Corresponding elastic distortion energy map, with an overlaid nematic director field (red). (**E**) Three-dimensional elastic distortion map revealing the presence of curvilinear rather than point-like singularities. An entangled network of lines coexists with isolated loops. (**F**) Hybrid lattice Boltzmann simulations yield a similar structure of 3D active nematics. All experimental samples consist of passive *fd* viruses at 25 mg/mL and microtubules at 1.33 mg/mL.

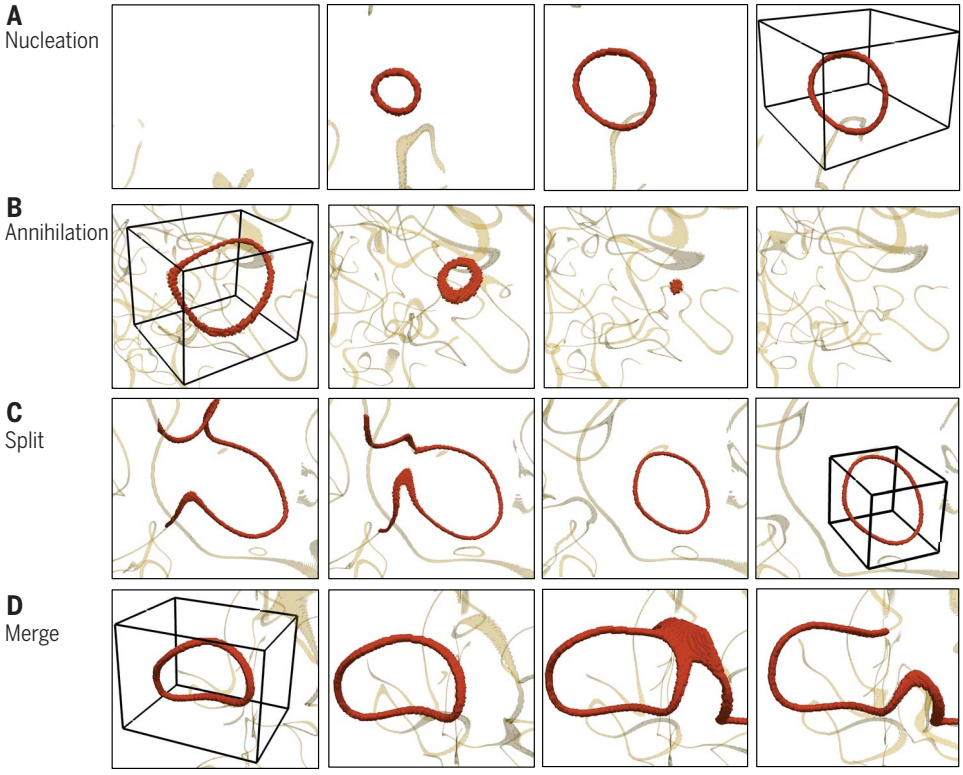


Fig. 2. Dynamics of experimentally observed disclination loops. (**A**) Loop nucleation from a defect-free region. (**B**) Loop self-annihilation leaves behind a defect-free nematic. (**C**) Disclination line self-intersects, reconnects, and emits a loop. (**D**) Disclination loop intersects, reconnects, and merges with a disclination line. Each bounding box is 30 × 30 × 38 μm. The time interval between two pictures is 12 s.

monopole charge or be topologically neutral, depending on its director winding structure. Because charged topological loops can only appear in pairs, nucleation of isolated loops as observed in our system implies their topological neutrality.

To establish that the closed-loop distortions are nematic disclination loops with no net charge, we characterized their topological structure. In 2D nematics, point-like disclination defects are characterized by the winding number or topological charge(s). The lowest-energy disclinations have $s = \pm 1/2$, which corresponds to a π rotation of the director field in the same sense or the opposite sense, respectively, as the traversal of any closed path encircling only the defect of interest. In 3D nematics, point-like defects

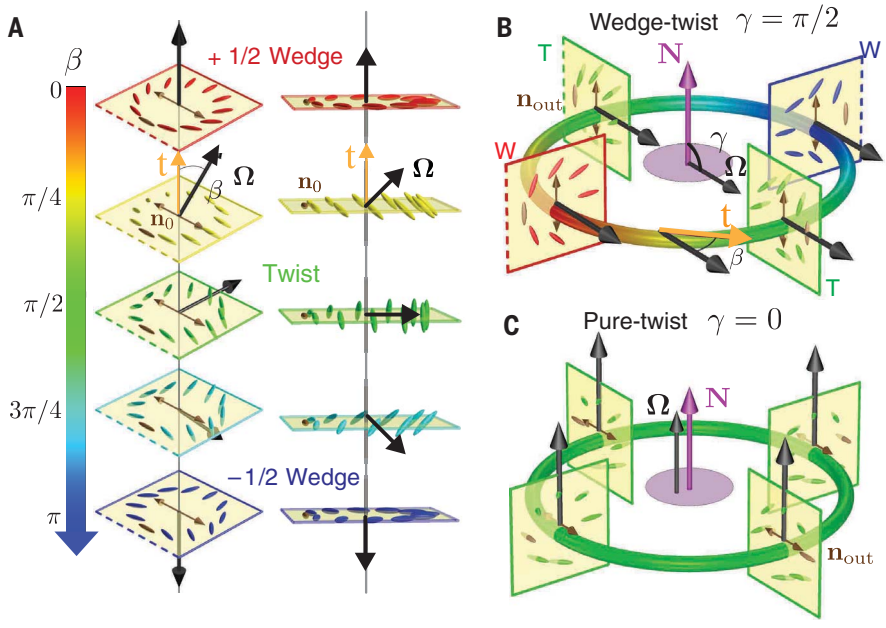


Fig. 3. Structure of disclinations lines, wedge-twist, and pure-twist loops. (**A**) Disclination line where a local +1/2 wedge winding continuously transforms into a −1/2 wedge through an intermediate twist winding. The director field winds by π about the rotation vector $\boldsymbol{\Omega}$ (black arrows), which makes angle β with the tangent **t** (orange arrow) and is orthogonal to the director field everywhere in each slice. For ±1/2 wedge windings, $\beta = 0$ and π. $\beta = \pi/2$ indicates local twist winding. Reference director $\mathbf{n_o}$ (brown) is held fixed. Color map indicates angle β. (**B**) Wedge-twist loop where local winding as reflected by angle β varies along the loop. $\boldsymbol{\Omega}$ is spatially uniform and forms an angle $\gamma = \pi/2$ with the loop's normal, **N**. The winding in the four illustrated planes corresponds to the profiles of the same colors shown in (A), with dashed edges of squares aligned to match the local director field. Double-headed brown arrows indicate $\mathbf{n_{out}}$, the director just outside the loop. (**C**) Pure-twist loop, with $\boldsymbol{\Omega}$ both uniformly parallel to loop normal **N** ($\gamma = 0$) and perpendicular to the tangent vector.

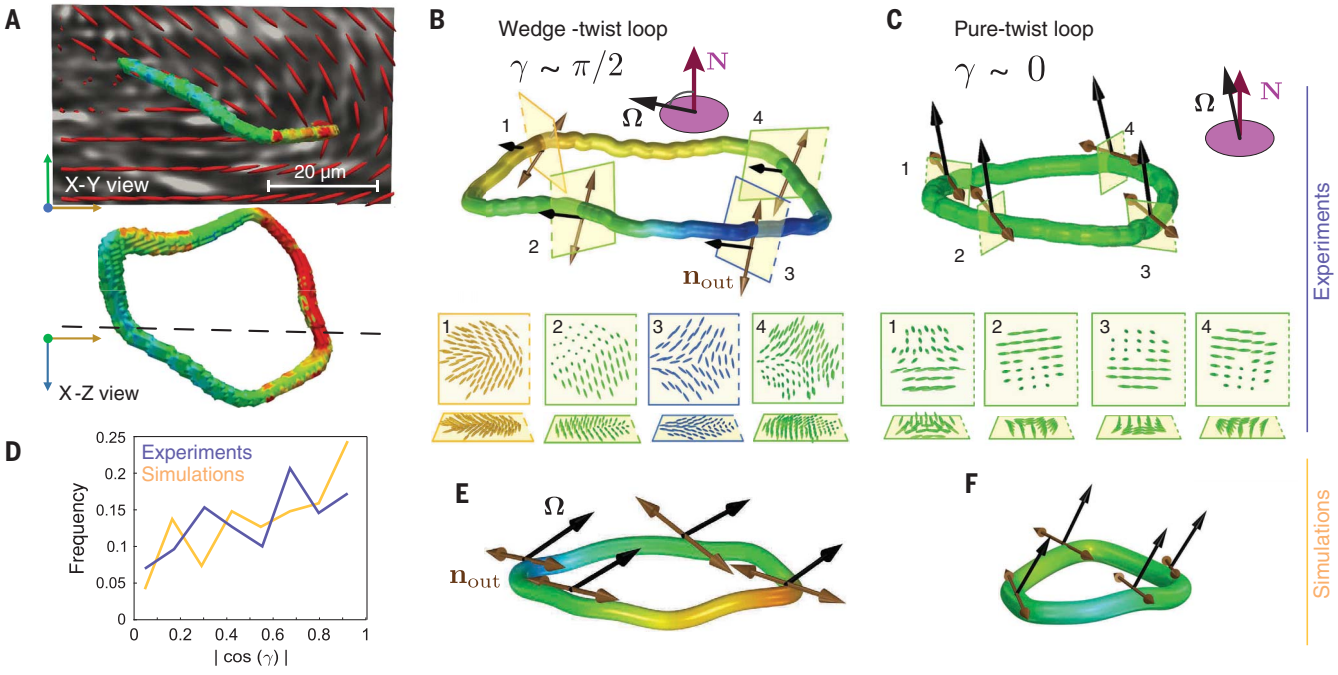


Fig. 4. Structure of disclination loops in experiments and theory. (**A**) Two orthogonal views of an experimental wedge-twist loop overlaid onto a fluorescent image of the microtubules. The nematic director is shown in red. (**B** and **E**) Structure of wedge-twist disclination loops in experiments and simulation. (**C** and **F**) Structure of pure-twist disclination loops from experiment and simulation. Panels show the director field's winding in the corresponding cross-sections on the experimental loops. (**D**) Distribution of loop types extracted from experiment ($N = 268$) and hybrid lattice Boltzmann simulations ($N = 94$). $|\cos(\gamma)| = 0$ for wedge-twist loops and 1 for pure-twist loops. Distributions of standard deviations of $|\cos(\gamma)|$ are shown in fig. S3. The count of simulated loops includes analysis of some loops at multiple time points because we did not track loop identity in the complex flow dynamics. Coloring of loops indicates the angle β. Scales and bounding boxes for the loops are shown in fig. S4.

from 2D systems are generalized to disclination lines, where the director similarly has a π winding, affording a broader variety of director configurations. We define **t** to be the disclination line's local tangent unit vector. The director field winds by π about a direction specified by **Ω**, the rotation vector, which can make an arbitrary angle β with **t** (*27*). If **Ω** points antiparallel or parallel to **t**, then the local director field rotates in the plane orthogonal to **t**, assuming the disclination profiles familiar from 2D nematics. These configurations in which β is equal to 0 or π are said to have a local wedge winding (Fig. 3A). If **Ω** is perpendicular to **t**, then $\beta = \pi/2$ and the director forms a spatially varying angle away from the orthogonal plane, locally creating what is called a twist winding. Because **Ω** may point in any direction relative to **t**, both **Ω** and β can vary continuously along a disclination line (movie S9).

For disclination lines forming loops, **Ω** can vary continuously providing it returns to its original orientation upon closure, leading to a broad range of possible winding variations. A family of loops of particular relevance to 3D active nematics is characterized by a spatially uniform **Ω**, interpolating between two emblematic geometries: wedge-twist and pure-twist loops. In the wedge-twist loop, **Ω** makes an angle $\gamma = \pi/2$ with the loop normal **N** (Fig. 3B). As the disclination's tangent **t** rotates by 2π upon traveling around the loop, the angle β varies from 0 (+1/2 wedge) to π/2 (twist), to π (−1/2 wedge), then back to π/2, and finally returning to 0 (movie S9) (*27*, *28*). The pure-twist loop has **Ω** uniformly parallel to **N**, so $\gamma = 0$ and **Ω** is perpendicular to **t** ($\beta = \pi/2$, twist profile) at all points on the loop (Fig. 3C) (*27*, *29*). In this family of loops, the director just outside the loop, $\mathbf{n}_{out}$, is also uniform. The lack of winding of both **Ω** and $\mathbf{n}_{out}$ implies that both wedge-twist and pure-twist loops are topologically neutral (*30*, *31*).

Experimental measurements of the director field allowed us to fully characterize the topological structure of the disclination loops (Fig. 4). Analysis of the director field indicated that the distortion lines and loops have the π winding indicative of disclinations (Fig. 1, E and F), with continuous variation of β, which indicates local winding. Furthermore, most of the analyzed loops were well approximated by the family of curves where **Ω** and $\mathbf{n}_{out}$ varied little along the loop circumferences. Categorizing loops according to their γ values revealed that the entire continuous family from wedge-twist (Fig. 4, A and B) to pure-twist (Fig. 4C) was represented, with the latter being more prevalent (Fig. 4D). Structural analysis revealed topological neutrality, as all 268 experimental loops and all 94 loops extracted from hybrid lattice Boltzmann simulations carried no charge. This demonstrates that among many possible configurations, topologically neutral loops are the dominant excitation mode of 3D active nematics. The same class of loop geometries also dominated the dynamics in our numerical simulations of bulk 3D active nematics and in confined active nematics (Fig. 4, E and F) (*25*, *26*, *32*, *33*). The phenomenology observed is a direct consequence of activity-induced flows and is insensitive to backflows induced by reactive stresses. This conclusion is supported by the agreement of results from the mechanical model considered in the hybrid lattice Boltzmann method and the purely kinematic Stokes method.

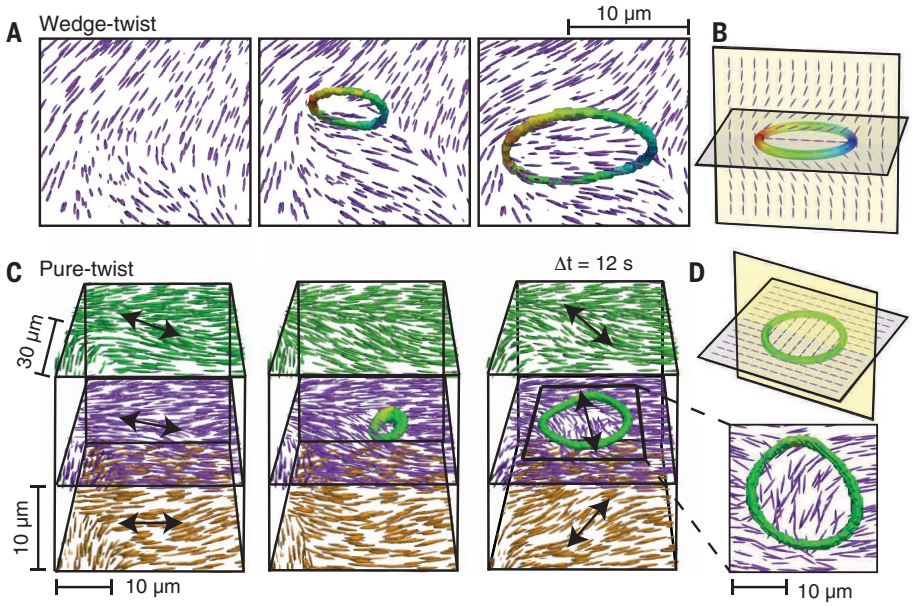


Fig. 5. Nucleation mechanism of wedge-twist and pure-twist loops. (**A**) Nucleation and growth of a wedge-twist disclination loop through a self-amplifying bend distortion. Purple rods represent the 2D director field through the local ±1/2 wedge profiles. (**B**) Schematic of a wedge-twist loop and the director field in the plane that intersects ±1/2 wedge profiles. (**C**) Pure-twist disclination loop nucleates and grows from a local twist distortion (movie S10). Black arrows indicate the local buildup of the twist distortion. Insert shows the top view of a growing twist disclination loop. (**D**) Schematic of a pure-twist loop and the director field in the loop's plane.

In 2D active nematics, self-amplifying bend distortions give rise to the nucleation of a pair of topological defects of opposite charge (*12*–*18*). Nucleation of isolated, topologically neutral wedge-twist loops are the 3D analog of the 2D defect-creation process. Specifically, a cross-section through the +1/2 and −1/2 wedge profiles recalls unbinding of a pair of point disclinations in 2D (Fig. 5, A and B). The +1/2 wedge profile typically appears on the side of the growing bend distortion, oriented away from the −1/2 wedge profile. Similarly, wedge-twist loops with the +1/2 wedge profile oriented inward toward the −1/2 wedge are driven to shrink by active and passive stresses. Unlike in 2D active nematics, after nucleation, the wedge profiles remain bound to each other through a disclination loop that includes points with a local twist winding. It is possible that some analyzed pure-twist loops have evolved from wedge-twist loops by continuous deformation of local winding character. However, both simulations and experiments showed cases of loop nucleation in nearly pure-twist ($\gamma \approx 0$) geometries from previously defect-free regions. Local active nematic stresses alone are not expected to drive growth of a pure-twist loop (Fig. 5D). One possibility is that long-range hydrodynamic flows build up twist distortions that locally relax through creation of a pure-twist loop (Fig. 5C and movie S10).

By coupling a flow field to an orientational order parameter with curvilinear topological defects, 3D active nematics display dynamics even more complex than the chaotic flows of 2D active systems. Combined with emerging theoretical work (*32*, *33*), the experimental model system described herein offers a platform with which to investigate the role of topology, dimensionality, and material order in the chaotic internally driven flows of active soft matter. Furthermore, the use of a multiview light sheet imaging technique demonstrates its potential to unravel dynamical processes in diverse nonequilibrium soft materials, such as relaxation of nematic liquid crystals upon a quench or their deformation under external shear flow (*3*, *34*).

REFERENCES AND NOTES

1. S. Galtier, *Introduction to Modern Magnetohydrodynamics* (Cambridge Univ. Press, ed. 1, 2016).
2. C. Blanch-Mercader *et al*., *Phys. Rev. Lett.* **120**, 208101 (2018).
3. M. J. Bowick, L. Chandar, E. A. Schiff, A. M. Srivastava, *Science* **263**, 943–945 (1994).
4. P. Poulin, H. Stark, T. C. Lubensky, D. A. Weitz, *Science* **275**, 1770–1773 (1997).
5. A. R. Bausch *et al*., *Science* **299**, 1716–1718 (2003).
6. W. T. Irvine, V. Vitelli, P. M. Chaikin, *Nature* **468**, 947–951 (2010).
7. M. W. Scheeler, W. M. van Rees, H. Kedia, D. Kleckner, W. T. M. Irvine, *Science* **357**, 487–491 (2017).
8. A. Martinez *et al*., *Nat. Mater.* **13**, 258–263 (2014).
9. U. Tkalec, M. Ravnik, S. Čopar, S. Žumer, I. Muševič, *Science* **333**, 62–65 (2011).
10. R. Aditi Simha, S. Ramaswamy, *Phys. Rev. Lett.* **89**, 058101 (2002).
11. D. Marenduzzo, E. Orlandini, M. E. Cates, J. M. Yeomans, *Phys. Rev. E Stat. Nonlin. Soft Matter Phys.* **76**, 031921 (2007).
12. S. Shankar, S. Ramaswamy, M. C. Marchetti, M. J. Bowick, *Phys. Rev. Lett.* **121**, 108002 (2018).
13. L. Giomi, M. J. Bowick, P. Mishra, R. Sknepnek, M. Cristina Marchetti, *Philos. Trans. A Math. Phys. Eng. Sci.* **372**, 20130365 (2014).
14. T. Gao, R. Blackwell, M. A. Glaser, M. D. Betterton, M. J. Shelley, *Phys. Rev. Lett.* **114**, 048101 (2015).
15. S. P. Thampi, R. Golestanian, J. M. Yeomans, *EPL* **105**, 18001 (2014).
16. X. Q. Shi, Y. Q. Ma, *Nat. Commun.* **4**, 3013 (2013).
17. T. Sanchez, D. T. Chen, S. J. DeCamp, M. Heymann, Z. Dogic, *Nature* **491**, 431–434 (2012).
18. V. Narayan, S. Ramaswamy, N. Menon, *Science* **317**, 105–108 (2007).
19. K. Kawaguchi, R. Kageyama, M. Sano, *Nature* **545**, 327–331 (2017).
20. T. B. Saw *et al*., *Nature* **544**, 212–216 (2017).
21. S. Zhou, A. Sokolov, O. D. Lavrentovich, I. S. Aranson, *Proc. Natl. Acad. Sci. U.S.A.* **111**, 1265–1270 (2014).
22. N. Kumar, R. Zhang, J. J. de Pablo, M. L. Gardel, *Sci. Adv.* **4**, eaat7779 (2018).
23. H. Li *et al*., *Proc. Natl. Acad. Sci. U.S.A.* **116**, 777–785 (2019).
24. U. Krzic, S. Gunther, T. E. Saunders, S. J. Streichan, L. Hufnagel, *Nat. Methods* **9**, 730–733 (2012).
25. G. Duclos *et al*., Experimental director field data, the code to detect and analyze the topological loops and the Stokes solver for: Topological structure and dynamics of three-dimensional active nematics, Dryad (2020); https://doi.org/10.25349/D9CS31.
26. D. Banerjee *et al*., Data from numerical simulations of topological structure and dynamics of three-dimensional active nematics. 4TU.Centre for Research Data (2020); https://doi.org/10.4121/uuid:5c8ea40a-19d5-4ecb-893a-c93f238a494c.
27. J. Friedel, P. De Gennes, *CR Acad. Sc. Paris B* **268**, 257–259 (1969).
28. T. Emeršič *et al*., *Sci. Adv.* **5**, eaav4283 (2019).
29. E. M. Terentjev, *Phys. Rev. E Stat. Phys. Plasmas Fluids Relat. Interdiscip. Topics* **51**, 1330–1337 (1995).
30. G. P. Alexander, B. G. Chen, E. A. Matsumoto, R. D. Kamien, *Rev. Mod. Phys.* **84**, 497–514 (2012).
31. S. Čopar, S. Žumer, *Proc. Royal Soc. Math. Phys. Eng. Sci.* **469**, 20130204 (2013).
32. S. Čopar, J. Aplinc, Ž. Kos, S. Žumer, M. Ravnik, *Phys. Rev. X* **9**, 031051 (2019).
33. T. N. Shendruk, K. Thijssen, J. M. Yeomans, A. Doostmohammadi, *Phys. Rev. E* **98**, 010601 (2018).
34. M. S. Lavine, A. H. Windle, *Macromol. Symp.* **124**, 35–47 (1997).

ACKNOWLEDGMENTS

We thank B. Lemma, R. Subramanian, and M. Ridilla for help in protein purification. D.A.B. acknowledges S. Čopar, S. Žumer, and M. Ravnik for helpful discussions on disclinations in 3D active nematics. **Funding:** Experimental work was supported by the U.S. Department of Energy, Office of Basic Energy Sciences, through award DE-SC0019733 (G.D., R.A., I.K., and Z.D.). G.D. and I.K. also acknowledge support from HFSP fellowships. R.A. acknowledges support from NSF-GRFP. Theoretical modeling was supported by NSF-DMR-1855914, NSF-MRSEC-1420382, and NSF-CBET-1437195 (D.A.B., M.P., M.V., Ar.B., Ap.B., M.F.H., R.A.P., and T.R.P.). Computational resources were provided by the NSF through XSEDE computing resources (MCB090163) and TU/e through the F&F computing cluster. We also acknowledge use of the Brandeis optical, HPCC, and biosynthesis facilities supported by NSF-MRSEC-1420382. D.B. was supported by FOM and NWO. V.V. was supported by the Army Research Office under grant W911NF-19-1-0268 and NSF-MRSEC (DMR-1420709). S.J.S. was supported by NIH-R00 award 5R00HD088708-05. D.A.B. thanks the Isaac Newton Institute for Mathematical Sciences for support during the program "The Mathematical Design of New Materials," supported by EPSRC grant EP/R014604/1. **Author contributions:** G.D., I.K., S.J.S., and R.A. conducted experimental research; G.D., I.K., S.J.S., R.A., M.S.P., and D.A.B. analyzed experimental and theoretical data. D.B., F.T., and V.V. developed hybrid lattice Boltzmann simulations. M.S.P., M.V., Ar.B., Ap.B., and M.F.H. developed and applied finite difference Stokes solver code. D.A.B., R.P., and T.R.P. conducted theoretical modeling and interpretation of data. G.D., V.V., Ap.B., M.F.H., D.A.B., and Z.D conceived the work. G.D., D.A.B., V.V., and Z.D. wrote the manuscript. All authors reviewed the manuscript. **Competing interests:** The authors declare no competing interests. **Data and materials availability:** Experimental director field data, the code to detect and analyze the topological loops, and the Stokes solver are available on Dryad (*25*). Lattice Boltzmann code and director generated by this code are available on REPOSITORY (*26*).

SUPPLEMENTARY MATERIALS

science.sciencemag.org/content/367/6482/1120/suppl/DC1
Materials and Methods
Supplementary Text
Figs. S1 to S4
Captions for Movies S1 to S10
References (*35*–*53*)

16 September 2019; accepted 7 February 2020
10.1126/science.aaz4547

ELECTRON MICROSCOPY

Single-atom vibrational spectroscopy in the scanning transmission electron microscope

F. S. Hage[1], G. Radtke[2]*, D. M. Kepaptsoglou[1,3], M. Lazzeri[2], Q. M. Ramasse[1,4]*

Single-atom impurities and other atomic-scale defects can notably alter the local vibrational responses of solids and, ultimately, their macroscopic properties. Using high-resolution electron energy-loss spectroscopy in the electron microscope, we show that a single substitutional silicon impurity in graphene induces a characteristic, localized modification of the vibrational response. Extensive ab initio calculations reveal that the measured spectroscopic signature arises from defect-induced pseudo-localized phonon modes—that is, resonant states resulting from the hybridization of the defect modes and the bulk continuum—with energies that can be directly matched to the experiments. This finding realizes the promise of vibrational spectroscopy in the electron microscope with single-atom sensitivity and has broad implications across the fields of physics, chemistry, and materials science.

Changes in the normal mode frequencies of dynamical systems that arise from the presence of impurities have been studied since the 19th century, which has resulted in the set of classical theorems now referred to as the Rayleigh theorems (*1*, *2*). However, the modern theory of defect modes in crystals was established in the 1940s with the pioneering work of Lifschitz (*3*). Many studies followed, mainly based on optical spectroscopies (*4*), which identified two types of nontrivial defect-induced modes known as localized and resonant modes. Resonant modes are also called quasi- or pseudo-localized modes because, despite being spatially extended, they involve a large-amplitude vibration of the impurity itself. Defect modes can control materials' properties such as electric and heat transport or, more generally, processes that are affected by the scattering of electrons or phonons. This can be exploited, for example, to suppress heat propagation in thermoelectrics using rattler modes (*5*), to tune the superconductivity in two-dimensional films (*6*), or to affect the optoelectronic properties of conducting polymers (*7*). Although the existence of an atomically localized spectroscopic signature of single-atom defects has long been discussed (*8*), conventional vibrational spectroscopies typically average information over much larger length scales.

Vibrational electron energy-loss spectroscopy (EELS) in the scanning transmission electron microscope (STEM) has recently emerged as a powerful means of probing the vibrational response of materials at a spatial resolution that is superior to that of other experimental techniques (*9*, *10*). Tip-enhanced Raman spectroscopy (TERS) (*11*) and inelastic electron tunneling spectroscopy (IETS) (*12*, *13*) provide high spatial and energy resolution alternatives, but they are strictly limited to surface experiments and, therefore, present challenges for a range of applications. Vibrational STEM-EELS, on the other hand, takes advantage of versatile probe-forming optics to offer ground-breaking capabilities: nanometer-scale thermometry (*14*), mapping of bulk and surface-phonon-polariton modes (*15*), establishing phonon dispersion diagrams from nano-objects (*16*), and site-specific isotopic labeling in molecular aggregates (*17*). These reports highlight the complementarity of STEM-EELS with conventional vibrational spectroscopies whose energy resolutions remain unmatched. However, the ultimate promise of vibrational STEM-EELS is the ability to reach the single-atom or molecular level, in the same way that modern microscopes have enabled electronic structure analysis (*18*), plasmonic (*19*) and UV-optical response fingerprinting (*20*), and energy-dispersive x-ray spectroscopy (*21*) from single atoms. Atomically resolved phonon maps of bulk systems are preliminary steps in this direction (*22*).

In this work, we use STEM-EELS to measure the localized vibrational signature of a single trivalent substitutional Si atom in single-layer graphene (Si@Gr). From ab initio simulations, we attribute the measured atomic-scale spectroscopic response to scattering by pseudo-localized vibrational modes arising from a resonance between the Si impurity–specific modes and the bulk continuum.

Figure 1A illustrates how electron beam deflectors are adjusted to displace the EEL spectrometer entrance aperture by 69 mrad (or an 8.87-Å^{-1} momentum transfer) with respect to the bright field (BF) disc so that these no longer overlap. Further details of the experimental geometry are provided in the supplementary materials (fig. S1). Compared with a conventional on-axis geometry, where the EELS aperture is centered on the BF disc, this off-axis or dark-field EELS geometry markedly suppresses the relative contributions of electrons having undergone elastic and delocalized phonon scattering, favoring instead highly localized impact phonon scattering (*23*). This approach makes it possible to record atomic-resolution phonon scattering maps of nanometer-thick flakes of hexagonal boron nitride (*22*) or of single-layer graphene (fig. S2), where the off-axis geometry is key because the on-axis EELS phonon response of graphene is vanishingly small (*24*). Note that the large beam convergence that is necessary for an atomic-sized probe results in spectral integration over a range of momentum transfer in the sample plane. To achieve a signal-to-noise ratio sufficient for resolving the phonon loss spectrum fine structure, the electron beam is scanned repeatedly over a small window, tightly defined around the impurity of interest, while the spectrum intensity is accumulated (*25*).

Figure 1B shows a dark-field EEL spectrum from a single Si atom impurity in graphene (labeled Si) alongside that acquired from a comparably sized region of pristine graphene (labeled C), located only a few atoms away from the Si impurity. The relative positions of the two scanned regions are indicated by red (Si) and blue (C) boxes on the high-angle annular dark-field (HAADF) image in Fig. 1C. A close-up of the probed Si atom (Fig. 1D) and the corresponding fine structure of the Si $L_{2,3}$ ionization edge (fig. S3C) confirm that the brighter-contrast Si atom is trivalently substituted into the graphene lattice. Asymmetric annular dark-field (aADF, thus denoted because of the off-axis geometry) movies were recorded during spectrum acquisition to monitor possible beam-induced structure modifications, while ensuring that the probed atom remained centered within the scanned region. Averaged aADF movies are shown as insets in Fig. 1B, with individual frames shown in the supplementary materials.

The Si and C spectra in Fig. 1B are normalized to the maximum of their respective zero-loss peaks (ZLPs). As a result, the tails of the ZLPs closely overlap immediately before the first observable loss features, which allows for a straightforward visual comparison of relative changes in energy loss caused by inelastic scattering by phonons. Any change in spectrum intensity above the coinciding ZLP tails should be representative of differences in relative phonon scattering probability. The fine structure in the phonon energy range of the two recorded spectra is strikingly different. Although the C spectrum is consistent with that of nondoped bulk graphene (*24*), the Si spectrum comprises phonon loss features at different energies.

[1]SuperSTEM Laboratory, SciTech Daresbury Campus, Daresbury WA4 4AD, UK. [2]Sorbonne Université, Muséum National d'Histoire Naturelle, UMR CNRS 7590, Institut de Minéralogie, de Physique des Matériaux et de Cosmochimie, 75005 Paris, France. [3]York Nanocentre and Department of Physics, University of York, Heslington, York YO10 5DD, UK. [4]School of Chemical and Process Engineering and School of Physics and Astronomy, University of Leeds, Leeds LS2 9JT, UK.
*Corresponding author. Email: qmramasse@superstem.org (Q.M.R.); guillaume.radtke@sorbonne-universite.fr (G.R.)

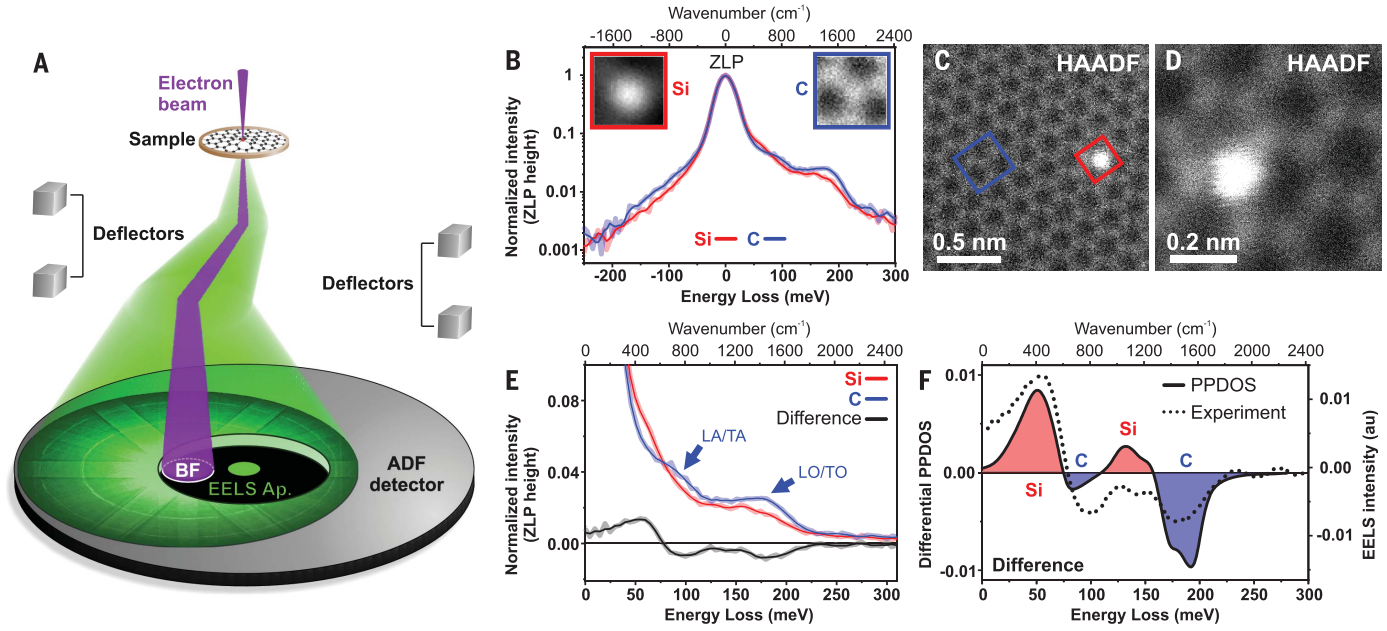


Fig. 1. Experimental geometry and vibrational STEM-EEL spectrum of a Si impurity in graphene. (**A**) Beam deflectors shift the BF disc away from the EEL spectrometer entrance aperture (Ap.) in the diffraction plane. (**B**) Normalized vibrational EEL spectra of a substitutional Si impurity and of defect-free graphene. Insets show aADF images of the repeatedly scanned sample regions. Smoothed spectra (thin lines) are superimposed on the raw data (shading around the lines). (**C**) HAADF overview of the experimental region. Red and blue boxes indicate the positions of the sub-scan regions from which the Si and C spectra, respectively, were acquired. (**D**) HAADF close-up of the (bright) trivalent Si impurity. (**E**) Detail of the normalized Si and C EEL spectra shown in (B) and the difference spectrum. L, longitudinal; T, transverse; A, acoustic; O, optical. (**F**) Comparison of the calculated differential PPDOS (broadened to match the experimental resolution) and the experimental difference spectrum. The blue and red shaded areas highlight energy ranges where the contributions of the Si impurity and its three nearest neighbors, or that of bulk graphene, are comparatively stronger. au, arbitrary units.

Figure 1E shows, in greater detail, the phonon loss region of the spectra. The C spectrum exhibits two distinct loss peaks at 85 meV (685 cm^{-1}) and 170 meV (1371 cm^{-1}). Following (*24*), we attribute these peaks to scattering by transverse (T) or longitudinal (L), acoustic (A) or optical (O) modes in graphene, respectively (the graphene-phonon dispersion diagram is presented for reference in fig. S10). Spectral contributions of out-of-plane phonon modes are expected to be negligible, as the incident electron beam is normal to the graphene plane. Despite stemming from a position only a few atoms away, the Si spectrum shows a remarkably different phonon fine structure comprising a prominent loss peak at about 55 meV (443 cm^{-1}) and weaker structures at 125 and 150 meV (1008 and 1209 cm^{-1}). To enhance the differences between the spectra, we subtracted the C from the Si spectrum, and the resulting difference spectrum is shown in Fig. 1, E and F. This has the additional benefit of effectively subtracting the elastic scattering ZLP tail (making the reasonable assumption that the tail contribution, before any expected loss contribution, is similar between spectra) without possible errors associated with common background removal techniques, as discussed in the supplementary materials (fig. S4). Thus, the difference can be interpreted as a relative change in phonon scattering probability induced by the presence of the single Si atom impurity. Virtually identical results (detailed in the supplementary materials) were obtained from complementary measurements carried out in a different area of the sample. These experimental results lead to the remarkable conclusion that the single Si atom impurity in graphene possesses a characteristic vibrational signature localized at the atomic scale.

To gain insights into the physics associated with these results, we have calculated, within the framework of density functional theory (DFT) (*26*) and using periodic boundary conditions, the vibrational spectrum of a large 96×96 supercell of graphene (96 unit cells by 96 unit cells) containing one substitutional Si atom. The structure of the defect and computational details are presented in the supplementary materials. As discussed therein, the important features observed in the vibrational EEL spectra of graphene can be safely interpreted in terms of the phonon density of states (DOS) of the bulk. The local behavior of the DOS can be quantified by the projected phonon DOS (PPDOS), defined as $n^{\kappa}(\omega) = \sum_{\nu} |\mathbf{e}_{\nu}^{\kappa}|^2 \delta(\omega - \omega_{\nu})$, where κ denotes a specific atom, ω_{ν} and $\mathbf{e}_{\nu}$ are the phonon angular frequency and normalized polarization, and the sum is carried over all the phonon modes, ν, of the supercell. Because the momentum transfer occurs predominantly in the plane perpendicular to the electron beam trajectory in our experiments, only the components of the phonon polarization that are parallel to the graphene plane are relevant. A tentative comparison to the experimental difference spectrum is then provided by combining the PPDOS projected on the Si atom, n^{Si}; the PPDOS projected on its three C neighbors, n^{C1}; and the bulk phonon DOS per atom, n^{bulk}: $\tilde{n}(\omega) = [n^{Si}(\omega) + 3n^{C1}(\omega) - 4n^{bulk}(\omega)]/4$. This differential PPDOS reflects the experimental spectrum averaging over the scanning window, which is expected to include contributions from the impurity's neighboring C atoms. The resulting differential PPDOS is shown in Fig. 1F, after broadening to match the experimental resolution. It predicts all the main features of the experimental difference spectrum, including a single peak at ~55 meV (443 cm^{-1}), two overlapping peaks at 125 and 150 meV (1008 and 1209 cm^{-1}), and dips centered around 100 and 180 meV (807 and 1452 cm^{-1}).

The physical origin of these spectral features can be understood by considering the individual in-plane PPDOS employed to construct the differential PPDOS, $\tilde{n}$, and the PPDOS of C atoms located at increasing distances away from the Si impurity (Fig. 2A). The Si PPDOS is dominated by an intense peak at 55 meV, closely matching the low-energy experimental

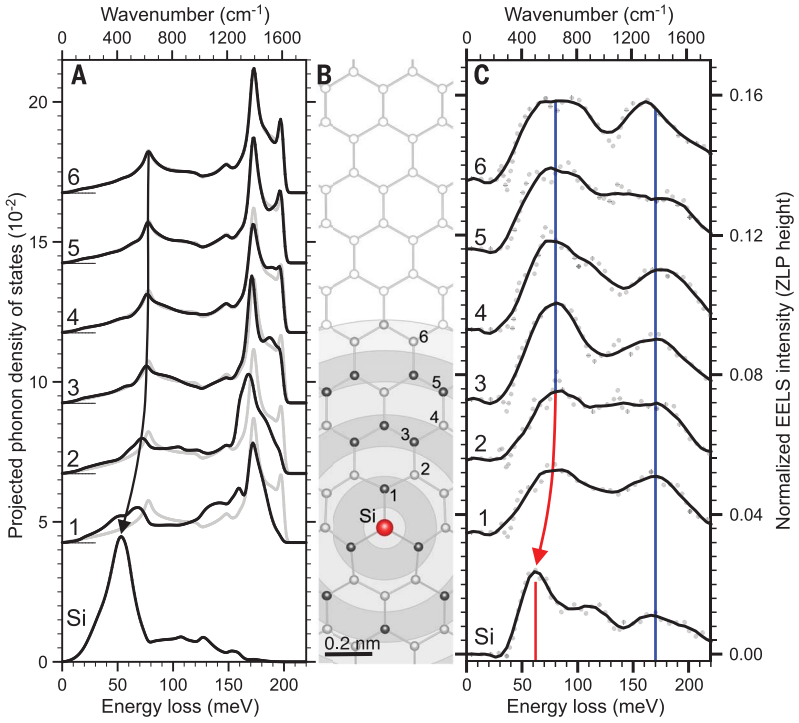


Fig. 2. Localization of the vibrational signal. (**A**) Calculated in-plane component of the phonon DOS projected on the Si and C atoms at increasing distances from the impurity. Overlaid light gray lines show the bulk graphene phonon DOS per atom, fully recovered from atom 6. The curves are vertically shifted and smeared by a 2-meV FWHM Lorentzian for clarity. (**B**) Sketch of the position of the C atoms, labeled 1 to 6, and Si impurity (red sphere). (**C**) Background-subtracted experimental spectra acquired at equivalent atomic positions. Smoothed (black lines) and raw (gray dots) data are overlaid.

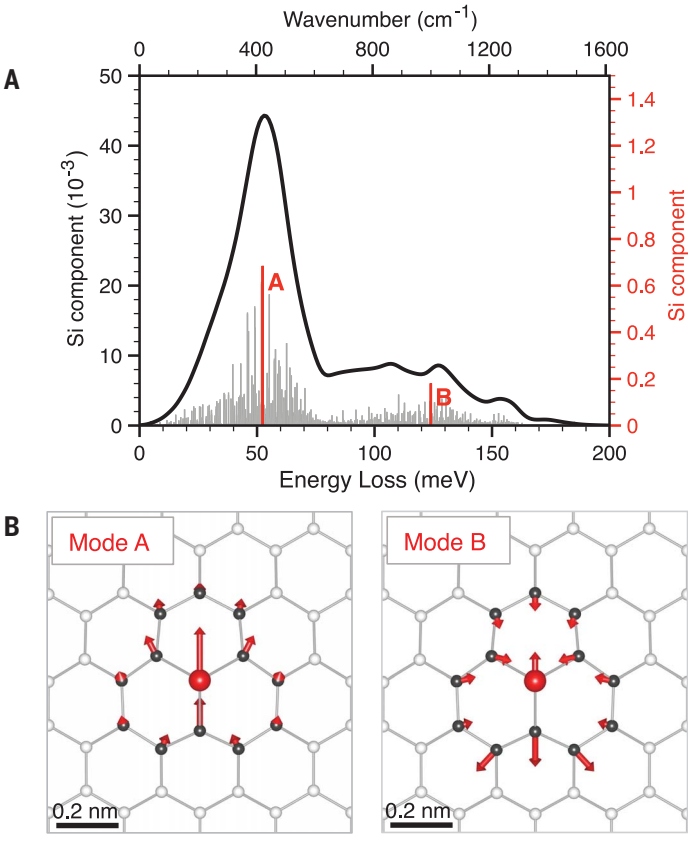


Fig. 3. Localized components of the Si vibrations. (**A**) Gray histogram shows the square of the phonon eigenmodes of the 96×96 supercell projected on the in-plane Si atom component. Black line indicates the in-plane component of the phonon DOS projected on the Si atom (same as the Si PPDOS shown in Fig. 2) obtained by broadening the gray histogram with a 2.0-meV FWHM Lorentzian. The red histogram is calculated from a 13-atom fragment centered on the impurity. Two dominant modes, denoted A and B, are observed. (**B**) Atomic model of the 13-atom fragment (the Si atom is shown in red), with relative atomic displacements for modes A and B indicated as arrows with lengths proportional to the displacement amplitudes.

feature seen in Fig. 1E. This peak is followed by a broad band with weaker structures at 105, 127, and 155 meV (847, 1024, and 1250 cm^{-1}).

The absence of intense features in the bulk graphene DOS at 55 meV implies that the corresponding modes should possess a degree of localization. By inspecting the PPDOS of neighboring C atoms in Fig. 2, it is evident that, although the first two C neighbor shells coordinating the impurity still display traces of the 55 meV peak, its contribution is weak. The PPDOS of subsequent neighbors rapidly tends toward the bulk signature, which is fully retrieved after six shells. Corresponding atomically resolved experimental spectra in Fig. 2C, from a full-spectrum image over equivalent C neighbor positions (fig. S8), exhibit an identical trend: The EELS signal reproduces the main features observed in the in-plane PPDOS.

It is instructive to consider a calculation performed on a smaller 13-atom fragment of C_{3v} symmetry centered on the impurity (fig. S9), decoupled from the supercell by artificially setting the interatomic force constants linking the fragment to the rest of the 96×96 supercell to zero. The fragment displays two modes with E symmetry at 52 and 124 meV (419 and 1000 cm^{-1}), involving large in-plane displacements of the Si atom either in phase (mode A) or out of phase (mode B) with the neighboring C atoms (Fig. 3). The resonances in the full Si@Gr system, simulated by the 96×96 supercell, can thus be interpreted as a hybridization of these local impurity modes with the vibrational continuum of the graphene bulk.

The associated atomic displacements, including those arising from the in-plane vibration of the Si atom, do not decay far from the defect; the full system presents a delocalized continuum, a concept quantified with the inverse participation ratio analysis shown in the supplementary materials. However, these delocalized phonon modes possess an enhanced component atomically localized on the impurity. The power of EELS is the technique's ability to probe this quasi-localization, thereby revealing the paradoxical nature of defect-induced resonant modes. It is also notable that the experimentally measured ~30 meV (242 cm^{-1}) full-width at half-maximum (FWHM) of the impurity peak at ~55 meV (Fig. 1F) closely matches the intrinsic theory-predicted width of the resonant mode (Fig. 3A). The experimental energy resolution is therefore not limiting, and the EEL spectra faithfully capture the fine structure of the Si@Gr system's vibrational response.

Localized and resonant modes arising from point defects have been widely discussed (*8*). The former are characterized by frequencies lying out of the continuum of the unperturbed crystal and atomic amplitudes dying off faster-than-exponentially with increasing distance from the defect (*27*). By contrast, the latter

occur at frequencies lying within the allowed bands of the host. The recognition of resonant modes was delayed by their peculiar characteristics, where the vibrational amplitude does not vanish far from the defect, extending instead over the entire crystal (*28*). Furthermore, experimental observations of these effects have, thus far, been limited to indirect fingerprints, often at the macroscopic scale. Volgmann *et al.* (*13*) used scanning probe microscope (SPM)–IETS to detect a local energy-dependent increase in phonon DOS on a Ag (100) surface, which they attributed to a substitutional Cu atom. However, the surface nature of these experiments and the lack of more direct visualization means precluded an unambiguous interpretation.

In contrast, the ability demonstrated in this work to directly measure, at the atomic scale, the localized component of the vibrational signature of a single impurity atom within a solid, and to match the observed spectral fine structure to theoretically predicted modes, realizes the potential of phonon spectroscopy in the STEM. The STEM-EELS technique, characterized by single-atom defect sensitivity combined with isotope selectivity (*17*) and the ability to operate at cryogenic temperatures (*29*), now enables potential experiments where a single functionalizing isotope is fingerprinted at the atomic scale through its vibrational signature. The approach should be applicable to three-dimensional structures, although challenges will arise from the complexity of the computational work necessary to inform these experiments. Nevertheless, this opens up a path to further applications in solid-state science, where the electron beam of the STEM can be used to assemble functional devices atom by atom (*30*) and to spectroscopically probe the resulting lattice dynamics and their coupling with other quasiparticles.

REFERENCES AND NOTES

1. W. R. Hamilton, *Philos. Trans. R. Soc.* **124**, 247–308 (1834).
2. J. W. Strutt, *The Theory of Sound* (Cambridge Univ. Press, 1887).
3. I. M. Lifšic, *Nuovo Cim.* **3**, 716–734 (1956).
4. A. S. Barker, A. J. Sievers, *Rev. Mod. Phys.* **47**, S1–S179 (1975).
5. D. J. Voneshen *et al.*, *Nat. Mater.* **12**, 1028–1032 (2013).
6. C. Brun *et al.*, *Nat. Phys.* **10**, 444–450 (2014).
7. M. Shao *et al.*, *Nat. Commun.* **5**, 3180 (2014).
8. R. F. Wallis, Ed., *Localized Excitations in Solids* (Springer, 1968).
9. O. L. Krivanek *et al.*, *Nature* **514**, 209–212 (2014).
10. T. Miyata *et al.*, *Microscopy* **63**, 377–382 (2014).
11. P. Z. El-Khoury *et al.*, *Adv. Phys. X.* **1**, 35–54 (2016).
12. H. Gawronski, M. Mehlhorn, K. Morgenstern, *Science* **319**, 930–933 (2008).
13. K. Volgmann *et al.*, *Nat. Commun.* **5**, 5089 (2014).
14. J. C. Idrobo *et al.*, *Phys. Rev. Lett.* **120**, 095901 (2018).
15. M. J. Lagos, A. Trügler, U. Hohenester, P. E. Batson, *Nature* **543**, 529–532 (2017).
16. F. S. Hage *et al.*, *Sci. Adv.* **4**, eaar7495 (2018).
17. J. A. Hachtel *et al.*, *Science* **363**, 525–528 (2019).
18. K. Suenaga, M. Koshino, *Nature* **468**, 1088–1090 (2010).
19. W. Zhou *et al.*, *Nature Nanotech.* **7**, 161–165 (2012).
20. F. S. Hage *et al.*, *ACS Nano* **12**, 1837–1848 (2018).
21. T. C. Lovejoy *et al.*, *Appl. Phys. Lett.* **100**, 154101 (2012).
22. F. S. Hage, D. M. Kepaptsoglou, Q. M. Ramasse, L. J. Allen, *Phys. Rev. Lett.* **122**, 016103 (2019).
23. C. Dwyer *et al.*, *Phys. Rev. Lett.* **117**, 256101 (2016).
24. R. Senga *et al.*, *Nature* **573**, 247–250 (2019).
25. Q. M. Ramasse *et al.*, *Nano Lett.* **13**, 4989–4995 (2013).
26. P. Giannozzi *et al.*, *J. Phys. Condens. Matter* **21**, 395502 (2009).
27. E. W. Montroll, R. B. Potts, *Phys. Rev.* **100**, 525–543 (1955).
28. R. Brout, W. Visscher, *Phys. Rev. Lett.* **9**, 54–55 (1962).
29. M. T. Hotz *et al.*, *Microsc. Microanal.* **24**, 1132–1133 (2018).
30. T. Susi *et al.*, *2D Mater.* **4**, 042004 (2017).

ACKNOWLEDGMENTS

The authors gratefully acknowledge R. Brydson, M. Bugnet, and E. Prestat for useful discussions. **Funding:** SuperSTEM is the UK National Research Facility for Advanced Electron Microscopy, supported by the Engineering and Physical Sciences Research Council (EPSRC). This work was granted access to the High-Performance Computing resources of the Institut du Développement et des Ressources en Informatique Scientifique (IDRIS) under allocation 2019-A0060910820, attributed by the Grand Equipement National de Calcul Intensif (GENCI). **Author contributions:** Q.M.R. conceived the project. F.S.H., Q.M.R., and D.M.K. designed and carried out the experiments and interpreted the data. G.R. and M.L. carried out and interpreted the theoretical calculations. All authors contributed to the preparation of the manuscript. **Competing interests:** The authors declare no competing interests. **Data and materials availability:** All data necessary for evaluating the conclusions of the paper are included in the main text and/or the supplementary materials. Data related to those presented here are available from the authors upon reasonable request.

SUPPLEMENTARY MATERIALS

science.sciencemag.org/content/367/6482/1124/suppl/DC1
Materials and Methods
Supplementary Text
Figs. S1 to S12
References (*31*–*43*)

7 November 2019; accepted 3 February 2020
10.1126/science.aba1136

QUANTUM SIMULATION

A scalable realization of local U(1) gauge invariance in cold atomic mixtures

Alexander Mil[1]*, Torsten V. Zache[2], Apoorva Hegde[1], Andy Xia[1], Rohit P. Bhatt[1], Markus K. Oberthaler[1], Philipp Hauke[1,2,3], Jürgen Berges[2], Fred Jendrzejewski[1]

In the fundamental laws of physics, gauge fields mediate the interaction between charged particles. An example is the quantum theory of electrons interacting with the electromagnetic field, based on U(1) gauge symmetry. Solving such gauge theories is in general a hard problem for classical computational techniques. Although quantum computers suggest a way forward, large-scale digital quantum devices for complex simulations are difficult to build. We propose a scalable analog quantum simulator of a U(1) gauge theory in one spatial dimension. Using interspecies spin-changing collisions in an atomic mixture, we achieve gauge-invariant interactions between matter and gauge fields with spin- and species-independent trapping potentials. We experimentally realize the elementary building block as a key step toward a platform for quantum simulations of continuous gauge theories.

Gauge symmetries are a cornerstone of our fundamental description of quantum physics as encoded in the standard model of particle physics. The presence of a gauge symmetry implies a concerted dynamics of matter and gauge fields that is subject to local symmetry constraints at each point in space and time (*1*). To uncover the complex dynamical properties of such highly constrained quantum many-body systems, enormous computational resources are required. This difficulty is stimulating great efforts to quantum simulate these systems, i.e., to solve their dynamics using highly controlled experimental setups with synthetic quantum systems (*2*–*4*). First experimental breakthroughs have used quantum-computer algorithms that implement gauge invariance exactly, but which are either limited to one spatial dimension (*5*, *6*), restrict the dynamics of the gauge fields (*7*, *8*), or require classical preprocessing resources that scale exponentially with system size (*9*). Recently, the dynamics of a discrete Z_2 gauge theory in a minimal model has been realized based on Floquet engineering (*10*–*12*). Despite these advances, the faithful realization of large-scale quantum simulators describing the continuum behavior of gauge theories remains highly challenging.

Our aim is the development of a scalable and highly tunable platform for a continuous U(1) gauge theory, such as realized in quantum electrodynamics. In the past years, ultracold atoms have become a well-established system for mimicking condensed-matter models with static electric and magnetic fields (*13*) and even dynamical background fields for moving particles (*14*–*16*). These systems possess global U(1) symmetries related to the conservation of total magnetization and atom number (*17*). However, a gauge theory is based on a local symmetry, which we enforce here through spin-changing collisions in atomic mixtures. This promising mechanism to protect gauge invariance has been put forward in various proposals (*18*–*21*) but not yet demonstrated experimentally. We demonstrate the engineering of an elementary building block in a mixture of bosonic atoms, demonstrate its high tunability, and verify its faithful representation of the desired model.

We further propose an extended implementation scheme in an optical lattice, where each lattice well constitutes an elementary building block that contains both matter and gauge fields. Repetitions of this elementary unit can be connected using Raman-assisted tunneling (*22*). Gauge and matter fields are spatially arranged in such a way that the spin-changing collisions occur within single-lattice wells, in contrast to previous proposals (*18*–*21*) where the gauge and matter fields were spatially separated and spin-changing collisions had to be accompanied by hopping across different sites of the optical lattice.

We specify our proposal for a one-dimensional gauge theory on a spatial lattice, as visualized

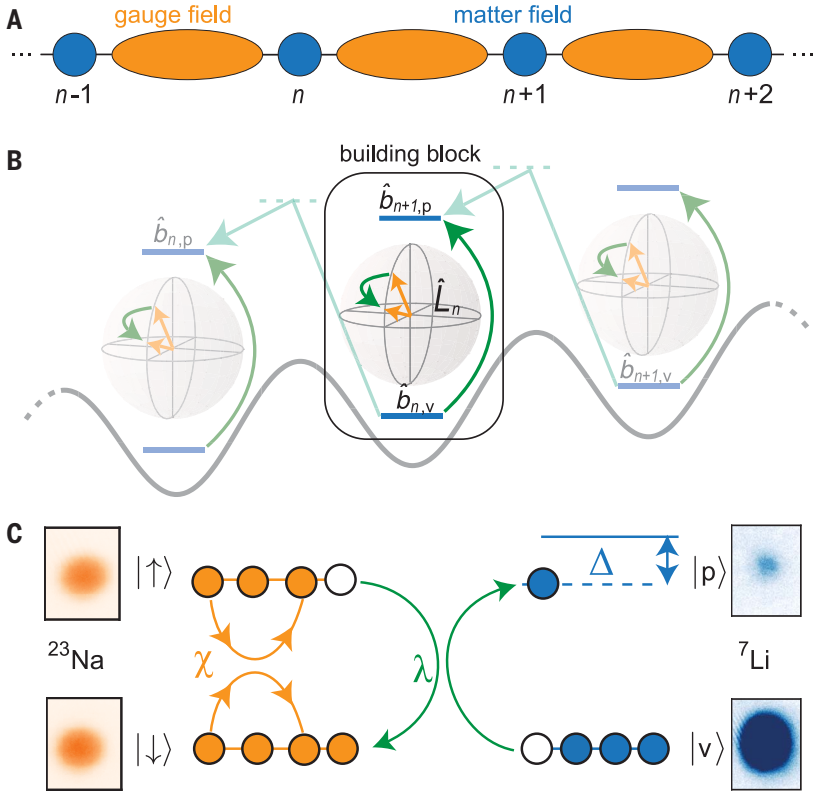


Fig. 1. Engineering a gauge theory. (**A**) Structure of a lattice gauge theory. Matter fields reside on sites and gauge fields on the links in between. (**B**) Proposed implementation of the extended system. Individual building blocks consist of long spins (representing gauge fields) and matter states, which are confined within the same well and whose interaction constitutes a local U(1) symmetry. An array of building blocks in an optical lattice is connected via Raman-assisted tunneling. (**C**) Experimental realization of the elementary building block with bosonic gauge (sodium) and matter (lithium) fields. The gauge-invariant interaction is realized by heteronuclear spin-changing collisions.

[1]Kirchhoff-Institut für Physik, Heidelberg University, Im Neuenheimer Feld 227, 69120 Heidelberg, Germany. [2]Institut für Theoretische Physik, Heidelberg University, Philosophenweg 16, 69120 Heidelberg, Germany. [3]INO-CNR BEC Center and Department of Physics, University of Trento, Via Sommarive 14, I-38123 Trento, Italy.
*Corresponding author. Email: block@synqs.org

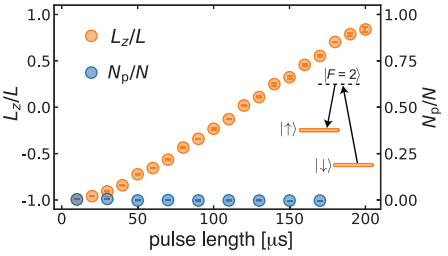


Fig. 2. Tunability of the initial conditions. The normalized spin z-component L_z/L of ^{23}Na atoms as a function of the preparation pulse length, which shows that the gauge field can be tuned experimentally over the entire possible range. Simultaneously, the particle number N_p/N of ^{7}Li is kept in the vacuum state. The inset shows a sketch of the experimental protocol used for tuning the initial conditions.

in Fig. 1A. Charged matter fields reside on the lattice sites n, with gauge fields on the links in between the sites (*23*). We consider two-component matter fields labeled "p" and "v", which are described by the operators $(\hat{b}_{n,\mathrm{p}}, \hat{b}_{n,\mathrm{v}})$. To realize the gauge fields with the atomic system, we use the quantum link formulation (*24*–*26*), where the gauge fields are replaced by quantum mechanical spins $\hat{\mathbf{L}}_n = (\hat{L}_{x,n}, \hat{L}_{y,n}, \hat{L}_{z,n})$, labeling link operators by the index of the site to the left. In this formulation, the spin z-component $\hat{L}_{n,z}$ can be identified with a discrete "electric" field. We recover the continuous gauge fields of the original quantum field theory in a controlled way by working in the limit of long spins (*20*).

Physically, this system of charged matter and gauge fields can be realized in a mixture of two atomic Bose–Einstein condensates (BECs) with two internal components each (in our experiment, we use ^{7}Li and ^{23}Na). An extended system can be obtained by use of an optical lattice. In our scheme, we abandon the one-to-one correspondence between the sites of the simulated lattice gauge theory and the sites of the optical-lattice simulator. This correspondence characterized previous proposals and necessitated physically placing the gauge fields in-between matter sites (*18*–*21*). Instead, as illustrated in Fig. 1B, here one site of the physical lattice hosts two matter components, each taken from one adjacent site ($\hat{b}_{n+1,\mathrm{p}}$ and $\hat{b}_{n,\mathrm{v}}$), as well as the link ($\hat{\mathbf{L}}_n$).

The enhanced physical overlap in this configuration decisively improved time scales of the spin-changing collisions, which until now were a major limiting factor for experimental implementations. Moreover, a single well of the optical lattice already contains the essential processes between matter and gauge fields and thus represents an elementary building block of the lattice gauge theory. These building blocks can be coupled by Raman-assisted tunneling of the matter fields [see supplementary materials (SM)].

The Hamiltonian $\hat{H} = \sum[\hat{H}_n + \hbar\Omega(\hat{b}^{\dagger}_{n,\mathrm{p}}\hat{b}_{n,\mathrm{v}} + \hat{b}^{\dagger}_{n,\mathrm{v}}\hat{b}_{n,\mathrm{p}})]$ of the extended system can thus be decomposed into the elementary building-block Hamiltonian $\hat{H}_n$ and the Raman-assisted tunneling (with Raman frequency ~Ω). Here, $\hat{H}_n$ reads (writing $\hat{b}_{\mathrm{p}} \equiv \hat{b}_{n+1,\mathrm{p}}$, $\hat{b}_{\mathrm{v}} \equiv \hat{b}_{n,\mathrm{v}}$, and $\hat{\mathbf{L}} \equiv \hat{\mathbf{L}}_n$)

$$\hat{H}_n/\hbar = \chi\hat{L}_z^2 + \frac{\Delta}{2}(\hat{b}^{\dagger}_{\mathrm{p}}\hat{b}_{\mathrm{p}} - \hat{b}^{\dagger}_{\mathrm{v}}\hat{b}_{\mathrm{v}}) + \lambda(\hat{b}^{\dagger}_{\mathrm{p}}\hat{L}_{-}\hat{b}_{\mathrm{v}} + \hat{b}^{\dagger}_{\mathrm{v}}\hat{L}_{+}\hat{b}_{\mathrm{p}}) \quad (1)$$

where $\hat{L}_{+} = \hat{L}_x + i\hat{L}_y$ and $\hat{L}_{-} = \hat{L}_x - i\hat{L}_y$. The first term on the right-hand side of Eq. 1, which is proportional to the parameter χ, describes the energy of the gauge field, and the second term, ~Δ, sets the energy difference between the two matter components. The last term, ~λ, describes the U(1) invariant coupling between matter and gauge fields, which is essential to retain the local U(1) gauge symmetry of the Hamiltonian $\hat{H}$ (see SM for more details).

We implemented the elementary building block Hamiltonian $\hat{H}_n$ with a mixture of $2L \sim 300 \times 10^3$ sodium and $N \sim 50 \times 10^3$ lithium atoms as sketched in Fig. 1C (see SM for details). Both species were kept in an optical dipole trap such that the external trapping potential is spin insensitive for both species. An external magnetic bias field of $B \approx 2$G suppressed any spin change energetically, such that only the two Zeeman levels, $m_F = 0$ and 1, of the $F = 1$ hyperfine ground state manifolds were populated during the experiment. The ^{23}Na states are labeled as $|\uparrow\rangle = |m_F = 0\rangle$ and $|\downarrow\rangle = |m_F = 1\rangle$, on which the spin operator $\hat{\mathbf{L}}$ associated to the gauge field acts. The first term of Eq. 1 is then identified with the one-axis twisting Hamiltonian (*27*, *28*). We label the ^{7}Li states as "particle" $|\mathrm{p}\rangle = |m_F = 0\rangle$ and "vacuum" $|\mathrm{v}\rangle = |m_F = 1\rangle$, in accordance with the matter field operators $\hat{b}_{\mathrm{p}}$ and $\hat{b}_{\mathrm{v}}$. With this identification, the second term arises from energy shifts due to the external magnetic field and density interactions. Finally, the term ~λ is physically implemented by heteronuclear spin-changing interactions (*29*).

The resulting setup is highly tunable, as we demonstrated experimentally on the building block. We achieved tunability of the gauge field through a two-pulse Rabi coupling of the Na atoms between $|\downarrow\rangle$ and $|\uparrow\rangle$ using an intermediate $|F = 2\rangle$ state, which yields a desired value of $L_z/L = (N_\uparrow - N_\downarrow)/(N_\uparrow + N_\downarrow)$ (Fig. 2). At the same time, we kept the ^{7}Li atoms in $|\mathrm{v}\rangle$, corresponding to the initial vacuum of the matter sector at $\Delta \to \infty$, with ≲1% detected in $|\mathrm{p}\rangle$ (Fig. 2).

When the gauge-invariant coupling was turned off by removing the Na atoms from the trap, we observed no dynamics in the matter sector beyond the detection noise. By contrast, once the gauge field was present, the matter sector clearly underwent a transfer from $|\mathrm{v}\rangle$ to $|\mathrm{p}\rangle$ for proper initial conditions, as illustrated in Fig. 3A for an initialization to $L_z/L = -0.188$ at a magnetic field of $B_{\mathrm{A}} = 2.118(2)$G (*30*). This observation demonstrated the controlled operation of heteronuclear spin-changing collisions implementing the gauge-invariant dynamics in the experiment.

To quantify our observations, we extracted the ratio N_p/N, with $N = N_p + N_v$, as a function of time as presented in Fig. 3B. We observed nonzero N_p/N, describing "particle production," on a time scale of a few tens of milliseconds, with up to 6% of the total N being transferred to $|\mathrm{p}\rangle$. This value is consistent with our expectations from conservation of the initial energy $E_0/h = \chi L_z^2 - \Delta N_v/2$, from which we estimated a maximum amplitude on the order of a few percent. Owing to the much larger ^{23}Na condensate, the expected corresponding change in L_z/L is ~2%, which is currently not detectable with our imaging routine (see SM for details). Coherent oscillations in N_p/N were seen to persist for about 100ms.

We display N_p/N over the entire range of initial L_z in Fig. 4, keeping a fixed time of 30ms. The upper panel (A) corresponds to the same experimental setting as in Fig. 3. A clear resonance for particle production can be seen around $L_z/L \simeq -0.5$, approximately captured by the resonance condition $2\chi L_z \sim \Delta$ (see SM

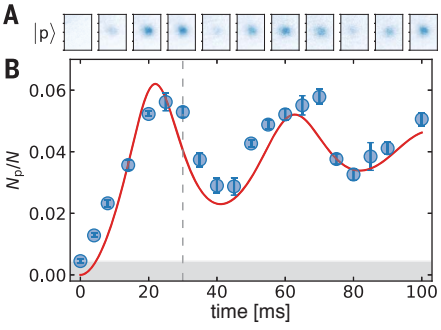


Fig. 3. Dynamics of particle production. (**A**) The number density distribution in state $|\mathrm{p}\rangle$ as a function of time for $L_z/L = -0.188$. (**B**) The corresponding particle number N_p/N. The blue circles give the experimental values with bars indicating the statistical error on the mean. The red curve is the theoretical mean-field prediction of Hamiltonian (Eq. 1) with parameters determined from a fit of the data in Fig. 4A and phenomenological damping. The shaded area indicates the experimental noise floor. The dashed line marks the time of 30 ms as it is used for the experimental sequence generating the data in Fig. 4.

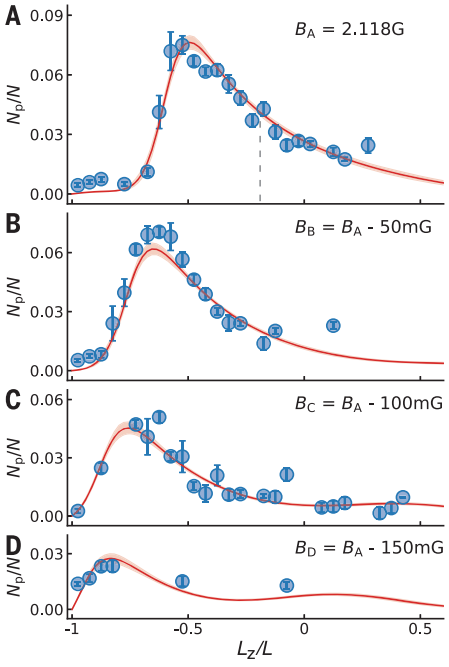


Fig. 4. Resonant particle production. (**A** to **D**) The number of produced particles as a function of initially prepared L_z/L after 30 ms for different-bias magnetic fields. Blue circles are experimental values with bars indicating the statistical error on the mean. The red curve in (A) arises from the theoretical model using the best estimate values of χ, λ, Δ_0, and Δ_L. The remaining curves in (B) to (D) are computed using the same parameters, including Δ_B. The shaded area indicates confidence intervals of the fit from bootstrap resampling. The dashed line in (A) indicates the L_z/L value corresponding to the time evolution shown in Fig. 3.

for details). The asymmetry of the resonance is a clear manifestation of the nonlinearity of the dynamics. As we reduced the magnetic field B, presented in Fig. 4, B to D, we observed a shift of the resonant particle production together with a reduction in amplitude, which continued to be qualitatively captured by the resonance condition $2\chi L_z \sim \Delta$. The maximal amplitude of the particle production was necessarily reduced by the conservation of total magnetization as the resonant peak was pushed closer to $L_z/L = -1$. For fields that were smaller than $B_{\min} \approx 1.96$G, the matter and gauge field dynamics became too off-resonant, and particle production was not observed any longer.

We compare the experimental results to the mean-field predictions of Hamiltonian (Eq. 1) for chosen χ, λ, and $\Delta(L_z, B) = \Delta_0 + \Delta_L L_z/L + \Delta_B(B - B_A)/B_A$ (see SM for the origin of the dependence on the magnetic field B and the initial spin L_z). A first-principle calculation of these model parameters, using only the experimental input of our setup, yielded $\chi^{\mathrm{th}}/2\pi \approx 14.92$mHz, $\lambda^{\mathrm{th}}/2\pi \approx 42.3\mu$Hz, $\Delta_0^{\mathrm{th}}/2\pi \approx -77$Hz, $\Delta_L^{\mathrm{th}}/2\pi \approx 4.474$kHz, and $\Delta_B^{\mathrm{th}}/2\pi \approx -1.669$kHz. These values were obtained by neglecting any residual spatial dynamics (*31*) of the atomic clouds within the trapping potential, which renormalized the model parameters. Moreover, the mean-field approximation was not able to capture the decoherence observed in Fig. 3 at later times. However, the features of the resonance data in Fig. 4 were more robust against the decoherence as it probed the initial rise of particle production.

We included the decoherence into the model phenomenologically by implementing a damping term characterized by $\gamma/2\pi = 3.54(94)$ Hz, which was determined by an exponential envelope fit to the data of Fig. 3B. Physically, the damping had several origins: quantum fluctuations; fluctuations of initial state preparation, as well as values of parameters; atom loss; and the spatial dynamics of the two species within the building block. In particular, the first two did not compromise gauge invariance. The last two sources of dissipation can in general be controlled by reducing the particle density and by implementing a deep optical lattice that freezes out the spatial dynamics within individual wells. Fixing γ, the best agreement (solid red line) with the data in Fig. 4A was obtained for $\chi/2\pi = 8.802(8)$ mHz, $\lambda/2\pi = 16.4(6)\mu$Hz, $\Delta_0/2\pi = -4.8(16)$Hz, and $\Delta_L/2\pi = 2.681(1)$kHz. The prediction with these model parameters showed excellent agreement with the data in Fig. 3B (red line) for all times observed. Notably, our established model also described the data in Fig. 4, B to D, by including $\Delta_B/2\pi = -519.3(3)$Hz (see SM). Compared to the ab initio estimates, all fitted values had the expected sign and lie in the same order of magnitude.

Our results demonstrated the controlled operation of an elementary building block of a U(1) gauge theory and thus open the door for large-scale implementations of lattice gauge theories in atomic mixtures. The potential for scalability is an important ingredient for realistic applications to gauge field theory problems. Digital quantum simulations of gauge theories on universal quantum computers (*5*, *9*) are challenging to scale up. This difficulty makes analog quantum simulators, as treated here, highly attractive, because they can be scaled up and still maintain excellent quantum coherence (*6*–*8*, *32*–*34*). Proceeding to the extended system requires optical lattices and Raman-assisted tunneling [see SM and (*22*)]. The resulting extended gauge theory will enable the observation of relevant phenomena, such as plasma oscillations or resonant particle production in strong-field quantum electrodynamics (*35*). Along the path to the relativistic gauge theories realized in nature, we will replace bosonic ^{7}Li with fermionic ^{6}Li, which will allow for the recovery of Lorentz invariance in the continuum limit (see SM).

REFERENCES AND NOTES

1. S. Weinberg, *The Quantum Theory of Fields* (Cambridge Univ. Press, 1995).
2. U.-J. Wiese, *Ann. Phys.* **525**, 777–796 (2013).
3. E. Zohar, J. I. Cirac, B. Reznik, *Rep. Prog. Phys.* **79**, 014401 (2016).
4. M. Dalmonte, S. Montangero, *Contemp. Phys.* **57**, 388–412 (2016).
5. E. A. Martinez *et al.*, *Nature* **534**, 516–519 (2016).
6. C. Kokail *et al.*, *Nature* **569**, 355–360 (2019).
7. H. Bernien *et al.*, *Nature* **551**, 579–584 (2017).
8. F. M. Surace *et al.*, Lattice gauge theories and string dynamics in Rydberg atom quantum simulators. arXiv:1902.09551 [cond-mat.quant-gas] (2019).
9. N. Klco *et al.*, *Phys. Rev. A* **98**, 032331 (2018).
10. L. W. Clark *et al.*, *Phys. Rev. Lett.* **121**, 030402 (2018).
11. F. Görg *et al.*, *Nat. Phys.* **15**, 1161–1167 (2019).
12. C. Schweizer *et al.*, *Nat. Phys.* **15**, 1168–1173 (2019).
13. N. Goldman, G. Juzeliūnas, P. Öhberg, I. B. Spielman, *Rep. Prog. Phys.* **77**, 126401 (2014).
14. F. Chevy, C. Mora, *Rep. Prog. Phys.* **73**, 112401 (2010).
15. F. Grusdt, E. Demler, in *Quantum Matter at Ultralow Temperatures* (Società Italiana di Fisica, 2016), p. 325.
16. T. Rentrop *et al.*, *Phys. Rev. X* **6**, 041041 (2016).
17. D. M. Stamper-Kurn, M. Ueda, *Rev. Mod. Phys.* **85**, 1191–1244 (2013).
18. E. Zohar, J. I. Cirac, B. Reznik, *Phys. Rev. A* **88**, 023617 (2013).
19. K. Stannigel *et al.*, *Phys. Rev. Lett.* **112**, 120406 (2014).
20. V. Kasper, F. Hebenstreit, M. K. Oberthaler, J. Berges, *Phys. Lett. B* **760**, 742–746 (2016).
21. T. V. Zache *et al.*, *Quantum Sci. Technol.* **3**, 034010 (2018).
22. M. E. Tai *et al.*, *Nature* **546**, 519–523 (2017).
23. J. B. Kogut, *Rev. Mod. Phys.* **51**, 659–713 (1979).
24. D. Horn, *Phys. Lett. B* **100**, 149–151 (1981).
25. S. Chandrasekharan, U. J. Wiese, *Nucl. Phys. B* **492**, 455–471 (1997).
26. D. Banerjee *et al.*, *Phys. Rev. Lett.* **109**, 175302 (2012).
27. C. Gross, T. Zibold, E. Nicklas, J. Estève, M. K. Oberthaler, *Nature* **464**, 1165–1169 (2010).
28. M. F. Riedel *et al.*, *Nature* **464**, 1170–1173 (2010).
29. X. Li *et al.*, *Phys. Rev. Lett.* **114**, 255301 (2015).
30. All uncertainties given in this manuscript correspond to a 68% confidence interval for the statistical uncertainty.
31. E. Nicklas *et al.*, *Phys. Rev. Lett.* **107**, 193001 (2011).
32. I. Bloch, J. Dalibard, W. Zwerger, *Rev. Mod. Phys.* **80**, 885–964 (2008).
33. J. I. Cirac, P. Zoller, *Nat. Phys.* **8**, 264–266 (2012).
34. J. Berges, *Nature* **569**, 339–340 (2019).
35. V. Kasper, F. Hebenstreit, J. Berges, *Phys. Rev. D Part. Fields Gravit. Cosmol.* **90**, 025016 (2014).
36. F. Jendrzejewski *et al.*, Realizing a scalable building block of a U(1) gauge theory with cold atomic mixtures, Dryad (2020); https://doi.org/10.5061/dryad.8gtht76k2.

ACKNOWLEDGMENTS

Funding: We acknowledge funding from the DFG Collaborative Research Centre "SFB 1225 (ISOQUANT)," the ERC Advanced Grant "EntangleGen" (Project-ID 694561), the ERC Starting Grant "StrEnQTh" (Project-ID 804305), and the Excellence Initiative of the German federal government and the state governments - funding line Institutional Strategy (Zukunftskonzept): DFG project number ZUK 49/Ü. F.J. acknowledges the DFG support through the project FOR 2724, the Emmy-Noether grant (project-id 377616843) and from the Juniorprofessorenprogramm Baden-Württemberg (MWK). P.H. acknowledges support by Provincia Autonoma di Trento, Quantum Science and Technology in Trento. **Author contributions:** A.M., A.H., A.X. and R.P.B. set up the experiment and performed the measurements; A.M. and T.V.Z. performed the data analysis; T.V.Z., P.H., and J.B. developed the theory; P.H., J.B., M.K.O., and F.J. supervised the project; all authors took part in writing the manuscript. **Competing Interests:** The authors declare no competing interests. **Data and materials availability:** The data are available on the Dryad database (*36*).

SUPPLEMENTARY MATERIALS

science.sciencemag.org/content/367/6482/1128/suppl/DC1
Materials and Methods
Supplementary Text
References (*37*–*42*)

17 September 2019; accepted 4 February 2020
10.1126/science.aaz5312

NEUROSCIENCE

Replay of cortical spiking sequences during human memory retrieval

Alex P. Vaz[1,2,3], John H. Wittig Jr.[1], Sara K. Inati[4], Kareem A. Zaghloul[1]*

Episodic memory retrieval is thought to rely on the replay of past experiences, yet it remains unknown how human single-unit activity is temporally organized during episodic memory encoding and retrieval. We found that ripple oscillations in the human cortex reflect underlying bursts of single-unit spiking activity that are organized into memory-specific sequences. Spiking sequences occurred repeatedly during memory formation and were replayed during successful memory retrieval, and this replay was associated with ripples in the medial temporal lobe. Together, these data demonstrate that human episodic memory is encoded by specific sequences of neural activity and that memory recall involves reinstating this temporal order of activity.

Retrieving individual episodic memories in the human brain relies on our ability to internally replay neural patterns of activity that were present when the memory was first experienced (*1*–*6*). This suggests a link with a parallel line of work in rodents that demonstrated that individual neurons in the medial temporal lobe (MTL) fire in sequences when animals are navigating spatial environments, and that these sequences are replayed during awake periods of rest and during sleep (*7*–*14*). Replay of sequences of spiking activity has been interpreted to reflect memory retrieval and consolidation (*13*) and even memory-related planning (*14*), but no direct evidence exists that demonstrates that replay of neural spiking sequences could also underlie episodic memory retrieval in humans. Neuronal sequences replayed in the rodent MTL are associated with fast oscillations termed "ripples" (*15*–*20*). Ripples are also relevant for episodic memory retrieval in humans (*21*–*26*), raising the possibility that ripples may also be associated with memory-relevant replay of spiking activity in the human brain.

We therefore investigated the relationship between cortical ripples and single-unit spiking activity in six participants (two female; 34.8 ± 4.7 years of age; mean ± SEM). We implanted a microelectrode array (MEA) to collect single-unit and micro–local field potential (micro-LFP) data from the anterior temporal lobe in each participant (*27*, *28*) while also collecting macro-scale intracranial electroencephalography (iEEG) signals from subdural electrodes placed over the lateral temporal cortex and along the MTL (Fig. 1, A and B). Recordings captured from the cortical iEEG contacts placed immediately above the MEA in the middle temporal gyrus (MTG) enabled us to simultaneously examine neural activity from the same brain region across spatial scales (Fig. 1A). We used the iEEG signals to detect ripple oscillations in the MTG and the MTL and any potential coupling between brain regions (*25*).

Ripples present in the iEEG recordings in the MTG were accompanied by ripples in the underlying micro-LFP signals and a burst of single unit spiking activity (Fig. 1C). Ripples exhibited band-limited power increases within 80 to 120 Hz at both macro-iEEG and micro-LFP spatial scales (fig. S1). Each ripple identified in each microelectrode was accompanied by an increase in single-unit spiking activity on that channel (Fig. 1C and figs. S2 and S3). Cortical spiking was tightly locked to the onset of the detected ripple oscillations at both the macro-iEEG and micro-LFP scales across participants (Fig. 1D and figs. S4 and S5). Within each micro-LFP ripple, spikes captured from the associated microelectrode channel in this cortical region were locked to the ripple trough, which is consistent with the relationship between spiking and ripple activity observed in rodents and humans (Fig. 1, E and F) (*18*, *29*).

Each participant performed a paired-associates verbal memory task (*25*, *27*) that required them to encode and subsequently retrieve new associations between pairs of randomly selected words on each trial (Fig. 2A and supplementary materials). Although we found a strong relation between cortical spiking and detected ripple oscillations, we focused our analyses on the bursts of single-unit spiking activity and their temporal structure during memory formation (*9*–*12*). We defined a burst event as the time indices during which the cortical spiking exceeded a population rate–based threshold for at least 25 ms (supplementary materials). Across all participants, burst events had a mean frequency of 1.4 ± 0.2 Hz, and each burst involved 39.9 ± 6.3% of all identified units within that session. Burst events occurred repeatedly throughout the duration of the word pair presentation (Fig. 2B). We reordered the units in each trial according to a template sequence that we derived from the relative timing of spiking activity between pairs of units during each encoding period. We used this template sequence to visualize, but not analyze, the temporal structure of unit activity across multiple burst events during both encoding and retrieval periods from the same trial (supplementary materials). Units within individual burst events appeared to preserve the same sequential order of firing throughout the duration of encoding (Fig. 2C).

Because we observed repeated sequences of neuronal firing while participants were encoding the word pairs, we quantified the extent to which the sequences of neuronal firing within the burst events were consistent within each individual trial and different between trials. For each burst event, we determined the sequence of spiking activity across units within that particular burst event by ordering each neuron according to when its maximum firing rate occurred in a ±75-ms window around the center index of the burst event (fig. S6). We found several examples of units that formed a sequence in one trial during word pair presentation and rearranged to form a different sequence in another trial (Fig. 2D). To examine how similar any sequence was to any other sequence, we computed the matching index (MI) (*12*). The MI compares the pairwise temporal relationships between all units that are common to both sequences and takes on a value of 1 for perfect forward replay and –1 for perfect reverse replay (supplementary materials). We computed the average pairwise MI between all sequences within each trial and compared this with the distribution of MI values that arises when comparing all pairwise combinations of sequences across different trials. Across participants, in correct, but not incorrect, encoding trials, sequences were significantly more similar to other sequences within the same trial than to sequences in other trials [$n = 6$ participants, paired t test; correct within-trial versus across-trial, $t(5) = 3.26$, $P = 0.023$; incorrect within-trial versus across-trial, $t(5) = 1.47$, $P = 0.202$; correct versus incorrect, $t(5) = 3.68$, $P = 0.014$] (Fig. 2E). This difference between correct and incorrect trials was not observed when calculating the similarity of unit identity (in which "identity" is defined as a binary vector on the basis of whether or not a unit fired within a burst event) (supplementary materials and fig. S7). This suggests that a necessary component of successful memory encoding, and later retrieval, involves repeated sequences of cortical spiking activity that are specific to each trial.

If successful memory encoding relies on the temporal order of neuronal firing, then we hypothesized that successful memory retrieval would involve replay of the same trial-specific sequence. In one trial, the sequence of cortical spiking observed in a single burst event during encoding was replayed in a burst event during

[1]Surgical Neurology Branch, National Institute of Neurological Disorders and Stroke (NINDS), National Institutes of Health, Bethesda, MD 20892, USA. [2]Medical Scientist Training Program, Duke University School of Medicine, Durham, NC 27710, USA. [3]Department of Neurobiology, Duke University, Durham, NC 27710, USA. [4]Office of the Clinical Director, NINDS, National Institutes of Health, Bethesda, MD 20892, USA.
*Corresponding author. Email: kareem.zaghloul@nih.gov

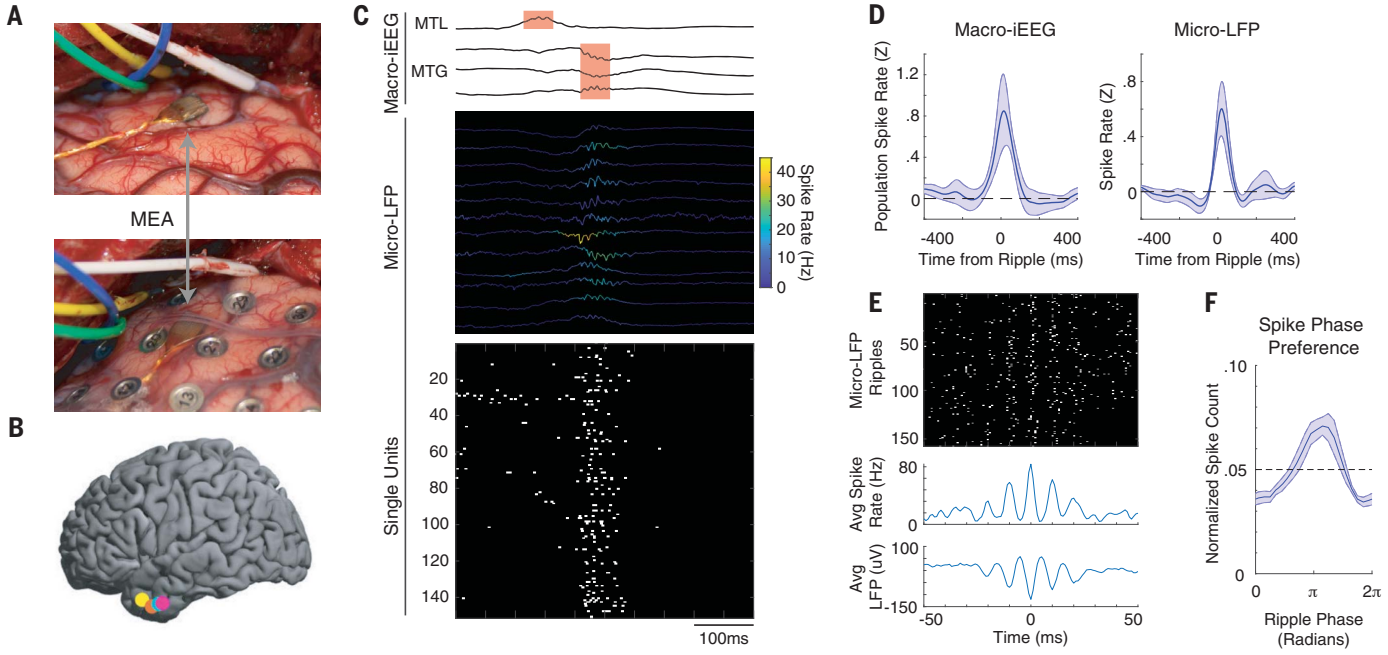


Fig. 1. Ripple oscillations reflect burst firing of cortical neurons. (**A**) Intraoperative photograph showing the implanted MEA in the MTG (top) and after placement of a macro-iEEG grid over the MEA (bottom). (**B**) Locations of the MEAs in five participants. Colors represent each participant. One participant with a right hemisphere implant is not shown. (**C**) Example of a coupled ripple oscillation between the MTL and MTG detected in macro-iEEG (top) with simultaneous cortical ripples present in the micro-LFP (middle; instantaneous spike rate of each channel indicated by color of trace) and burst firing of cortical single units (bottom). All 151 units measured during this session are shown, and 82 of these units spiked during this cortical ripple event. Spikes are shown with width of 5 ms for visualization purposes. (**D**) Average population spike rate relative to onset of ripples in the macro-iEEG (left) and average single-channel spike rate relative to onset of ripples in the micro-LFP (right). t = 0 indicates start index of detected ripple oscillation. Error bars represent SEM across all participants. (**E**) A representative single-channel spike raster locked to the maximum trough of each ripple oscillation recorded in that channel (top), with average spike rate (middle) and LFP (bottom) across all ripple events. t = 0 indicates trough of detected ripple oscillation. (**F**) Phase preference of spikes with respect to ripple phase (80 to 120 Hz). Dotted line indicates uniform distribution that would be expected by chance given the number of histogram bins. Error bars represent SEM across all participants.

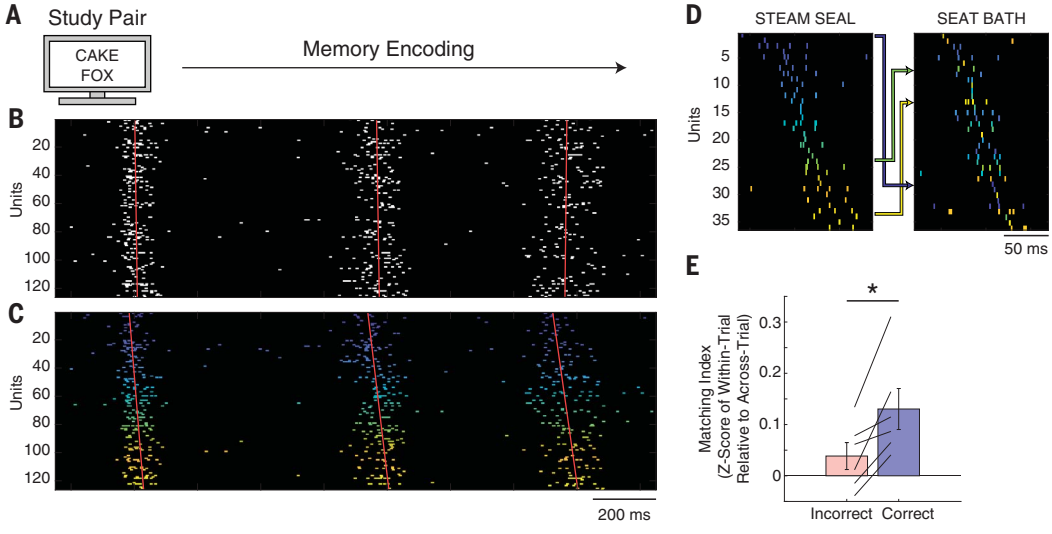


Fig. 2. Burst events are organized into trial-specific sequences during successful memory formation. (**A**) Memory-encoding portion of the paired-associates verbal memory task, during which participants are instructed to memorize associations between pairs of words. (**B**) Repeated cortical burst events during memory formation. (**C**) Same units as in (B) but reorganized according to the extracted average temporal sequence for that trial. Colors represent the average temporal ordering, with cooler and warmer colors representing earlier and later spiking in the template sequence, respectively. Red lines indicate the linear regression through the maximum spike rate times of all units within each burst event. The slope of the regression line indicates the temporal sequence of firing times for the respective burst event. (**D**) Spike sequences for burst events during two separate correct encoding trials. Units are colored according to the ordering in the first sequence (left) to demonstrate rearrangement of units to form the second sequence (right). Arrows indicate rearrangement for example individual units between the two sequences. Spikes are shown with width of 2 ms for visualization purposes. (**E**) Sequences in correct trials, but not incorrect trials, demonstrated higher within-trial compared with across-trial similarity (*P < 0.05).

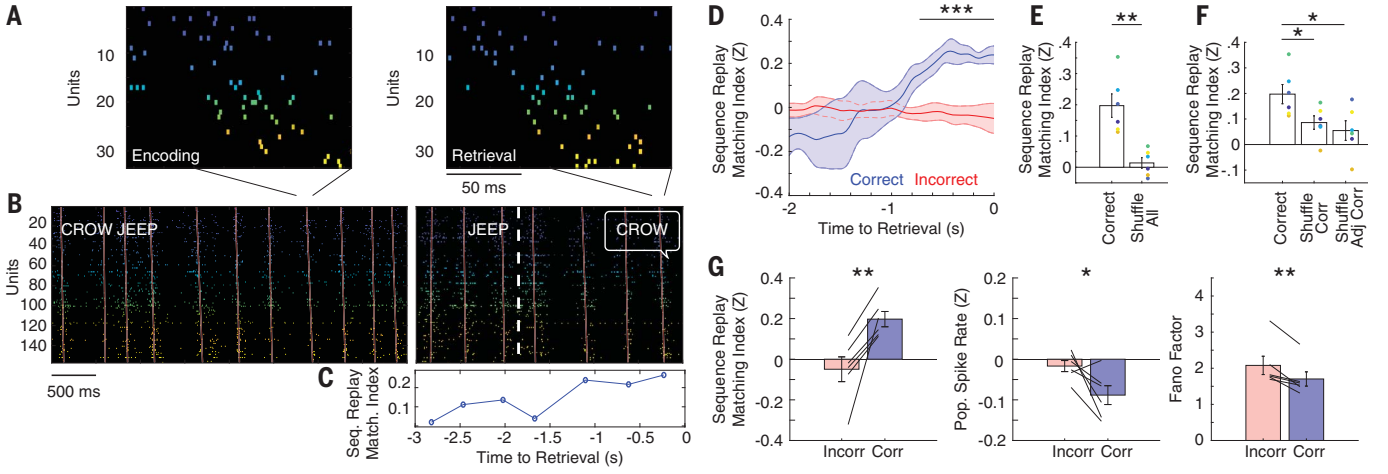


Fig. 3. Memory-specific sequence replay occurs during successful memory retrieval. (**A**) Example sequence replay event during memory retrieval. MI = 0.42 ($P < 0.001$) for this encoding-retrieval sequence pair. Colors represent the average temporal ordering during the encoding period, with cooler and warmer colors representing earlier and later in the sequence, respectively. (**B**) Encoding (left) and retrieval (right) rasters of the corresponding trial in (A) during the paired associates task. Inset text indicates the study pair to be memorized (CROW JEEP), the test probe (JEEP), and the verbalized response (CROW). The white dashed line indicates the time of test probe presentation. Red lines indicate the linear regression through the maximum spike rate times of all units within each burst event. (**C**) Average sequence similarity of each retrieval burst event to all encoding events for the trial shown in (B). (**D**) Average similarity of retrieval sequences to encoding sequences across all participants during memory retrieval. Bars indicate SEM across all participants. Correct retrieval demonstrated significantly increased sequence similarity compared with incorrect retrieval (***$P < 0.001$, permutation test). (**E**) Sequence replay for true encoding-retrieval comparisons versus replay after shuffling encoding labels for all trials (**$P < 0.01$). Each colored dot represents a replay value for one participant, and bars indicate SEM across all participants. (**F**) Sequence replay for correct trials versus shuffled correct trial conditions. True encoding-retrieval pairs were significantly more similar than shuffled correct and shuffled adjacent correct trials (*$P < 0.05$). (**G**) Increased sequence replay during correct retrieval (left) was accompanied by decreased population spike rate (middle) and decreased Fano factor (right). Each line indicates a single participant, and bars indicate SEM across all participants (*$P < 0.05$, **$P < 0.01$).

memory retrieval (Fig. 3A and fig. S8). Across the entire trial, we observed repeated burst events during both the encoding and retrieval portions of the paired associates memory task (Fig. 3B). We calculated the average sequence similarity (MI) of each retrieval burst event to all encoding events. Over the course of memory retrieval, sequences appeared to become more similar to the encoding sequences until the moment when the participant vocalized their response (Fig. 3C and fig. S9). Across participants, we found that this pattern of increasing sequence similarity was recapitulated in correct, but not incorrect, trials (Fig. 3D and fig. S10). Before vocalization, retrieval sequences were significantly more similar to encoding sequences during correct compared with incorrect trials ($P < 0.001$, permutation test) (Fig. 3D).

We replicated these results within individual participants (fig. S11) and performed an *N*-way (factorial) analysis of variance (ANOVA) with participants and correctness of response (binary between correct and incorrect) as the independent variables for each trial and the corresponding sequence replay value as the observation. We observed significant effects for correctness of response [$F_6 = 4.55$, $P < 0.001$] but not for participants [$F_5 = 1.14$, $P = 0.340$]. We also confirmed this difference between correct and incorrect trials by using an alternative metric of sequence similarity and by using nonparametric statistical tests (fig. S12). Sequence similarity was not correlated with the similarity in unit identity between burst events [correlation coefficient (r) = 0.07 ± 0.03; $n = 6$ participants, $t(5) = 1.80$, $P = 0.132$] or with the number of units that were common to both sequences [$r = 0.06 \pm 0.03$; $n = 6$ participants, $t(5) = 2.04$, $P = 0.096$] (fig. S13), and the difference in sequence similarity between correct and incorrect trials did not arise owing to a difference in burst rates or ripple rates between conditions (figs. S14 and S15). We found significant differences in sequence similarity between correct and incorrect trials in both the presence of detected cortical macro-iEEG ripples and even when ripples were not explicitly detected when using our criteria (fig. S16). We did not find that sequences were replayed during the rest period between retrieval trials or during the math distractor period (fig. S17). We also did not find any evidence of significant reverse replay during correct retrieval and found that the duration of the sequences were not significantly different between correct encoding and retrieval [108.0 ± 10.4 ms versus 107.8 ± 10.8 ms; $n = 6$ participants, $t(5) = 0.180$, $P = 0.865$] (fig. S6).

Our data, which demonstrates that trial-specific sequences observed during encoding are replayed during retrieval, suggest that sequence replay should also be specific to each retrieval trial. We compared each sequence during the last second of the retrieval period with sequences from other encoding trials by using a shuffling procedure. We first shuffled all trials by calculating the replay of each correct retrieval trial for all nonmatching encoding trials. The true encoding-retrieval replay value was significantly greater than the values computed by using the shuffled pairs across all participants [$n = 6$ participants, paired t test, $t(5) = 3.49$, $P = 0.018$] (Fig. 3E). We next shuffled the encoding trial labels using only the correct trials and then by swapping only the encoding trial labels from adjacent correct trials. The true unshuffled average sequence similarity between retrieval and encoding was significantly greater than the average in each shuffled condition (one-way ANOVA across all categories: $F_2 = 4.70$, $P = 0.026$; post-hoc paired t test $P < 0.05$ for each category pair) (Fig. 3F), demonstrating that the replay of cortical spiking sequences is specific for each retrieved memory. This memory specificity extended even to individual encoding-retrieval sequence pairs (fig. S18). Moreover, both correct encoding and retrieval had a lower population spike rate and lower Fano factor compared with those of incorrect trials (supplementary materials), suggesting that successful retrieval involves replaying precise sequences of sparse neural firing (Fig. 3G and fig. S19).

Burst events observed during retrieval were closely associated with ripple oscillations captured at both the macro-iEEG and micro-LFP

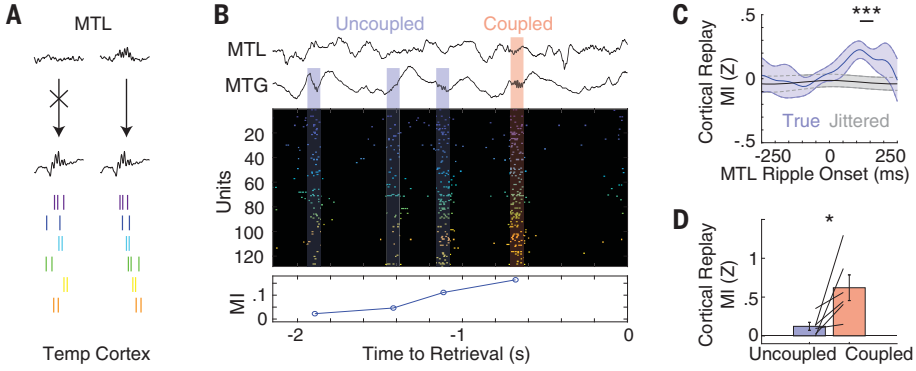


Fig. 4. MTL ripples precede cortical sequence replay. (**A**) Schematic of proposed mechanism for sequence replay in the cortex. Units are not sequentially organized when cortical bursts occur in isolation (left), whereas sequence replay occurs when MTL ripples occur in coordination with cortical bursts (right). (**B**) Example of dynamic coupling between MTL and cortical ripples (top), bursting events (middle), and sequence replay during successful memory retrieval (bottom). (**C**) Average cortical replay values relative to onset of MTL ripples in correct retrieval trials (blue), and the same data when MTL ripple temporal indices were jittered randomly (gray). Error bars represent SEM across all participants (***$P < 0.001$, permutation test). (**D**) Sequence replay during retrieval after dividing all sequences into those that were uncoupled and those that were coupled to MTL ripples. Each line indicates a single participant, and bars indicate SEM across all participants. Coupled sequences exhibited higher replay values than those of uncoupled sequences (*$P < 0.05$).

scale (Fig. 1C), yet only some of these cortical events were also coupled to ripples in the MTL. Previous evidence has suggested that successful memory retrieval involves a ripple-mediated interaction between the cortex and the MTL (*18*, *25*). Although each cortical ripple may reflect an underlying burst of spiking activity, only cortical burst events that are coupled to MTL ripples may be preferentially relevant for memory retrieval (Fig. 4A). We therefore hypothesized that sequences of spiking activity that occurred in association with MTL ripples during retrieval were more similar to encoding sequences than bursts of spiking that were not coupled with the MTL. In correct retrieval trials, we found several examples in which burst events associated with MTL ripples exhibited higher average sequence similarity to the encoding period than those burst events that occurred in the absence of a MTL ripple (Fig. 4B). We explicitly quantified replay in the cortex triggered to the onset of MTL ripples and found that maximal replay occurred ~100 ms after MTL ripple onset (significant replay compared with jittered ~100 to 175 ms) (Fig. 4C). We therefore used this temporal relationship to designate every cortical burst event as coupled or uncoupled to a MTL ripple (supplementary materials) and examined the replay content of each type of cortical burst event. In correct retrieval trials across all participants, burst events coupled to MTL ripples demonstrated significantly greater replay of the sequences present during encoding compared with uncoupled events [$n = 6$ participants, $t(5) = 2.85$, $P = 0.036$] (Fig. 4D).

Together, our data demonstrate that ripple oscillations reflect bursts of spiking activity in the human cortex and that these bursts contain item-specific sequences of single-unit spiking that are established during memory encoding and replayed during memory retrieval. Cortical spike replay is enhanced during retrieval when bursts of spiking in the cortex are coupled with ripples in the MTL. Our data therefore suggest that successful memory encoding and retrieval of individual items involves a specific temporal ordering of cortical spiking activity and provide a link between previous evidence regarding the role of ripple oscillations in human memory (*21*–*26*) and evidence regarding the replay of neuronal sequences observed in rodents (*7*–*14*). Studies of spike replay in rodents have largely focused on sequences of spiking activity that emerge during spatial navigation and that are replayed during sleep or during awake periods of rest. These data have inspired models of memory that posit that memory formation involves an initial encoding state, in which the temporal order of spiking activity is established through sequential experience, and a subsequent consolidation state, during which these sequences of spiking activity are replayed in a temporally compressed manner in the MTL (*17*, *30*). Our task requires participants to memorize abstract associations between word pairs and to retrieve those associations following only a brief distractor period. Hence, our data provide direct evidence that awake human memory retrieval involves replay of sequences of spiking activity in the cortex. Whether such cortical spike replay plays a similar role in longer-term memory consolidation in the human brain remains an open question. Moreover, whereas temporal compression and reverse replay may be common features of spike replay observed in rodents, their absence here may be related to our task involving neither sequential experience nor reward. Instead, our data suggest that spiking sequences may represent individual concepts in the human brain through a temporally stereotyped activation of a neural ensemble that emerges during the initial experience of an event and that is replayed when its memory is retrieved.

REFERENCES AND NOTES

1. E. Tulving, in *Organization of Memory*, E. Tulving, W. Donaldson, Eds. (Academic Press, 1972), pp. 381–403.
2. J. L. McClelland, B. L. McNaughton, R. C. O'Reilly, *Psychol. Rev.* **102**, 419–457 (1995).
3. J. D. Johnson, M. D. Rugg, *Cereb. Cortex* **17**, 2507–2515 (2007).
4. B. P. Staresina, R. N. A. Henson, N. Kriegeskorte, A. Alink, *J. Neurosci.* **32**, 18150–18156 (2012).
5. L. Deuker *et al*., *J. Neurosci.* **33**, 19373–19383 (2013).
6. R. B. Yaffe *et al*., *Proc. Natl. Acad. Sci. U.S.A.* **111**, 18727–18732 (2014).
7. W. E. Skaggs, B. L. McNaughton, *Science* **271**, 1870–1873 (1996).
8. Z. Nádasdy, H. Hirase, A. Czurkó, J. Csicsvari, G. Buzsáki, *J. Neurosci.* **19**, 9497–9507 (1999).
9. A. K. Lee, M. A. Wilson, *Neuron* **36**, 1183–1194 (2002).
10. D. J. Foster, M. A. Wilson, *Nature* **440**, 680–683 (2006).
11. K. Diba, G. Buzsáki, *Nat. Neurosci.* **10**, 1241–1242 (2007).
12. D. Ji, M. A. Wilson, *Nat. Neurosci.* **10**, 100–107 (2007).
13. M. F. Carr, S. P. Jadhav, L. M. Frank, *Nat. Neurosci.* **14**, 147–153 (2011).
14. B. E. Pfeiffer, D. J. Foster, *Nature* **497**, 74–79 (2013).
15. G. Girardeau, K. Benchenane, S. I. Wiener, G. Buzsáki, M. B. Zugaro, *Nat. Neurosci.* **12**, 1222–1223 (2009).
16. S. P. Jadhav, C. Kemere, P. W. German, L. M. Frank, *Science* **336**, 1454–1458 (2012).
17. G. Buzsáki, *Hippocampus* **25**, 1073–1188 (2015).
18. D. Khodagholy, J. N. Gelinas, G. Buzsáki, *Science* **358**, 369–372 (2017).
19. H. R. Joo, L. M. Frank, *Nat. Rev. Neurosci.* **19**, 744–757 (2018).
20. A. Fernández-Ruiz *et al*., *Science* **364**, 1082–1086 (2019).
21. N. Axmacher, C. E. Elger, J. Fell, *Brain* **131**, 1806–1817 (2008).
22. B. P. Staresina *et al*., *Nat. Neurosci.* **18**, 1679–1686 (2015).
23. H. Zhang, J. Fell, N. Axmacher, *Nat. Commun.* **9**, 4103 (2018).
24. Y. Liu, R. J. Dolan, Z. Kurth-Nelson, T. E. J. Behrens, *Cell* **178**, 640–652.e14 (2019).
25. A. P. Vaz, S. K. Inati, N. Brunel, K. A. Zaghloul, *Science* **363**, 975–978 (2019).
26. T. M. Norman *et al*., *Science* **365**, eaax1030 (2019).
27. A. I. Jang, J. H. Wittig Jr., S. K. Inati, K. A. Zaghloul, *Curr. Biol.* **27**, 1700–1705.e5 (2017).
28. J. H. Wittig Jr., A. I. Jang, J. B. Cocjin, S. K. Inati, K. A. Zaghloul, *Nat. Neurosci.* **21**, 808–810 (2018).
29. M. Le Van Quyen *et al*., *J. Neurosci.* **28**, 6104–6110 (2008).
30. G. Buzsáki, *Neuroscience* **31**, 551–570 (1989).

ACKNOWLEDGMENTS

We thank N. Brunel, A. Sanzeni, A. Zadeh, L. Bachschmid-Romano, V. Sreekumar, J. Chapeton, and Z. Xie for helpful and insightful comments on the manuscript. We are indebted to all patients who have selflessly volunteered their time to participate in this study. **Funding:** This work was supported by the Intramural Research Program of the National Institute for Neurological Disorders and Stroke (NINDS). This work was also supported by National Institute of General Medical Sciences grant T32 GM007171 and NINDS grant F31 NS113400 to A.P.V. **Author contributions:** A.P.V. and K.A.Z. conceptualized the study; A.P.V. performed all data analysis, software development, and visualization; A.P.V., J.H.W., S.K.I., and K.A.Z. curated the data; A.P.V. and K.A.Z. wrote the original draft; K.A.Z. supervised the study; and A.P.V., J.H.W., S.K.I., and K.A.Z. reviewed and edited the final manuscript. **Competing interests:** The authors declare no competing interests. **Data and materials availability:** The data that support the findings of this study are available for public download at https://neuroscience.nih.gov/ninds/zaghloul/downloads.html.

SUPPLEMENTARY MATERIALS

science.sciencemag.org/content/367/6482/1131/suppl/DC1
Materials and Methods
Supplementary Text
Figs. S1 to S27
Table S1
References (*31*–*37*)

View/request a protocol for this paper from *Bio-protocol*.

1 November 2019; accepted 5 February 2020
10.1126/science.aba0672

SOLAR CELLS

Efficient tandem solar cells with solution-processed perovskite on textured crystalline silicon

Yi Hou[1]*, Erkan Aydin[2]*, Michele De Bastiani[2]*, Chuanxiao Xiao[3]*, Furkan H. Isikgor[2], Ding-Jiang Xue[1], Bin Chen[1], Hao Chen[1], Behzad Bahrami[4], Ashraful H. Chowdhury[4], Andrew Johnston[1], Se-Woong Baek[1], Ziru Huang[1], Mingyang Wei[1], Yitong Dong[1], Joel Troughton[2], Rawan Jalmood[2], Alessandro J. Mirabelli[2], Thomas G. Allen[2], Emmanuel Van Kerschaver[2], Makhsud I. Saidaminov[1], Derya Baran[2], Qiquan Qiao[4], Kai Zhu[3], Stefaan De Wolf[2]†, Edward H. Sargent[1]†

Stacking solar cells with decreasing band gaps to form tandems presents the possibility of overcoming the single-junction Shockley-Queisser limit in photovoltaics. The rapid development of solution-processed perovskites has brought perovskite single-junction efficiencies >20%. However, this process has yet to enable monolithic integration with industry-relevant textured crystalline silicon solar cells. We report tandems that combine solution-processed micrometer-thick perovskite top cells with fully textured silicon heterojunction bottom cells. To overcome the charge-collection challenges in micrometer-thick perovskites, we enhanced threefold the depletion width at the bases of silicon pyramids. Moreover, by anchoring a self-limiting passivant (1-butanethiol) on the perovskite surfaces, we enhanced the diffusion length and further suppressed phase segregation. These combined enhancements enabled an independently certified power conversion efficiency of 25.7% for perovskite-silicon tandem solar cells. These devices exhibited negligible performance loss after a 400-hour thermal stability test at 85°C and also after 400 hours under maximum power point tracking at 40°C.

Through an intensive worldwide effort, perovskite solar cell (PSC) power conversion efficiencies (PCEs) have increased from an initial 3.8% to a certified 25.2% during the past decade (*1*, *2*). This progress is based on the combination of materials properties such as a low energy required for crystal formation (*3*), a sharp optical absorption edge (*4*), and a tunable band gap (*5*) ideally suited for photovoltaic (PV) applications. The rapid development of PSCs is further enabled through the use of solution-based coating methods to deposit the semiconductors (*6*).

These properties also make PSCs attractive as top cells for tandem applications that use lower band gap bottom cells such as crystalline silicon (c-Si) and copper indium gallium selenide (CIGS) (*7*–*18*). By reducing thermalization losses, stacking PV absorbers of decreasing band gap in a multijunction device can overcome the Shockley-Queisser efficiency limit of 33.7% for single-junction solar cells. The combination with a c-Si bottom cell is of particular appeal, because single-junction c-Si–based technology has come to dominate the PV market. However, as c-Si solar cell efficiencies approach their practical limits, multijunction technologies using a c-Si bottom cell are of interest to drive further efficiency improvements.

[1]Department of Electrical and Computer Engineering, University of Toronto, Toronto, Ontario M5S 1A4, Canada. [2]KAUST Solar Center (KSC), Physical Sciences and Engineering Division (PSE), King Abdullah University of Science and Technology (KAUST), Thuwal 23955-6900, Kingdom of Saudi Arabia. [3]National Renewable Energy Laboratory (NREL), Golden, CO 80401, USA. [4]Department of Electrical Engineering, Center for Advanced Photovoltaics, South Dakota State University, Brookings, SD 57007, USA.
*These authors contributed equally to this work.
†Corresponding author. Email: stefaan.dewolf@kaust.edu.sa (S.D.W.); ted.sargent@utoronto.ca (E.H.S.)

Silicon heterojunction technology is attractive for tandem solar cells because of its high PCE and comparatively straightforward tandem integration. At present, most reported monolithic perovskite-silicon tandem devices are based on a single-side texturing configuration: c-Si wafers with their front flat-polished so that it is compatible with existing solution-based perovskite fabrication processes and a textured back side for enhanced light trapping relative to that of a double-side polished c-Si device (*8*, *14*–*16*, *18*). This configuration, however, provides limited light-trapping benefits and requires additional antireflection foils that do not provide sufficient light trapping compared with the textured counterpart (*18*). Furthermore, the effectiveness of antireflection foils can be compromised upon encapsulation. The preparation of such atomically smooth surfaces is also not practiced industrially owing to the high processing costs involved. Building up efficient tandems using double-side textured wafers—the industry-compatible c-Si approach—still challenges the PV community.

As a result, recent attention has shifted to combining perovskites with fully textured c-Si (*7*). The benefits of fully textured tandems have been demonstrated previously by Sahli *et al.* using a hybrid two-step deposition method combining sequential coevaporation of PbI_2 and CsBr and solution conversion (*7*). Unfortunately, the fill factor (FF) was moderate, a result of the limited perovskite quality achieved using this approach (*19*, *20*). More efficient, but also more complex, thermal coevaporation enables textured tandems; however, the large vapor-pressure difference between the organic and inorganic components demands a high level of control over the deposition rates of each precursor during the evaporation process (*21*).

Early efforts to deposit perovskites by using solution techniques on top of micrometer-sized Si pyramids quickly revealed a number of hurdles: uncovered Si pyramids, shunt paths, and inefficient charge collection in films with variable thickness. In addition, the application of conventional surface-passivation techniques—a prerequisite for state-of-the-art PSC device performance—are incompatible with the rough perovskite surfaces that result from the underlying c-Si texture (*7*). So far, insulating solution-processed passivants have failed to cover rough surfaces with the needed consistency of a thickness of a few nanometers.

Previous reports of perovskite-silicon tandems atop textured c-Si bottom cells have relied on physical vapor deposition of the perovskite front cell, rather than solution-processed perovskite cells on textured c-Si bottom cells. We sought to develop a high-quality micrometer-thick perovskite to cover the pyramids and, simultaneously, to enhance charge collection in these thick films through improved drift and diffusion of photogenerated carriers. We combined solution-processed, micrometer-thick, wide–band gap perovskite solar cells with pyramidal-textured c-Si bottom cells. This approach achieved a threefold enhanced depletion width in the perovskite semiconductor at the valleys of Si pyramids, improving carrier collection, as revealed using nanometer-scale kelvin probe force microscopy (KPFM).

To further increase carrier diffusion length, we introduced a conformal surface-passivation strategy for rough surfaces by anchoring a self-limiting passivant on the wide–band gap perovskite surface. This passivant also suppresses phase segregation. In addition, micrometer-thick perovskites allowed us to maintain a plateau of external quantum efficiency (EQE) of 92 to 93% across the spectral range of 650 to 730 nm. The fully textured bottom cells minimized reflection losses and efficient light trapping was achieved for the bottom cells, crucial to satisfying current-matching conditions. Overall, with the combined enhancements in charge drift and diffusion, the best tandem cells herein achieved an independently certified efficiency of 25.7%, combined with negligible performance loss after 400-hour thermal-stability tests at 85°C and also after 400 hours under maximum power point (MPP) tracking at 40°C.

As seen in the scanning electron microscope (SEM) top-view images, the textured c-Si features 2-μm-sized (111) faceted pyramids that were fabricated by alkaline wet-chemical etching (Fig. 1A). When forming tandems atop a textured c-Si bottom cell, it is important that one control the perovskite morphology and film thickness. When the perovskite film was deposited under fabrication conditions used for conventional planar perovskites (generally

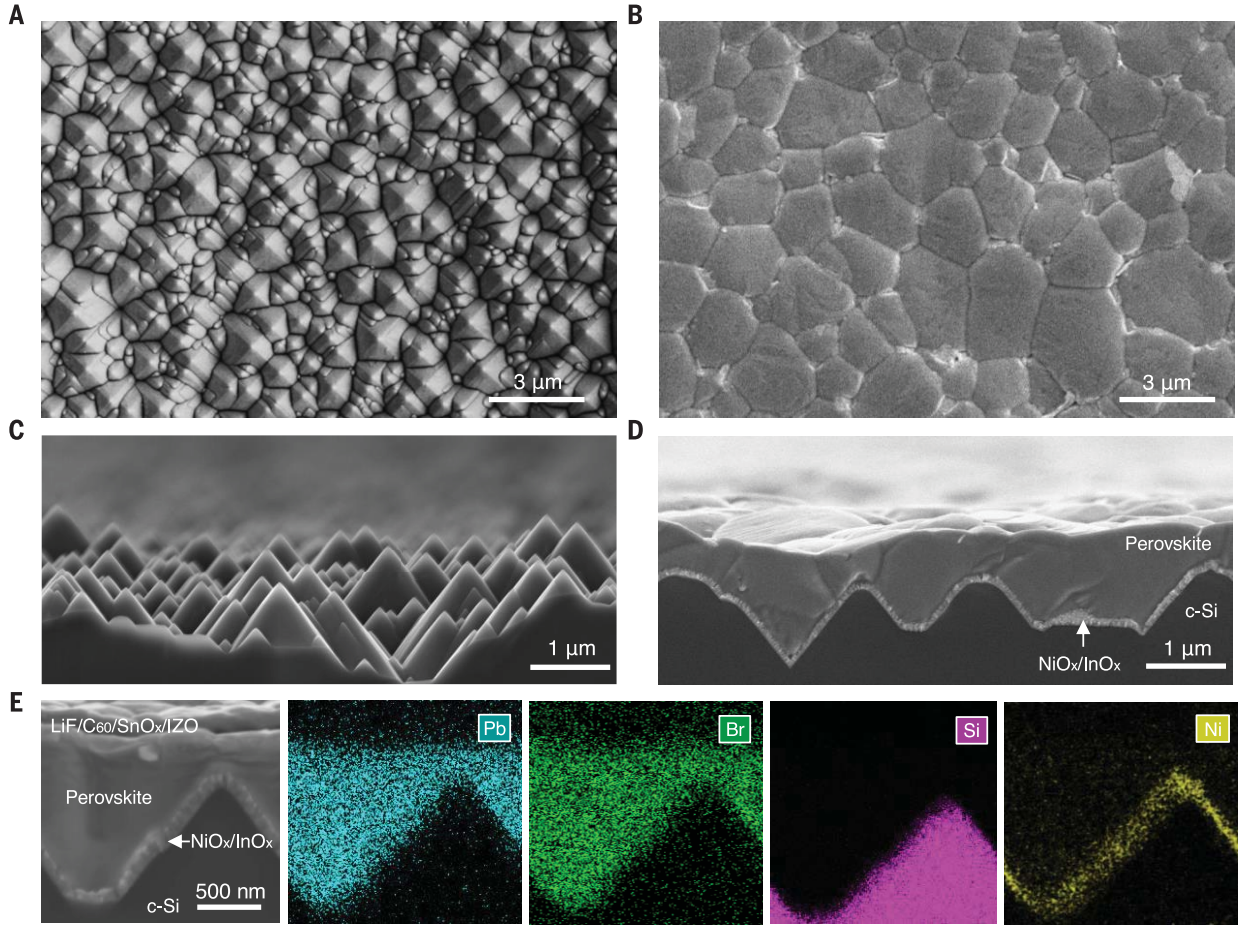


Fig. 1. Microstructure of solution-processed perovskite top cells on textured c-Si bottom cells. (**A** and **B**) SEM top-view images of the textured c-Si surface with an average pyramid size of 2 μm (A) and corresponding substrates covered by solution-processed perovskite crystal (B). (**C** and **D**) SEM cross-section images of a textured c-Si with an average pyramid size of 2 μm (C) and corresponding substrates covered by solution-processed perovskite crystal (D). (**E**) SEM image with corresponding EDS maps indicating the distribution of lead (Pb, aqua), bromide (Br, green), silicon (Si, purple), and nickel (Ni, yellow) inside the solar cell. Lead and bromide distribution were confined to the perovskite layer.

resulting in 400- to 600-nm-thick films), pyramids that were not capped with perovskite were observed, and these regions created shunt paths in devices (fig. S1). To fully cover the micrometer-sized pyramids, we used a concentrated (1.65 to 1.75 M) precursor that resulted in a micrometer-thick perovskite with large (2 to 4 μm) grain sizes (Fig. 1B). This process enabled us to achieve uniform perovskite coverage of the pyramids and eliminated the need for additional flattening processes (Fig. 1, C and D).

To achieve current matching, we opted to broaden the band gap of the micrometer-thick perovskite rather than reduce the thickness of a smaller–band gap perovskite because the latter approach would uncover pyramids. This thick, wide–band gap perovskite (1.68 eV, $Cs_{0.05}MA_{0.15}FA_{0.8}PbI_{2.25}Br_{0.75}$) top cell also provided a path toward a higher ultimate efficiency limit in tandem solar cells (fig. S2).

Because the size of the Si pyramids and perovskite thickness were similar, this infiltrated morphology differs from previously reported flat and conformal architectures used in perovskite-silicon tandem devices (fig. S3) (*7*, *8*, *14*, *15*). These images also suggest that the textured structures substantially modified the surface geometry by increasing the contact area. Rather than producing a conformal coating with uniform thickness, which would be similar to the evaporation case, the solution-processed perovskite smoothly overcoated the pyramid geometry while retaining the curvature of the textured surface beneath (Fig. 1D). The elemental distribution within the tandems measured by means of energy-dispersive x-ray spectroscopy (EDS; Fig. 1E) confirmed the presence of a textured layer stack. From the detailed features of the perovskite and conformal NiO_x interface, we did not see undesired accumulation of hole-transport layer (HTL) material at the bottom, nor did we observe HTL material absence at the facets of the Si pyramids (*7*, *8*, *14*, *15*).

Thick perovskite layers require sufficiently long charge-carrier diffusion lengths to enable efficient charge collection. This condition demands perovskite crystals and surfaces of high electronic quality. To increase the performance of single-junction wide–band gap PSCs, much research has focused on developing surface treatments (*22*). Trioctylphosphine oxide (TOPO) can substantially reduce nonradiative recombination and increase perovskite stability (*23*), but its insulating nature inhibits charge transport in devices. In addition, the rough surface of textured c-Si devices sets an additional challenge in the search for surface passivation. A passivant film must conformally coat and passivate the rough top perovskite surface with readily controlled thickness and functional groups without being overly sensitive to surface topography, treatment time, and perovskite thickness. Moreover, this treatment should not dissolve the perovskite nor alter its crystal structure (*24*).

We pursued an approach in which we exposed the rough perovskite top surface to 1-butanethiol vapor, a technique adapted in light of previous work performed on thiol-based self-assembled monolayer growth on metal surfaces. The thiol group anchored to the perovskite surface by strong coordination of the thiol on Pb^{2+}. The thiol molecules rapidly

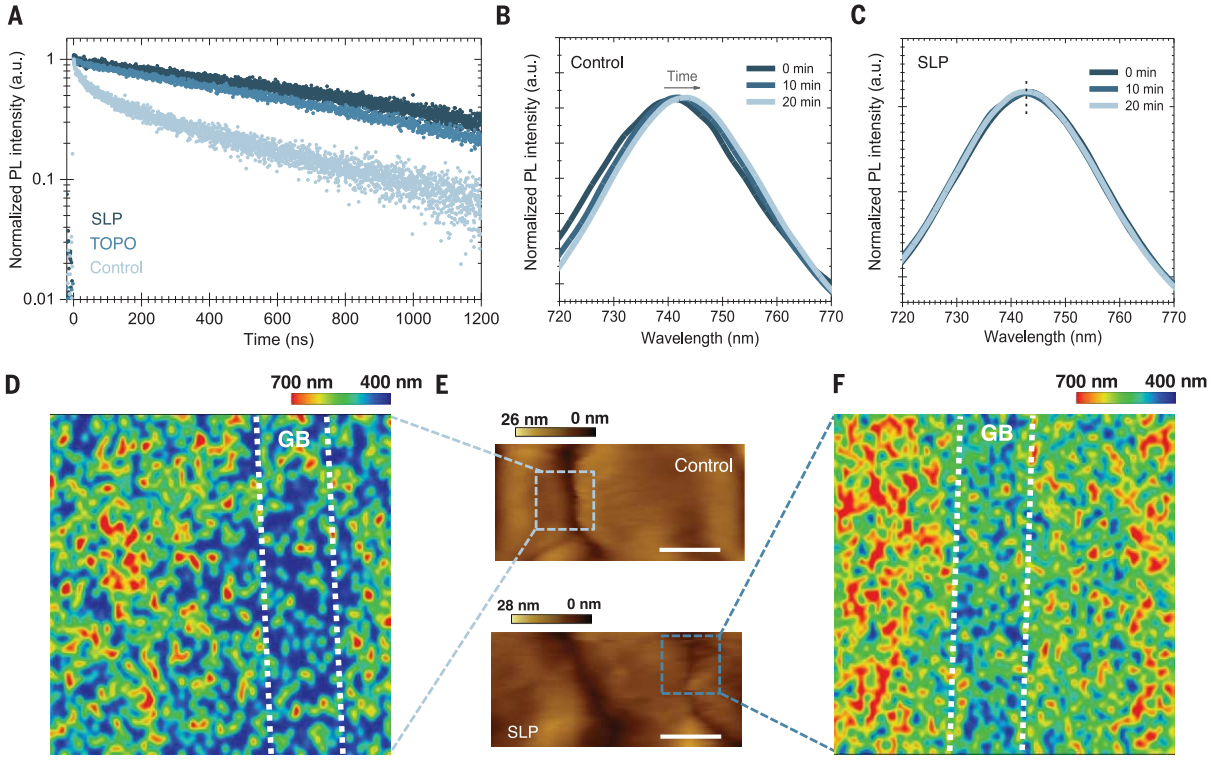


Fig. 2. Effects of SLP on diffusion length and phase segregation in micrometer-thick wide–band gap perovskite. (**A**) TRPL spectra of 1.68-eV–band gap thin films under different surface treatments. a.u., arbitrary units. (**B**) Normalized PL spectra of control perovskite films after illuminating for 0, 10, and 20 min. (**C**) Normalized PL spectra of SLP-treated perovskite films after illuminating for 0, 10, and 20 min. (**D**) Nanoscale-resolved mapping of the area indicated by the light blue square in (E) (100 nm by 100 nm) of the diffusion length of the control perovskite. The white dashed line shows the corresponding grain-boundary (GB) area. (**E**) Contact-mode atomic force microscopy (AFM) topography of the control sample (top) and SLP perovskite (bottom) (scale bar, 100 nm). (**F**) Nanoscale-resolved mapping of the area indicated by the dark blue square in (E) (100 nm by 100 nm) of the diffusion length of the SLP perovskite. The white dashed line shows the corresponding GB area.

diffused through the vapor phase to the perovskite surface, in contrast with thiol passivation of PbS colloidal quantum dots, where ligand exchange occurred in solution. Because of the self-limiting nature of thiol passivation, no anchoring sites were present after the initial passivation for further growth of additional layers. Thus, prolonged exposure did not damage the perovskite.

We used ultrafast transient absorption spectroscopy to investigate the phase distribution of 1.68-eV–band gap perovskite films after different treatment times. The two classes of treated films each showed a single ground-state bleaching peak centered at ~725 nm (fig. S4). This result indicated that the perovskite films existed compositionally within a single phase and that the bulk properties of the perovskite film could be stabilized with the thiol self-limiting passivation (SLP) treatment. We confirmed identical recombination kinetics for the film after 30-min and 20-hour SLP treatments: The data (fig. S4) attest to the time-insensitivity of the passivation process. Similarly, there were no differences in surface-sensitive grazing-incidence wide-angle x-ray scattering (GIWAXS) measurements between the samples with different SLP treatment times. After different treatment times, the perovskite peaks maintained their intensities and positions, suggesting no change in crystal structure and orientation (fig. S5).

After SLP treatment, we observed in time-resolved photoluminescence (TRPL) an increase in the carrier lifetime from 570 to 900 ns when we measured the samples from air-perovskite sides. This is ~15% higher than that of similar films treated with TOPO (Fig. 2A) and ~60% higher than that of control samples. We propose that passivation using smaller-sized thiols provided increased diffusion through the vapor phase and reduced steric hindrance. When we illuminated from the glass-perovskite side, the carrier lifetime was essentially similar in these three samples (fig. S6). Passivation was most effective on the top surface of thick perovskite, where, in the pristine case, major carrier recombination would otherwise have occurred.

The SLP treatment also enhanced phase stability of the perovskite. After 20 min of continuous light exposure, the SLP-treated films exhibited a stable PL peak position, whereas the control sample showed a red shift in the peak position, indicative of phase segregation (Fig. 2, B and C). This result is in agreement with earlier conclusions from Belisle *et al.* demonstrating that charge accumulation and carrier trapping at perovskite surfaces are drivers of photoinduced halide segregation and that efficiently passivating the perovskite surfaces suppresses phase segregation and stabilizes wide–band gap perovskites (*25*).

A representative, randomly selected 100-nm–by–100-nm area for topographic imaging that included grain boundaries (red square in fig. S7) was mapped for the nanoscale charge-carrier diffusion length, which is related to the local charge-carrier transport time (fig. S8) and charge-carrier recombination lifetime (fig. S9). Figure 2, D to F, presents nanoscale diffusion-length maps of both control sample and SLP-treated perovskite at similar regions, indicated by the blue squares. The diffusion length was improved in both grain and grain boundaries for SLP perovskites compared with control samples. The diffusion length in SLP perovskites within grains was ~570 nm. At the grain boundaries, the diffusion length of the SLP perovskite decreased by ~50 nm, whereas the diffusion length in the control sample decreased by ~100 nm (fig. S10). Thus,

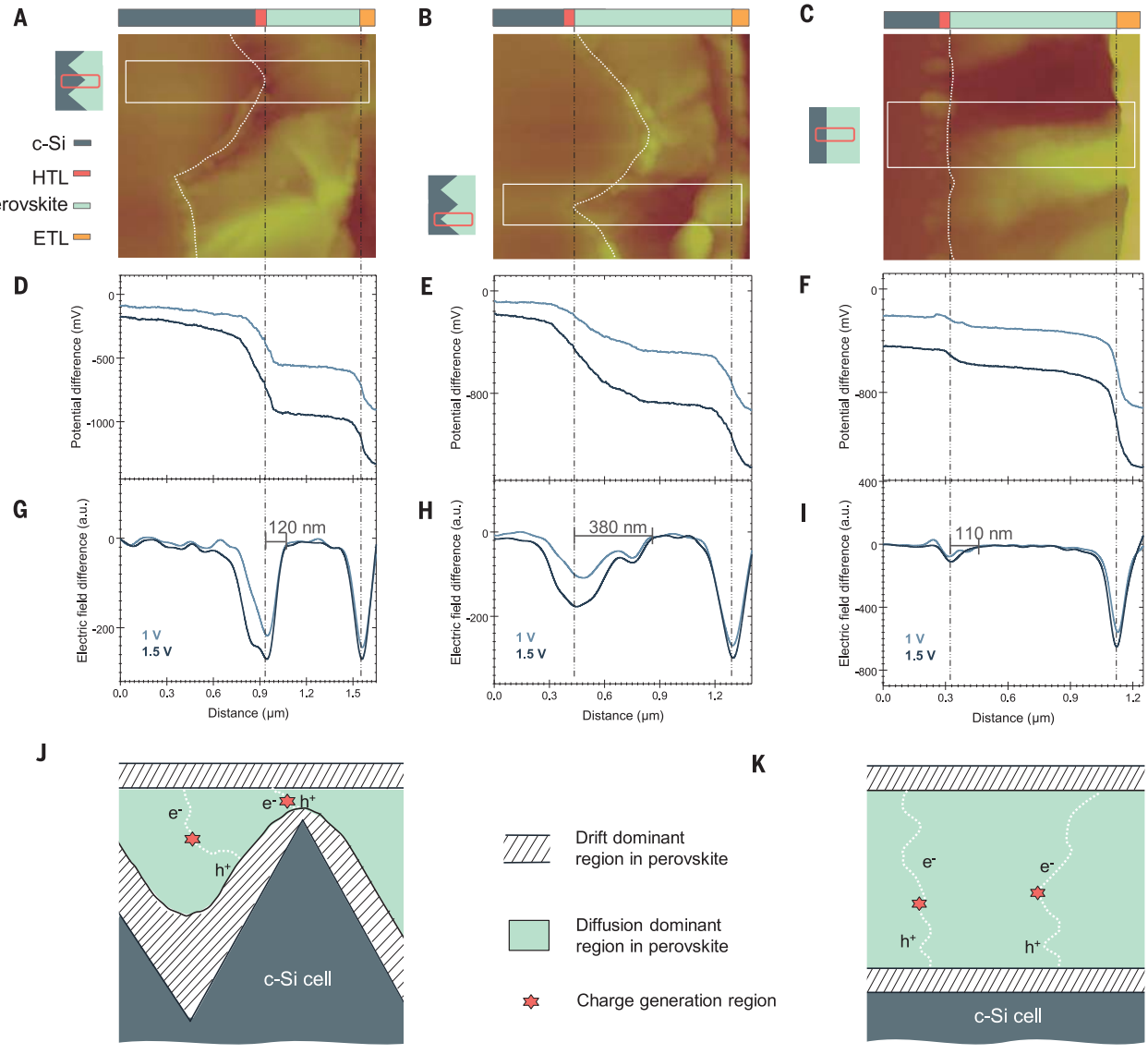


Fig. 3. Enhanced charge extraction in textured structured tandem cells. (**A** to **C**) AFM image of a cross section of the peak of a pyramid in the textured and flat tandem with a schematic showing each layer across the top of the Si bottom cell and the corresponding measured electric-potential zone. (**D** to **F**) Potential-difference profiling across the device under different bias voltages subtracted from the 0 V curve. (**G** to **I**) Electric-field difference across the device, taken by the first derivative in (D) to (F). (**J** and **K**) Schematics of electric-field distribution in textured (J) and flat tandem devices (K). h^+, holes; e^-, electrons.

passivation of the grain boundaries for the SLP perovskite increased the charge diffusion length compared with the control sample.

To probe the effects of the textured structure on the electrical field in the vertical direction, we used nanometer-scale KPFM to profile and observe the differences in electric-potential (or electric-field) distribution across the flat and textured devices. To determine the bulk profile from the surface measurement, we applied different forward-bias voltages of 1 and 1.5 V to the device and imaged the cross-sectional surface potential under each voltage (figs. S11 to S20). The junction characteristic was assessed from the small current flow, or equivalent shunt resistance, under bias, which was acquired by measuring the voltage drop across the cross-sectional surface.

By taking the first derivative of the potential difference, we determined the electric-field distribution relative to the metallurgical interfaces (Fig. 3, A to I). We observed two prominent junction peaks at the HTL-perovskite and perovskite–electron-transport layer (ETL) interfaces, whereas the electric field was near zero inside the perovskite layer. The perovskite-ETL junction has a similar strength and depletion width for both flat and textured cells, which agreed with the perovskite-ETL interfaces being identical for these two devices. Interestingly, the electric field at the HTL-perovskite interface was enhanced when a textured substrate was used (Fig. 3, J and K).

We determined that the depletion region in the perovskite (at the HTL-perovskite interface) was much wider at the valley of Si pyramids (~380 nm) than at their top (~120 nm) or compared with flat perovskite cells. This result implies that where the perovskite was the thickest, the depletion width was the largest, which would be desirable for effective charge collection. At the pyramid valleys, the perovskite was more confined and was subjected to electrical fields superimposed from neighboring HTL-coated pyramids. When Si

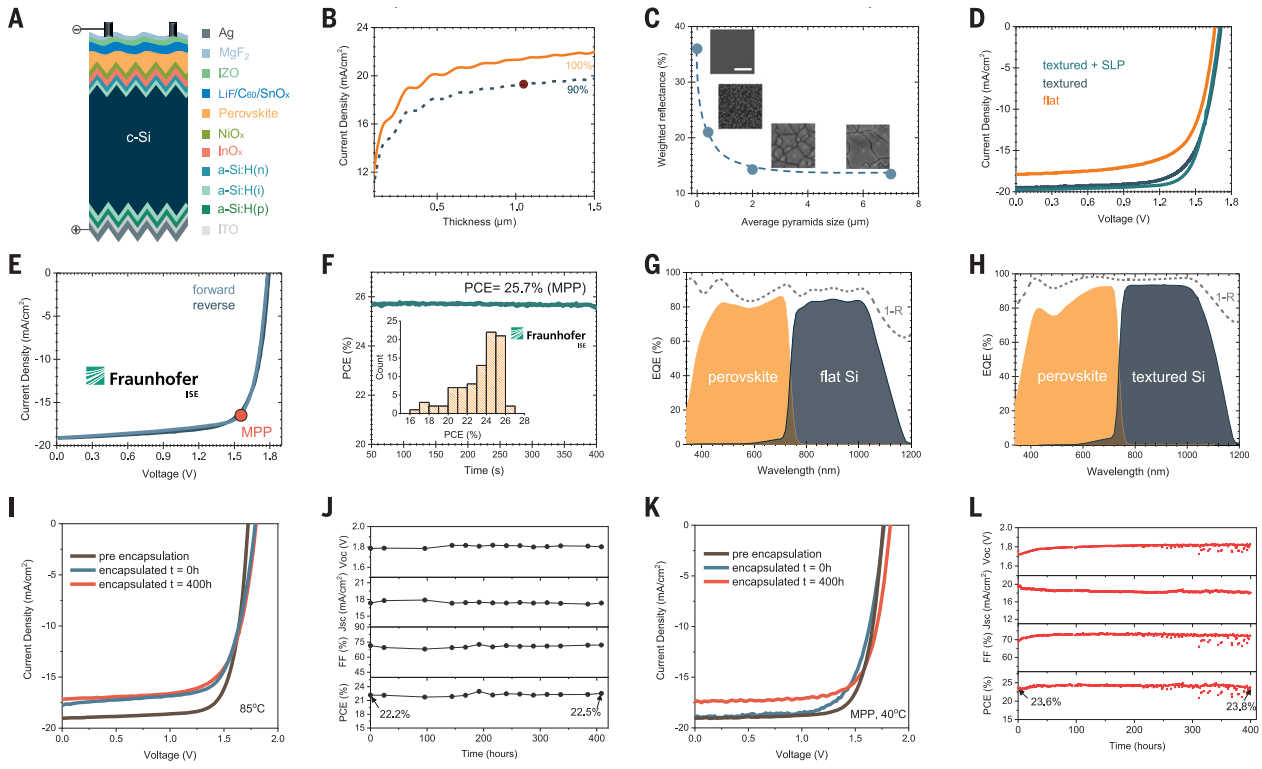


Fig. 4. Device characterization and stability of tandems. (**A**) Schematic of solution-processed perovskite–textured silicon tandem architecture. a-Si:H(n), n-doped hydrogenated amorphous silicon; a-Si:H(i), intrinsic hydrogenated amorphous silicon; a-Si:H(p), p-doped hydrogenated amorphous silicon. (**B**) Calculated J_{SC} values of the perovskite cells as a function of perovskite layer thickness. The red dot represents the EQE-integrated J_{SC} value in the textured tandem top cell. (**C**) Measured weighted reflectance as a function of pyramid sizes of c-Si. Texturing size refers to the pyramid base. The SEM images of different texturing sizes are reported in the insets (scale bar, 2 µm). (**D**) *J-V* characteristics of flat, textured, and SLP-treated textured tandems. (**E**) *J-V* characteristics of certified SLP-treated textured tandems. (**F**) MPP tracking of certified SLP-treated textured tandems and PCE distributions of 88 individual tandem devices. (**G** and **H**) EQE of the flat (G) and textured (H) devices (integrated current of 18.2 mA/cm^2 for the top cell and 16.8 mA/cm^2 for the bottom cell in the flat device; 19.3 mA/cm^2 for the top cell and 19.2 mA/cm^2 for the bottom cell in the Fraunhofer ISE CalLab PV Cells–certified textured device). (**I**) *J-V* curves of tandem devices before encapsulation (glass and butyl rubber) at the beginning and the end of the 85°C stability test. (**J**) *J-V* parameters measured over a 400-hour stability test at 85°C (relative humidity ~45 to 50%). (**K**) *J-V* curves of the tandem devices before encapsulation (glass and POE) at the beginning and the end of the MPP stability tests. (**L**) *J-V* parameters measured over >400 hours of light-soaking under MPP load at 40°C.

pyramid valleys were sharper, depletion regions were wider (in a linear relation; detailed values are shown in tables S1 and S2), which further suggested that the depletion width correlates with the geometry factor. In contrast with the case of other deposition methods (such as coevaporation), this geometry was only observed when the solution-processed perovskite cells smoothed out the textured silicon cell and caused this beneficial geometry-dependent electric-field distribution. This finding agrees with the simulated results (fig. S21).

The KPFM observation accounted for device performance trends, in that charge collection was enhanced in the best pyramid devices. The stronger and wider depletion at the valley of the pyramids benefited charge collection of charge carriers photogenerated with long-wavelength incident light. Outside of the depletion region, the carriers needed to diffuse through the perovskite absorber layer to be collected. At the top of the Si pyramids, the depletion width was not broadened. However, here the distance between hole contact and electron contact was much shorter (100 to 300 nm), which was well within the typical range of efficient charge diffusion in a PSC (Fig. 3, J and K). In light of the surrounding pyramidal structure, charges generated in the textured perovskite had a shortened transport distance to both contacts compared with a flat perovskite cell.

Figure 4A sketches the cross section of the textured tandem. To explore the role of the thick perovskite, we studied the thickness-dependent current generation theoretically. As presented in Fig. 4B, the short-circuit current density (J_{SC}) of the perovskite cell increased with layer thickness. The red dot represents the experimental J_{SC} value of the ~1.1-µm-thick perovskite used in this work (fig. S22), which is within <10% of the theoretical limit. This certified ~19.3 mA/cm^2 value is among the highest values for a single-pass device with 1.68-eV–band gap perovskites (Fig. 4H). In contrast with opaque devices with reflection from the rear electrode, single-junction devices required a thicker absorber to capture more photons near the band edge. With more photons absorbed by the top cell, we expect an enhanced upper limit of tandem efficiency.

Spectrally weighted reflectances were calculated from the air mass (AM) 1.5 G spectrum in the range of 350 to 900 nm (Fig. 4C). To investigate the effect of pyramid size on the reflection loss, we also selected different Si pyramid sizes by tailoring the texturing process. Although the pyramids in commercial Si are typically in the range of 2 to 7 µm, the benefit to reflection began to saturate when the pyramid size reached 2 µm or less (see fig. S23). This result is encouraging for perovskite-silicon tandems because it suggests that well-established solution-processing techniques can be united with textured silicon (fig. S24).

We observed enhanced J_{SC} and FF in tandems (Fig. 4D and figs. S24 and S25) in the case of fully textured c-Si bottom cells. EQE measurements highlight the advantage of switching from a polished front side to a double-side textured architecture (Fig. 4, G and H). Reflections occurring in the flat design

induced more current loss in the 330- to 1200-nm range. The introduction of a front texture reduced the overall reflectance, especially at wavelengths of 550 and 800 nm. The J_{SC} integrated from the EQE spectra is in excellent agreement with that derived from the 1-sun current density–voltage (*J-V*) curve with enhanced J_{SC} in both the top cell and bottom cell on the double-side textured device.

Both differential EQE and absorption confirm the ~1.68-eV perovskite band gap (fig. S2). We observed narrower EQE overlap between the perovskite and Si cell. The textured-device EQE maintained a plateau at 92 to 93% in this region. This result is distinct from previous work based on 400- to 600-nm-thick perovskite on flat devices in which the perovskite lost EQE at wavelengths of 550 and 800 nm. This high EQE photocurrent, combined with enhanced charge extraction, resulted in high FF, leading to an improved device performance from 20.3 to 24.0% (table S3). In particular, by further adding SLP treatment, we observed a distinct increase of FF from 72 to 77% (Fig. 4D). By reducing the recombination area and improving the top contact design (fig. S26), we achieved a Fraunhofer ISE CalLab PV Cells–certified stabilized (at MPP) PCE of 25.7% (Fig. 4, E and F, and fig. S27).

The tandems reported herein show low hysteresis (Fig. 4E), high reproducibility (Fig. 4F and fig. S28), and excellent operational stability under accelerated tests (Fig. 4, I to L). We monitored the stability of devices encapsulated with glass and butyl rubber. We heated these devices to 85°C for 400 hours in the dark at ~40% relative humidity and found that the devices retained their original performance (Fig. 4, I and J). We also monitored 400-hour operating stability of devices encapsulated using glass and POE (polyolefin encapsulant): Here, we used 1-sun-equivalent illumination (fig. S29) at 40°C and ~40 to 50% relative humidity (Fig. 4, K and L). *J-V* curves in both scan directions [open-circuit voltage (V_{OC}) to J_{SC} and J_{SC} to V_{OC}] were measured at 10-min intervals at 100 mV/s from −0.1 to +1.9 V, and vice versa. Between measurements, the tandem solar cell was held at the MPP voltage as determined by the most recent *J-V* scan. Devices retained their original performance after 400 hours. In Fig. 4, I to K, the *J-V* curves of the tandem were reported before encapsulation, at the beginning of the test, and after 400 hours, and images are provided of devices at the end of the test. Overall, we attribute this good operating lifetime to the replacement of organic carrier-selective layers with NiO_x inorganic materials, which prevent iodine reaction with small-molecule organic HTLs (table S4).

REFERENCES AND NOTES

1. A. Kojima, K. Teshima, Y. Shirai, T. Miyasaka, *J. Am. Chem. Soc.* **131**, 6050–6051 (2009).
2. National Renewable Energy Laboratory, Best research-cell efficiencies (2020); www.nrel.gov/pv/cell-efficiency.html.
3. J. S. Manser, M. I. Saidaminov, J. A. Christians, O. M. Bakr, P. V. Kamat, *Acc. Chem. Res.* **49**, 330–338 (2016).
4. S. De Wolf *et al*., *J. Phys. Chem. Lett.* **5**, 1035–1039 (2014).
5. D. P. McMeekin *et al*., *Science* **351**, 151–155 (2016).
6. Y. Deng *et al*., *Nat. Energy* **3**, 560–566 (2018).
7. F. Sahli *et al*., *Nat. Mater.* **17**, 820–826 (2018).
8. M. Jošt *et al*., *Energy Environ. Sci.* **11**, 3511–3523 (2018).
9. Q. Han *et al*., *Science* **361**, 904–908 (2018).
10. S. Essig *et al*., *Nat. Energy* **2**, 17144 (2017).
11. M. Saliba *et al*., *Science* **354**, 206–209 (2016).
12. G. E. Eperon *et al*., *Science* **354**, 861–865 (2016).
13. J. Tong *et al*., *Science* **364**, 475–479 (2019).
14. B. Chen *et al*., *Joule* **3**, 177–190 (2019).
15. K. A. Bush *et al*., *Nat. Energy* **2**, 17009 (2017).
16. H. Shen *et al*., *Sci. Adv.* **4**, eaau9711 (2018).
17. F. Fu *et al*., *Nat. Energy* **2**, 16190 (2016).
18. J. Zheng *et al*., *Energy Environ. Sci.* **11**, 2432–2443 (2018).
19. W. S. Yang *et al*., *Science* **356**, 1376–1379 (2017).
20. Q. Jiang *et al*., *Nat. Photonics* **13**, 460–466 (2019).
21. L. Gil-Escrig *et al*., *Adv. Energy Mater.* **8**, 1703506 (2018).
22. E. Aydin, M. De Bastiani, S. De Wolf, *Adv. Mater.* **31**, e1900428 (2019).
23. I. L. Braly *et al*., *Nat. Photonics* **12**, 355–361 (2018).
24. D. W. deQuilettes *et al*., *Science* **348**, 683–686 (2015).
25. R. A. Belisle *et al*., *ACS Energy Lett.* **3**, 2694–2700 (2018).

ACKNOWLEDGMENTS

The manuscript was improved by the insightful reviews provided by anonymous reviewers. **Funding:** This publication is based upon work supported by the King Abdullah University of Science and Technology (KAUST) Office of Sponsored Research (OSR) under award no. OSR-2018-CPF-3669.02, KAUST OSR-CARF URF/1/3079-33-01, KAUST OSR-CRG URF/1/3383, and KAUST OSR-CRG2018-3737, and in part on work supported by the U.S. Department of the Navy, Office of Naval Research (grant award no. N00014-17-1-2524). This work was authored in part by the National Renewable Energy Laboratory, operated by Alliance for Sustainable Energy, LLC, for the U.S. Department of Energy (DOE) under contract no. DE-AC36-08GO28308 (De-risking Halide Perovskite Solar Cells program of the National Center for Photovoltaics, funded by the DOE Office of Energy Efficiency and Renewable Energy, Solar Energy Technologies Office). The views expressed in the article do not necessarily represent the views of the DOE or the U.S. government. The U.S. government retains and the publisher, by accepting the article for publication, acknowledges that the U.S. government retains a nonexclusive, paid-up, irrevocable, worldwide license to publish or reproduce the published form of this work, or allow others to do so, for U.S. government purposes. This work has been partially supported by NSF MRI (1428992), the U.S.-Egypt Science and Technology (S&T) Joint Fund, and the EDA University Center Program (ED18DEN3030025). This work is derived from the subject data supported in whole or part by NAS and USAID, and any opinions, findings, conclusions, or recommendations expressed in the paper are those of the authors alone, and do not necessarily reflect the views of USAID or NAS. **Author contributions:** Y.H., E.A., and M.D.B. conceived the idea and designed the experiments. Y.H., E.A., M.D.B., and A.J.M. fabricated the devices and conducted the *J-V* and EQE characterizations. C.X. conducted the KPFM study, C.X. and K.Z. analyzed and discussed the KPFM results, and C.X. wrote the KPFM portion of the manuscript. E.A. and F.H.I. developed the perovskite holes extraction layer. E.A. performed the optimization of the top electrodes and contact layout. J.T. developed the setup for stability and performed the MPP test. M.D.B. and R.J. developed the silicon texturing. M.D.B, T.A., E.V.K., and R.J. developed the silicon bottom cell. D.B. supervised the stability test. B.C. contributed to SEM measurements. D.-J.X. and H.C. contributed to perovskite development and passivation analysis. M.W., Z.H., and Y.D. contributed to PL and transient reflection spectroscopy measurements. A.J. performed GIWAXS measurements. S.-W.B. contributed to finite-difference time domain simulations. Q.Q., B.B., and A.H.C. developed and implemented the mapping of transient photovoltage/transient photocurrent (TPV/TPC), analyzed the results, and wrote the TPV/TPC mapping portion of the manuscript. D.B., M.I.S., K.Z., and E.H.S. provided advice. Y.H., E.A., M.D.B., C.X., S.D.W., and E.H.S. composed the manuscript. All authors discussed the results and commented on the manuscript. **Competing interests:** None declared. **Data and materials availability:** All data needed to evaluate the conclusions in the paper are present in the paper or the supplementary materials.

SUPPLEMENTARY MATERIALS

science.sciencemag.org/content/367/6482/1135/suppl/DC1
Materials and Methods
Figs. S1 to S29
Tables S1 to S4
References (*26*–*31*)

5 September 2019; resubmitted 21 December 2019
Accepted 7 February 2020
10.1126/science.aaz3691

MOLECULAR BIOLOGY

Pervasive functional translation of noncanonical human open reading frames

Jin Chen[1,2], Andreas-David Brunner[3], J. Zachery Cogan[1,2], James K. Nuñez[1,2], Alexander P. Fields[1,2]*, Britt Adamson[1,2]†, Daniel N. Itzhak[4], Jason Y. Li[4], Matthias Mann[3,5], Manuel D. Leonetti[4], Jonathan S. Weissman[1,2]‡

Ribosome profiling has revealed pervasive but largely uncharacterized translation outside of canonical coding sequences (CDSs). In this work, we exploit a systematic CRISPR-based screening strategy to identify hundreds of noncanonical CDSs that are essential for cellular growth and whose disruption elicits specific, robust transcriptomic and phenotypic changes in human cells. Functional characterization of the encoded microproteins reveals distinct cellular localizations, specific protein binding partners, and hundreds of microproteins that are presented by the human leukocyte antigen system. We find multiple microproteins encoded in upstream open reading frames, which form stable complexes with the main, canonical protein encoded on the same messenger RNA, thereby revealing the use of functional bicistronic operons in mammals. Together, our results point to a family of functional human microproteins that play critical and diverse cellular roles.

Efforts to bioinformatically discover and annotate protein-coding open reading frames (ORFs) in genomes, termed coding sequences (CDSs), have traditionally relied on rules such as amino acid conservation and homology, translation initiation from an AUG start codon, and minimum length (i.e., 100 amino acids) (*1*). These rules have been widely adopted on the basis of the assumption that short peptides are unlikely to fold into stable structures to perform functions. However, the generality of these rules has been challenged. For example, the ribosomal protein RPL41 is a 25–amino acid (aa) peptide and both sarcolipin (SLN, 31 aa) and phospholamban (PLN, 52 aa) bind to and regulate the sarcoplasmic Ca^{2+} transporter SERCA (*2*, *3*). Additionally, MYC can be translated from a noncanonical start codon CUG (*4*), which demonstrates that non-AUG initiation can produce functional proteins. Recent studies have added a handful of examples of short proteins, or microproteins (also called micropeptides or just peptides), performing diverse functions (*5*–*18*), some encoded on transcripts annotated as long noncoding RNAs (lncRNAs). Finally, upstream ORFs (uORFs), located in the 5′ untranslated regions of mRNAs, have long been implicated in cis-acting translational control of the main, canonical CDS (*19*–*21*), though it has remained unclear whether they can generate stable, functional peptides.

Systematic identification of functional short CDSs remains challenging. Recent ribosome profiling (deep sequencing of ribosome-protected fragments) and mass spectrometry (MS) studies have identified thousands of previously unannotated CDSs (*22*–*25*) across bacteria, yeasts, viruses, and mammalian cells. However, for most cases, the cellular functions of these identified CDSs or their peptide products remain unexplored. We reasoned that the advent of CRISPR and its ability to precisely disrupt protein-coding regions (*26*), when combined with ribosome profiling, provides an opportunity to define and empirically characterize the functional protein-coding capacity of a given genome. In this work, we applied various types of approaches—including ribosome profiling, MS, and multiple CRISPR-based techniques—to systematically discover noncanonical CDSs encoded in the human genome and validate their critical roles in diverse cellular pathways.

To annotate potential CDSs comprehensively and accurately, we first investigated genome-wide translation by ribosome profiling across multiple cell types and conditions, including human induced pluripotent stem cells (iPSCs), iPSC-derived cardiomyocytes, human foreskin fibroblasts (HFFs), and HFFs infected with cytomegalovirus (*27*, *28*) (fig. S1A). We leveraged the ORF-RATER algorithm to annotate ORFs (*27*), incorporating multiple lines of evidence to identify ORFs undergoing active translation. This included consideration of the accumulation of ribosome densities at the start and stop codons, three-nucleotide periodicity, and additional experimental results, such as data from harringtonine-treated cells in which ribosomes are stalled at initiation sites (*27*). In iPSCs and cardiomyocytes, in addition to 9490 annotated CDSs (62% of the identified CDSs), we identified 3455 distinct, noncanonical CDSs (22%, i.e., with no in-frame overlap with previously annotated CDSs) and 2466 variant CDSs of annotated proteins (16%) in our high–statistical confidence set (Fig. 1A and materials and methods) (*27*). Among the distinct CDSs, 818 were CDSs on transcripts lacking prior protein-coding annotations ("new", i.e., lncRNAs), 2342 were upstream CDSs (i.e., uORFs or start overlaps: CDSs that overlap annotated start codons in a different reading frame), and only 13 were downstream CDSs. Similar numbers of CDSs were present in HFFs (fig. S1B), with 75% of the CDSs shared between the two cell types. Of the distinct CDSs, 96% are less than 100 aa in length, and 36% of the CDSs use non-AUG start codons (Fig. 1, B and C; see also fig. S2 for further characterizations).

Multiple lines of evidence suggest that the noncanonical CDSs are actively translated. The average ribosome density (metagene) of the lncRNA CDSs and of the translated uORFs closely mirrors footprints from that of annotated coding regions with strong three-nucleotide periodicities, a hallmark of active translation, as exemplified by traces from the lncRNA *LINC00998* transcript and a uORF of *ARL5A* (Fig. 1, D and E, and fig. S3). Our analysis also successfully recapitulated well-characterized short ORFs, such as the uORF on *ATF4* (*29*) and the recently discovered lncRNA-encoded microproteins MOXI/mitoregulin (*11*, *12*) and NoBody (*10*). Bona fide lncRNAs, such as *XIST*, *HOTAIR*, and *NEAT1*, were not identified to be protein coding (fig. S3E). Moreover, many of the CDSs were differentially translated during iPSC differentiation or viral infection (fig. S3F), providing evidence for translational control in different cell states.

MS-based proteomics in iPSCs and major human leukocyte antigen class I (HLA-I) peptidomics confirmed the stable expression of hundreds of noncanonical CDS peptides (Fig. 1F and figs. S4 and S5). HLA-I peptidomics identified 240 noncanonical peptides, which suggests that these peptides enter the HLA-I presentation pathway and contribute to the antigen repertoire and possible immunogenicity (Fig. 1F) (*30*). HLA-I prediction analysis cross-validated strong binding ($K_d \leq 50$ mM, where K_d is the dissociation constant) of noncanonical CDS HLA-I peptides to their respective allotypes (fig. S6) (*30*). MS-based proteomics using tryptic digestion identified far fewer noncanonical peptides, which may be due to challenges in detecting the trypsin-digested products from short, noncanonical CDSs or possibly to more rapid turnover of these noncanonical peptides (fig. S7).

To test whether translation of the noncanonical CDSs is important for cell growth and potentially yields functional peptides, we measured the growth phenotypes resulting from CRISPR-mediated ORF knockout in

[1]Department of Cellular and Molecular Pharmacology, University of California, San Francisco, CA 94158, USA. [2]Howard Hughes Medical Institute, University of California, San Francisco, CA 94158, USA. [3]Department of Proteomics and Signal Transduction, Max Planck Institute of Biochemistry, Martinsried 82152, Germany. [4]Cell Atlas Initiative, Chan Zuckerberg Biohub, San Francisco, CA 94158, USA. [5]Clinical Proteomics Group, Proteomics Program, Novo Nordisk Foundation Center for Protein Research, University of Copenhagen, Copenhagen 2200, Denmark.
*Present address: GRAIL, Inc., Menlo Park, CA 94025, USA.
†Present address: Department of Molecular Biology and Lewis-Sigler Institute for Integrative Genomics, Princeton University, Princeton, NJ 08544, USA.
‡Corresponding author. Email: jonathan.weissman@ucsf.edu

pooled screens (*26*). We designed a Cas9 ORF single guide RNA (sgRNA) library to specifically knock out thousands of the noncanonical CDSs identified by ribosome profiling (Fig. 2A and materials and methods) (*31*, *32*), targeting 1098 uORFs, 613 lncRNA CDSs, 352 extensions of annotated coding regions, 283 start overlaps, and 7 downstream CDSs. We performed pooled Cas9 knockout screens in iPSC and K562 chronic myeloid leukemia cells expressing Cas9 and the sgRNA library, akin to conventional pooled screens for essential proteins (*26*, *31*). We measured sgRNA abundance in the cell populations shortly after library transduction and after 10 additional population doublings by deep sequencing to quantify the fitness defect conferred by each sgRNA. We then calculated a phenotype score (γ) and

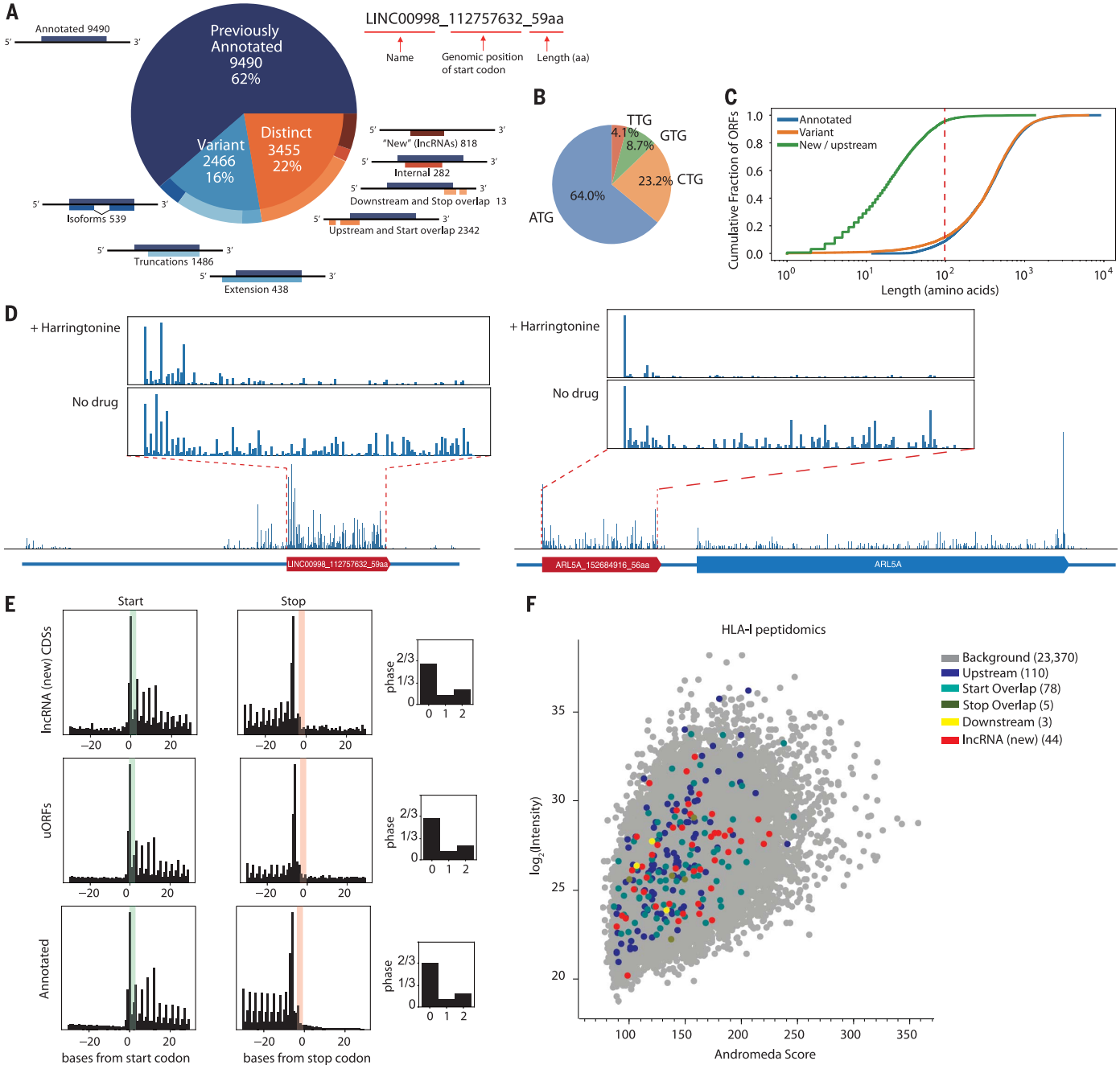
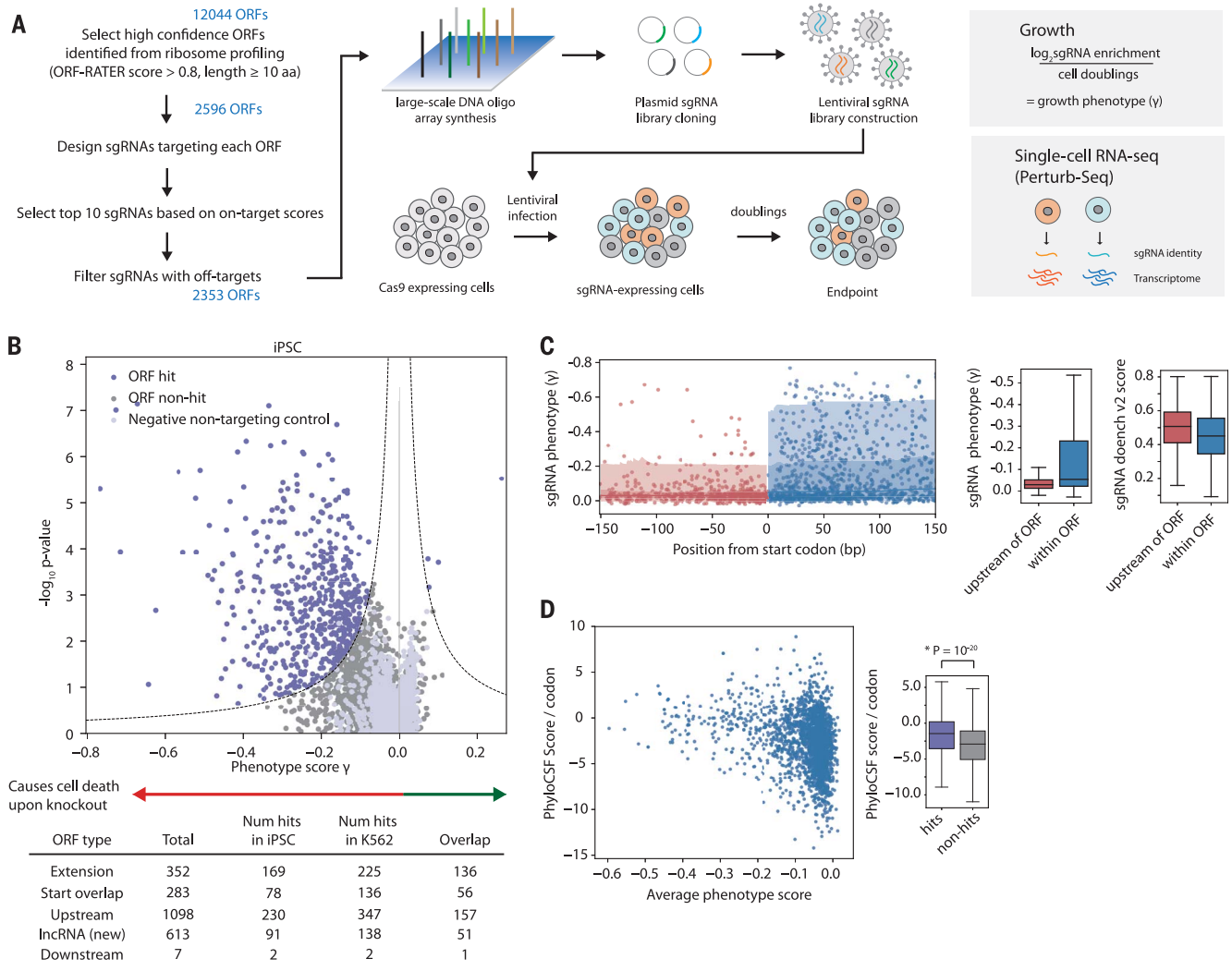


Fig. 1. Ribosome profiling and MS reveal translation of unannotated CDSs. (**A**) ORF-RATER analysis of ribosome profiling data: 62% are previously annotated coding sequences, whereas 16% are variants of canonical coding sequences that share portions of the coding sequence and 22% are distinct from annotated coding sequences. The naming convention of the identified ORFs is shown on the right. (**B**) Start-codon usage of the identified CDSs. (**C**) Cumulative distribution of CDS length. For distinct CDSs, 96% are smaller than 100 amino acids. (**D**) Example ribosome profiling traces of a lncRNA peptide from *LINC00998* and a uORF peptide from *ARL5A* displaying the hallmarks of translation, including peaks of density around the start codon following harringtonine treatment and three-nucleotide periodicities along the coding region. (**E**) Metagene analysis shows that the signatures of translation, including three-nucleotide periodicity in the expected reading frame, for uORFs and lncRNA CDSs are similar to those for annotated coding regions. (**F**) Identification of >200 noncanonical CDS peptides from HLA-I peptidomics, cross-validating their existence across the whole abundance range, with a mean Andromeda score of 141 compared with a total mean Andromeda score of 144. See materials and methods for further details.



ORF type	Total	Num hits in iPSC	Num hits in K562	Overlap
Extension	352	169	225	136
Start overlap	283	78	136	56
Upstream	1098	230	347	157
lncRNA (new)	613	91	138	51
Downstream	7	2	2	1

Fig. 2. Genome-scale CRISPR screens to identify functional, non-canonical CDSs. (**A**) Schematic of CRISPR library design and screening strategies, either by growth screens or Perturb-seq. For growth screens, frequencies of cells expressing a given sgRNA are determined by next-generation sequencing, and phenotype scores are quantified with the formula shown. For Perturb-seq, single-cell transcriptomes and sgRNA identities were obtained by single-cell RNA-seq. (**B**) Volcano plot summarizing knockout phenotypes and statistical significance (determined by Mann-Whitney *U* test) for ORFs targeted in the pooled screen in iPSCs. Each dot represents a targeted ORF, and ORF hits are labeled in purple, with a more negative phenotype score indicating a stronger growth defect. See materials and methods for further details. (**C**) Plot of the sgRNA phenotypes and distance from the start codon across all ORF hits. sgRNAs targeting the genome immediately upstream of the ORF (shown in red) have significantly lower phenotype scores than sgRNAs targeting within the ORF (shown in blue). Note the axis is increasingly negative (stronger) phenotype. The sgRNA phenotypes are quantified by the boxplot to the right. The difference is not because of differences in sgRNA on-target efficiencies, as quantified by the Doench v2 score. (**D**) The PhyloCSF score per codon (higher scores are more conserved across the Euarchontoglires) is generally higher for ORF hits (*$P = 10^{-20}$, Kolmogorov-Smirnov test) and ORFs with a stronger phenotype. Note that lack of a growth phenotype does not necessarily imply a low PhyloCSF score.

confidence (*P* value) for each ORF from the relative enrichment or depletion of sgRNAs targeting a particular ORF (Fig. 2B and materials and methods). In iPSCs, our screen identified >500 ORF knockout hits that resulted in statistically significant phenotypes. The hits include 169 genes that are variants of annotated proteins, 78 start overlap hits, 230 uORF hits, 91 lncRNA CDS hits, and 2 downstream CDS hits. iPSC and K562 cells had 401 shared hits, suggesting housekeeping or general cellular roles as well as CDSs that may play cell-specific functions (fig. S8). A fraction of the uORF hits do not have main, canonical CDSs with fitness defects upon knockout. This suggests an independent function of the uORFs or that disruption of the uORFs leads to increases in main CDS expression, which results in the growth phenotype (fig. S8E). Thus, unannotated CDSs with important functions across multiple cell types are an abundant feature of the genome.

Several lines of evidence further suggested that our screen reported specifically on the phenotypes of the selected ORFs. First, the phenotypes of control sgRNAs targeted directly upstream of each ORF in the genome (Fig. 2C) are significantly weaker than those of sgRNAs targeted within the ORF ($P = 10^{-26}$, Mann-Whitney test). Second, sgRNA phenotypes are independent of distance to other annotated proteins, splice sites, or transcriptional start sites (fig. S9A). Functionally, ORF hits are, on average, more phylogenetically conserved with a higher conservation score than non-hits (PhyloCSF score per codon, $P = 10^{-20}$, Kolmogorov-Smirnov test; Fig. 2D) (*33*), and they have other distinguishing sequence features (e.g., enrichment for Kozak consensus

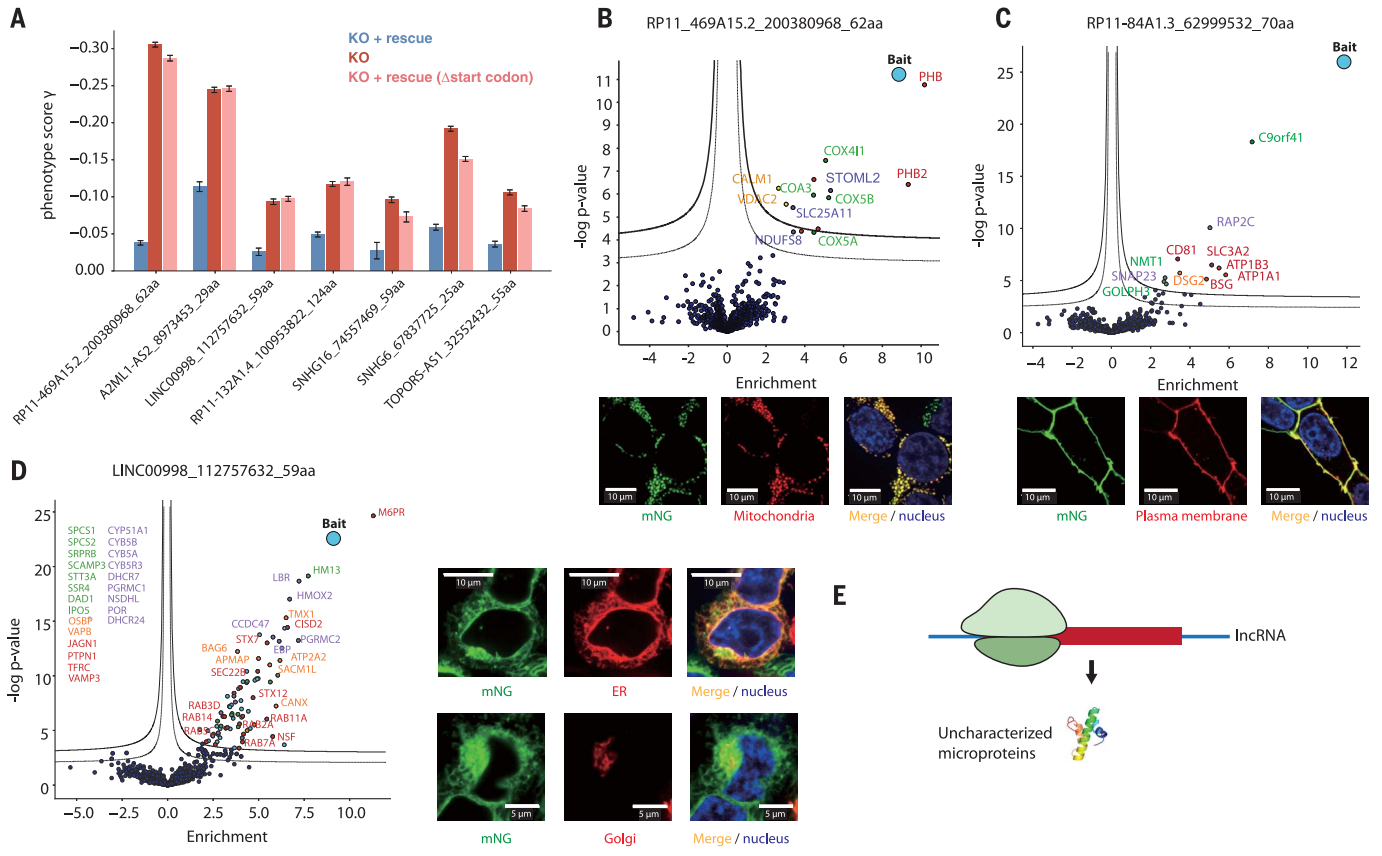


Fig. 3. Short lncRNA CDSs encode functional microproteins. (**A**) Rescue of lncRNA CDS knockout growth phenotypes by ectopic expression of the transcript encoding the peptide, as well as controls in which the initiating start codon is removed (Δstart codon). Error bars represent standard deviation of triplicates. $P < 0.05$ for all comparisons between knockout (KO) and KO + rescue. (**B** to **D**) Microscopy images and volcano plots of the co-IP MS of three example lncRNA-encoded microproteins tagged with mNG11, expressed ectopically (in the native transcript context) in a HEK293T cell line expressing mNG1-10. Green is mNG, red is the indicated organelle localization, and blue is Hoechst 33342, which stains for the nucleus. Scale bar dimensions are labeled. Statistically significant interactors are shown in the top, right corner of the volcano plots. Thick threshold line is 1% FDR (false discovery rate), and the thin threshold line is 5% FDR. The bait (the tagged peptide) is labeled in blue. The interactors are colored according to their functional groups. (**E**) lncRNA-encoded microproteins are uncharacterized proteins that may play important regulatory roles in cells.

sequence) (fig. S10). However, the noncanonical CDSs, on average, have lower PhyloCSF scores compared with canonical proteins (fig. S2B). Finally, sgRNAs targeting ORF hits versus non-hits have indistinguishable off-target and on-target scores (fig. S9B) (*32*). We then performed validation follow-ups with individual sgRNAs, which recapitulated the growth phenotypes from our genome-scale screen (fig. S8D). Sequencing of the targeted genomic regions revealed insertions and deletions (indels) of <50 base pairs (bp) (fig. S9, C and D). Together, these analyses independently support the conclusion that our screen phenotypes result specifically from the disruption of the target ORFs.

To survey function of the noncanonical CDSs at scale, we combined CRISPR screening with single-cell RNA sequencing (Perturb-seq) (*34*, *35*). Disruptions of the various noncanonical CDSs resulted in broad and diverse changes in RNA-sequencing profiles across a variety of critical pathways, suggesting that the candidate CDSs play diverse cellular roles (fig. S11). As an example, disruption of the CDS on *LINC00998* resulted in differentially expressed genes related to glycosylation ($P < 10^{-10}$), suggesting a function at the Golgi or endoplasmic reticulum (ER). The transcriptional phenotype also allowed us to functionally profile CDSs that are not essential for robust growth (fig. S11C). Furthermore, we found that CRISPR-targeted transcripts did not show detectable changes in abundance that might result from processes such as nonsense-mediated decay, which indicates that the phenotypes we observed were not caused by decreasing the abundance of the entire transcript (fig. S11D). Thus, similar to screens for essential protein-coding genes (*26*, *31*), our screen for noncanonical CDSs required for robust cell growth underestimated the true number of functional CDSs in the genome. This finding further underscores the pervasiveness of functional, unannotated CDSs in the genome that affect a wide range of cellular activities.

We next explored the functional role of the peptides encoded by the noncanonical CDSs identified from our screen, focusing first on lncRNA CDSs. For seven lncRNAs, we ectopically expressed the transcript encoding for the peptide and found, in all cases, that knockout-induced growth defect was partially or completely rescued. This rescue was abrogated by the removal of the initiating start codon (Δstart codon) (Fig. 3A), which suggests an essential role of the peptide itself in cell growth. To further investigate the specific functions of the noncanonical microproteins, we adopted a split-fluorescent protein approach using mNeonGreen (mNG), in which we fused each peptide with a minimally disruptive 16-aa tag (mNG11). Coexpression of the tagged peptide with the remainder of the mNG protein (mNG1-10) results in a fluorescence signal upon complementation (*36*, *37*). This creates

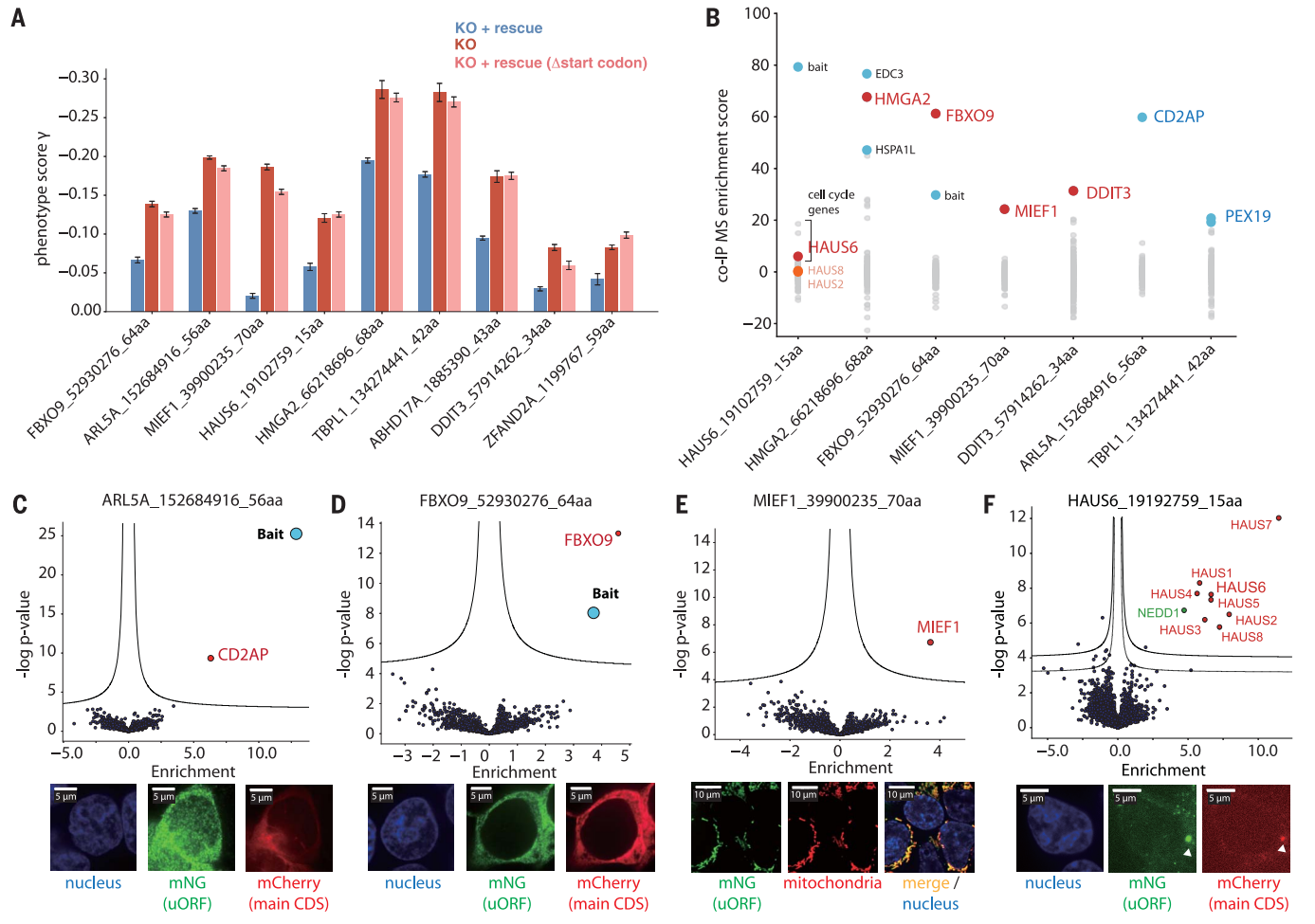
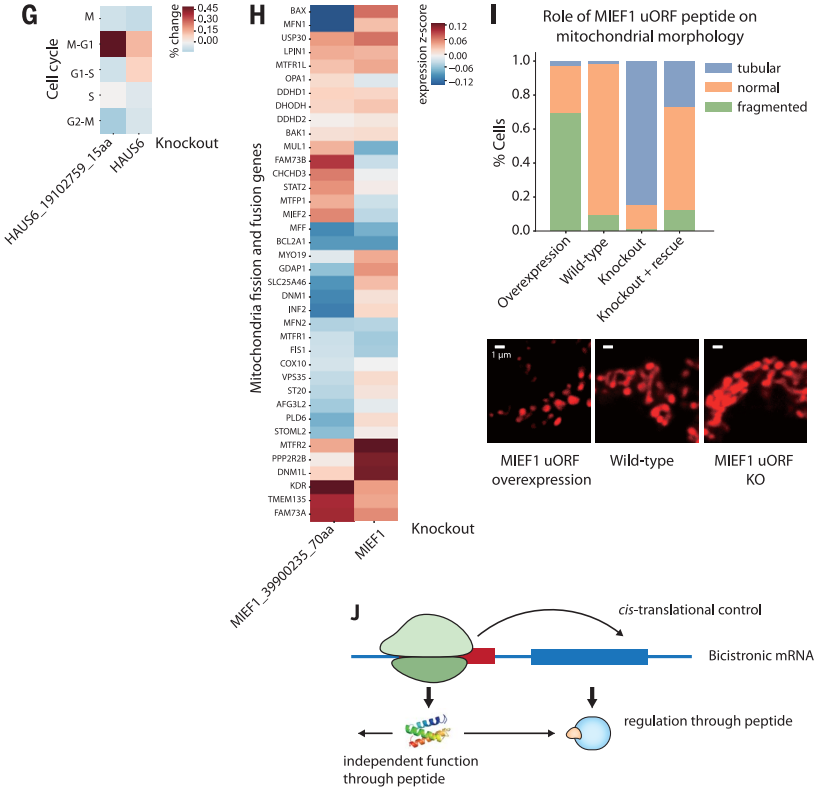


Fig. 4. Bicistronic mRNAs can encode uORF peptides that function in trans. (**A**) Rescue of uORF knockout growth phenotypes by ectopic expression of a transcript encoding the uORF peptide alone, as well as controls in which the initiating start codon is removed (Δstart codon). Error bars represent standard deviation of triplicates. $P < 0.05$ for all comparisons between KO and KO + rescue. (**B**) Summary of co-IP MS interactions of uORF peptides tagged with mNG11, showing five uORF peptides that interact with their downstream-encoded protein (shown in red). The tagged peptides are expressed alone ectopically (in the native transcript context) in an HEK293T cell line expressing mNG1-10. Other statistically significant interactors are shown in blue. (**C** to **E**) Example volcano plots of co-IP MS in (B) reveal statistically significant interactors with uORF peptides. Threshold line is 1% FDR. The bait (the tagged peptide) is labeled in blue. For microscopy in (C) and (D), the main, canonical protein tagged with mCherry (red) is coexpressed. For (E), the mNG11-tagged MIEF1 uORF peptide (green) localizes to the mitochondria (red). (**F**) Volcano plot of co-IP MS from endogenously mNG11-tagged HAUS6 uORF. For microscopy, the mNG11-tagged uORF is expressed alone ectopically (green), and the canonical HAUS6 tagged with mCherry (red) is coexpressed. (**G**) Percent change for each cell cycle state for HAUS6 knockout (KO) and HAUS6 uORF KO, compared with control cells. (**H**) Transcriptome response of the MIEF1 uORF KO compared with the main CDS KO from Perturb-seq. (**I**) Quantification of mitochondria morphology upon MIEF1 uORF peptide overexpression and knockout, as well as rescue of knockout phenotype. Representative microscopy images of the different mitochondria morphologies are shown to the right. (**J**) Possible model of uORF peptide functions and regulatory roles in cells.



both a fluorescent reporter to detect stable expression and cellular localization and a handle for coimmunoprecipitation (co-IP) and MS to define interaction partners (*36*) (fig. S12A). We probed the functions of six essential lncRNA CDSs and found that five of them formed specific complexes that were consistent with their subcellular localization. For example, the 62-aa peptide encoded by lncRNA *RP11_469A15.2* specifically localized to the mitochondria. The peptide has a predicted transmembrane domain and coimmunoprecipitates with the cytochrome c oxidase (COX) complex and the mitochondrial Prohibitin complex (Fig. 3B). Moreover, the 70-aa peptide encoded by *RP11-84A1.3* localizes to the plasma membrane and interacts with various cell surface proteins (Fig. 3C). Third, the 59-aa peptide encoded by lncRNA *LINC00998*, which contains two predicted transmembrane domains, localizes specifically to both the ER and Golgi and coimmunoprecipitates with lysosomal and vesicular transport proteins (Fig. 3D). Finally, the 55-aa peptide encoded on *TOPORS-AS1* and the 124-aa peptide on *RP11-132A1.4* also form functional complexes consistent with their cellular localization (fig. S12, C and D, and fig. S13). Consistent with prior studies (*5*–*18*), these examples demonstrate that lncRNAs can encode uncharacterized proteins, and they highlight the need to fully extend the annotation of lncRNAs and the proteome.

We next explored the functional effects of uORF translation, which is complicated by the fact that phenotypes can, in principle, be mediated by the peptide product (*24*, *38*–*41*), the effect of uORF translation on expression of the main, canonical CDS (*20*), or both. To distinguish between these possibilities, we first separately tagged the uORF and the main CDS and used Western blot to confirm the independent expression of uORF peptides from the canonical protein (fig. S14). Furthermore, we established that ectopic expression of a transcript encoding only the uORF peptide could at least partially rescue the growth phenotype caused by disruption of the endogenous uORF. In all cases this rescue is dependent on the initiating start codon in the ectopically expressed message, which demonstrates that the rescue is the result of production of the expressed peptide (Fig. 4A). Consistent with this, in all cases we tested, deleting the start codon for the uORFs only minimally increased (~20% to 60%) the expression of the main CDS. This suggests that the growth defect observed is mediated by the peptide and not by increased expression of the canonical protein (fig. S14, E and F). Taken together, these findings establish that uORFs could function through the peptide they produce independently of any cis-regulatory effects.

To explore the functions of uORF-encoded microproteins, we examined their localization and protein binding partners by tagging the uORF peptides with mNG11. Out of the 10 uORF peptides further tested by co-IP MS, we failed to detect statistically significant interaction partners for three of the tagged peptides. Two peptides, encoded by the uORFs of *TBPL1* and *ARL5A*, localize generally to the cytoplasm, whereas the main CDS proteins exhibit different cellular localization patterns. Consistent with our observed cellular localizations, these two uORF peptides specifically immunoprecipitate proteins with functions that are independent of the main CDS protein (Fig. 4, B and C, and fig. S12). Thus, these uORF peptides and their main CDS protein have independent functions.

We found that 5 of the 10 uORF peptides colocalized and formed a stable physical complex with the downstream-encoded, canonical protein on their shared mRNA. These include *MIEF1*, *DDIT3*, *FBXO9*, *HMGA2*, and *HAUS6* (Fig. 4, B, D, and E, and fig. S12). In all cases, we expressed the tagged peptides in their native transcript context but without the downstream CDS, thereby eliminating the possibility of stop codon read-through. We further confirmed this interaction by co-IP of the canonical protein and immunoblotting for the uORF peptide (fig. S12F), as well as with endogenously tagged clonal lines (fig. S15 and Fig. 4F). This physical interaction between the proteins encoded by the uORF and the canonical CDS on the same transcript is notable (*39*, *42*, *43*) because it implies an additional layer of regulation beyond the propensity of uORFs to modulate translation of downstream CDSs.

Next, we further investigated the function of uORF-expressed microproteins in *HAUS6* and *MIEF1*. In both cases, disrupting the uORF led to minimal increase in the expression of the main CDS protein, and the ectopic expression of a peptide-encoding transcript rescued the knockout-induced growth phenotype (Fig. 4A and fig. S14). mNG11-tagged HAUS6 uORF expressed from its endogenous locus efficiently pulled down key components of the HAUS6 complex, localized to the centrosome, and knockout of the uORF caused cells to arrest in the G1 stage, consistent with the role of HAUS6 microtubule attachment to the kinetochore and central spindle formation (Fig. 4, F and G, fig. S12, and fig. S15). Similarly, the MIEF1 uORF peptide localized to the mitochondria, consistent with the localization of the MIEF1 protein (Fig. 4E), which regulates mitochondrial fission and fusion (*44*). The MIEF1 uORF peptide knockout induced differential expression of mitochondrial fusion and fission genes, with a transcriptional signature that was distinct from that seen in the knockout of the MIEF1 protein (Fig. 4H). We observed that overexpression of the MIEF1 uORF peptide alone induced a fragmented mitochondrial phenotype (increased fission), whereas a clonal knockout of the MIEF1 uORF (with the sequence disrupted but nonetheless preserving an upstream ORF; see fig. S15) resulted in a tubular and more elongated mitochondrial phenotype (increased fusion). Notably, this knockout morphology could be rescued by the exogenous expression of the MIEF1 uORF peptide (Fig. 4I). Together, our results indicated a possible role of the uORF-encoded peptide in regulating the downstream-encoded protein, thereby challenging the monocistronic assumption about mammalian genomes. We speculate that this type of genomic architecture may be general, opening the doors to investigation of the cooperative and regulatory nature of bicistronic human mRNAs. Indeed, a number of stress-regulated alternate translation initiation factors can modulate translation initiation site choice and uORF usage, which suggests that regulation of bicistronic expression could play roles in both normal biology and diseases states (*21*, *45*).

We described a strategy that combines ribosome profiling, MS-based proteomics, microscopy, and CRISPR-based genetic screens to discover and characterize widespread translation of functional microproteins and define the protein-coding potential of complex genomes. We identified a subset of lncRNAs that can encode stable, functional proteins, which suggests that they may be misannotated RNAs or potentially have dual roles at the RNA and protein levels. Furthermore, we provided examples of uORFs encoding functional peptides, highlighting the diverse cellular roles that uORFs may play beyond translational control. We also identified uORF-encoded peptides binding to the downstream-encoded protein on the same mRNA. Thus, our data highlight a previously unappreciated complexity of the functional mammalian proteome, as well as the full spectrum of antigens presented by the HLA system.

REFERENCES AND NOTES

1. M. A. Basrai, P. Hieter, J. D. Boeke, *Genome Res.* **7**, 768–771 (1997).
2. A. Odermatt *et al.*, *Genomics* **45**, 541–553 (1997).
3. D. H. MacLennan, E. G. Kranias, *Nat. Rev. Mol. Cell Biol.* **4**, 566–577 (2003).
4. S. R. Hann, M. W. King, D. L. Bentley, C. W. Anderson, R. N. Eisenman, *Cell* **52**, 185–195 (1988).
5. R. Jackson *et al.*, *Nature* **564**, 434–438 (2018).
6. T. Kondo *et al.*, *Science* **329**, 336–339 (2010).
7. B. R. Nelson *et al.*, *Science* **351**, 271–275 (2016).
8. D. M. Anderson *et al.*, *Cell* **160**, 595–606 (2015).
9. E. G. Magny *et al.*, *Science* **341**, 1116–1120 (2013).
10. N. G. D'Lima *et al.*, *Nat. Chem. Biol.* **13**, 174–180 (2017).
11. C. S. Stein *et al.*, *Cell Rep.* **23**, 3710–3720e8 (2018).
12. C. A. Makarewich *et al.*, *Cell Rep.* **23**, 3701–3709 (2018).
13. A. Matsumoto *et al.*, *Nature* **541**, 228–232 (2017).
14. S. A. Slavoff, J. Heo, B. A. Budnik, L. A. Hanakahi, A. Saghatelian, *J. Biol. Chem.* **289**, 10950–10957 (2014).
15. P. Bi *et al.*, *Science* **356**, 323–327 (2017).
16. J.-Z. Huang *et al.*, *Mol. Cell* **68**, 171–184.e6 (2017).
17. Q. Zhang *et al.*, *Nat. Commun.* **8**, 15664 (2017).
18. A. Pauli *et al.*, *Science* **343**, 1248636 (2014).
19. T. G. Johnstone, A. A. Bazzini, A. J. Giraldez, *EMBO J.* **35**, 706–723 (2016).
20. G. L. Chew, A. Pauli, A. F. Schier, *Nat. Commun.* **7**, 11663 (2016).

21. S. R. Starck *et al*., *Science* **351**, aad3867 (2016).
22. N. T. Ingolia *et al*., *Cell Rep.* **8**, 1365–1379 (2014).
23. N. T. Ingolia, L. F. Lareau, J. S. Weissman, *Cell* **147**, 789–802 (2011).
24. S. A. Slavoff *et al*., *Nat. Chem. Biol.* **9**, 59–64 (2013).
25. A. A. Bazzini *et al*., *EMBO J.* **33**, 981–993 (2014).
26. T. Wang, J. J. Wei, D. M. Sabatini, E. S. Lander, *Science* **343**, 80–84 (2014).
27. A. P. Fields *et al*., *Mol. Cell* **60**, 816–827 (2015).
28. N. Stern-Ginossar *et al*., *Science* **338**, 1088–1093 (2012).
29. K. M. Vattem, R. C. Wek, *Proc. Natl. Acad. Sci. U.S.A.* **101**, 11269–11274 (2004).
30. M. Bassani-Sternberg, S. Pletscher-Frankild, L. J. Jensen, M. Mann, *Mol. Cell. Proteomics* **14**, 658–673 (2015).
31. L. A. Gilbert *et al*., *Cell* **159**, 647–661 (2014).
32. A. R. Perez *et al*., *Nat. Biotechnol.* **35**, 347–349 (2017).
33. M. F. Lin, I. Jungreis, M. Kellis, *Bioinformatics* **27**, i275–i282 (2011).
34. B. Adamson *et al*., *Cell* **167**, 1867–1882.e21 (2016).
35. P. Datlinger *et al*., *Nat. Methods* **14**, 297–301 (2017).
36. M. D. Leonetti, S. Sekine, D. Kamiyama, J. S. Weissman, B. Huang, *Proc. Natl. Acad. Sci. U.S.A.* **113**, E3501–E3508 (2016).
37. S. Feng *et al*., *Nat. Commun.* **8**, 370 (2017).
38. Z. Ji, R. Song, A. Regev, K. Struhl, *eLife* **4**, e08890 (2015).
39. S. Samandi *et al*., *eLife* **6**, e27860 (2017).
40. A. Rathore *et al*., *Biochemistry* **57**, 5564–5575 (2018).
41. V. Delcourt *et al*., *Mol. Cell. Proteomics* **17**, 2402–2411 (2018).
42. D. Bergeron *et al*., *J. Biol. Chem.* **288**, 21824–21835 (2013).
43. C. F. Lee, H. L. Lai, Y. C. Lee, C. L. Chien, Y. Chern, *J. Biol. Chem.* **289**, 1257–1270 (2014).
44. R. Yu *et al*., *Sci. Rep.* **7**, 880 (2017).
45. A. Sendoel *et al*., *Nature* **541**, 494–499 (2017).

ACKNOWLEDGMENTS

We thank the Weissman laboratory members, particularly T. M. Norman, M. Jost, M. J. Shurtleff, M. A. Horlbeck, L. A. Gilbert, M. Y. Hein, S. E. Torres, C. R. Liem, D. A. Santos, J. M. Replogle, and A. Xu. We also thank B. R. Conklin and M. P. Olvera (Gladstone Institute) for iPSC culturing; N. Cho (Chan-Zuckerberg Biohub) for endogenous tagging; and S. E. O'Leary and I W. Lin for discussions. **Funding:** This work was funded by NIH (RM1 HG009490), DARPA (HR0011-17-2-0043), and the Chan-Zuckerberg Initiative. J.S.W. is a HHMI Investigator. A.-D.B. and M.M. are supported by the Max Planck Society. J.C. is funded by the Jane Coffin Childs Memorial Fund for Medical Research and the NIH K99/R00 Pathway to Independence Award (K99 GM134154). J.K.N. is a fellow of the Hanna H. Gray Fellows Program. Oligonucleotide pools were courtesy of the Innovative Genomics Institute. **Author contributions:** J.C. designed and performed all experiments and analyzed and interpreted all the data with guidance from J.S.W. A.-D.B. and M.M. performed the proteomic MS and analysis. J.Z.C. and J.K.N. assisted with sample preparation, experiments, and key discussions. A.P.F. performed preliminary experiments and provided key analytical pipelines. B.A. contributed to Perturb-seq experiments. M.D.L. and J.Y.L. performed the pull-downs. M.D.L. designed the endogenous tagging methods. D.N.I. performed MS for the pull-downs. J.C. and J.S.W. conceived the study and wrote the manuscript with input from all authors. **Competing interests:** J.S.W. consults for and holds equity in KSQ Therapeutics and Maze Therapeutics and consults for 5AM Ventures. B.A. is an advisory board member and has restricted stock in Celsius Therapeutics, Inc. **Data and materials availability:** Raw sequencing data are deposited on the National Center for Biotechnology Information Gene Expression Omnibus database with accession number GSE131650. MS-based proteomics data are deposited to the ProteomeXchange Consortium via the Proteomics Identifications Database (PRIDE) partner repository with the dataset identifier PXD014031. Processed data are included as supplementary tables.

SUPPLEMENTARY MATERIALS

science.sciencemag.org/content/367/6482/1140/suppl/DC1
Materials and Methods
Figs. S1 to S15
Tables S1 to S8
References (*46*–*70*)

View/request a protocol for this paper from *Bio-protocol*.

26 May 2019; resubmitted 22 November 2019
Accepted 13 January 2020
10.1126/science.aay0262

MICROBIOLOGY

PE/PPE proteins mediate nutrient transport across the outer membrane of *Mycobacterium tuberculosis*

Qinglan Wang[1], Helena I. M. Boshoff[1], Justin R. Harrison[2], Peter C. Ray[2,3], Simon R. Green[2], Paul G. Wyatt[2], Clifton E. Barry III[1,4]*

Mycobacterium tuberculosis has an unusual outer membrane that lacks canonical porin proteins for the transport of small solutes to the periplasm. We discovered that 3,3-*bis*-di(methylsulfonyl)propionamide (3bMP1) inhibits the growth of *M. tuberculosis*, and resistance to this compound is conferred by mutation within a member of the proline-proline-glutamate (PPE) family, PPE51. Deletion of PPE51 rendered *M. tuberculosis* cells unable to replicate on propionamide, glucose, or glycerol. Growth was restored upon loss of the mycobacterial cell wall component phthiocerol dimycocerosate. Mutants in other proline-glutamate (PE)/PPE clusters, responsive to magnesium and phosphate, also showed a phthiocerol dimycocerosate–dependent growth compromise upon limitation of the corresponding substrate. Phthiocerol dimycocerosate determined the low permeability of the mycobacterial outer membrane, and the PE/PPE proteins apparently act as solute-specific channels.

Mycobacterium tuberculosis thrives in the hostile environment of the human lung despite an onslaught of host responses that prevent the growth of nearly all other bacteria (*1*). *M. tuberculosis* survives because it is covered by a highly impermeable envelope and is able to manipulate the host defense mechanisms (*2*). Outside of the cytoplasmic membrane is the mycobacterial envelope, which consists of a complex heteropolymer composed of peptidoglycan covalently attached to arabinogalactan terminated by mycolic acids, which are specific to mycobacteria (*3*). Cryo–electron microscopy shows that the outer lipid layer of the mycobacterial outer membrane is ~8 to 9 nm in width (*4*, *5*). No canonical porin protein has been identified in slow-growing mycobacteria, such as *M. tuberculosis*, although a major porin (MspA) has been identified in fast-growing mycobacterial species, such as *M. smegmatis* (*6*). However, porin-like activity has been observed in membrane preparations from slow-growing mycobacteria (*7*, *8*), but no protein determinants of this activity have been identified. Expression of the porin from fast-growing mycobacteria in *M. tuberculosis* substantially reduces virulence and enhances antibiotic susceptibility (*9*, *10*). A canonical porin is incompatible with the need for a permeability barrier that is extreme enough to allow the intracellular survival of *M. tuberculosis*.

As part of our drug discovery efforts, we identified a small-molecule whole-cell inhibitor from a library of agrichemicals. This simple molecule, 3,3-*bis*-di(methylsulfonyl)propionamide (3bMP1), displayed a modest minimum inhibitory concentration (MIC) of ~3 μg/ml independent of growth media and was highly bactericidal, reducing starting colony forming units (CFU) by 3 logs after 4 days and achieving near-sterilization after 8 days of incubation (Fig. 1, A and B). To identify the mechanism of action of this compound, we selected for resistant mutants by plating wild-type *M. tuberculosis* cells on media containing 10-fold the MIC of 3bMP1, and we observed mutants growing after 5 weeks of incubation. The resistance of these mutants was confirmed in liquid cultures, showing an MIC of 25 μg/ml in 7H9/OAD medium containing 0.05% Tween 80 [a detergent typically added to tuberculosis (TB) cultures to disperse the bacteria] and a much higher MIC in the same medium without Tween 80 (Fig. 1, C and D). Whole-genome sequencing of 10 clones from this experiment revealed that all had scattered mutations in a single protein, proline-proline-glutamate (PPE) family protein 51 (PPE51) (fig. S1A). Complementation of these mutants with a wild-type copy of the *ppe51* gene fully restored sensitivity to 3bMP1 (Fig. 1, C and D), which is consistent with what were apparently loss-of-function mutations in *ppe51* (fig. S1A).

The PE/PPE family of proteins, named for the homologous proline-glutamate (PE) or proline-proline-glutamate (PPE) repeated regions in their N terminus, comprises 169 orthologs. These proteins represent nearly 10% of the *M. tuberculosis* genome, and many are substrates for the type VII secretion systems of *M. tuberculosis* (*11*). Because they are secreted

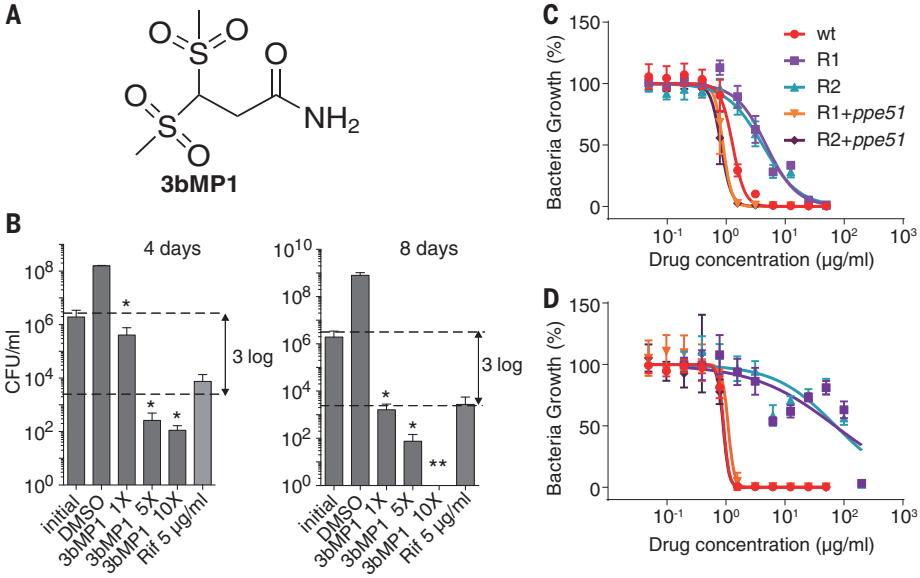


Fig. 1. Loss-of-function mutations in *ppe51* result in the resistance to compound 3bMP1. (**A**) The chemical structure of 3bMP1. (**B**) Logarithmically growing *M. tuberculosis* cells were exposed for 4 and 8 days to 3bMP1 at 1×, 5×, and 10× MIC values. Rifampicin (Rif) and dimethyl sulfoxide (DMSO) were used as positive and negative controls, respectively. Data are generated from two independent experiments and shown as mean ± SD (*$P < 0.05$, **$P < 0.01$, versus DMSO control, unpaired *t* test). (**C** and **D**) Susceptibility of *M. tuberculosis* strains to 3bMP1 in 7H9/OAD media with (C) or without (D) 0.05% Tween 80. Bacterial growth was quantified using an alamarBlue-based assay. R1 contains a G18D (Gly^{18}→Asp) mutation in the PPE51. R2 contains insertion sequence IS6110 at codon 247 in the *ppe51* gene. Data are representative of two independent experiments, both done as technical duplicates, and error bars represent SD [in (C): $P = 0.0007$, wild type (wt) versus R1; $P = 0.0107$, wt versus R2; no significant difference among wt, R1+*ppe51*, and R2+*ppe51*; in (D): $P < 0.0001$, wt versus R1; $P < 0.0001$, wt versus R2; no significant difference among wt, R1+*ppe51*, and R2+*ppe51*; data were analyzed using two-way analysis of variance (ANOVA) of matched values].

[1]Tuberculosis Research Section, Laboratory of Clinical Immunology and Microbiology, National Institute of Allergy and Infectious Diseases, National Institutes of Health, Bethesda, MD 20892, USA. [2]Drug Discovery Unit, College of Life Sciences, James Black Centre, University of Dundee, Dundee DD1 5EH, UK. [3]Exscientia Ltd., Oxford OX1 3LD, UK. [4]Institute of Infectious Disease and Molecular Medicine, University of Cape Town, Cape Town 7925, South Africa.
*Corresponding author. Email: cbarry@niaid.nih.gov

and numerous, they are commonly thought to play a role in interacting with the human immune system (*12*). However, these proteins do not appear to show sequence variation driven by immune recognition (*13*). The PE/PPE proteins are clearly associated with the outermost layer of the mycobacterial cell envelope (*14*–*16*). Many PE/PPE proteins have been implicated in various aspects of the pathogenesis of TB disease, but their molecular mechanisms have not been identified (*17*). Two recent studies have linked individual PPE proteins to heme and glycerol acquisition, yet the biological function of many of these proteins remains elusive (*16*, *18*).

Studies on analogs of 3bMP1 revealed that the propionamide core was essential for antitubercular activity (table S1). To understand whether resistance resulted from restricting drug uptake, we cultured *M. tuberculosis* in media containing only propionamide, a substructure of 3bMPl, as a carbon source. As expected, given the metabolic plasticity of this organism for growth on lipid substrates (*19*), wild-type *M. tuberculosis* was capable of florid growth on propionamide. The PPE51 mutant resistant to 3bMP1 was, however, incapable of growth on propionamide (fig. S1B). In contrast, the longer lipid substrate hexanamide supported the growth of both strains (fig. S1C). These results suggested that the resistance of this mutant might be due to impaired uptake of 3bMP1. We also screened this mutant for growth on other carbon sources and found that the mutant was also unable to optimally use glycerol and glucose as its sole carbon

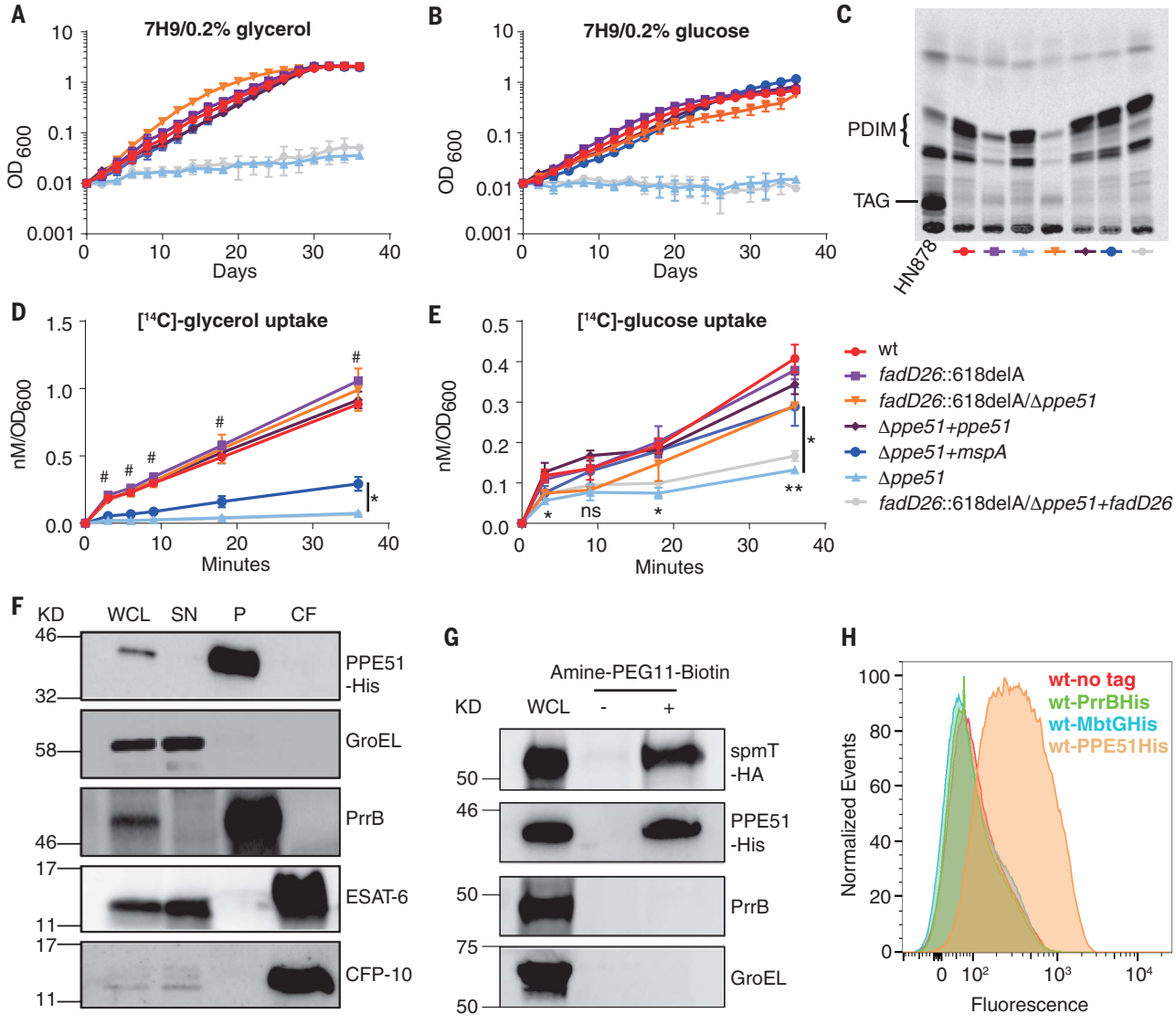


Fig. 2. PPE51 is required for uptake of glycerol and glucose by *M. tuberculosis*. (**A** and **B**) Growth of *M. tuberculosis* strains on 0.2% glycerol (A) or 0.2% glucose (B) as sole carbon source. Data are from three independent experiments and represent mean ± SD. (**C**) Thin-layer chromatographic analysis of PDIM production by *M. tuberculosis* strains. An *M. tuberculosis* clinical isolate, HN878, was included as a control. OD_{600}, optical density at a wavelength of 600 nm. (**D** and **E**) [^{14}C]-glycerol and [^{14}C]-glucose uptake by *M. tuberculosis* strains. Uptake experiments were done as two independent biological replicates, and mean values are shown with SD [in (D): #P < 0.001, wt versus Δ*ppe51* at different time points; *P < 0.05, Δ*ppe51* versus Δ*ppe51+mspA* at the last time point; in (E): *P < 0.05, **P < 0.01, ns = not significant, wt versus Δ*ppe51* at different time points; *P < 0.05, Δ*ppe51* versus Δ*ppe51+mspA* at the last time point, unpaired t test]. (**F**) Western blot analysis of whole-cell lysates (WCL), water-soluble supernatant (SN), membrane-associated pellet (P), and culture filtrate fractions (CF) obtained by ultracentrifugation of *M. tuberculosis*–expressing His-tagged PPE51. GroEL (cytosol) ESAT-6 and CFP-10 (secreted) and PrrB (inner membrane) were used as fractionation controls. KD, kilodaltons; ESAT-6, early secreted antigen of tuberculosis 6 kDa. (**G**) Cell surface protein biotinylation. Proteins of known subcellular localization served as control for cytosolic proteins (GroEL), inner membrane–associated proteins (PrrB), and surface-accessible proteins (spmT). (**H**) Cell surface accessibility of PPE51 by flow cytometry.

sources (fig. S1, D and E). Uptake assays for ^{14}C-glycerol and ^{14}C-glucose showed that the mutant was deficient because it could not transport glycerol and glucose, whereas both the parent and the complemented strain could (fig. S1, F and G).

To confirm that loss of PPE51 function was responsible for these phenotypes, we created a site-specific deletion of the *ppe51* gene (fig. S2A). This knockout did not recapitulate the phenotype of the drug-selected mutant—it showed less resistance to 3bMP1 in the medium without Tween 80 and was able to use glycerol and glucose as its sole carbon sources, unlike the drug-selected mutant (fig. S2, B and C, and Fig. 2, A and B). After further analysis, we discovered that the mutant had lost the ability to synthesize an abundant cell wall–associated nonpolar wax phthiocerol dimycocerosate (PDIM), containing a single nucleotide deletion (618delA) in the *fadD26* gene, which encodes a fatty acid–coenzyme A ligase in the PDIM biosynthesis pathway (Fig. 2C and fig. S1H). PDIM loss is a common occurrence during in vitro culture of *M. tuberculosis* (*20*). PDIM makes up 46% of the total lipids of *M. tuberculosis*, amounting to 11% of the total weight of dried bacteria (*21*). When we reselected a PDIM-positive deletion mutant of *ppe51*, the deletion mutant displayed a level of resistance to 3bMP1 similar to that of the drug-selected mutant, as well as an inability to grow on glycerol and glucose (fig. S2, B and C, and Fig. 2, A and B). No obvious growth difference was observed in standard rich medium or in media containing oleic acid or hexanamide as sole carbon sources, indicating that the PDIM-positive *ppe51* knockout mutant did not have a general growth defect (fig. S2, D to F). The PDIM-positive *ppe51* deletion mutant also showed a defect in uptake of ^{14}C-labeled glycerol and glucose (Fig. 2, D and E). Restoration of PDIM production in the original *ppe51* deletion mutant was achieved by providing a wild-type copy of *fadD26*, which resulted in an inability to grow on glycerol and glucose and showed defective uptake of ^{14}C-labeled glycerol and glucose (Fig. 2, A to E). Notably, both growth and uptake defects in the PDIM-positive *ppe51* knockout mutant were complemented by expression of wild-type *ppe51* or partially complemented by expression of the porin gene *mspA* of *M. smegmatis* (Fig. 2, A to E). Together with the observation that loss of PDIM rescued growth and uptake defects, this result indicates that PPE51 was localized to the outer membrane of *M. tuberculosis* and had a similar channel function to MspA.

Subcellular fractionation of *M. tuberculosis* cells expressing His-tagged PPE51 showed that this protein was membrane-associated (Fig. 2F). To distinguish between the inner and outer membrane proteins, we performed a cell-surface protein biotinylation assay—which is based on surface detection of proteins in whole cells using antibodies—using a membrane-impermeable biotinylation reagent (*22*) and flow cytometry analyses. As shown in Fig. 2, G and H, His-tagged PPE51 was biotinylated with amine-PEG11-biotin and was detected with a monoclonal anti-His antibody in flow cytometry experiments, whereas an inner membrane protein (PrrB), an inner membrane–associated protein (MbtG), and a cytosolic protein (GroEL) were not detected. The functionality of His-tagged PPE51 was confirmed by showing that it restored sensitivity to 3bMP1 (fig. S2G). These experiments indicate that PPE51 is localized to the outer membrane of *M. tuberculosis*.

The PE/PPE proteins are thought to assemble as heterodimers. The first reported crystallographic structure of a PE and PPE protein heterodimer (PE25 and PPE41) revealed that the proteins are tightly associated via hydrophobic regions along the long axis of a four-helix bundle (*23*). The similarity of this heterodimer to the structure of an ESAT-6 secretion system 1 (ESX-1)–secreted protein in *M. tuberculosis*, EspB, has been invoked to explain the substrate specificity of the type VII secretion system, which also transports PE/PPE proteins across the cytoplasmic membrane (*24*). EspB oligomerizes into heptamers that form pores in the phagosomal membrane of the host cell during infection by *M. tuberculosis*. Our data were consistent with a similar porin-like role for PPE51, in combination with a PE protein, embedded in the PDIM (fig. S4).

To identify the partner PE protein for PPE51, we performed saturating transposon mutagenesis on wild-type *M. tuberculosis*, selecting for resistance to 3bMP1. In addition to hits in *ppe51*, we identified transposon hits in *pe19* that conferred resistance (table S2). We subsequently constructed a series of mutants lacking each of the individual genes in

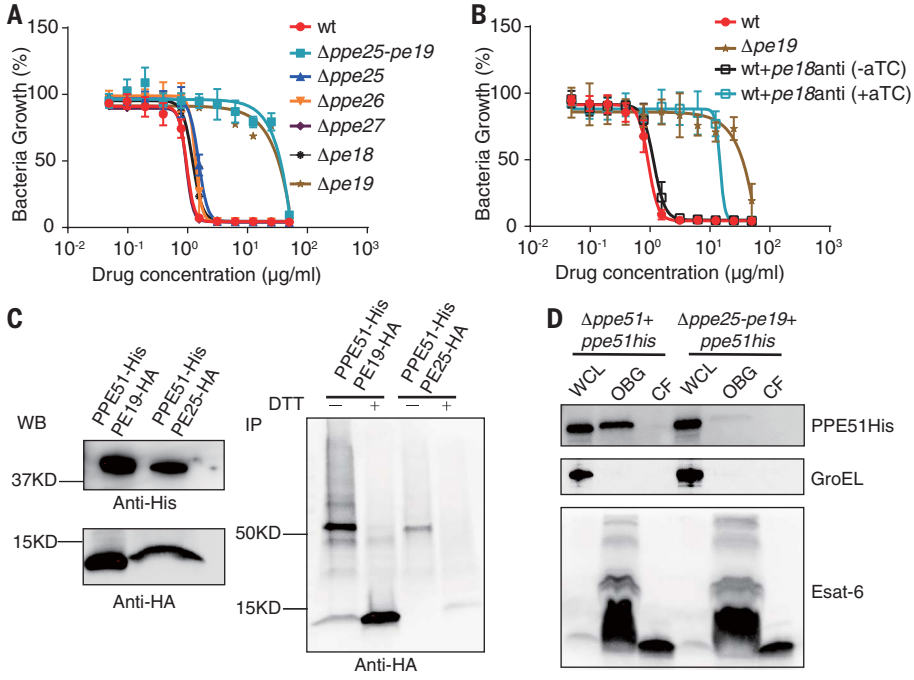


Fig. 3. PPE51 interacts with PE19 in *M. tuberculosis*. (**A**) Loss of *pe19* in *M. tuberculosis* leads to resistance to 3bMP1. (**B**) The *pe19* gene is negatively regulated by the antisense expression of *pe18*. Antisense expression of *pe18* was induced using 100 ng/ml anhydrotetracycline (aTC). In (A) and (B), experiments were performed in 7H9/OAD medium containing 0.02% tyloxapol. Data are generated from at least two independent experiments, both done as technical duplicates, and error bars represent SD [in (A): $P < 0.0001$, wt versus Δ*pe19*; in (B): $P = 0.0008$, wt versus wt+*pe18*anti (+aTC); $P = 0.0082$, wt+*pe18*anti (−aTC) versus wt+*pe18*anti (+aTC); two-way ANOVA of matched values]. (**C**) In vivo interaction between PPE51 and PE19. *M. tuberculosis* coexpressing His-tagged PPE51 and HA-tagged PE19 (or PE25) were cross-linked by DSP. PPE51 was precipitated using nickel–nitrilotriacetic acid resin, and coprecipitated PE proteins were visualized by Western blot (WB) using anti-HA antibodies. DTT, dithiothreitol; IP, immunoprecipitation. (**D**) Export of PPE51 in Δ*ppe51* and Δ*ppe25-pe19* mutants. The Δ*ppe51* and Δ*ppe25-pe19* cells expressing His-tagged PPE51 were grown in detergent-free Sauton's medium. Surface proteins were extracted by 1% *n*-octyl-β-D-glucopyranoside (OBG). The presence of PPE51 in WCL, OBG extracts, and culture filtrate (CF) was examined by anti-His antibodies.

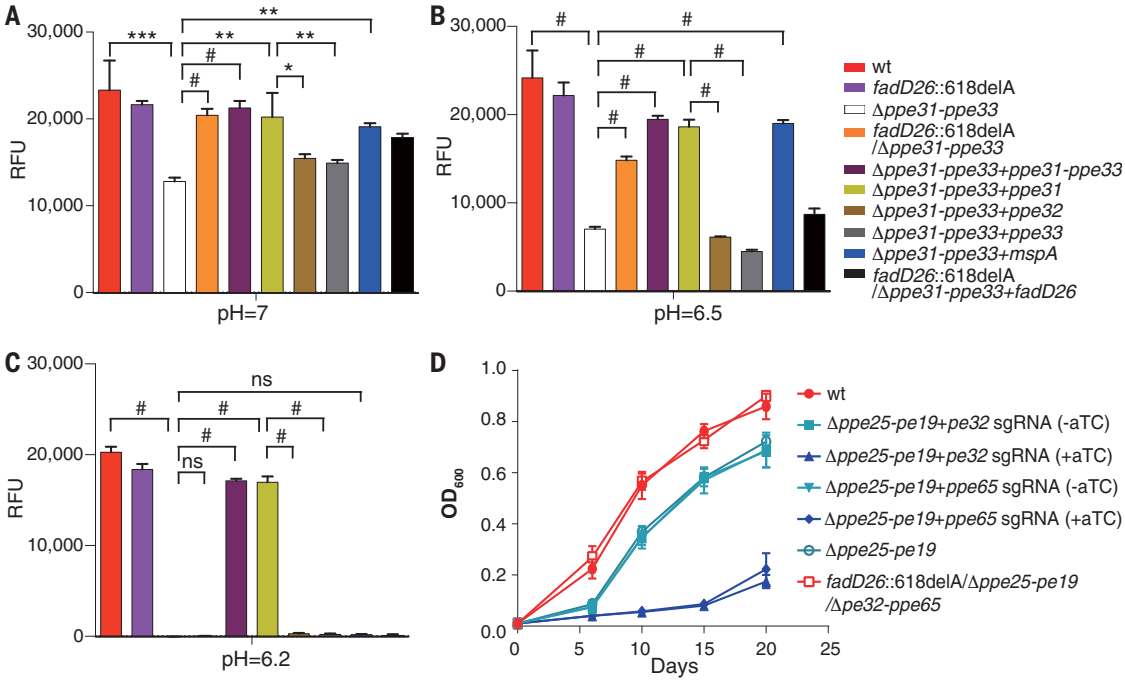


Fig. 4. PE20/PPE31 and PE32/PPE65 are required by *M. tuberculosis* for growth during Mg^{2+} and PO_3^{2-} restriction. Growth of *M. tuberculosis* strains in modified detergent-free Sauton's medium containing 10 μM Mg^{2+} at pH 7.0 (**A**), pH 6.5 (**B**), and pH 6.2 (**C**). Media were buffered with 50 mM MOPS [3-(*N*-morpholino)propanesulfonic acid]. After growth in 24-well plates for 15 days at 37°C, cells were treated with 0.1% Tween 80 overnight to prepare homogeneous cell suspensions, and cell growth was quantified by alamarBlue assay. Data are from technical triplicates corresponding to fig. S6 (*$P < 0.05$, **$P < 0.01$, ***$P < 0.001$, #$P < 0.0001$, unpaired *t* test). (**D**) *M. tuberculosis* requires *ppe25-pe19* and *pe32-ppe65* for efficient growth during phosphate limitation. Growth of *M. tuberculosis* strains in modified Sauton's medium containing 30 μM Pi buffered with 50 mM MOPS. A final concentration of 100 ng/ml aTC was used to knock down the expression of *pe32-ppe65* in the *ppe25-pe19* mutant. Data are generated from three independent experiments and shown as mean ± SD. RFU, relative fluorescence units.

this locus, as well as the entire *ppe25-pe19* locus, noting the high sequence identity between *ppe25* and *ppe27* genes (86.2%) and *pe18* and *pe19* genes (78.4%) in this locus (fig. S3, A and C). As shown in Fig. 3A, only the Δ*ppe25-pe19* and Δ*pe19* mutants showed resistance to 3bMP1. The growth defect of the Δ*ppe25-pe19* mutant was also rescued by loss of PDIM (fig. S3, B and D). PE18 and PE19 are highly conserved (89% identity), and extra-chromosomal expression of either PE18 or PE19 restored the susceptibility of the Δ*ppe25-pe19* mutant to 3bMP1 and rescued the growth of the Δ*ppe25-pe19* mutant on glycerol (fig. S3D and table S3). It is known that *pe18* produces antisense transcripts naturally (*25*), indicating that the expression of PE19 is negatively regulated by the antisense expression of *pe18*. Overexpression of the antisense transcript of *pe18* in wild-type H37Rv caused resistance to 3bMP1 (Fig. 3B), which is consistent with this regulatory role. To confirm the interaction between PPE51 and PE19 biochemically, we coexpressed His-tagged PPE51 and HA-tagged PE19 in *M. tuberculosis* cells and performed a coimmunoprecipitation assay with the cross-linker dithiobis(succinimidyl propionate) (DSP). As expected, PE19 coprecipitated with PPE51, and PE25 showed only slight coprecipitation with PPE51, likely because the N-terminal half of PE25 is nearly 50% identical to PE19 (Fig. 3C). Because PE/PPE proteins are usually exported as pairs by ESX systems, we examined the export of PPE51 in the Δ*pe19* mutant and found that export of PPE51 was blocked by the deletion of *pe19* (Fig. 3D).

We next asked whether this porin-like function was specific for the PE19/PPE51 pair or if other PE/PPE pairs had similar functions. The genomic locus encoding PE20-PPE33 has been shown to be up-regulated during Mg^{2+} limitation. This locus clustered with the *mgtC* gene, which is known to be involved in virulence and is also up-regulated upon magnesium deprivation (*26*). Furthermore, a magnesium riboswitch (Mbox) was found upstream of the *pe20-ppe33* locus (*27*), indicating that these proteins play a role in magnesium homeostasis. We therefore generated Δ*pe20* and Δ*ppe31-ppe33* mutants in *M. tuberculosis* in both a PDIM-positive and a PDIM-negative background (fig. S5, A and B, and fig. S8A). As expected, both PDIM-positive mutants showed a growth defect in Mg^{2+}-limiting media, especially at mildly acidic pH, while the PDIM-negative mutants grew similarly to wild type (Fig. 4, A to C, and figs. S6, S7, and S8, D to F). The phenotype of Δ*ppe31-ppe33* could be complemented by expressing *ppe31-ppe33*, *ppe31* alone, or *mspA* from *M. smegmatis*, but not by expressing *ppe32* or *ppe33* (Fig. 4, A to C, and fig. S6). PE20 and PPE31 were also found to associate by coprecipitation (fig. S8B). Together, these results suggest that PE20/PPE31 form a complex, possibly with other proteins, to mediate Mg^{2+} transport across the outer membrane. PE20 was also found to interact with PPE33 (fig. S8B); however, PPE33 did not affect Mg^{2+} uptake (Fig. 4, A to C, and fig. S6). Further studies will be needed to identify the substrate transported by PE20/PPE33.

Finally, the genomic loci *ppe25-pe19* and *pe32-ppe65* are known to be strongly up-regulated by starvation for inorganic phosphate (*28*). First, we tested the growth of a Δ*ppe25-pe19* mutant in defined media containing various concentrations of phosphate. The Δ*ppe25-pe19* mutants were impaired slightly for growth at 100 μM phosphate, and at 30 μM, growth was severely restricted (fig. S9). We were unable to obtain a single knockout of the *pe32-ppe65* locus or the double knockout of the *pe32-ppe65* locus in the Δ*ppe25-pe19* background that retained PDIM. Therefore, we knocked down the expression of *pe32* or *ppe65* in the Δ*ppe25-pe19* mutant using CRISPR interference. As shown in Fig. 4D and fig. S10, silencing the expression of *pe32-ppe65* in Δ*ppe25-pe19* resulted in a pronounced growth defect in phosphate-limiting media, whereas the PDIM-negative Δ*ppe25-pe19*/Δ*pe32-ppe65* double knockout mutant grew similarly to the wild type.

In slow-growing *M. marinum*, the ESX-5 secretion system is essential for PDIM outer-membrane permeability, but the substrates it transports were not identified (*29*). The ESX-5 secretion system maps closely to the *ppe25-pe19* gene cluster, and it seems likely that the observed phenotype was the result of

a lack of transport of PE19. The phylogeny and distribution of the PE/PPE proteins is such that all slow-growing mycobacteria seem to have an expanded repertoire of heterodimer combinations, and these species lack any detectable homolog of the porin seen in the fast-growing mycobacteria that have few PPEs (table S4). Our data, coupled with the distribution of PE/PPE among the mycobacteria, suggest that slow-growing mycobacteria have co-opted at least some of these proteins as small molecule–selective channels in place of porins. The need for these porins is intimately associated with the production of PDIM. Despite the fact that PDIM accounts for as much as 46% of the total lipids present in *M. tuberculosis* and for 11% of the total bacterial mass in culture (*21*), its molecular role in the envelope has been unclear. PDIM, like the PE/PPE proteins, is also restricted in distribution to the slow-growing mycobacteria, and our results indicate that its role is to enhance the impermeability of the mycobacterial cell wall. Fully 1% of the coding capacity of the organism is devoted to the biosynthesis of PDIM, and PDIM-deficient mutants are highly attenuated in virulence (*30*, *31*). PDIM is easily lost during in vitro culture yet never absent from freshly isolated clinical strains (*20*). Our results suggest that PDIM acts within the outer leaflet of the mycobacterial cell envelope to enhance its impermeability, presumably thereby directly allowing growth in the hostile environment of the host. At least some of the PE/PPE proteins appear to act as solute-selective pores, allowing *M. tuberculosis* access to nutrients required to proliferate in this environment. Understanding the transport properties and selectivity of these particular channels would enable rational approaches to optimize the uptake properties of newly designed drugs.

REFERENCES AND NOTES

1. C. J. Queval, R. Brosch, R. Simeone, *Front. Microbiol.* **8**, 2284 (2017).
2. S. A. Stanley, J. S. Cox, *Curr. Top. Microbiol. Immunol.* **374**, 211–241 (2013).
3. P. J. Brennan, H. Nikaido, *Annu. Rev. Biochem.* **64**, 29–63 (1995).
4. C. Hoffmann, A. Leis, M. Niederweis, J. M. Plitzko, H. Engelhardt, *Proc. Natl. Acad. Sci. U.S.A.* **105**, 3963–3967 (2008).
5. B. Zuber *et al*., *J. Bacteriol.* **190**, 5672–5680 (2008).
6. M. Faller, M. Niederweis, G. E. Schulz, *Science* **303**, 1189–1192 (2004).
7. B. Kartmann, S. Stenger, M. Niederweis, *J. Bacteriol.* **181**, 6543–6546 (1999).
8. T. Lichtinger *et al*., *FEBS Lett.* **454**, 349–355 (1999).
9. O. Lamrabet *et al*., *Microb. Pathog.* **76**, 10–18 (2014).
10. C. Mailaender *et al*., *Microbiology* **150**, 853–864 (2004).
11. L. S. Ates, E. N. G. Houben, W. Bitter, *Microbiol. Spectr.* **4**, VMBF-0011-2015 (2016).
12. G. Delogu, M. J. Brennan, R. Manganelli, *Adv. Exp. Med. Biol.* **1019**, 191–207 (2017).
13. R. Copin *et al*., *mBio* **5**, e00960-13 (2014).
14. M. J. Burggraaf *et al*., *Microb. Cell Fact.* **18**, 44 (2019).
15. A. Cascioferro *et al*., *Mol. Microbiol.* **66**, 1536–1547 (2007).
16. A. Mitra, A. Speer, K. Lin, S. Ehrt, M. Niederweis, *mBio* **8**, e01720-16 (2017).
17. S. Fishbein, N. van Wyk, R. M. Warren, S. L. Sampson, *Mol. Microbiol.* **96**, 901–916 (2015).
18. J. J. Baker, R. B. Abramovitch, *Sci. Rep.* **8**, 4168 (2018).
19. R. R. Lovewell, C. M. Sassetti, B. C. VanderVen, *Curr. Opin. Microbiol.* **29**, 30–36 (2016).
20. P. Domenech, M. B. Reed, *Microbiology* **155**, 3532–3543 (2009).
21. R. J. Anderson, *J. Biol. Chem.* **83**, 502–522 (1929).
22. A. Speer *et al*., *Mol. Microbiol.* **97**, 881–897 (2015).
23. M. Strong *et al*., *Proc. Natl. Acad. Sci. U.S.A.* **103**, 8060–8065 (2006).
24. M. Solomonson *et al*., *Structure* **23**, 571–583 (2015).
25. S. S. Shell *et al*., *PLOS Genet.* **11**, e1005641 (2015).
26. C. Belon, L. Gannoun-Zaki, G. Lutfalla, L. Kremer, A. B. Blanc-Potard, *PLOS ONE* **9**, e116052 (2014).
27. K. B. Arnvig *et al*., *PLOS Pathog.* **7**, e1002342 (2011).
28. S. R. Elliott, A. D. Tischler, *Mol. Microbiol.* **100**, 510–526 (2016).
29. L. S. Ates *et al*., *PLOS Genet.* **11**, e1005190 (2015).
30. J. Quigley *et al*., *mBio* **8**, e00148-17 (2017).
31. J. S. Cox, B. Chen, M. McNeil, W. R. Jacobs Jr., *Nature* **402**, 79–83 (1999).

ACKNOWLEDGMENTS

We thank DuPont Agriculture for providing the library of compounds that included 3bMP1. We also thank G. Prosser and K. Kolbe for the modification of plasmids used in this study, and A. Bohrer for help with flow-cytometry assays. **Funding:** This work was funded, in part, by the Intramural Research Program of the NIAID, NIH, and by the Bill and Melinda Gates Foundation through the TB Drug Accelerator program. **Author contributions:** Q.W., J.R.H., P.C.R., and S.R.G. performed the experiments. P.G.W., H.I.M.B., and C.E.B. designed the experiments. Q.W., H.I.M.B., and C.E.B. wrote the manuscript. **Competing interests:** The authors declare no competing interests. **Data and materials availability:** All data are available in the main text or the supplementary materials.

SUPPLEMENTARY MATERIALS

science.sciencemag.org/content/367/6482/1147/suppl/DC1
Materials and Methods
Figs. S1 to S10
Tables S1 to S6
References (*32*–*42*)

View/request a protocol for this paper from *Bio-protocol*.

9 October 2018; resubmitted 31 October 2019
Accepted 5 February 2020
10.1126/science.aav5912

TRANSCRIPTION

Sequencing metabolically labeled transcripts in single cells reveals mRNA turnover strategies

Nico Battich*, Joep Beumer, Buys de Barbanson, Lenno Krenning†, Chloé S. Baron‡, Marvin E. Tanenbaum, Hans Clevers, Alexander van Oudenaarden*

The regulation of messenger RNA levels in mammalian cells can be achieved by the modulation of synthesis and degradation rates. Metabolic RNA-labeling experiments in bulk have quantified these rates using relatively homogeneous cell populations. However, to determine these rates during complex dynamical processes, for instance during cellular differentiation, single-cell resolution is required. Therefore, we developed a method that simultaneously quantifies metabolically labeled and preexisting unlabeled transcripts in thousands of individual cells. We determined synthesis and degradation rates during the cell cycle and during differentiation of intestinal stem cells, revealing major regulatory strategies. These strategies have distinct consequences for controlling the dynamic range and precision of gene expression. These findings advance our understanding of how individual cells in heterogeneous populations shape their gene expression dynamics.

Mammalian cells use diverse strategies to regulate mRNA levels by controlling their synthesis and degradation rates (*1*, *2*). High synthesis or degradation rates allow cells to rapidly respond to extracellular and intracellular signals (*2*, *3*), whereas low degradation rates allow them to integrate transcriptional information over time (*4*). The extent to which mammalian cells exploit different regulatory strategies during complex dynamical processes such as cell cycle progression or organ formation remains unclear. This is partially due to the difficulty in distinguishing these strategies when only transcript levels are measured.

Additionally, the study of these regulatory strategies in bulk assays is hindered by the presence of heterogeneous cell types in the same tissue and unsynchronized cell states that result from the cell and circadian cycles (*1*, *5*–*7*). Advances in single-cell RNA sequencing help to resolve cellular heterogeneity (*8*–*14*), yet do not provide insights into how the dynamic control of transcription and degradation leads to the observed expression patterns. The kinetic parameters that govern the life of mRNA can be measured by its metabolic labeling during transcription (*1*, *5*, *6*). Here, we demonstrate that mRNA labeled with 5-ethynyluridine (EU) can be detected in thousands of single cells by sequencing. We determined transcription and degradation rates in heterogeneous and unsynchronized cell populations and uncovered mRNA control strategies during the cell cycle of human cells and differentiation of mouse intestinal stem cells.

To measure newly synthesized transcripts in single cells, we labeled mRNA by incubating cells with EU, an analog of uridine that can be biotinylated with click chemistry, a method we have named "single-cell EU-labeled RNA sequencing" (scEU-seq) (*15*). Briefly, after EU incubation, cells were dissociated, fixed, and permeabilized, and EU-labeled RNA was biotinylated in situ. We sorted single cells and generated mRNA/cDNA hybrids using poly-T primers containing a cell barcode, a unique molecular identifier (UMI), a 5′ sequencing adapter, and the T7 promoter. Cells were pooled, EU labeled and unlabeled hybrids were separated using streptavidin magnetic beads, and libraries were generated for both fractions (Fig. 1A). The UMI counts for labeled mRNA were higher in EU-treated cells compared with dimethyl sulfoxide (DMSO)–treated cells or empty control wells, resulting in a high signal-to-noise ratio and low across-well cross-contamination rates (Fig. 1B). Only 12 of 11,848 detected genes were affected by the EU treatment itself (fig. S1A). When we compared the total mRNA (unlabeled and EU-labeled UMIs; total UMIs) from EU-treated versus DMSO-treated RPE1-FUCCI cells, we found high recovery efficiency (99.5 ± 0.4%) of labeled mRNA (fig. S1B). After 120 min of EU incubation, the labeled mRNA fraction was on average 8.9 ± 0.7% (fig. S1B), which agrees with an expected average production of 8 to 10% of the transcriptome during a period of 2 hours in unsynchronized cells with a cell cycle length of ~20 to 24 hours (*16*).

To assess whether scEU-seq specifically enriches transcripts synthesized during the EU-labeling window, we performed pulse and chase experiments varying either the EU incubation time or the length of a chase phase with uridine (U) after EU treatment for 22 hours (Fig. 1C and fig. S1, C to G). As expected, we detected an increase in labeled UMIs as a function of the EU pulse length (Fig. 1D) and a decrease as a function of the U chase length (Fig. 1E). We could still detect significantly higher UMI counts for very short labeling times (15 and 30 min) compared with the DMSO control (Fig. 1D and fig. S1G). In these short EU pulses, we found that labeled UMIs were enriched in transcripts that contained unspliced introns (Fig. 1F).

Next, we incubated K562 cells at either 37°C or 42°C for a period of 45 min in the presence of EU or DMSO. The differential gene expression signature upon heat shock was more pronounced in the fraction of EU-labeled mRNAs compared with the unlabeled fraction or with cells treated with DMSO (fig. S2). Consistently, the functional annotation analysis (*17*) for up-regulated genes in the EU-labeled fraction revealed an enrichment for genes encoding heat shock or stress response proteins (fig. S2B). In addition, UMIs of these stress response genes represented a large percentage in the EU-labeled samples but not in the DMSO-treated or unlabeled controls.

Using data from the scEU-seq pulse and chase experiments, we can estimate the synthesis rate κ and the degradation rate constant γ for all detected transcripts. Furthermore, we can place individual cells along cell cycle or differentiation trajectories and thus infer how synthesis and degradation rates change over time. We first estimated κ and γ with high resolution along the mammalian cell cycle. For each of the 5422 cells that passed quality controls in the pulse and chase experiments, we calculated the relative position along the cell cycle using the Geminin-GFP and the Cdt1-RFP signals from the FUCCI system (fig. S3, A and B) (*18*). The expression of known cell cycle markers followed the expected pattern relative to the Geminin-GFP and Cdt1-RFP (*18*), whereas the housekeeping gene *HPRT1* displayed constant expression during the cell cycle (Fig. 2A and fig. S3C). The level of labeled transcripts of cell cycle–controlled genes changed as a function of the cell cycle (fig. S4 and fig. S5), with the total UMI counts per cell approximately doubling during one cell cycle (fig. S6, A and B). These results suggest that our estimation of the cell cycle progression in single cells is accurate.

To fit κ and γ to the experimental datasets, we simulated the dynamics of the pulse and chase experiments and quantified the accuracy of the fitting procedures. The simulations defined the range of κ and γ values for which we can accurately determine these rates, and demonstrated that a model that does not assume steady-state dynamics of gene expression is more fitting for our datasets (fig. S7).

Next, we used the cell cycle progression estimates to pool cells from different EU-labeling

Oncode Institute, Hubrecht Institute-KNAW (Royal Netherlands Academy of Arts and Sciences) and University Medical Center Utrecht, 3584 CT Utrecht, Netherlands.
*Corresponding author. Email: n.battich@hubrecht.eu (N.B.); a.vanoudenaarden@hubrecht.eu (A.v.O.)
†Present address: Division of Cell Biology, Oncode Institute, Netherlands Cancer Institute, Amsterdam, the Netherlands.
‡Present address: Stem Cell Program and Division of Hematology/Oncology, Boston Children's Hospital and Dana-Farber Cancer Institute, Howard Hughes Medical Institute, Harvard Medical School, Harvard Stem Cell Institute, Stem Cell and Regenerative Biology Department, Harvard University, 1 Blackfan Circle, Boston, 02115 MA, USA.

time points and fitted κ and γ using the non–steady-state model (Fig. 2B and fig. S8) on 528 genes that showed high expression changes during the cell cycle (fig. S9). Separate fits of the pulse and chase experiments with the non–steady-state model resulted in accurate γ values, but simultaneous fits of both experiments further reduced uncertainty (Fig. 2B and fig. S10, A and B). We averaged the degradation rates over the cell cycle and obtained good agreement between our data and a published dataset (Spearman r = 0.585, fig. S10C) (*5*). The estimated values of κ and γ for the 528 genes allowed us to predict their transcript levels at any position during cell cycle progression. Our predictions matched measurements of CEL-seq2 (*19*), an independent single-cell mRNA-sequencing method, for expression changes along the cell cycle (median correlation of 0.730 for 528 genes; Fig. 2C and fig. S10D).

We found widespread changes of both synthesis and degradation rates during the cell cycle (Fig. 2, B and C). Clustering of the expression levels, synthesis rates, and degradation rate constants with self-organizing maps (SOMs) revealed distinct strategies of mRNA regulation during the cell cycle (Fig. 2, B and D). To find common properties between the different strategies regardless of the position of the expression peak, we computed the cosine similarity between synthesis and degradation dynamics (Fig. 2B and fig. S11A). We observed three types of regulatory strategies during the cell cycle: cooperative, neutral, and destabilizing. The cooperative strategy describes an increase in the synthesis rate that is accompanied by a decrease in the degradation rate constant and vice versa, thus having a negative cosine similarity. The neutral strategy is characterized by small relative changes in the degradation rate constant compared with the synthesis rate. The destabilizing strategy is characterized by a simultaneous increase or decrease of the synthesis rate and the degradation rate constant, resulting in positive cosine similarity. Among the groups of genes that follow the cooperative strategy, we found a subset of genes that have an expression peak in G_2 and are involved in microtubule spindle assembly and mitosis regulation (strategy group B); genes with a functional enrichment for signaling and protein phosphorylation (group F); and genes that are expressed during S phase and are involved in DNA replication, repair, and maintenance (group D; Fig. 2C and fig. S11B). We validated the changes of the degradation rate constant during the cell cycle for these genes (groups B, D, and F) by performing a bulk chase experiment of 500 pooled cells gated for G_1, S, or G_2 (Pearson r between 0.290 and 0.611; fig. S11C). Genes that follow the neutral strategy were functionally enriched in microtubule activity (group A), homology recombination repair (group E), or cytokine activity, G_1/S transition, and DNA replication initiation (group C; Fig. 2C and fig. S11B). Further simulations in which we varied the regimes of κ and γ throughout the cell cycle (fig. S12, A to C) validated that we can accurately determine the strategy type for most of the parameter combinations tested (fig. S12, D to G). These results indicate that genes with similar cellular functions tend to be controlled by similar strategies and may share posttranscriptional regulators.

We next investigated the change in predicted expression by assuming either a model with constant γ or constant κ (Fig. 2, D and E). These constants were chosen to match the expression averaged over the cell cycle as observed in the experimental data. The model assuming dynamic γ and κ could accurately

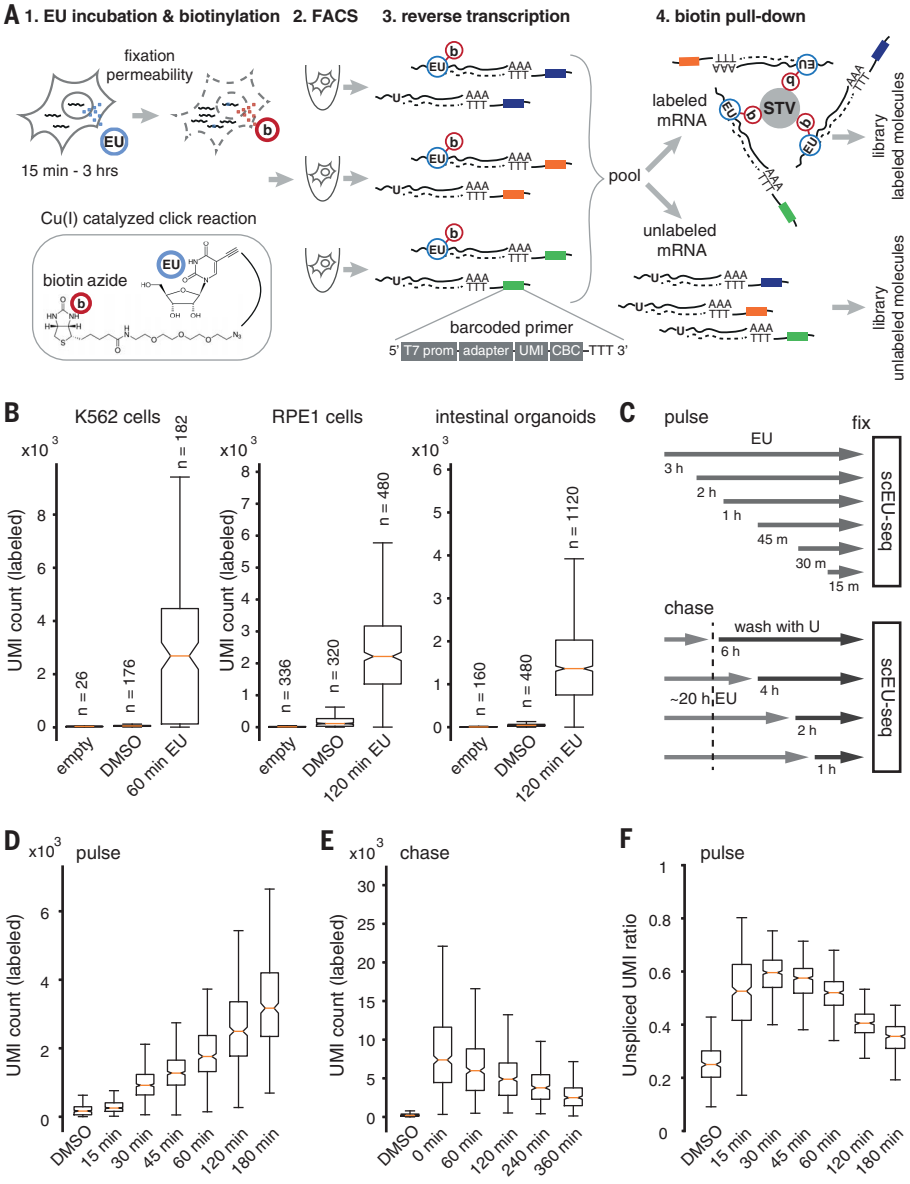


Fig. 1. Single-cell EU RNA sequencing (scEU-seq). (**A**) Schematics of the scEU-seq workflow. (**B**) Boxplots showing UMI counts of labeled mRNAs per well either containing single cells or left empty. Cell types are indicated. No cutoff was applied to the UMI counts per well. Signal-to-noise ratios are 49.74 ($P = 2.4 \times 10^{-26}$) for K562 cells, 19.69 ($P = 2.4 \times 10^{-77}$) for FUCCI-expressing RPE1 cells, and 32.48 ($P = 1.7 \times 10^{-157}$) for cells derived from mouse intestinal organoids; P values are from a Mann–Whitney U test. Estimated cross-contamination rates per well are 37.31 ± 4.11, 21.13 ± 1.80, and 8.26 ± 0.87 (mean UMIs per cell ± SEM) for K562, RPE1-FUCCI, and organoid cells, respectively. (**C**) Design of pulse and chase experiments. (**D**) Boxplots showing UMI counts of labeled mRNAs per cell. RPE1-FUCCI cells were treated with EU for the indicated times. (**E**) As in (D), but RPE1-FUCCI cells were treated with EU for 22 hours and then washed and treated with U for the indicated times. Cells shown in (D) and (E) were filtered as described in (*15*). (**F**) Fractions of UMI of labeled mRNAs containing unspliced introns for RPE1-FUCCI cells.

predict the dynamic range and the expression timing of our CEL-seq2 dataset. However, when either rate was assumed constant, we observed changes in both expression properties. As expected, the synthesis rate κ had an impact on the dynamic range of all genes (Fig. 2F), whereas the impact on timing was strongest for the strategy groups A and G, which show constant degradation rates during the cell cycle (Fig. 2G). Strong effects on the dynamic range could be observed by assuming a constant γ for the groups of genes showing cooperative strategies (groups B, D, and F; Fig. 2F). In addition, for three of the four clusters in group B, the effects on expression timing obtained by assuming constant degradation were similar to the results obtained by the constant synthesis model (Fig. 2G). These results imply that the degradation and synthesis rates are coordinated to achieve precise expression dynamics during the cell cycle.

Next, we asked whether scEU-seq could reveal similar mRNA regulatory strategies during cellular differentiation. We used intestinal organoids expressing the GFP-Lgr5 reporter in intestinal stem cells (*20*, *21*) (Fig. 3A) and performed a pulse experiment using an EU incubation time of 120 min and chase experiments with a 0-, 45-, or 360-min U chase phase. The UMAP (Uniform Manifold Approximation and Projection for Dimension Reduction) representation of the 3831 cells that passed quality controls places stem cells in the center and shows two branches representing the differentiation trajectories of enterocytes and secretory cells (Fig. 3, B to D). We did not observe batch effects between the experiments (fig. S13A). The expression of the GFP-Lgr5 fusion closely matches the measured expression of the *Lgr5*

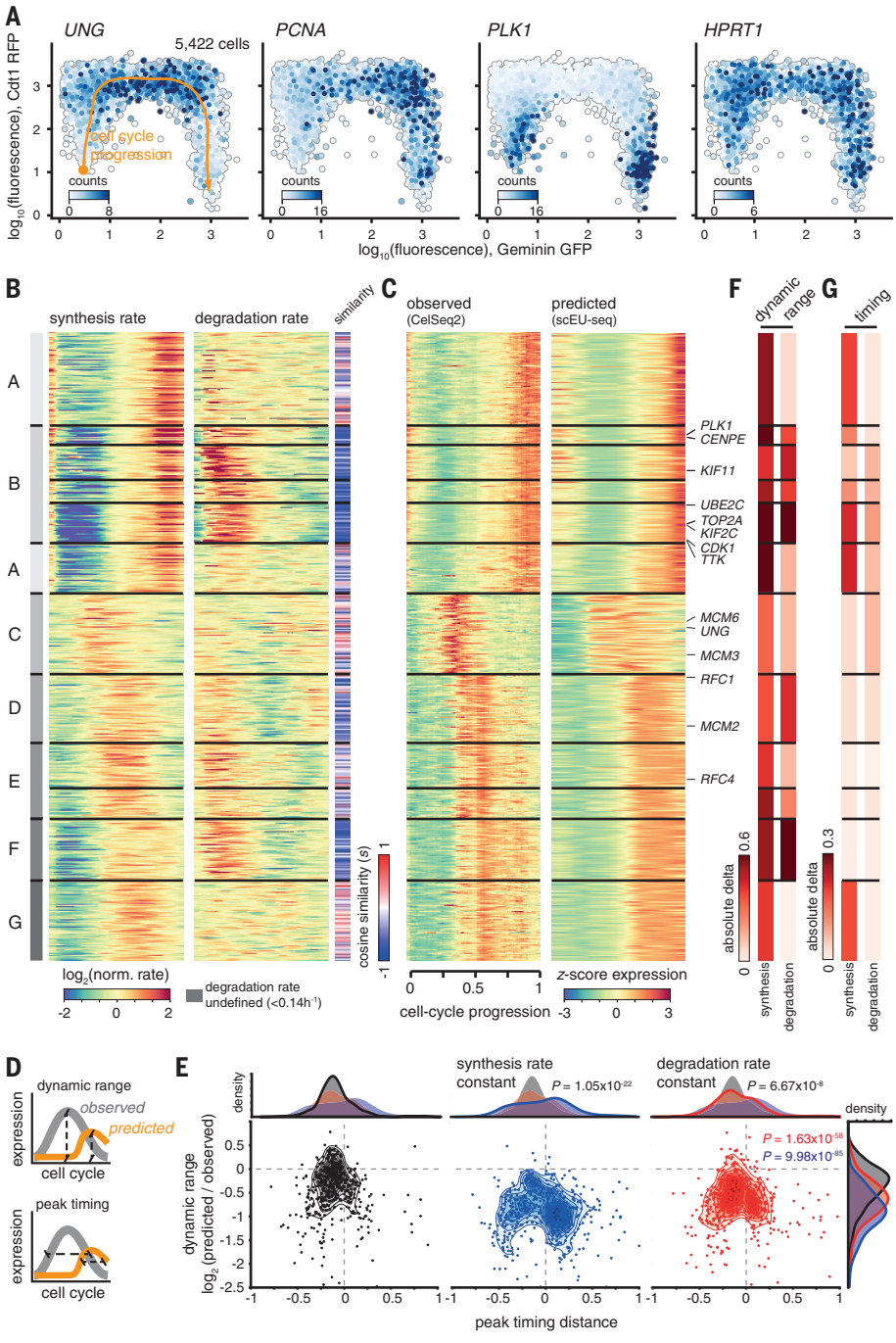


Fig. 2. scEU-seq reveals mRNA control strategies during the cell cycle. (**A**) Scatter plot of the Geminin-GFP- and Cdt1-RFP–corrected signals of RPE1-FUCCI cells (n = 5422 cells). Expression levels (total UMI counts per cell) of four example genes are indicated in blue. (**B**) Clustered heat maps of estimated synthesis and degradation rates. Leftmost panel shows the cosine similarity (s) between the rates (n = 528 genes). (**C**) As in (B) but showing the observed expression levels (left, data generated using CELSeq2) and predicted expression levels (right) along cell cycle progression. (**D**) Schematics of the calculation of the dynamic range (top) and the timing of the expression peak (bottom). (**E**) Density plot of the peak timing distance against the dynamic range of the predicted relative to the observed expression for models with dynamic synthesis and degradation rates (black, left), a constant synthesis rate (blue, middle), and a constant degradation rate (red, right). Top panels compare the distributions of peak timing distances (blue versus black: $P = 1.05 \times 10^{-22}$, red versus black: $P = 6.67 \times 10^{-8}$, F test for variance). Rightmost panel compares the distributions of dynamic ranges (blue versus black: $P = 9.98 \times 10^{-85}$, red versus black: $P = 1.63 \times 10^{-58}$, Wilcoxon test, n = 528 genes). (**F**) Median absolute differences (delta) in dynamic range between the constant synthesis model [blue in (E)] and the full dynamic model [black in (E)] and between the constant degradation model [red in (E)] and the full dynamic model [black in (E)]. (**G**) As in (F) but for the peak timing distance.

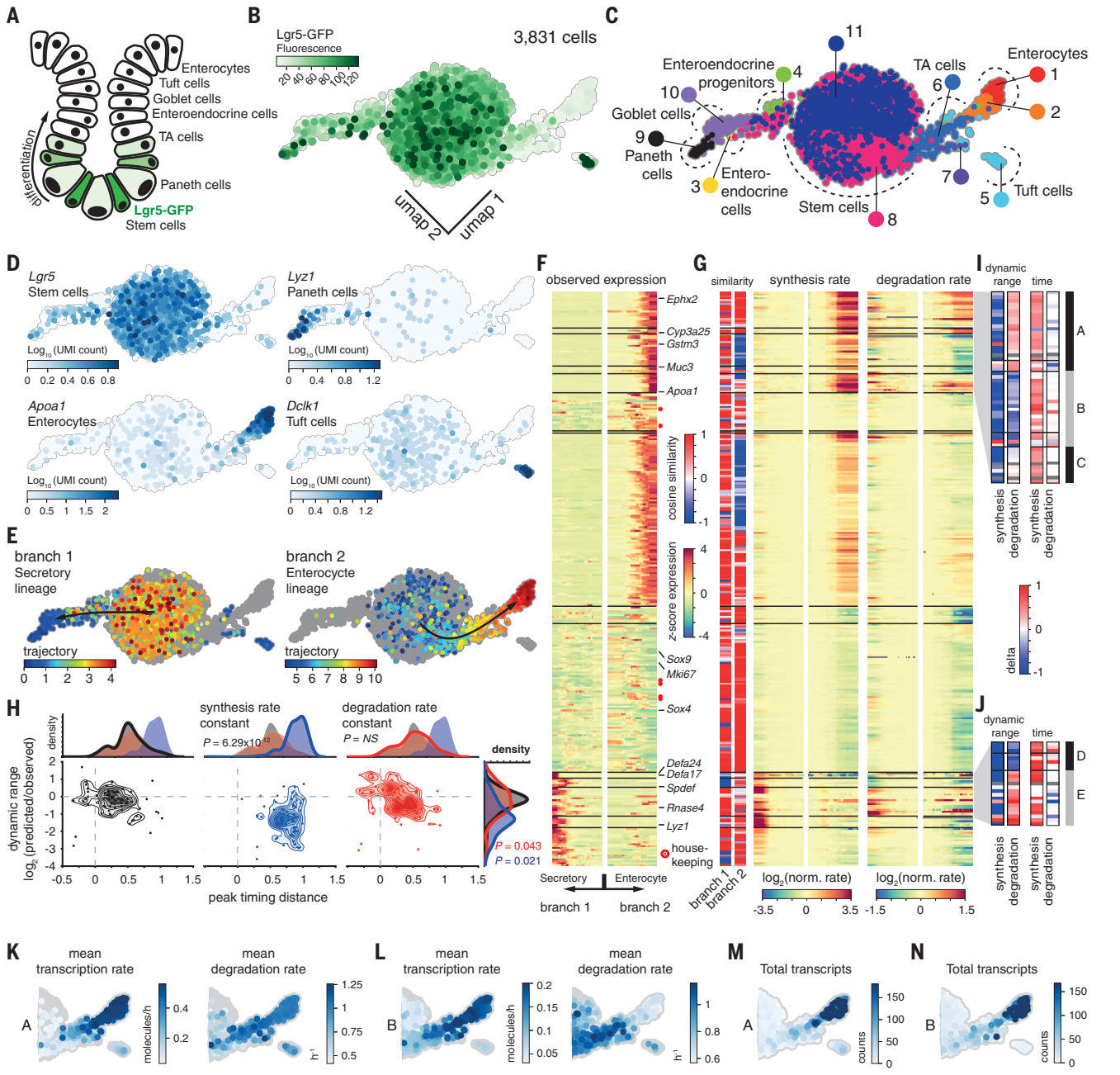


Fig. 3. mRNA control strategies during intestinal organoid differentiation. (**A**) Schematics of intestinal organoid crypts. (**B**) UMAP showing the expression levels of Lgr5-GFP (green) in 3831 cells from intestinal organoids. (**C**) UMAP showing clusters of cells with similar gene expression (SOM analysis, cluster number indicated) and their respective cell identity. (**D**) UMAP showing the expression levels (blue) of four genes that are markers for stem cells, Paneth cells, enterocytes, and tuft cells, respectively. (**E**) UMAP showing the Monocle2 differentiation branches 1 and 2, as indicated by arrows. Colors indicate the monocle trajectory values. (**F**) Heat maps of the observed expression levels along the two differentiation branches, the secretory lineage into Paneth cells (branch 1) and the enterocyte lineage (branch 2) (n = 301 genes). Red dots mark the position of housekeeping genes. (**G**) As in (F) but showing the estimated synthesis (left panels) and degradation rates (right panels). Genes are clustered and the cosine similarity is indicated independently for the two branches. Strategies with strong changes in the synthesis and the degradation rates are highlighted in (I) and (J). (**H**) Density plot of the peak timing distance against the dynamic range of the predicted relative to the observed expression for models with dynamic synthesis and degradation rates (black, left), constant synthesis rate (blue, middle), and constant degradation rate (red, right) [n = 72 genes with strong cooperative and destabilizing strategies (groups A, B C, D and E); see (I) and (J)]. Top panels compare the distributions of peak timing distances (blue versus black: $P = 6.29 \times 10^{-12}$, red versus black: P = nonsignificant, Wilcoxon test). Rightmost panel compares the distributions of dynamic ranges (blue versus black: P = 0.021, red versus black: P = 0.043, F test for variance, n = 72 genes). (**I** and **J**) Delta values of data shown in (H) for genes with strong cooperative and destabilizing strategies (groups A, B C, D, and E). Shown are differences in dynamic range and timing, respectively, between the constant synthesis model [blue in (H)] and the full dynamic model [black in (H)] and between the constant degradation model [red in (H)] and the full dynamic model [black in (H)]. (**K**) Mean synthesis and degradations rates for genes in group A. (**L**) Mean synthesis and degradation rates for genes in group B. (**M**) Total number of UMIs detected for genes in group A. (**N**) Total number of UMIs detected for genes in group B.

transcript (Fig. 3, B and D). We clustered single-cell expression levels using SOMs and identified stem cells (clusters 8 and 11), fully differentiated cells (clusters 1, 3, 5, 9, and 10), and potentially intermediate stages (clusters 10, 4, 6, and 2; Fig. 3C).

We selected 295 genes that showed a high coefficient of variation compared with the mean expression and differences in expression between the stem cells and cells in intermediate or differentiated stages (fig. S13, B and C). We used monocle2 (*22*) to sort cells along the differentiation trajectories of secretory cells (branch 1) and enterocytes (branch 2; Fig. 3E and fig. S14, A to C). We added six housekeeping genes as a control and calculated the synthesis rates and degradation rate constants throughout differentiation for these 301 genes (fig. S14, D to F).

We used SOMs to cluster genes by their expression level, synthesis rates, and degradation rate constants. The results demonstrate that cells use both the synthesis and degradation rate to control gene expression during differentiation. The housekeeping genes clustered separately from differentially regulated genes between branches 1 and 2 (Fig. 3, F and G, and fig. S15A). For 24% of genes (72 genes), the degradation rate changed during differentiation, whereas the synthesis rate increased, displaying cooperative and destabilizing strategies, respectively, as observed for the cell cycle. Among the genes with destabilizing strategies (group A), we identified functional enrichment for oxidoreductase activity and drug metabolism (fig. S15B). These genes were up-regulated in enterocytes and six of them belong to the cytochrome P450 family localized to the endoplasmic reticulum (*23*). Gene groups with cooperative strategies (group D and B) were enriched for genes encoding secreted proteins or components of the endoplasmic reticulum or Golgi complex (fig. S15B).

When we analyzed the gene expression dynamics as before, assuming a constant synthesis rate, we observed that the dynamic range decreased and the expression timing and dynamics changed (Fig. 3H). By contrast, a constant degradation rate had little effect on the timing of the expression peak but increased the variance of the dynamic range; although the dynamic range of genes with destabilizing strategies increased (groups A and E), it decreased for genes with cooperating strategies (groups B and D; Fig. 3, I and J). In agreement with this, we found that the absolute increase in the synthesis rate of genes in group A was higher than those in group B (Fig. 3, K and L), whereas the expression levels in both groups changed along the differentiation trajectory with similar dynamics and magnitude (Fig. 3, M and N). This effect is explained by the stabilization of transcripts in group B toward the end of differentiation branch 2 (Fig. 3L and fig. S15C).

Here, we show that cells use cooperative, neutral, or destabilizing strategies to actively regulate gene expression during the cell cycle and during differentiation. Both synthesis and degradation rates control the accuracy and precision of the dynamic range and the timing of the expression peak. By contrast, during differentiation, the degradation rate seems to affect only the dynamic range of expression, whereas the timing is fully encoded by the dynamics of the mRNA synthesis rate. Thus, our data support findings that the modulation of mRNA degradation rates plays a role in mammalian cellular homeostasis such as T cell homeostasis (*24*) and differentiation of mammalian embryonic stem cells (*25*).

REFERENCES AND NOTES

1. B. Schwalb *et al.*, *Science* **352**, 1225–1228 (2016).
2. M. Rabani *et al.*, *Cell* **159**, 1698–1710 (2014).
3. O. Shalem *et al.*, *Mol. Syst. Biol.* **4**, 223 (2008).
4. S. C. Little, M. Tikhonov, T. Gregor, *Cell* **154**, 789–800 (2013).
5. H. Tani *et al.*, *Genome Res.* **22**, 947–956 (2012).
6. M. Rabani *et al.*, *Nat. Biotechnol.* **29**, 436–442 (2011).
7. A. Raghavan *et al.*, *Nucleic Acids Res.* **30**, 5529–5538 (2002).
8. T. Hashimshony, F. Wagner, N. Sher, I. Yanai, *Cell Rep.* **2**, 666–673 (2012).
9. D. A. Jaitin *et al.*, *Science* **343**, 776–779 (2014).
10. A. B. Rosenberg *et al.*, *Science* **360**, 176–182 (2018).
11. D. Grün *et al.*, *Nature* **525**, 251–255 (2015).
12. E. Z. Macosko *et al.*, *Cell* **161**, 1202–1214 (2015).
13. A. M. Klein *et al.*, *Cell* **161**, 1187–1201 (2015).
14. B. Pijuan-Sala *et al.*, *Nature* **566**, 490–495 (2019).
15. See supplementary materials.
16. T. Zerjatke *et al.*, *Cell Rep.* **19**, 1953–1966 (2017).
17. W. da Huang, B. T. Sherman, R. A. Lempicki; W. Huang da, *Nat. Protoc.* **4**, 44–57 (2009).
18. L. Krenning, F. M. Feringa, I. A. Shaltiel, J. van den Berg, R. H. Medema, *Mol. Cell* **55**, 59–72 (2014).
19. T. Hashimshony *et al.*, *Genome Biol.* **17**, 77 (2016).
20. T. Sato *et al.*, *Nature* **459**, 262–265 (2009).
21. H. Tian *et al.*, *Nature* **478**, 255–259 (2011).
22. X. Qiu *et al.*, *Nat. Methods* **14**, 979–982 (2017).
23. F. Xie, X. Ding, Q. Y. Zhang, *Acta Pharm. Sin. B* **6**, 374–383 (2016).
24. S. Geula *et al.*, *Science* **347**, 1002–1006 (2015).
25. P. J. Batista *et al.*, *Cell Stem Cell* **15**, 707–719 (2014).

ACKNOWLEDGMENTS

We thank R. van der Linden and A. Lyubimova for experimental help; A. Alemany and D. Berchtold for critical comments on modeling, experiments, and the manuscript; and the members of the van Oudenaarden laboratory for comments on the manuscript. **Funding:** This work was supported by the European Research Council (grants ERC-AdG 742225-IntScOmics and EU/ERC-677936 RNAREG) and a Nederlandse Organisatie voor Wetenschappelijk Onderzoek (NWO) TOP award (NWO-CW714.016.001). N.B. was supported by the Swiss National Science Foundation (P2ZHP3_171695) and the Human Frontier Science Program (LT 000877/2017). This work is part of the Oncode Institute that is partly financed by the Dutch Cancer Society. **Contributions:** N.B. and A.v.O. designed, supervised the research work and wrote the manuscript; N.B. developed techniques and performed experiments with assistance from J.B., L.K., C.S.B., M.E.T., and H.C.; N.B. performed computational analyses with assistance from B.d.B., and A.v.O. **Competing interests:** The authors declare no competing interests. **Data and materials availability:** The datasets have been uploaded to the Gene Expression Omnibus with accession number GSE128365.

SUPPLEMENTARY MATERIALS

science.sciencemag.org/content/367/6482/1151/suppl/DC1
Materials and Methods
Supplementary Text
Figs. S1 to S15
Captions for Tables S1 to S4
References (*26–38*)

15 March 2019; accepted 6 February 2020
10.1126/science.aax3072



Flow Reactor for Kilogram-Scale Production
The FlowSyn Maxi from Uniqsis is a high-throughput flow reactor for process chemists looking to optimize reaction conditions before scaling-up synthetic production to multiple kilograms per day. It combines the benefits of Uniqsis' proven FlowSyn technology with high flow rates (up to 100 mL/min) in a compact, benchtop design. The highly intuitive user interface quickly guides you through the process for setting up a flow chemistry reaction. Once set up, the reactor automatically runs the experiment unattended, ensuring that critical parameters remain within defined limits. Robustly constructed from epoxy-coated and bead-blasted stainless steel, it can be specified with stainless steel, Hastelloy, or polytetrafluoroethylene (PTFE) flow paths. The unit is fitted with larger-bore inlet tubing and upgraded inlet/outlet solenoid valves with bigger fluidic channels to cope with the increased flow rate. The FlowSyn Maxi is designed to carry out superheated reactions up to +260°C (1,400 psi) and cooled reactions down to –70°C—making it one of the most versatile process-scale flow reactors available.
Uniqsis
For info: +44-(0)-845-864-7747
www.uniqsis.com/paproductsdetail.aspx?id=flw_maxi

Knockout Cell Lines
CRISPR-Cas9 knockout cell lines from Abcam provide you with reliable, off-the-shelf, single-gene knockouts, so that you can confidently interrogate the relationship between genotype and phenotype without spending months establishing your own knockout cell line. We provide a large and expanding range of knockouts in immortalized mammalian cell lines, such as HeLa and HEK293T. All knockout cell lines are Sanger sequenced, and many have additional Western blot data to confirm knockout at the proteomic level. With our large range of ready-made knockouts in commonly used cell lines, and our ever-expanding range of new targets and cell lines, obtaining your knockout cell line of choice is as easy as buying a reagent. Don't see the cell line you need in our catalog? Register your interest for your desired knockout cell line and we will be in touch if it's in our pipeline.
Abcam
For info: 888-772-2226
www.abcam.com

Recombinant Antibodies for In Vivo Research
Absolute Antibody offers VivopureX recombinant mouse antibodies for in vivo research in mouse models. The collection consists of popular antibody clones, many originally obtained from rats or hamsters, which Absolute Antibody has engineered into mouse anti-mouse recombinant versions to improve research results. The antibodies are available in discounted bulk sizes ranging from 1 mg to 100 mg. VivopureX antibodies are species-matched chimeric antibodies, consisting of a clone's original antigen-binding variable domain with a mouse-constant domain, which means they do not induce neutralizing antibodies in mouse models. In addition, the antibodies feature engineered effector functions, with fragment crystallizable (Fc) receptor binding tailored to best suit popular applications such as depletion, agonism, or blocking. All antibodies are produced recombinantly for ensured batch-to-batch reproducibility and offer high purity and low endotoxin levels ideal for in vivo applications. The antibodies are targeted against key immune system proteins, including clinically relevant checkpoint proteins such as PD-1, CTLA-4, and OX40.
Absolute Antibody
For info: 617-377-4057
absoluteantibody.com

Heparanase and Hyaluronidase Activity Kits
AMS Biotechnology supplies Razie assay kits to measure enzyme activity of heparanase and hyaluronidase in cell culture supernatants, human plasma, biological fluids, and tissue samples. Our kits have been used for research into anti-inflammatory responses, kidney disease, cancer research, and intervertebral disc degeneration. Heparanase and hyaluronidase enzymes play an important role in the extracellular matrix. Our kits provide a solution to the performance and standardization problems found with traditional measurement techniques used for these types of enzymes. Each assay is available in two formats: (1) with enzyme as positive control to demonstrate digestion/activity, and (2) without positive control, for end-users who have their own enzyme for use as positive control.
AMS Biotechnology
For info: 800-987-0985
www.amsbio.com

Antigen and Antibody Conjugation Kits
The Native Antigen Company offers a selection of complementary, easy-to-use antibody conjugation kits, with a wide range of labels suitable for use in most applications. On request we can also undertake custom conjugation of proteins and antibodies. The kits utilize a novel chemistry to generate highly reproducible antigen and antibody conjugates with a range of different labels, including enzymes, fluorochromes, and biotin. No reconstitution is required, and these kits can be used to generate liquid stable conjugates, which are fully scalable from 0.01 mg to gram scale. Incorporation is highly efficient, helping to ensure lot-to-lot consistency, low backgrounds, and improved assay sensitivity.
The Native Antigen Company
For info: +44-(0)-1865-595230
thenativeantigencompany.com/conjugation-kits

pQA Portable Quadrupole Analyzer
The Hiden pQA portable gas analyzer is a versatile mass spectrometer and offered with a range of interchangeable sampling inlets to suit a broad application range. Membrane introduction mass spectrometry (MIMS) inlets are offered for analysis of dissolved species in ground water, fermentation cultures, soil samples, and general applications where analysis of dissolved species in a liquid sample is required. The system is suited to gas analysis applications, where sample volume is small, and for environmental applications where detection of low concentration levels is required. The pQA system has a mass range of 200 atomic mass units (amu) and sub-ppb detection levels; extended mass range to 300 amu is optional. The system is supplied in a Pelican case and can be powered by a 12-V supply for field use, battery and/or solar powered, or a 220-V supply for laboratory use.
Hiden Analytical
For info: +44-(0)-1925-445225
www.hidenanalytical.com

Electronically submit your new product description or product literature information! Go to www.sciencemag.org/about/new-products-section for more information.

Newly offered instrumentation, apparatus, and laboratory materials of interest to researchers in all disciplines in academic, industrial, and governmental organizations are featured in this space. Emphasis is given to purpose, chief characteristics, and availability of products and materials. Endorsement by *Science* or AAAS of any products or materials mentioned is not implied. Additional information may be obtained from the manufacturer or supplier.

Chair, Biochemistry and Structural Biology

UT Health San Antonio
Joe R. & Teresa Lozano Long School of Medicine

The University of Texas Health Science Center San Antonio, dba as UT Health San Antonio (UTHSA), seeks a dynamic academic leader to serve as Chair of the Department of Biochemistry and Structural Biology (BSB) in the Long School of Medicine. UTHSA is the only academic health center in South Texas and combines scientific discovery with clinical care in innovative and transformative ways

Reporting to the Dean, the Chair of BSB is responsible for the overall vision and strategic plan for the department and oversight of administrative, academic and research activities of the Department. This is a unique opportunity to lead an outstanding basic science department with strategic vision and direction. UTHSA views diversity as a core value which embodies inclusiveness, mutual respect, and multiple perspectives and serves as a catalyst for change resulting in health equity. Inclusion fosters innovation, creativity and a sense of belonging—reflecting differing ideas, beliefs, experiences, perspectives and backgrounds—that lead to biomedical discovery and scientific advancement.

The UT Health San Antonio is an Equal Employment Opportunity/Affirmative Action Employer and is committed to excellence through diversity among its faculty, staff and students including protected veterans and persons with disabilities.

Candidates must have a PhD and/or MD, and academic credentials that merit appointment at the rank of Professor with tenure. The ideal candidate will have a widely recognized national reputation in their field. The ability to foster a culture of collaboration, innovation, and accountability across the Health Science Center is important. This is a wonderful opportunity for a visionary leader. UT Health San Antonio is a research-intensive institution located in San Antonio and it sits in the gateway to the picturesque Texas Hill Country. San Antonio is a vibrant, multicultural city with year-round recreational activities and an attractive cost-of-living.

To Apply: submit a letter of interest along with a current CV electronically via the UT Health Careers portal at **https://uthscsa.referrals.selectminds.com/faculty/jobs/chair-department-of-biochemistry-structural-biology-2851**. Inquiries and to receive a full job prospectus email Shelly Evans, Long School of Medicine Chief of Staff at elliss@uthscsa.edu.

All faculty appointments are designated as security sensitive positions.

Director, Institute for Integration of Medicine and Science

UT Health San Antonio
Joe R. & Teresa Lozano Long School of Medicine

The University of Texas Health Science Center San Antonio, dba UT Health San Antonio (UTHSA), is seeking a dynamic academic leader to serve as its **Director of the Institute for Integration of Medicine & Science (IIMS)**, the academic home for UTHSA's Clinical and Translational Science Award from the National Institutes of Health.

UTHSA is a comprehensive academic health university and research center in South Texas. The Director of the IIMS reports directly to the Dean of the Long School of Medicine, and is responsible for the overall administrative, academic, and research activities of the IIMS. This is a unique opportunity to lead an outstanding research institute with strategic vision and direction. UT Health San Antonio combines scientific discovery with clinical care in innovative and transformative ways.

The UT Health San Antonio is an Equal Employment Opportunity/Affirmative Action Employer and is committed to excellence through diversity among its faculty, staff and students including protected veterans and persons with disabilities.

Candidates must have a MD and/or PhD, and academic credentials that merit appointment at the rank of Professor with tenure. The ideal candidate will have a widely-recognized national reputation in their field. The ability to foster a culture of collaboration, innovation, and accountability across the Health Science Center is important. This is a wonderful opportunity for a visionary leader. UT Health San Antonio is a research-intensive institution located in San Antonio and it sits in the gateway to the picturesque Texas Hill Country. San Antonio is a vibrant, multicultural city with year-round recreational activities and an attractive cost-of-living.

To Apply: submit a letter of interest along with a current CV electronically via the UT Health Careers portal at **https://uthscsa.referrals.selectminds.com/faculty/jobs/director-institute-for-integration-of-medicine-science-2845**. Inquiries and to receive a full job prospectus email Shelly Evans, Long School of Medicine Chief of Staff at elliss@uthscsa.edu.

All faculty appointments are designated as security sensitive positions.

Director, Greehey Children's Cancer Research Institute

UT Health San Antonio
Joe R. & Teresa Lozano Long School of Medicine

The Long School of Medicine at the University of Texas Health Science Center at San Antonio (dba UT Health San Antonio) seeks an individual with an outstanding record of leadership, scientific and educational achievement, and faculty/trainee recruitment and mentoring as its **Director, Greehey Children's Cancer Research Institute (GCCRI)**. Dynamic leadership, clear communication, strong interpersonal skills, and a keen strategic vision are crucial characteristics required for success. Reporting to the Dean of the Long School of Medicine, the Director will be responsible for continuing to build and maintain excellence in research programs, high quality educational programs, and a collegial interactive culture.

The UT Health San Antonio is an Equal Employment Opportunity/Affirmative Action Employer and is committed to excellence through diversity among its faculty, staff and students including protected veterans and persons with disabilities.

Candidates must have a PhD and/or MD, and academic experience consistent with eligibility for full Professor with tenure. The ideal candidate will have a widely-recognized national reputation in their field. The ability to foster a culture of collaboration, innovation, and accountability across the Health Science Center is important. This is a wonderful opportunity for a visionary leader. UT Health San Antonio is a research-intensive institution located in San Antonio and it sits in the gateway to the picturesque Texas Hill Country. San Antonio is a vibrant, multicultural city with year-round recreational activities and an attractive cost-of-living.

To Apply: submit a letter of interest along with a current CV electronically via the UT Health Careers portal at **https://uthscsa.referrals.selectminds.com/faculty/jobs/director-of-greehey-childrens-cancer-research-institute-2763**. Inquiries and to receive a full job prospectus email Shelly Evans, Long School of Medicine Chief of Staff at elliss@uthscsa.edu.

All faculty appointments are designated as security sensitive positions.

The National Academies of
SCIENCES • ENGINEERING • MEDICINE

ARL Distinguished Postdoctoral Fellowships

The Army Research Laboratory (ARL) Distinguished Postdoctoral Fellowships provide opportunities to pursue independent research in ARL laboratories. Fellows benefit by working alongside some of the nation's best scientists and engineers, while enhancing the mission and capabilities of the U.S. Army and the warfighter in times of both peace and war.

ARL invites exceptional young researchers to apply. Fellows must display extraordinary abilities in scientific research and show clear promise of becoming future leaders. Candidates are expected to have already successfully tackled a major scientific or engineering problem or to have provided a new approach or insight, evidenced by a recognized impact in their field. ARL offers five named Fellowships; two of these positions are open for the 2020 competition.

Fellowships are one-year appointments, renewable for up to three based on performance. The award includes a $100,000 annual stipend, health insurance, paid relocation, and a professional travel allowance. Applicants must have completed all requirements for a Ph.D. or Sc.D. degree by October 1, 2020, and may not be more than five years beyond their doctoral degree as of the application deadline. For more information and to apply, visit www.nas.edu/arldpf.

Online applications must be submitted by May 29, 2020 at 5 PM EST.

U.S.ARMY
DEVCOM ARMY RESEARCH LABORATORY

Faculty Position in Host-Pathogen Interactions and Microbial Immunology

Department of Microbiology-Immunology

Northwestern Medicine
Feinberg School of Medicine

The Department of Microbiology-Immunology at Northwestern University Feinberg School of Medicine seeks a full-time, tenure-track Investigator at the rank of Assistant, Associate, or Full Professor within the broad field of host-pathogen interactions and microbial immunology. Applicants working at the interface between bacteriology and immunology or virology and immunology are particularly encouraged to apply.

Qualified candidates are expected to have a Ph.D., M.D., or equivalent degree as well as postdoctoral training or equivalent status. The successful candidate will be expected to establish and maintain a vigorous, extramurally funded research program and to participate in our strong graduate and medical student training programs. All applicants should have substantial peer-reviewed publications that demonstrate productivity and the ability to perform cutting edge research. Candidates for an Assistant Professor position should have current or pending external funding, which could include an NIH K-level award or equivalent. Candidates at the Associate Professor or Full Professor level should have substantial research productivity, current grant support and academic service. The primary criteria for selection will be excellence and creativity in research and scholarship. We offer a highly interactive collegial research environment with state-of-the-art research and core facilities.

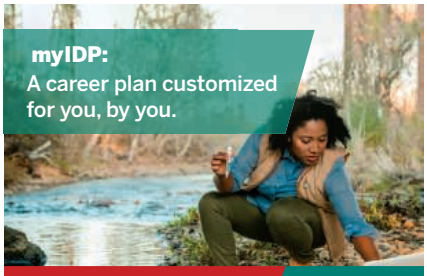
The start date is negotiable, and the position will remain open until filled.

Please read ALL instructions and make preparations before proceeding to the application page:

- Applications will only be accepted via online submission (see link below).
- Please prepare all documents in advance as Adobe PDF files, and please be sure all information is entered correctly and accurately (especially names and email addresses), as there will be no opportunity for online revision after your application has been submitted.
- All required fields in the application form are marked with an asterisk and must be filled before clicking the "Submit" button.
- Be aware that incomplete applications cannot be saved.

Applications accepted here: **https://facultyrecruiting.northwestern.edu/apply/ODg1**

Northwestern University is an Equal Opportunity, Affirmative Action Employer of all protected classes, including veterans and individuals with disabilities. Women, racial and ethnic minorities, individuals with disabilities, and veterans are encouraged to apply. Hiring is contingent upon eligibility to work in the United States.



There's only one Science

Features in myIDP include:

- Exercises to help you examine your skills, interests, and values.
- A list of 20 scientific career paths with a prediction of which ones best fit your skills and interests.

myIDP

Visit the website and start planning today!

myIDP.sciencecareers.org

Science Careers

In partnership with:

UCSF University of California San Francisco

UIC

BURROUGHS WELLCOME FUND

University of Massachusetts Medical School

FASEB

UT Health San Antonio

The University of Texas Health Science Center San Antonio, dba as UT Health San Antonio (UTHSA), is seeking a dynamic, academic leader to serve as its **Chair of the Department of Microbiology, Immunology & Molecular Genetics** (MIMG).

The Department of Microbiology, Immunology & Molecular Genetics (MIMG) is the nucleus for research and education in immunology and microbiology at UT Health San Antonio and provides a dynamic environment for scientific discovery and training. This is a unique opportunity to lead an outstanding basic science department with strategic vision and direction. Reporting to the Dean of the Long School of Medicine, the Chair will be responsible for overall administrative, academic and research activities of this strong department.

For more information, contact Abby Walsh at **abby@grantcooper.com** or 314-449-1599.

The UT Health Science Center San Antonio dba as UT Health San Antonio (UTHSA) is an Equal Employment Opportunity/ Affirmative Action Employer and is committed to excellence through diversity among its faculty, staff and students including protected veterans and persons with disabilities. All faculty appointments are designated as security sensitive positions.

STAND UP TO CANCER™

Applications Requested for Stand Up To Cancer (SU2C) Convergence Grants Exploring Cancer's Communications among the Immune System and the Microbiome Using Organoids and Mice

Goal: develop a set of experimental platforms using organoid systems in vitro, and mouse models, that will permit a detailed exploration and understanding of the interactions and chemical communications among the cancerous/normal organoid, the immune system, and the microbiome.

Convergence 3.1416 aims to bring together several independent research laboratories with complementary skill sets and technological approaches:

- Laboratories able to make and maintain organoids from multiple types of human or mouse tissues;
- Cellular immunologists exploring the innate immune system and the adaptive immune system;
- Virologists and microbiologists who study the microbiomes of various tissues;
- Individuals using mass spectroscopy to characterize changes in metabolism and to identify metabolites that act as signaling agents between organ systems;
- Researchers who use multiplex mass spectroscopy of peptides to identify proteins that could be communicating among microbes, lymphocytes, and tissues of the body;
- Engineers who can create "chemostats" for organoids and their fellow lymphoid and microbial travelers, with both aerobic and anaerobic compartments;
- Quantitative biologists and physicists studying diffusion of nutrients and signals for communicating, who can analyze large data sets of information collected from sequencing, microscopy, and time lapse filming of cultures.

Applications: A letter of intent describing current research directions, capabilities, and a list of recent publications, information about present position, institution, and laboratory size and scope. Current funding should be included, as well as any conflicts of interest. Please submit your applications to: **StandUpToCancer.org/Convergence** by **June 1, 2020**. Questions can be addressed to: alustig@su2c.org.

Notification: Applications will be screened by a committee, and 10-15 investigators will be invited to a three day ideas laboratory to be held at the Institute for Advanced Study, in Princeton, New Jersey, at which invited investigators will give a short talk about their work and capabilities, and break up into groups to determine if collaborative efforts can be planned. Following this meeting, a subset of the group will be selected to write proposals of no more than 10 pages, and supply a budget for a three to four year period. The review committee will determine which proposals are acceptable for funding.

FOCUS ON DIVERSITY AND INCLUSION

ILLINOIS

Now recruiting faculty and postdocs to help improve photosynthesis for increased yields at the University of Illinois

The Grainger College of Engineering at the University of Illinois at Urbana-Champaign invites applications for **up to two full-time tenured or tenure-track faculty positions** in the broad area of photosynthesis engineering. The application closes on March 20, 2020. Learn more and apply at http://bit.ly/2w1tmIb.

The Carl R. Woese Institute for Genomic Biology at Illinois has an **open call for postdoctoral research fellows** from a variety of fields and disciplines to assist with research efforts such as RIPE (https://ripe.illinois.edu), ROGUE (https://rogue.illinois.edu), and CABBI (https://cabbi.bio) that are supported by the Bill & Melinda Gates Foundation, the U.S. Department of Energy, and others. Applicants must have obtained a Ph.D. (or equivalent) in the last 8 years in molecular biology, mathematical modeling of biological systems, plant physiology, crop sciences, or related fields. We are now accepting applications to fill at least seven vacancies but will consider adding positions to recruit more top talent to Illinois. Labs with openings include Donald R. Ort, Stephen P. Long, and Carl J. Bernacchi. To be given full consideration, applications must be received by **April 13, 2020**, at **http://bit.ly/polysynpostdoc**.

The University of Illinois is a world leader in photosynthesis research and has contributed to some of the most seminal discoveries in photosynthesis. Here we seek to build upon and expand our leadership in this area. Illinois is uniquely positioned to capitalize on the traditional strengths in photosynthesis research with the emerging engineering/technological capabilities associated with genomics and DNA editing, and modeling whole plant-environment interactions.

Illinois is an Equal Opportunity, Affirmative Action Employer. Minorities, women, veterans, and individuals with disabilities are encouraged to apply. For more information, visit http://go.illinois.edu/EEO.

POSITIONS OPEN

KEK
HIGH ENERGY ACCELERATOR RESEARCH ORGANIZATION

Call for Nomination for Next Director General of KEK

KEK, High Energy Accelerator Research Organization, invites nominations for the next Director General whose term will begin April 1, 2021.

In view of his/her role that presides over the business of KEK as a representative of the Inter-University Research Institute Corporation, nominees shall be:
(1) persons of noble character, with relevant knowledge and experience and having abilities to manage its educational and research activities properly and effectively.
(2) persons expected to promote with long-term vision and strong scientific leadership, the highly advanced, internationalized, and inter-disciplinary research activities of KEK by getting support from the public.
(3) persons expected to establish and carry out the medium-term goals and plans.

The term of appointment is three years until March 31, 2024 and shall be eligible for reappointment only twice. Thus, he/she may not remain in office continuously over a period 9 years. We widely accept the nomination of the candidates regardless of their nationalities. We would like to ask you to recommend the best person who satisfies requirements for the position written above.

Nomination should be accompanied by: (1) letter of recommendation, (2) brief personal history of the candidate, and (3) list of major achievements (publications, academic papers, commendations and membership of councils, etc.). The nomination should be submitted to the following address **no later than May 29, 2020**:
• Documents should be written either in English or in Japanese.
• Forms are available at: **https://www.kek.jp/en/newsroom/2020/03/02/1000/**

Inquiries concerning the nomination should be addressed to: General Affairs Division, General Management Department, KEK, High Energy Accelerator Research Organization, 1-1 Oho, Tsukuba, Ibaraki 305-0801, Japan; Tel +81-29-864-5114 • Fax +81-29-864-5560; Email: kek.dgsc@ml.post.kek.jp.

FOCUS ON DIVERSITY AND INCLUSION

LSU Health SHREVEPORT

The Department of Cellular Biology and Anatomy at the LSU Health Sciences Center School of Medicine in Shreveport is currently seeking a candidate holding a Ph.D. or equivalent degree for a tenure-track position at the level of Assistant and Associate Professor. To be successful, the candidate should have expertise in the area of the Anatomical Sciences/Cellular Biology. Candidates having established research expertise in vascular biology, especially in the areas of stroke and/or the neurobiological sequeliae associated with stroke will be given special consideration.

This position is part of a continued expansion of the research program in the department. The requirements for Assistant Professor include a minimum of two years of post-doctoral research experience and for Associate Professor a minimum of five years of experience at the level of Assistant Professor. Applicants are expected to have a record of scholarly and research activity. The successful candidate should also have teaching experience in Gross Anatomy, and in one or more of the following disciplines: Cellular Biology, Neurosciences, or Histology. For the Associate Professor level, extramural funding (NIH R01 or equivalent) is expected. Salary and start-up packages will be commensurate with experience.

This is an exciting opportunity for the appropriate candidate to play a significant role in an active, dynamic work environment. It is also expected that the new faculty member will take an active role in the continued growth of the Center for Cardiovascular Diseases and Sciences.

Please submit application with full curriculum vitae and names of three references via email to: **Dr. Kevin McCarthy (kmccar2@lsuhsc.edu), Professor and Chair, Department of Cellular Biology and Anatomy, LSU Health Sciences Center, School of Medicine in Shreveport, Shreveport, LA 71130**. Please include with your packet a letter that summarizes your future research plans. Review of applications will begin immediately and will continue until the position is filled.

LSU Health Shreveport is committed to diversity and is an Equal Opportunity/Equal Access Employer.

VCU

TENURE TRACK POSITIONS
DEPARTMENT OF BIOCHEMISTRY AND MOLECULAR BIOLOGY
Virginia Commonwealth University School of Medicine

The Department of Biochemistry and Molecular Biology at Virginia Commonwealth University School of Medicine has openings for two tenure-track positions. The candidates should have a Ph.D. and strong background in cellular and molecular biology, with emphasis on bioactive lipids, cancer, cardiovascular disease, or neuroscience. The successful candidate will be required to have a well-developed scholarly/research portfolio with evidence of multi-disciplinary applications and external funding appropriate to complement and expand existing expertise in the department. At the associate or full professor level, successful applicants will have an outstanding publication record, complemented by substantial extramural support. At the assistant professor level, positions require a strong publication record, and postdoctoral experience with potential for, or evidence of, the ability to secure extramural funding. As promoted by VCU, the faculty member should also demonstrate experience working in and fostering a diverse faculty, staff, and student environment or commitment to do so as a faculty member at VCU. The Department belongs to a very active community of investigators and is committed to providing an outstanding research environment. Interested candidates should apply online at https://www.vcujobs.com.

Interested candidates should apply at **https://www.vcujobs.com**
Search Job: F65930 & F65940

Virginia Commonwealth University is an Equal Opportunity, Affirmative Action University providing access to education and employment without regard to age, race, color, national origin, gender, religion, sexual orientation, veteran status, political affiliation or disability.

HIGH-LEVEL GLOBAL TALENTS RECRUITMENT



Welcome back to hometown.
Thousands of academic job vacancies are in fast-developing China.

2020 Global Online Job Fair

March 13, 2020 High-level Global Talents Recruitment
March 25, 2020 Northeast China Doctoral Talents Recruitment
April 09, 2020 Southwest China Doctoral Talents Recruitment
April 17, 2020 Southeast China Doctoral Talents Recruitment
April 24, 2020 Specialty Session (Engineering)
May 08, 2020 North and Northeast China Doctoral Talents Recruitment
May 09, 2020 Hong Kong, Macao and Taiwan Doctoral Talents Recruitment
May 15, 2020 High-level Global Talents Recruitment

Qualification for Applicants

Global scholars, Doctor and Post-doctor

Key Disciplines

Life Sciences, Medicine, Material Sciences, Physical Sciences

Participating Approach

Please send your CV to consultant@acabridge.edu.cn for 2020 Global Online Job Fair

Scan the QR code to apply for 2020 Global Online Job Fair

Job Vacancies in China's Universities and Institutes
Please visit https://www.acabridge.edu.cn/
Contact consultant@acabridge.edu.cn

By **Ellen K. W. Brennan**

Learning to say 'yes, and'

I stood behind the curtain, my hands shaking. As I listened to the crowd laugh at the host's jokes, all I could think was, "Why did I believe I could do this?" Two months earlier, I had signed up for improv classes at a local theater, along with four other grad students. We hoped that improv training—which involves acting out unscripted scenes—would improve our science communication skills. That sounded great in principle, and our program would pay the fees. But when the host gave us the cue to come on stage, I seriously wondered what I'd gotten myself into.

When I first heard about the improv classes, I was torn. As an introvert, I feared getting on stage and improvising in front of strangers. However, I knew I wanted to work as a science communicator after finishing my Ph.D., so it seemed like the perfect opportunity to improve my speaking ability and gain confidence thinking on my feet. I signed up, knowing the experience would take me well outside my comfort zone.

During our first class, we learned a core concept of improv: "yes, and." It means that, as improvisers, we accept what fellow performers say. If someone says that rhinos are librarians, for example, then rhinos are librarians. We do not question the logic; we say "yes" and continue with the scene as if nothing is awry.

To do this effectively, our teacher warned us that we'd have to avoid second-guessing ourselves. Sometimes scenes go in unexpected directions. The best improv happens when performers stay open to different possibilities and say whatever pops into their minds.

I got a taste of how difficult that is when acting out my first scene. My classmate turned to me and said, "Mom is going to be so mad." Mad about what? My mind spun out ideas, and my inner critic shot them all down. We broke the car? No, that's too easy. We failed a test? No, you don't want your classmates thinking you're stupid on the first day. I finally landed on an answer: "Yes, we're going to be late for dinner." The scene proceeded from there, and we eventually finished as two sisters who lost their way on a hiking trail.

The first few scenes were hard, but as weeks turned into months, I became more comfortable thinking on my feet and even started to enjoy our classes. I never silenced my inner critic entirely, but over time, I didn't police my words with quite so much vigor. I also became better at listening, relating to my conversation partners, and communicating clearly in the moment.



"I feared getting on stage and improvising in front of strangers."

That training came in handy 6 months ago, when I was giving a seminar about my science. An audience member surprised me with a question that didn't grow out of the information I'd presented. Instead of getting flustered, I implemented the "yes, and" approach—accepting the question at face value and letting my mind focus on why it was asked. That helped me shift gears and find an appropriate answer.

The benefits of improv go beyond communication. Early on in grad school, I would get stuck when my experiments generated unexpected data; my inner critic would assume I had made a mistake. But now, after embracing the "yes, and" concept, I no longer go into an experiment thinking that I already know the story my data are going to tell.

Last year, I used that approach after encountering confusing data. Instead of getting discouraged, I kept exploring the data and ended up identifying a new type of cell—one that wasn't behaving as expected. If I hadn't stayed open to the possibility that the results were real, I would have missed out on the most exciting finding of my Ph.D. so far.

All scientists can benefit from this lesson. If the data say rhinos are librarians, then it's worth investigating whether rhinos are, in fact, librarians. Our job as scientists isn't to generate data that support a preconceived story. Our job is to say "yes, and."

As for that debut performance, I must admit that I cannot remember much of it. In front of the deafeningly loud crowd, it went by in a blur. But I do recall that when we left the stage, my face ached from grinning. That very night, I registered for the next level of classes—excited to discover what else I'd learn from improv. ■

Ellen K. W. Brennan is a Ph.D. candidate at the University of Michigan, Ann Arbor. Send your career story to SciCareerEditor@aaas.org.

ILLUSTRATION: ROBERT NEUBECKER

Published by AAAS